ISSN 1580-3155 Pages 389–662 ■ Year 2025, Vol. 72, No. 3

Slovensko kemijsko društvo
Slovenian Chemical Society

Acta Chimica Slovenica

3

72/2025

http://acta.chem-soc.si

EDITOR-IN-CHIEF

FRANC PERDIH
University of Ljubljana, Facuty of Chemstry and Chemical Technology, Večna pot 113, SI-1000 Ljubljana, Slovenija
E-mail: ACSi@fkkt.uni-lj.si, Telephone: (+386)-1-479-8514

ASSOCIATE EDITORS

Alen Albreht, *National Institute of Chemistry, Slovenia*
Mirela Dragomir, *Jožef Stefan Institute, Slovenia*
Krištof Kranjc, *University of Ljubljana, Slovenia*
Matjaž Kristl, *University of Maribor, Slovenia*
Maja Leitgeb, *University of Maribor, Slovenia*
Helena Prosen, *University of Ljubljana, Slovenia*
Miha Pavšič, *University of Ljubljana, Slovenia*
Martina Hrast Rambaher, *University of Ljubljana, Slovenia*
Jernej Stare, *National Institute of Chemistry, Slovenia*
Irena Vovk, *National Institute of Chemistry, Slovenia*

ADMINISTRATIVE ASSISTANT

Eva Mihalinec, *Slovenian Chemical society, Slovenia*

EDITORIAL BOARD

Wolfgang Buchberger, *Johannes Kepler University, Austria*
Alojz Demšar, *University of Ljubljana, Slovenia*
Stanislav Gobec, *University of Ljubljana, Slovenia*
Marko Goličnik, *University of Ljubljana, Slovenia*
Günter Grampp, *Graz University of Technology, Austria*
Wojciech Grochala, *University of Warsaw, Poland*
Danijel Kikelj, *University of Ljubljana*
Janez Košmrlj, *University of Ljubljana, Slovenia*
Mahesh K. Lakshman, *The City College and The City University of New York, USA*
Blaž Likozar, *National Institute of Chemistry, Slovenia*
Janez Mavri, *National Institute of Chemistry, Slovenia*
Jiři Pinkas, *Masaryk University Brno, Czech Republic*
Friedrich Srienc, *University of Minnesota, USA*
Walter Steiner, *Graz University of Technology, Austria*
Jurij Svete, *University of Ljubljana, Slovenia*
David Šarlah, *University of Illinois at Urbana-Champaign, USA; Università degli Studi di Pavia, Italy*
Ivan Švancara, *University of Pardubice, Czech Republic*
Gašper Tavčar, *Jožef Stefan Institute, Slovenia*
Ennio Zangrando, *University of Trieste, Italy*
Polona Žnidaršič Plazl, *University of Ljubljana, Slovenia*

ADVISORY EDITORIAL BOARD

Chairman
Branko Stanovnik, Slovenia

Members
Udo A. Th. Brinkman, The Netherlands
Attilio Cesaro, Italy
Vida Hudnik, Slovenia
Venčeslav Kaučič, Slovenia
Željko Knez, Slovenia
Radovan Komel, Slovenia
Stane Pejovnik, Slovenia
Anton Perdih, Slovenia
Slavko Pečar, Slovenia
Andrej Petrič, Slovenia
Boris Pihlar, Slovenia
Milan Randić, Des Moines, USA
Jože Škerjanc, Slovenia
Đurđa Vasić-Rački, Croatia
Marjan Veber, Slovenia
Gorazd Vesnaver, Slovenia
Jure Zupan, Slovenia
Majda Žigon, Slovenia

Acta Chimica Slovenica is indexed in: *Academic Search Complete, Central & Eastern European Academic Source, Chemical Abstracts Plus, Chemical Engineering Collection (India), Chemistry Citation Index Expanded, Current Contents (Physical, Chemical and Earth Sciences), Digitalna knjižnica Slovenije (dLib.si), DOAJ, ISI Alerting Services, PubMed, Science Citation Index Expanded, SciFinder (CAS), Scopus, Web of Science and Portico.* Impact factor for 2022 is IF = 1.20.

Articles in this journal are published under the
Creative Commons Attribution 4.0 International License

Izdaja – Published by:
SLOVENSKO KEMIJSKO DRUŠTVO – SLOVENIAN CHEMICAL SOCIETY
Naslov redakcije in uprave – Address of the Editorial Board and Administration
Hajdrihova 19, SI-1000 Ljubljana, Slovenija
Tel.: (+386)-1-476-0252; Fax: (+386)-1-476-0300; E-mail: chem.soc@ki.si

Slovensko kemijsko društvo
Slovenian Chemical Society

Izdajanje sofinancirajo – Financially supported by:
National Institute of Chemistry, Ljubljana, Slovenia
Jožef Stefan Institute, Ljubljana, Slovenia
Faculty of Chemistry and Chemical Technology, University of Ljubljana, Slovenia
Faculty of Chemistry and Chemical Engineering, University of Maribor, Slovenia
University of Nova Gorica, Slovenia

Acta Chimica Slovenica izhaja štirikrat letno v elektronski obliki na spletni strani http://*acta.chem-soc.si*. V primeru posvečenih številk izhaja revija tudi v tiskani obliki v omejenem številu izvodov.

Acta Chimica Slovenica appears quarterly in electronic form on the web site *http://acta.chem-soc.si*. In case of dedicated issues, a limited number of printed copies are issued as well.

Transakcijski račun: 02053-0013322846 Bank Account No.: SI56020530013322846-Nova Ljubljanska banka d. d., Trg republike 2, SI-1520 Ljubljana, Slovenia, SWIFT Code: LJBA SI 2X

Oblikovanje ovitka – Design cover: KULT, oblikovalski studio, Simon KAJTNA, s. p. Grafična priprava za tisk: OSITO, Laura Jankovič, s.p.

ActaChimicaSlo
ActaChimicaSlo
SlovenicaActaC
Year 2025, Vol. 72, No. 3

Graphical Contents

REVIEW

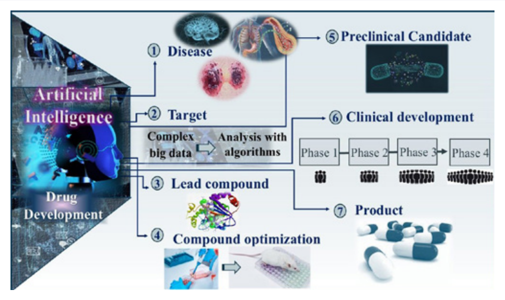

SCIENTIFIC PAPER

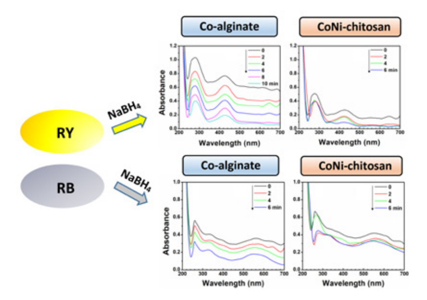

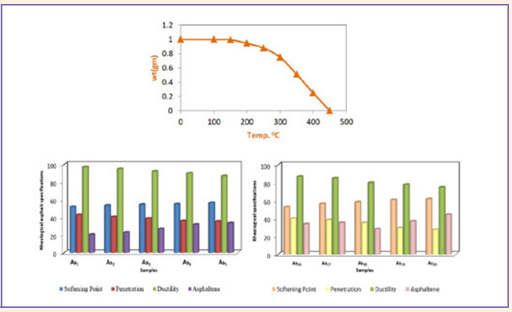

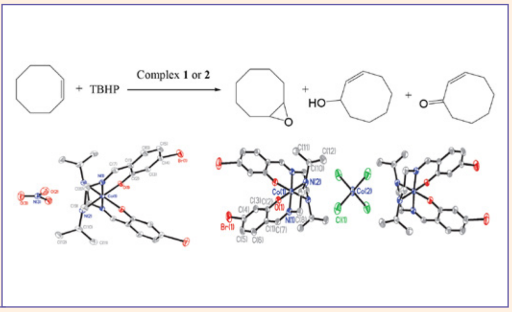
+ TBHP
Complex 1 or 2
HO

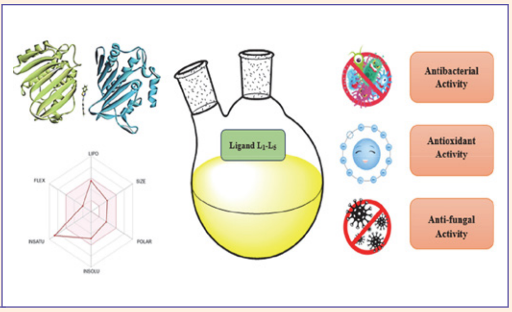
Ligand L1-L6
Antibacterial Activity
Antioxidant Activity
Anti-fungal Activity
LIPO
SIZE
POLAR
INSOLU
INSATU
FLEX

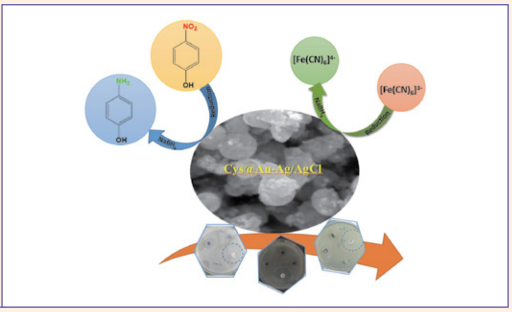
NO2
OH
NH2
OH
[Fe(CN)6]4-
[Fe(CN)6]3-
Cys@Au-Ag/AgCl

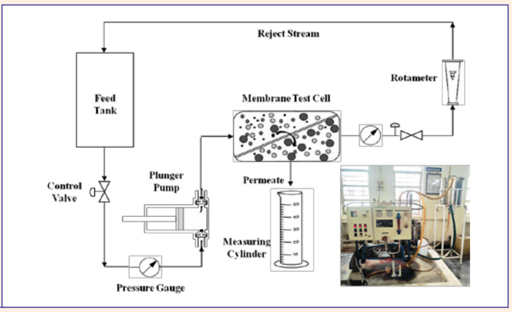
Reject Stream
Rotameter
Feed Tank
Membrane Test Cell
Control Valve
Plunger Pump
Permeate
Measuring Cylinder
Pressure Gauge

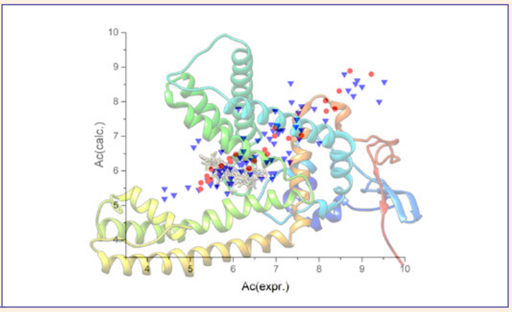
Ac(calc.)
Ac(expr.)
10
9
8
7
6
5
4
5
6
7
8
9
10

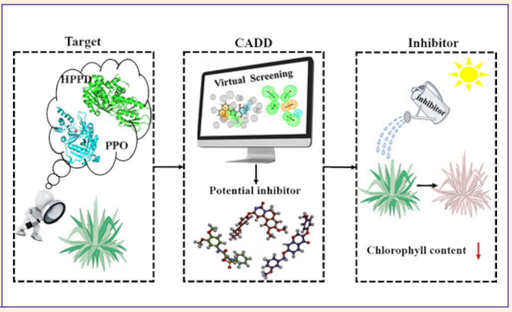
Target
CADD
Inhibitor
HPPD
PPO
Virtual Screening
Potential inhibitor
Inhibitor
Chlorophyll content ↓

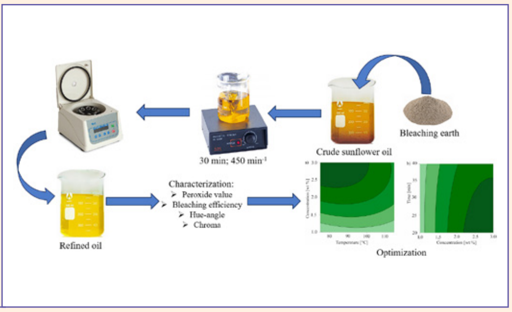
30 min; 450 min⁻¹
Crude sunflower oil
Bleaching earth
Characterization:
➢ Peroxide value
Bleaching efficiency
➢ Hue-angle
➢ Chroma
Refined oil
Optimization

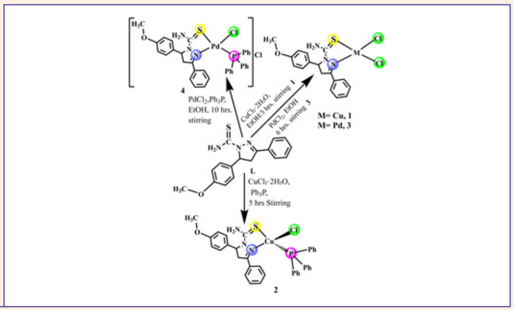
PdCl₂.Ph₃P, EtOH, 10 hrs. stirring
CuCl₂.2H₂O, EtOH 5 hrs. stirring 1
PdCl₂, EtOH 6 hrs. stirring 3
M= Cu, 1
M= Pd, 3
L
CuCl₂.2H₂O, Ph₃P, 5 hrs Stirring
4
2

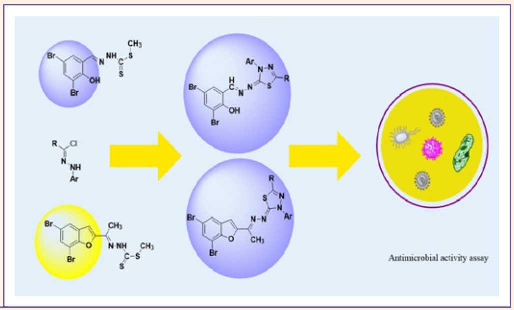
Antimicrobial activity assay

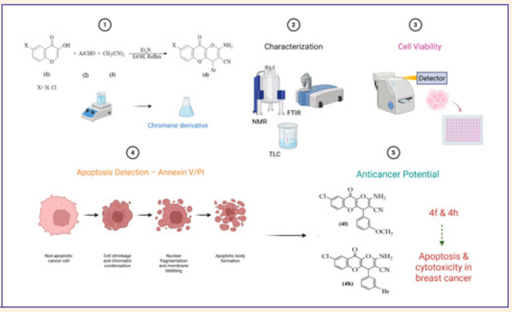
①
②
③
Characterization
Cell Viability
Chromene derivative
NMR
FTIR
TLC
Detector
④
⑤
Apoptosis Detection – Annexin V/PI
Anticancer Potential
4f & 4h
Apoptosis & cytotoxicity in breast cancer

524–531 Biomedical applications

Design, Synthesis and Anticonvulsant Activity of 2 and 5-disubstituted 1,3-dioxoisoindoline

Asghar Davood, Maryam Yadavar Nikravesh,
Mahsa Hadipour Jahromy, Sepideh Taghizad

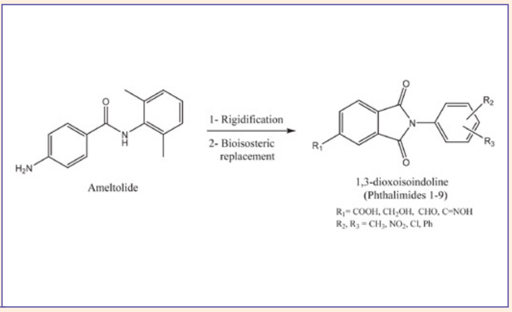

532–544 Biomedical applications

Therapeutic Potential and *In silico* Evaluation of Phytochemicals in the Leaves of *Eucalyptus Globulus*, *Jasminum Officinale* and *Solanum Nigrum*

Imran Ali, Afshan Kaleem, Farah Akram, Muhammad Talal,
Roheena Abdullah, Mehwish Iqtedar, Irfana Iqbal, Xiaoming Chen

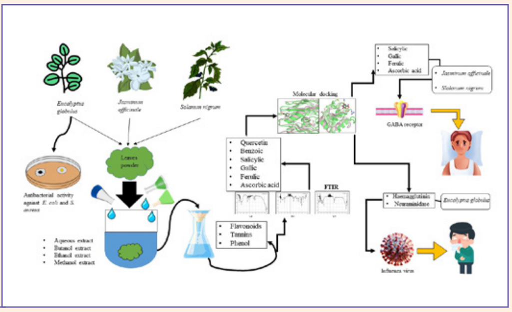

545–552 Organic chemistry

Preparation and Characterization of Ionic Liquid Supported on Fe_3O_4-Lignin and Investigation of Its Catalytic Activity in the Synthesis of Dihydropyrano[3,2-*c*]chromene Derivatives

Majidreza Gerami and Mahnaz Farahi

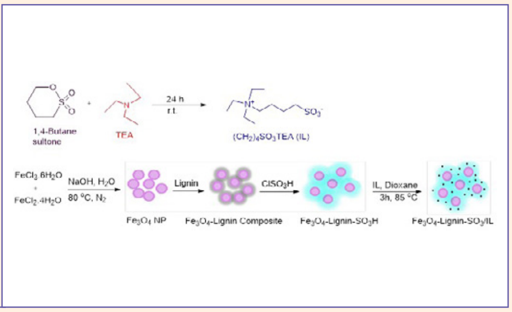

553–561 Inorganic chemistry

Adsorption and Corrosion Inhibition Effect of Expired Prednisolone on AISI 1020 Carbon Steel: Electrochemical, Gravimetric, and Surface Studies

Sihem Kherraf, Malika Foudia, Zohra Djetoui, Leila Kherraf,
Nour El Houda Sobhi

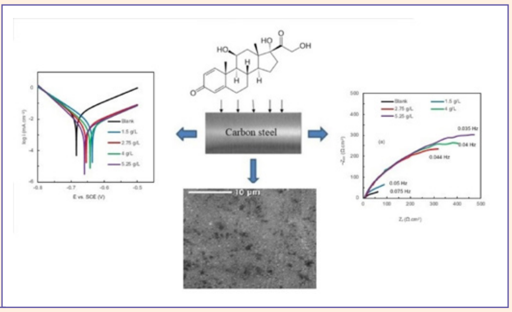

562–572 Organic chemistry

Synthesis, DFT, and Molecular Docking Studies of Anti-cancer Imidazolidine-2,4-dione and Thiazolidine-2,4-dione Derivatives

Osama Alharbi

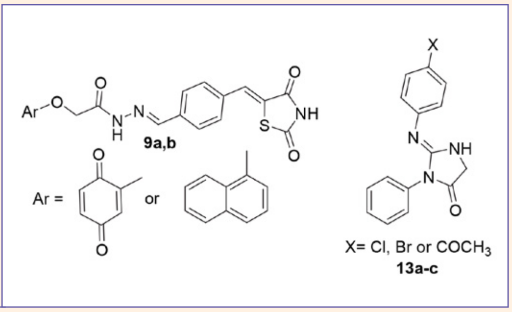

573–580 Inorganic chemistry

Synthesis, Characterization, and Theoretical Calculation of a Copper Complex of 3-Hydroxy-2-methylquinolin-4-carboxylate and 1,10-Phenanthroline

Yan-Hua Li, Xing-Jian Liu, Jian Huang, Yu Xie, Fei Deng, Xiu-Guang Yi

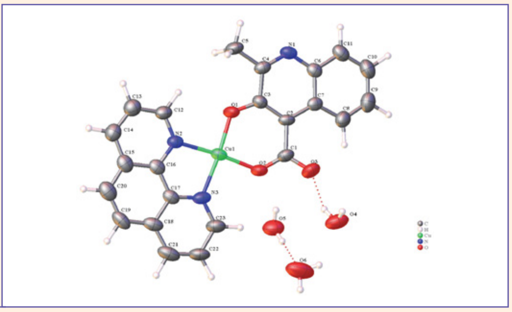

601–612 Biochemistry and molecular biology

HPLC-DAD Analysis, Antioxidant and Antibacterial Properties of Fruit Extracts from *Pistacia atlantica* Desf.

Younes Douffa, Karima Saffidine, Nour Elhouda Belabes, Nadjet Azzi, Haifaa Laroui, Hafsa Silini Cherif, Thoraya Guemmaz, Fatima Zerargui and Abderahmane Baghiani

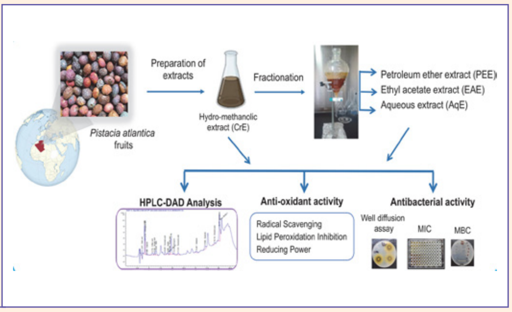

613–621 Inorganic chemistry

Fibrous Silica KCC-1 as a Platform for Mn-Based Dual Metal Oxide Adsorbents for CO_2 Capture

Syawal Mohd Yusof, Azizul Hakim Lahuri, Nurul Asikin Mijan, Umar Kalmar Nizar, Siti Sarahah Sulhadi, Salma Samidin, Ainil Hafiza Abdul Aziz

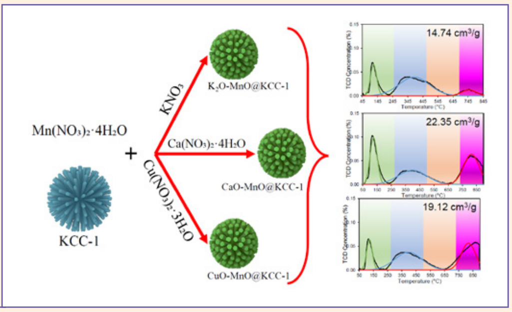

DOI: 10.17344/acsi.2024.8702 *Acta Chim. Slov.* **2025,** *72,* 389–399

Scientific paper

Green Synthesis of Co-alginate and CoNi-chitosan Catalysts for Catalytic Reduction of Organic Azo Dyes

Filiz Akti[*]

Department of Chemical Engineering, Hitit University, Corum 19030, Turkey

** Corresponding author: E-mail: filizakti@hitit.edu.tr*

Received: 02-16-2024

Abstract

Cobalt and nickel doped catalysts were synthesized by using chitosan and alginate and used in the degradation of Remazol Yellow 4GL (RY) and Remazol Black B (RB) dyes. XRD pattern of catalysts exhibited that amorphous and semi-crystalline form for CoNi-chitosan and Co-alginate, respectively. SEM images showed catalyst's surface was rough, grainy and rod-like structures. The surface functional groups were determined by FTIR analysis method and it was seen clearly presence of alginate and chitosan. The Co-alginate catalysts exhibited higher dye degradation (74% for RY) and lower reaction time (6 min for RB). The reduction reaction was in good agreement with pseudo-first-order kinetic model and reaction rate constant was determined as 0.140 min^{-1} and 0.174 min^{-1} for RY and RB, respectively. The RY reduction percent over both catalysts was higher than RB. Co-alginate showed approximately 70% reduction efficiency for RY even after 4 runs. The dye reduction efficiency and catalytic activity of the catalysts were promise for organic pollutant dyes catalytic reduction applications.

Keywords: Remazol Yellow 4GL; Remazol Black B; cobalt/nickel bead catalyst; catalytic reduction

1. Introduction

Dyes are widely used in textile, cosmetics, paper, leather, food, plastic and many other industries. Azo dyes (–N=N– group) are among the most harmful dyes due to their high physicochemical stability.[1] From these azo dyes, Remazol Yellow 4GL (RY) and Remazol Black B (RB) is a synthetic highly toxic dyes with a diazo group of symmetrical aromatic nature. They pose significant risks to human health such as mutagen, carcinogen, respiratory disorder, skin irritation and allergic reactions.[2–8] Their discharge to water pollutes both environment and threat to human and many vivid species health due to their toxic, carcinogenic and mutagenic properties.[9–13] Therefore, require efficient treatment before being released into aqueous media. Many methods such as adsorption, advanced oxidation, coagulation and reverse osmosis have been used for the treatment of wastewater containing organic dyes. Adsorption process is the most effective and reliable technique for removal of dyes from wastewater. Although adsorption has the advantage of high processing efficiency, ease of use, and relatively low cost, it is difficult to remove contaminants from the adsorbent. In recent years, the chemical reduction strategy using $NaBH_4$ in the presence of suitable catalysts has gained more and more research attention due to its advantages of environment friendly, low cost, high efficiency and easy operation. This process, while thermodynamically favorable, is kinetically unfavorable.[14–21] Therefore, electrons need a catalyst for their rapid transfer from borohydride ions to dye molecules.[22] Moreover, there may be a large redox potential difference between the electron donor (BH_4^- ion) and acceptor (dyes) species and this is also can hinder relaying of electrons. Metal nanoparticles (MNPs) are feasible enough to reduce the potential difference due to their high Fermi potentials for which they can exhibit excellent dye degradation efficiency. Au, Pt, Pd and Ag noble metal nanoparticles have been utilized in catalytic dye degradation due to their good electron transfer capabilities resulting from favorable redox potentials. However, they are expensive, which greatly limits their industrial applications. Co, Ni, Fe and Cu transition metals having low cost are good candidates to replace the noble metals.[16,23–26] The biggest obstacle to the use of these metal nanoparticles is instability and agglomeration problem that causes the reduction of their active sites due to their high surface energy. Also, they cannot be easily separated from the reaction medium, and this restricts their large-scale applications. To overcome this problem, many polymeric hydrogel networks, support materials such as SBA-

15, biochar, graphene have been used in preparation of metal nanoparticles.[9,15,27–33] Chitosan and alginate which are a natural biodegradable polysaccharide having non-toxic, environmentally friendly, is used for providing of polymeric hydrogel networks. Both of them provides excellent chelating ability and binding capacity to divalent metal cations thanks to its functional groups (RCOO−, OH−, CO−, NH_2−).[15,28,34,35] This attractive crosslinking character ensures them various shapes such as bead and membrane, as well as it make them more attractive for environmental applications which are adsorption, filtration, oxidation and catalytic reduction of organic pollutants.[15]

In the removal of RB and RY from wastewater adsorption and photocatalytic methods are generally used[2–8,36], while the use of catalytic reduction method is encountered. In study performed by Almeida et al. RB has been degraded photocatalytically using electric arc furnace dust and provided catalytic performance and degradation time of 81% and 150 min.[7] Secundino-Sánchez et al., have been declared that RB was degraded 50% and at 20 min in the presence of TiO_2-NF's-anatase photocatalysts.[4] In other work[5], GO/$CoFe_2O_4$ photocatalyst has been used for degradation of RB and observed 53% degradation efficiency within 60 min. On the other hand, there are very limited studies for the removal of RY. One of these studies is the study conducted by Akti[7] and the other is the study conducted by Akti and Balci.[8] Photocatalytic method was used in these studies. Akti removed 96% of RY in 60 min using PANI-SnO_2@diatomite, while Akti and Balci removed 58.2% in 150 min.[7,8] All these materials have exhibited promising results in removing pollutants from wastewater. However, there is still a need for effective, cheap, economical, environmentally friendly and non-toxic catalysts.

This paper deal with the synthesis, characterization and activity test of chitosan and alginate network-structured cobalt and cobalt-nickel bead type catalysts for catalytic reduction of RY and RB, selected as a model pollutant. The novelty of the present study lies in the fact that the synthesized catalysts have been reported in a limited number of studies in the literature for reduction, and their catalytic activity is highly competitive.

2. Materials and Methods

2. 1. Materials

$CoCl_2.6H_2O$ (≥ 95%), $NiCl_2.6H_2O$ (≥ 95%), sodium alginate, chitosan (low molecular weight), $CaCl_2$ (≥ 93%) and NaOH (≥ 99%) were supplied from Sigma-Aldrich. Acetic acid (glacial 100%) and $NaBH_4$ (≥ 98%) were taken Isolab and Merck, respectively. The Remazol Yellow 4GL (C. I. Reactive Yellow 160; $C_{25}H_{22}ClN_9Na_2O_{12}S_3$) and Remazol Black B (C. I. Reactive Black 5; $C_{26}H_{21}N_5Na_4O_{19}S_6$) were obtained from a local textile company in Turkey. All chemicals were of analytical grade and were used directly.

2. 2. Synthesis of Co-alginate and CoNi-chitosan Bead Type Catalysts

Co-alginate bead type catalysts synthesis; 0.2 g $CoCl_2.6H_2O$ was dissolved in 50 mL distilled water, 1 g of sodium alginate (2 w/v%) added and mixture was stirred for 3h at room temperature. Afterward obtained gel was dropped into 100 mL of 1% (w/v) $CaCl_2$ solution using a syringe for bead formation and stirred at 150 rpm for 2 h for stable structure. And then formed beads were filtered, rinsed several times with distilled water for remove unreacted $CaCl_2$ and dried at room condition.

CoNi-chitosan bead type catalysts synthesis; 0.1 g $CoCl_2.6H_2O$ and 0.1 g $NiCl_2.6H_2O$ were dissolved in 50 mL acetic acid (1 v/v%) and added a solution containing 2% chitosan (w/v). The mixture was stirred for 3 h at room temperature and then dropped into 100 mL of 1 M NaOH solution with a syringe. The occurred beads were kept in NaOH solution at 150 rpm for 2 h for stable structure and then filtered, washed several times with distilled water for remove unreacted NaOH on the surface of beads and dried at room condition.

2. 3. Characterization of Co-alginate and CoNi-chitosan Bead Type Catalysts

X-ray diffraction (XRD) patterns were taken in the 2θ range of 10–90° with 0.02° step size and scan speed of 1°/min using Philips PW 3040 device with CuKα radiation (λ = 0.15406 nm). The crystallite sizes (D) of metal species within polymer matrix were determined from Debye Scherrer equation ($D = 0.9\ \lambda)/(\beta\cos\theta)$) where β is full width half maximum (FWHM) of the strongest peak corresponding to metal species.[37]

Scanning electron microscopy (SEM) images were taken on Quanta 400F Field Emission model electron microscope at 30 kV. Before the analysis samples were attached on carbon tape and covered with a very thin layer of Au-Pd.

Fourier transforms infrared (FTIR) spectra (resolution of less than 0.09 cm^{-1}) were recorded on a Thermo Scientific/Nicolet IS50 instrument with a Pike ATR (attenuated total reflectance) adapter. FTIR data were collected with 0.5 cm^{-1} increment in the wavelength range of 600–4000 cm^{-1}.

2. 4. Catalytic Activity Evaluation of Co-alginate and CoNi-chitosan Bead Type Catalysts

The activity of the catalysts was tested in the reduction reaction of Remazol Yellow 4GL (RY) and Remazol Black B (RB) dyes in the presence of $NaBH_4$. All solutions were freshly prepared before reaction test. 1.5 mL of dye solution (20 mg/L) and 1 mL of $NaBH_4$ solution (0.3 M) were mixed. And then mixture was taken to a quartz cuvette, followed by addition of 30 mg of catalyst. Catalytic reduction was monitored at regular intervals of time using a Thermo Scientific/Evolution-201 UV-vis spectrophotometer in the wavelength range of 200–700 nm. Kinetic data were collected by measuring the absorbance values of RY and RB dye solutions at 429 nm and 562 nm, respectively. The kinetics of the reduction were investigated by implying the reaction process pursuing the pseudo-first order and pseudo second-order law, with the following equations: Eqs. (1) and (2), respectively. Reduction rate % was calculated using Eq. (3).

$$\ln\left(\frac{A_t}{A_o}\right) = -k_{app}t \qquad (1)$$

$$1/A_t = -k_{app}t \qquad (2)$$

$$\text{Reduction rate } \% = (A_o - A_e)/A_o x100 \qquad (3)$$

Where k_{app} (min^{-1}) is the rate constant, A_t is absorbance at time t, A_o is initial absorbance and A_e is absorbance at equilibrium of dye solutions.

3. Results and Discussion

3. 1. Characterization of Catalysts

XRD patterns are given in Fig. 1. Co-alginate exhibited semi-crystalline structure while CoNi-chitosan showed an amorphous structure. The semi-crystallinity due to chitosan derives from the presence of inter- and intramolecular hydrogen bonds between the hydroxyl and amine groups on glucosamine units that lead to the formation of parallel and closely packed polymer chains.[38] Two broad peaks corresponding to crystalline plane of chitosan were obtained at ~ 20° and 40° Bragg angle values for CoNi-chitosan[39,40]. No obvious diffraction peaks related to the cobalt and nickel phases were obtained due to the metals might be embedded/settled as very small particle to the chitosan structure. Co-alginate exhibited oxide (2θ: 29.14°, 33.96° and 36.98°) and metallic (2θ: 44.54°) forms of cobalt species[41,42] and crystallite size of cobalt was calculated as 25.12 nm from the highest peak intensity at 33.96 ° by Scherrer equation.

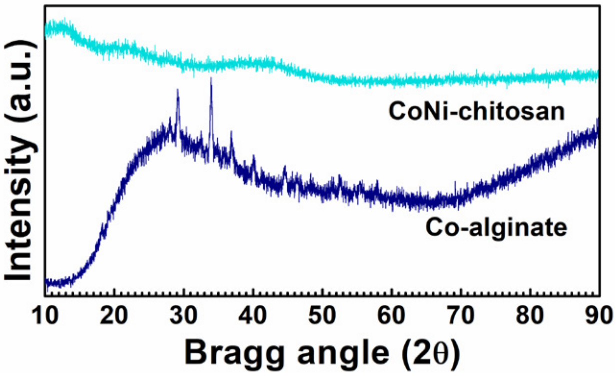

Figure 1. XRD patterns of Co-alginate and CoNi-chitosan bead type catalysts.

Fig. 2 shows the surface morphology of Co-alginate and CoNi-chitosan. Grainy structure of 4–25 µm size were observed on the surfaces of catalysts (Fig. 2a and c). It was observed that the surface of CoNi-chitosan (Fig. 2d) was rougher than Co-alginate (Fig. 2b). In addition to, grainy and rod-like structures were also observed for CoNi-chitosan. This different morphological structure may be related to the interaction between metals and alginate and chitosan.

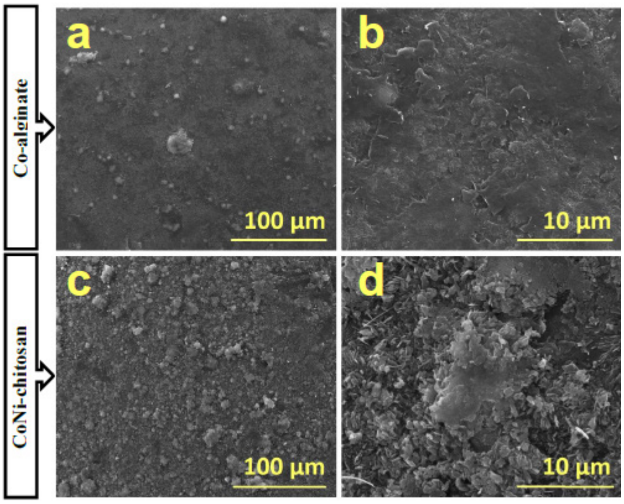

Figure 2. SEM images bead type catalysts of Co-alginate (**a, b**) and CoNi-chitosan (**c, d**).

FTIR spectrums of catalysts are shown in Fig. 3. The peak at 850 cm^{-1} related to the C–H band in the chitosan structure. The peak observed at around 1030 cm^{-1} indicates the C–O vibration, while the peaks obtained at 1350 cm^{-1} and 1460 cm^{-1} shows the C–H vibration originating from the CH_2/CH_3 groups. The peak detected at 1644 cm^{-1} was assigned the C=O bond found in chitosan and

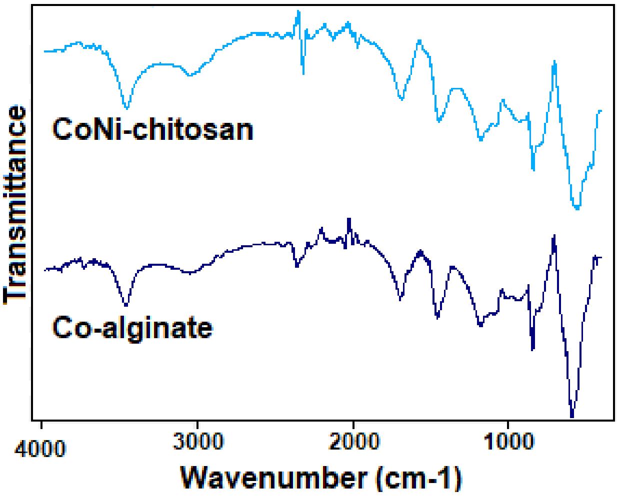

Figure 3. FTIR spectrums of Co-alginate and CoNi-chitosan bead type catalysts.

alginate structures. Addition, the N–H groups of chitosan were observed at 1557 cm^{-1} and 3270 cm^{-1} wavenumbers. The peak obtained at approximately 3450 cm^{-1} is due to the O–H band in the structure of chitosan and alginate.[40,43–46]

3. 2. Catalytic reduction of RY and RB over catalysts

The Co-alginate and CoNi-chitosan catalysts were tested in RY and RB reduction reaction and monitored results by UV-vis absorption spectra with time-dependent (Fig. 4). The dyes were reduced immediately in a short time. The rapid decrease in the absorption peaks observed at 429 nm and 562 nm clearly indicated the degradation of RY and RB, respectively. The reduction rate of RY in the first 2 min was about 18% for both catalysts. In total, RY was degraded by 74.0% in 10 min with Co-alginate and 50.4% in 6 min with CoNi-chitosan. RB degraded by 33% with CoNi–chitosan and by 4% with Co–alginate within the first 2 min. As can be predicted from the reduction in the absorption peak intensity at 562 nm, 66.4% and 21.9% of RB degraded by Co-alginate and CoNi-chitosan, respectively (Fig. 4a-d and Fig. 5b).

The difference in degradation performance of two dyes with different structures on different catalysts is due to the different physicochemical properties and molecular and electronic structures of the catalysts and dyes. It is well known that functional groups such as sulfonic (SO_3), hydroxyl (OH), methyl (CH_3), nitro (NO_2), and azo linkages (N=N) present in dye structures play a significant role in influencing the degradation process.[47–49] Khataee and Kasiri reported that monoazo dyes exhibited a higher degradation rate.[49] Rauf et al. stated that dye degradation occur primarily due to the cleavage of –N=N– azo bonds.[50] The –NH group in dye molecule is the fragile group. Besides, the sulfonic group may be increased the adsorb ability of the dye molecules on the catalyst contributing to higher degradation rate. On the other hand, the electron donating group attached

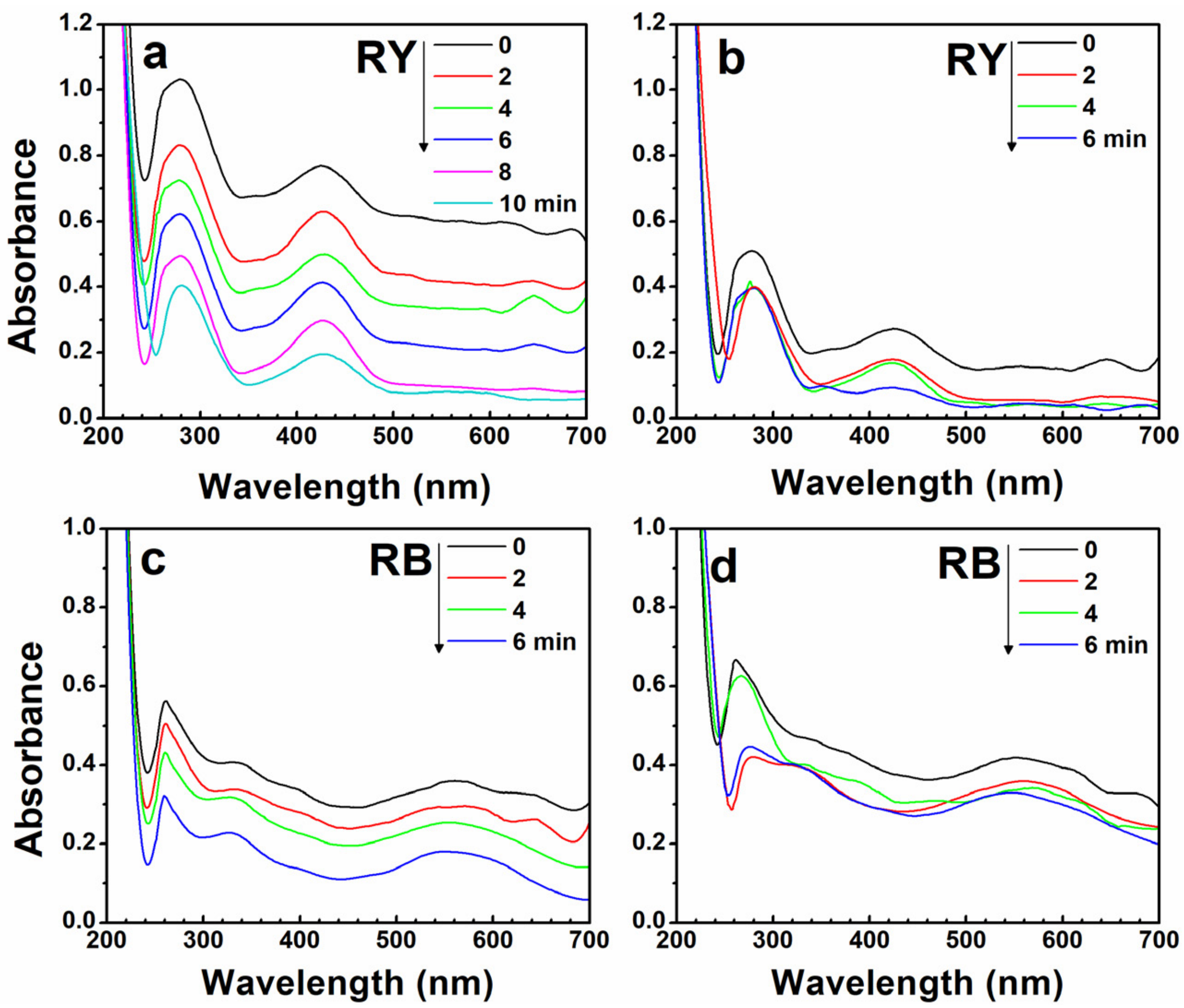

Figure 4. Time dependent UV–Vis absorption monitoring reduction of RY dye (**a:** Co-alginate, **b:** CoNi-chitosan) and RB dye (**c:** Co-alginate, **d:** CoNi-chitosan) over catalysts.

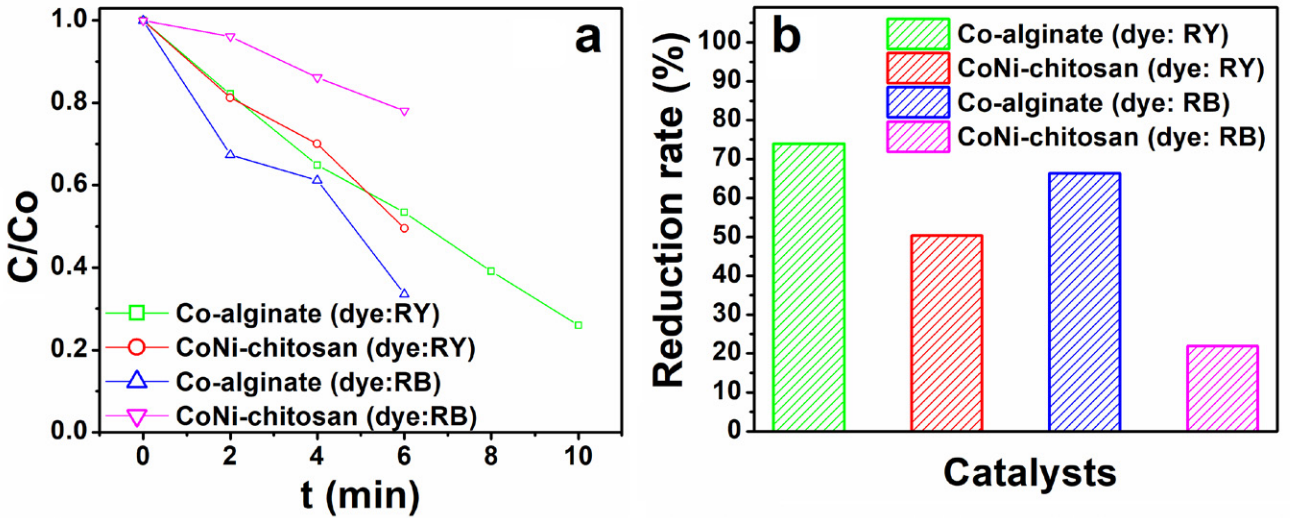

Figure 5. **(a)** The relationships of (C/C_o) versus reaction time **(b)** Reduction rate percent of dyes over catalysts.

to the molecular structure of dyes becomes more nucleophilic by donating some of its electron density.[48] Pervez et al. stated that the presence of $-CH_3$ group has a significant effect on the molecular mobility of dye molecules in the catalytic degradation of dyes.[47] Khataee and Kasiri explained that the number of –OH groups in dye molecule can increase the dye degradation rate.[49] Apart from these discussions, Von-Kiti et al. stated that the topological polar surface area (TPSA) of dyes is effective in dye removal, and that dyes with a low TPSA can show better removal performance.[51]

In the present study, the reduction rate of RY was found to be higher than that of RB. There could be several reasons for this. For example, RY is a monoazo dye (with a

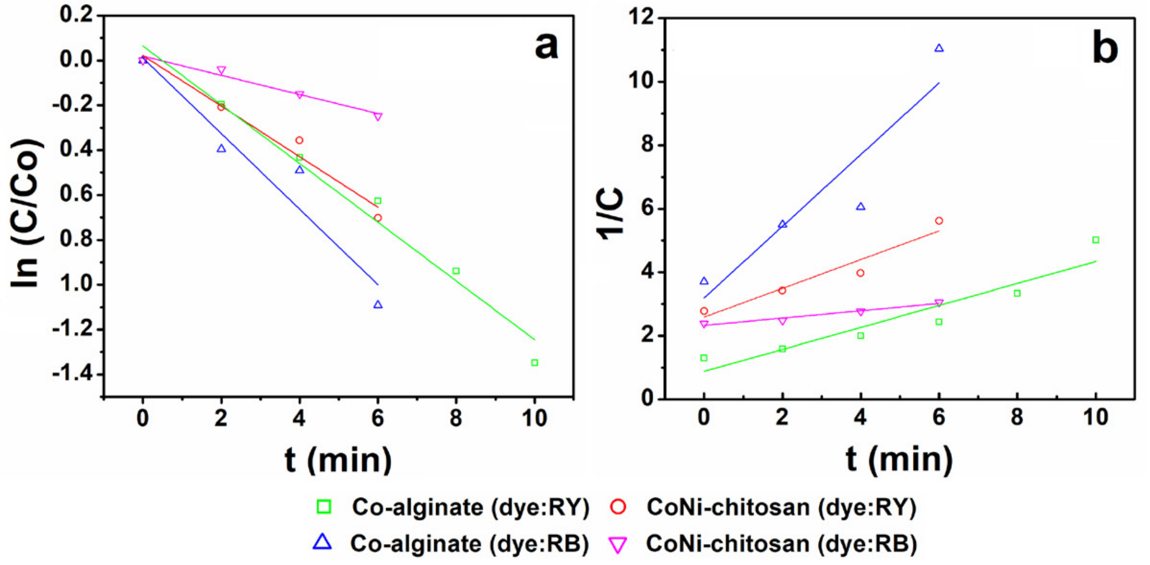

Figure 6. Kinetic plots of catalytic reduction of RY and RB dyes over Co-alginate and CoNi-chitosan bead type catalysts **(a)** first-order **(b)** second-order.

Table 1. Properties of dyes.

Dye	**Properties**							
	$N_{N=N}$	N_{SO3}	N_{OH}	N_{NH}	N_{CH3}	**HBDC***	**TPSA (Å)^{2*}**	**Complexity***
Remazol Yellow 4GL	1	2	–	4	2	5	355	1720
Remazol Black B	2	4	1	1	–	2	462	2030

N: number of groups; *: Ref: https://pubchem.ncbi.nlm.nih.gov/

Table 2. First-order and second-order kinetic parameters for the reduction of RY and RB over catalysts.

Catalyst	Dye	Pseudo-first-order k_{app} (min^{-1})	 R^2	Pseudo-second-order k_{app} (Lg^{-1}min^{-1})	 R^2
Co-alginate	Remazol Yellow 4GL	0.140	0.979	0.346	0.887
CoNi-chitosan	Remazol Yellow 4GL	0.124	0.969	0.452	0.928
Co-alginate	Remazol Black B	0.174	0.930	1.127	0.860
CoNi-chitosan	Remazol Black B	0.052	0.968	0.115	0.960

single –N=N– bond), and it has a higher number of –NH and $-CH_3$ groups compared to RB. Additionally, the hydrogen bond donor count (HBDC) of RY is higher than that of RB. Moreover, the topological polar surface area (TPSA) and complexity values of RY are lower than those of RB. Although RB has a higher number of SO_3 and –OH groups compared to RY, its lower removal percentage may be due to the reduced interaction between the catalyst and the dye molecules, or its higher complexity and greater number of N=N groups (Table 1).

To discuss the kinetics of the dye reduction, pseudo-first-order and pseudo-second-order kinetic models were applied.[52,53] The k_{app} values were estimated from the slope of the lines in Fig. 6. The rate constants and coefficients of determination (R^2) calculated for the models are presented in Table 2. As the kinetic models were compared, kinetic data fitted well pseudo-first-order kinetic model ($R^2 \leq 0.979$). The k_{app} values for RY were found to be 0.140 and 0.124 min^{-1} for the Co-alginate and CoNi-chitosan, respectively and for RB as 0.174 and 0.052 min^{-1}. Both higher dye reduction and a higher reaction rate constant were obtained with Co-alginate. Possible reasons for this include the combination of cobalt with alginate may be improve the steric structure inside the alginate, thereby increasing the adsorption of dye onto the catalyst surface.[35]

Reusability test was performed for Co-alginate in degradation of RY. Firstly, the catalyst was easily collected after completing of reaction thanks to their bead shape, washed with deionized water and then reused under the same reaction conditions. The catalyst could be successfully recycled up to 4 runs and the reduction efficiency of RY was determined as 70% even after 4 runs (Fig. 7).

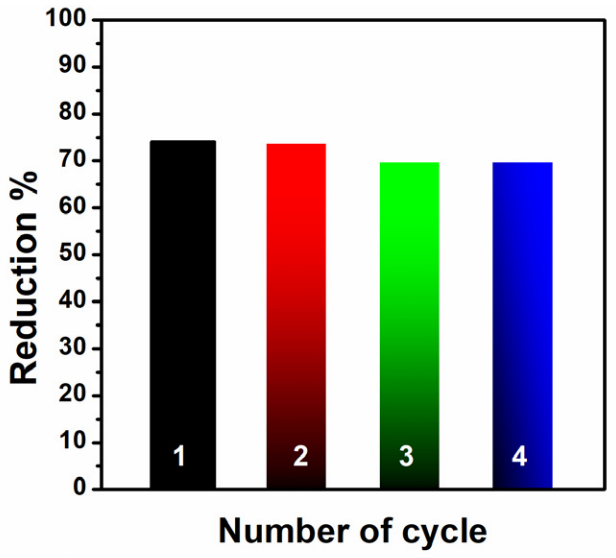

Figure 7. Reusability of Co-alginate for RY dye.

The dye reduction performance of the synthesized catalysts was compared with that of different materials and

Table 3. The catalytic degradation reaction kinetic of RY and RB over different catalysts.

Sample	Dye	Dye concentration (mg/L)	Degradation method	Degradation (%)	Degradation time (min)	k_{app} (min^{-1})	Reference
Co-alginate	Remazol Yellow 4GL	20	Catalytic reduction	74.0	10	0.140	This work
CoNi-chitosan	Remazol Yellow 4GL	20	Catalytic reduction	50.4	6	0.124	This work
PANI-SnO_2@Diatomite	Remazol Yellow 4GL	50	Photocatalytic	96.0	60	0.042	[7]
Sn/SBA-15@APTES(EA)	Remazol Yellow 4GL	50	Photocatalytic	58.2	150	0.0016	[8]
α-Fe_2O_3 NPs	Remazol Yellow RR	50	Photocatalytic	75.0	250	0.006	[54]
Fe^{2+} ions	Remazol Yellow FG	100	Contact glow discharge electrolysis	51.3	180	–	[55]
Co-alginate	Remazol Black B	20	Catalytic reduction	66.4	6	0.174	This work
CoNi-chitosan	Remazol Black B	20	Catalytic reduction	21.9	6	0.052	This work
Electric arc furnace dust	Remazol Black B	40	Photocatalytic	81.0	150	0.002	[2]
TiO_2-NF's-anatase	Remazol Black B	20	Photocatalytic	50.0	20	0.068	[4]
GO/$CoFe_2O_4$	Remazol Black B	10	Photocatalytic	53.0	60	0.102	[5]

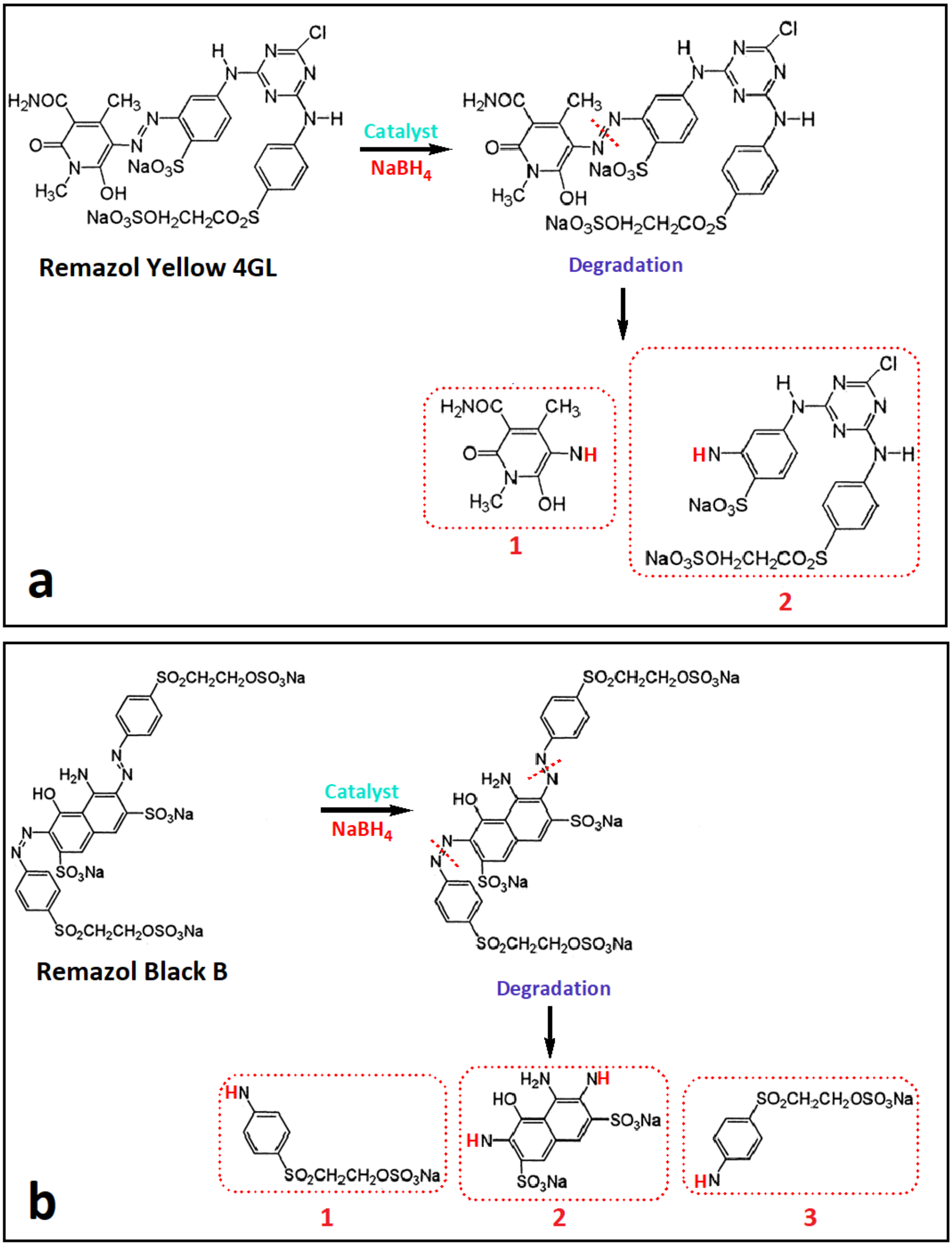

Scheme 1. Possible mechanism of reduction reaction of two dyes by catalysts.

reduction methods, and the results are presented in Table 3. In the present study, both high reduction capacity and a high reaction rate constant value were achieved with the synthesized catalysts, and it was observed that reduction or degradation occurred in a shorter time. From this perspective, it can be said that the catalysts are promising for dye reduction.

3. 3. Possible Catalytic Reduction Mechanism of RY and RB Dyes

The reduction reaction of dyes in the presence of $NaBH_4$ proceeds via Langmuir–Hinshelwood mechanism, where the reaction occurs due to interaction between adsorbed species (both dye and reductant). In this dye reduction process, the first step involves the diffusion of reactants into the pores of catalysts, and it is generated that electrons from $NaBH_4$ and hydrides from aqueous media. In the second step, these electrons and active hydride species are transferred to metal nanoparticles, resulting in the formation of metal–hydride bonds. Dye molecules incline to capture hydrogen and electrons from the metal–hydride complex.[26,56–59] According to the previously reported literature studies[19,26,59–62], the possible mechanism of dye reduction by catalyst and resulting products are proposed in Scheme 1. The H atom attaches to the N atom of heterocyclic ring in dye and breaks down azo double bond (–N=N–) between N and aromatic ring via conjugation. The broken bonds reduce to hydrazine group (–HN–NH–) and convert to products. The products occur according to azo double bond number of RY (single azo class) and RB (double azo class) (Scheme 1a and 1b).

4. Conclusion

Co-alginate and CoNi-chitosan catalysts were successfully designed for the catalytic reduction of RY and RB dyes. Co-alginate demonstrated high catalytic efficiency within a short time. The RY degraded 74% and 50% with Co-alginate and CoNi-chitosan, and also RB 66% and 22%, respectively. Different results were obtained with the same catalyst for RY and RB reduction. This behavior is thought to be due to the interaction between the dye and the catalyst. The rate constant, reaction time and reusability obtained in this study are quite assertive. The catalysts may serve as potential candidates not only for the dye reduction but also for the removal of various harmful organic and inorganic pollutants.

5. References

1. Alene, A. N.; Teshager, A. A.; Adugna, A. G.; Kndie, T. M.; Feleke, M. K.; Atlabachew, M.; Abate, G. Y.; Nguyen, D. T. A. Nanocatalytic reductive removal of Congo-red dye using boron-loaded cobalt oxide nanocomposites from aqueous solutions. *Results in Chemistry* **2025**, *15*, 102222. **DOI:**10.1016/j.rechem.2025.102222
2. Almeida, M. M.; Saczk, A. A.; da Silva Felix, F.; Penido, E. S.; Santos, T. A. R.; de Souza Teixeira, A.; Magalhães, F. Characterization of electric arc furnace dust and its application in photocatalytic reactions to degrade organic contaminants in synthetic and real samples. *Journal of Photochemistry and Photobiology A: Chemistry* **2023**, *438*, 114585. **DOI:**10.1016/j.jphotochem.2023.114585
3. Cardoso, N. F.; Pinto, R. B.; Lima, E. C.; Calvete, T.; Amavisca, C. V.; Royer, B.; Cunha, M. L.; Fernandes, T. H.; Pinto, I. S. Removal of remazol black B textile dye from aqueous solution by adsorption. *Desalination* **2011**, *269* (1–3), 92–103. **DOI:**10.1016/j.desal.2010.10.047
4. Secundino-Sánchez, O.; Díaz-Reyes, J.; Sánchez-Ramírez, J.; Arias-Cerón, J.; Galván-Arellano, M.; Vázquez-Cuchillo, O. Controlled synthesis of electrospun TiO2 nanofibers and their photocatalytic application in the decolouration of Remazol Black B azo dye. *Catalysis Today* **2022**, *392*, 13–22. **DOI:**10.1016/j.cattod.2021.10.003
5. Sheshmani, S.; Falahat, B.; Nikmaram, F. R. Preparation of magnetic graphene oxide-ferrite nanocomposites for oxidative decomposition of Remazol Black B. *International journal of biological macromolecules* **2017**, *97*, 671–678. **DOI:**10.1016/j.ijbiomac.2017.01.041
6. Shakeri, N.; Amooey, A. A.; Amoei, A.; Tahmasebizadeh, M. Evaluation of an Anaerobic/Aerobic System for Reactive Black 5 Removal: Kinetic Study. *Iranian Journal of Chemistry and Chemical Engineering* **2021**, *40* (5), 1512–1521.
7. Akti, F. Photocatalytic degradation of remazol yellow using polyaniline–doped tin oxide hybrid photocatalysts with diatomite support. *Applied Surface Science* **2018**, *455*, 931–939. **DOI:**10.1016/j.apsusc.2018.06.019
8. Akti, F.; Balci, S. Synthesis of APTES and alcohol modified Sn/SBA-15 in presence of competitive ion: Test in degradation of Remazol Yellow. *Materials Research Bulletin* **2022**, *145*, 111496. **DOI:**10.1016/j.materresbull.2021.111496
9. ALSamman, M. T.; Sanchez, J. Recent advances on hydrogels based on chitosan and alginate for the adsorption of dyes and metal ions from water. *Arabian Journal of Chemistry* **2021**, *14* (12), 103455. **DOI:**10.1016/j.arabjc.2021.103455
10. Suvarna, A. R.; Shetty, A.; Anchan, S.; Kabeer, N.; Nayak, S. Cyclea peltata leaf mediated green synthesized bimetallic nanoparticles exhibits methyl green dye degradation capability. *Bionanoscience* **2020**, *10*, 606–617. **DOI:**10.1007/s12668-020-00739-9
11. Balci, B.; Aksoy, N.; Erkurt, F. E.; Budak, F.; Basibuyuk, M.; Zaimoglu, Z.; Turan, E. S.; Yilmaz, S. Removal of a reactive dye from simulated textile wastewater by environmentally friendly oxidant calcium peroxide. *International Journal of Chemical Reactor Engineering* **2021**, *19* (11), 1231–1243. **DOI:**10.1515/ijcre-2021-0062
12. Benredjem, Z.; Barbari, K.; Chaabna, I.; Saaidia, S.; Djemel, A.; Delimi, R.; Douas, S.; Bakhouche, K. Comparative investigation on the removal of methyl orange from aqueous solution using three different advanced oxidation processes. *International Journal of Chemical Reactor Engineering* **2021**, *19* (6), 597–604. **DOI:**10.1515/ijcre-2020-0243
13. Ali, A.; Garg, U.; Khan, K. U.; Azim, Y. Removal of organic and inorganic pollutants using CSFe3O4@ CeO2 nanocatalyst via adsorption–reduction catalysis: A focused analysis on methylene blue. *Journal of Polymers and the Environment* **2022**, *30* (10), 4435–4451. **DOI:**10.1007/s10924-022-02522-1
14. Dorraj, M.; Sadjadi, S.; Heravi, M. M. Pd on poly (1-vinylimidazole) decorated magnetic S-doped grafitic carbon nitride: An efficient catalyst for catalytic reduction of organic dyes. *Scientific Reports* **2020**, *10* (1), 13440. **DOI:**10.1038/s41598-020-70457-5
15. Abdelkrim, S.; Mokhtar, A.; Djelad, A.; Hachemaoui, M.; Boukoussa, B.; Sassi, M. Insights into catalytic reduction of

dyes catalyzed by nanocomposite beads Alginate@ Fe3O4: Experimental and DFT study on the mechanism of reduction. *Colloids and Surfaces A: Physicochemical and Engineering Aspects* **2022**, *650*, 129595. **DOI:**10.1016/j.colsurfa.2022.129595

16. Zahid, M.; Segar, A. S. M.; Al-Majmaie, S.; Shather, A.; Khan, M. F.; Alguno, A. C.; Capangpangan, R. Y.; Ismail, A. Elettaria cardamomum seed extract synthesized silver nanoparticles for efficient catalytic reduction of toxic dyes. *Environmental Nanotechnology, Monitoring & Management* **2023**, *20*, 100809. **DOI:**10.1016/j.enmm.2023.100809
17. Khakyzadeh, V. Evaluation of the performance of a hybrid advanced oxidation process for degradation of organic pollutants in aqueous media. *International Journal of Environmental Analytical Chemistry* **2022**, 1–10.
18. Hachemaoui, M.; Mokhtar, A.; Abdelkrim, S.; Ouargli-Saker, R.; Zaoui, F.; Hamacha, R.; Habib Zahmani, H.; Hacini, S.; Bengueddach, A.; Boukoussa, B. Improved catalytic activity of composite beads calcium alginate@ MIL-101@ Fe3O4 towards reduction toxic organic dyes. *Journal of Polymers and the Environment* **2021**, *29* (12), 3813–3826. **DOI:**10.1007/s10924-021-02177-4
19. Wang, G.; Zhao, K.; Gao, C.; Wang, J.; Mei, Y.; Zheng, X.; Zhu, P. Green synthesis of copper nanoparticles using green coffee bean and their applications for efficient reduction of organic dyes. *Journal of Environmental Chemical Engineering* **2021**, *9* (4), 105331. **DOI:**10.1016/j.jece.2021.105331
20. Deng, L.; Ren, H.; Fu, L.; Liao, M.; Zhou, X.; Chen, S.; Wang, H.; Wang, L. Ferrous and manganese oxalate for efficient heterogenous-Fenton degradation of organic pollutants: composite active site and mechanism perception. *International Journal of Chemical Reactor Engineering* **2023**, (0). **DOI:**10.1515/ijcre-2023-0024
21. Heidari, H.; Aliramezani, F. Ni/Fe3O4@ nanocellulose and Ni/nanocellulose green nanocomposites: Inorganic-organic hybrid catalysts for the reduction of organic pollutants. *Iran. J. Chem. Chem. Eng. Research Article Vol* **2022**, *41* (10).
22. Naseem, K.; Farooqi, Z. H.; Begum, R.; Irfan, A. Removal of Congo red dye from aqueous medium by its catalytic reduction using sodium borohydride in the presence of various inorganic nano-catalysts: a review. *Journal of cleaner production* **2018**, *187*, 296–307. **DOI:**10.1016/j.jclepro.2018.03.209
23. Linxu, X.; Zhigang, Y.; Xue, S.; Jin, W.; Sisi, X.; Rupeng, L.; Feiyong, C. Facile synthesis of CuO/Co3O4 nanoribbons with excellent catalytic performance for reduction of organic dyes. *Solid State Sciences* **2022**, *134*, 107048. **DOI:**10.1016/j.solidstatesciences.2022.107048
24. Rahmani, A.; Rahmani, H.; Zonouzi, A. Sponge like M-doped Ni/NiO (M= Cu, Co) composites and their catalytic activity toward dye reduction. *Materials Today Communications* **2020**, *25*, 101304. **DOI:**10.1016/j.mtcomm.2020.101304
25. Ajmal, M.; Siddiq, M.; Al-Lohedan, H.; Sahiner, N. Highly versatile p (MAc)–M (M: Cu, Co, Ni) microgel composite catalyst for individual and simultaneous catalytic reduction of nitro compounds and dyes. *RSC Advances* **2014**, *4* (103), 59562–59570. **DOI:**10.1039/C4RA11667D
26. Moussadik, A.; Brigiano, F. S.; Tielens, F.; Halim, M.; Kacimi, M.; El Hamidi, A. Self-supported Ag nanoparticles on AgTi2 (PO4) 3 for hazardous dyes reduction in industrial wastewater. *Journal of Environmental Chemical Engineering* **2022**, *10* (1), 106939. **DOI:**10.1016/j.jece.2021.106939
27. Bao, Y.; Shao, L.; Xing, G.; Qi, C. Cobalt, nickel and iron embedded chitosan microparticles as efficient and reusable catalysts for Heck cross-coupling reactions. *International journal of biological macromolecules* **2019**, *130*, 203–212. **DOI:**10.1016/j.ijbiomac.2019.02.143
28. Kurczewska, J. Chitosan-montmorillonite hydrogel beads for effective dye adsorption. *Journal of Water Process Engineering* **2022**, *48*, 102928. **DOI:**10.1016/j.jwpe.2022.102928
29. Maslamani, N.; Khan, S. B.; Danish, E. Y.; Bakhsh, E. M.; Zakeeruddin, S. M.; Asiri, A. M. Carboxymethyl cellulose nanocomposite beads as super-efficient catalyst for the reduction of organic and inorganic pollutants. *International journal of biological macromolecules* **2021**, *167*, 101–116. **DOI:**10.1016/j.ijbiomac.2020.11.074
30. Vandarkuzhali, S. A. A.; Pachamuthu, M.; Srinivasan, V.; Mohamed, S. K.; Abd-Rabboh, H. S.; Hamdy, M. S.; Balamurugan, V. Efficient reduction of dyes to leuco form over silver nanoparticles on functionalised SBA-15 and aminoclay. *International Journal of Environmental Analytical Chemistry* **2020**, 1–14. **DOI:**10.1080/03067319.2020.1811257
31. Ajmal, M.; Demirci, S.; Siddiq, M.; Aktas, N.; Sahiner, N. Simultaneous catalytic degradation/reduction of multiple organic compounds by modifiable p (methacrylic acid-co-acrylonitrile)–M (M: Cu, Co) microgel catalyst composites. *New Journal of Chemistry* **2016**, *40* (2), 1485–1496. **DOI:**10.1039/C5NJ02298C
32. Daneshafruz, H.; Barani, H.; Sheibani, H. Palladium nanoparticles-decorated β-cyclodextrin–cyanoguanidine modified graphene oxide: a heterogeneous nanocatalyst for suzuki–miyaura coupling and reduction of 4-nitrophenol reactions in aqueous media. *Journal of Inorganic and Organometallic Polymers and Materials* **2022**, *32* (3), 791–802. **DOI:**10.1007/s10904-021-02218-4
33. Zarei, M.; Mohammadzadeh, I.; Saidi, K.; Sheibani, H. Fabrication of biochar@ Cu-Ni nanocatalyst for reduction of aryl aldehyde and nitroarene compounds. *Biomass Conversion and Biorefinery* **2024**, *14* (2), 2761–2776. **DOI:**10.1007/s13399-022-02490-5
34. Srivastava, V.; Choubey, A. K. Investigation of adsorption of organic dyes present in wastewater using chitosan beads immobilized with biofabricated CuO nanoparticles. *Journal of Molecular Structure* **2021**, *1242*, 130749. **DOI:**10.1016/j.molstruc.2021.130749
35. Sun, Y.; Li, Y.; Chen, B.; Wang, M.; Zhang, Y.; Chen, K.; Du, Q.; Wang, Y.; Pi, X. Methylene Blue Removed from Aqueous Solution by Encapsulation of Bentonite Aerogel Beads with Cobalt Alginate. *ACS omega* **2022**, *7* (45), 41246–41255. **DOI:**10.1021/acsomega.2c04904
36. Ahmadi, S.; Rahdar, A.; Rahdar, S.; Igwegbe, C. A. Removal of Remazol Black B from aqueous solution using P-γ-Fe2O3 nanoparticles: synthesis, physical characterization, isotherm,

kinetic and thermodynamic studies. *Desalination and water treatment* **2019**, *152*, 401–410. **DOI:**10.5004/dwt.2019.23978

37. Niemantsverdriet, J. W. *Spectroscopy in catalysis: an introduction*; John Wiley & Sons, 2007. **DOI:**10.1002/9783527611348
38. Vakili, M.; Deng, S.; Liu, D.; Li, T.; Yu, G. Preparation of aminated cross-linked chitosan beads for efficient adsorption of hexavalent chromium. *International journal of biological macromolecules* **2019**, *139*, 352–360. **DOI:**10.1016/j.ijbiomac.2019.07.207
39. Sowmya, A.; Meenakshi, S. Zr (IV) loaded cross-linked chitosan beads with enhanced surface area for the removal of nitrate and phosphate. *International Journal of Biological Macromolecules* **2014**, *69*, 336–343. **DOI:**10.1016/j.ijbiomac.2014.05.043
40. Abdeen Z, M. S., Mahmoud M Adsorption of Mn (II) ion on polyvinyl alcohol/chitosan dry blending from aqueous solution. *Environmental Nanotechnology, Monitoring & Management* **2015**, *3*, 1–9. **DOI:**10.1016/j.enmm.2014.10.001
41. Akti, F. Green synthesis of pistachio shell-derived biochar supported cobalt catalysts and their catalytic performance in sodium borohydride hydrolysis. *International Journal of Hydrogen Energy* **2022**, *47* (83), 35195–35202. **DOI:**10.1016/j.ijhydene.2022.08.101
42. Zhang, M.; Jia, L.; Zhang, Y.-h.; Li, W.; Li, J.-l.; Hong, J.-p. Preparation of highly dispersed silicon spheres supported cobalt-based catalysts and their catalytic performance for Fischer-Tropsch synthesis. *Journal of Fuel Chemistry and Technology* **2023**, *51* (5), 608–615. **DOI:**10.1016/S1872-5813(22)60078-1
43. Kumirska, J.; Czerwicka, M.; Kaczyński, Z.; Bychowska, A.; Brzozowski, K.; Thöming, J.; Stepnowski, P. Application of spectroscopic methods for structural analysis of chitin and chitosan. *Marine drugs* **2010**, *8* (5), 1567–1636. **DOI:**10.3390/md8051567
44. Lustriane, C.; Dwivany, F. M.; Suendo, V.; Reza, M. Effect of chitosan and chitosan-nanoparticles on post harvest quality of banana fruits. *Journal of Plant Biotechnology* **2018**, *45* (1), 36–44. **DOI:**10.5010/JPB.2018.45.1.036
45. Su, C.; Berekute, A. K.; Yu, K.-P. Chitosan@ TiO2 composites for the adsorption of copper (II) and antibacterial applications. *Sustainable Environment Research* **2022**, *32* (1), 1–15. **DOI:**10.1186/s42834-022-00138-7
46. Benali, F.; Boukoussa, B.; Benkhedouda, N.-E.-H.; Cheddad, A.; Issam, I.; Iqbal, J.; Hachemaoui, M.; Abboud, M.; Mokhtar, A. Catalytic Reduction of Dyes and Antibacterial Activity of AgNPs@ Zn@ Alginate Composite Aerogel Beads. *Polymers* **2022**, *14* (22), 4829. **DOI:**10.3390/polym14224829
47. Pervez, M. N.; Mishu, M. M. R.; Tanvir, N. P.; Talukder, M. E.; Cai, Y.; Telegin, F. Y.; Zhao, Y.; Naddeo, V. Insights into the structures and properties of dyes in the Fenton catalytic process for treating wastewater effluent. *Water Environment Research* **2023**, *95* (12), e10948. **DOI:**10.1002/wer.10948
48. Khalik, W. F.; Ho, L.-N.; Ong, S.-A.; Wong, Y.-S.; Yusoff, N. A.; Lee, S.-L. Revealing the influences of functional groups in azo dyes on the degradation efficiency and power output in solar photocatalytic fuel cell. *Journal of Environmental Health Science and Engineering* **2020**, *18*, 769–777. **DOI:**10.1007/s40201-020-00502-y
49. Khataee, A.; Kasiri, M. B. Photocatalytic degradation of organic dyes in the presence of nanostructured titanium dioxide: Influence of the chemical structure of dyes. *Journal of Molecular Catalysis A: Chemical* **2010**, *328* (1–2), 8–26. **DOI:**10.1016/j.molcata.2010.05.023
50. Rauf, M.; Meetani, M.; Hisaindee, S. An overview on the photocatalytic degradation of azo dyes in the presence of TiO2 doped with selective transition metals. *Desalination* **2011**, *276* (1–3), 13–27. **DOI:**10.1016/j.desal.2011.03.071
51. Von-Kiti, E.; Oduro, W. O.; Animpong, M. A.; Ampomah-Benefo, K.; Boafo-Mensah, G.; Kwakye-Awuah, B.; Williams, C. D. Evidence of electronic influence in the adsorption of cationic and zwitterionic dyes on zeolites. *Heliyon* **2023**, *9* (9). **DOI:**10.1016/j.heliyon.2023.e20049
52. Li, H.; Jiang, D.; Huang, Z.; He, K.; Zeng, G.; Chen, A.; Yuan, L.; Peng, M.; Huang, T.; Chen, G. Preparation of silver-nanoparticle-loaded magnetic biochar/poly (dopamine) composite as catalyst for reduction of organic dyes. *Journal of colloid and interface science* **2019**, *555*, 460–469. **DOI:**10.1016/j.jcis.2019.08.013
53. Veisi, H.; Joshani, Z.; Karmakar, B.; Tamoradi, T.; Heravi, M. M.; Gholami, J. Ultrasound assisted synthesis of Pd NPs decorated chitosan-starch functionalized Fe3O4 nanocomposite catalyst towards Suzuki-Miyaura coupling and reduction of 4-nitrophenol. *International Journal of Biological Macromolecules* **2021**, *172*, 104–113. **DOI:**10.1016/j.ijbiomac.2021.01.040
54. Bhuiyan, M. S. H.; Miah, M. Y.; Paul, S. C.; Aka, T. D.; Saha, O.; Rahaman, M. M.; Sharif, M. J. I.; Habiba, O.; Ashaduzzaman, M. Green synthesis of iron oxide nanoparticle using Carica papaya leaf extract: application for photocatalytic degradation of remazol yellow RR dye and antibacterial activity. *Heliyon* **2020**, *6* (8), e04603. **DOI:**10.1016/j.heliyon.2020.e04603
55. Budikania, T. S.; Afriani, K.; Widiana, I.; Saksono, N. Decolorization of azo dyes using contact glow discharge electrolysis. *Journal of Environmental Chemical Engineering* **2019**, *7* (6), 103466. **DOI:**10.1016/j.jece.2019.103466
56. Abay, A. K.; Chen, X.; Kuo, D.-H. Highly efficient noble metal free copper nickel oxysulfide nanoparticles for catalytic reduction of 4-nitrophenol, methyl blue, and rhodamine-B organic pollutants. *New Journal of Chemistry* **2017**, *41* (13), 5628–5638. **DOI:**10.1039/C7NJ00676D
57. Farooqi, Z. H.; Sultana, H.; Begum, R.; Usman, M.; Ajmal, M.; Nisar, J.; Irfan, A.; Azam, M. Catalytic degradation of malachite green using a crosslinked colloidal polymeric system loaded with silver nanoparticles. *International Journal of Environmental Analytical Chemistry* **2022**, *102* (16), 4104–4120. **DOI:**10.1080/03067319.2020.1779247
58. Khan, N.; Shahida, B.; Khan, S. A.; Ahmad, Z.; Saeeduddin; Sheikh, Z.; Bakhsh, E. M.; Alraddadi, H. M.; Fagieh, T. M.; Khan, S. B. Anchoring Zero-Valent Cu and Ni Nanoparticles on Carboxymethyl Cellulose-Polystyrene–Block Polyisoprene–Block Polystyrene Composite Films for Nitrophenol

Reduction and Dyes Degradation. *Journal of Polymers and the Environment* **2023**, *31* (2), 608–620. **DOI:**10.1007/s10924-022-02579-y

59. Mahmoud, M. E.; Amira, M. F.; Abouelanwar, M. E.; Salam, M. A. Green synthesis and surface decoration of silver nanoparticles onto δ-FeOOH-Polymeric nanocomposite as efficient nanocatalyst for dyes degradation. *Journal of Environmental Chemical Engineering* **2021**, *9* (1), 104697. **DOI:**10.1016/j.jece.2020.104697
60. Ali, A.; Garg, U.; Khan, K. U.; Azim Y. Removal and inorganic pollutants using CSFe$_3$O$_4$@ CeO$_2$ nanocatalyst via adsorption–reduction catalysis: A focused analysis on methylene blue. *Journal of Polymers and the Environment* **2022**, *30* (10), 4435–4451. **DOI:**10.1007/s10924-022-02522-1
61. Deka, J. R.; Saikia, D.; Cheng, T.-H.; Kao, H.-M.; Yang, Y.-C. Bimetallic AgCu nanoparticles decorated on zeolitic imidazolate framework derived carbon: An extraordinarily active and recyclable nanocomposite catalyst for reduction of nitroarenes and degradation of organic dyes. *Journal of Environmental Chemical Engineering* **2023**, *11* (3), 109777. **DOI:**10.1016/j.jece.2023.109777
62. Mallakpour, S.; Azadi, E.; Dinari, M. Mesoporous Ca-alginate/melamine-rich covalent organic polymer/cupric oxide-based microgel beads as heterogeneous catalyst for efficient catalytic reduction of hazardous water pollutants. *Journal of Environmental Chemical Engineering* **2023**, *11* (2), 109294. **DOI:**10.1016/j.jece.2023.109294

Povzetek

Katalizatorji, dopirani s kobaltom in nikljem, so bili sintetizirani z uporabo hitozana in alginata ter uporabljeni pri degradaciji barvil Remazol Yellow 4GL (RY) in Remazol Black B (RB). XRD vzorec katalizatorjev je pokazal amorfno obliko za CoNi-hitozan in polikristalinično obliko za Co-alginat. SEM slike so pokazale, da je bila površina katalizatorja groba, zrnata in z valjastimi strukturami. Površinske funkcionalne skupine so bile določene z metodo FTIR analize in jasno je bila opažena prisotnost alginata in hitozana. Katalizatorji Co-alginat so pokazali višjo degradacijo barvila (74% za RY) in tudi krajši čas reakcije (6 min za RB). Reakcija redukcije je bila dobro skladna s kinetičnim modelom pseudo-prvega reda, konstanta hitrosti reakcije pa je bila določena kot 0,140 min^{-1} za RY in 0,174 min^{-1} za RB. Delež redukcije RY z obema katalizatorjema je bila višja kot pri RB. Co-alginat je pokazal približno 70% učinkovitost redukcije za RY celo po 4 ponovitvah. Učinkovitost redukcije barvila in katalitska aktivnost katalizatorjev obetata možnosti za aplikacije katalitske redukcije organskih onesnaževalnih barvil.

DOI: 10.17344/acsi.2024.8923 *Acta Chim. Slov.* **2025,** *72,* 400–408

Scientific paper

Studying the Effect of Adding Polymeric Wastes on the Rheological Properties of Asphalt

Semaa I. Khaleel*

Department of Petroleum and Refining Engineering, College of Petroleum and Mining Engineering, University of Mosul, Mosul, Iraq

** Corresponding author: E-mail: semaaibraheem@uomosul.edu.iq*

Received: 08-08-2024

Abstract

This research aims to develop various types of asphalt materials with enhanced rheological properties compared to unmodified asphalt. Three types of polymeric materials (PS), (PFR), and (PP)-were used to modify Al-Doura asphalt, with the goal of evaluating their impact on the rheological characteristics of the resulting asphalt systems. These modified materials were then compared with each other with both local and international standards to assess their suitability for specific applications. Polymeric waste materials were used instead of virgin polymers to reduce environmental pollution and lower modification costs. The modification process was carried out using two approaches: physical treatment and chemical treatment. The chemical method involved a catalytic reaction using 2% ($FeCl_3$) and 1% (S). Results showed that chemical treatment had a more significant positive impact on the rheological properties of the asphalt systems compared to physical treatment. In both approaches, the addition of polymers led to an increase in de-asphaltene %, with the highest values recorded for AsPS (44.5%), AsPFR (40%), and AsPP (40%). Furthermore, chemically modifying asphalt with PS produced the most notable improvements among the tested polymers. Based on key performance indicators such as softening point, penetration, ductility, penetration index (PI), and asphaltene %, the modified asphalt samples demonstrated suitability for use in producing mastic, which are widely applied as waterproofing material.

Keywords: Rheological properties, Polymeric wastes, Asphalt, Softening point, Penetration Index

1. Introduction

Pure asphalt is a complex structure chemical substance that can be obtained through the distillation process of crude oil and has many properties such as: little cost and widely spread, It also have associative viscoelastic, water-resistant properties, which can be used in various applications such as paving and others.[1,2] The chemical composition of asphalt consists mainly of hydrocarbon compounds (paraffinic, naphthenic, and aromatic) in which carbon atoms reach 88% and hydrogen about 11%. It also includes cyclic or non-cyclic compounds containing oxygen, nitrogen, and sulfur, which are called heterogeneous atoms, and these last atoms are responsible. About the polarity of bitumen.[3] Mineral elements that are polar in nature affect the physical and chemical properties in addition to increasing the interaction between molecules of asphalt. Asphalt have a chemical composition consisting of four parts called SARA (i.e. Saturates, Aromatics, Resins, and Asphaltene). These components differ in their properties such as solubility and polarity. And its molecular weight, as maltin consists of non-polar parts that are characterized by a low molecular weight (Aromatics, Saturates), which represent the dispersed part in the asphalt. As for the polar part, which have a higher molecular weight compared to the first two parts, it is the resin. These three parts have the ability to dissolve in n-heptane.[4] Asphaltene represents the part responsible for gaining asphalt stability and hardness properties.[5] Asphalt is known by several names around the world, In North America, the word asphalt is called bitumen, while abroad it is called mixtures of bitumen with a mixture of mineral materials.[6]

The chemical inertness that characterizes asphalt, coupled with its physical properties, is what makes it eligible for wide uses in construction and industry, and the physical properties is what determines the nature of the use more than the chemical ones.[7] Given the physical properties of asphalt its wide availability in nature, its different sources, and its diverse applications many researchers have conducted studies in order to improve and develop many of its characteristics, for example: softening, ductility, and penetration using different types of additives, in various ways and methods, and by referring to the literature, many studies in this field, including:

Awaeed et al.[8] was able to use polymeric waste such as poly (ethylene-terephthalate) taken from plastic water bottles in modifying the rheological specifications of asphalt. Different percentages of polymer were used, the best of which was (8%) by weight of the asphalt mixture. The Marshall test was conducted and it was found that these the mixtures give maximum stability and rigidity voids are filled with asphalt when using this type of modification.

Firyal and Mohanad[9] were able to improve the flow properties of asphalt by adding several different polymers, namely Poly (Acrylonitrile-Co-Maleic anhydride), Poly (Indene-Co-Maleic anhydride), and Poly (Dipentine-Co-Maleic anhydride), and using sulfur. The results are high properties of these mixtures when compared with original asphalt. All improvements include increased asphalt viscosity, thermal sensitivity, increased asphalt cohesion, increased resistance to permanent deformation, improved impact resistance at low temperatures, and improved binder adhesion (viscosity is higher than that of the binder).

Soultan[10] studied the addition of different percentages (1, 2, 3, 4, 5, 6, 7, 8%) of polypropylene to bitumen (60–70). It was able to improve the properties of asphalt in terms of increasing its resistance and tolerance to high temperatures under various climatic conditions. The study was conducted Tests on modified bitumen samples included penetration, ductility, softening, penetration index calculation, and using the RTFOT rotary thin-layer oven. Bitumen compounds were also identified by performing a structural diagnosis of its constituent groups. Results showed that the ideal percentage of polypropylene added was (7%).

Lin et al.[11] were able to improve the attributes of asphalt by using quick waste bags (WEBs), which are difficult to recycle. The results showed increase in viscosity and decrease in penetration and softening. Results of FT-IR spectroscopy showed that the modification was physical without a chemical reaction occurring. Khiavi et al.[12] modified the rheological properties at high temperature to bitumen by adding Polymer 2 hydroxyethyl methacrylate (PHEMA) in different proportions (3%, 5% and 7% by weight), the samples were in the form of homogeneous mixtures. The obtained results show that enhancement in the resistance of permanent deformation of the asphalt at high temperatures, from through multiple measurements light scanning, penetration, softening and viscosity. Fournier et al. [13]studied the possibility of using construction and demolition waste (CDW) to obtain recycled coarse aggregate suitable for manufacturing hot mix asphalt (HMA), which makes this mixture economically beneficial due to reducing the acquisition of aggregate from natural sources as well as maintaining a healthy and clean environment.

Hamedi et al. [14]were also able to modify asphalt with the polymer styrene-butadiene rubber (SBR), and the results obtained showed that the polymer added to the mixture produced a good improvement through the change observed in the moisture susceptibility of the axle asphalt, and this was confirmed by repeated loading tests under dry and wet conditions. Salih et al.[15] using solid waste represented by PVA in addition to spent lubricating oils to enhance the characteristics of the bitumen. The process was carried out at a temperature of (180 °C) in the presence of anhydrous aluminum chloride at one time and sulfur at other times. The results showed an enhancement in the properties of bitumen compared to original bitumen. The measurements were repeated again after 12 months. AL-Shabani and Obaid[16] were able to study the use of reclaimed asphalt paving (RAP) with a ratio of (15, 30, and 45%) and the polymer polystyrene butadiene styrene (SBS) with a ratio of 4% on the properties of the asphalt mixture. Mineral fillers made of Ordinary Portland Cement (OPC) were also used. It was concluded that the use of polymer in the asphalt mixture led to a significant improvement in its performance.

The process of obtaining good asphalt samples that can be used in different fields is a difficult process, especially since their use varies according to the weather conditions of the area of use. This research is focused on using waste industrial polymers PS, PFR, and PP for the purpose of modifying the rheological characteristics of asphalt to determine its suitability for use in a specific field. Waste polymeric materials used instead of virgin materials for purpose of reducing environmental pollution, reducing costs of modification. The treatment was carried out using two methods: physical treatment based on mixing thermally broken down polymeric materials with asphalt and Chemical treatment.

2. Experimental

2. 1. Material and Characterization

This section includes an explain of the initialization mechanism for carrying out the asphalt improvement process by mentioning the materials used, and the devices used to measure the properties of asphalt. It also mentions the initialization of the polymeric materials that will be used in the asphalt treatment process.

2. 1. 1. Raw Materials

Asphalt: AL-Doura asphalt was used as a raw material for treatment and was characterized by the properties shown below:

Table 1. Rheological properties of asphalt material

Properties	Experimental Value
Softening point (°C)	50
Penetration, mm (100g, 5sec, 25 °C)	45.5
Ductility (cm, 25 °C)	+100
Asphaltene %	18

n-Hexane (Obtained from Fluka company), and Polystyrene, Phenol-Formaldehyde Resin, Polypropylene Obtained from waste materials from which they are manufactured, Anhydrous Ferric Chloride (Obtained from Fluka company), Sulfur.

2. 1. 2. Characterization Methods

Ring and Ball Apparatus: The measurement was conducted using ASTM (D36-95), which are internationally dependent.[17] Penetrometer: The measurement was based on ASTM (D5/D5 M-13), which are internationally approved.[18] Ductility: The measurement was conducted using ASTM(D113-07) internationally dependent.[19]

Treatment apparatus asphalt by polymers: The device consists of the following parts:

1. A large glass round (200 ml) three necked flask
2. A mechanical motor mounted on the middle opening of the flask.
3. Electrical mental equipped with a regulator to control the temperature.
4. A thermometer installed in one of the side openings.
5. An iron stand equipped with a holder to fixed the flask.

2. 2. Preparing the Polymeric Materials for the Reaction

The polymeric waste was subjected to a mechanical and thermal crushing process before being mixed and reacted with asphalt to obtain polymeric materials that have a little molecular weight. This process was carried out based on thermo-gravimetric analysis.

The polystyrene sheets were crushed into small pieces, then placed in a ceramic crucible and heated for a full hour at a temperature of (350 °C). Then it was cooled and ground until it became a fine powder. The phenol-formaldehyde resin was prepared in the same way as the previous thermal cracking method, with the difference in heating time, which reached half an hour and at a temperature of (400 °C). By thermal cracking method, which was done on polystyrene sheets, polypropylene was broken.

2. 3. Asphalt Treatment

Asphalt was treated with polymeric materials through two paths:

2. 3. 1. The First Path: Physical Treatment Procedure

This treatment included physical mixing of polymeric materials in weight ratios (3%, 6%, 9%, 12%, 15%) with specific weights of asphalt that were weighed accurately and using the processing device described as above. The mixing continues for an hour at a temperature (160)°C, and after completing the treatment, the necessary rheological measurements were carried out for the prepared asphalt samples.

2. 3. 2. The Second Path: Chemical Treatment Procedure

This treatment was carried out by conducting a chemical reaction between certain quantities of accurately weighed asphalt and weight percentages (3%, 6%, 9%, 12%, 15%) of the polymeric materials, using anhydrous ferric chloride as a catalyst, and in the presence of sulfur, as the asphalt is mixed well with the polymer. And also, using the treatment device referred as above, then 2% by weight of the catalyst and 1% sulfur were added, and the reaction continued for an hour at a temperature of (160 °C). After the end of the treatment, rheological measurements were carried out on the prepared asphalt samples.

2. 3. 3. De-Asphaltene

Placed a (2) g of asphalt material in a glass flask and weigh it accurately, add (80) ml of n-hexane at a ratio of (1:40) (g/ml), and shake the mixture using an electric shaker for two hours at zero degrees Celsius, and then leave the solution for Half an hour at laboratory temperature, then the precipitate was filtered and washed with sufficient amounts of n-hexane until the wash drops became colorless. The precipitate was then dried at laboratory temperature, then the percentage of the precipitate (asphaltenes) was weighed and calculated. Here we chose this ration of n-hexane according to research.[20]

3. Results and Discussion

Obtaining asphalt with excellent rheological specifications to suit the purposes for which it is used is extremely important. From this standpoint, this research focused on the use of three types of different polymers in terms of their compositional forms. The polymers (polystyrene, phenol-formaldehyde resin, polypropylene) were treated as described in the method of work, as the temperature used in these polymeric materials was inferred from the results of thermo-gravimetric analysis (TGA), which gives information about the temperatures at which the polymeric materials begin to break down. The amount of loss in polymer weight at those temperatures. (Table 2–4) and (Figure 1–3) show the curve of the results obtained.

The reason to use polymeric waste instead of commercial virgin materials is to reduce the cost of modification as well as the many environmental and economic benefits.

Table 2. TGA results for polystyrene

Temperature (°C)	Loss in Weight (gm)
0	*0.5006
100	0.4963
150	0.4932
200	0.4908
250	0.4271
300	0.3753
350	0.2506
400	0.1011
450	0.0664
500	0.0035

* Original weight

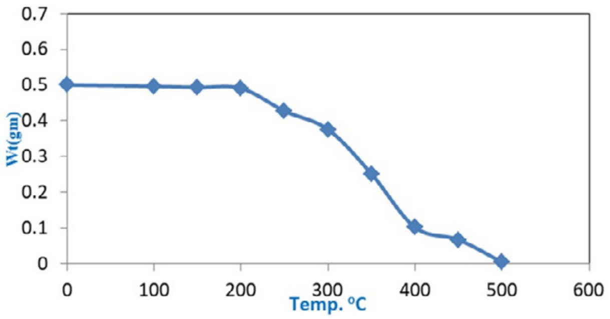

Figure 1. TGA curve for polystyrene

Table 3. TGA results for phenol-formaldehyde resin

Temperature (°C)	Loss in Weight (gm)
0	*1.0673
100	1.0412
150	0.9763
200	0.8345
250	0.5674
300	0.5210
350	0.4833
400	0.3075
450	0.2013
500	0.1909

* Original weight

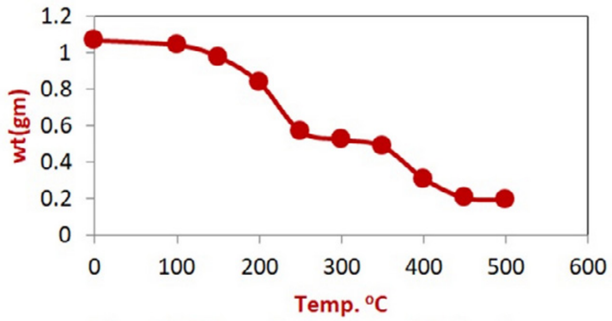

Figure 2. TGA curve for phenol-formaldehyde resin

Table 4. TGA results for polypropylene

Temperature (°C)	Loss in Weight (gm)
0	*1
100	0.9995
150	0.9975
200	0.9944
250	0.9424
300	0.8794
350	0.7478
400	0.5103
450	0.250
500	0.0001

* Original weight

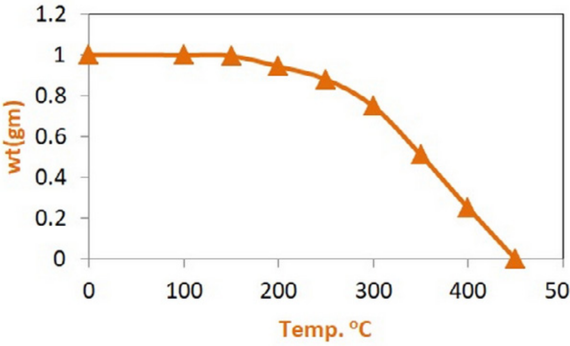

Figure 3. TGA curve for polypropylene

3. 1. Modifying Rheological Attributes of Asphalt by Physical Treatment

3.1.1. Asphalt Treatment with Polystyrene (AsPS)

Asphalt was treated with different percentages ranging between (3, 6, 9, 12, 15%) of polystyrene waste under the conditions shown below at a temperature of (160 °C) for one hour. The rheological properties of the treated asphalt were measured, including softening point, penetration, ductility, and the percentage of separated asphaltene, and the penetration index was calculated. These character-

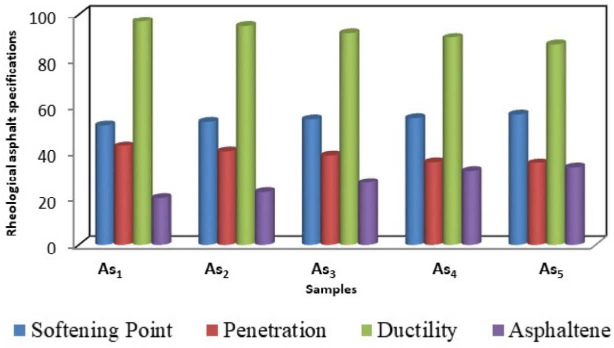

Figure 4. Rheological asphalt specifications mixed with various proportions of polystyrene

Table 5. Rheological asphalt specifications mixed with various proportions of polystyrene (PS) at temperature (160°C) for 1 hr.

Sample	%PS	Softening Point (°C)	Penetration, (100 g, 5 sec, 25 °C)	Ductility (cm, 25 °C)	Asphaltene %	Penetration Index (PI)
As_0	0	50	45.5	+100	18	–1.404
As_1	3	52	42.9	97	20.5	–1.052
As_2	6	53.5	40.5	95	23	–1.198
As_3	9	54.5	38.8	92	27	–1.415
As_4	12	55	36	90	32	–0.755
As_5	15	56.5	35.5	87	33.5	–0.567

As_0: Asphalt AL-Doura without treatment.

istics determine the suitability of the modified asphalt for use and the success of the treatment process. (Table 5) and (Figure 4) show the results of this treatment.

It is clear to us from Table 5 that the asphalt physically treated with polystyrene waste (AsPS) differed in its rheological properties from the original asphalt (As) by changing the degree of softening point, penetration and ductility. When the percentage of added polymer increased, it was observed that values of softening point increased, and values of penetration and ductility decreased. That is, the relationship between percentage of added polymer and softening point is a direct relationship, while the relationship is inverse with both penetration and ductility.

As for the Penetration Index (PI), it is a developed relationship linking the softening point of the sample and its penetration. The PI is considered a function of the extent of the sensitivity of the asphalt material and its effect on temperatures, and it can be calculated from the following mathematical relationship:[21]

$$\frac{20-\mathrm{PI}}{10+\mathrm{PI}} = 50\left[\frac{\log 800-\log \mathrm{pen.}}{T_{RB}-T}\right] \tag{1}$$

T_{RB} = softening point
T = temperature at which the penetration was measured 25 °C

3. 1. 2. Asphalt Treatment with Phenol-Formaldehyde Resin (AsPFR)

Mixing asphalt with different weight ratio of phenol-formaldehyde resin waste for the purpose of studying this type of additives on the resulting asphalt systems, (Table 6) and (Figure 5) shows the treatment results.

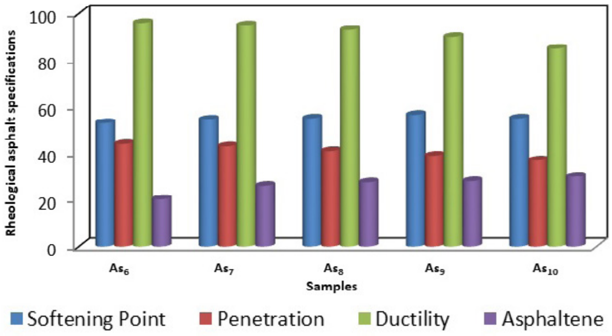

Figure 5. Rheological asphalt specifications mixed with various proportions of phenol-formaldehyde resin

It was observed from the table above a clear update in rheological asphalt specifications physically treatment by phenol-formaldehyde resin waste (AsPFR) comparison with source asphalt (As), where values of the softening point of the treated asphalt changed and increased with the increase in the ratio of added polymer, with the exception of (As_{10}) due to heterogeneity. The values of penetration and ductility decreased with increasing polymer ratio.

3. 1. 3. Asphalt Treatment with Polypropylene (AsPP)

Physically mixing asphalt with different ratio of polypropylene (AsPP), (Table 7) and (Figure 6) shows the treatment results.

It was noted from (Table 7) that asphalt physically treated with different ratio of AsPP generally led to product asphalt systems by rheological characteristics different

Table 6. Rheological asphalt specifications mixed with various proportions of phenol-formaldehyde resin (PFR) at temperature (160 °C) for 1 hr.

Sample	%PFR	Softening Point (°C)	Penetration, (100 g, 5 sec, 25 °C)	Ductility (cm, 25 °C)	Asphaltene %	Penetration Index (PI)
As_0	0	50	45.5	+100	18	–1.404
As_6	3	53	44	96	20.3	–0.769
As_7	6	54.5	43	95	26	–0.482
As_8	9	55	41	93	27.5	–0.479
As_9	12	56.5	39	90	28	–0.266
As_{10}	15	55	37	85	30	–0.697

Table 7. Rheological asphalt specifications mixed with various proportions of polypropylene (PP) at temperature (160°C) for 1 hr.

Sample	%PP	Softening Point (°C)	Penetration, mm (100 g, 5 sec, 25 °C)	Ductility (cm, 25 °C)	Asphaltene %	Penetration Index (PI)
As_0	0	50	45.5	+100	18	–1.404
As_{11}	3	52	41.9	95	21	–1.103
As_{12}	6	54.2	40.5	90	22	–0.680
As_{13}	9	55	39.4	81	28	–0.566
As_{14}	12	55.5	37.5	79	30	–0.560
As_{15}	15	57	36.8	75	32	–0.275

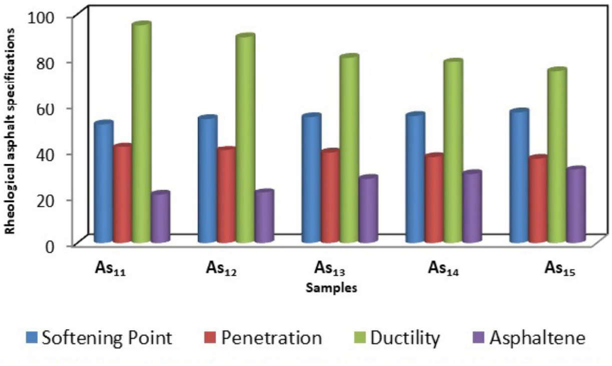

Figure 6. Rheological asphalt specifications mixed with various proportions of polypropylene

from original (As). Also note that the softening point is directly proportional to the ratio of PP added and inversely proportional to both penetration and ductility.

It was observed from the (Tables 5–7) shown previously that most of the asphalt samples (AsPP, AsPFR, AsPS) were characterized by good resistance to thermal sensitivity. This was demonstrated by calculating the PI values for these samples, as they generally increase with the increase in the ratio of polymer added.

It was also observed that there was a clear increase in the ratio of asphaltene for the three asphalt systems compared to the original (As), accompanied by an increase in the ratio of added polymer. This is due to the fact that the addition of polymers led to a change in the nature of the existing balances within the components of the asphalt system due to the relatively high molecular weight of these polymers.

When comparing the rheological properties of the three physically treated asphalt systems, it becomes clear to us that in terms of the softening point they were close, as the effect of physical mixing on the softening point is very similar despite the difference in the polymers used. The reason may be the lack of complete mixing with the asphalt.

As for the penetration point, it was observed that its values were similar for all the prepared asphalt systems. As for the ductility values, it was noted that the ductility values of the asphalt samples modified with polystyrene with a linear composition were higher than the ductility values of the asphalt modified with polypropylene. As for the asphalt modified with phenol-formaldehyde resin, the prepared samples appeared with higher values. Average between the rest of the other modified samples.

As for the ratio of asphaltene for the three asphaltene systems, it was noted that it was higher compared to the original asphalt. It is believed that the reason for this is due to the interference of some of the polymeric molecules with asphaltene-like materials, and thus they will precipitate and the ratio of asphaltene will increase.

3. 2. Modifying the Rheological Properties of Asphalt Through Chemical Treatment

Asphalt was treated by conducting a chemical reaction between the asphalt and the polymeric material, using anhydrous ferric chloride as a catalyst and in the presence of sulfur. This catalyst was chosen based on what was indicated in the scientific literature, and the choice of the sulfur percentage of 1% was based on a previous study.[22]

3. 2. 1. Asphalt Treatment with Polystyrene (AsPS)

This treatment depends on linking the polystyrene molecule with the asphalt molecule with existence sulfur, anhydrous ferric chloride as a catalyst for this process, (Table 8) and (Figure 7) shows the results of this treatment.

It was noted from the table above that the chemical treatment of asphalt with polystyrene (AsPS) led to a change in its rheological properties from the original (As), and a clear increase in softening values was also observed

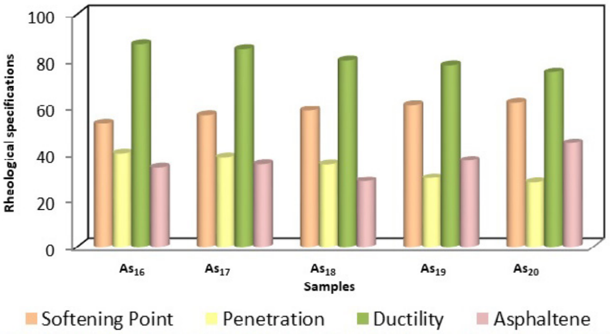

Figure 7. Rheological specifications of chemically treated asphalt with various ratio of polystyrene

Table 8. Rheological specifications of chemically treated asphalt with various ratio of polystyrene (PS) at temperature (160 °C), catalyst ratio (2% $FeCl_3$) and (1%) sulfur for an hour

Sample	%PP	Softening Point (°C)	Penetration, mm (100 g, 5 sec, 25 °C)	Ductility (cm, 25 °C)	Asphaltene %	Penetration Index (PI)
As_0	0	50	45.5	+100	18	−1.404
As_{16}	3	53	40.1	87	34	−0.966
As_{17}	6	56.5	38.5	85	35.4	−0.297
As_{18}	9	58.5	35.3	80	28.2	−0.076
As_{19}	12	61	29.5	78	37	+0.045
As_{20}	15	62	27.6	75	44.5	+0.077

with an increase in the ratio of added polymer in the prepared asphalt samples, accompanied by a decrease in the values of penetration and ductility.

3. 2. 2. Asphalt Treatment with Phenol-Formaldehyde resin (AsPFR)

This treatment depends on linking the phenol-formaldehyde resin (PFR) molecule with the asphalt molecule with existence sulfur and anhydrous ferric chloride as a catalyst for this process. (Table 9) and (Figure 8) shows the results of this treatment.

Looking at the results recorded in (Table 9), it was noted that treating asphalt with this polymeric material led to increase softening point of modified asphalt samples (AsPFR), while remaining constant at (58 °C) despite the increase in the ratio of polymer, while the values of the penetration point and ductility decreased. It also led to this is due to the increase in the ratio of asphaltene, which increases with the increase in the ratio of polymer.

3. 2. 3. Asphalt Treatment with Polypropylene (AsPP)

This treatment depends on linking the polypropylene molecule with the asphalt molecule with existence sulfur, anhydrous ferric chloride as a catalyst for this process. (Table 10) and (Figure 9) shows the results of this treatment.

Following the samples shown in (Table 10), it was observed that there was a clear increase in the softening values of the modified asphalt samples (AsPP) with an increase in the ratio of added polymer, accompanied by a decrease in the values of penetration and ductility.

Table 9. Rheological specifications of chemically treatment asphalt with various ratio of phenol-formaldehyde resin (PFR) at temperature (160 °C), catalyst ratio (2% $FeCl_3$) and (1%) sulfur for an hour

Sample	%PFR	Softening Point (°C)	Penetration, mm (100 g, 5 sec, 25 °C)	Ductility (cm, 25 °C)	Asphaltene %	Penetration Index (PI)
As_0	0	50	45.5	+100	18	−1.404
As_{21}	3	55.5	38	90	27	−0.430
As_{22}	6	56	35	86	30	−0.598
As_{23}	9	57	33.5	83	32.5	−0.485
As_{24}	12	58	31	73	33	−0.442
As_{25}	15	58	29.5	70	40	−0.542

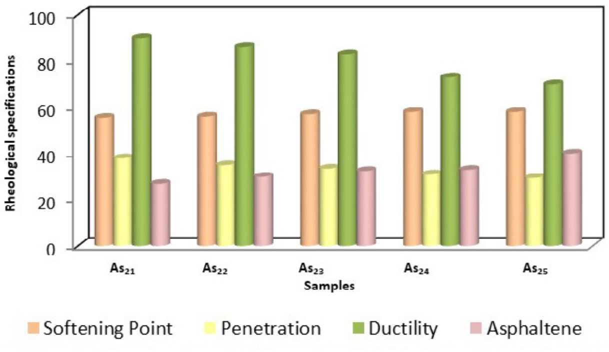

Figure 8. Rheological specifications of chemically treatment asphalt with various ratio of phenol-formaldehyde resin

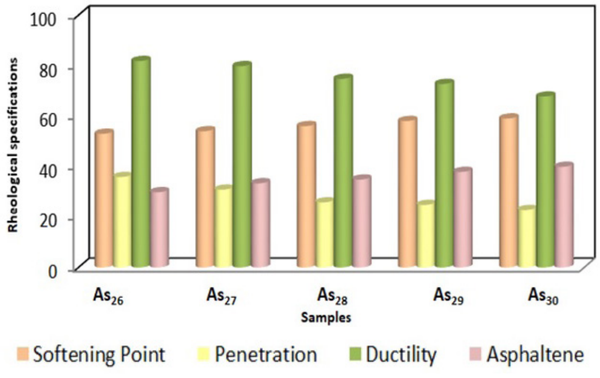

Figure 9. Rheological specifications of chemically treated asphalt with various ratio of polypropylene

Table 10. Rheological specifications of chemically treated asphalt with various ratio of polypropylene (PP) at temperature (160 °C), catalyst ratio (2% $FeCl_3$), and (1%) sulfur for an hour.

Sample	%PP	Softening Point (°C)	Penetration, mm (100 g, 5 sec, 25 °C)	Ductility (cm, 25 °C)	Asphaltene %	Penetration Index (PI)
As_0	0	50	45.5	+100	18	−1.404
As_{26}	3	53	36	82	30	−1.189
As_{27}	6	54	31	80	33.5	−1.263
As_{28}	9	56	26	75	35	−1.179
As_{29}	12	58	25	73	38	−0.856
As_{30}	15	59	23	68	40	−0.817

When comparing the rheological specifications of chemically treated asphalt systems (AsPP, AsPFR, AsPS), it was noted that there is a clear discrepancy in terms of the values of the softening point. It was found that the asphalt modified with polystyrene has the highest values of softening, the lowest than that treated with polypropylene, and the least than both treated with phenol-formaldehyde resin. It is believed The reason for this is that thermally broken polystyrene has more active sites, which makes the possibility of chemical bonding (chemical reaction in the presence of $FeCl_3$, sulfur) of the polystyrene molecule to the asphalt molecule to a greater degree than the other two polymers. This is clear from the rise in asphaltene values and also reflected in the decrease penetration values.

The increase in the polymer ratio led to an increase in the amount of non-reactive polymeric materials, which affected the ductility and penetration values and made them lower than the original, and this may also be reflected in the penetration index (PI) values.

As for the ductility values of asphalt treated with polystyrene (AsPS), we find that they are higher than the ductility values of polypropylene (AsPP), despite the lower penetration values and higher softening point of the (AsPS) system compared to the (AsPFR) system. The reason for this may be attributed to the association of the linear polystyrene molecule with asphalt chemical compositions, it contributed to imparting ductility properties to a higher degree than asphalt linked to PP.

After looking at the results obtained, it was found that part of these samples, especially those resulting from chemical treatment were characterized by high softening points and low penetration and ductility values that qualify them for use in the production of Mastic, which is used as water proofing material. It has many uses and in wide fields, such as its use for the purposes of roofing, surfacing, and covering pipes for transporting liquids and gases under the surface of the earth to prevent their corrosion and collapse, based on the standard specifications shown in (Table 11–13).

Table 11. American standard specifications ASTMD (D491-41) for asphalt used to produce mastic[23]

Rheological Measurements	Minimum	Maximum
Softening point (°C)	54	65
Penetration, mm (100g, 5sec, 25 °C)	20	40
Ductility (cm, 25 °C)	15	---

Table 12. Specifications of American standards ASTM (D491-41) for mastic asphalt used as a moisture insulating material[24]

Rheological Measurements	Minimum	Maximum
Softening point (°C)	50	70
Penetration, mm (100g, 5sec, 25°C)	15	40
Ductility (cm, 25 °C)	15	---

Table 13. Iraqi standard specifications for asphalt used in surfacing[25]

Rheological Measurements	Minimum	Maximum
Softening point (°C)	57	66
Penetration, mm (100g, 5sec, 25°C)	18	40
Ductility (cm, 25°C)	10	---

4. Conclusions

Chemical treatment yields more favorable effects on the rheological properties of the asphalt systems compared to physical treatment methods. Both treatment approaches-chemical and physical-led to an increase in the separated asphaltene percentage within the modified asphalt, with the highest values recorded for AsPS (44.5%), AsPFR (40%), and AsPP (40%). Among the tested polymers, chemically modifying asphalt with polystyrene had the most significant impact on enhancing rheological characteristics. Notably, some of the modified asphalt samples demonstrated rheological properties that make them suitable for applications as moisture and leakage-resistant materials (mastic), particularly when evaluated against both local and international performance standards.

Acknowledgements: At the end of this research, I can only extend my sincere thanks and appreciation to the University of Mosul and to the College of Engineering for the facilities provided to complete this research.

Conflicts of interest: The author has no potential conflict of interest.

5. References

1. C. Fang, C. Wu, J. Hu, R. Yu, Z. Zhang, L. Nie, S. Zhou, X. Mi, *J. Vinyl Addit. Technol.* **2014**, *20*, 31–35. **DOI:**10.1002/vnl.21328
2. H. Zhang, Z. Chen, G. Xu, C. Shi, *Fuel.* **2018**, *211*, 850–858. **DOI:**10.1016/j.fuel.2017.09.111
3. S. Sultana, A. Bhasin, *Constr. Build. Mater.* **2014**, *72*, 293–300. **DOI:**10.1016/j.conbuildmat.2014.09.022
4. A. M. Nejes, Y. F. Mustafa, H. Adewachi, *Int. J. Pave. Eng.* **2020**, *23*, 39–45. **DOI:**10.1080/10298436.2020.1728534
5. S. Mozaffari, P. Tchoukov, J. Atias, J. Czarnecki, N. Nazemifard, *Energ. Fuel* **2015**, *29*, 5595–5599. **DOI:**10.1021/acs.energyfuels.5b00918
6. K. A. A. AL-Ghannam, *PhD Thesis, University of Mosul.* **1996**.
7. D. Lesueur, *Adv. Colloid Inter. Sci.* **2009**, *145*, 42–82. **DOI:**10.1016/j.cis.2008.08.011
8. K. M. Awaeed, B. M. Fahad, D. A. Rasool, *J. Eng. Devel.* **2018**, *20*, 1–21. https://www.researchgate.net/publication/327848627
9. M. A. Firyal, Q. H. Mohanad, *J. Babylon University/ Pure and Appl. Sci.* **2018**, *26*, 150–162. https://www.researchgate.net/publication/371010059
10. B. Soultan, *Tishreen University J. Res. Sci. Stud. Eng. Sci. Ser.* **2018**, *40*, 12–22. https://journal.tishreen.edu.sy/index.php/engscnc/article/view/5743
11. Y. Lin, C. Hu, S. Adhikari, C. Wu, M. Yu, *Appl. Sci.* **2019**, *9*, 1–12. **DOI:**10.3390/app9061242
12. A. K. Khiavi, A. Ghanbari, E. Ahmadi, *J. Mater. Civil Eng.* **2020**, *32*, 1–11. **DOI:**10.1061/(ASCE)MT.1943-5533.0003070
13. J. M. Fournier, D. A. Alvarez, A. A. Aenlle, A. J. Tenza-Abril, S. Ivorra, *MDPI*. **2020**, *12*, 1–16. **DOI:**10.3390/su12135356
14. G. H. Hamedi, A. Sahraei, M. H. Pirbasti, *Peri. Polytech. Civil Eng.* **2021**¸ *65*, 546–555. **DOI:**10.3311/PPci.16691
15. W. M. Salih, A. A. Hamdoon , F. Abeed , M. Y. Saleh, M. A. Abdelzaher, *Egyptian J. Chem.* **2022**, *65*, 727–734. **DOI:**10.21608/ejchem.2022.144144.6287
16. Z. J. Al-Shabani, I. A. Obaid, *Iraq E3S Web of Confer.* **2023**, *427*, 1–10. **DOI:**10.1051/e3sconf/202342703019
17. American Society for Testing and Materials, D36–95. **2000**. Scribd.com/document/46807506/ASTM-D-36-95-softening-point-of-Bitumen-Ring-Ball-Apparatus-E. http://www.shxf17.com/pdf/ASTMD36-95.pdf
18. American Society for Testing Materials, D5/D5M-13, Standard test method for penetration of bituminous materials. **2013**.https://cdn.standards.iteh.ai/samples/ 83801/71be4df-9cbc845b3b7457816aab94d27/ASTM-D5-D5M-13.pdf
19. ASTM D 113-07, Standard Test Method for Ductility of Bituminous Materials, Annual Book of ASTM Standards. **2007**. https://cdn.standards.iteh.ai/samples/58339/257d8bb9b51d473999f33d590ee09fb6/ASTM-D113-07.pdf
20. L. H. Ali, K. A. AL-Ghannam, *Fuel.* **1981**, *60*, 1043–1046. **DOI:**10.1016/0016-2361(81)90047-8
21. American Society for Testing and Materials, D1559-2004, Standard Specification. **2004**. https://www.epa.gov/sites/default/files/2020-01/documents/sedc_2004-2005_append.pdf
22. N. Tang, W. Huang, J. Hu, F. Xiao, *Road Mater. Pave. Desi.* **2017**, *19*, 1288–1300. **DOI:**10.1080/14680629.2017.1305436
23. M. A. Abdelzaher, A. S. Hamouda, I. M. Ismail, M. A. El-Sheikh, *Key Eng. Mater.* **2018**, *786*, 248–257. **DOI:**10.4028/www.scientific.net/KEM.786
24. ASTM, American Society for Testing Materials, Part 11, D491–41. **1969**.
25. R. R. Matti, K. A. Owaid, *J. Edu. Sci.* **2019**, *29*, 26–44. **DOI:**10.33899/edusj.2020.165302

Povzetek

Namen raziskave je bil razvoj različnih vrst asfaltnih materialov z izboljšanimi reološkimi lastnostmi v primerjavi z nespremenjenim asfaltom. Uporabljene so bile tri vrste polimernih materialov (PS), (PFR) in (PP) za modifikacijo asfalta Al-Doura, s ciljem oceniti njihov vpliv na reološke lastnosti nastalih asfaltnih sistemov. Ti spremenjeni materiali so bili nato primerjani med seboj s tako lokalnimi kot mednarodnimi standardi za oceno njihove primernosti za specifične aplikacije. Uporabljeni so bili polimerni odpadni materiali namesto deviških polimerov za zmanjšanje okoljske onesnaženosti in znižanje stroškov modifikacije. Postopek modifikacije je bil izveden z uporabo dveh pristopov: fizikale in kemijske obdelave. Kemijska metoda je vključevala katalizirano reakcijo z uporabo 2% ($FeCl_3$) in 1% (S). Rezultati so pokazali, da je imela kemijska obdelava pomembnejši pozitiven učinek na reološke lastnosti asfaltnih sistemov v primerjavi s fizikalno obdelavo. V obeh pristopih je dodatek polimera pripeljal do povečanja % de-asfaltena, pri čemer so najvišje vrednosti beležili za AsPS (44,5%), AsPFR (40%) in AsPP (40%). Poleg tega je kemijsko modificiranje asfalta s PS prineslo najbolj opazne izboljšave med preizkušenimi polimeri. Na podlagi ključnih kazalnikov uspešnosti, kot so točka mehčanja, penetracija, duktilnost, indeks penetracije (PI) in odstotek asfaltenov, so modificirani vzorci asfalta pokazali primernost za uporabo pri proizvodnji mastik, ki se široko uporabljajo kot vodoodporen material.

DOI: 10.17344/acsi.2025.9313 *Acta Chim. Slov.* **2025,** *72,* 409–415

Scientific paper

Synthesis, Characterization and Crystal Structures of Nitrate and Tetrachloridocobalt(II) Salts of Cobalt(III) Complexes with Catalytic Epoxidation of Cyclooctene

Li-Fei Zou[1], Ya-Li Sang[1,*], Su-Wen Liu[2], Kai Wang[1], and Li-Min Wang[1]

[1] *Inner Mongolia Key Laboratory of Photoelectric Functional Materials, College of Chemistry and Life Science, Chifeng University, Chifeng 024000, P. R. China*

[2] *Professional Basic Teaching Department, Chifeng Industry Vocational Technology College, Chifeng 024000, P. R. China*

** Corresponding author: E-mail: sangyali0814@126.com*

Received: 05-08-2025

Abstract

Two new cobalt(III) complexes, $[CoL_2]NO_3$ (**1**) and $[CoL_2]_2[CoCl_4]$ (**2**), where L is 5-bromo-2-(((2-isopropylamino)ethyl)imino)methyl)phenolate, have been prepared and characterized by physico-chemical methods and single crystal X-ray analysis. X-ray analysis indicated that the Co atoms in both complexes are in octahedral coordination except for that in $[CoCl_4]$ unit which in a tetrahedral coordination. Crystal structures of complexes are stabilized by hydrogen bonds and π···π interactions. Catalytic property of both cobalt complexes was studied on the epoxidation of cyclooctene with *tert*-butylhydroperoxide (TBHP) as oxidant. Both complexes show good catalytic activity and high epoxides selectivity.

Keywords: Schiff base; Cobalt complex; Crystal structure; Catalytic property

1. Introduction

Schiff bases are readily synthesized by condensation reaction of carbonyl compounds with primary amines. Schiff bases have been widely investigated for their biological activities, such as antibacterial and antitumor activities.[1] Metal complexes of Schiff bases have also been received much attention. These complexes show interesting properties in catalytic and enzymatic reactions, magnetism and molecular architectures,[2] as well as biological activities.[3]

In the last years, Schiff base complexes have been widely used as catalysts for sulfoxidation,[4] epoxidation,[5] etc. Among the complexes, those with cobalt center have received particular attention in the field of catalytic epoxidation reaction.[6] The oxygen binding ability of cobalt complexes stimulated the study on reversible oxygen binding of cobalt complexes and their usage as catalysts.[7] Epoxides are important precursors for the production of a variety of fine chemicals. Thus, the catalytic epoxidation of alkenes is an important reaction. A number of cobalt complexes have shown remarkable and interesting catalytic properties for the epoxidation of olefins.[8] During search of literature, cobalt complexes with Schiff bases derived from 4-bromosalicylaldehyde are seldom reported. As continuation of this work to explore more efficient new catalysts, we report herein the synthesis, characterization, crystal structures, and catalytic properties of two new cobalt(III) complexes, $[CoL_2]NO_3$ (**1**) and $[CoL_2]_2[CoCl_4]$ (**2**), where L is 5-bromo-2-(((2-isopropylamino)ethyl)imino)methyl) phenolate (HL; Scheme 1).

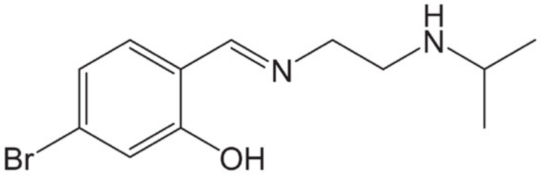

Scheme 1. The Schiff base HL.

2. Experimental

2. 1. Materials and Measurements

4-Bromosalicylaldehyde and *N*-isopropylethane-1,2-diamine with AR grade were obtained from Aldrich and used as received. Cobalt nitrate and cobalt chloride were purchased from TCI. Elemental analyses were performed using a Perkin-Elmer 240C analytical instrument. Infrared spectra were recorded on a Nicolet 5DX FT-IR spectrophotometer with KBr pellets. Molar conductance was measured with a Shanghai DDS-11A conductometer.

2. 2. Synthesis of $[CoL_2]NO_3$ (1)

4-Bromosalicylaldehyde (0.20 g, 1.0 mmol) and *N*-isopropylethane-1,2-diamine (0.10 g, 1.0 mmol) were dissolved in methanol (30 mL). To the mixture was added cobalt nitrate hexahydrate (0.29 g, 1.0 mmol). A brown solution was formed immediately. After 20 min stirring, the solution was filtered and the filtrate was kept for slow evaporation. The diffraction quality colorless single crystals that deposited over a period of a few days were collected by filtration and washed with methanol. The yield was 0.13 g (38%). Anal. Calcd. for $C_{24}H_{32}Br_2CoN_5O_5$ (%): C, 41.82; H, 4.68; N, 10.16. Found: C, 41.66; H, 4.61; N, 10.33. IR data (KBr, cm^{-1}): 3164, 1647, 1585, 1521, 1466, 1450, 1408, 1385, 1344, 1323, 1288, 1245, 1203, 1175, 1139, 1084, 1062, 1031, 977, 935, 913, 853, 798, 790, 730, 678, 620, 600, 561, 470. UV-Vis data in methanol [λ_{max} (nm), ε (L mol^{-1} cm^{-1})]: 225, 15370; 257, 18210; 378, 1923.

2. 3. Synthesis of $[CoL_2]_2[CoCl_4]$ (2)

4-Bromosalicylaldehyde (0.20 g, 1.0 mmol) and *N*-isopropylethane-1,2-diamine (0.10 g, 1.0 mmol) were dissolved in methanol (30 mL). To the mixture was added cobalt chloride hexahydrate (0.24 g, 1.0 mmol). A brown solution was formed immediately. After 20 min stirring, the solution was filtered and the filtrate was kept for slow evaporation. The diffraction quality colorless single crystals that deposited over a period of a few days were collected by filtration and washed with methanol. The yield was 0.22 g (30%). Anal. Calcd. for $C_{48}H_{64}Br_4Cl_4Co_3N_8O_4$ (%): C, 39.61; H, 4.43; N, 7.70. Found: C, 39.45; H, 4.53; N, 7.76. IR data (KBr, cm^{-1}): 3177, 1647, 1585, 1523, 1465, 1450, 1410, 1345, 1326, 1291, 1245, 1203, 1175, 1141, 1082, 1062, 1027, 975, 935, 911, 853, 798, 787, 722, 667, 635, 593, 560, 543, 475. UV-Vis data in methanol [λ_{max} (nm), ε (L mol^{-1} cm^{-1})]: 225, 16120; 260, 17870; 380, 2105.

2. 4. X-Ray Crystallography

Suitable single crystals of the complexes were selected and mounted on a Bruker Smart 1000 CCD area-detector diffractometer with graphite monochromatized Mo-Ka radiation (l = 0.71073 Å). Diffraction data for the compounds were collected by ω scan mode at 298(2) K. Data reduction and cell refinement were performed by the SMART and SAINT programs.[9] Empirical absorption correction was applied by using SADABS.[10] The structures were solved by direct methods and refined with the full-matrix least-squares technique using SHELXL97.[11] The non-H atoms in the structures were subjected to refined anisotropic refinement. The hydrogen atoms were located in geometrically and treated with the riding mode. Crystallographic data and experimental details for the compounds are summarized in Table 1. Selected bond lengths and angles for the compounds are listed in Table 2.

2. 5. Catalytic Oxidation Reaction

The two cobalt complexes were tested as catalysts for the oxidation of cyclooctene with TBHP as oxidant. The reaction was monitored by gas chromatography at 60 min

Table 1. Crystallographic data for the two cobalt complexes

	1	2
Molecular formula	$C_{24}H_{32}Br_2CoN_5O_5$	$C_{48}H_{64}Br_4Cl_4Co_3N_8O_4$
Molecular weight	689.30	1455.30
Crystal system	Monoclinic	Orthorhombic
Space group	*C2/c*	*Fddd*
a, Å	21.4695(15)	16.4270(17)
b, Å	12.7142(13)	25.7287(18)
c, Å	12.4588(13)	27.0688(18)
α, °	90	90
β, °	125.178(1)	90
γ, °	90	90
V, Å^3	2779.7(5)	11440.5(16)
Z	4	8
ρ_{calcd}, g cm^{-3}	1.647	1.690
μ, mm^{-1}	3.535	3.889
Reflections collected/unique	14875/2589	14744/2676
Observed reflections ($I \geq 2\sigma(I)$)	2229	1902
Data/restraints/parameters	2589/0/171	2676/0/164
GOOF on F^2	1.048	1.011
R_1, wR_2 ($I \geq 2\sigma(I)$)	0.0289, 0.0718	0.0444, 0.1019
R_1, wR_2 (all data)	0.0367, 0.0761	0.0699, 0.1166

Table 2. Selected bond distances (Å) and angles (°) for the two cobalt complexes

1			
Co(1)–O(1)	1.8970(17)	Co(1)–N(1)	1.905(2)
Co(1)–N(2)	2.034(2)		
O(1)–Co(1)–O(1A)	87.74(11)	O(1)–Co(1)–N(1A)	86.65(8)
O(1)–Co(1)–N(1)	94.29(8)	N(1)–Co(1)–N(1A)	178.69(13)
O(1)–Co(1)–N(2A)	90.39(8)	N(1)–Co(1)–N(2A)	94.46(8)
O(1)–Co(1)–N(2)	177.89(8)	N(1)–Co(1)–N(2)	84.62(8)
N(2)–Co(1)–N(2A)	91.50(12)		
Symmetry code: A) 1 – *x*, –*y*, –*z*.			
2			
Co(1)–O(1)	1.891(3)	Co(1)–N(1)	1.911(4)
Co(1)–N(2)	2.030(4)		
O(1)–Co(1)–O(1B)	88.93(18)	O(1)–Co(1)–N(1B)	84.55(14)
O(1)–Co(1)–N(1)	92.88(14)	N(1)–Co(1)–N(1B)	176.4(2)
O(1)–Co(1)–N(2B)	90.32(13)	O(1)–Co(1)–N(2)	177.38(13)
N(1)–Co(1)–N(2)	84.55(15)	N(1)–Co(1)–N(2B)	97.99(15)
N(2)–Co(1)–N(2B)	90.5(2)		
Cl(1)–Co(2)–Cl(1B)	106.50(8)	Cl(1)–Co(2)–Cl(1C)	109.95(11)
Cl(1)–Co(2)–Cl(1D)	112.01(11)		
Symmetry codes: B) 5/4 – *x*, *y*, 5/4 – *z*; C) 5/4 – *x*, 5/4 – *y*, *z*; D) *x*, 5/4 – *y*, 5/4 – *z*.			

intervals in different solvents and conditions. The retention times for the starting materials and the products were determined by comparison with authentic samples. In the absence of the catalysts, very little products were formed. Cycloocteneoxide is the major product of the oxidation process with cyclooctene as the starting material. The catalyst (10 μmol) was dissolved in solvent (10 mL) and cyclooctene (15 mmol) and TBHP (30 mmol) were added. The mixture was stirred under reflux and with the reaction monitored at 60 min intervals by gas chromatography.

3. Results and Discussion

3. 1. Chemistry

Complexes **1** and **2** were prepared by *in situ* reaction of 4-bromosalicylaldehyde, *N*-isopropylethane-1,2-diamine, with cobalt nitrate and cobalt chloride, respectively in methanol (Scheme 2). As usually observed for the preparation of cobalt complexes, Co^{II} in $[CoL_2]$ units underwent aerial oxidation to Co^{III} in the synthetic route of both complexes. The molar conductivities of the complex-

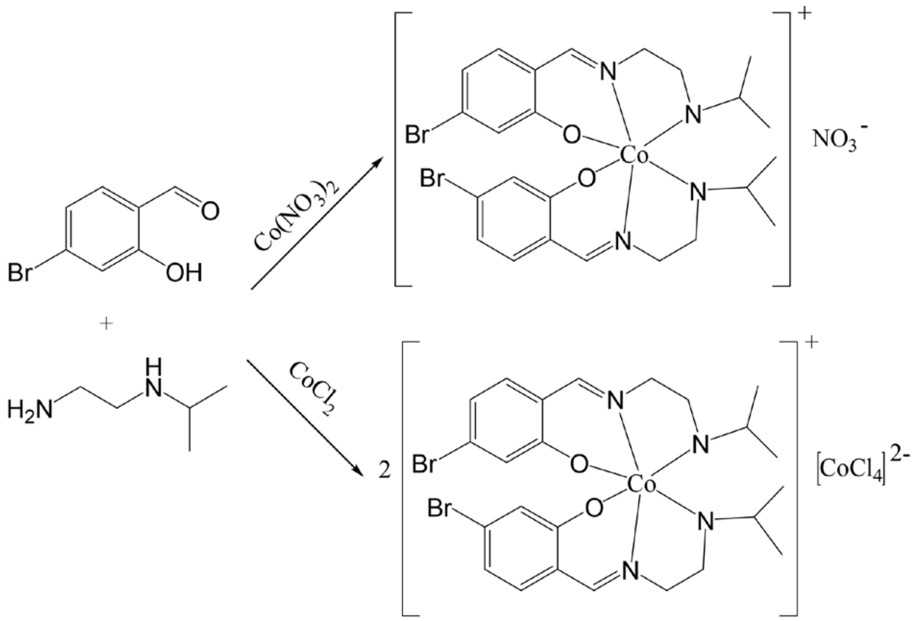

Scheme 2. The synthetic route for both complexes.

es **1** and **2** measured in methanol at concentration of 10^{-3} mol L^{-1} are 223 and 345 Ω^{-1} cm^2 mol^{-1}, indicating the 1:1 and 1:2 electrolytic nature of the complexes in solution.[12]

3. 2. Infrared and Electronic Spectra

In the infrared spectra of the complexes, the weak absorptions in the range 3164–3177 cm^{-1} are assigned to the N–H vibrations of the Schiff base ligands. The characteristic imine stretching is observed at 1647 cm^{-1} as strong signal.[13] The spectrum of complex **1** shows an intense band at 1385 cm^{-1} characteristic of ionic nitrate.[14] The Schiff base ligands coordination is substantiated by the phenolic C–O stretching bands at 1175 cm^{-1} in the complexes.[15] Coordination of the Schiff bases is further confirmed by the appearance of weak bands in the low wave numbers 400–600 cm^{-1}, corresponding to ν(Co–N) and ν(Co–O).[16]

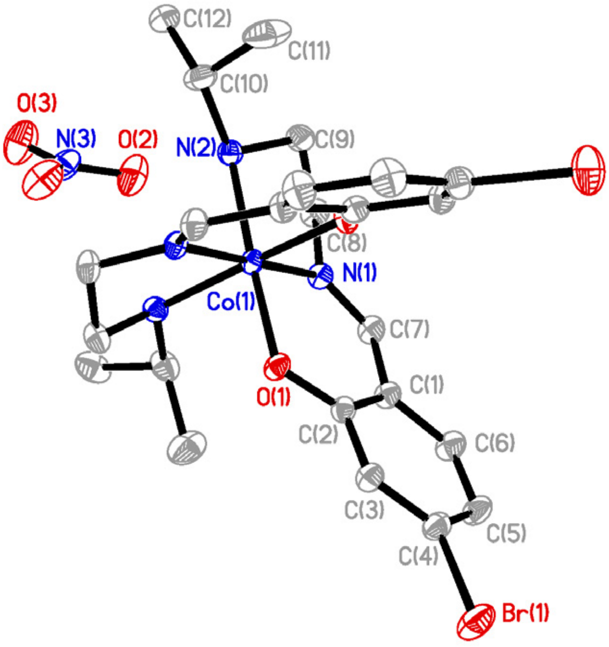

Fig. 1. Molecular structure of complex **1**. Unlabeled atoms are related to the symmetry operation 1 – *x*, *y*, ½ – *z*.

In the UV-Vis spectra of the complexes, the bands at 225 nm and 257–260 nm are attributed to the *π*-*π** and *n*-*π** transitions.[17] The bands at 378–380 nm can be attributed to the ligand to metal charge transfer transition (LMCT).[18]

3. 3. Crystal Structure Description of the Complexes

Molecular structures of complexes **1** and **2** are shown in Figs. 1 and 2, respectively. Complex **1** contains a $[CoL_2]^+$ cation and a nitrate anion, and complex **2** contains two $[CoL_2]^+$ cations and a $[CoCl_4]^{2-}$ anion. The Co atom in each $[CoL_2]^+$ cation is coordinated by two phenolate oxygen, two imino nitrogen and two amino nitrogen from two Schiff base ligands, forming octahedral coordination. The equatorial plane of the octahedral coordination is defined by O(1), N(1), N(2) and N(1A) atoms, and the axial positions are occupied by O(1A) and N(2A) atoms. The octahedral geometry is distorted from ideal model, as evidenced by the bond angles. The *cis* and *trans* angles in the octahedral coordination are in the ranges of 84.62(8)–94.46(8)° and 177.89(8)–178.69(8)° for **1**, and 84.55(15)–97.99(15)° and 176.4(2)–177.38(13)° for **2**, respectively. The Co–O and Co–N bond lengths are comparable to those observed in Schiff base cobalt complexes.[19] The Co atom in the $[CoCl_4]^{2-}$ anion is in a tetrahedral coordination, with the bond angles ranging from 106.50(8) to 112.01(11)°.

As shown in Fig. 3, the nitrate anions in complex **1** are linked to the complex cations through N–H···O hydrogen bonds (Table 3), to form a dimer. In addition, there are π···π interactions among the molecules (Cg(3)···Cg(3)^b 4.320(5) Å, symmetry code: b) –*x*, 1 – *y*, 1 – *z*; Cg(3) is the centroid of C(1)–C(2)–C(3)–C(4)–C(5)–C(6)). As shown in Fig. 4, the $[CoCl_4]^{2-}$ anions and the complex cations in complex **2** are linked through N–H···Cl and C–H···Cl hydrogen bonds (Table 3), to form two-dimensional sheets parallel to the *bc* plane. In addition, there are π···π interac-

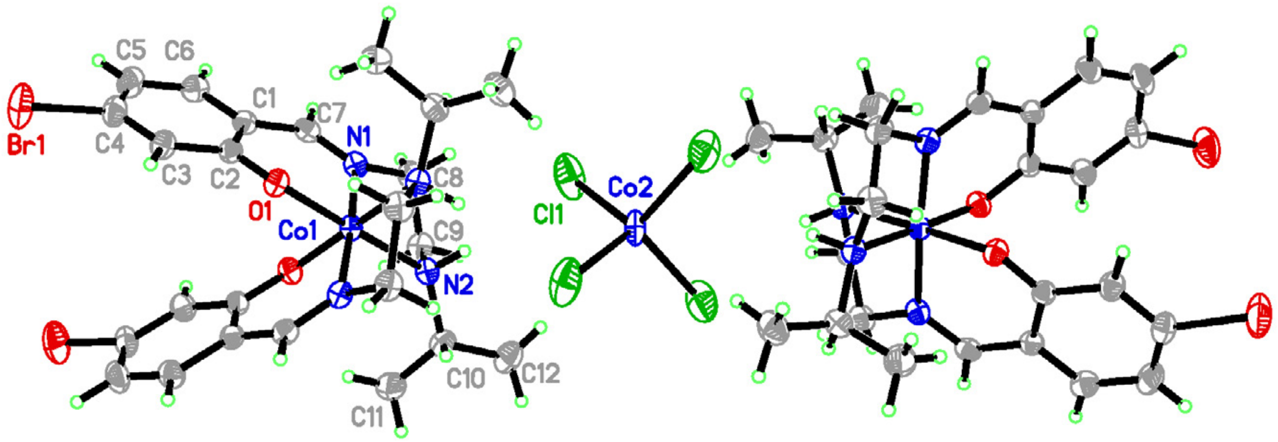

Fig. 2. Molecular structure of complex **2**. Unlabeled atoms are related to the symmetry operations 5/4 – *x*, *y*, 5/4 – *z* and 5/4 – *x*, 5/4 – *y*, *z*.

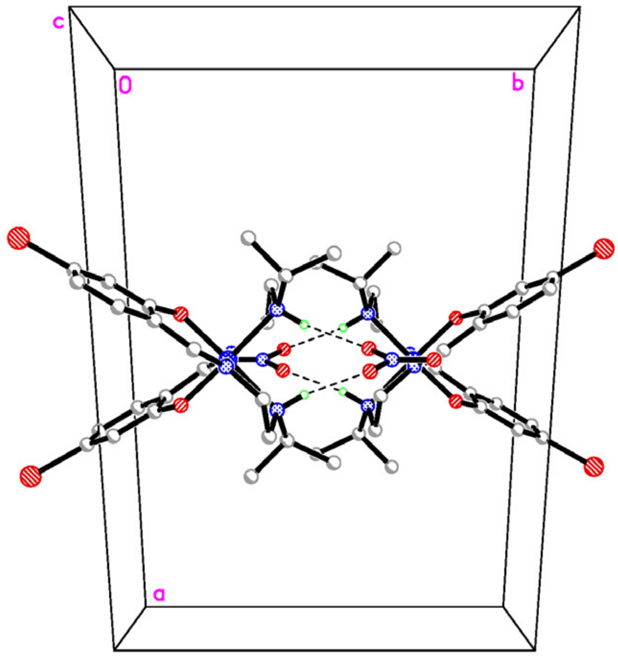

Fig. 3. Molecular packing structure of complex **1**, viewed along the *c* axis. Hydrogen bonds are shown as dashed lines.

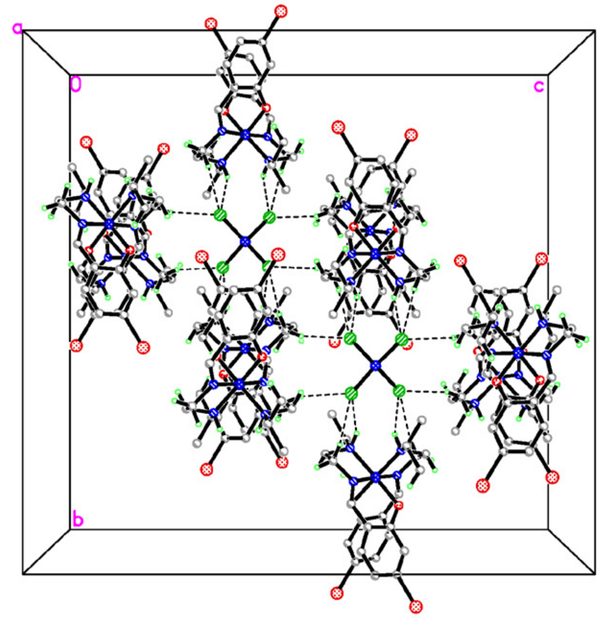

Fig. 4. Molecular packing structure of complex **2**, viewed along the *a* axis. Hydrogen bonds are shown as dashed lines.

tions among the molecules (Cg(4)···Cg(4)^{c} 4.461(5) Å, symmetry code: c) ¼ – *x*, *y*, ¼ – *z*; Cg(4) is the centroid of C(1)–C(2)–C(3)–C(4)–C(5)–C(6)).

3. 4. Catalytic Property

The catalytic oxidation of cyclooctene with the two cobalt complexes as catalysts produced three products 9-oxa-bicyclo[6.1.0]nonane, cyclooct-2-enol and cyclooct-2-enone. Reaction conditions such as solvent, reaction time, catalyst, as well as oxidant to substrate ratio were optimized. Each catalyst (10 μmol) was dissolved in methanol (10 mL). Then, cyclooctene (15 mmol) and TBHP (30 mmol) were added. The mixture was stirred at reflux for 36 h. The reaction was monitored at 60 min intervals by gas chromatography. As a result, the conversion increased up to 20 h and reached the limit. Thus, 20 h was chosen as the optimized reaction time. Both complexes have similar properties and complex **1** was chosen to investigate the effect of other variables. The solvent type, catalyst load, and the oxidant to substrate ratio were shown as Fig. 5. Methanol is the best solvent for this reaction. The conversion of both complexes as catalysts is over than 75%, and epoxide selectivity is over 56% (Table 4). The catalytic performance of the present complexes is comparable with those reported in literature.[20]

Table 4. The catalytic results for the two cobalt complexes.

Complex	Conversion (%)	Selectivity (%)		TON
		Epoxide	Other products	
1	78	58	42	1167
2	75	56	44	1128

Table 3. Hydrogen bond distances (Å) and bond angles (°) for the complexes

D–H···*A*	*d*(*D*–H)	*d*(H···*A*)	*d*(*D*···*A*)	Angle (*D*–H···*A*)
1				
N(2)–H(2)···O(2)$^{\#1}$	0.91	2.59	3.375(3)	146(5)
N(2)–H(2)···O(2)$^{\#2}$	0.91	2.18	3.059(3)	161(5)
2				
N(2)–H(2)···Cl(1)$^{\#3}$	0.91	2.68	3.501(4)	151(6)
C(8)–H(8A)···Cl(1)$^{\#3}$	0.97	2.66	3.478(4)	142(6)
C(8)–H(8B)···Cl(1)$^{\#4}$	0.97	2.66	3.585(4)	159(6)
C(11)–H(11A)···O(1)$^{\#5}$	0.96	2.46	3.151(4)	129(6)

Symmetry codes: #1: –*x*, –*y*, 1 – *z*; #2: *x*, –*y*, –½ + *z*; #3: –½ + *x*, ½ + *y*, *z*; #4: ½ – *x*, ½ – *y*, –*z*; #5: ¼ – *x*, *y*, ¼ – *z*.

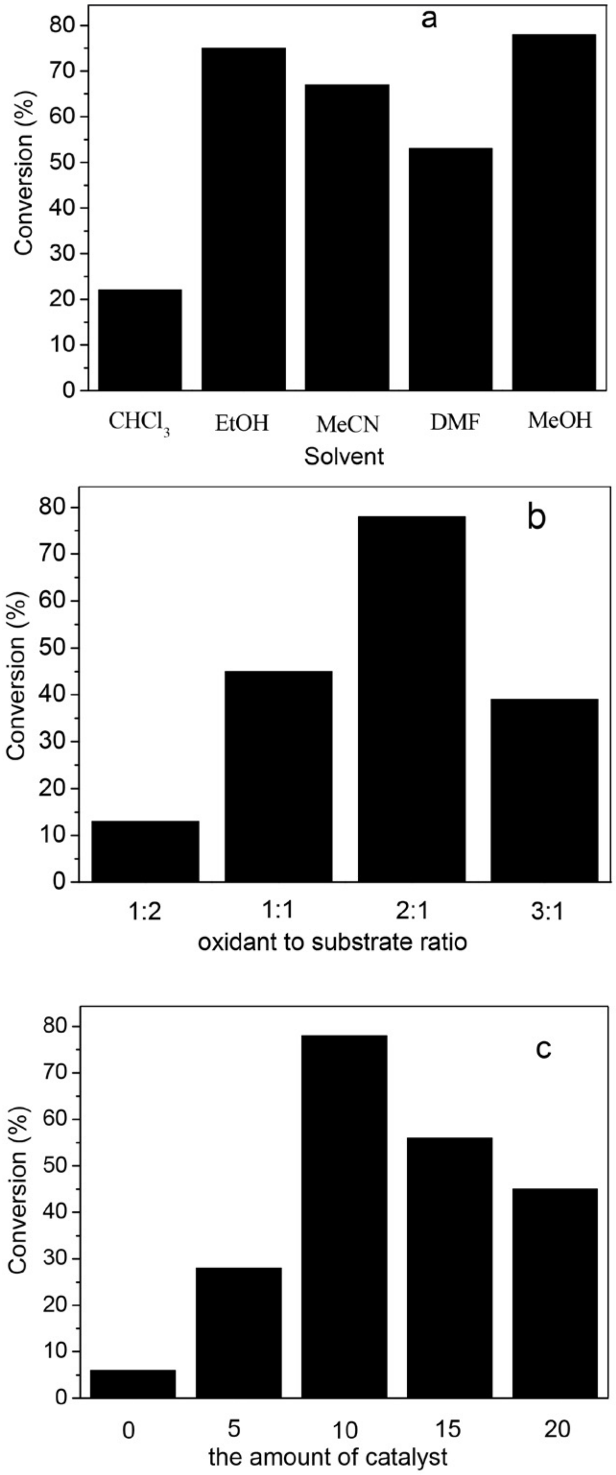

Fig. 5. The influence of solvent type (a), the oxidant to substrate ratio (b) and the amount of catalyst (c).

4. Conclusion

Two new cobalt complexes have been prepared and characterized. Structures of the complexes were characterized by spectroscopic methods, and confirmed by single crystal X-ray determination. One complex is a nitrate salt of a cobalt(III) complex, and the other one is a cobalt(II) tetrachloride salt of a cobalt(III) complex. The Schiff base ligand coordinates to the cobalt atoms through phenolate oxygen, imino nitrogen and amino nitrogen atoms. Both complexes are good catalysts for the oxidation of cyclooctene with TBHP as oxidant and methanol as solvent. The catalytic activity and epoxide selectivity were in high level.

Supplementary Material

CCDC reference numbers 2061676 (**1**) and 2061677 (**2**) contain the supplementary crystallographic data for this paper. These data can be obtained free of charge at www.ccdc.cam.ac.uk, or from Cambridge Crystallographic Data Center, 12, Union Road, Cambridge CB2 1EZ, UK; Fax: +44 1223 336 033; e-mail: deposit@ccdc.cam.ac.uk.

Acknowledgments

We gratefully acknowledge the financial support by the National Natural Science Foundation of China (22361001), the Natural Science Foundation of Inner Mongolia Autonomous Region (2023LHMS05032), and the Natural Science Foundation of Inner Mongolia Autonomous Region (2025MS02028).

5. References

1. (a) I. Mushtaq, M. Ahmad, M. Saleem, A. Ahmed, *Future J. Pharm. Sci.* **2024**, *10*, 16; **DOI:**10.1186/s43094-024-00594-5
   (b) R. Sahu, K. Shah, *Curr. Pharm. Des.* **2025**, *31*, 37–56; **DOI:**10.2174/0113816128339161240913055034
   (c) Nidhia, Siddharam, D. P. Rao, A. K. Gautam, A. Verma, Y. Gautam, *Res. Chem.* **2025**, *13*, 101941. **DOI:**10.1016/j.rechem.2024.101941
2. (a) M. Fallah-Mehrjardi, H. Kargar, K. S. Munawar, *Inorg. Chim. Acta* **2024**, *560*, 121835; **DOI:**10.1016/j.ica.2023.121835
   (b) V. K. Juyal, A. Pathak, M. Panwar, S. C. Thakuri, O. Prakash, A. Agrwal, V. Nand, *J. Organomet. Chem.* **2023**, *999*, 122825; **DOI:**10.1016/j.jorganchem.2023.122825
   (c) J. Jiang, P. Liang, Y. Han, H. Zhang, Z. You, *Acta Chim. Slov.* **2023**, *70*, 353–360; **DOI:**10.17344/acsi.2023.8253
   (d) W.-G. Zhang, J.-H. Liang, *Acta Chim. Slov.* **2023**, *70*, 421–429; **DOI:**10.17344/acsi.2023.8144
   (e) Y. Lei, Q. Yang, X. Xiao, Y. Liu, *Acta Chim. Slov.* **2024**, *71*, 288–294. **DOI:**10.17344/acsi.2024.8720
3. (a) R. Qurrat-ul-ain, M. U. Rahman, H. M. Javed, S. Hassan, T. Munir, R. Asghar, *Inorg. Chem. Commun.* **2024**, *170*, 113396; **DOI:**10.1016/j.inoche.2024.113396
   (b) S. M. Bufarwa, R. M. El-Sefait, D. K. Thbayh, M. Belaidi, R. K. Al-Shemary, R. M. Abdusamea, M. M. El-Ajaily, B. Fiser, H. A. Bader, A. A. Saleh, M. M. Bufarwa, *Rev. Inorg. Chem.* **2025**, *45*, 105–124; **DOI:**10.1515/revic-2024-0007
   (c) M. Zabiszak, J. Frymark, K. Ogawa, M. Skrobanska, M.

Nowak, R. Jastrzab, M. T. Kaczmarek, *Coord. Chem. Rev.* **2023**, *493*, 215326. **DOI:**10.1016/j.ccr.2023.215326

4. (a) J. Tang, F. P. Huang, Y. Wei, H. D. Bian, W. Zhang, H. Liang, *Dalton Trans.* **2016**, *45*, 8061–8072; **DOI:**10.1039/C5DT04507J
   (b) K. Madejska, M. Karman, G. Romanowski, A. Chylewska, A. Dabrowska, *Polyhedron* **2021**, *209*, 115481. **DOI:**10.1016/j.poly.2021.115481
5. (a) S. Mistri, K. Mondal, *Top. Curr. Chem.* **2024**, *382*, 35; **DOI:**10.1007/s41061-024-00480-x
   (b) S. Naderi, R. Sandaroos, S. Peiman, B. Maleki, *Chem. Methodol.* **2023**, *7*, 392–404.
6. (a) S. T. Hulushe, G. M. Watkins, S. D. Khanye, *Dalton Trans.* **2024**, *53*, 11326–11343; **DOI:**10.1039/D4DT00739E
   (b) M. Ghasemiyan, A. Abbasi, M. S. Hosseini, *J. Mol. Struct.* **2024**, *1311*, 138413. **DOI:**10.1016/j.molstruc.2024.138413
7. (a) J. B. Gordon, T. Albert, S. Yadav, J. Thomas, M. A. Siegler, P. Moenne-Loccoz, D. P. Goldberg, *Inorg. Chem.* **2023**, *62*, 392–400; **DOI:**10.1021/acs.inorgchem.2c03484
   (b) A. B. Valiotti, R. A. Abakumova, *Russ. J. Appl. Chem.* **2004**, *77*, 1623–1626. **DOI:**10.1007/s11167-005-0084-7
8. (a) R. Sandaroos, R. Sandaroos, A. Allahresani, *Res. Chem. Interm.* **2024**, *50*, 1313–1329; **DOI:**10.1007/s11164-023-05204-2
   (b) B. Rezazadeh, A. R. Pourali, A. R. Banaei, S. Tabari, *Russ. J. Coord. Chem.* **2021**, *47*, 424–437. **DOI:**10.1134/S107032842106004X
9. *SMART and SAINT. Area Detector Control and Integration Software*, Siemens Analytical X-Ray Systems, Inc., Madison, Wisconsin, USA, **1996**.
10. G. M. Sheldrick, *SADABS. Program for Empirical Absorption Correction of Area Detector Data*, University of Göttingen, Germany, **1996**.
11. G. M. Sheldrick, *SHELXTL V5.1 Software Reference Manual*, Bruker AXS, Inc., Madison, Wisconsin, USA, **1997**.
12. W. J. Geary, *Coord. Chem. Rev.* **1971**, *7*, 81–122. **DOI:**10.1016/S0010-8545(00)80009-0
13. Y. Luo, J. Wang, X. Ding, R. Ni, M. Li, T. Yang, J. Wang, C. Jing, Z. You, *Inorg. Chim. Acta* **2021**, *516*, 120146. **DOI:**10.1016/j.ica.2020.120146
14. S. Chandra, A. K. Sharma, *J. Coord. Chem.* **2009**, *62*, 3688–3700. **DOI:**10.1080/00958970903121305
15, Y. Luo, J. Wang, B. Zhang, Y. Guan, T. Yang, X. Li, L. Xu, J. Wang, Z. You, *J. Coord. Chem.* **2020**, *73*, 1765–1777. **DOI:**10.1080/00958972.2020.1795645
16. Z. You, Y. Luo, S. Herringer, Y. Li, S. Decurtins, K. W. Kramer, S.-X. Liu, *Crystals* **2020**, *10*, 592. **DOI:**10.3390/cryst10070592
17. A. Jayamani, M. Sethupathi, S. O. Ojwach, N. Sengottuvelan, *Inorg. Chem. Commun.* **2017**, *84*, 144–149. **DOI:**10.1016/j.inoche.2017.08.013
18. S. Shit, P. Talukder, J. Chakraborty, G. Pilet, M. S. El Fallah, J. Ribas, S. Mitra, *Polyhedron* **2007**, *26*, 1357–1363. **DOI:**10.1016/j.poly.2006.11.013
19. (a) N. C. Jana, M. Patra, P. Brandao, A. Panja, *Polyhedron* **2019**, *164*, 23–34; **DOI:**10.1016/j.poly.2019.02.024
    (b) L. Pogany, J. Moncol, M. Gal, I. Salitros, R. Boca, *Inorg. Chim. Acta* **2017**, *462*, 23–29. **DOI:**10.1016/j.ica.2017.03.001
20. (a) S. Shit, D. Saha, D. Saha, T. N. Guru Row, C. Rizzoli, *Inorg. Chim. Acta* **2014**, *415*, 103–110; **DOI:**10.1016/j.ica.2014.02.036
    (b) M. Maiti, D. Sadhukhan, S. Thakurta, E. Zangrando, G. Pilet, S. Signorella, S. Bellu, S. Mitra, *Bull. Chem. Soc. Jpn.* **2014**, *87*, 724–732; **DOI:**10.1246/bcsj.20130334
    (c) Z. Xiong, P. Zhang, *Acta Chim. Slov.* **2023**, *70*, 155–162. **DOI:**10.17344/acsi.2022.7903

Povzetek

Pripravili smo dva nova kobaltova(III) kompleksa, $[CoL_2]NO_3$ (**1**) and $[CoL_2]_2[CoCl_4]$ (**2**), kjer je L 5-bromo-2-(((2-izopropilamino)etil)imino)metil)fenolat, ter ju okarakterizirali s fizikalno-kemijskimi metodami in monokristalno rentgensko analizo. Rentgenska analiza je pokazala, da so atomi Co v obeh kompleksih oktaedrično koordinirani, razen v enoti $[CoCl_4]$, kjer so tetraedrično koordinirani. Kristalne strukture kompleksov stabilizirajo vodikove vezi in π···π interakcije. Katalitične lastnosti obeh kobaltovih kompleksov smo preučevali na epoksidaciji ciklooktena s *t*-butilhidroperoksidom (TBHP) kot oksidantom. Oba kompleksa kažeta dobro katalitično aktivnost in visoko selektivnost.

Scientific paper

Synthesis, Characterization and Biological Evaluation of Substituted Pyridine Based Benzo-thiazol Derivatives: *In Silico* Calculations and ADME Prediction

Iram Akbar,[1] Amir Karim,[2] Muhammad Iqbal,[1,*] Rahime Eshaghi Malekshah,[2,3] Najeeb Ullah,[2] Yu-Ting Chu,[2] Saqib Ali,[4,*] Sodio C. N. Hsu,[2,5,*] and Muhammad Nawaz Tahir[6]

[1] *Department of Chemistry Bacha Khan University Charsadda 24420, KPK, Pakistan.*

[2] *Department of Medicinal and Applied Chemistry, Kaohsiung Medical University, Kaohsiung 80708, Taiwan.*

[3] *Department of Chemistry, Semnan University, Semnan, Iran.*

[4] *Department of Chemistry, Quaid I Azam University, Islamabad, Pakistan.*

[5] *Department of Medical Research, Kaohsiung Medical University Hospital, Kaohsiung 80708, Taiwan.*

[6] *Department of Physics, University of Sargodha, Sargodha, Pakistan*

* *Corresponding author: E-mail: iqbal@bkuc.edu.pk, iqbalmo@yahoo.com*
Fax: +92-91-6540060

Received: 02-18-2025

Abstract

In this study, a series of new condensation products $\mathbf{L_1}$–$\mathbf{L_5}$ have been synthesized from substituted pyridinecarbaldehydes and 2-aminobenzothiazole and characterized by FTIR, UV-Visible, ^{1}H NMR spectroscopy and ESI-MS analysis. Additionally, compound $\mathbf{L_1}$ was structurally characterized through single-crystal X-ray diffraction study exhibiting four crystallographically independent molecules in the asymmetric unit. All the synthesized compounds exhibited antibacterial activity against Gram-negative and Gram-positive bacteria as well as against *Candida albicans* ATCC 60193 and *Candida tropicalis* ATCC 13803. All the compounds were optimized by using DFT-D method. Total energy values for compounds were calculated then, the reactivity descriptors were theoretically proven by computing the HOMO and LUMO energies. The prediction of ADME properties indicated that all of the compounds exhibit good drug-likeness and pharmacokinetic properties.

Keywords: (*E*)-*N*-((6-methoxypyridin-3-yl)methylene)benzo[*d*]thiazol-2-amine; Crystal structure; Bioactivities; Computational Studies; Swiss ADME.

1. Introduction

2-Aminobenzothiazole (2-ABT) has a significant role in the synthesis of organic compounds due to the presence of the electrophilic amino group (–NH_2) which can yield fused heterocycles.[1] It is an important compound due to its high reactivity, and can be modified according to the needs by the substitution on the benzene ring, making such derivatives ideal for medicinal chemistry.[2] Riluzole is 2-ABT derivative which has been extensively investigated for its role as a central muscle relaxant and glutamate neurotransmission inhibitor since the 1950s.[3] Its derivatives showed to be promising anticancer candidates, emphasizing targeted delivery systems to enhance efficacy and reduce side effects.[4] 2-Aminobenzothiazole derivatives have been extensively explored for antimicrobial, anticonvulsant, anti-HIV, analgesic, anti-viral, anti-inflammatory, antileishmanial, antitubercular and anticancer activities. The unique structural features of benzothiazole make them versatile scaffolds for drug development.[5–15] The presence of electronegative substitution such as halogen (–X) on aromatic ring has shown potent antimicrobial and anti-tuberculosis activities.[16] Another study demonstrated that these compounds have significant role in antifungal and antibacterial activities against *Candida albicans*, *Aspergillus niger*, *Staphylococcus. aureus*, *Streptococci*, *Escherichia coli*, and *Pseudomonas.*[17]

Schiff base is usually obtained by treating amines with an aldehyde or ketone, making an imine or azomethine functionality.[18] This imine (–C=N–) group in Schiff bases is crucial for their impressive biological activities, including anti-bacterial, antifungal, anti-viral, anti-oxidant, anti-leishmanial, anti-convulsant, anti-tumor, analgesic, anti-inflammatory, anti-glutamate, anti-tuberculosis, anti-diabetic, anti-malarial, anthelmintic and herbicidal properties.[19–22] 2-Aminobenzothiazol derivatives serve as ideal precursors for the synthesis of Schiff base ligands. The aromatic moiety significantly enhances DNA binding capacity through effective stacking interactions, contributing to the stabilization of the DNA double helix.[23] Schiff bases derived from 2-ABT are suitable for the synthesis of metal complexes as well. These compounds can also be used as catalysts in various industrial applications, including polymerization and fine chemical synthesis.[24] Schiff bases of 2-ABT have shown potential ability as chemo-sensors for detecting Hg^{2+} ions, indicating interesting applications in medicinal and environmental fields.[16] Upadhyay *et al.* synthesized three novel Schiff bases using 4,6-difluoro-2-aminobenzothiazole. One of those compounds *N*-((1*H*-indol-3-yl)methylene)-4,6-difluorobenzothiazole-2-amine demonstrated excellent antimicrobial activity, particularly against fungal strains.[25] Moustafa *et al.* synthesized a series of compounds derived from 2-ABT showing significant antitumor activity against HeLa cells and COS-7 cells suggesting their potential as new antitumor agents.[26]

To develop medicinal drugs with minimum side effects, computational studies such as molecular docking, density functional theory (DFT) and absorption, distribution, metabolism, elimination and toxicity (ADMET) are used extensively. These theoretical methods help in prediction of the geometry, interaction with specific target enzyme and possible pharmacokinetic, pharmacodynamics and physicochemical significance.[27–29]

Inspired by excellent biological potential of 2-aminobenzothiazole compounds, we have synthesized five new Schiff bases using substituted pyridine carboxaldehydes. All compounds were characterized using different analytical techniques including single crystal XRD, ^{1}H NMR, ESI-MS, FTIR and UV-Visible spectrophotometry. All the compounds were tested for antibacterial, antioxidant and anti-fungal activities experimentally. Furthermore, DFT-D, molecular docking and drug-likeness studies were applied in predicting possible biological activities.

2. Experimental

2. 1. Reagents and Materials

All the chemicals utilized in this study were obtained from Fluka (Switzerland) and all solvents were purchased from Merck (Germany). Both, chemicals and solvents in current study were used without further purification. Distilled water was employed throughout the experiments. Thin layer chromatography was performed using Silica Gel G (Merck Index) pre-coated plates and the spots were visualized by exposure to UV light.

2. 2. Instrumentations

The melting points of the prepared compounds were checked by capillary tube using a Gallenkamp, serial number C040281, UK, an electro thermal M.P. apparatus. FT-IR spectra of the compounds were obtained on Perkin 1,600,300 Laintrisant S.No 95,120 UK from 4000 to 400 cm^{-1}. The UV-Visible spectrophotometer Shimadzu Mod. UV 1800-240 V with 1.0 cm quartz cells was used for spectral analysis. Bruker Avance Digital 300 MHz NMR spectrometer was used for ^{1}H NMR study. ESI mass spectra were collected on a Waters ZQ 4000 mass spectrometer using methanol as solvent and are presented in Figures 7S–9S. Suitable crystals of $\mathbf{L_1}$ were obtained by slow evaporation of toluene solution. Single crystal X-ray diffraction data was collected on XtaLAB Pro II AFC12 (RINC): Kappa single diffractometer using Mo Kα Radiation (λ = 0.71073). The crystal was kept at a temperature of 100 K (± 2 K) and the data was collected by PLATON.[30] The structure was solved by direct methods and was refined on F^2 by the full-matrix least-squares method using the SHELXL-2019 program.[31]

2. 3. Syntheses of Compounds $\mathbf{L_1}$–$\mathbf{L_5}$

All the compounds $\mathbf{L_1}$–$\mathbf{L_5}$ were synthesized based on the following method as presented in Scheme 1.

2. 3. 1. Synthesis of $\mathbf{L_1}$

Compound $\mathbf{L_1}$ was synthesized by refluxing an equimolar solution of 6-methoxy-3-pyridinecarboxaldehyde (0.275 g, 2 mmol) with 2-aminobenzothiazole (0.300 g, 2 mmol) in dry toluene for 3 h. The reaction progress was continuously monitored by TLC. After 3 h the reaction mixture was filtered, concentrated to 10 mL and kept for crystallization at room temperature. Yellow crystals appeared in 3 days. Crystals were filtered off and washed with diethyl ether and characterized by single crystal XRD, ^{1}H NMR, ESI-MS, FTIR and UV-Vis spectrophotometry. Yellow color; m.p. 170 °C; yield: 0.413 g (77%). UV-Vis: ($1.57 \cdot 10^{-3}$ M, MeOH) λ_{max} = 263, 294, 350 nm. Selected FT-IR data (solid): ν_{max}/cm^{-1} 3061(w), 2981(w), 2949(w), 2852(w), 1690(m), 1600(s), 1560(m), 1492(s), 1473(w), 1452(m), 1427(m), 1346(s), 1311(s), 1284(s), 1257(m), 1219(w), 1154(m), 1102(m), 1059(w), 1010(s), 861(w), 840(s), 818(w), 759(s), 723(s), 664(s), 628(w), 612(m), 527(m). ^{1}H NMR (300 MHz, $CDCl_3$): δ 8.83 (s, 1H), 8.19–8.15 (m, 1H), 7.87–7.84 (m, 1H), 7.48 (dd, *J* =

7.0, 1.8 Hz, 1H), 7.38 (dd, J = 7.2, 1.6 Hz, 1H), 7.35 (s, 1H), 7.33 (d, J = 5.5 Hz, 1H), 7.34–7.29 (m, 1H), 6.79 (d, J = 8.7 Hz, 1H), 3.97 (s, 3H). ESI-MS: m/z calculated for [$\mathbf{L_1}$ = $C_{14}H_{11}N_3OS$]$^+$: 269.06, found: [$\mathbf{L_1}$ + H^+ = 270.02]$^+$.

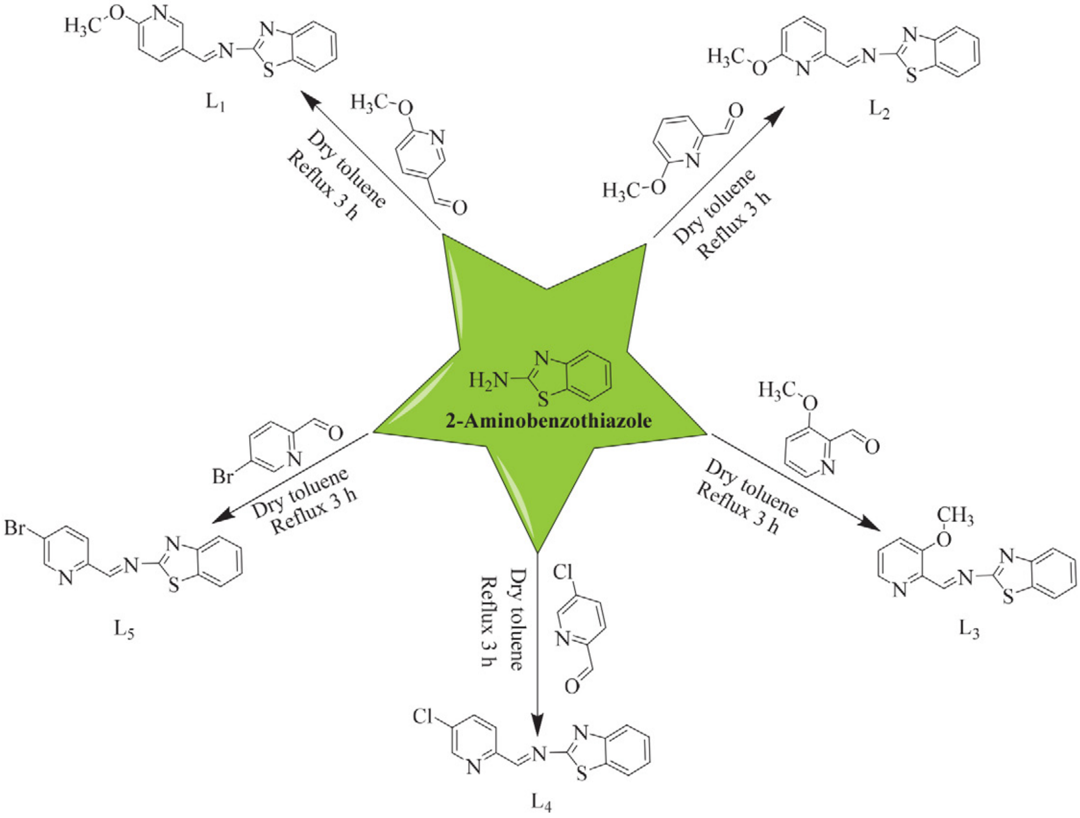

Scheme 1. Synthetic rout followed for compounds $\mathbf{L_1}$–$\mathbf{L_5}$.

2. 3. 1. Synthesis of $\mathbf{L_2}$

For $\mathbf{L_2}$, the same procedure was followed as for $\mathbf{L_1}$ but using 6-methoxy-2-pyridinecarboxaldehyde (0.275 g, 2 mmol). The final product was characterized by ^{1}H NMR, FTIR and UV-Vis spectrophotometry. Yellow color; m.p. 130 °C; yield: 0.392 g (73%). UV-Vis: (1.57 · 10^{-3} M, MeOH) λ_{max} = 263, 294, 350 nm. Selected FT-IR data (solid) ν_{max}/cm^{-1} 3075(w), 3048(w), 3001(w), 2861(m), 1702(s), 1675(w), 1573(m), 1552(m), 1465(m), 1382(w), 1367(m), 1292(m), 1260(w), 1206(s), 1122(w), 1107(s), 1012(s), 985(w), 934(w), 847(s), 827(s), 725(m), 707(s), 626(s), 543(s), 480(s), 414(s). ^{1}H NMR (300 MHz, $CDCl_3$): δ 9.05 (s, 1H), 8.62 (s, 1H), 8.37 (d, J = 6.0 Hz, 1H), 8.35 (d, J = 6.0 Hz, 1H), 7.97 (d, J = 6.0 Hz, 1H), 7.84 (d, J = 3.0 Hz, 1H), 7.50–7.35 (m, 1H), 7.88 (t, J = 6.0 Hz, 1H), 4.02 (s, 3H).

2. 3. 1. Synthesis of $\mathbf{L_3}$

For $\mathbf{L_3}$, the same procedure was followed as for $\mathbf{L_1}$ but using 3-methoxy-2-pyridinecarboxaldehyde (0.275 g, 2 mmol). The final product was characterized by ^{1}H NMR, FTIR and UV-Vis spectrophotometry. Yellow color; m.p. 133 °C; yield: 0.427 g (79%). UV-Vis (1.57 · 10^{-3} M, MeOH) λ_{max} = 263, 294, 350 nm. Selected FT-IR data (solid): ν_{max}/cm^{-1} 3393(w), 3270(w), 3056(w), 2913(w), 2726(w), 1629(m), 1525(m), 1440(m), 1368(w), 1105 (m), 1068(w), 1018(w), 962(w), 917(m), 886(m), 841(w), 737(s), 715(s), 681(m), 628(w), 429(s). ^{1}H NMR (300 MHz, $CDCl_3$): δ 9.03 (s, 1H), 8.61 (s, 1H), 8.35 (d, J = 6.0 Hz, 1H), 7.95 (d, J = 6.0 Hz, 1H), 7.82 (d, J = 6.0 Hz, 1H), 7.46 (d, J = 3.0 Hz, 1H), 7.40–7.33 (m, 1H), 6.87 (t, J = 6.0 Hz, 1H), 4.02 (s, 3H).

2. 3. 1. Synthesis of $\mathbf{L_4}$

For $\mathbf{L_4}$, the same procedure was followed as for $\mathbf{L_1}$ but using 5-chloro-2-pyridinecarboxaldehyde (0.283 g, 2 mmol). The final product was characterized by ^{1}H NMR, ESI-MS, FTIR and UV-Vis spectrophotometry. Yellow color; m.p.134 °C; yield: 0.445 g (81%). UV-Vis (1.57 · 10^{-3} M, MeOH) λ_{max} = 263, 294, 350 nm. Selected FT-IR data (solid): ν_{max}/cm^{-1} 3390(w), 3273(w), 3059(w), 2912(w), 2725(w), 1916(w), 1632(s), 1526(s), 1444(s), 1365(w), 1105(s), 1064(w), 1016(m), 961(w), 914(m), 886(m), 842(m), 739(s), 719(s), 685(m), 431(s). ^{1}H NMR (300 MHz, $CDCl_3$): δ 10.16 (s, 1H), 8.43–8.39 (m, 2H), 8.39 (s, 1H), 8.10 (d, J = 2.0 Hz, 2H), 8.09–8.05 (m, 2H), ESI-MS:

m/z calculated for [$\mathbf{L_4}$ = $C_{13}H_8ClN_3S$]$^+$: 273.01, found: [$\mathbf{L_4}$ + H^+ = 273.93]$^+$.

2. 3. 1. Synthesis of $\mathbf{L_5}$

For $\mathbf{L_5}$, the same procedure was followed as for $\mathbf{L_1}$ but using 5-bromo-2-pyridinecarboxaldehyde (0.372 g, 2 mmol). The final product was characterized by ^{1}H NMR, ESI-MS, FTIR and UV-Vis spectrophotometry. Yellow color; m.p. 160 °C; yield: 0.482 g (76%). UV-Vis ($1.57 \cdot 10^{-3}$ M, MeOH) λ_{max} = 263, 294, 350 nm. Selected FT-IR data (solid): ν_{max}/cm^{-1} 3390(w), 3270(w), 3053(w), 3026(w), 2918(w), 2731(w), 1921(w), 1622(m), 1499(w), 1439(w), 1107(s), 1065(w), 1012(w), 966(w), 920(m), 885(m), 849(m), 740(s), 715(s), 486(m), 429(s). ^{1}H NMR (300 MHz, $CDCl_3$): δ 10.18 (s, 1H), 8.43 (d, *J* = 1.7 Hz, 2H), 8.40 (s, 1H), 8.12–8.09 (m, 2H), 8.08 (s, 2H), ESI-MS: *m/z* calculated for [$\mathbf{L_5}$ = $C_{13}H_8BrN_3S$]$^+$: 316.90, found: [$\mathbf{L_5}$ + H^+ = 317.83]$^+$.

2. 4. Biological Studies

2. 4. 1. Antibacterial Activity

The *in vitro* antibacterial evaluation of the synthesized compounds $\mathbf{L_1}$–$\mathbf{L_5}$ was performed against five types of pathogens: three Gram-negative bacteria (*Escherichia coli, Klebsiella pneumoniae* and *Pseudomonas aeruginosa*) and two Gram.positive bacteria (*Staphylococcus aureus* and *Streptococcus pyogenes*). The antibacterial assay was conducted at pH 7.4 ± 0.2, with a final inoculum concentration of 10^5 cfu/mL. The test solutions were prepared for all compounds in dimethyl sulfoxide (DMSO) at concentrations of 2, 10, 20, 40, 60, 80 and 100 μg/mL and diluted in Mueller–Hinton broth. Then the solutions were incubated at 37 °C and evaluated after 24 h against bacteria.

2. 4. 2. Antioxidant Activity

All the compounds were tested for free radical scavenging ability using 1,1-diphenyl-2-picryl-hydrazyl free radical (DPPH) as standard.[32] The absorbance of the samples was estimated at 515 nm on a UV-Visible spectrophotometer as compared to a blank of ethanol. Three different concentrations 50, 100 and 200 μg mL^{-1} were prepared and stored in the dark. A 500 μL solution of DPPH added to 250 μL of each test samples of $\mathbf{L_1}$–$\mathbf{L_5}$. Then all compounds containing DPPH were incubated for 30 min at room temperature. The experiments were performed in triplicate and percentage of inhibition based on the DPPH scavenging ability was calculated using the following formula (1):

$$\text{DPPH scavenging effect \%} = \frac{A_0 - A_S}{A_0} \qquad (1)$$

where A_o, is the absorbance of the control sample (DPPH solution) and A_s is the absorbance of the sample along with DPPH solution after incubating for 30 min.

2. 4. 3. Anti-fungal Activity

All the ligands were examined for antifungal activity using fungal colony of *Candida albicans* ATCC 60193 and *Candida tropicalis* ATCC 13803 and percent inhibition was calculated using formula (2).

$$\text{Fungal growth inhibition (\%)} = \frac{A-B}{A} \times 100 \qquad (2)$$

where *A* is the diameter of the fungal colony in the control plate and *B* is the diameter of the fungal colony after treating with samples.

2. 5. Computational Studies

2. 5. 1. DFT-D Calculations

In current study, all compounds were designed in Material Studio 2017 and the computational calculations were attained using DFT-D in gaseous phase.[33,34] In order to describe the exchange correlation effects, the generalized gradient approximation (GGA) with the Perdew–Burke–Ernzerhof (PBE) function was applied in the calculations and performed by the Dmol^3 software in this package.[33] The resultant optimized structures, HOMO/LUMO distributions, energies and the chemical reactivity descriptors are given in Figures 6 and 7, and Tables 5 and 6, respectively. All optimized compounds were saved in Mol2 file format to study molecular docking.

2. 5. 2. Molecular Docking Study

All the compounds were docked with Gram-negative bacteria *E. coli* DNA gyrase B in complex with small molecule inhibitor (PDB code 4DUH) and Gram-positive bacteria *Streptococcus pneumonia* (PDB code 4MOT) which were downloaded from the Protein Data Bank server https://www.rcsb.org/structure/4mot and https://www.rcsb.org/experimental/4duh. Molecular docking calculations were performed using Molegro Virtual Docker (MVD). The dimensions for 4DUH and 4MOT were set 21.24 · 11.84 · 24.16 and 21.38 · 29.05 · 2.13, respectively. Additionally, five poses were set in the software. The binding interactions for specific receptor sites with ligands were studied by Biovia Discovery Studio 2016.[35]

2. 6. ADMET Profiling

In order to understand biological efficacy of compounds presented in this work ADMET study was employed. This method helps in predicting pharmacokinetic and pharmacological studies containing log $P_{o/w}$, blood–brain barrier (BBB) permeate, gastrointestinal (GI) absorption, total polar surface area (TPSA), bioavailability and Lipinski's rule of the newly synthesized compounds. ADME studies were performed by Swiss ADME using an online platform. After that, the predictive model of Egan's Boiled-egg and the bioavailability radar were calculated to investigate the central nervous system (CNS) and measure their oral bioavailability for human health.

3. Results and Discussion

3. 1. FTIR Discussion

FTIR spectroscopy is a highly valuable technique for the structural determination of the synthesized compounds. The formation of a Schiff base can be confirmed by the disappearance of characteristic carbonyl (C=O) and amine ($-NH_2$) peaks and the appearance of distinct azomethine (HC=N–), band in the FTIR spectrum. FTIR spectra of Schiff bases are presented in Figure 1S. The spectra of $\mathbf{L_1}$–$\mathbf{L_5}$ showed medium to strong band in the range of 1622–1690 cm^{-1} typically corresponding to the stretching vibration of azomethine (HC=N–), while the weak band in the region of 3048–3061 cm^{-1} corresponded to aromatic (Ar-H).[36] The weak absorption bands in the range of 2861–2918 cm^{-1} typically indicated azomethine C–H group. The presence of strong band in the region of 725–759 cm^{-1} belongs to (C–S–C) thiazine group.[25] The stretching frequency of pyridine group (–C=N–) was observed in the range of 1499–1560 cm^{-1}.[37]

3. 2. UV-Visible Spectroscopic Study

The UV-Visible spectral study of the synthesized compounds $\mathbf{L_1}$–$\mathbf{L_5}$ was conducted at room temperature in methanol. All the absorption spectra of $\mathbf{L_1}$–$\mathbf{L_5}$ were compared to the starting material, 2-aminobenzothiazole as shown in Figure 1. The absorption band at 263 nm is primarily attributed to the $\pi \rightarrow \pi^*$ transitions of the pyridine moiety.[38] The small shoulder peak at 294 nm revealed distinctive $\pi \rightarrow \pi^*$ transitions reinforcing the presence of aromatic rings which could be particularly ascribed to the π-electrons present in 2-aminobenzothiazole part of the Schiff base as observed in unreacted form as well. The appearance of new absorption band at 350 nm is evidence of $n \rightarrow \pi^*$ transitions of azomethine group.[20,36,39]

3. 3. ^{1}H NMR Study

The ^{1}H NMR spectra of compounds $\mathbf{L_1}$–$\mathbf{L_5}$ were measured in $CDCl_3$ by using TMS as an internal reference and are presented in Figures 2S–6S. The multiple signals corresponding to aromatic protons were observed in the range of 8.11–6.78 ppm.[25] A signal in range 8.6–7.9 ppm corresponded to aromatic protons in the pyridine ring. The peaks in the range of 3.97–4.2 ppm confirm the presence of methoxy substituents in compounds $\mathbf{L_1}$–$\mathbf{L_3}$.[40] The peaks observed at 8.82 ($\mathbf{L_1}$), 8.83 ($\mathbf{L_2}$), 9.03($\mathbf{L_3}$), 10.16 ($\mathbf{L_4}$), and 10.18 ($\mathbf{L_5}$) ppm are assigned to azomethine protons which is a strong evidence for the synthesis of the mentioned Schiff bases.[41,42] The observed shifting of azomethine protons due to the influence of electron-withdrawing and electron-donating substitution on pyridine group of the Schiff bases is in line with the literature.[41,42]

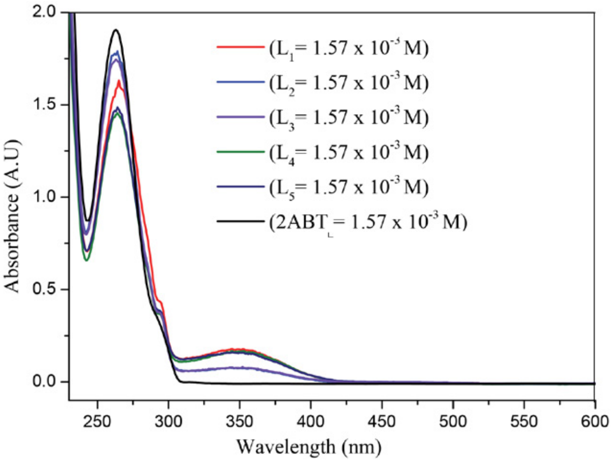

Figure 1. UV-Visible spectra of compounds $\mathbf{L_1}$–$\mathbf{L_5}$ and 2-aminobenzothizole.

3. 4. Structural Description

Compound $\mathbf{L_1}$ crystalizes in monoclinic crystal system with space group *C* 2/*c* while the crystal structure and atomic numbering scheme are illustrated in Figure 2. The unit cell dimensions and crystallographic parameters are summarized in Table 1, while the important bond lengths and bond angles are listed in Table 2. The azomethine (–C=N–) bond length was found to be consistent with values reported in the literature.[16] The torsion angles C_8–C_9–C_{13}–S_{12} = 179.2(3)° and C_7–N_2–C_8–C_9 = –179.7(3)° show that the configurations about the C=N bonds are *anti* (1*E*).[43] The specific spatial orientation of the molecules enables O-atom of methoxy group to participate in C–H···O interaction with the adjacent molecule of the lattice. This interaction of molecules is shown in Figure 3. Since there are no O/N/F–H···O/N/F functionalities in the molecule, there is no H-bonding in the crystal lattice and the packing diagram is shown in Figure 4.

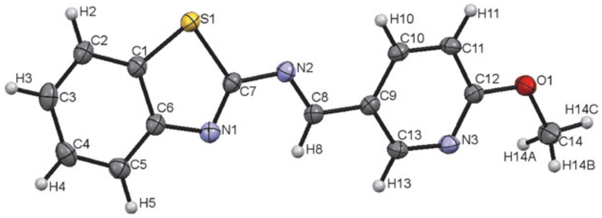

Figure 2. Structure and atom numbering scheme of $\mathbf{L_1}$.

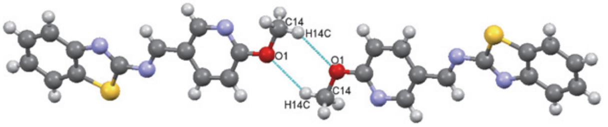

Figure 3. C–H···O interactions (shown blue) exhibited by molecules in lattice.

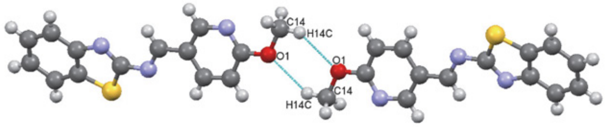

Figure 4. Packing diagram of molecules of L_1 as viewed along *b*-axis.

Table 1. Crystal data and structure refinement for compound L_1.

Empirical formula	$C_{14}H_{11}N_3O_S$
Formula weight	269.32
Crystal system	monoclinic
Space group	*C* 2/*c*
a/Å, b/Å, c/Å	47.9676(16), 4.5345(3), 11.3392(7)
α/°, β/°, γ/°	90, 92.390(5), 90
Volume/Å^3	2464.2(2)
Z	8
ρ_{calc} g/cm^3	1.452
μ/mm^{-1}	0.257
F(000)	1120
Goodness-of-fit on F^2	1.051
Reflections collected	2416
Independent reflections	2166 [R_{int} = 0.1242,]
Data/restraints/parameters	2416/0/173

3. 5. Antibacterial Assay

All the synthesized compounds L_1–L_5 prevented growth of the microorganisms (Gram-negative and Gram-positive bacteria) as shown by the data given in Table 3. All the compounds were found to be good antibacterial agents against five different types of bacteria. The minimum inhibitory concentrations (MICs, µg/mL) of compounds L_1–L_3 demonstrated excellent antibacterial activity compared to compounds L_4 and L_5. All compounds were compared to the standard antibiotic ciprofloxacin. In addition, MIC of compound L_1 was lower than inhibitory concentration of ciprofloxacin and other compounds against *E. coli, P. aeruginosa* (–), *S. aureus* (+) and *S. pyogenes* (+). The results demonstrated that compounds L_1–L_5 showed good activity against Gram-negative compared to Gram-positive bacterial stains. The experimental data were found to be in good agreement with the theoretical results (quantum molecular descriptors and molecular docking). Also, these compounds can obstruct and destroy respiration process of the studied organisms due to the presence of heterocyclic rings containing S and N atoms.[44,45] Lipophilicity is a significant factor to control antimicrobial activity. Compounds L_1–L_5 showed high lipophilicity, which may subsequently promote penetration through the lipid layer of the cell membrane.[46] Additionally, lipophilicity and delocalization of π-electrons in the structure of a bioactive molecule have been found to play parallel roles in the enhancement of cell death.[47]

3. 6. Antioxidant Studies

Reactive oxygen and nitrogen species (RONS) as free radicals that can induce severe oxidative damage on biomacromolecules like DNA, lipids and proteins. Hence, recent investigations have focused on synthesizing novel heterocyclic compounds as potent antioxidants due to their pharmaceutical significance.[48] In this study, compounds with methoxy substituent (L_1–L_3) exhibited slightly higher activity than the compounds containing halogen groups as shown in Figure 5. Furthermore, L_1 having OMe group on *para* position with respect to the azomethine functionality revealed good antioxidant activity as compared with other compounds L_2, L_3 and other halogen-substituted compounds. Halo groups destabilize the free radicals while methoxy groups stabilize the radicals to some extent which might be attributed to the high electronic density. Furthermore, increase in concentration of the compounds resulted in a decrease in the DPPH radical scavenging ability, indicating that the oxidants at low concentrations were most effective.[49]

3. 7. Anti-fungal Activity

The anti-fungal screening data revealed that all the compounds L_1–L_5 were active against *C. albicans* ATCC

Table 2. Selected bond lengths, bond angles, and torsion angles for compound L_1

Bond lengths (Å)		Bond angles (°)		Torsion angles (°)	
C_1–S_1	1.7302(18)	C_2–C_1–N_1	115.07	C_8–N_2–C_7–S_1	166.6 (2)
C_7–N_1	1.301(2)	C_2–N_1–C_7	110.52	C_8–N_2–C_7–N_1	−13.7 (5)
S_1–C_7	1.7511(16)	C_2–S_1–C_7	88.910	C_8–C_9–C_{13}–S_{12}	179.2 (3)
C_7–N_2	1.391(2)	N_1–C_7–S_1	116.30	C_7–S_1–C_2–C_1	−0.2 (2)
N_1–C_7	1.301(2)	S_1–C_7–N_2	115.41	C_7–S_1–C_2–C_3	180.0 (3)
N_2–C_8	1.284(2)	N_1–C_7–N_2	128.23	C_7–N_1–C_1–C_6	179.8 (3)
N_3–C_{12}	1.324(2)	C_7–N_2–C_8	118.26	C_7–N_1–C_1–C_2	−0.3 (4)
C_{13}–N_3	1.343(2)	C_{10}–N_3–C_{11}	116.09	C_7–N_2–C_8–C_9	−179.7 (3)
C_{12}–O_1	1.349(2)	N_3–C_{11}–O_1	119.55	—	—
O_1–C_{14}	1.4403(19)	C_{11}–O_1–C_{14}	117.01	—	—

60193 and *C. tropicalis* ATCC 13803 with diameter of inhibition area ranging from 20–26 and 32–34 mm, respectively. As can be seen from Table 4, all compounds showed higher antifungal effects compared to the standard drug fluconazole.

3. 8. DFT-D Calculations

Optimization based on DFT-D was performed to obtain the most stable structures for all compounds as shown in Figure 6. Total energies for compounds **L_1–L_5** were calculated to be –1169.372, –1169.372, –1171.135, –1514.971, and –1068.565 kcal/mol, respectively as shown in Table 5.

3. 9. HOMO and LUMO Orbitals

The HOMO electron density of compounds **L_1–L_5** is mainly distributed over aromatic groups and imine group while the LUMO electron density distribution extends to N and S atoms as shown in Figure 7.

3. 10. Quantum Molecular Descriptors

Recently, researches are employing DFT calculations to obtain quantum chemical parameters for prediction of biological properties. The quantum chemical descriptors such as the ionization potential (I), electron affinity (A),

Table 3. Minimum inhibitory concentration (MIC) values of the compounds **L_1–L_5** (μg/mL).

Compound	*E. coli* (–)	*K. pneumoniae* (–)	*P. aeruginosa* (–)	*S. aureus* (+)	*S. pyogenes* (+)
L_1	7.5 ± 0.11	6.5 ± 0.81	8.4 ± 1.73	8.9 ± 0.21	9.3 ± 0.42
L_2	7.9 ± 0.64	6.9 ± 0.98	8.6 ± 1.73	9.6 ± 0.24	10.8 ± 0.47
L_3	7.0 ± 0.45	6.9 ± 0.25	7.0 ± 0.35	9.3 ± 0.55	10.0 ± 0.43
L_4	9.5 ± 0.01	7.6 ± 0.43	9.3 ± 0.32	9.8 ± 0.89	11 ± 0.12
L_5	9.9 ± 0.82	7.9 ± 0.76	10.9 ± 0.19	9.8 ± 0.72	12 ± 1.12
Ciprofloxacin	9.8 ± 1.28	4.8 ± 0.08	9.8 ± 0.08	9.12 ± 0.85	10.5 ± 0.41

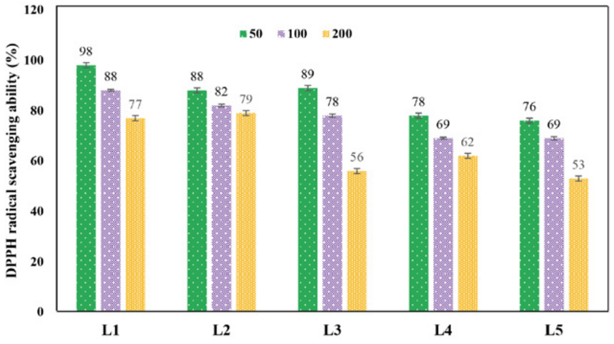

Figure 5. Histogram representation of DPPH free radicals scavenging potentials of the compounds **L_1–L_5** relative to ascorbic acid taken as 100%.

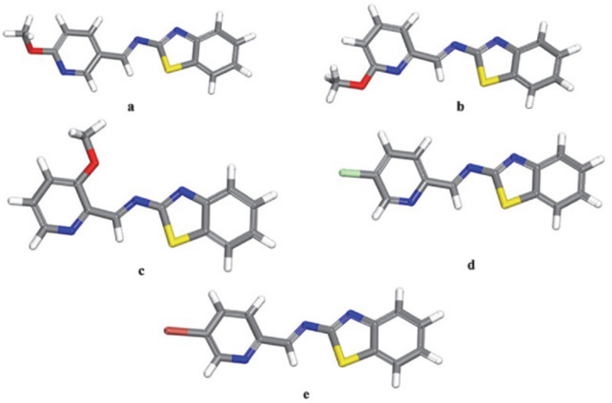

Figure 6. Optimized structures **L_1–L_5** (a–e) based on DFT-D method using DMol^3 module in Material Studio 2017.

Table 4. The diameter of antifungal studies of compounds **L_1–L_5** against *C. albicans* ATCC 60193 and *C. tropicalis* ATCC 13803

Compounds	**L_1**	**L_2**	**L_3**	**L_4**	**L_5**	**Fluconazole**
C. albicans ATCC 60193	24	23	26	22	20	17
C. tropicalis ATCC 13803	32	32	33	32	34	31

Table 5. The energy parameters resulted from DFT-D method for compounds **L_1–L_5**.

compounds	Sum of atomic energies	Kinetic	Electrostatic	Exchange-correlation	Spin polarization	DFT-D correction	Total DFT-D energy
L_1	–1169.372	–30.443	0.278	1.867	–67.441	–0.029	–1239.331
L_2	–1169.372	–30.434	0.272	1.866	–67.441	–0.029	–1239.331
L_3	–1171.135	–10.245	0.155	2.275	1.661	–0.021	–1177.310
L_4	–1514.971	–31.533	0.620	1.639	–78.003	–0.024	–1593.868
L_5	–1068.565	–27.667	0.660	1.625	–61.716	–0.025	–1132.322

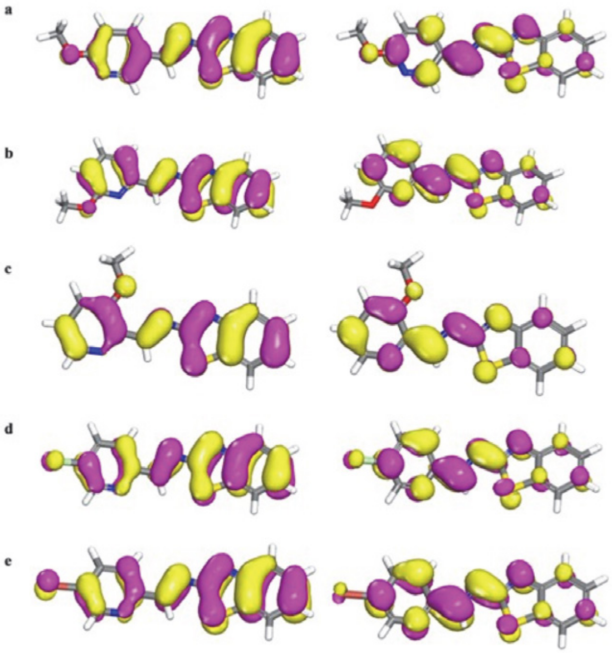

Figure 7. Electron density distributions, HOMO (left) and LUMO (right) orbitals of the compounds L_1–L_5 (corresponding to a–e, respectively).

Table 6. The calculated quantum chemical parameters obtained from energy gap.

compounds	HOMO	LUMO	E_g	I	A	$\eta = I - A/2$	X	$\mu = -X$	$w = \mu \cdot \mu / 2\eta$
L_1	−6.224	−3.727	2.5	6.22	3.73	1.25	4.98	−4.98	9.914
L_2	−6.306	−3.574	2.73	6.31	3.57	1.37	4.94	−4.94	8.93
L_3	−5.768	−3.707	2.06	-5.77	-3.71	1.03	4.74	−4.74	10.889
L_4	−6.435	−3.625	2.81	6.44	3.63	1.41	5.03	−5.03	9.00
L_5	−6.369	−3.636	2.73	6.36	3.5	1.37	4.93	−4.93	8.49

chemical potential (μ), global hardness (η), dipole moment (μ), and the electrophilicity index (ω) were calculated by HOMO and LUMO energy gaps obtained from the DFT-D results. The higher energy gap (ΔE = HOMO – LUMO) imparts less reactivity, less polarizability and more stability to molecule and vice versa. Based on the observed ADME results of energy gaps as listed in Table 6, compound $\mathbf{L_3}$ is less stable and more lipophilic indicating more reactivity. Soft molecules have a lower energy gap than hard molecules and may easily transfer electrons to acceptors, making them more reactive and interacting with biomacromolecules as targets in the biological systems. Consequently, $\mathbf{L_3}$ and $\mathbf{L_1}$ showed more inhibitory activities. Additionally, $\mathbf{L_4}$ had high chemical hardness (η) as compared to other compounds, leading to the most stable and least reactive compound for the biological activity. Compound $\mathbf{L_4}$ exhibited the highest Lewis acid character due to high electronegativity (χ). Global electrophilicity (ω) was found to be significant, indicating that the electrophilic index confirms biocidal property to kill the microbes.[50,51] In addition, $\mathbf{L_3}$ and $\mathbf{L_1}$ can kill cancer cells more than others due to higher value of electrophilicity index (ω).[15]

3. 11. Molecular Modeling Studies

To understand protein-ligand interactions and drug development affinity of the synthesized compounds toward the targeted proteins, the *in silico* molecular docking technique using MVD was employed. The molecular docking results and the interactions with receptors are presented in Table 7. The compounds showed good binding orientation in the binding pocket of *E. coli* (PDB code 4DUH) and *S. pneumoniae* (PDB code 4MOT). Compounds $\mathbf{L_1}$–$\mathbf{L_5}$ with 4DUH revealed a binding affinity of −95.750, −89.837, −98.960, −90.801, and −91.229 kcal/mol. While with 4MOT the lowest possible binding energies for compounds $\mathbf{L_1}$–$\mathbf{L_5}$ were displayed at −107.148, −117.347, −122.728, −103.724, and −104.470 kcal/mol, respectively. Compounds $\mathbf{L_1}$–$\mathbf{L_3}$ revealed the higher binding affinity as compared with $\mathbf{L_4}$–$\mathbf{L_5}$ in both of receptors in good accord with energy gap (E_g). 3D and 2D predictions on both of proteins displayed the intermolecular interactions of ligands with amino acid residues in active site from the best docking pose. Docking score of all investigated compounds with *S. pneumoniae* exhibited negative binding energy, suggesting their high hydrophobic interactions. 2D and 3D views of the non-bonded interactions between structures were docked onto *E. coli* (PDB code 4DUH) or *S. pneumoniae* (PDB code 4MOT) and are shown in Figures 8 and 9.

3. 12. Drug Likeness and *In-Silico* Bioactivity Prediction Using Swiss ADME

The behavior of molecules in humans is influenced by the structural features including bioavailability, transport properties, affinity, reactivity, toxicity, and metabolic stability.[52] Table 8 presents the permeability levels of compounds $\mathbf{L_1}$–$\mathbf{L_5}$, describing their potential for molecular transport across the blood–brain barrier (BBB) and intestinal membranes. But these compounds were not cleared from the central nervous system (CNS) by the P-glycoprotein. Moreover, these compounds had high gastrointestinal (GI) absorption, indicating a high absorbance in the human intestine, showing high GI absorption.[53] Furthermore, all of the tested compounds have a bioavailability score of 0.55, showing a moderate level of bioavailability.[54] They obey Lipinski's first rule, signifying that these compounds can be developed as orally active small anti-in-

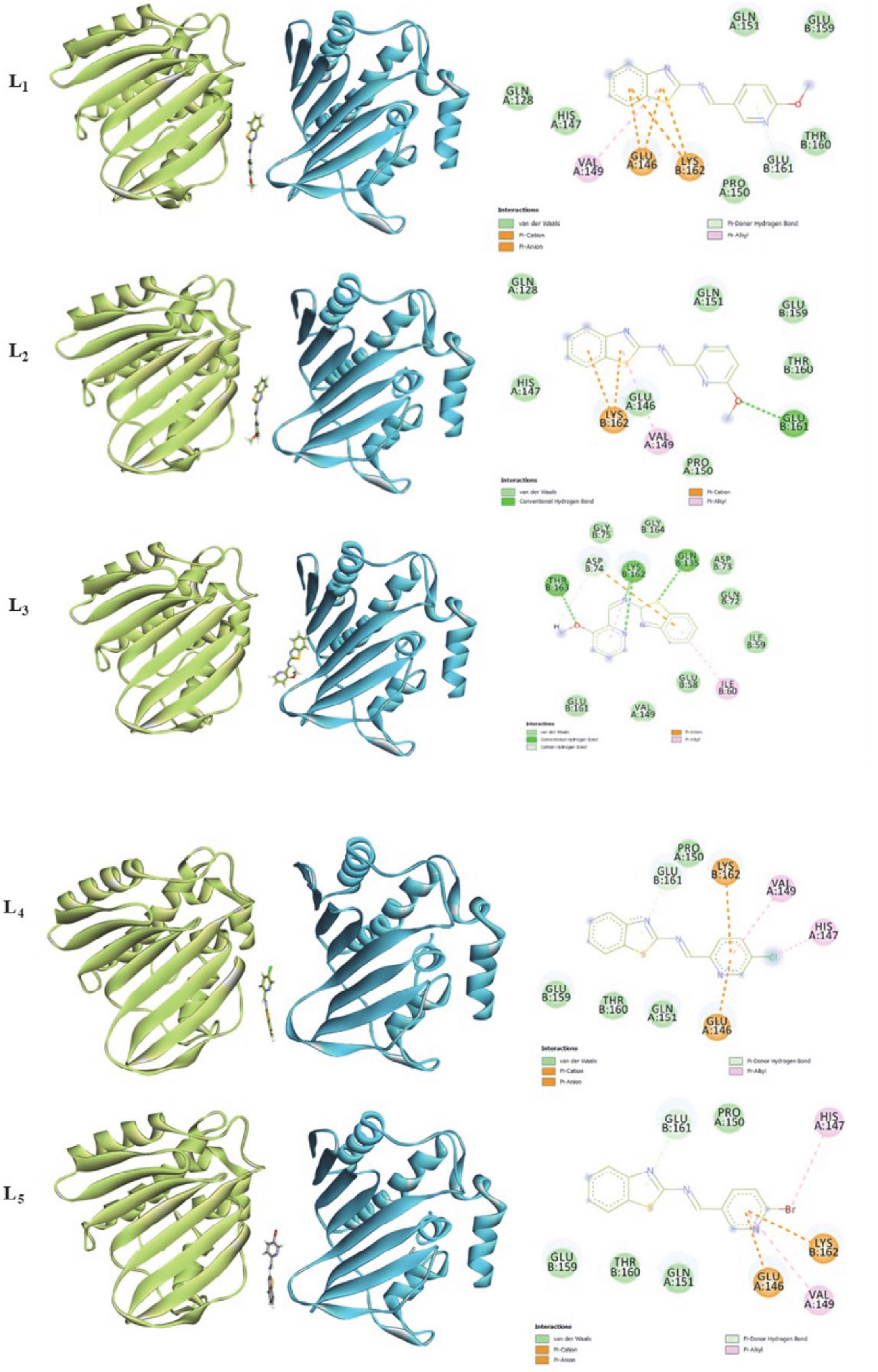

Figure 8. 3D and 2D dimensions of results of intramolecular interactions for compounds $\mathbf{L_1}$–$\mathbf{L_5}$ with *E. coli*.

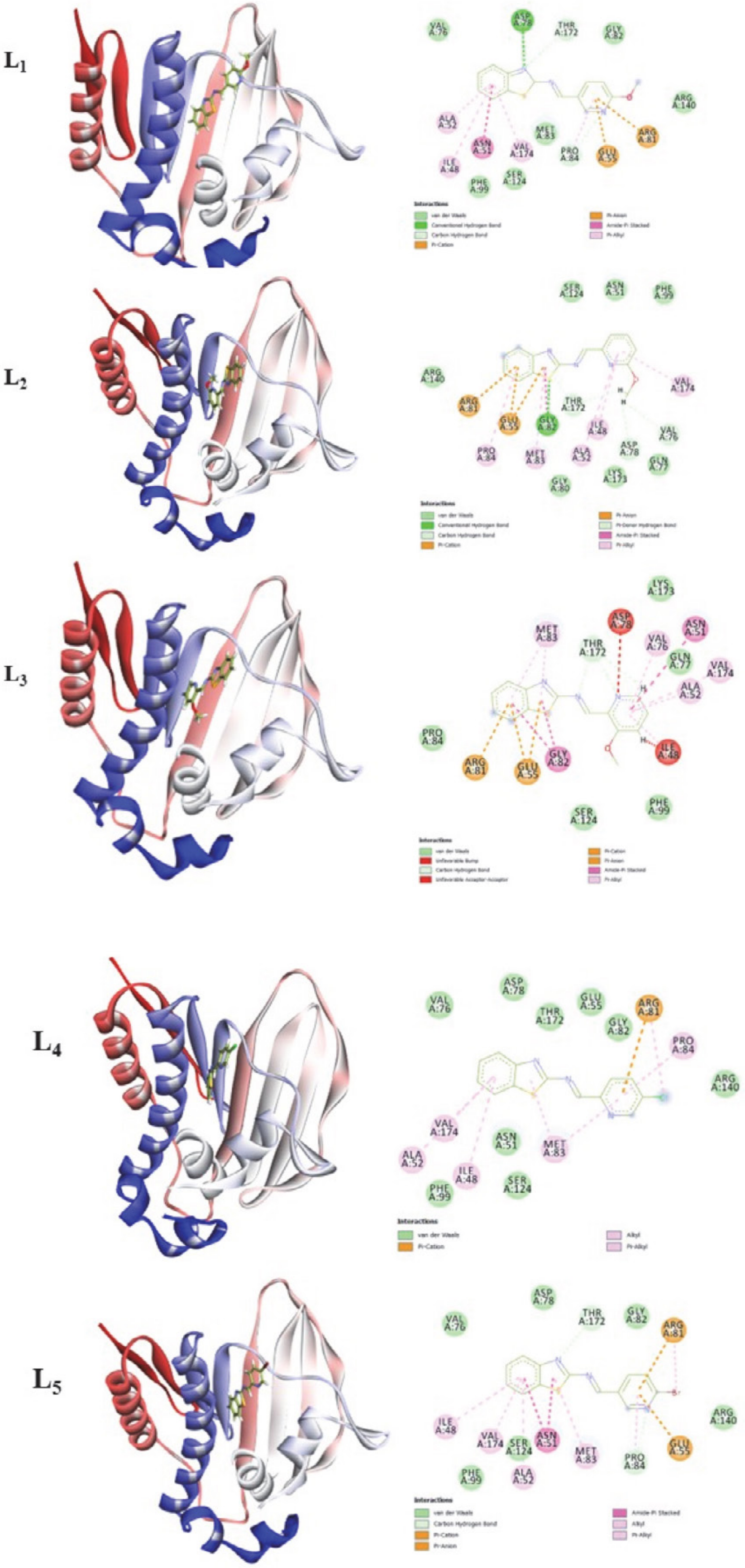

Figure 9. 3D and 2D diagrams of intramolecular interactions of compounds **L$_1$–L$_5$** with *S. pneumoniae.*

Table 7. Docking of compounds into *E. coli* (PDB code 4DUH) and *S. pneumoniae* (PDB code 4MOT)

compounds	Docking score (kcal/mol)	Interacting residues with 4DUH
L$_1$	−95.750	Van der Waals (Pro A:150, Thr B:160, Glu B:159, Gln A:151, His A:147, Gln A:128), π-donor hydrogen bond (Gln B:161), π-alky (Val A:149).
L$_2$	−89.837	Van der Waals (Gln A:128, His A:147, Gln A:151, Thr B:160, Glu B:159, Glu B:146, Pro A:150), π-alky (Val A:149), hydrogen bond (Glu B:161).
L$_3$	−98.960	Van der Waals (Gly B:75, Gly B:164, Asp B:73, Gln B:72, Ile B:59, Glu B:58, Val A:149, Glu B:161), hydrogen bond (Thr B:163, Lys B:162, Gln B:135), π-alky (Ile B:60).
L$_4$	−90.801	Van der Waals (Gln A:151, Thr B:160, Glu B:159, Pro A:150), carbon hydrogen bond (Gln B:161), π-alky (His A:147, Val A:149).
L$_5$	−89.837	Van der Waals (Glu B:161, Glu B:159, Thr B:160, Glu B:159, Pro A:150, Thr B:151), π-alky (His A:147, Val A:149), hydrogen bond (Glu B:161).
	Docking score (kcal/mol)	**Interacting residues with 4MOT**
L$_1$	−107.148	Van der Waals (Val A:76, Thr A:172, Phe A:99, Ser A:124, Gly A:82, Arg A:84), carbon hydrogen bond (Pro A:84), alkyl and π-alkyl (Ile A:48, Pro A:84, Met A:83, Ala A:52, Val A:174), hydrogen bond (Asp A:78), amid π-stacked (Asn A:51).
L$_2$	−122.728	Van der Waals (Ser A:124, Phe A:99, Asn A:51, Gln A:77, Lys A:173, Gly A:80), hydrogen bond (Gly A:82), carbon hydrogen bond (Asp A:78, Thr A:172), alkyl and π-alkyl (Pro A:84, Met A:83, Ala A:52, Val A:174, Ile A:48).
L$_3$	−122.728	Van der Waals (Pro A:84, Lys A:173, Gln A:77, Ser A:124, Phe A:99), amid-π stacked (Asn A:51, Gly A:82), π-alkyl (Met A:83, Val A:174, Ala A:52, Val A:76, Ile A:48), carbon hydrogen bond (Thr A:172).
L$_4$	−103.724	Van der Waals (Val A:76, Asp A:78, Thr A:172, Glu A:55, Phe A:99, Ser A:124, Gly A:82, Asn A:51), alkyl and π-alkyl (Ile A:48, Pro A:84, Met A:83, Ala A:52, Val A:174).
L$_5$	−104.470	Van der Waals (Val A:76, Asp A:78, Glu A:55, Ser A:124, Phe A:99, Gly A:82, Arg A:140), carbon hydrogen bond (Thr A:172), amid π-stacked (Asn A:51), alkyl and π-alkyl (Pro A:84, Met A:83, Ala A:52, Val A:174, Ile A:48).

Table 8: Prediction of the toxicity pharmacokinetic properties based on Swiss ADMET results of the synthesized compounds **L$_1$**–**L$_5$**.

compounds	H-bond acceptors	H-bond donors	log $P_{o/w}$	log S	BBB	GI absorption	Lipinski	Bioavailability Score	TPSA	Ghose, Veber, Egan, Muegge	Class
L$_1$	4	0	3.30	−3.94	Yes	High	Yes	0.55	75.61	Yes	Soluble
L$_2$	4	0	3.02	−3.80	Yes	High	Yes	0.55	66.38	Yes	Moderately soluble
L$_3$	4	0	3.02	−3.78	Yes	High	Yes	0.55	66.38	Yes	Moderately soluble
L$_4$	3	0	3.77	−4.48	Yes	High	Yes	0.55	66.38	Yes	Moderately soluble
L$_5$	3	0	2.94	−4.88	Yes	High	Yes	0.55	66.38	Yes	Poorly soluble

flammatory drugs with minimum ulcerogenic properties. All compounds based on Veber's rules and Egan's rules represented the oral bioavailability of a possible drug molecule. Furthermore, log $P_{o/w}$ values of less than five with good lipophilicity value, indicate strong cell membrane permeability of the compounds and their biological activity. The compounds did not exhibit as CYP2D6 inhibitors, concluding that they would not show any adverse drug reactions.[55] TPSA of compounds were measured to be less than 160 Å, demonstrating very helpful statistic for forecasting the transport of drug molecules.[56] The drug-likeness parameters of an orally available bioactive drug are provided by the bioavailability radar and its graphical snapshot as a pink hexagonal part indicating size, flexibility, unsaturation, lipophilicity, solubility, and polarity as shown in Figure 10.

4. Conclusion

The series of five synthesized compounds **L$_1$**–**L$_5$** in this study were prepared, purified in quantitative yield and characterized using FTIR, UV-Visible, ^{1}H NMR, ESI-MS and single crystal XRD. The azomethine group (–C=N–) was indicated in FTIR in the range of 1622–1690 cm^{-1}. The UV-Visible spectra showed distinct absorption band at 350 nm as an evidence of n → π* transitions of azomethine group. The ^{1}H NMR spectra of the

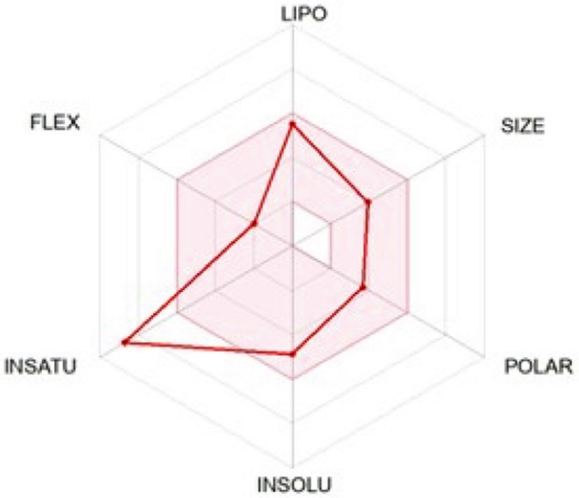

Figure 10. The bioavailability radar of the compounds $\mathbf{L_1}$–$\mathbf{L_5}$ using Swiss ADME web tool.

compounds were recorded in $CDCl_3$ showing a peak in the range of 8.82–10.18 indicating the presence of azomethine group. All compounds demonstrated significant bioactivity against various target microbes. The antibacterial activity of all compounds were examined against Gram-negative (*E. coli, K. pneumoniae* and *P. aeruginosa*) and Gram-positive (*S. aureus* and *S. pyogenes*) bacterial strains. The activities of compounds $\mathbf{L_1}$–$\mathbf{L_5}$ against various antibacterial targets showed that compounds containing a methoxy group exhibited better activity compared to those with halogenated groups. The antioxidant activity of compounds $\mathbf{L_1}$–$\mathbf{L_5}$ was found to be in the order of $\mathbf{L_1} > \mathbf{L_2} > \mathbf{L_3} > \mathbf{L_5} > \mathbf{L_4}$. The anti-fungal screening studies exhibited that all the compounds were active against *C. albicans* ATCC 60193 and *C. tropicalis* ATCC 13803 with stronger inhibitory properties compared to standard drugs. Interestingly methoxy-substituted compounds showed better bioactivities compared to halogen-substituted compounds. All compounds were optimized by DFT-D and then their quantum chemical parameters were investigated by using energy difference between the HOMO and LUMO orbitals. The chemical parameters, including energy gap and electrophilicity, obtained from DFT-D calculations, provided supportive insights into the biological activity of the compounds $\mathbf{L_1}$–$\mathbf{L_5}$.

Molecular docking study exhibited good interaction in the binding pocket of *E. coli* (PDB code 4DUH) and *S. pneumoniae* (PDB code 4MOT). Finally, Swiss ADME prediction modeling evaluated the physicochemical characteristics such as solubility, permeability, and drug-likeness. Results obtained from ADME study showed GI absorption for all compounds. Observation revealed that every anticipated derivative had favorable gastric absorption, signifying noteworthy oral bioavailability. All compounds showed a wide range of lipophilicity, suggesting diverse cellular permeability and dissolution properties.

Appendix A. Supplementary data

CCDC 2455335 corresponds to the crystallographic data of compound $\mathbf{L_1}$, deposited with the Cambridge Crystallographic Data Centre. Copies of the data may be obtained free of charge from The Director, CCDC, 12, Union Road Cambridge CB21EZ [Fax: +44 (1223)336 033] or e.mail: deposit@ccdc.cam.ac.uk.

Author's Contribution

Iram Akbar and Amir Karim: Synthesis, Conceptualization, Methodology, Formal analysis, Investigation, Writing original-draft. Rahime Eshaghi Malekshah: Computational study, Biological activities, Investigation and Writing original-draft. Najeeb Ullah: Writing original-draft, Characterizations. Yu-Ting Chu and Muhammad Nawaz Tahir: X-ray Crystallography. Muhammad Iqbal: Supervision, Data curation, Formal analysis, and editing. Saqib Ali: Project administrator, Data curation, Formal analysis. Sodio C. N. Hsu: Supervision, Data curation, Formal analysis, and editing.

Acknowledgments

We thank Bacha Khan University Charsadda and Quaid I Azam University Islamabad for supporting this work. We also acknowledge Mr. Qi-Xin Guo from Department of Medicinal and Applied Chemistry of KMU for the help on the ESI-MS determination.

Declaration of Interest

The authors declare that they have no known competing financial interests or personal relationships that could have appeared to influence the work reported in this paper.

5. References

1. J. K. Malik, F. Manvi, B. Nanjwade, S. Singh, P. Purohit, *Pharm. Lett.* **2010**, *2*, 347–359.
2. L. V. Zhilitskaya, B. A. Shainyan, N. O. Yarosh, *Molecules* **2021**, *26*, 2190. **DOI:**10.3390/molecules26082190
3. G. N. Raju, S. Karishma, K. R. Sowjanya, N. R. Rao, *Int. J. Adv. Pharm.* **2015**, *6*, 2776–2783.
4. O. M. Salih, M. A. Al-Sha'er, H. A. Basheer, *ACS Omega* **2024**, *9*, 13928–13950. **DOI:**10.1021/acsomega.3c09212
5. M. Singh, S. Kumar Singh, B. Thakur, P. Ray, S. K Singh, *Anticancer Agents Med. Chem.* **2016**, *16*, 722–739. **DOI:**10.2174/1871520615666151007160115
6. S. Shafi, M. M. Alam, N. Mulakayala, C. Mulakayala, G. Vanaja, A. M. Kalle, R. Pallu, M. Alam, *Eur. J. Med. Chem*, **2012**, *49*, 324–333. **DOI:**10.1016/j.ejmech.2012.01.032
7. G. A. Pereira, A. C. Massabni, E. E. Castellano, L. A. S. Cos-

ta, C. Q. F. Leite, F. R. Pavan, A. Cuin, *Polyhedron*, **2012**, *38*, 291–296. **DOI:**10.1016/j.poly.2012.03.016

8. A. Abdelhameed, X. Liao, C. A. McElroy, A. C. Joice, L. Rakotondraibe, J. Li, C. Slebodnick, P. Guo, W. D. Wilson, K. A. Werbovetz, *Bioorg. Med. Chem. Lett.* **2020**, *30*, 126725. doi: 10.1016/j.bmcl.2019.126725.
9. M. Gollapalli, M. Taha, M. T. Javid, N. B. Almandil, F. Rahim, A. Wadood, A. Mosaddik, M. Ibrahim, M. A. Alqahtani, Y. A. Bamarouf, *Bioorg. Chem.* **2019**, *85*, 33–48. **DOI:**10.1016/j.bioorg.2018.12.021
10. M. Amir, S. Asif, I. Ali, M. Z. Hassan, *Med. Chem. Res.* **2012**, *21*, 2661–2670. **DOI:**10.1007/s00044-011-9791-1
11. E. Kashiyama, I. Hutchinson, M.-S. Chua, S. F. Stinson, L. R. Phillips, G. Kaur, E. A. Sausville, T. D. Bradshaw, A. D. Westwell, M. F. Stevens, *J. Med. Chem.* **1999**, *42*, 4172–4184. **DOI:**10.1021/jm990104o
12. N. Karalı, Ö. Güzel, N. Özsoy, S. Özbey, A. Salman, *Eur. J. Med. Chem.* **2010**, *3*, 1068–1077. **DOI:**10.1016/j.ejmech.2009.12.001
13. F. Arjmand, B. Mohani, S. Ahmad, *Eur. J. Med. Chem.* **2005**, *40*, 1103–1110. **DOI:**10.1016/j.ejmech.2005.05.005
14. F. Arjmand, F. Sayeed, S. Parveen, S. Tabassum, A. S. Juvekar, S. M. Zingde, *Dalton Trans.* **2013**, *42*, 3390–3401. **DOI:**10.1039/C2DT32155F
15. J. Haribabu, V. Garisetti, R. E. Malekshah, S. Srividya, D. Gayathri, N. Bhuvanesh, R. V. Mangalaraja, C. Echeverria, R. Karvembu, *J. Mol. Struct.* **2022**, *1250*, 131782. **DOI:**10.1016/j.molstruc.2021.131782
16. J. K. Suyambulingam, R. Karvembu, N. S. Bhuvanesh, I. V. M. V. Enoch, P. M. Selvakumar, D. Premnath, C. Subramanian, P. Mayakrishnan, S.-H. Kim, I.-M. Chung, *J. Adhes. Sci. Technol.* **2020**, *34*, 2590–2612. **DOI:**10.1080/01694243.2020.1775032
17. M. Vedavathi, B. Somashekar, G. Sreenivasa, E. Jayachandran, *Int. J. Pharm. Sci. Res.* **2010**, 2, 53.
18. S. Salman, N. Bakr, M. Mahmood, *Physics and Astronomy, ILCPA*. **2015**, *40*, 36–42. **DOI:**10.56431/p-q9tzpl
19. N. D. Amnerkar, B. A. Bhongade, K. P. Bhusari, *Arab. J. Chem.* **2015**, *8*, 545–552. **DOI:**10.1016/j.arabjc.2014.11.034
20. A. Rambabu, M. P. Kumar, S. Tejaswi, N. Vamsikrishna, *J. Photochem. Photobiol. B.* **2016**, *165*, 147–156. **DOI:**10.1016/j.jphotobiol.2016.10.027
21. M. N. Bhoi, M. A. Borad, H. D. Patel, *Synth. Commun.* **2014**, *44*, 2427–2457. **DOI:**10.1080/00397911.2014.907426
22. H. S. Lihumis, A. A. Alameri, R. H. Zaooli, *Prog. Chem. Biochem. Res.* **2022**, *5*, 147–164. **DOI:**10.22034/pcbr.2022.330703.1214
23. L. Lerman, *J. Mol. Biol.* **1961**, *3*, 18–14. **DOI:** 10.22034/pcbr.2022.330703.1214
24. S. Dayan, M. Tercan, F. A. Özdemir, G. Aykutoğlu, N. Özdemir, Z. Şerbetçi, M. Dinçer, O. Dayan, *Polyhedron*, **2021**, *199*, 115106. **DOI:**10.1016/j.poly.2021.115106
25. S. Upadhyay, R. Zala, K. Bhatt, *Med. Anal. Chem. Int. J.* **2020**, *4*, 1–7. **DOI:**10.23880/macij-16000157
26. M. T. Gabr, N. S. El-Gohary, E. R. El-Bendary, M. M. El-Kerdawy, N. Ni, *Chin. Chem. Lett.* **2016**, *27*, 380–386. **DOI:**10.1016/j.cclet.2015.12.033
27. Y. Belay, A. Muller, P. Leballo, O. A. Kolawole, A. S. Adeyinka, T. Y. Fonkui, L. R. Motadi, *J. Mol. Struct.* **2023**, *1286*, 135617. **DOI:**10.1016/j.molstruc.2023.135617
28. K. Gholivand, M. Sabaghian, R. E. Malekshah, *Bioorg. Chem.* **2021**, *115*, 105193. **DOI:**10.1016/j.bioorg.2021.105193
29. R. Eshaghi Malekshah, M. Salehi, M. Kubicki, A. Khaleghian, *J. Coord. Chem.* **2018**, *71*, 952–968. **DOI:**10.1080/00958972.2018.1447668
30. A. L. Spek, *Biol. Crystallogr.* **2009**, *65*, 148–155. **DOI:**10.1107/S090744490804362X
31. J. Lübben, C. M. Wandtke, C. B. Hübschle, M. Ruf, G. M. Sheldrick, B. Dittrich, *Found. Crystallogr.* **2019**, *75*, 50–62. **DOI:**10.1107/S2053273318013840
32. A. Abdelmadjid, D. Haffar, F. Benghanem, S. Ghedjati, L. Toukal, V. Dorcet, R. Bourzami, *J. Mol. Struct.* **2021**, *1227*, 129368. **DOI:**10.1016/j.molstruc.2020.129368
33. H. Ighnih, R. Haounati, R. E. Malekshah, H. Ouachtak, Y. Toubi, F. Alakhras, A. Jada, A. A. Addi, *JPPA*, **2023**, *445*, 115071. **DOI:**10.1016/j.jphotochem.2023.115071
34. M. Haghbin, R. Eshaghi Malekshah, M. Sobhani, Z. Izadi, B. Haghshenas, M. Ghasemi, B. S. Kalani, H. Samadian, *Int. J. Biol. Macromol.* **2023**, *235*, 123766. **DOI:**10.1016/j.ijbiomac.2023.123766
35. S. Parvarinezhad, M. Salehi, R. Eshaghi Malekshah, M. Kubicki, A. Khaleghian, *Appl. Organomet. Chem.* **2022**, *36*, e6563. **DOI:**10.1002/aoc.6563
36. G. Alpaslan, B. Boyacioglu, N. Demir, Y. Tümer, G. Yapar, N. Yıldırım, M. Yıldız, H. Ünver, *J. Mol. Struct.* **2019**, *1180*, 170–178. **DOI:**10.1016/j.molstruc.2018.11.065
37. E. Ogbonda-Chukwu, O. Abayeh, O. Achugasim, *J. Appl. Sci. Environ. Manage.* **2022**, *26*, 2033–2037. **DOI:**10.4314/jasem.v26i12.17
38. E.-A. D. M. Abd, E. S. Eldin H, Ali Elham A. *J. Mol. Struct.* **2013**, *1048*, 487–499. **DOI:**10.1016/j.molstruc.2013.05.051
39. S. Noreen, S. H. Sumrra, *ACS Omega*, **2021**, *6*, 33085–33099. **DOI:**10.1021/acsomega.1c05290
40. M. Sunjuk, L. Al-Najjar, M. Shtaiwi, B. El-Eswed, M. Al-Noaimi, L. Al-Essa, K. Sweidan, *Inorganics*, **2022**, *10*, 43. **DOI:**10.3390/inorganics10040043
41. S. Chacko, S. Samanta, *J. Biopha.* **2017**, *89*, 162–176. **DOI:**10.1016/j.biopha.2017.01.108
42. A. Ahlawat, V. Singh, S. Asija, *Chem. Pap.* **2017**, *71*, 2195–2208. **DOI:**10.1007/s11696-017-0213-9
43. Y. S. Demircioğlu, H. C. Sakarya, Y. Süzen, *Bulg. Chem. Commun.* **2020**, *52*, 9–13. **DOI:** 10.34049/bcc.52.1.4835
44. O. A. El-Gammal, A. A. El-Bindary, F. S. Mohamed, G. N. Rezk, M. A. *J. Mol. Liq.* **2022**, 34, xx–xx. **DOI:**10.1016/j.molliq.2021.117850
45. F. Lemilemu, M. Bitew, T. B. Demissie, R. Eswaramoorthy, M. Endale, *BMC Chemistry,* **2021**, *15*, 67. **DOI:**10.1186/s13065-021-00791-w
46. N. Ranjitha, G. Krishnamurthy, M. Manjunatha, H. B. Naik, M. Pari, N. Vasantakumarnaik, J. Lakshmikantha, K. Pradeepa, *J. Mol. Struct.* **2023**, *1274*, 134483. **DOI:**10.1016/j.molstruc.2022.134483
47. H. A. K. Kyhoiesh, K. J. Al-Adilee, *Inorganica Chim. Acta.*

2023, *555*, 121598. **DOI:**10.1016/j.ica.2023.121598
48. Y. Cai, Q. Luo, M. Sun, H. Corke, *Life Sci.* **2004**, *74*, 2157–2184. **DOI:**10.1016/j.lfs.2003.09.047
49. A. C. Ekennia, A. A. Osowole, L. O. Olasunkanmi, D. C. Onwudiwe, E. E. Ebenso, *Res. Chem. Intermed.* **2017**, *43*, 3787–3811. **DOI:**10.1007/s11164-016-2841-z
50. S. Sakthivel, T. Alagesan, S. Muthu, C. S. Abraham, E. Geetha, *J. Mol. Struct.* **2018**, *1156*, 645–656. **DOI:**10.1016/j.molstruc.2017.12.024
51. R. Gandhimathi, S. Anbuselvi, R. Saranya, *JICS* **2023**, *100*, 101033. **DOI:**10.1016/j.jics.2023.101033
52. B. Belhani, M. Aissaoui, H. K'tir, T. Khaldi, L. Khattabi, Y. Laichi, A. Boulebnane, M. Berredjem, S. E. Djilani, *J. Mol. Struct.* **2023**, *1293*, 136221. **DOI:**10.1016/j.molstruc.2023.136221
53. A. Bayazeed, H. Alharbi, A. I. Alalawy, N. A. H. Alshammari, A. M. Alqahtani, M. Alsahag, A. Alisaac, N. M. El-Metwaly, *J. Mol. Struct.* **2025**, *1320*, 139579. **DOI:**10.1016/j.molstruc.2024.139579
54. W. M. Alamoudi, *J. Saudi Chem. Soc.* **2024**, *28*, 101897. **DOI:**10.1016/j.jscs.2024.101897
55. A. Bhardwaj, M. Kumar, S. Garg, D. Kumar, *Inorg. Chem. Commun.* **2023**, 157, 111332. **DOI:**10.1016/j.inoche.2023.111332
56. S. Banwala, S. Sardana, R. K. Sindhu, *REDVET* **2024**, *25*, 584–599. **DOI:**10.53555/redvet.v25i1.601

Povzetek

V tej študiji smo sintetizirali serijo novih kondenzacijskih produktov **L$_1$**–**L$_5$**, ki so nastali med substituiranimi piridinkarbaldehidi in 2-aminobenzotiazolom. Spojine smo karakterizirali s FTIR, UV-Vis, ^{1}H NMR spektroskopijo in ESI-MS analizami. Dodatno smo spojino **L$_1$** strukturno določili s pomočjo rentgenske difrakcije monokristala; ugotovili smo, da v asimetrični enoti vsebuje štiri kristalografsko neodvisne molekule. Vse pripravljene spojine izkazujejo antibakterijsko aktivnost proti Gram-negativnim in Gram-pozitivnim bakterijam ter so aktivne tudi proti *Candida albicans* ATCC 60193 in *Candida tropicalis* ATCC 13803. Strukture vseh spojin smo optimizirali s DFT-D metodo nato pa zanje izračunali vrednosti celokupnih energij ter vrednosti HOMO in LUMO energij ter določili teoretične parametre reaktivnosti. Napovedane ADME lastnosti nakazujejo, da vse spojine izkazujejo dobro podobnost z zdravili in da imajo ustrezne farmakokinetične lastnosti.

DOI: 10.17344/acsi.2025.9185 *Acta Chim. Slov.* **2025,** *72,* 430–440

Scientific paper

Synthesis, Characterization and Catalytic Properties of L-Cysteine-Mediated Self-Assembled Au-Ag/AgCl Nanoparticles

Moein Rezazadeh and Zeinab Moradi–Shoeili

Department of Inorganic Chemistry, Faculty of Chemistry, University of Guilan, P.O. Box 41335–1914, Rasht, Iran

** Corresponding author: E-mail: zmoradi@guilan.ac.ir*
Tel.: +98 13 33333262; fax: +98 13 33320066

Received: 02-07-2025

Abstract

In this study, the self-assembly of gold and silver-based nanoclusters modified by L-cysteine (Cys@Au-Ag/AgCl) was prepared using a simple and straightforward hydrothermal method. Cys@Au-Ag/AgCl exhibited efficient catalytic activity for the rapid reduction of 4-nitrophenol (4-NP) to the less toxic 4-aminophenol (4-AP) in the presence of $NaBH_4$ as a reducing agent, completing the reaction within a few minutes with a rate constant of 6.1×10^{-3} s^{-1}. The catalytic performance of Cys@Au-Ag/AgCl was optimized by studying the effect of various parameters on the catalytic reduction. In addition, Cys@Au-Ag/AgCl nanocomposite was used for catalytic reduction of $K_3[Fe(CN)_6]$ in the presence of $NaBH_4$, and the reaction rate constant was found to be 1.73×10^{-2} s^{-1}. The antibacterial activity of Cys@Au-Ag/AgCl nanocomposite was also evaluated against common drug-resistant Gram-positive bacteria (*Bacillus subtilis* and *Staphylococcus aureus*) and Gram-negative bacteria (*Pseudomonas aeruginosa* and *Escherichia coli*). The results demonstrated that the multifunctional Cys@Au-Ag/AgCl nanocomposite exhibited good antibacterial activity against these clinical drug-resistant bacteria.

Keywords: Gold; Silver; Nanoclusters; 4-Nitrophenol; $K_3[Fe(CN)_6]$; Antibacterial activity

1. Introduction

Over the past decade, noble metal nanoparticles (MNPs), such as gold, silver, palladium, and platinum, have attracted considerable attention due to their unique advantages such as high strength, stability, and cost-effective production.[1,2] These nanoparticles exhibit multiple applications, including in electronics, photonics, catalysis, drug delivery, biological imaging, magnetic recording devices, biosensors, and as enzyme mimetic nanoparticles.[3,4] Bimetallic nanoparticles of noble metals usually possess advantages in comparison with their monometallic counterparts due to the synergy between the two components which allows them to exhibit a wide range of new properties and applications.[5,6] Structural and physico-chemical properties of bimetallic nanoparticles strongly depend on the elemental composition and the method used to produce them.[7] Recently, many efforts have been devoted to the construction of a ternary Au/Ag/AgCl heterostructure. Results have shown that the incorporation of AgCl in bimetallic nanostructure can provide a much higher photocatalytic performance in comparison with pure Ag, Au and bimetallic Ag/Au nanoparticles.[8] Moreover, Au/Ag/AgCl hybrid materials can provide the multifunctionality of catalytic and optical properties that can be utilized in sensor and catalytic systems. Kuo et al. developed a cost-effective, highly sensitive and specific sensing system for easy and rapid detection of nanomolar concentrations of spermine in complex urine samples based on high peroxidase-like catalytic activity of Ag-Au/AgCl nanohybrid. They reported that the catalytic activity of Ag-Au/AgCl nanohybrid was at least 150-fold higher than that of its Ag, Au and AgCl components.[9] Sapkota et al. described the facile, efficient and ecofriendly synthesis route for Au-Ag@AgCl nanomaterials possessed high catalytic activity for multicomponent tandem synthesis of various quinoline derivatives.[10] Given its excellent surface-enhanced Raman scattering (SERS), Barveen and co-workers have demonstrated a facile hydrothermal and photoreduction approach to fabricate the Ag/Au/AgCl heterostructure for the SERS detection of antibiotics and analgesics. This unique properties of Ag/Au/AgCl heterostructure in the SERS process was related to the coupling of bimetal Au and Ag with the semiconductor (AgCl) which provides the large surface area, high enhancement of Raman signal, improvement of detection sensitivity, reproducibility and uniformity and also the reusable properties of SERS substrate due to the photodegradation ability of AgCl.[11] Devi et al. reported the catalytic and antimicrobial properties of Ag/Au/AgCl nanoparticles fabricated by using *Aquilaria agallocha* leaf juice. They found that the Au@Ag@AgCl nanoparticles showed better antimicrobial properties than the monometallic Ag and Au nanoparticles because of the medicinal properties of the leaf. The as-prepared Ag/Au/AgCl nanoparticles demonstrated an excellent catalytic activity in the reduction of toxic nitrocompounds.[12] Recently, Au@Ag@AgCl nanoparticles were employed for visible-light-driven photocatalytic degradation of various organic pollutants by Ryu and and co-workers.[13] In another precedent on photocatalytic activity of Ag/Au/AgCl hybrid materials, Lio et al. fabricated one-dimensional (1D) Ag/Au/AgCl hollow heterostructures. It was found that the synthesized Ag/Au/AgCl hollow heterostructures showed the higher catalytic and photocatalytic activity as compared to pure Ag nanowires. However, the AgCl semiconductor could act as supporting materials, but the excess AgCl is the obstacle for contact of Ag/Au bimetals with reactive species. Moreover, they showed that the Ag/Au bimetals enhanced the photocatalytic performance of AgCl semiconductor via the localized surface plasmon resonance (LSPR) and plasmon resonance energy transfer (PRET) mechanisms.[14]

4-Nitrophenol (4-NP) is highly toxic pollutant which can cause several negative impacts on human health such as formation of methemoglobin, liver and kidney damage, anemia, skin irritation, eye irritation, and systemic poisoning.[15] This pollutant has been listed as a priority pollutant by the US Environmental Protection Agency. Over the years, various methods such as photocatalytic degradation, chemical oxidation, electrochemical treatments, adsorption and coagulation have been developed to minimize the pollution of nitrophenols from wastewater.[16] In recent years, chemically reduction of nitrophenols to the useful product aminophenols using sodium borohydride ($NaBH_4$) as a reducing agent has been commonly used as the effective removal methodology for such hazardous substrate compounds from polluted waters.[17,18] In addition, there is a high industrial demand for aromatic amine compounds.[19] As an example, in pharmaceutical industry, the conversion of nitrophenols to aminophenols can be widely used in the production of many analgesics and antipyretics such as paracetamol and phenacetin.[20,21] These reactions have been also utilized as model reaction to assess the catalytic performance of various nanocatalytic systems especially metallic nanoparticles.[17,22] This is because the progress of the reduction reaction can be easily followed by UV-vis spectroscopy during the conversion of nitrophenols to aminophenols. Up to now, there have been a large number of mono and bimetallic nanoparticles consisting of Au and Ag have been reported for the catalytic reduction of nitroaromatic compounds.[23-28] However, the combination of Au, Au and AgCl nanoparticles is rarely investigated.

The World Health Organization (WHO) reported that antimicrobial resistance is one of the top 10 health threats to humans in recent years. According to the WHO report, bacterial infection has been one of the main causes of death worldwide in the past 15 years.[29] Although antibiotics have achieved remarkable success as conventional antibacterial drugs in the treatment of bacterial infections, the widespread and inappropriate use of antibiotics leads to antimicrobial resistance.[30] MNPs have been found as effective mineral agents in presenting antibacterial properties and optimizing their antibacterial performance is a major area of interest in new antibacterial treatments.[31,32] The chemical and physical nature of MNPs such as their elemental composition and morphology can significantly contribute to the interactions between MNPs and the target biosystem enhancing the development of more efficient antibacterial agents.[33-35]

Herein, novel L-cysteine-modified Au and Ag/AgCl nanoclusters (Cys@Au-Ag/AgCl) were developed via a simple hydrothermal method. This work advances prior research on mono/bimetallic Au/Ag nanoparticles by introducing a ternary system with unique synergistic properties. The Cys@Au-Ag/AgCl nanocomposite demonstrates enhanced catalytic efficiency for reducing both organic (4-NP) and inorganic ($K_3[Fe(CN)_6]$) pollutants to less toxic products, along with potent antibacterial activity against clinical drug-resistant Gram-positive and Gram-negative bacteria. These dual capabilities make the Cys@Au-Ag/AgCl nanocomposite a promising candidate for environmental and biomedical applications.

2. Experimental

2. 1. Materials and Characterization

All the chemicals used in this study were obtained from either Sigma-Aldrich or Merck and used as received without further purification. Deionized water was used throughout all the experiments.

Scanning electron microscopy (SEM) images were obtained using a field-emission scanning electron microscope (FE-SEM, TESCAN MIRA3, TESCAN Co., Czech Republic) at an acceleration voltage of 3 KV. UV-vis spectroscopic measurements were performed using a UV–vis spectrophotometer) Shimadzu UV-1800, Japan). FTIR spectra were recorded on an FTIR spectrophotometer (Alpha-Bruker) using KBr disks at room temperature. X-ray diffraction (XRD) spectroscopy was performed using an X-ray diffractometer (Philips PW 1730, Netherlands) with Cu Kα radiation (λ = 1.54 Å, 40 kV × 30 mA), and 2θ was scanned from 10° to 80°. X-ray energy diffraction (EDAX) was performed using an X-ray energy diffractometer (EM8000F, KY KY CO.,China).

2. 2. Synthesis of L-Cysteine Modified Cys@Au-Ag/AgCl Nanocomposite

Self-assembled gold-silver nanoparticles with L-cysteine were prepared by a facile hydrothermal reduction method using l-cysteine as reducing and stabilizing agent.[36] In this method, 1ml of $HAuCl_4$ solution (0.01M) and 1 ml of $AgNO_3$ solution (0.01M) were added to 10 mL deionized water. Then, 2 ml of l-cysteine solution (0.1M) was added dropwise under vigorous stirring for 10 minutes at room temperature. The pH of the solution was adjusted to 12 using NaOH (0.1M). A dark-brown colloidal precipitate was obtained, which was kept in autoclave at 120 °C for 2 hours. Then final precipitate was separated by centrifugation, washed three times with water and once with ethanol and dried at room temperature and washed three times with water and once with ethanol and dried at room temperature.

2. 3. Reduction of 4-Nitrophenol to 4-Aminophenol

To assess the catalytic performance of Cys@Au-Ag/AgCl nanocomposite, the reduction of 4-NP to 4-AP was used as a model reaction. In a typical experiment, 300 μl solution of freshly prepared aqueous $NaBH_4$ (0.1M) was added to 2.5 ml aqueous solution of 4-NP (0.1 mM) in a quartz cuvette with 1.0 cm path length. The color of the solution changed immediately from pale to bright yellow upon the addition of $NaBH_4$. Then, 5 mg of the synthesized Cys@Au-Ag/AgCl nanocomposite was added to the reaction mixture and the initial yellow color of the solution faded to colorless as the reaction proceeded. The progress of the reduction reaction was followed by monitoring the absorbance of the solution over the wavelength range of 250–500 nm in the same time interval.

The reduction percentage of 4-NP to 4-AP was calculated using eq. (1):

$$\%Reduction\ of\ 4-NP = \frac{A_0 - A_t}{A_0} \times 100\% \qquad (1)$$

where A_0 is initial absorbance and A_t the absorbance after a time interval.

2. 4. Investigation of the Effect of Different Parameters on the Catalytic Activity

In order to investigate the effect of catalyst dispersion on reaction rate, 0.01 g of the synthesized nanocomposite was dispersed in 10 mL of water and sonicated for 15 minutes. Then, Cys@Au-Ag/AgCl aqueous dispersion (1 mg/mL, 500 μL) was added to the aqueous solutions of 4-NP (0.1 mM, 2.5 mL) and $NaBH_4$ (0.1M, 300 μL) and the absorbance of the reaction solution was analyzed at 250-500 nm during the time course.

To optimize the amount of catalyst, reduction reaction of 4-NP was repeated four times under the same concentration of 4-NP (0.1 mM, 2.5 mL) and $NaBH_4$ (0.1M, 300 μL), except that different amount of the catalyst was added (200, 500 and 700 μL, 1 mg/mL) to the reaction mixture.

The effect of concentration of $NaBH_4$ on the rate of the catalytic reducing of 4-NP was also studied. In this regards, different amount of $NaBH_4$ (200, 300, 400 and 700 μL, 0.1 M) were added to the 4-NP solution (0.1 mM, 2.5 mL) and Cys Au/Ag nanocomposite (1 mg/mL, 500 μL).

To investigate the effect of the complex water environment on the catalytic performance of Cys@Au-Ag/AgCl nanocomposite in the reduction of 4-NP, the same molar concentration of 4-NP solutions were also prepared in tap water and seawater instead of the deionized water and the absorbance of the reaction solution was analyzed at 250-500 nm during the time course. The tap water directly obtained from the laboratory (without any treatment) and the Caspian seawater were used instead of deionized water when preparing the 4-NP solution.

2. 5. Reduction of $K_3[Fe(CN)_6]$

The catalytic activity of Cys@Au-Ag/AgCl nanocomposite was also studied in the reduction of $K_3[Fe(CN)_6]$. In a typical experiment, freshly prepared aqueous $NaBH_4$ solution (0.1 M, 200 μL) was mixed with aqueous solution of $K_3[Fe(CN)_6]$ (0.2 mM, 2.5 mL) in a quartz cuvette and then the Cys@Au-Ag/AgCl aqueous suspension (500 μL, 1 mg/mL) was injected without any stirring. The reaction was monitored by taking the absorption spectra between 250–500 nm at a time interval of 1 minutes. The reduction percentage of $K_3[Fe(CN)_6]$ was calculated using eq. (2):

$$\%reduction\ of\ K_3Fe(CN)_6 = \frac{A_0 - A_t}{A_0} \times 100\ \% \qquad (2)$$

where A_0 is initial absorbance and A_t the absorbance after a time interval at λ = 400 nm.

2. 6. Antibacterial Activity Assessment Method

The in vitro antibacterial activity of the prepared Cys@Au-Ag/AgCl nanocomposite was tested using the zone inhibition method,[37] against four pathogenic bacteria including *Pseudomonas aeruginosa* (*P. aeruginosa*), *Escherichia coli* (*E. coli*), *Staphylococcus aureus* (*S. aureus*), and *Bacillus subtilis* (*B. subtilis*). The nutrient agar and nutrient broth cultures were prepared according to manufactures' instructions and were incubated at 37 °C. After incubation for the appropriate time, a suspension of 100 μL of each bacterial test organism was spread onto the nutrient agar plates. Agar wells were prepared with the help of a sterilized glass tube. Then 100μL of the test agents at a concentration of 1000 μg/mL in DMSO were added to each well. All the bacterial strains were incubated at 37 °C for 24

h. Clear zones around the wells showed inhibition of bacterial growth and turbidity indicated bacterial resistance to the compound at the concentration present in the medium. The diameter of inhibition zones was determined in millimeters (mm). The concentration of DMSO in the medium did not affect growth of any of the microorganisms tested. Antibacterial activity of Cys@Au-Ag/AgCl nanocomposite was compared with tetracycline as standard drugs. DMSO was used as a negative control.

3. Results and Discussion

3. 1. Characterization

XRD analysis was carried out to confirm the crystal structure and particle size of the synthesized nanocomposite within the range of 2θ = 10°–80°. It clearly shows that the sample is composed of metallic Ag/Au and cubic AgCl crystals. Ag and Au crystals cannot be distinguished in the XRD patterns because the XRD diffraction peak pattern of single metallic gold and silver NPs as well as their bimetallic NPs are close together and they have similar crystal structure and lattice constants.[25] As shown in Fig. 1a, the XRD pattern of the Cys@Au-Ag/AgCl nanocomposite showed four diffraction peaks at 2θ= 38.27°, 44.42°, 64.58°, and 77.72° (labeled as circles) correspond to (111), (200), (220), and (311) lattice planes of fcc structure for Au and Ag in this bimetallic system.[38,39] In addition, the XRD pattern of the nanocomposite showed diffraction peaks at 2θ = 27.88°, 32.28°, 46.28°, 54.82°, 57.47°, 67.48°, 74.47 and 77.72° (labeled as stars) were can be attributed to the (111), (200), (220), (311), (222), (400), (331) and (420) planes of the cubic crystals of AgCl.[40] Therefore, the XRD result confirms the successful formation of Cys@Au-Ag/AgCl nanocomposite. FTIR spectroscopic measurement was used to identify the binding of the L-Cysteine as capping molecules on the surface of Cys@Au-Ag/AgCl nanocomposite. Fig. 1b shows the FTIR spectra of pure L-Cysteine and Cys@Au-Ag/AgCl. In the spectrum of pure L-Cysteine, characteristic bands of O–H stretching (3424 cm^{-1}) and CH$_2$ stretching (2968 cm^{-1}) were observed.[41] The broad absorption at around 3200 cm^{-1} can be attributed to the stretching mode of ammonium. The bands at 1544 cm^{-1} and 1593 cm^{-1} was ascribed to the symmetric bending mode of the N-H and COO asymmetric mode, respectively.[42] In the case of Cys@Au-Ag/AgCl nanocomposite, several peaks of L-cysteine are seen, indicating the incorporation of the L-cysteine into the structure of final nanocomposite. In addition, comparing with the two spectra shows the decrease in intensity or shifting of some bands which indicates the interaction of L-Cysteine with the Au, Ag and AgCl nanoparticles in the prepared nanocomposite. The FTIR spectrum of L-cysteine exhibits a typical S–H vibrational band at 2553 cm^{-1} which is absent in FTIR spectrum of Cys@Au-Ag/AgCl, indicating that the sulfur–hydrogen bond was broken and the L-cysteine molecules were associated with Au-Ag/AgCl nanoparticles through the formation of Au/Ag–sulfur bond. Binding of L-cysteine on the surface of nanoparticles through a thiolate linkage has already been reported in the literature.[43]

The morphology and particle size distribution of the as-prepared Cys@Au-Ag/AgCl nanocomposite were characterized by scanning electron microscopy (SEM). As shown in Fig. 2 at different magnifications, the nanocomposite exhibits a crystalline structure composed of spherical nanoparticles with diameters predominantly below 100 nm. While most particles self-assemble into larger spherical aggregates (<500 nm), isolated nanoparticles (~20 nm) are also observed. This agglomeration behavior, commonly observed in metal nanocomposites, can be attributed to the high surface energy of these particles due to their nano-size regime.[44] The SEM analysis confirms the successful formation of a nanostructured composite with the expected morphological features.

EDX and EDS spectroscopy was performed to determine the elemental composition of Cys@Au-Ag/AgCl nanocomposite. Fig. 3a shows the EDX spectrum, which displays the peaks corresponding to Au, Ag and Cl elements,

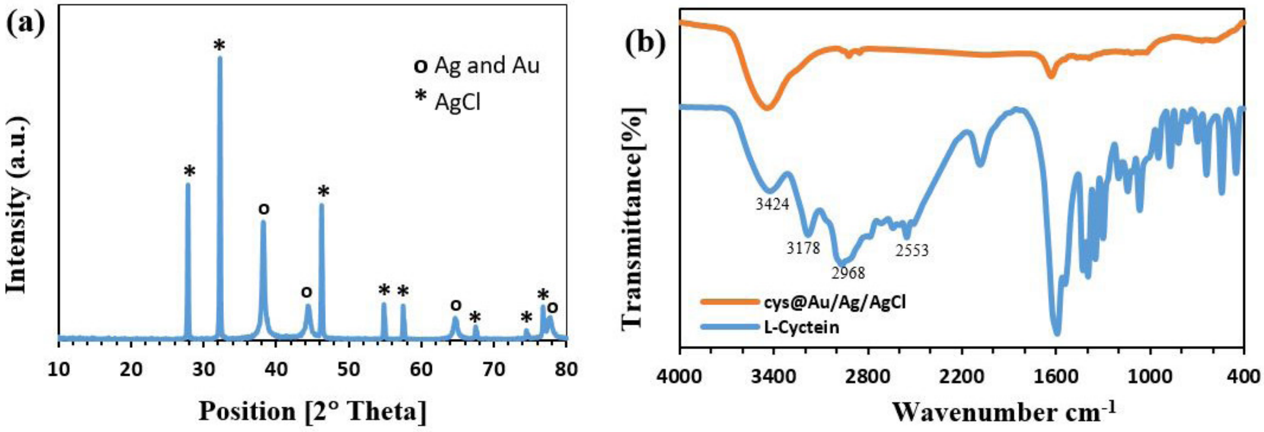

Fig. 1. (a) XRD pattern of Cys@Au-Ag/AgCl and (b) FTIR spectra of Cys@Au-Ag/AgCl and L-Cyctein

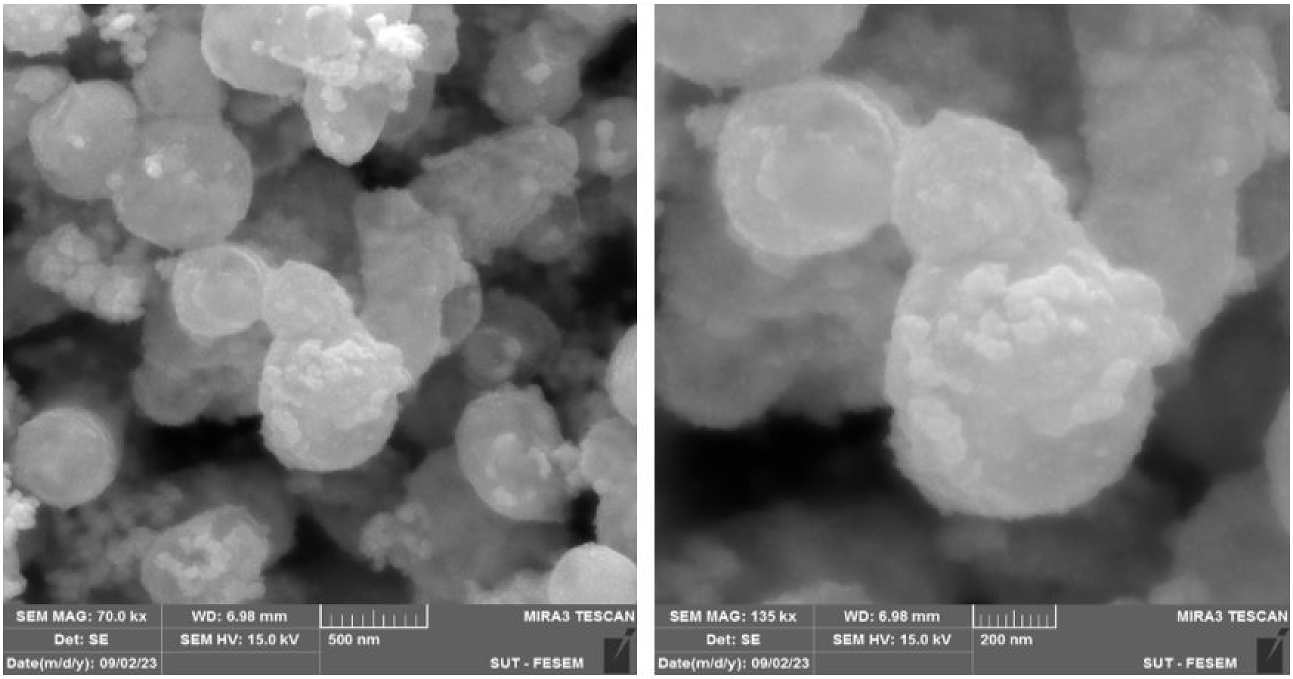

Fig. 2. SEM images of Cys@Au-Ag/AgCl nanocomposite at different magnifications (70 kx and 135 kx).

confirms the formation of Au, and Ag/AgCl NPs. The remaining elements (C, O, N and S,) due to the presence of cysteine molecules confirm the formation of Cys@Au-Ag/AgCl nanocomposite. EDS mapping of the synthesized nanocomposite (Fig. 3b) shows that all these elements are well dispersed in the structure of Cys@Au-Ag/AgCl nanocomposite.

3. 2. Catalytic Performance of Cys@Au-Ag/AgCl Nanocomposite

3. 2. 1. Catalytic Activity of Cys@Au-Ag/AgCl in the Reduction of 4-NP

The reduction of 4-NP to 4-AP was investigated as a model reaction to study the catalytic activity of Cys@Au-Ag/AgCl nanocomposite in the presence of $NaBH_4$ (scheme 1). In the absence of catalyst, the reduction of 4-NP was negligible whereas the addition of 5 mg Cys@Au-Ag/AgCl to 2.5 mL of the reaction mixture achieved a reduction of about 84% within 20 minutes (no stirring or sonication applied). Time-dependent UV-vis absorption spectra were recorded to monitor the reaction progress. Upon adding $NaBH_4$ to the 4-NP solution, the absorption peak shifted from 317 nm to 400 nm, accompanied by a color change from light yellow to bright yellow (Fig. 4a). This shift corresponds to the formation of 4-nitrophenolate ion (4-NP$^-$) in alkaline conditions. In the absence of the catalyst, this peak remained the same even after a long time without a change in intensity which indicates that $NaBH_4$ alone is not able to proceed fast enough the reduction reaction. In the presence of the Cys@Au-Ag/AgCl nanocomposite, the peak at 400 nm gradually decreased while a new peak appeared at about ~300 nm, indicative of 4-AP formation. After about 20 minutes, the complete disappearance of the 400 nm peak and the decolorization of the solution mixture confirmed the successful reduction of 4-NP to 4-AP (Fig. 4b).

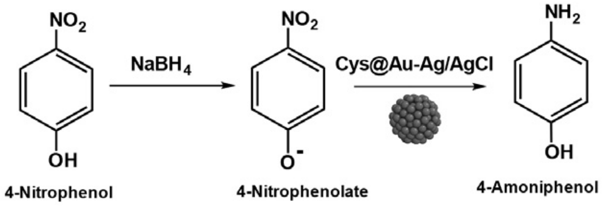

Scheme 1. Reduction of 4-NP to 4-AP in the presence of Cys@Au-Ag/AgCl nanocomposite

The catalytic activity of the prepared Cys@Au-Ag/AgCl nanocomposite in reduction of 4-NP was studied under different conditions including the effect of catalyst dispersion and different molar equivalents of catalyst and $NaBH_4$. In order to investigate the effect of catalyst dispersion on the reaction rate, the 10 mg of Cys@Au-Ag/AgCl was dispersed in 10 mL of H_2O using ultrasonication and appropriate amount was added to the reaction mixture. The results indicated that dispersing the catalyst in the reaction medium significantly increased the reaction rate as shown on Fig. 5a which provides the conversion of about 93% from 4-NP to 4-AP. The post-reaction analyses were similarly conducted under sonication to ensure sample

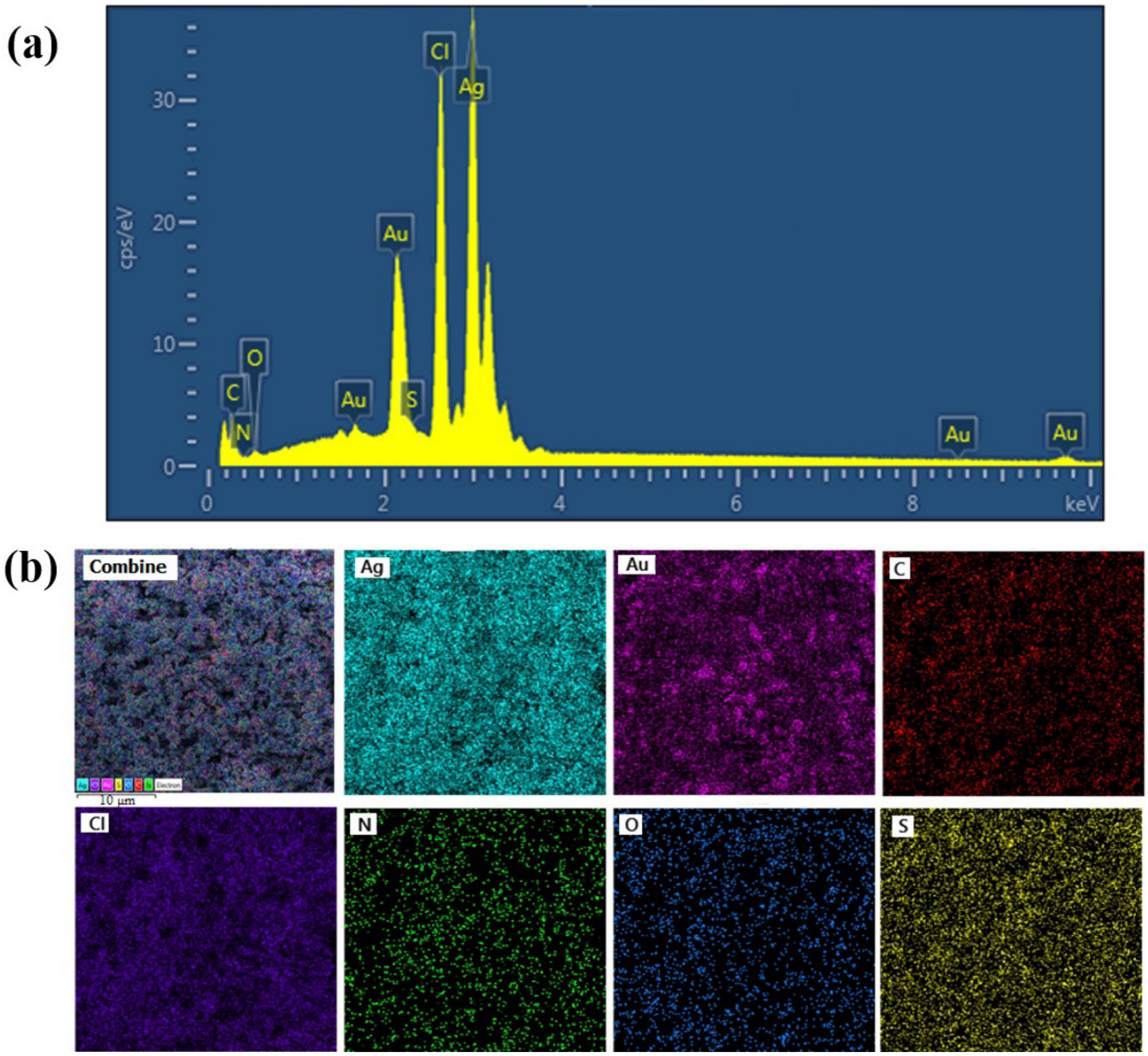

Fig. 3. (a) EDX spectrum and (b) EDS elemental mapping of the Cys@Au-Ag/AgCl nanocomposite

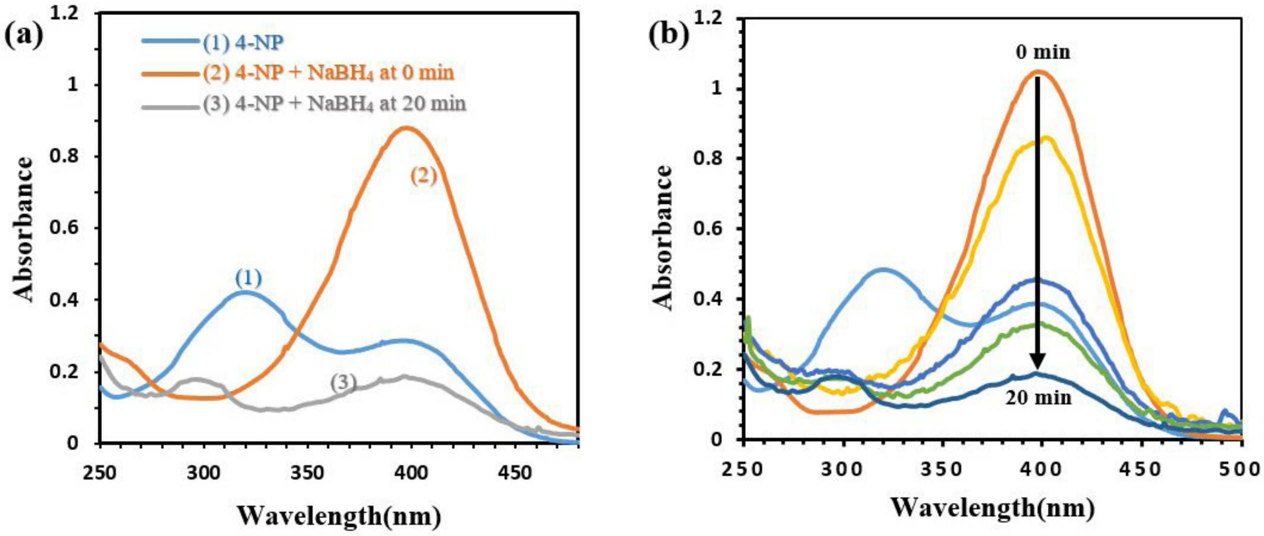

Fig. 4. (a) UV-Vis spectral profile of 4-NP and (b) Successive UV-vis absorption spectra for the reduction of 4-NP in the presence of Cys@Au-Ag/AgCl over time.

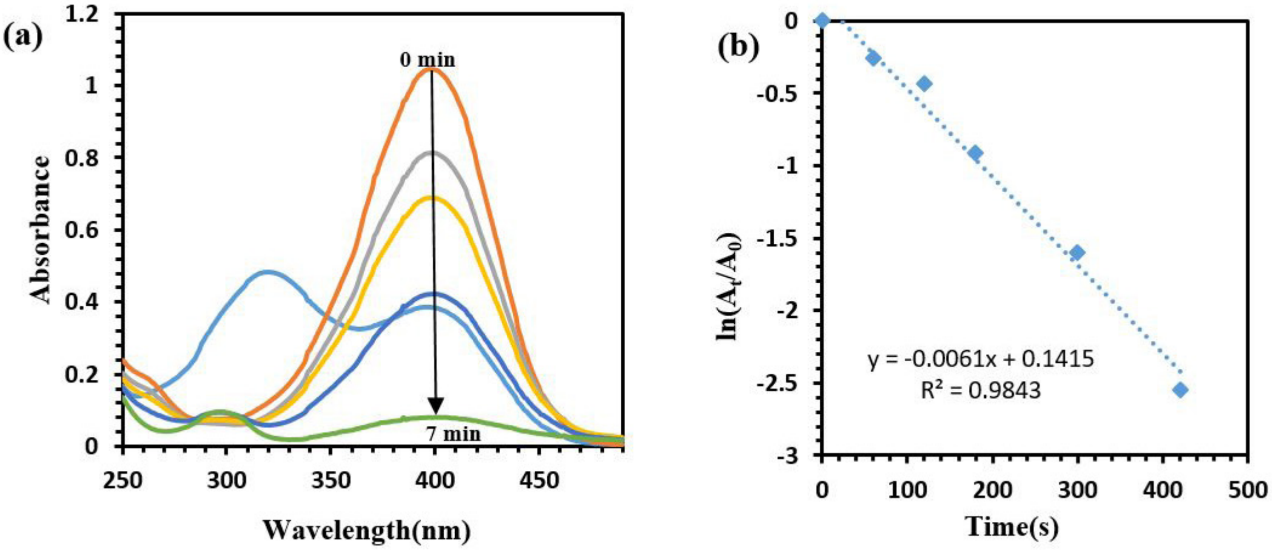

Fig. 5. (a) Sequential UV-vis absorption spectra for the sonication-assisted reduction of 4-NP by $NaBH_4$ in the presence of Cys@Au-Ag/AgCl. (b) The fitting plot curve of $\ln(A_t/A_0)$ versus time for the catalytic reduction reaction.

uniformity. The reaction rate for the sonication-assisted reduction reaction was determined by plotting the graph of ln (A_t/A_0) over time, where A_0 and A_t are the absorbances at 400 nm at time $t = 0$ and time t (Fig. 5b). A linear relation with a correlation coefficient of 0.9843 was obtained indicating a pseudo-first-order kinetics and the rate constant (k_{app}) was found to be 6.1×10^{-3} s^{-1}.

The optimization of the catalyst amount was achieved by varying the amount of Cys@Au-Ag/AgCl nanocomposite and the other reaction parameters during the mentioned reaction were kept constant. All optimization experiments were evaluated after a consistent 7-minute reaction period to enable direct comparison. As shown in Fig. 6a, the 0.2 mg/mL catalyst concentration achieved 93% conversion within 7 minutes, while increasing the amount to 0.28 mg/mL only marginally improved the conversion to 95%. Therefore, 0.2 mg/mL concentration was selected as optimal due to its near-identical catalytic efficiency coupled with significantly lower material consumption. In order to investigate the effects of the $NaBH_4$ concentration on the reaction rate, different amounts of $NaBH_4$ were added to the reaction vessel and the concentration of 4–NP and Cys@Au-Ag/AgCl (0.2 mg/mL) were kept constant. According to the Fig. 6b, the highest conversion percentage (96%) was achieved at a $NaBH_4$ concentration of 0.012 M after 7 minutes of reaction time, while other concentrations showed progressively reduced efficiency. This optimal concentration was therefore selected for the further studies. R Madhushree et al. have also found comparable optimized conditions for 4–NP reduction using MoS_2/ZnO nanocomposite.[45]

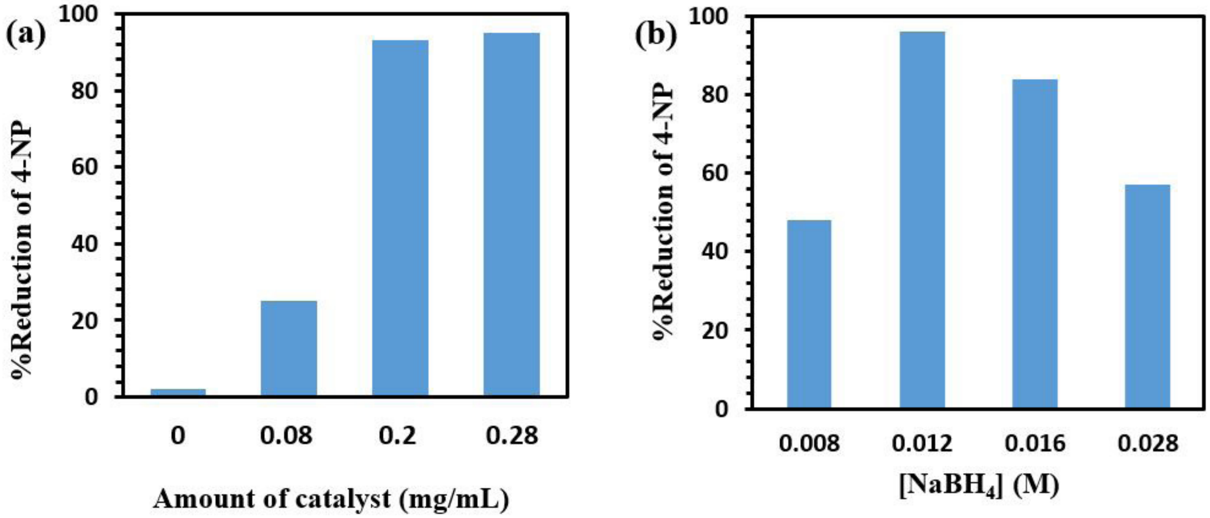

Fig. 6. Conversion of 4–NP to 4–AP in the presence of different (a) catalyst amounts (b) $NaBH_4$ concentrations after 7 minutes reaction time.

Table 1. Comparison of the catalytic performance of Cys@Au-Ag/AgCl with different nano-catalysts for 4–NP reduction.

Catalyst	**Reaction conditions (4–NP, $NaBH_4$, catalyst)**	k_{app} (s^{-1})	**%Reduction, Time**	**Ref.**
MoS_2/ZnO	0.5 mM (100 mL), 500 mg, 0.1 g	0.81×10^{-3}	99%, 15 min	45
Fe_2O_3-Pt@DSL-Pt	0.1mM, 50 mM, 0.5 mg	6.32×10^{-3}	99% , 8 min	46
PtNPs@C-PZS	0.1mM, 5mM,0.2 mg	4.6×10^{-3}	87.6%, 16 min	47
PZS@Ag-Au	0.05 mM, 3.8 mM,0.05 mg	4.63×10^{-3}	99% , 8 min	48
Ag–Fe_3O_4@chitin	0.1 mM, 0.1 M, 0.075 mg	5.23×10^{-3}	99%, 10 min	49
$CoMn_2O_4$/APTPOSS@FPS	0.2 mM, 0.5M, 0.4 mg	1.83×10^{-2}	99%, 100 s	50
Cys@Au-Ag/AgCl	0.1 mM , 0.012 M, 0.5 mg	6.1×10^{-3}	96%, 7 min	This work

As evidenced by the data in Table 1, the synthesized Cys@Au-Ag/AgCl catalyst demonstrates superior performance to previously reported nanocatalysts in terms of rate constant (k) and reaction completion time.

The catalytic performance of Cys@Au-Ag/AgCl was also investigated in different water environments such as seawater system and tap water system instead of deionized water. As shown in Fig. 7, the synthesized nanocomposite exhibited good catalytic activity in both seawater and drinking water and the presence of interfering ions such as sulfate and carbonate salts or organic species in the water environment did not interfere significantly in 4-NP reduc-

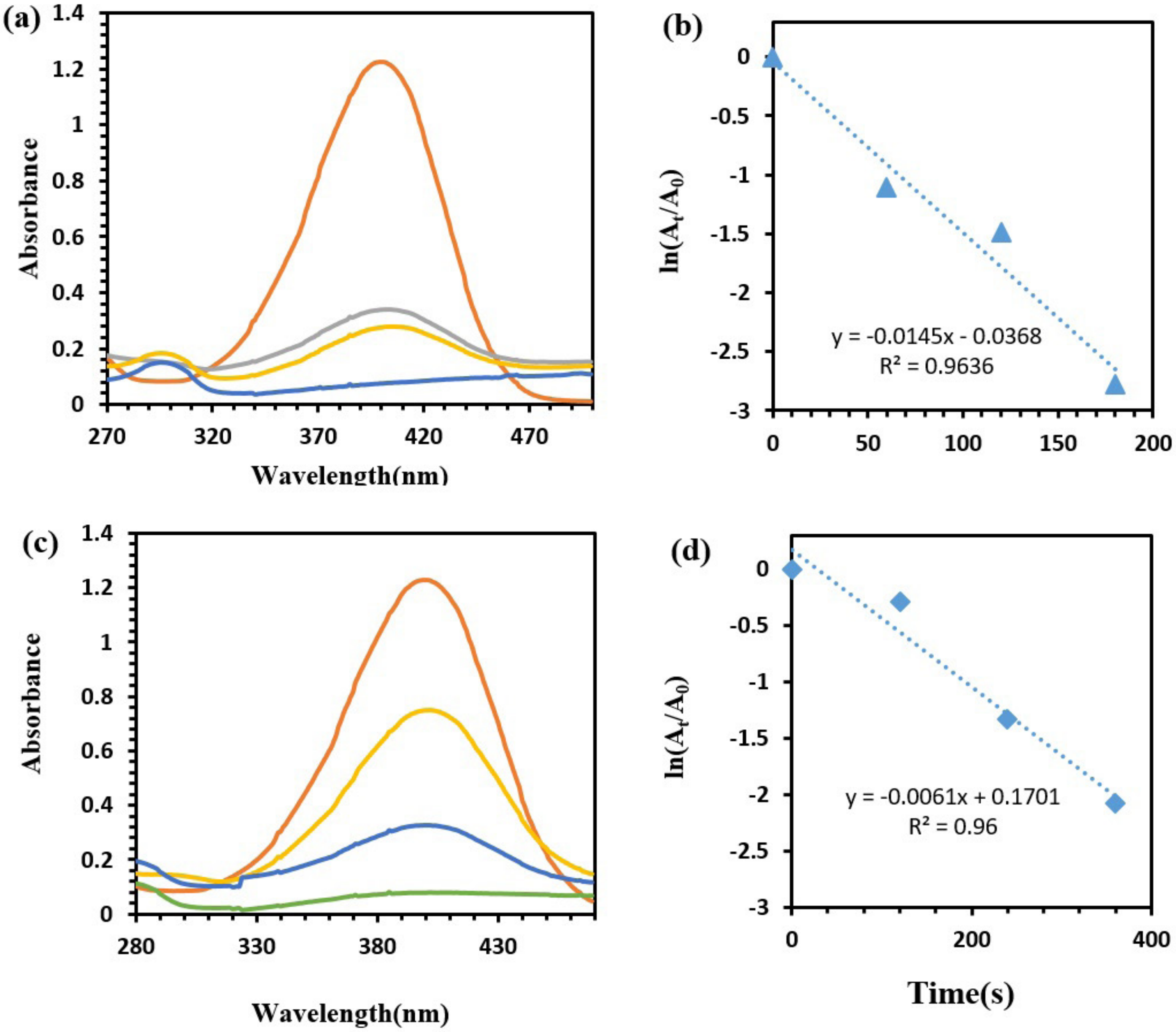

Fig. 7. Sequential UV-vis absorption spectra and the fitting plot curve of ln(At/A0) versus time for reduction of 4-NP in (a and b) tap water and (c and d) seawater in the presence of Cys@Au-Ag/AgCl nanocomposite.

tion process. The conversion efficiency of all three systems exceeds 95%.

3. 2. 2. Catalytic Activity of Cys@Au-Ag/AgCl in the Reduction of $K_3[Fe(CN)_6]$

The catalytic activity of Cys@Au-Ag/AgCl nanocomposite was also evaluated in reduction of $K_3[Fe(CN)_6]$ to $K_4[Fe(CN)_6]$ in the presence of $NaBH_4$ (Fig. 8a). As shown in Fig. 8b, from $\ln(A_t/A_0)$ vs. time plot, Cys@Au-Ag/AgCl shows pseudo-first-order kinetics reaction in reduction of $K_3[Fe(CN)_6]$ with k_{app} value of 1.73×10^{-2} s^{-1} and the conversion of 96% was achieved during 3 minutes (Fig 8b).

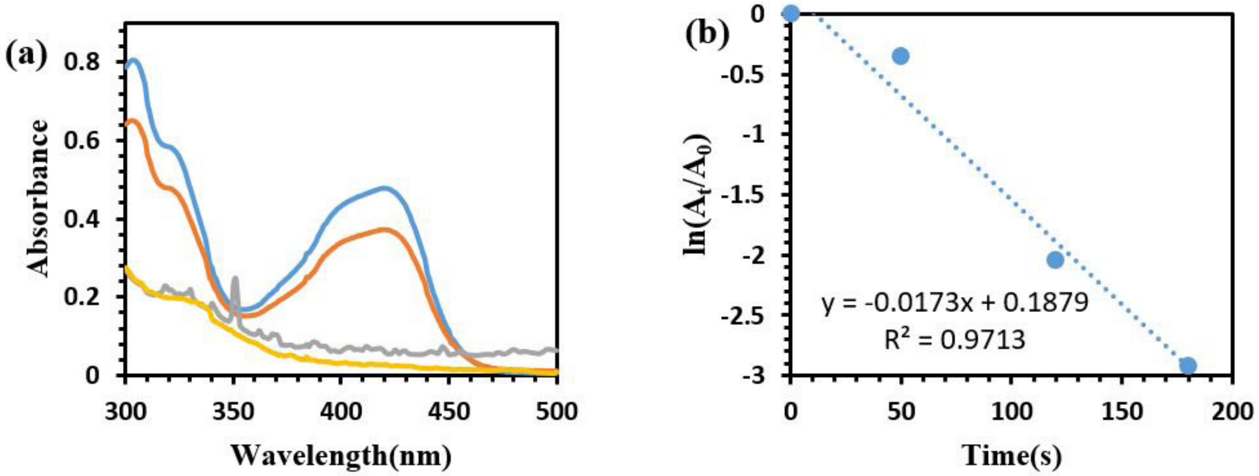

Fig. 8. (a) UV-vis spectra of the reduction of $K_3[Fe(CN)_6]$ pollutant in the presence of Cys@Au-Ag/AgCl nanocomposite. (b) The fitting plot curve of $\ln(A_t/A_0)$ versus time for the catalytic reduction reaction.

3. 3. Cys@Au-Ag/AgCl Antibacterial Test on Gram-positive and Gram-negative Bacteria

The antibacterial activity of Cys@Au-Ag/AgCl nanocomposite was studied against Gram-positive bacteria, *B. subtilis* and *S. aureus*, and also Gram-negative bacteria, *P. aeruginosa* and *E. coli*, using the zone inhibition method. Tetracycline was used as positive controls. The antibacterial activity was monitored at a concentration of 1000 μg/mL in DMSO and the experiments were performed by measuring the inhibition zone around the well. The results showed that the Cys@Au-Ag/AgCl nanocomposite has significant antibacterial activity against Gram-negative bacteria compared to Gram-positive bacteria. The inhibition zone was about 15 mm for *E. coli* and 18 mm for *P. aeruginosa*. While *B. subtilis* showed resistance and no inhibition halo was observed, the inhibition zone for *S. aureus* was 18 mm. The probable antibacterial mechanism of Cys@Au-Ag/AgCl nanocomposite can be attributed to the presence of gold and silver in the structure and their interactions with bacterial cells. Noble metal nanoparticles, particularly Ag and Au, are well-known for their bactericidal properties[51]. Research indicates that Ag- and Au-based nanomaterials exert antimicrobial effects through multiple pathways, including electrostatic adhesion to negatively charged bacterial membranes, penetration into cells due to their nanoscale size[52], and subsequent disruption of vital cellular processes. In addition, these nanoparticles induce oxidative stress via reactive oxygen species (ROS) generation, interfere with DNA/RNA replication, and disrupt enzymatic activity by binding to essential metabolites[53]. Notably, Au is less reactive than Ag in oxygen-rich environments, leading to lower ROS production[54]. However, studies indicate that Ag–Au nanocomposites often exhibit superior antimicrobial activity compared to their monometallic counterparts, likely due to synergistic effects[55]. Therefore, Cys@Au-Ag/AgCl nanocomposite can be used as an antibacterial agent in various industries such as pharmaceuticals, food, and medicine.

3. 4. Conclusion

In this study, L-cysteine was used as a biocompatible and stabilizing reducing agent to electrostatically immobilize Au, Ag and AgCl nanoparticles. The results showed that the prepared Cys@Au-Ag/AgCl nanocomposite exhibited high catalytic activity towards the reduction of toxic 4-NP to less toxic 4-AP within a few minutes using $NaBH_4$ as a reducing agent. The catalytic reduction performance of Cys@Au-Ag/AgCl was optimized by studying the effect of various parameters on the catalytic reduction of 4-NP. Furthermore, the Cys@Au-Ag/AgCl nanocomposite was used for the catalytic reduction of $K_3[Fe(CN)_6]$

in the presence of $NaBH_4$. Additionally, the antibacterial activity of the nanocomposite was evaluated using disk diffusion method against some pathogenic Gram-positive and Gram-negative bacteria. The results showed that the Cys@Au-Ag/AgCl nanocomposite exhibited good antibacterial activity against drug-resistant clinical bacteria. Facile preparation, quick reduction time and antibacterial activity of Cys@Au-Ag/AgCl nanocomposite may open a new window to synthesize new nano-catalysts with enhanced properties for decontamination of organic and inorganic pollutants from water sources and reduce the spreading of diseases and infections in medical and industrial environments.

Acknowledgements

The authors are grateful to the University of Guilan for financial support.

Compliance with Ethical Standards

The authors declare that they have no conflict of interest. This article does not contain any studies involving animals or human participants performed by any of the authors.

4. References

1. M. J. Ndolomingo, N. Bingwa, R. Meijboom, *J. Mater. Sci.* **2020**, *55,* 6195–6241. **DOI:**10.1007/s10853-020-04415-x
2. M. Azharuddin, G. H. Zhu, D. Das, E. Ozgur, L. Uzun, A. P. Turner, H. K. Patra, *Chem. Comm.* **2019**, *55,* 6964–6996. **DOI:**10.1039/C9CC01741K
3. T. H. Yang, J. Ahn, S. Shi, P. Wang, R. Gao, D. Qin, *Chem. Rev.* **2020**, *121,* 796–833. **DOI:**10.1021/acs.chemrev.0c00940
4. N. Gao, J. Xu, X. Li, G. Ling, P. Zhang, *Chem. Eng. J.* **2023**, 465, 142817–142831. **DOI:**10.1016/j.cej.2023.142817
5. I. Mustieles Marin, J. M. Asensio, B. Chaudret, *ACS nano*, **2021**, *15,* 3550–3556. **DOI:**10.1021/acsnano.0c09744
6. M. S. Qatan, F. Arshad, M. Miskam, G. A. Naikoo, *Int. J. Environ. Sci. Technol.* **2024**, *21,* 5247–5268. **DOI:**10.1007/s13762-023-05429-z
7. K. Loza, M. Heggen, M. Epple, *Adv. Funct. Mater.* **2020**, 30, 1909260–1909273. **DOI:**10.1002/adfm.201909260
8. J. Wang, C. An, M. Zhang, C. Qin, X. Ming, Q. Zhang, *Can. J. Chem.* **2012**, *90,* 858–864. **DOI:**10.1139/v2012-079
9. P. C. Kuo, C. W. Lien, J. Y. Mao, B. Unnikrishnan, H. T. Chang, H. J. Lin, C. C. Huang, *Anal. Chim. Acta*, **2018**, *1009,* 89–97. **DOI:**10.1016/j.aca.2018.01.018
10. K. Sapkota, S. S. Han, *New J. Chem.* **2017**, *41,* 5395–5402. **DOI:**10.1039/C7NJ00764G
11. N. R. Barveen, T. J. Wang, Y. H. Chang, *Chem. Eng. J.* **2021**, *423,* 130191–130203. **DOI:**10.1016/j.cej.2021.130191
12. T. B. Devi, M. Ahmaruzzaman, *ChemistrySelect*, **2017**, *2,* 5950–5957. **DOI:**10.1002/slct.201700601
13. H. J. Ryu, H. L. Kim, J. H. Joo, J. S. Lee, *Catal.* **2020**, *10,* 405–408 **DOI:**10.3390/catal10040405
14. J. Liu, Z. Wu, Q. He, Q. Tian, W. Wu, X. Xiao, C. Jiang, *Nanoscale Res. Lett.* **2019**, *14,* 1–13. **DOI:**10.1186/s11671-019-2862-9
15. R. Nehru, T. W. Chen, S. M. Chen, T. W. Tseng, X. Liu, *Int. J. Electrochem. Sci.* **2018**, *13,* 7778–7788. **DOI:**10.20964/2018.08.14
16. P. Sarkar, A. Dey, *J. Environ. Chem. Eng.* **2020**, *8,* 104347–104355. **DOI:**10.1016/j.jece.2020.104347
17. T. K. Das, N. C. Das, *Int. Nano Lett.* **2022**, *12,* 223–242. **DOI:**10.1007/s40089-021-00362-w
18. A. O. Cardoso Juarez, E. Ivan Ocampo Lopez, M. K. Kesarla, N. K. R. Bogireddy, *ACS omega*, **2024**, *9,* 33335–33350. **DOI:**10.1021/acsomega.4c04185
19. K. S. Hayes, *Appl. Catal. A: Gen.* **2001**, 221, 187–195. **DOI:**10.1016/S0926-860X(01)00813-4
20. C. Zhang, R. Zhang, S. He, L. Li, X. Wang, M. Liu, W. Chen, *ChemCatChem.* **2017**, *9*, 980–986. **DOI:**10.1002/cctc.201601364
21. Z. F. Jiang, F. M. Tian, K. M. Fang, Z. G. Wang, L. Zhang, J. J. Feng, A. J. Wang, *J. Colloid. Interface Sci.* **2025**, *677*, 718–728. **DOI:**10.1016/j.jcis.2024.08.027
22. M. J. Vaidya, S. M. Kulkarni, R. V. Chaudhari, *Org. Process Res. Dev.* **2003**, *7,* 202–208. **DOI:**10.1021/op025589w
23. N. Arora, A. Mehta, A. Mishra, S. Basu, *Appl. Clay Sci.* **2018**, *151*, 1–9. **DOI:**10.1016/j.clay.2017.10.015
24. M. Rocha, C. Pereira, C. Freire, *Colloids Surf. A: Physicochem. Eng. Asp.* **2021**, *621*, 126614–126627. **DOI:**10.1016/j.colsurfa.2021.126614
25. K. Hareesh, R. P. Joshi, D. V. Sunitha, V. N. Bhoraskar, S. D. Dhole, *Appl. Surf. Sci.* **2016**, *389*, 1050–1055. **DOI:**10.1016/j.apsusc.2016.08.034
26. S. D. Oh, M. R. Kim, S. H. Choi, J. H. Chun, K. P. Lee, A. Gopalan, C. G. Hwang, K. Sang-Ho, O. J. Hoon, *J. Ind. Eng. Chem.* **2008**, *14*, 687–692. **DOI:**10.1016/j.jiec.2008.04.008
27. S. Velpula, S. R. Beedu, K. Rupula, *Int. J. Biol. Macromol.* **2021**, *190*, 159–169. **DOI:**10.1016/j.ijbiomac.2021.08.211
28. A. M. Mostafa, E. A. Mwafy, N. S. Awwad, H. A. Ibrahium, *J. Mater. Sci.: Mater. Electron.* **2021**, *32*, 11978–11988. **DOI:**10.1007/s10854-021-05827-4
29. S. Kumar, *EClinicalMedicine*, **2021**, *41*, 101221 **DOI:**10.1016/j.eclinm.2021.101221
30. S. K. Ahmed, S. Hussein, K. Qurbani, R. H. Ibrahim, A. Fareeq, K. A. Mahmood, M. G. Mohamed, *J. Med. Surg. Public Health,* **2024**, *2*, 100081–100089. **DOI:**10.1016/j.glmedi.2024.100081
31. A. Brandelli, A. C. Ritter, F. F.Veras, Antimicrobial activities of metal nanoparticles. Metal nanoparticles in pharma, Springer, **2017**, pp.337–363. **DOI:**10.1007/978-3-319-63790-7_15
32. K. Gold, B. Slay, M. Knackstedt, A. K. Gaharwar, *Adv. Therap.* **2018**, *1*, 1700033–1700049. **DOI:**10.1002/adtp.201700033
33. A. Laganà, G. Visalli, F. Corpina, M. Ferlazzo, A. Di Pietro, A. Facciolà, *Eur. Rev. Med. Pharmacol. Sci.* **2023**, *27*, 3645–3663.

34. C. Silvia Pop, D. Hussien, M. Popa, A. Mares, A. Mihai Grumezescu, R. Grigore, V. Lazar, M. Carmen Chifiriuc, M. Sakizlian, E. Bezirtzoglou, S. Bertesteanu, Curr. *Top. Med. Chem.* **2015**, *15*, 1577–1582. **DOI:**10.2174/1568026615666150414125015
35. M. C. Sportelli, R. A. Picca, N. Cioffi: Nano-Antimicrobials Based on Metals. Novel antimicrobial agents and strategies: Wiley-VCH, Weinheim, Germany, **2014**, pp. 181–218. **DOI:**10.1002/9783527676132.ch8
36. S. Siddiqui, S. Shawuti, Sirajuddin, J. H. Niazi, A. Qureshi, *Ind. Eng. Chem. Res.* **2019**, *58*, 8035–8043. **DOI:**10.1021/acs.iecr.9b00016
37. Z. Piri, Z. Moradi–Shoeili, A. Assoud, *Inorg. Chim. Acta,* **2019**, *484*, 338–346. **DOI:**10.1016/j.ica.2018.09.054
38. S. Yallappa, J. Manjanna, B. L. Dhananjaya, *Spectrochim. Acta-A: Mol. Biomol. Spectrosc.* **2015**, *137*, 236–243. **DOI:**10.1016/j.saa.2014.08.030
39. S. S. Godipurge, S. Yallappa, N. J. Biradar, J. S. Biradar, B. L. Dhananjaya, G. Hegde, K. Jagadish, G. Hegde, *Enzyme Microb. Technol.* **2016**, *95*, 174–184. **DOI:**10.1016/j.enzmictec.2016.08.006
40. Y. H. Li, P. Tan, X. Q. Liu, D. D. Zu, C. L. Huang, L. B. Sun, *J. Nanosci. Nanotechnol.* **2015**, *15*, 4373–4379. **DOI:**10.1166/jnn.2015.9590
41. S. F. Parker, Chem. Phys. **2013**, *424*, 75–79. **DOI:**10.1016/j.chemphys.2013.04.020
42. I. Feliciano-Ramos, M. Caban-Acevedo, M. A. Scibioh, C. R. Cabrera, *J. Electroanal. Chem.* **2010**, *650*, 98–104. **DOI:**10.1016/j.jelechem.2010.09.001
43. S. Diamai, D. P. Negi, *Spectrochim. Acta-A: Mol. Biomol. Spectrosc.* **2019**, *215*, 203–208. **DOI:**10.1016/j.saa.2019.02.101
44. Z. Xu, H. Zhang, S. Liu, B. Zhang, H. Zhong, D. S. Su, *Int. J. Hydrogen Energy.* **2012**, *37*, 17978–17983. **DOI:**10.1016/j.ijhydene.2012.09.050
45. R. Madhushree, J. R. J. UC, D. Pinheiro, S. D. KR, *Appl. Surf. Sci. Adv.* **2022**, *10*, 100265–100273. **DOI:**10.1016/j.apsadv.2022.100265
46. Y. Gao, J. Fang, Y. Zhang, C. Zhang, S. Zhao, Y. Zhou, M. Huang, X. Sheng, *Appl. Organomet. Chem.* **2018**, *32*, 4208–4219.
47. J. Fu, S. Wang, X. Wang, Y. Yan, K. Wang, M. Gao, Q. Xu, *J. Porous Mater.* **2017**, *25*, 1081–1089. **DOI:**10.1007/s10934-017-0519-6
48. Y. Yan, J. Fu, M. Wang, S. Liu, Q. Xin, Z. Chen, Q. Xu, *RSC Advances*, **2016**, *6*, 24921–24928. **DOI:**10.1039/C6RA02158A
49. B. Duan, F. Liu, M. He, L. Zhang, *Green Chemistry*, **2014**, *16*, 2835–2845. **DOI:**10.1039/C3GC42637H
50. Y. Chen, L. Feng, S. M. Sadeghzadeh, *RSC advances*, **2020**, *10*, 19553–19561. **DOI:**10.1039/D0RA01136C
51. R. Aguilar-Garay, L. F. Lara-Ortiz, M. Campos-López, D. E. Gonzalez-Rodriguez, M. M. Gamboa-Lugo, J. A. Mendoza-Pérez, Á. Anzueto-Ríos, D. E. Nicolás-Álvarez, *Pharmaceuticals*, **2024**, *17*, 1134. **DOI:**10.3390/ph17091134
52. Y. Wang, J. Wan, R. J. Miron, Y. Zhao, Y. Zhang, *Nanoscale*, **2016**, *8*, 11143–11152. **DOI:**10.1039/C6NR01114D
53. Q. Li, F. Lu, H. Ye, K. Yu, B. Lu, R. Bao, Y. Xiao, F. Dai, G. Lan, *ACS Sustain. Chem. Eng.* **2018**, *6,* 9813–9821. **DOI:**10.1021/acssuschemeng.8b00931
54. S. Wang, Y. Wang, Y. Peng, X. Yang, *ACS appl. Mater. Interfaces*, **2019**, *11,* 8461–8469. **DOI:**10.1021/acsami.8b22143
55. X. Hu, X. Xu, F. Fu, B. Yang, J. Zhang, Y. Zhang, S. S. B. Touhid, L. Liu, Y. Dong, X. Liu, J. Yao, *Carbohydr. Polym*. **2020**, *248,* 116777. **DOI:**10.1016/j.carbpol.2020.116777

Povzetek

V tej raziskavi smo s preprosto hidrotermalno metodo pripravili strukturo nanoklastrov na osnovi zlata in srebra, modificiranih z L-cisteinom (Cys@Au-Ag/AgCl). Cys@Au-Ag/AgCl je pokazal učinkovito katalitsko aktivnost pri hitri redukciji 4-nitrofenola (4-NP) v manj toksičen 4-aminofenol (4-AP) ob prisotnosti $NaBH_4$ kot reducenta, pri čemer je bila reakcija zaključena v nekaj minutah s hitrostno konstanto $6{,}1 \times 10^{-3}\ s^{-1}$. Katalitsko učinkovitost Cys@Au-Ag/AgCl smo optimirali s preučevanjem vpliva različnih parametrov na katalitsko redukcijo. Poleg tega smo nanokompozit Cys@Au-Ag/AgCl uporabili tudi za katalitsko redukcijo $K_3[Fe(CN)_6]$ v prisotnosti $NaBH_4$, pri čemer je bila izmerjena konstanta reakcijske hitrosti $1{,}73 \times 10^{-2}\ s^{-1}$. Ocenili smo tudi protibakterijsko aktivnost nanokompozita Cys@Au-Ag/AgCl proti pogostim na zdravila odpornim gram-pozitivnim bakterijam (Bacillus subtilis in Staphylococcus aureus) ter gram-negativnim bakterijam (Pseudomonas aeruginosa in Escherichia coli). Rezultati so pokazali, da multifunkcionalni nanokompozit Cys@Au-Ag/AgCl izkazuje dobro protibakterijsko delovanje proti tem klinično pomembnim odpornim bakterijam.

DOI: 10.17344/acsi.2025.9163 *Acta Chim. Slov.* **2025**, *72*, 441–449

Scientific paper

Modelling and Prediction of Permeate Flux in the Ultrafiltration Recovery of Sodium Lignosulfonate from Aqueous Solution

Vinay B. Patel[1,2], Haresh K. Dave[2], Tejal M. Patel[2] and Kaushik Nath[2,*]

[1] *Research scholar, Gujarat Technological University, Ahmedabad, Gujarat, India*

[2] *Department of Chemical Engineering G H Patel College of Engineering & Technology (The CVM University), Vallabh Vidyanagar-388120, Gujarat, India*

* *Corresponding author: E-mail: kaushiknath@gcet.ac.in*

Received: 01-21-2025

Abstract

Modelling and data fitting for the prediction of permeate flux during ultrafiltration (UF) of a model feed solution of sodium lignosulfonate was carried out following resistance in series, gel polarization and Kedem Katchalsky equations. The experiments were conducted in a laboratory UF unit equipped with PES/HFUF asymmetric membrane under specific operating conditions by altering some parameters including solute concentration, transmembrane pressure (TMP), and cross flow velocity (CFV). The maximum experimental permeate flux was observed at TMP of 3.92 bar and CFV 0.527 ms^{-1} was 19.6×10^{-6} $m^3m^{-2}s^{-1}$. The theoretical and experimental volumetric flux was plotted, and their extent of resemblance was compared and validated statistically. The study sheds light on the effective upcycling of sodium lignosulfonate from spent liquor via ultrafiltration.

Keywords: Lignosulfonate, ultrafiltration, transmembrane pressure, model, flux

1. Introduction

Spent sulphite liquor, apparently considered to be a waste stream, produced in the sulphite pulping could be a rich source of sodium lignosulfonate – an invaluable product with innumerable upcycling options. Lignosulfonates (LS) have sparked interest due to its variety of applications as surfactants, dispersants of pesticides and dyes, cement and detergent builders, binders in ceramics, tanning and ingredients of fine chemical production.[1,2] There are multiple processing routes for the isolation and extraction of sodium lignosulfonate from commercial spent pulping liquor. The Howard process is one of the classical and widely used methods in which precipitation of lignosulfonate is accomplished by addition of excess lime. Fractionation based on solubility and molecular weight of the components includes solvent extraction, and precipitation.[3, 4] Selective adsorption using different sorbents such as synthetic polymeric resins, sandstone, lime stone, dolomite etc. has been reported by several authors.[1,5] Other methods include amine extraction using long chain alkali amines followed by alkali extraction, ion-exchange via exchange of sodium ion with hydrogen ion from the resin and membrane processes.[1,6,7] Despite being unique in their application and having several advantages, most of these methods have met with limited success. Adsorption is constrained by equilibrium and regeneration of spent sorbents. The same is true for ion exchange method as well, where the resin requires frequent replacement resulting in repeated plant shutdown and incurring high operational cost. Additionally, these methods are relatively tedious, and at times fail to recover a substantial quantity of LS.

In recent years, the use of semipermeable membranes, both commercial and indigenously functionalized have broadened the application of ultrafiltration (UF) in various sectors. Selective separation and fractionation of lignosulfonates from dilute spent liquor holds much promise in the development of biorefinery operations. Application of membranes with a variety of molecular weight cutoffs can shed much light on some rough, preliminary information on molecular weight distribution. Study of earlier literature reveals that ultrafiltration could yield a significant percentage of purified LS.[1] Various authors reported the combination of ultrafiltration and nanofiltration for the production of pure lignin fractions.[8,9] Even ultrafiltration could greatly reduce the polydispersity of the purified LS.[10,11] Fernández-Rodríguez 2015[12] carried out the fractionation of spent sulphite liquor by combining three ceramic UF membranes (molecular weight cut off of 15kDa, 5 kDa and 1kDa) in series and reported total LS rejection up to 72.56%. Parameters that affect the final product in UF comprise of trans-membrane pressure, feed temperature, cross-flow velocity, and the Reynolds number. In one of our earlier papers, [13]we reported the feasibility of UF to concentrate sodium lignosulfonate along with the analysis of dilution factor on permeate flux and solute retention.

The design and operation of ultrafiltration system entail accurate prediction of performance and rigorous analysis in terms of specific performance parameters such as water flux (membrane throughput) and solute rejection. However, UF rejection data have been analyzed less quantitatively than flux data in pertinent literature. To that end the present work bridges a research gap.Thus, the key focus of this work was to predict the permeate flux following resistance in series, gel polarization and Kedem-Katchalsky (K-K) equations and to compare the resemblance of experimental and predicted flux following statistical validation. These phenomenological models incorporate some of the important hallmarks of membrane separation, such as concentration polarization and formation of gel layer along with illustration of mass transfer across membrane. Modelling was carried out assuming that each of the hydraulic, osmotic pressure and concentration polarization resistances was dependent on the operating conditions. Modelling and data fitting was carried out by writing a program using Google Colab Python 3.10 version following resistance in series, gel polarization and Kedem Katchalsky equations.[14] It is expected that the results and model of the present study will be advantageous in a wide spectra of UF applications and facilitate commercial leverage at higher scale. Although the present experimental study is limited to the beneficiation of sodium lignosulfonate from dilute solution, the model used herein would certainly be applicable to other feed solutions within the framework of well-defined physical properties.

2. Materials and Methods

2. 1. Chemicals and Membranes

A hydrophilic commercial ultrafiltration membrane made of polyether sulfone was selected in the present experiment. It was supplied by M/s Aquaneel Separation Pvt Ltd, Vadodara, India. The molecular weight cut off the membrane was 5 kDa with maximum operating temperature 45 °C and pH range being 1–14. Distilled water of conductivity in the range of 10–15 μs cm^{-1} was used to prepare reagents. Various chemicals including sodium lignosulfonate (SLS, 96%) involved in experiments were of AR grades purchased from Merck Limited, Mumbai, India. The chemicals were used as purchased without any further treatment. The permeability of the membrane was evaluated after plotting permeate flux against trans-membrane pressure (TMP) using distilled water at ambient temperature.

2. 2. Ultrafiltration Study of Lignosulfonate Solution

Ultrafiltration of model feed solution of sodium lignosulfonate was carried out in a laboratory scale UF system. The schematic description of the experimental set up is given elsewhere.[13] A polyether sulfone flat sheet membrane with molecular weight cut off 5 kDa was used. LS feed solution was prepared by dissolving suitable quantity (the range being 1.2 to 1.24 g l^{-1}) of sodium lignosulfonate powder in deionized water. While evaluating the effect of selected operating conditions on model parameters, a number of experimental measurements were carried out at varying cross flow velocity and trans membrane pressure. The flux measurement study was carried out at four different cross flow velocities (ms^{-1}) like 0.323, 0.357, 0.425 and 0.527. The experimental flux calculation was carried out at four different trans-membrane pressures, namely 1.96, 2.94, 3.92 and 4.9 bar. The used membranes were cleaned using distilled water after each measurement followed by chemical cleaning, with EDTA (0.8% (w) of Na-EDTA (sodium salt of ethylaminediamine-tetraacetic acid) and detergent solution (2.0% (w) of STPP (sodium tripolyphosphate) ($Na_5P_3O_{10}$) and 0.025% (w) Na-DDBS ($C_6H_5(CH_2)_{12}$-SO_3Na) (sodium salt of dodecylbenzene sulfonate).

2. 3. Concentration of the Feed, Permeate and Reject Stream

The concentration of feed solution, permeate solution and reject solution was determined using a UV–VIS spectrophotometer (Model: Lambda 19, Perkin Elmer, USA) in a linear absorbance mode (scan speed 0.3–1200 nm min^{-1}, resolution 0.8 nm, deuterium lamp) out at a wavelength of 280 nm.

2. 4. Permeability and Flux Measurement of Membrane

The permeability of the used membrane was determined at various operating pressure using deionized water. The membrane permeability was determined from the slope of the permeate flux against trans-membrane pressure plot. The pure water flux J_w($m^3 m^{-2} s^{-1}$) was calculated using Eq. (1)

$$J_w = V/At \tag{1}$$

Where V is the volume of the permeate sample (m^3), A is the effective area (m^2) and Δt is the permeation time (s). The experiments were carried out at room temperature and average of three reading was reported.

2. 5. Modelling of the Present Study

Resistance in series model

Resistance in series model quantifies a number of mass transfer resistances during membrane transport. Total resistance Rtot can be expressed by Eq. (2).[15,16]

$$R_{tot} = R_m + R_{ad} + R_{cp} + R_p \tag{2}$$

R_m, R_{ad}, R_{cp} and R_p were calculated following the method described elsewhere.[17] The model was developed using principles of solution-diffusion and film theory and correlation for concentration polarization resistance. The transport equation through the porous membrane can be given by the Darcy's law to describe the osmotic pressure-controlled flux (Eq. 3)[18]

$$Vw^{osm} = L_p(\Delta P - \Delta\pi) \tag{3}$$

Where, $Lp = (1/\mu Rm)$, which indicates the permeability of the membrane. This permeability is related to the traditional Darcy's permeability (ko) as, $Lp = ko/\mu\delta$, where δ is the thickness of the membrane skin and μ is the viscosity of the permeating solution. The osmotic pressure difference across the membrane is given by Eq. (4)

$$\Delta\pi = \pi_m - \pi_p \tag{4}$$

Osmotic pressure of feed solution at membrane surface and in the permeate was estimated by using Vant Hoff's equation considering dilute solution. Accordingly, incorporating the osmotic coefficient 'a' at room temperature and considering molecular weight of sodium lignosulfonate (average molecular weight: 534.502 g mol^{-1}; universal gas constant R: 8314 J $mol^{-1}K^{-1}$; T: 303 K), the osmotic pressure becomes

$$\pi = 4713.C_p \tag{5}$$

Real retention (R_r) can be defined as the ratio of difference between membrane surface and permeate concentration to membrane surface concentration. It is a constant for a particular membrane-solute system.

$$R_r = 1 - \frac{C_p}{C_m} \tag{6}$$

Using Eqs. (3) to (5), the osmotic pressure-controlled flux is expressed as

$$Vw^{osm} = L_p(\Delta P - 4713 C_m R_r) \tag{7}$$

The osmotic pressure controlled flux; vw^{osm} cannot be calculated from Eq. (7), as

C_m is unknown. For that, the film theory for steady state mass transfer (Eq. 8) is used

$$Vw^{osm}.C + D.\frac{dc}{dy} = Vw^{osm}.C_p \tag{8}$$

On integrating Eq. (8) from $y = 0$, $c = c_m$ to $y = \delta$, $c = c_o$, the standard film theory equation is obtained as represented by Eq. (9)

$$Vw^{osm} = kln\left[\frac{C_m - C_p}{C_o - C_p}\right] \tag{9}$$

The permeate concentration C_p can be expressed in terms of the membrane surface concentration, c_m and R_r from Eq. (6). Eq. (9) can be expressed as

$$Vw^{osm} = kln\left(\frac{C_m.R_r}{C_o - C_m(1 - R_r)}\right) \tag{10}$$

In general, the Sherwood (*Sh*) number is related to the Schmidt (*Sc*) and Reynolds (*Re*) numbers for laminar flow as Eq. (11)

$$S_h = \frac{k.de}{D} = 1.85\left(Re.Sc.\frac{de}{L}\right)^{1/3} \tag{11}$$

For turbulent flow conditions (Re > 2000–4000) Harriott-Hamilton correlation (Eq. 12) was used to calculate Sh.[19]

$$S_h = 0.0096.R_e{}^{0.91}.S_c{}^{0.35} \tag{12}$$

Diffusivity D, was determined using the correlation of Wilke and Chang[20] (Eq. 13).

$$D = \frac{(117.3 \times 10^{-18})(\varphi.M)^{0.5}.T}{\mu.v^{0.6}} \tag{13}$$

Combining Eq. (7) and (9), Eq. (14) was obtained

$$\begin{aligned} Vw^{osm} &= L_p(\Delta P - 4713 C_m R_r) \\ &= kln\left(\frac{C_m.R_r}{C_o - C_m(1 - R_r)}\right) \end{aligned} \tag{14}$$

Eq. (14) was solved using Newton-Raphson trial and error method, to determine C_m and hence Vw^{osm}. Once C_m is calculated from Eq. (14) the permeate concentration C_p can be estimated from Eq. (6). For the determination of various resistances and models parameters a schematic algorithm of Python-designed computational program is presented in Fig. 1.

Gel polarization model

The mass transfer coefficient was calculated from Sherwood number[21] after calculating Reynold's number

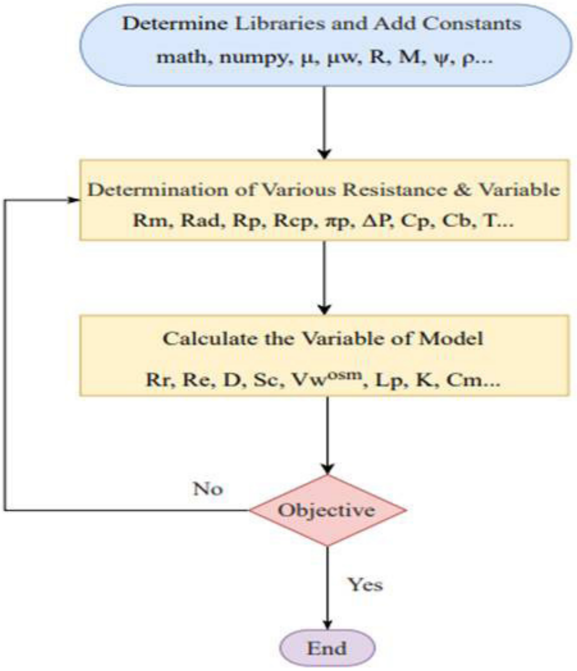

Fig. 1 Schematic algorithm of Python-designed computational program

and Schmidt number from cross flow velocity of the solution. The value of mass transfer coefficient was used to predict membrane surface concentration and then predicted flux calculation.[22] The predicted flux calculation from gel polarization model compared with experimental flux calculation.

$$R_{obs}=1-\frac{C_p}{C_o} \tag{15}$$

$$J=k\ln\left[\left(\frac{C_m-C_p}{C_o-C_p}\right)\right] \tag{16}$$

$$C_m=C_p+\left(C_o-C_p\right)\exp\left(\frac{J}{k}\right) \tag{17}$$

$$S_h=0.023\mathrm{Re}^{0.875}\,Sc^{0.25} \tag{18}$$

Kedem Katchalsky Model

Pure water permeability (L_p) was calculated by doing the experiments at different TMP. The predicted solvent flux was calculated by Eq. (19) [23] and compared with experimental flux. The reflection coefficient was assumed to be 0.9.

$$J=L_p(\Delta P-\sigma\Delta\pi)=\text{Solvent flux} \tag{19}$$

Where $\Delta\pi = RT(C_o - C_p)$. Incorporating Eq. (17) in Eq. (19) and substituting Δπ solvent flux was estimated.

2. 6. Statistical Analysis

The difference between measured or estimated value and the true value was expressed as a ratio of the absolute difference to the true value.

$$\text{Relative Error}=\frac{|\text{True Value}-\text{Measured Value}|}{\text{True Value}}$$

Root mean square error can be estimated following Eq. (20), in which the smaller the value of RMSE, the better will be the fit between the predicted and experimental data.

$$\text{RMSE}=\sqrt{\frac{1}{\text{N}}\sum_{\text{i}=1}^{\text{N}}\left(\text{J}_{\text{i,exp}}-\text{J}_{\text{i,theory}}\right)^2} \tag{20}$$

Where RMSE = Root mean square error

Chi-square test is a statistical analysis used to compare actual results with an expected hypothesis. It combines both curve-fitting and model testing by considering measurement uncertainties following Eq. (21).

$$\text{x}^2=\sum\frac{(\text{O}_\text{i}-\text{E}_\text{i})^2}{\text{E}_\text{i}} \tag{21}$$

Where O_i = observed value and E_i = expected value

A smaller value of x^2 is indicative of good fit of model data with those of experimental.

3. Results and Discussion

Membrane flux or throughput is an important performance index for any pressure driven membrane process including UF. Forecasting of permeate flux is an important consideration for long-term UF operation. Membrane durability as well as permeate flux is influenced by the phenomena named concentration polarization (i.e., solute build-up) and fouling (due to adhesion of microbial cells, solute particles, gel layer formation etc.) at the membrane surface. Similar to other filtration process UF is also encountered with the drop of permeate flux largely due to aforementioned factors.[24,25] In the present study, prior to modelling of permeate flux, effect of trans-membrane pressure on it and its time evolution under specific experimental conditions were investigated. Later, three mathematical models namely resistance in series, gel polarization and Kedem-Katchalsky (K-K) were applied. Predicted flux estimated from these three models was then compared with experimental flux. These are highlighted in the following subsections.

3. 1. Effect of Trans-membrane Pressure

It was observed in the present experiment, that permeate-flux increased proportionally with the trans-membrane pressure within the pressure range studied in all cases. This implies that the operation was within the pressure-controlled region. Fig 2 represents the experimental permeate flux as a function of trans-membrane pressure at four different cross flow velocities for a run time of 60 min and at constant initial feed concentration of 1.24 gL^{-1}. A perusal of Fig 2 reveals that at 3.92 bar pressure, experimental flux was found to be maximal for all cross flow velocities. At a cross flow velocity of 0.527 ms^{-1} the values of permeate flux were estimated to be 13.4 × 10^{-6} and 17.4 × 10^{-6} m^3 m^{-2}s^{-1} at trans-membrane pressure of 2.94 and 3.92 bar respectively.

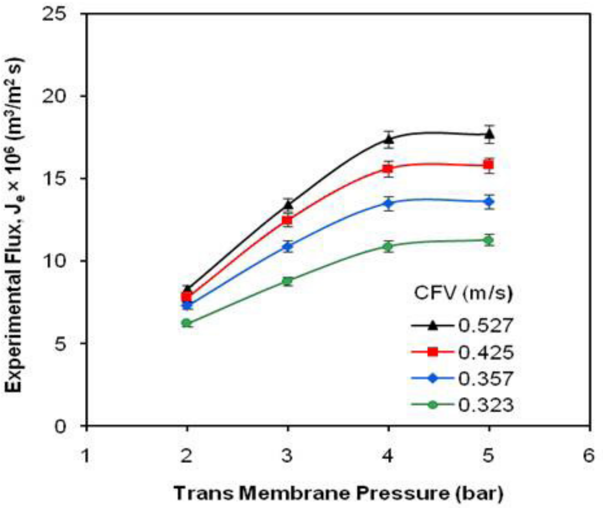

Fig. 2 Experimental flux as a function of trans-membrane pressure at various cross flow velocities (Feed concentration: 1.24 g/L; run time: 60 min, temp: ambient).

The figure also indicates that increase in cross flow velocity resulted in substantial flux improvement. For example, at CFV of 0.323m s^{-1}, the maximum permeate flux at 3.92 bar TMP was found out to be 10.9 × 10^{-6} m^3 m^{-2}s^{-1} and this rose to 17.4 × 10^{-6} m^3 m^{-2}s^{-1} when CFV was increased to 0.527 ms^{-1} thereby, registering a 59.6% increase. A higher cross flow velocity can effect a sweeping action across the membrane, minimizing the concentration gradient towards the membrane surface and subsequently results in flux increment.[25] As the trans-membrane pressure increases, the osmotic pressure also increases, which can partly nullify the increase in flux. Thus, beyond 3.92 bar pressure there was negligible increase in permeate flux. It means the attainment of the "critical flux" region of UF, which is where the flux starts to plateau. At this point, further increasing the pressure generally does not augment the flux. These observations follow the similar trend as reported by Bhattacharya et al (2005)[27] for the ultrafiltration of sodium lignosulfonate from spent sulphite liquor. Our study indicates that 3.92 bar trans-membrane pressure was found to be the most appropriate under the present experimental conditions.

3. 2. Time Evolution of Permeate Flux

Fig 3 represents the experimental flux as a function of time for a feed solution having initial concentration of 1.24 gL^{-1}, and TMP 3.92 bar at four different cross flow velocities (CFVs). At CFV of 0.527 ms^{-1}, and transmembrane pressure of 3.92 bar permeation flux was estimated to be 19.6 × 10^{-6} m^3 m^{-2}s^{-1} after 15 min of operation which however reduced to 17.4 × 10^{-6} and 15.2 × 10^{-6} m^3/m^{-2}s^{-1} after 45 and 60 min respectively. This corresponds to 28.9% reduction of initial flux. For other cross flow velocities the percentage flux reduction was in the range of 25–28% under similar experimental conditions.

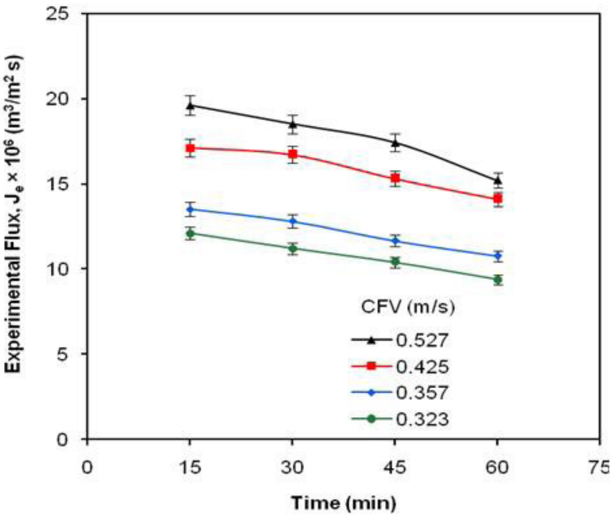

Fig 3. Experimental flux as a function of time at various cross flow velocities (Feed concentration = 1.24 g/L; trans membrane pressure: 3.92 bar, run time: 60 min, temp: ambient)

The declining trend of permeate flux with time, as shown in Fig 3, is ascribed to the phenomenon of solute build up (concentration polarization) on the surface layer of membrane imparting resistance to solvent transport.

Although concentration polarization could be reversible during the initial period of operation, it becomes irreversible phenomena like solute adsorption and gel layer. A perusal of the profile of permeate flux as a function of time indicates gradual decline of flux with time. Initially the decline was sharp followed by a steady decline in line with the classical filtration theory. At the beginning of operation smaller solutes presumably block the membrane pores resulting in flux decline, which further aggravated due to gradual concentration polarization on the membrane surface. It has been reported by many authors that resistance arising out of the concentration polarization is the dominating cause for the permeate flux decline reaching values somewhat two times higher than the hydraulic membrane resistance.[28,29] At the end of each experimental run, the used membrane was thoroughly washed and reused. It was found that original membrane permeability could be largely regained. This possibly indicates that the

Table 1: Comparison with similar other studies of ultrafiltration of spent sulfite liquor from literature

Sr No	Membrane types and features	Average permeate flux (L/m^2 h)	Trans membrane pressure (bar)	Major findings	Reference
1	TiO_2 ceramic membranes are used (MWCO: 1, 5 and 15 kDa)	55.45, 5.77 and 6.00 for 15, 5 and 1 kDa membranes respectively	1.8 to 2.0	Fractionation of spent sulfite liquor into monomeric sugars and LS. Highest LS rejection (65.68 %)	[12]
2	Polysulfone membrane (GR 60-P)	Not presented	6.0 to 11.5	Concentration polarization model was used to determine lignosulfonate rejection. Average molecular mass was also estimated	[21]
3	Polysulfone and fluoropolymer membranes (MWCO 10–100 kDa)	100–700 (a wider range for different membranes)	0 to 10	High MWCO GR membranes are very suitable for UF of SSL for the recovery of lignosulphonates.	[27]
4	Ceramic hollow fiber membranes with MWCO 20 kDa, 20 kDa, 30 nm, 8 nm, and 3 nm	252 to 261	3.0 to 7.0	Ceramic hollow fiber membranes were comparable and even better than tubular membrane to concentrate spent sulfite liquor	[30]
5	Polysulfone, polyethersulfone and fluoropolymer composite membranes (MWCO:1–10 kDa)	10 to 50	2 to 5	Could not fractionate lignosulphonates from sugars due to overlapping molecular weights of LS and sugars	[31]
6	Polyether sulfone membrane (MWCO: 5 kDa)	13.4 to 17.4	1.9 to 4.9	Modelling and data fitting was carried out following RIS, GP and K-K equations.	Present study

fouling due to pore blocking was reversible. Additionally, Table 1 summarizes the comparison of major experimental findings from similar other studies of ultrafiltration of spent sulfite liquor from pertinent literature.

3. 3. Experimental and Predicted Flux Using Various Models

Predicting the permeate flux is critical for evaluating and optimizing the performance of the ultrafiltration process. In modelling, along with model description it is vitally important to analyse and validate the capacity of the models to predict the permeation flux. This, in turn, impacts the further use of these models for scaling up to industrial level**.** In the present study three models namely resistance in series, gel polarization and K-K were applied for predicting flux of permeate in ultrafiltration of sodium lignosulfonate solution. Fig 4 presents graphical comparison of the theoretically predicted versus experimentally determined volumetric permeate flux using three different models at four different cross flow velocities (CFV). A perusal of Fig 4 indicates that theoretically predicted permeate flux following resistance in series and gel polarization models, conforms more closely to the experimental values compared to K-K model.

Theoretically, the resistances against solvent flux are the summation of the membrane hydraulic resistance, reversible pore-blocking resistance, and a deposited gel-layer resistance. Using K-K model, predicted flux values become exorbitantly higher than those of experimentally determined ones. The extent of matching between the predicted permeation flux and the experimental data, following all the three models was evaluated using statistical performance parameters such as root mean square error (RMSE), chi square test, and percentage relative error (RE) (Table 2). The smaller the values of RMSE and RE, the better would be the matching between the predicted and the experimental fluxes. The same is true for the chi square test as well. Thus, from a further observation of Table 1, it is evident that at a cross flow velocity of 0.527 ms^{-1}, RMSE, RE and chi squared parameters are minimal for resistance in series and gel polarization models. It also indicates that increase in cross flow velocity resulted in a marginally better fit between experimental and predicted flux values. The highest relative error and root mean square errors (in bracket) estimated for the predicted permeate flux using resistance-in-series, gel polarization and K-K models were 0.603 (6.765), 0.684 (7.640), 2.892 (30.292) respectively. The results obtained, within the statistically validated models, showed that K-K model presents a high variability of prediction (values of percentage relative error in the range of 2.89–3.32), and root Mean Square Error (RMSE) in the range of 26.53–30.29 within the experimental framework. The chi square test analysis also shows that x^2 values for curve fitting by using resistance in series and gel polarization models are very low

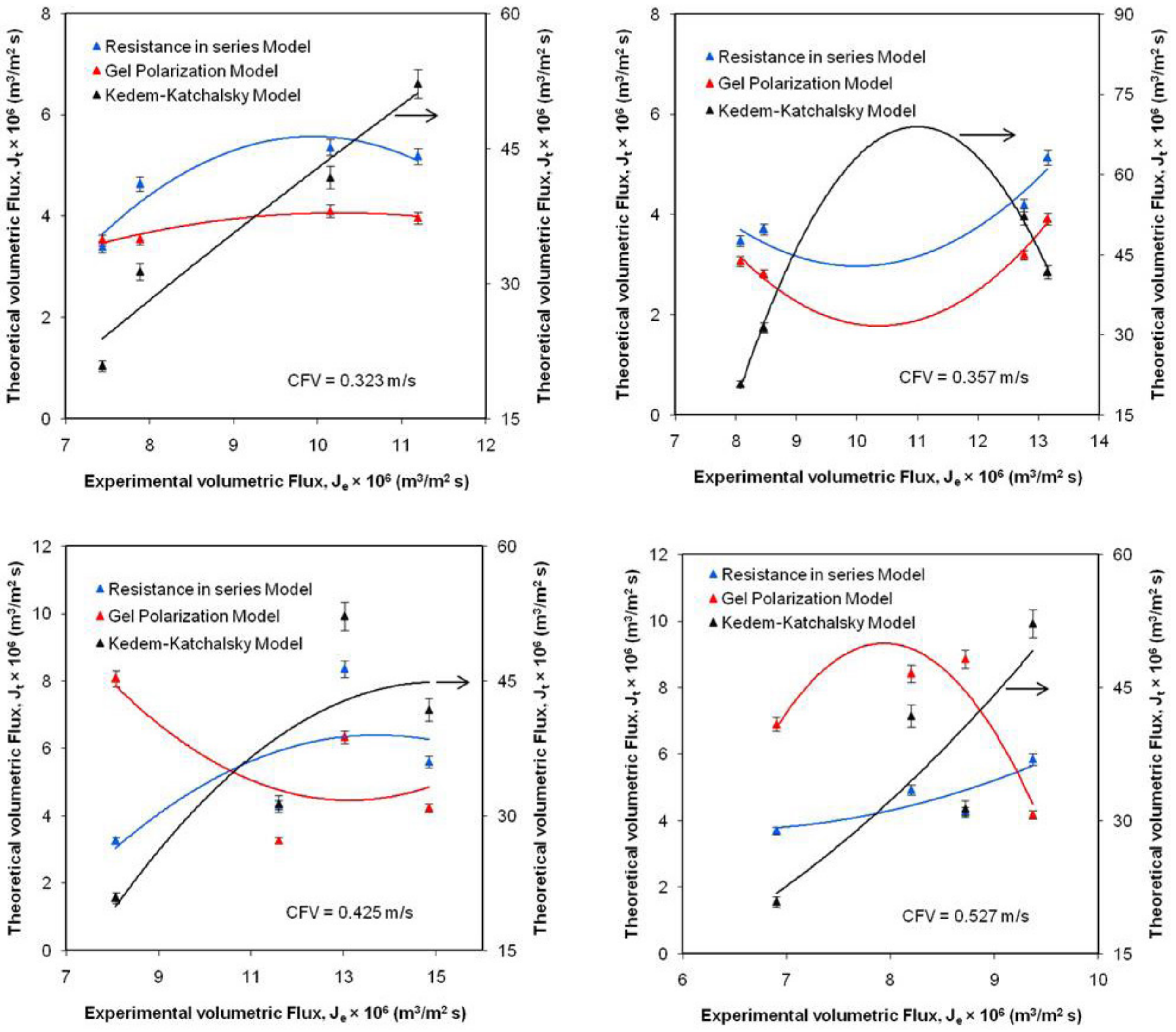

Fig 4: Graphical comparison theoretical Vs Experimental volumetric flux using three different models at four different cross flow velocities (CFV). (a) CFV: 0.323 m/s (b) CFV: 0.357 m/s (c) CFV: 0.425 m/s (d) 0.527 m/s; (Feed concentration = 1.24 g/L; trans membrane pressure: 3.92 bar; run time: 60 min, temp: ambient).

compared to those obtained in K-K model for all the cross flow velocities.

The significant deviation between the experimental data and those predicted by the K-K model might be due to fluctuating interference of the operating parameters and experimental inaccuracies. Kedem-Katchalsky equations are based on the linear thermodynamics of irreversible processes. The equations are valid for membrane systems with two-component solutions, suitably diluted and well stirred. Since, under the present experimental set

Table 2: Statistical analysis of goodness of fit between experimental and predicted volumetric flux of ultrafiltration SLS solution *(Resistance in series: RIS; Gel Polarization: GP; Kedem-Katchalsky:KK)*

CFV	Chi square			RMSE			% RE		
(m/s)	RIS	GP	KK	RIS	GP	KK	RIS	GP	KK
0.323	4.312	1.700	21.394	4.633	5.542	29.216	0.491	0.579	2.892
0.357	4.153	1.748	23.992	6.732	7.640	27.676	0.603	0.684	2.390
0.425	3.175	1.648	17.009	6.765	7.519	26.534	0.551	0.486	2.029
0.527	1.604	1.4	7.833	3.636	2.592	30.292	0.436	0.128	3.322

up the feed solution was not sufficiently well stirred, the K-K model showed a deviation from the predicted values. In literature mostly it is applied for RO and NF systems, where applied pressures are relatively high. The reason why two proposed models worked well, whilst the other fared poorly is not obvious at this stage. Nevertheless, there is a strong likelihood of other forms of membrane-solute interaction which was not investigated in the present work. In future, another form of interaction should be taken into account. In essence, the findings of data fitting show that the osmotic pressure difference, the cross-flow velocity of the feed solution, and the water permeability coefficient has a significant impact on water flux.

4. Conclusion

The performance of the resistance in series and gel polarization model, studied in our work for the prediction of permeate flux is quite satisfactory, since the model predictions are in consonance with the experimental data. In both of these models statistical fit parameters such as root mean square error, percentage relative error and chi square test values were estimated to be in the lower range compared to Kedem Katchalsky model thereby indicating conformation between theoretical and experimental flux data. However, Kedem Katchalsky model represents substantial difference between experimental and theoretical values. However, the phenomenological models used in this study, despite presenting a moderate variability of prediction stand as unique tools for scaling-up and for better understanding of the UF process. The developed models may be utilized for any other ultrafiltration system and could be a useful tool for the scaling-up of processes from laboratory to pilot or industrial dimensions. In conclusion, the phenomenological models presented in this paper provide an initial framework for advancing a problem of considerable practical as well as theoretical interest. Nevertheless, the application to more complex matrices needs elaborate further investigation.

Nomenclature:

J = Permeate flux ($m^3m^{-2}\ s^{-1}$)
R_m = Intrinsic membrane resistance (m^{-1})
R_{ad} = Adsorption resistance (m^{-1})
R_{cp} = Concentration polarization (m^{-1})
R_p = Pore blocking resistance (m^{-1})
R_{tot} = Summation of a number of resistances
Vw^{osm} = Osmotic pressure controlled flux ($m^3m^{-2}.s^{-1}$)
L_p = Permeability of the membrane ($m^3m^{-2}\ s^{-1}\ Pa^{-1}$)
ΔP = Transmembrane Pressure drop (bar)
$\Delta\pi$ = Osmotic pressure difference
π_m = Osmotic pressure at the membrane surface (bar)
π_p = Osmotic pressure at the permeate stream (bar)
C_p = Permeate concentration (mg l^{-1})
C_m = Membrane surface concentration (mg l^{-1})
C_0 = Feed concentration (mg l^{-1})
R = Universal gas constant (J $mole^{-1}\ K^{-1}$)
R_r = Real retention
k = Mass transfer coefficient ($m\ s^{-1}$)
L = Effective membrane length (m)
M = Molecular weight of the solvent (kg $kgmol^{-1}$)
μ = Solution viscosity ($kg\ m^{-1}\ s^{-1}$)
ν = Solute molar volume ($kg\ mol\ m^{-3}$)
φ = Association factor for solvent
R_e = *Reynolds number,* $^{\rho.u.d}/\mu$ (Dimensionless)
S_c = *Schmidt number,* $^{\mu}/\rho.D$ (Dimensionless)
S_h = *Sherwood number,* $^{k.d}/D$ (Dimensionless)
T = Temperature (K)
D = Diffusivity ($m^2\ s^{-1}$)
d_e = Equivalent diameter (m)
σ = reflection coefficient
R_{obs} = Rejection observed

Declaration of Competing Interest

The authors declare that they have no known competing financial interests or personal relationships that could have appeared to influence the work reported in this paper.

5. References

1. I. Sumerskii, P. Korntner, G. Zinovyev, T. Rosenau, A. Potthast, *RSC Advances*. **2015**, *5*, 92732–92742. **DOI:**10.1039/C5RA14080C
2. K. Nath, S.C.Panchani, T. M. Patel, H. K. Dave, V. B. Patel, K. K. Tiwari, N. Sahoo, *J. Wood Chem. Tech.* **2020**, *40*, 331–347. **DOI:**10.1080/02773813.2020.1809677
3. D. Tarasov, M. Leitch, P. Fatehi, *Biotech. Prog.* **2015**, *31*, 1508–1514. **DOI:**10.1002/btpr.2149
4. W. Fang, M. Alekhina, O. Ershova, S. Heikkinen, H. Sixta, *De Gruyter* **2015,** *69,* 943–950. **DOI:**10.1515/hf-2014-0200
5. P. Fatehi, J. Chen, in: Z. Fang, Jr. R. Smith, Jr. (Eds.), Production of Biofuels and Chemicals from Lignin. Biofuels and Biorefineries. Springer, Singapore, 2016. pp.35–54. **DOI:**10.1007/978-981-10-1965-4_2
6. G. E. Fredheim, S. M. Braaten, B. E. Christensen, *J. Chromat.* A **2002**, *942*, 191–199. **DOI:**10.1016/S0021-9673(01)01377-2
7. K. Gawluk, A. Modrzejwska-Sikorska, T. Rębiś, G. Milczarek, *Catalysts* **2017**, *7*, 392–401. **DOI:**10.3390/catal7120392
8. A. Arkell, J. Olsson, O. Wallberg, *Chem. Eng. Res. Des.* **2014**, *92*, 1792–1800. **DOI:**10.1016/j.cherd.2013.12.018
9. A-S Jönsson, A-K Nordin, O Wallberg, *Chem. Eng. Res. Des.* **2008**, *86,* 1271–1280. **DOI:**10.1016/j.cherd.2008.06.003
10. Y. Deng, W. Zhang, Y. Wu, H. Yu, X. Qiu, *J. Phys. Chem. B* **2011**, *115*, 14866–14873. **DOI:**10.1021/jp208312a
11. O. Ringena, B. Saake, *Holzforschung* **2005**, *59*, 405–412. **DOI:**10.1515/HF.2005.066

12. J. Fernández-Rodríguez, A. Garcíab, A. Coza, J. Labidi, *Chem. Eng. Trnsac.* **2015**, *45*, 553–558. **DOI**: 10.3303/CET1545093
13. K. Nath, V. B. Patel, H. K. Dave, S. C. Panchani, *Ind. Chem. Eng.* **2022**, *64*, 553–564. **DOI:**10.1080/00194506.2022.2028197
14. C. Quezada, H. Estay, A. Cassano, E. Troncoso, R. Ruby-Figueroa, *Membranes* **2021**, *11*, 368. **DOI:**10.3390/membranes11050368
15. C. Fersi, L. Gzara, M. Dhahbi, *Desalination* **2009**, *244*, 321–332. **DOI:**10.1016/j.desal.2008.04.046
16. A. Simon, N. Gondrexon, S. Taha, J. Carbon, G. Dorange, *Sep. Sci. Tecnol.* **2000**, *35*, 2619–2637. **DOI:**10.1081/SS-100102359
17. T. M. Patel, K. Nath, *Korean J. Chem. Eng.* **2014***, 31*, 1865–1876. **DOI:**10.1007/s11814-014-0139-7
18. V. Karthik, S. Das Gupta, S. De, *J. Membr. Sci.* **2002**, *199*, 29–40. **DOI:**10.1016/S0376-7388(01)00674-3
19. G. B.van den Berg, I. G.Racz, C. A. Smolders, *J. Membr. Sci.* **1989**, *47*, 25–51. **DOI:**10.1016/S0376-7388(00)80858-3
20. R. E. Treybal,1981, Mass transfer operations, 3rd Edition, McGraw-Hill Book Company, New Delhi pp. 104–123.
21. K. Kovasin, H. V. Norden, *1984* Svensk Papperstidning. Reprinted from Svensk Papperstidning **1984,** *87,* 6, R44–R47
22. Z. Rizki, M. Ottens, *Sep. Purif. Technol.* **2023**, *315*, 123682. **DOI:**10.1016/j.seppur.2023.123682
23. J. Geens, K. Boussu, C. Vandecasteele, B. Van der Bruggen, *J. Membr. Sci.* **2006**, *281*, 139–148. **DOI:**10.1016/j.memsci.2006.03.028
24. G. E. Wetterau, M. M. Clark, C. J. Anselme, *J. Memb. Sci.* **1996**, *109*, 185–204. **DOI:**10.1016/0376-7388(95)00200-6
25. G. F. Crozes, J. G. Jacangelo, C. Anselme, J. M. Laîné, *J. Memb. Sci.* **1997**, *124*, 63–76. **DOI:**10.1016/S0376-7388(96)00244-X
26. K. Katsikaris, C. Boukouvalas, K. Magoulas, *Desalination* **2005**, *171*, 1–11. **DOI:**10.1016/j.desa1.2004.02.103
27. P. K. Bhattacharya, R. K. Todi, M. Tiwari, C. Bhattacharjee, S. Bhattacharjee, S. Datta, *Desalination* **2005**, *174*, 287–297. **DOI:**10.1016/j.desal.2004.09.017
28. D. M. Kanani, R. Ghosh, *J. Membr. Sci.* **2007**, *290*, 207–215. **DOI:**10.1016/j.memsci.2006.12.030
29. C. Serra, M. J. Clifton, P. Moulin, J. C. Rouch, P. Aptel, *J. Membr. Sci.* **1998**, *145*, 159–172. **DOI:**10.1016/S0376-7388(98)00075-1
30. D. Humpert, M. Ebrahimi, A. Stroh, P. Czermak, *Membranes* **2019**, *9*, 45. **DOI:**10.3390/membranes9040045
31. J. A. Restolho, A. Prates, M. N. de Pinho, M. D. Afonso, *Biomass bioener.* **2009**, *33* 1558–1566. **DOI:**10.1016/j.biombioe.2009.07.022

Povzetek

Modeliranje in prilagajanje podatkov za napovedovanje pretoka permeata med ultrafiltracijo (UF) modelne hranilne raztopine natrijevega lignosulfonata je bilo izvedeno z zasledovanjem upora v serijah, gelne polarizacije in enačbami Kedem Katchalsky. Eksperimenti so potekali v laboratorijski enoti za UF, opremljeni s PES/HFUF asimetrično membrano, pod določenimi delovnimi pogoji z spreminjanjem nekaterih parametrov, vključno s koncentracijo topila, transmembranskim tlakom (TMP) in hitrostjo pretoka (CFV). Najvišji eksperimentalni pretok permeata je bil opažen pri TMP 3,92 bar in CFV 0,527 ms^{-1}, in je znašal 19,6 × 10^{-6} $m^3m^{-2}s^{-1}$. Teoretični in eksperimentalni volumetrični fluks sta bila prikazana grafično, njuna stopnja podobnosti pa je bila primerjana in statistično potrjena. Študija osvetljuje učinkovito recikliranje natrijevega lignosulfonata iz odpadne tekočine s pomočjo ultrafiltracije.

DOI: 10.17344/acsi.2025.9199 *Acta Chim. Slov.* **2025,** *72,* 450–462

Scientific paper

Development of Novel Analgesics Related to TRPV1 Antagonism – *In Silico* Approach

Mladjan Golubovic[1,2], Velimir Peric[1,2], Marija Stosic[1,2], Vladimir Stojiljkovic[1,2], Tomislav Kostic[1,3], Aleksandar Kamenov[1,2], Milan Lazarevic[1,2], Dalibor Stojanovic[2], Aleksandar M. Veselinović[4*]

[1] *Faculty of Medicine, University of Niš, Niš, Serbia*

[2] *University Clinical Center Niš, Clinic for Cardiosurgery, Niš, Serbia*

[3] *University Clinical Center Niš, Clinic for Cardiovascular Disease, Niš, Serbia*

[4] *Faculty of Medicine, Departmant of Chemistry, University of Niš, Niš, Serbia*

** Corresponding author: E-mail: aveselinovic@medfak.ni.ac.rs*
Fax: +381 18 4238770; Phone: +381 18 4570029

Received: 02-08-2025

Abstract

In the context of pharmacological intervention for pain, Transient Receptor Potential Vanilloid, member 1 (TRPV1), as a non-selective cation channel belonging to the transient receptor potential (TRP) family of ion channels, has emerged as a promising target. However, the availability of selective TRPV1 antagonists and their associated pharmacological properties remains limited. This research paper explores various QSAR modeling techniques applied to a range of piperazinyl-aryl compounds acting as TRPV1 antagonists. The descriptors utilized in the creation of conformation-independent QSAR models included local molecular graph invariants and the SMILES notation, along with the incorporation of the Monte Carlo optimization method as a model development technique. Several statistical methods were employed to evaluate the quality, robustness, and predictive capacity of the developed models, yielding positive results. For the best developed QSAR model following statistical parameters were obtained for training set $R^2 = 0.7155$, CCC = 0.8134, IIC = 0.7430, $Q^2 = 0.6970$, RMSE = 0.645, MAE = 0.489 and F = 157; and for test set $R^2 = 0.9271$, CCC = 0.9469, IIC = 0.9635, $Q^2 = 0.9241$, RMSE = 0.367, MAE = 0.329 and F = 328. Additionally, molecular fragments derived from SMILES notation descriptors, which explain observed changes in the evaluated activity, were identified, leading to the design of four new antagonists. The final validation of the QSAR model and the designed antagonists was conducted through molecular docking, which demonstrated strong correlation with the QSAR modeling results.

Keywords: TRPV1, Pain treatment, QSAR, Molecular modeling, Drug design

1. Introduction

TRPV1 (transient receptor potential cation channel, subfamilyV, member 1) is a non-selective cation channel activated by a variety of exogenous and endogenous stimuli. Cloning of TRPV1 and demonstration of its therapeutic value have led to intense research in understanding the molecular mechanisms encompassing the responses of sensory neurons to stimuli such as heat, protons, some endogenous activators such as an and amide and exogenous activators such as capasaicin[1–5]. TRPV1, also known as VR1 (Vanilloid Receptor 1), is primarily expressed on unmyelinated pain-sensing nerve fibers (C-fibers) and small A fibers in the dorsal root and trigeminal ganglia[6,7]. Activation of the channel leads to an influx of calcium and sodium ions into the cell, causing depolarization, and that in turn results in the excitation of primary sensory neurons and ultimately in the perception of pain, though a reduction of the activation thresholds of the channel to other stimuli indicate that agonists of the channel can cause desensitization with therapeutic application in the management of pain. However, such desensitization leads to the side effects of burning sensation, irritation, and neurotoxicity, resulting from continuous influx of calcium ions into the cells, thus limiting the clinical use of agonists[8–10]. Blocking the TRPV1- mediated pain signaling pathways with receptor antagonists is an alternative promising strategy for the development of novel analgesic drugs with potentially fewer side effects[11–14]. The chemistry and pharmacology of several classes of competitive TRPV1 antagonists, based on chemotypes containing thiourea, urea, and amide groups, have been described and reviewed[15–18]. They have been classified into four profiles based on their ability to differentially modulate TRPV1 activation by different modes such as capsaicin, pH 5 and heat[19].

Over the years, many antagonists that have entered and progressed into various clinical phases have failed due to the development of hyperthermia as an undesired on-target side-effect. With increased structural, mechanistic and biophysical knowledge on TRPV1, there is an unrecognized need to find more and diverse chemo types for TRPV1 antagonists. New chemo types are needed to evolve functionally-selective or modality-selective antagonists that can probe and prove if hyperthermia can be dissociated from the other functions of this ion channel[21,22]. The need for new chemotypes is encouraged by the fact that there numerous new indications attributed to TRPV1 for which small molecule chemical probes are required for validation[23–25]. Apart from validation for newer indications, probes are required to decipher the potential consequences of targeting a single indication. In this regard, a generally applicable TRPV1 antagonist pharmacophore that can enable discovery of novel chemotypesis critical.

Drug discovery and development are inherently time-consuming processes, requiring substantial time, effort, and financial resources. These challenges arise from the need to identify effective and safe therapeutic compounds through extensive experimental screening, optimization, and validation. To mitigate these constraints, chemoinformatics has emerged as an essential discipline, leveraging computational tools and in silico methodologies to accelerate various stages of the drug development pipeline. Chemoinformatic approaches offer a wide range of applications, including the identification of novel lead compounds, optimization of pharmacological activity, and improvement of pharmacokinetic and toxicological profiles of compounds with known biological activity[26–28]. Among the numerous chemoinformatic techniques, quantitative structure-activity relationship (QSAR) modeling is recognized as the most extensively applied and impactful approach. QSAR studies aim to establish predictive relationships between the chemical structure of compounds and their biological activity, providing valuable insights into molecular interactions and activity mechanisms. Contemporary QSAR models are developed using a variety of molecular descriptors, which are computationally derived parameters that capture distinct chemical, physical, and structural features of molecules. These descriptors vary widely, encompassing properties such as electronic, steric, hydrophobic, and topological characteristics. The construction of QSAR models involves a systematic process. Initially, molecular descriptors are calculated from well-defined molecular structures, each descriptor contributing unique insights into the molecule's behavior. These descriptors are then analyzed to identify their relevance and predictive capacity, enabling the development of robust mathematical equations that quantitatively relate molecular descriptors to observed biological activities. Such models provide a powerful framework for predicting the activity of untested compounds, guiding the rational design of new drugs, and prioritizing experimental validation.

Despite their strengths, QSAR models are not without limitations. The accuracy and reliability of a QSAR model depend heavily on the quality and diversity of the training dataset, the choice of molecular descriptors, and the statistical methods employed. Moreover, the interpretability of these models can sometimes be challenging, especially when complex machine learning algorithms are used. Nevertheless, QSAR remains a cornerstone of modern drug discovery, contributing to significant time and cost savings by enabling the prioritization of promising candidates for further experimental testing[29–33]. As computational power and chemoinformatics methodologies continue to evolve, the integration of QSAR with other in silico approaches, such as molecular docking, pharmacophore modeling, and machine learning, promises to further enhance its predictive capabilities. This integration will likely play a pivotal role in addressing the growing demand for efficient, cost-effective, and innovative drug development strategies.

This research employed various in silico methods to identify novel compounds with potential antagonistic effects on the TRPV1 receptor. The study focused on developing QSAR models using conformation-independent molecular descriptors derived from SMILES notation and local graph invariants, integrated with the Monte Carlo optimization method. A key objective was to identify molecular fragments or structural features responsible for TRPV1 antagonism and to explore correlations among the different computational approaches used. The study successfully pinpointed molecular fragments present in small molecules that are critical for ligand-receptor interactions. These findings provide valuable insights into the structural basis of TRPV1 antagonism, offering a foundation for the rational design and development of novel analgesic agents. The identified fragments could be strategically employed to enhance the efficiency and specificity of future drug discovery efforts targeting TRPV1-related pathways.

2. Materials and Method

In this study, a dataset comprising 98 molecules known to TRPV1antagonism effect was collected from the scientific literature[34]. The compounds analyzed in this study were evaluated for their ability to inhibit capsaicin- (CAP, 500 nM) or acid- (pH 5.0) induced uptake of $^{45}Ca^{2+}$ in Chinese Hamster Ovary (CHO) cells stably expressing rat TRPV1 (rTRPV1), as previously described[35,36]. Functional activity was reported as IC_{50} ± SEM (nM), based on experimental measurements. These IC_{50} values were collected from [insert database or literature reference], and converted to pIC_{50} values using the standard equation: $pIC_{50} = -\log_{10}(IC_{50} \times 10^{-9})$. The dataset was curated to remove duplicates, inconsistent records, and extreme outliers prior to model development. The SMILES notation for all the molecules used in the study, along with their corresponding pIC_{50} values, is provided in Table S1 within the Supplementary Material. To ensure the robustness of the analysis, the dataset was randomly divided into three random splits with two sets: a training set consisting of 73 compounds (75%) and a test set comprising 25 compounds (25%). The normality of the activity distribution for all the dataset splits was assessed following the methodology described in a published reference[37].

2. 1. QSAR Modeling Utilizing the Monte Carlo Optimization Method

The Monte Carlo optimization method was employed to construct a conformation-independent QSAR model using a hybrid approach that combined molecular graph-based and SMILES notation-based descriptors. The molecular graph-based descriptors included local graph invariants derived from fundamental graph theory concepts, such as paths and walks, with detailed mathematical definitions available in the literature[38]. The optimal descriptors identified from the graph-based approach encompassed Morgan extended connectivity indices (EC0), valence shell descriptors for ranges 2 and 3 (s2, s3), path numbers for lengths 2 and 3 (p2, p3), the number of neighboring carbon atoms (Number of Carbon), and the number of neighboring non-carbon atoms (Number of Non Carbon). In parallel, SMILES notation-based descriptors offered mechanistic insights by representing molecular fragments. Each descriptor contributes to the molecule's Descriptor Correlation Weight (DCW), which is computed as the sum of the correlation weights (CW) assigned to all relevant SMILES descriptors. This relationship is mathematically formalized in Equation 1. By combining these two descriptor systems, the hybrid approach provides a robust framework for characterizing molecular features, enabling enhanced predictive accuracy and interpretability in identifying key structural determinants of biological activity.

$$\begin{aligned} DCW(T,Nepoch) = {} & zCW(ATOMPAIR) + \\ & xCW(NOSP) + yCW(BOND) + tCW(HALO) + \\ & rCW(HARD) + \alpha\Sigma CW(S_k) + \beta\Sigma CW(SS_k) + \\ & \gamma\Sigma CW(SSS_k) \end{aligned} \tag{1}$$

In Equation 1, the variables z, x, y, t, α, β, γ represent binary values – 1 indicating "yes" and 0 indicating "no" – that determine whether the corresponding SMILES descriptor is included in the QSAR model development. The symbol S_k refers to a SMILES atom represented by a single SMILES notation symbol (or a pair of inseparable symbols) and is associated with local molecular descriptors. Descriptors constructed as linear combinations of two and three SMILES atoms are denoted by SS_k and SSS_k, respectively, to account for interactions between multiple atomic components. The second category of SMILES notation-based descriptors used in the study comprises global descriptors, which capture the overall properties of the studied molecule. These include descriptors such as ATOMPAIR, HALO, BOND, NOSP, and HARD, each defined according to methodologies outlined in references[39,40]. These global descriptors provide a comprehensive overview of molecular structure and complement the local descriptors in capturing the nuances of molecular behavior. The QSAR model developed in this study integrated both SMILES notation-based descriptors (local and global) and local graph invariants. This hybrid approach facilitated the calculation of the Descriptor Correlation Weight (DCW) for molecules as described in Equation 2, providing a robust and versatile framework for accurately modeling the relationship between molecular features and biological activity.

$$\begin{aligned} DCW(T,N_{epoch}) = {} & \Sigma CW(S_k) + \Sigma CW(SS_k) + \\ & \Sigma CW(SSS_k) + \Sigma CW(EC0_k) + \Sigma CW(PT2_k) + \\ & \Sigma CW(PT3_k) + \Sigma CW(VS2_k) + \Sigma CW(VS3_k) + \\ & \Sigma CW(NNC_k) \end{aligned} \tag{2}$$

In addition to the previously defined symbols S_k, SS_k and SSS_k, Equation 2 incorporates the following symbols: The Morgan connectivity index of zero order (the hydrogen-suppressed graph was used in this research) – $EC0_k$, paths of length of 2 and 3 – $PT2_k$ and $PT3_k$, valence shell 2 and 3 – $VS2_k$, and $VS3_k$, and Nearest Neighbors – NNC_k[38]. The linear regression approach is used to compute the QSAR model (utilizing the training set) as indicated in Equation 3. This is achieved when the numerical data regarding the correlation weights are derived from the model, leading to favorable statistical results for the test set. In this specific study, the search for the optimal combination of T and N_{epoch} was carried out within the ranges of 1–5 for T and 0–50 for N_{epoch}.

$$Ac = C_0 + C_1 \times DCW(T,N_{epoch}) \tag{3}$$

To thoroughly evaluate the quality, robustness, and predictive reliability of the developed conformation-independent QSAR models, a comprehensive set of validation metrics was employed. These included widely used statistical parameters such as the squared correlation coefficient (R^2), which measures the proportion of variance explained by the model, and the root-mean-squared error (RMSE), a standard indicator of prediction error magnitude. Cross-validation coefficients (Q^2) were calculated to assess the model's performance in predicting data excluded from the training set, while the F-value was used to determine the statistical significance of the regression. Additionally, the mean absolute error (MAE) was included as a measure of the average deviation between observed and predicted values, providing further insights into model accuracy[41–44]. To strengthen the reliability of the QSAR models, advanced validation metrics were also applied. These included R_m^2 and MAE-based metrics, which emphasize the model's predictive power for new datasets. The concordance correlation coefficient (CCC) was used to evaluate the agreement between predicted and observed values, while the index of ideality of correlation (IIC) offered insights into the degree to which the correlation between the predicted and observed values aligned with an ideal relationship[45]. The inclusion of these metrics ensured a thorough validation process and a holistic assessment of model performance. A pivotal component of any QSAR model is the establishment of its applicability domain (AD), which defines the chemical space within which the model can make reliable predictions. The AD ensures that predictions are made for compounds structurally and chemically similar to those in the training set, preventing extrapolation into areas of chemical space where the model may be unreliable. In this study, a literature-derived method was employed to determine the AD, as recommended in references[46–48]. This involved systematic evaluation of the chemical structures and descriptors used in the model, ensuring that predictions adhered to the established AD criteria. A key aspect of this study was the analysis of "statistical defects" in conformation-independent molecular descriptors, particularly d(A), to define the AD. These descriptors, previously utilized in QSAR model construction[39–40], were scrutinized to identify potential outliers or anomalies that could affect model reliability. The calculations for AD determination were performed using the CORAL software, which allowed for precise evaluation and correction of these statistical defects. Equation 4 formalized the methodology for this process, ensuring consistency and rigor.

$$d(A) = \frac{|P(A_{train}) - P(A_{test})|}{N(A_{train}) - N(A_{trest})} \tag{4}$$

In the equation above, $P(A)_{train}$ and $P(A)_{calib}$ denote the probabilities of a conformation-independent attribute or descriptor (A) in the training and test sets, respectively. Meanwhile, $NA(_{train})$ and $NA(_{calib})$ represent the frequency of occurrence of a conformation-independent attribute or descriptor (A) in the training set and the test set, respectively. The statistical SMILES defect (D) is the cumulative sum of the defects, d(A), of all the attributes found in the SMILES notation of the molecules. It is computed according to Equation 5.

$$D = defect(SMILES) = \sum_{k=1}^{NA} d(A) \tag{5}$$

A molecule is labeled as an outlier if it falls outside the defined applicability domain (AD), which happens when its D exceeds 2 times Dav, where Dav represents the average D calculated for the relevant set (whether it's the training or test set) in which the molecule is located.

2. 2. Molecular Docking

Docking studies were carried out using the Molegro Virtual Docker (MVD) software to evaluate the interactions between potential ligands and the TRPV1 receptor. Ligands were geometrically optimized prior to docking using the MMFF94 force field to ensure accurate structural representations. The three-dimensional structure of the TRPV1 receptor used for docking studies was obtained from the Protein Data Bank (PDB ID: 5IRX), representing the rat TRPV1 channel in complex with the antagonist capsazepine, resolved at 3.27 Å resolution[41]. This structure was selected based on its biological relevance and compatibility with the experimental system used in the QSAR dataset. The binding site was defined based on the position of the co-crystallized antagonist and included amino acid residues known to participate in ligand interactions, such as Tyr511, Ser512, Met547, Thr550, and Glu570[42]. These residues form the hydrophobic pocket and polar environment critical for antagonist binding. Protein preparation included removal of crystallographic water molecules, assignment of charges, and optimization of hydrogen bonding network using default MVD settings. The docking grid was centered on the native ligand position, with a radius of 15 Å to ensure full coverage of the binding cavity. Standard MolDock scoring function and search algorithm parameters were applied (maximum iterations = 1500; population size = 50; number of poses = 10 per ligand). MVD employs a hybrid approach in which the receptor structure is treated as rigid, while the ligand structures are allowed flexibility. This approach balances computational efficiency with the ability to account for conformational adaptability of ligands during docking. MVD identifies and quantifies both hydrophobic and hydrophilic interactions between the receptor and the ligands. Hydrophobic interactions primarily encompass Van der Waals forces and steric effects, while hydrophilic interactions involve hydrogen bond formation between ligand atoms and specific amino acid residues in the active site. These interactions are quantified through the use of "scoring" functions, which calculate numerical values corresponding to binding energies[51,52]. In molecular docking studies, the strength and nature of ligand-receptor interactions are critical indicators of potential inhibitory activity. A general principle applies to enzyme and receptor studies: stronger and more favorable interactions typically correlate with enhanced inhibition potential. For this reason, the "scoring" functions calculated by MVD provide valuable insights into the binding affinity and potential efficacy of the studied ligands[40]. In this research, two primary scoring functions were calculated and utilized for the evaluation of inhibitory potential: MolDock Score and Rerank Score. The MolDockScore represents the primary binding energy calculated during docking, encompassing contributions from steric, electrostatic, and hydrogen bonding interactions. The Rerank Score is a secondary evaluation that re-assesses the binding interactions using additional weighting for certain interaction types, providing a more refined prediction of binding affinity. The docking protocol employed in this study was meticulously validated to ensure its reliability and accuracy. The validation was performed in accordance with established methodologies from the literature[53], which involve comparing docking results with experimentally determined binding modes or known inhibitors. This validation step is crucial for confirming that the docking simulations accurately represent the ligand-receptor interactions. Furthermore, the results of these docking studies provide a quantitative basis for ranking ligands based on their predicted binding affinity and inhibitory potential. These findings contribute to the identification of promising compounds for further experimental validation and drug development.

To complement molecular docking and provide an additional layer of binding affinity prediction, we applied KDEEP, a deep learning-based tool for structure-based binding affinity estimation. KDEEP uses 3D convolutional neural networks trained on experimentally validated protein–ligand complexes to predict binding strength and utilizes 3D Convolutional Neural Networks (3DCNN) to enhance the accuracy of binding predictions[54]. It classifies input molecules into eight pharmacophore properties: hydrophobic, aromatic, hydrogen-bond donor and acceptor, positive and negative ionizable, metallic, and total excluded volume. The molecules are then processed using a Deep Convolutional Neural Network (DCNN) model trained on the PDBbind 2016 database (available at https://playmolecule.com/Kdeep/)[55]. The docking results for ligand orientation within the TRPV1 receptor active site obtained with MolDock were used to estimate absolute binding affinity with KDeep. For each ligand–TRPV1 complex, KDEEP calculated three key parameters: pKd, binding free energies (ΔG) and ligand efficiencies (LE).

By integrating computational and statistical rigor, the study establishes a robust framework for exploring ligand interactions with the TRPV1 receptor, paving the way for the development of novel therapeutic agents targeting this receptor.

3. Results and Discussion

Table 1 summarizes the numerical values of all the validation metrics used to comprehensively evaluate the quality and performance of the conformation-independent QSAR models developed through the Monte Carlo

Table 1. The statistical quality of the developed conformational-independent QSAR models for TRPV1 antagonism by piperazinyl-aryl compounds

		Training set								Test set							
		R^2	CCC	IIC	CII	Q^2	RMSE	MAE	F	R^2	CCC	IIC	CII	Q^2	RMSE	MAE	F
Split 1	1 run	0.7926	0.8843	0.8200	0.8828	0.7775	0.517	0.410	271	0.8263	0.8851	0.8401	0.9097	0.7799	0.547	0.433	109
	2 run	0.7928	0.8844	0.8201	0.8833	0.7798	0.517	0.398	272	0.8410	0.8923	0.7270	0.9305	0.8077	0.529	0.424	122
	3 run	0.7858	0.8800	0.7743	0.8715	0.7732	0.525	0.399	260	0.8487	0.8859	0.8449	0.9344	0.8124	0.534	0.421	129
	Av	0.7904	0.8829	0.8048	0.8729	0.7768	0.520	0.402	268	0.8387	0.8878	0.8040	0.9249	0.8000	0.537	0.426	120
Split 2	1 run	0.7219	0.8385	0.7826	0.8298	0.7090	0.591	0.413	184	0.8367	0.8657	0.8352	0.8931	0.8087	0.591	0.505	118
	2 run	0.7478	0.8557	0.7539	0.8406	0.7360	0.563	0.398	210	0.8379	0.8485	0.8394	0.8979	0.8100	0.616	0.512	119
	3 run	0.7781	0.8752	0.7690	0.8658	0.7672	0.528	0.373	249	0.8770	0.8894	0.8858	0.9212	0.8535	0.538	0.441	164
	Av	0.7493	0.8565	0.7685	0.8545	0.7374	0.561	0.395	214	0.8505	0.8679	0.8535	0.9041	0.8241	0.582	0.486	134
Split 3	1 run	0.7472	0.8553	0.7757	0.8447	0.7316	0.578	0.439	213	0.9158	0.9535	0.9155	0.9568	0.8977	0.363	0.311	239
	2 run	0.7244	0.8297	0.7895	0.8255	0.7156	0.636	0.481	164	0.9119	0.9448	0.9299	0.9430	0.8932	0.384	0.338	228
	3 run	0.7155	0.8134	0.7430	0.7766	0.6970	0.645	0.489	157	0.9271	0.9469	0.9635	0.9593	0.9241	0.367	0.329	328
	Av	0.7290	0.8328	0.7694	0.8156	0.7147	0.620	0.470	178	0.9183	0.9484	0.9363	0.9530	0.9050	0.371	0.326	265

R^2 – Correlation coefficient CCC – Concordance correlation coefficient IIC – Index of ideality of correlation Q^2 – Cross-validated correlation coefficient RMSE – Root mean squared error MAE – Mean absolute error F – Fischer ratio Av – Average value for statistical parameters obtained from three independent Monte Carlo optimization runs optimization method. These metrics demonstrate the robustness, predictive accuracy, and reproducibility of the models, providing a clear indication of their reliability. The results highlight the strong predictive potential of the QSAR models, with no significant deviations or inconsistencies observed across the dataset. Among the various splits examined during the optimization process, the second split, utilizing a T value of 4 and N_{epoch} of 15, produced the most favorable results. This configuration led to a model with superior performance, as indicated by its validation metrics. Notably, no outliers were identified during the analysis, as the methodology applied for defining the applicability domain (AD) confirmed that all molecules fell within the defined chemical space. This is a crucial finding, as the absence of outliers ensures that the model's predictions are both valid and reliable within the specified AD, thereby enhancing its applicability to unseen compounds. Figure 1 provides a graphical representation of the best-performing QSAR model, which achieved the highest R^2 value across all three splits during the optimal Monte Carlo optimization run. The graph visually illustrates the close agreement between observed and predicted values, highlighting the model's predictive accuracy and its capability to generalize across the dataset. To ensure further validation, the concordance correlation coefficient (CCC) was calculated for all QSAR models. The CCC is a robust metric that evaluates the reproducibility of predictions by measuring the degree of agreement between observed and predicted values. The results demonstrated high reproducibility across all splits, confirming that the models are consistent and reliable across different configurations. In addition, the mean absolute error (MAE)-based metric was used to evaluate the precision of the models, and the outcomes were rated as "GOOD," further solidifying the models' robustness and reliability. The final layer of validation involved the calculation of the index of ideality of correlation (IIC). This metric assesses how closely the correlation between predicted and observed values aligns with an ideal relationship. The IIC values obtained were highly favorable, suggesting that the developed QSAR models not only perform well but also exhibit a high degree of predictive reliability and alignment with theoretical expectations. The findings of this study strongly indicate that the QSAR models developed using the Monte Carlo optimization method possess exceptional predictive potential, making them valuable tools for future applications in drug discovery and other computational research domains. The comprehensive validation of these models using multiple metrics – including R^2, RMSE, Q^2, F-value, MAE, CCC, and IIC – underscores their robustness and generalizability. By incorporating a rigorous methodology for defining and adhering to the applicability domain, the study ensures that these models can be reliably employed for predictions involving structurally similar compounds within the defined chemical space. Furthermore, the absence of outliers and the high concordance between predicted and observed values across all validation steps provide additional confidence in the utility of these models. This thorough validation process paves the way for the practical application of these QSAR models in tasks such

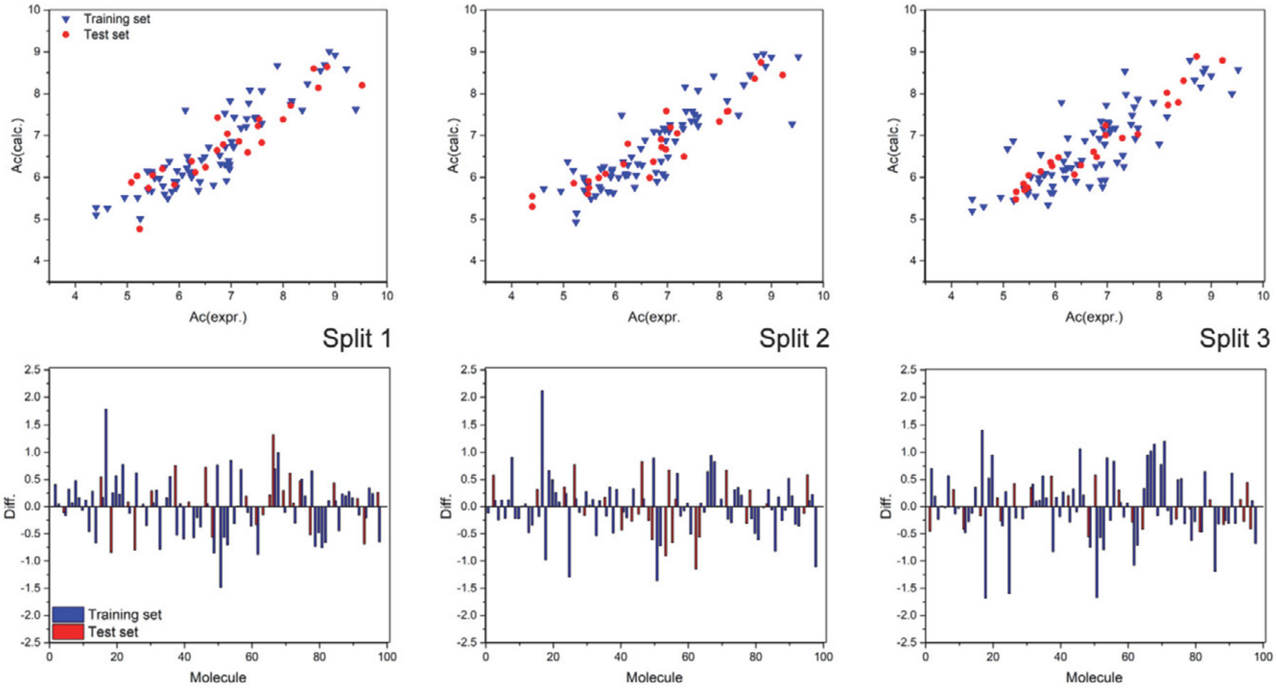

Figure 1. Above) Graphical presentation of the best Monte Carlo optimization runs (the highest value for R^2) for the developed QSAR models; Bellow) Diff. – Difference between experimental and calculated values for pIC_{50}.

as virtual screening, lead optimization, and the prediction of biological activity for new compounds. Ultimately, these models represent a significant advancement in the integration of computational tools into modern drug discovery workflows.

The mathematical formulations for the top-performing QSAR models, as determined by the test set R^2 values for all the splits, are provided in Equations 6–8.

$$\text{Split 1: } pIC_{50} = -0.4579(\pm 0.0534) + 0.0398(\pm 0.0003)\times DCW(3,24) \tag{6}$$

$$\text{Split 2: } pIC_{50} = 0.3013(\pm 0.0420) + 0.0297(\pm 0.0002)\times DCW(1,10) \tag{7}$$

$$\text{Split 3: } pIC_{50} = 2.1931(\pm 0.0443) + 0.0339(\pm 0.0003)\times DCW(3,23) \tag{8}$$

The equations (Eq. 6–8) show that for split 1, the preferred values for T and N_{epoch} are 3 and 24, respectively. For split 2, the preferred values are 1 for T and 10 for N_{epoch}, while for split 3, the preferred values are 3 for T and 23 for N_{epoch}.

There have been significant efforts to apply ligand-based methodologies for developing pharmacophore and QSAR models aimed at TRPV1 antagonists. These studies have utilized various computational approaches, demonstrating the versatility and effectiveness of such methods in exploring the molecular basis of TRPV1 antagonism. Some studies have employed molecular field-based techniques like CoMFA (Comparative Molecular Field Analysis) and CoMSIA (Comparative Molecular Similarity Indices Analysis), as well as Phase QSAR methodologies[56]. These approaches focus on the spatial and electronic properties of molecules to identify patterns correlating with antagonistic activity. Others have used descriptor-based algorithms to determine molecular descriptors most strongly associated with TRPV1 antagonism, enabling the development of predictive QSAR models[57]. In other efforts, 3D alignments of TRPV1 antagonists have been analyzed in the context of homology models. These studies have leveraged the structural insights provided by homology models to explore the spatial arrangements and interactions of antagonists within the receptor binding site[54.58]. For example, Goldmann et al. utilized publicly available data on TRPV1 antagonists to construct pharmacophore models. Their research involved extensive validation of these models, which were then applied to virtually screen the LifeChem database comprising 305,841 compounds. This exercise identified 12 hits with promising activity and diversity compared to reference antagonists and other active compounds. Goldmann and colleagues further hypothesized that pharmacophore modeling of public data could reveal "pharmacophoric ensembles," helping to differentiate safe compounds from those with undesirable profiles[59]. Similarly, Feng et al. reported constructing human TRPV1 (hTRPV1) homology models based on the recently released rat TRPV1 (rTRPV1) structure. Their study involved validation using known agonists and antagonists, prediction of binding modes for well-known antagonists, and a virtual screening exercise targeting the putative antagonist binding site. This approach provided valuable insights into the molecular interactions governing TRPV1 antagonism and highlighted potential candidates for further investigation[60]. Kristam et al. developed and validated predictive 3D-QSAR models for a collection of TRPV1 receptor antagonists using CoMFA and Topomer-CoMFA methodologies. These models were applied to screen databases for alternative fragments that could replace key functional groups in known antagonists, such as the disubstituted dimidazolyl moiety (R1 fragment) or the piperazine aryl moiety (R2 fragment)[34]. Their work underscores the potential of 3D-QSAR techniques in guiding the rational design of structurally optimized TRPV1 antagonists. Together, these studies demonstrate the power of ligand-based methodologies, including pharmacophore modeling, QSAR, and homology modeling, in advancing our understanding of TRPV1 receptor antagonists. They highlight the potential of computational tools to identify novel candidates, optimize known scaffolds, and reveal critical molecular features that differentiate efficacious and safe compounds from those with less desirable profiles. These approaches continue to contribute significantly to the field of TRPV1-targeted drug discovery, offering pathways to innovative therapeutic agents for pain management and other conditions.

A primary objective of this research was to identify molecular fragments, defined as optimal descriptors in SMILES notation, that contribute positively or negatively to the studied activity, as supported by prior studies[39,40,61,62]. These fragments are essential for understanding the structural features that influence the biological activity of compounds, providing valuable insights for drug design and optimization. The complete set of calculated molecular descriptors, derived from both SMILES notation and molecular graph-based approaches, is provided in Table S2 in the Supplementary Material. These descriptors encompass a wide range of molecular properties and were systematically analyzed to determine their relevance to the studied activity. To aid in understanding, an example calculation of a molecule's summarized Descriptor Correlation Weight (DCW) and its corresponding studied activity (pIC_{50}) is detailed in Table 2. For simplicity, molecular graph-based descriptors are excluded from the example, allowing for a more focused interpretation of the contributions from SMILES-based descriptors. This example highlights the methodology used to link molecular features to biological activity, demonstrating how individual descriptor contributions are aggregated into the DCW. Furthermore, a graphical representation of the molecular fragments associated with the same molecule is provided in Figure 2. This visualization illustrates the structural components of the

Table 2. Example of DCW calculation

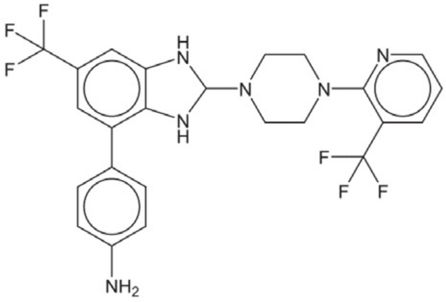

SMILES notation:
Nc1ccc(cc1)c1cc(cc2c1NC(N2)N1CCN(CC1)c1ncccc1C(F)(F)F)C(F)(F)F
DCW = 115.8633
pIC_{50}(calc.) = 6.1255

SA_k	$CW(SA_k)$	SA_k	$CW(SA_k)$	SA_k	$CW(SA_k)$	SA_k	$CW(SA_k)$
10001000	−0.0545	C...(.......	0.4633	c...c...1...	−0.1625	N...(...C...	1.6575
(...(.......	0.2736	c...(...c...	0.2654	C...C...1...	−0.11	N...........	−0.1445
(...........	0.1116	c...........	0.0465	c...c...2...	−2.6721	n...........	0.2927
(...C...(...	0.3527	C...........	−0.3361	c...c...c...	0.1654	N...1.......	−0.7082
(...F...(...	−0.0813	c...1...(...	0.2406	C...N...(...	−0.1388	n...1.......	−0.5053
1...(.......	0.8061	C...1...(...	0.1533	c...N.......	0.1804	N...1...C...	−0.0284
1...........	0.2906	c...1.......	0.0952	C...N...1...	0.1723	n...1...c...	0.1866
1...c...(...	−0.3129	C...1.......	−0.5409	c...n...1...	0.0845	N...2.......	0.5679
1...C...(...	0.4098	c...1...c...	0.7524	F...(...(...	0.3315	N...C...(...	−0.2294
1...N...(...	0.1976	c...1...C...	0.2782	F...(.......	0.0918	N...C.......	−0.1215
2...(.......	0.3586	c...1...N...	−0.424	F...(...C...	1.0121	n...c.......	0.7165
2...........	0.4303	c...2.......	0.0583	F...(...F...	0.0196	N...c...1...	0.4924
2...c...1...	−0.6572	c...2...c...	0.1318	F...........	0.3709	N...C...C...	−2.8109
BOND00000	0.1922	c...c...(...	0.1144	HALO10000	−0.6764	n...c...c...	2.3328
c...(.......	0.1999	C...C...(...	0.0764	N...(.......	1.8556	NOSP10000	0.6488
c...c.......	0.1336	C...C.......	−0.4259	N...(...2...	0.6523		

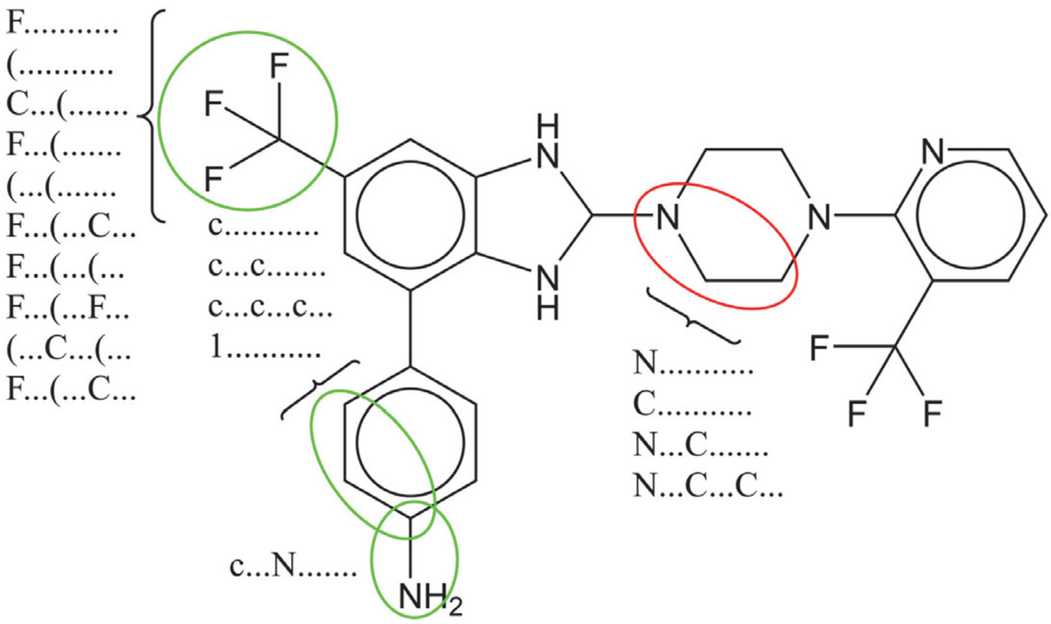

Figure 2. Contribution of molecular fragments to TRPV1antagonism (Green – Increase, Red – Decrease).

molecule and their respective roles, offering a clear depiction of how specific fragments correlate with the observed activity. Together, these analyses provide a comprehensive framework for identifying and understanding the molecular determinants of TRPV1 antagonism, facilitating the rational design of new compounds with improved efficacy and safety profiles.

The results from QSAR modeling revealed specific molecular fragments, identified through SMILES notation, that significantly influence pIC_{50} activity, either positively or negatively. These findings provide a structural basis for designing new TRPV1 antagonists with enhanced activity.Molecular fragments that positively influenced pIC_{50} activity included those associated with trifluoromethyl groups, such as “F..........”, “(..........”, “C...(.......”, “F...(.......”, “(...(.......”, “F...(...C...”, “F...(...(...”, “F...(...F...”, “(...C...(...”, and “F...(...C...”. Fragments associated with aromatic carbon atoms, including “c..........”, “c...c.......”, and “c...c...c...”, as well as the nitrogen atom bonded to aromatic carbon (“c...N.......”), also demonstrated positive effects. Fragments that negatively influenced pIC_{50} activity included the nitrogen atom (“N..........”), carbon atom (“C..........”); and combinations of nitrogen bonded to one or two carbon atoms (“N...C.......” and “N...C...C...” respectively). These negatively correlated fragments provided insights into structural features that should be avoided or minimized in antagonist design.

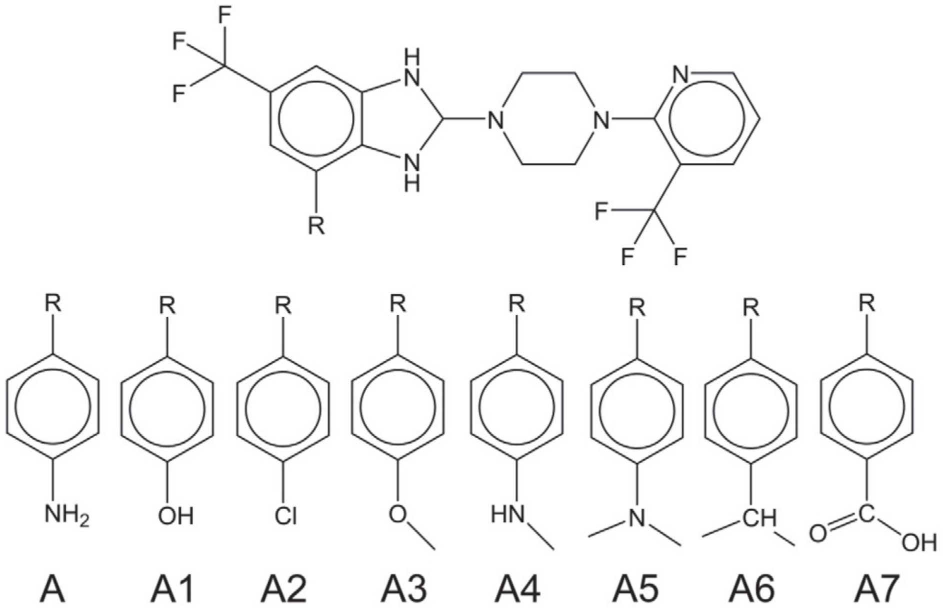

Figure 3. Chemical structures of designed molecules.

The molecular fragments identified as positively influencing activity were applied in a Computer-Aided Design (CAD) process to develop seven novel compounds with enhanced pIC_{50} values. These compounds were designed by introducing functional groups that incorporated new fragments positively associated with activity. Molecule A1 was created by replacing the amino group with a hydroxyl group in the para position, resulting in the addition of the fragment “O............”. Molecule A2 introduced a chlorine atom at the same position, adding the “Cl...........” fragment, while molecule A3 incorporated a methoxy group with the fragment “C...O.......”. Molecule A4 introduced an aminomethyl group, adding the “C...N.......” fragment, enhancing hydrogen bonding potential. Molecule A5 featured a dimethylamino group, adding the fragments “C...(.......”, “(..........”, “N...(.......”, and “N...(...C...”, which indicated increased molecular branching around the nitrogen atom. Molecule A6 incorporated an isopropyl group, resulting in fragments such as “C...(.......”, “(..........”, “C...(.......”, and “C...(...C...” that also indicated increased branching on carbon atoms. Molecule A7 introduced a carboxyl group, contributing fragments such as “=..........”, “=...C...(...”, “C...=.......”, “O...(.......”, “O...(...C...”, “O...=.......”, “O...C...(...”, and “O...C.......” that enhanced electron-withdrawing and polar interaction properties. All introduced fragments in molecules A1–A7 were associated with a positive impact on pIC_{50} activity, leading to higher predicted activity values. The substitution strategy and resulting molecular modifications were validated through increased pIC_{50} values, as summarized in Table 3. These results demonstrate the effectiveness of the CAD approach in integrating QSAR insights for the rational design of novel TRPV1 antagonists with improved biological activity.

All the designed molecules, along with the template molecule A, were subjected to molecular docking studies targeting TRPV1 to evaluate and further validate the predictive accuracy of the developed QSAR models. Table 3 provides the numerical values of the calculated "scoring" functions, which reflect the strength of interactions be-

Table 3. The list of all the designed molecules with their calculated activities, score values (kcal/mol), ΔG (kcal/mol), ligand efficiency (LE) (kcal/mol) and pKd

Molecule	pIC_{50}(calc.)	Rerank	MolDock	ΔG	LE	pKd
A0	6.1255	−121.35	−118.85	−7.437	−0.1957	5.5089
A1	6.4688	−133.49	−128.49	−8.3795	−0.2328	6.207
A2	6.6225	−137.85	−121.65	−9.3946	−0.2610	6.9590
A3	6.5881	−136.35	−134.32	−8.6117	−0.2328	6.3790
A4	6.4472	−133.22	−130.66	−8.7899	−0.2376	6.5110
A5	7.0963	−139.59	−136.57	−9.2786	−0.2577	6.8730
A6	7.2891	−144.43	−137.47	−9.7236	−0.2559	7.2027
A7	6.7976	−138.48	−130.3	−9.1377	−0.2405	6.7686

tween the ligands and the receptor. Since different scoring functions capture distinct ligand-amino acid interactions, a comprehensive assessment of inhibitory potency requires consideration of all relevant factors. Based on the results obtained for the MolDock and ReRank scoring functions, molecule A6 emerged as the compound with the highest potential inhibitory activity. This finding aligns well with the predictions from QSAR modeling, reinforcing the consistency and reliability of the models. In contrast, the template molecule A exhibited the lowest MolDock and ReRank scores, a result that also corresponds to the predictions made by the QSAR models. These correlations between docking results and QSAR predictions provide strong validation for the approach used in this study. Table 3 presents a list of the designed TRPV1 antagonist candidates, along with their predicted biological activity (pIC_{50}), binding free energy (ΔG), ligand efficiency (LE), and predicted dissociation constant pKd These values were calculated using a combination of QSAR modeling, molecular docking, and KDEEP-based binding affinity estimation. As expected, compounds with higher predicted pIC_{50} values–which indicate stronger biological activity and lower effective concentration–generally correspond to more favorable binding energies (lower ΔG values). This relationship is consistent with the principle that stronger binding (i.e., more negative ΔG) often correlates with increased ligand efficiency and potency. For instance, compound A6 shows the highest predicted pIC_{50} (7.2891), in line with its strong binding affinity (ΔG = −9.72 kcal/mol) and the highest pKd (7.20), indicating a tighter ligand–receptor complex. Ligand efficiency (LE), defined as the binding energy per heavy atom, also supports this trend and reflects the balance between molecular size and binding strength. Compounds A5 and A6 exhibit both high pIC_{50} and LE values, suggesting that they are not only potent but also structurally efficient binders. Overall, these results demonstrate a high level of consistency between ligand-based (QSAR) and structure-based (docking and deep learning) predictions, further validating the designed molecules as promising candidates for future experimental testing.

The best-calculated binding poses of all designed molecules within the active site of TRPV1 are illustrated in Figure 4. Further in Figure 4 sufraces of active site (aromatic, hydrophobic, H-Bond and solvent accessibility surface – SAS). These visual representations highlight the spatial orientation and interaction profiles of each molecule, further supporting the docking results and their alignment with QSAR-based predictions. Together, these findings underscore the effectiveness of combining QSAR

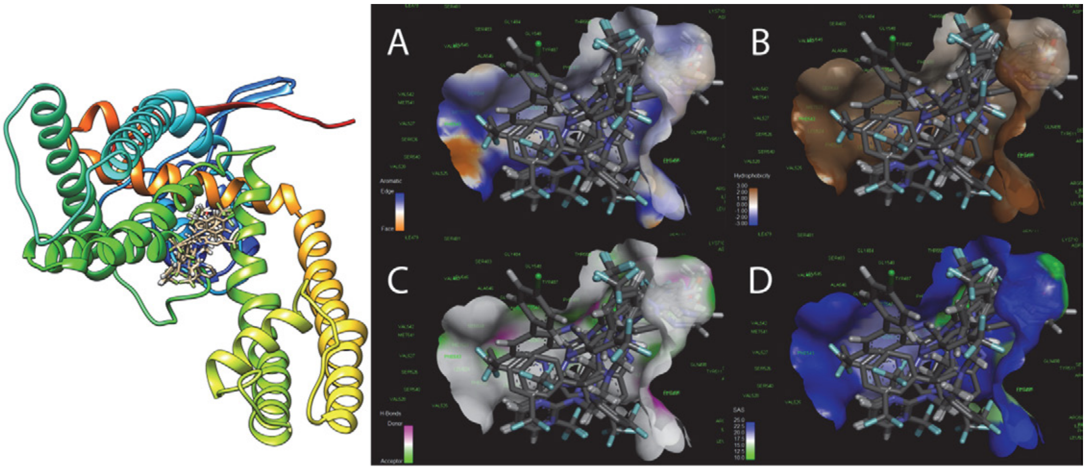

Figure 4. Left) The best calculated poses for all the designed molecules within the active site of TRPV1; Right) Surfaces inside active site: A) Aromatic, B) Hydrophobic, C) H-Bond and D) SAS

modeling and molecular docking studies in identifying and validating promising TRPV1 antagonists.

This study highlights the potential of the Monte Carlo optimization method for generating diverse and informative QSAR models. However, certain limitations merit further investigation to enhance the method's applicability and reliability. One notable limitation involves the interpretability of certain SMILES-based descriptors. The inclusion of two- and three-atom combinations can result in descriptors such as "(...2......." or "#.../.......", which lack clear physical or chemical meaning. This ambiguity makes it challenging to derive mechanistic insights into their influence on biological properties, such as vaginal permeability predictions. Improving the clarity and interpretability of these descriptors would significantly enhance the practical utility of the models. Fragment identification also poses challenges. The method may struggle to detect rare but biologically significant molecular fragments, which could provide valuable insights into permeability or activity. Additionally, the focus on smaller fragments, such as those comprising three atoms, may overlook the contributions of larger structural motifs or long-range interactions that play a critical role in biological processes. The CORAL algorithm, employed within the Monte Carlo optimization framework, introduces another limitation. Its potential prevalence bias may prioritize common fragments within the dataset, potentially underestimating the significance of truly active fragments that are present across all SMILES descriptors. This bias could reduce the algorithm's ability to identify unique features critical for model predictions. While the hybrid approach incorporates descriptors derived from both SMILES notation and molecular graphs, some molecular graph-based descriptors also lack clear mechanistic interpretation. This limitation restricts the ability to connect model predictions with underlying chemical or biological principles, which is essential for advancing scientific understanding and rational compound design. To address these limitations, data preprocessing strategies could be implemented. Preliminary analysis and filtering of molecular fragments and descriptors might help identify those that are most informative and relevant to the studied activity. This approach could reduce noise, improve model interpretability, and enhance the mechanistic insights derived from the models. Additionally, incorporating techniques that balance the emphasis on rare and common fragments may improve the identification of biologically significant features. Future research should focus on addressing these challenges to enhance the capabilities of the Monte Carlo optimization method. Efforts could include refining descriptor definitions, exploring alternative algorithms with reduced bias, and expanding the scope of descriptors to capture larger and more complex molecular interactions. By overcoming these limitations, the Monte Carlo optimization method could become an even more powerful tool in the development of QSAR models and their application in drug discovery and beyond.

4. Conclusion

The primary goal of this study was to develop reliable QSAR models with strong predictive power for TRPV1 antagonism, validated through a comprehensive set of statistical parameters. Conformation-independent QSAR models were constructed using the Monte Carlo optimization method, leveraging optimal descriptors derived from both local graph invariants and SMILES notation. These descriptors provided a robust foundation for the modeling process, enabling the identification of structural features influencing TRPV1 antagonism. The robustness and predictive capabilities of the QSAR models were thoroughly evaluated using various statistical techniques. The validation metrics confirmed the high applicability of the models, demonstrating their effectiveness in predicting biological activity. The Monte Carlo optimization method facilitated the identification of molecular fragments, represented as SMILES notation fragments, with both positive and negative effects on TRPV1 antagonism. These insights offered a deeper understanding of the molecular features contributing to or detracting from activity, supporting the rational design of more effective antagonists. Molecular docking studies served as the final validation step, further confirming the predictive accuracy of the developed QSAR models. The docking results provided an additional layer of evidence for the potential inhibitory effects of the designed molecules. A strong inter-correlation was observed between the calculated pIC_{50} values from the best QSAR model and the interaction energies derived from docking studies with the TRPV1 active site. To further strengthen the predictive workflow, we incorporated KDEEP-a deep learning-based method for protein–ligand binding affinity estimation–which provided additional independent predictions of pKd and ΔG values. The strong concordance between these results and the QSAR-predicted pIC_{50} values supports the internal validity of the designed compounds and adds confidence to their prioritization. KDEEP thus served as a third, AI-powered validation layer within our CADD pipeline, highlighting its utility in guiding early-phase drug discovery even in the absence of experimental data. This concordance highlights the reliability of the combined QSAR and molecular docking approach in predicting ligand-receptor interactions. The methodology described in this study demonstrates significant potential for broader applications, including the discovery of novel therapeutics for conditions such as atherosclerosis. By targeting the antagonism of Transient Receptor Potential Vanilloid, member 1 (TRPV1), the outlined approach provides a versatile framework for identifying and optimizing drug candidates for a variety of therapeutic areas.

Competing Interests

The authors declare that there are no conflicts of interest in this study.

Acknowledgment

The authors would like to thank the Ministry of Education, Science and Technological Development of Republic of Serbia (Grant No: 451-03-136/2025-03/200113) for financial support.

5. References

1. M. J. Caterina, M. A. Schumacher, M. Tominaga, T. A. Rosen, J. D. Levine, D. Julius, *Nature* **1997**, *389*, 816–824. **DOI:**10.1038/39807
2. M. M. Moran, M. A. McAlexander, T. Bíró, A. Szallasi, *Nat. Rev. Drug Discov.* **2011**, *10*, 601–620. **DOI:**10.2174/138161208783330763
3. R. Vennekens, G. Owsianik, B. Nilius, *Curr. Pharm. Des.* **2008**, *14*, 18–31. **DOI:**10.2174/138161208783330763
4. M. Zhang, Y. Ma, X. Ye, N. Zhang, L. Pan, B. Wang, *Signal Transduct. Target Ther.* **2023**, *8*, 261. **DOI:**10.1038/s41392-023-01464-x
5. L. Basso, C. Altier, *Curr. Opin. Pharmacol.* **2017**, *32*, 9–15. **DOI:**10.1016/j.coph.2016.10.002
6. Y. Kaneko, A. Szallasi, *Br. J. Pharmacol.* **2014**, *171*, 2474–2507. **DOI:**10.1111/bph.12414
7. M. G. Tsagareli, I. Nozadze, *Behav. Pharmacol.* **2020**, *31*, 413–434. **DOI:**10.1097/FBP.0000000000000524
8. A. Szallasi, P. M. Blumberg, *Pharmacol. Rev.* **1999**, *51*, 159–212. **DOI:**10.1016/S0031-6997(24)01403-0
9. O. M. E. Abdel-Salam, G. Mózsik, *Neurochem. Res.* **2023**, *48*, 3296–3315. **DOI:**10.1007/s11064-023-03983-z
10. J. E. Krause, B. L. Chenard, D. N. Cortright, *Curr. Opin. Investig. Drugs* **2005**, *6*, 48–57.
11. M. M. Moran, *Annu. Rev. Pharmacol. Toxicol.* **2018**, *58*, 309–330. **DOI:**10.1146/annurev-pharmtox-010617-052832
12. L. A. Roberts, M. Connor, *Recent Pat. CNS Drug Discov.* **2006**, *1*, 65–76. **DOI:**10.2174/157488906775245309
13. B. Nilius, *Curr. Top. Med. Chem.* **2013**, *13*, 244–246. **DOI:**10.2174/1568026611313030002
14. A. Szallasi, D. N. Cortright, C. A. Blum, S. R. Eid, *Nat. Rev. Drug Discov.* **2007**, *6*, 357–372. **DOI:**10.1038/nrd2280
15. D. Y. Okuhara, A. Y. Hsia, M. Xie, *Expert Opin. Ther. Targets* **2007**, *11*, 391–401. **DOI:**10.1517/14728222.11.3.391
16. J. Lázár, L. Gharat, N .K. Joshi, P. M. Blumberg, A. Szallasi, *Expert Opin. Drug Discov.* **2009**, *4*, 159–180. **DOI:**10.1517/17460440802681300
17. D. Souza Monteiro de Araujo, R. Nassini, P. Geppetti, F. De Logu, *Expert Opin. Ther. Targets* **2020**, *24*, 997–1008. **DOI:**10.1080/14728222.2020.1815191
18. C. C. Correll, A. Palani, *Expert Opin. Ther. Pat.* **2006**, *16*, 783–795. **DOI:**10.1517/13543776.16.6.783
19. G. Y. Wong, N.R. Gavva, *Brain Res. Rev.* **2009**, *60*, 267–277. **DOI:**10.1016/j.brainresrev.2008.12.006
20. P. Holzer, *Br. J. Pharmacol.* **2008**, *155*, 1145–1162. **DOI:**10.1038/bjp.2008.351
21. A. Fernández-Carvajal, G. Fernández-Ballester, I. Devesa, J. M. González-Ros, A. Ferrer-Montiel, *Pharmaceuticals* **2012**, *5*, 16–48. **DOI:**10.3390/ph5010016
22. K. Kaszas, J. M. Keller, C. Coddou, S. K. Mishra, M. A. Hoon, S. Stojilkovic, K .A. Jacobson, M. J. Iadarola, *J. Pharmacol. Exp. Ther.* **2012**, *340*, 152–160. **DOI:**10.1124/jpet.111.183053
23. J. Chen, D. H. Hackos, *Naunyn Schmiedebergs Arch. Pharmacol.* **2015**, *388*, 451–463. **DOI:**10.1007/s00210-015-1088-3
24. B. Nilius, A. Szallasi, *Pharmacol. Rev.* **2014**, *66*, 676–814. **DOI:**10.1124/pr.113.008268
25. M. J. Gunthorpe, A. Szallasi, *Curr. Pharm. Des.* **2008**, *14*, 32–41. **DOI:**10.2174/138161208783330754
26. P. V. Desai, *Future Med. Chem.* **2016**, *8*, 1717–1720. **DOI:**10.4155/fmc-2016-0161
27. S. Ekins, J. Mestres, B. Testa, *Br. J. Pharmacol.* **2007**, *152*, 9–20. **DOI:**10.1038/sj.bjp.0707305
28. S. De Vita, M. G. Chini, G. Bifulco, G. Lauro, *Bioorg. Med. Chem. Lett.* **2023**, *83*, 129171. **DOI:**10.1016/j.bmcl.2023.129171
29. P. G. R. Achary, *Mini Rev. Med. Chem.* **2020**, *20*, 1375–1388. **DOI:**10.2174/1389557520666200429102334
30. S. J. Macalino, V. Gosu, S. Hong, S. Choi, *Arch. Pharm. Res.* **2015**, *38*, 1686–1701. **DOI:**10.1007/s12272-015-0640-5
31. T. Wang, M. B. Wu, J. P. Lin, L. R. Yang, *Expert Opin. Drug Discov.* **2015**, *10*, 1283–1300. **DOI:**10.1517/17460441.2015.1083006
32. M. R. Hasan, A. A. Alsaiari, B. Z. Fakhurji, M. H. R. Molla, A. H. Asseri, M. A. A. Sumon, M. N. Park, F. Ahammad, B. Kim, *Molecules* **2022**, *27*, 4169. **DOI:**10.3390/molecules27134169
33. K. Funatsu, T. Miyao, M. Arakawa, *Curr. Comput. Aided Drug Des.* **2011**, *7*, 1–9. **DOI:**10.2174/157340911793743556
34. R. Kristam, S. N. Rao, A. S. D'Cruz, V. Mahadevan, V. N. Viswanadhan, *J. Mol. Graph. Model.* **2017**, *72*, 112–128. **DOI:**10.1016/j.jmgm.2017.01.010
35. V. I. Ognyanov, C. Balan, A. W. Bannon, Y. Bo, C. Dominguez, C. Fotsch, V. K. Gore, L. Klionsky, V. V. Ma, Y. X. Qian, R. Tamir, X. Wang, N. Xi, S. Xu, D. Zhu, N. R. Gavva, J. J. Treanor, M. H. Norman, *J. Med. Chem.* **2006**, *49*, 3719–3742. **DOI:**10.1021/jm060065y
36. V. K. Gore, V. V. Ma, R. Tamir, N. R. Gavva, J. J. Treanor, M. H. Norman, *Bioorg. Med. Chem. Lett.* **2007**, *17*, 5825–5830. **DOI:**10.1016/j.bmcl.2007.08.044
37. P. K. Ojha, K. Roy, *Chemometr. Intell. Lab.* **2011**, *109*, 146–161. **DOI:**10.1016/j.chemolab.2011.08.007
38. A. A. Toropov, P. Duchowicz, E. A. Castro, *Int. J. Mol. Sci.* **2003**, *4*, s272–283. **DOI:**10.3390/i4050272
39. A. M. Veselinović, J. B. Veselinović, J. V. Živković, G. M. Nikolić, *Curr. Top. Med. Chem.* **2015**, *15*, 1768–1779. **DOI:**10.2174/1568026615666150506151533
40. M. Zivkovic, M. Zlatanovic, N. Zlatanovic, M. Golubović, A. M. Veselinović, *Mini Rev. Med. Chem.* **2020**, *20*, 1389–1402. **DOI:**10.2174/1389557520666200212111428
41. A. Golbraikh, A. Tropsha, *J. Mol. Graph. Model.* **2020**, *20*, 269–276. **DOI:**10.1016/S1093-3263(01)00123-1
42. P. P. Roy, J. T. Leonard, K. Roy, *Chemometr. Intell. Lab.* **2008**, *90*, 31–42. **DOI:**10.1016/j.chemolab.2007.07.004
43. P. K. Ojha, I. Mitra, R. N. Das, K. Roy, *Chemometr. Intell. Lab.* **2011**, *107*, 194–205. **DOI:**10.1016/j.chemolab.2011.03.011

44. K. Roy, R. N. Das, P. Ambure, R. B. Aher, *Chemometr. Intell. Lab.* **2016**, *152*, 18–33. **DOI:**10.1016/j.chemolab.2016.01.008
45. A. P. Toropova, A. A. Toropov, *Sci. Total Environ.* **2017**, *586*, 466–472. **DOI:**10.1016/j.scitotenv.2017.01.198
46. K. Roy, S. Kar, P. Ambure, *Chemometr. Intell. Lab.* **2015**, *145*, 22–29. **DOI:**10.1016/j.chemolab.2015.04.013
47. P. Gramatica, *QSAR Comb. Sci.* **2007**, *26*, 694–701. **DOI:**10.1002/qsar.200610151
48. A. A. Toropov, A. P. Toropova, A. Lombardo, A. Roncaglioni, E. Benfenati, G. Gini, *Eur. J. Med. Chem.* **2011**, *46*, 1400–1403. **DOI:**10.1016/j.ejmech.2011.01.018
49. Y. Gao, E. Cao, D. Julius, Y. Cheng, *Nature* **2016**, *534*, 347–351. **DOI:**10.1038/nature17964
50. M. Liao, E. Cao, D. Julius, Y. Cheng, *Nature* **2013**, *504*, 107–112. **DOI:**10.1038/nature12822
51. R. Thomsen, M. H. Christensen, *J. Med. Chem.* **2006**, *49*, 3315–3321. **DOI:**10.1021/jm051197e
52. G. Bitencourt-Ferreira, W. F. de Azevedo Jr., *Methods Mol. Biol.* **2019**, *2053*, 149–167. **DOI:**10.1007/978-1-4939-9752-7_10
53. Manisha, S. Chauhan, P. Kumar, A. Kumar, *SAR QSAR Environ. Res.* **2019**, *30*, 145–159. **DOI:**10.1080/1062936X.2019.1568299
54. J. Jiménez, M. Škalič, G. Martínez-Rosell, G. De Fabritiis, *J. Chem. Inf. Model.* **2018**, *58*, 287–296. **DOI:**10.1021/acs.jcim.7b00650
55. M. Torrens-Fontanals, P. Tourlas, S. Doerr, G. De Fabritiis, *J. Chem. Inf. Model.* **2024**, *64*, 584–589. **DOI:**10.1021/acs.jcim.3c01776
56. V. N. Viswanadhan, Y. Sun, M. H. Norman, *J. Med. Chem.* **2007**, *50*, 5608–5619. **DOI:**10.1021/jm070261k
57. W. S. Cheung, R. R. Calvo, B. A. Tounge, S. P. Zhang, D. R. Stone, M. R. Brandt, T. Hutchinson, C. M. Flores, M. R. Player, *Bioorg. Med. Chem. Lett.* **2008**, *18*, 4569–4572. **DOI:**10.1016/j.bmcl.2008.07.035
58. P. R. Kym, M. E. Kort, C. W. Hutchins, *Biochem. Pharmacol.* **2009**, *78*, 211–216. **DOI:**10.1016/j.bmcl.2008.07.035
59. D. Goldmann, P. Pakfeifer, S. Hering, G. F. Ecker, *Future Med. Chem.* **2015**, *7*, 24–256. **DOI:**10.4155/fmc.14.168
60. Z. Feng, L. V. Pearce, X. Xu, X. Yang, P. Yang, P. M. Blumberg, X. Q. Xie, *J. Chem. Inf. Model.* **2015**, *55*, 572–588. **DOI:**10.1021/ci5007189
61. S. A. Amin, N. Adhikari, S. Gayen, T. Jha, *J. Biomol. Struct. Dyn.* **2019**, *37*, 4528–4541. **DOI:**10.1080/07391102.2018.1552895
62. P. Kumar, A. Kumar, J. Sindhu, *SAR QSAR Environ. Res.* **2019**, *30*, 525–541. **DOI:**10.1080/1062936X.2019.1629998

Povzetek

V kontekstu farmakološkega posega pri lajšanju bolečine se je transientni receptorski potencial vaniloid tip 1 (TRPV1), nespecifični kationski kanal iz družine TRP ionskih kanalov, izkazal kot obetavna tarča. Kljub temu pa je razpoložljivost selektivnih antagonistov TRPV1 in njihovih farmakoloških lastnosti še vedno omejena. V tem raziskovalnem članku predstavljamo različne tehnike QSAR modeliranja, uporabljene na nizu piperazinil-arilnih spojin, ki delujejo kot antagonisti TRPV1. Opisi, uporabljeni pri oblikovanju konformacijsko neodvisnih QSAR modelov, vključujejo lokalne molekulske grafe in SMILES notacijo, pri čemer je bila za razvoj modela uporabljena tudi Monte Carlo optimizacija. Za oceno kakovosti, robustnosti in napovedne sposobnosti razvitih modelov smo uporabili več statističnih metod, ki so dale pozitivne rezultate. Za najboljši QSAR model so bili doseženi naslednji statistični parametri: za učno množico $R^2 = 0.7155$, CCC = 0.8134, IIC = 0.7430, $Q^2 = 0.6970$, RMSE = 0.645, MAE = 0.489 in F = 157; za testno množico pa $R^2 = 0.9271$, CCC = 0.9469, IIC = 0.9635, $Q^2 = 0.9241$, RMSE = 0.367, MAE = 0.329 in F = 328. Poleg tega smo identificirali molekulske fragmente, izpeljane iz deskriptorjev SMILES notacije, ki pojasnjujejo opažene spremembe v ocenjeni aktivnosti, kar je vodilo do zasnove štirih novih antagonistov. Končna validacija QSAR modela in zasnovanih antagonistov je bila izvedena z molekulskim sidranjem, ki je pokazalo dobro ujemanje z rezultati QSAR modeliranja.

DOI: 10.17344/acsi.2025.9188 *Acta Chim. Slov.* 2025, *72,* 463–477

Scientific paper

Identification of Novel HPPD/PPO Dual-Target Inhibitors Through Virtual Screening of Multiple Pharmacophore Models

Pan-Xiu Zhang[1], Juan Shi[1], Ying Fu[1,2,*]

[1] *Department of Chemistry, College of Arts and Sciences, Northeast Agricultural University, Harbin 150030, China*

[2] *Key Laboratory of Agricultural Functional Molecule Design and Utilization of Heilongjiang Province, Harbin 150030, China*

* *Corresponding author: E-mail: fuying@neau.edu.cn*

Received: 02-03-2025

Abstract

The development and identification of dual target herbicides was one of primary approach to addressing the issue of weed resistance. Protoporphyrinogen oxidase (PPO) and *p*-hydroxyphenylpyruvate dioxygenase (HPPD) are two important targets of photosynthesis in plants. Different from the traditional single target drug design, this study focuses on HPPD and PPO dual target drug design. Hiphop pharmacophore models of HPPD and PPO targets were constructed use commercial pesticides, and CBP pharmacophore models were constructed based on protein complexes. Over millions of molecules were screened using pharmacophore models and 8 compounds were obtained. Candidate compounds chelated with Fe(II) in HPPD and formed stable π-π interactions with key residues in HPPD active pocket. Most compounds produced hydrogen bond interactions and π-π interactions with residues in PPO. Combined with a multiple visual screen process, potential compounds with dual-target inhibition effect were obtained.

Keywords: Dual target herbicide, Target-based drug design, HPPD, PPO, Virtual screening

1. Introduction

Weeds are a major hazard to crops, competing with them for sunlight, water and nutrients in the soil.[1,2] As an economical, efficient, and reliable solution for weed control, herbicide application is key role to ensuring high and stable crop yields. The continuous application of herbicides led the weed resistance increasing, and the impact of herbicide residues on crops and the environment. There is an urgent need to develop of safety, low-impact, low toxicity and highly efficient novel herbicides.[3,4]

During plant photosynthesis, the action sites of pigment synthesis are tetrapyrrole, carotenoid and plastoquinone. As shown in Figure 1, the synergistic effect of three enzymes, protoporphyrinogen oxidase (PPO) phytoene desaturase (PDS) and p-hydroxyphenylpyruvate dioxygenase (HPPD) in plants were illustrated.[5] In the process of chlorophyll synthesis, PPO is the key catalytic enzyme in the process of tetrapyrrole biosynthesis. PPO catalyzes protoporphyrinogen IX to produce protoporphyrin IX in plants under the oxygen and sunlight conditions.[6,7] Protoporphyrin IX chelates with metal ions in chloroplasts to produce chlorophyll.[8–10] Protoporphyrinogen IX is unable to bind to the active site of PPO after being treated with PPO inhibitors in the presence of light and oxygen, protoporphyrinogen IX is accumulated in cytoplasm and converted to photosensitive protoporphyrin IX, causing the cell to rupture and the plant death.[11–13] In addition to chlorophyll, carotenoids, acting as light-harvesting pigments in photosynthetic reaction, protect photosynthesis from chlorophyll triplet and singlet oxygen damage.[14] PDS is a rate-limiting enzyme in carotenoid synthesis and catalyzes the symmetric desaturation of phytoene to carotenoid.[15,16] Inhibition of PDS causes the phytoene accumulation in plants, disrupting carotenoid and chlorophyll synthesis and ultimately resulting in weeds death.[17] In plants, HPPD is an important oxidoreductase involved in the tyrosine metabolic pathway, catalyzing the conversion of p-hydroxyphenylpyruvate (HPPA) to homogentisic acid (HGA), which further reacts to produce plastoquinone and tocopherol.[18–20] Plastoquinone is the key cofactor of PDS. HPPD inhibitors hinder the synthesis of plastoquinone and tocopherol,[21,22] and the synthesis of carotenoid is indirectly affected by the decrease of the content of plas-

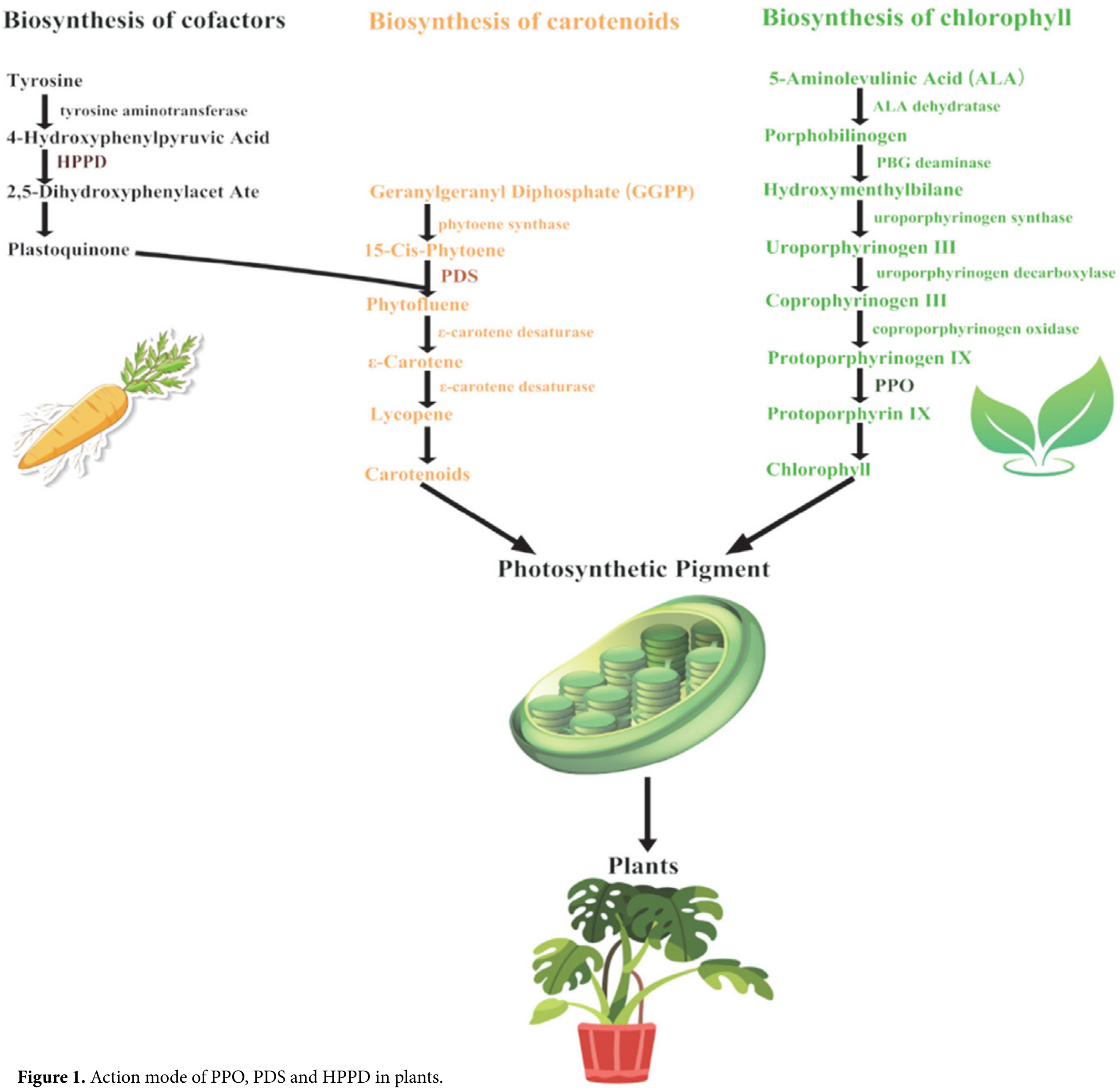

Figure 1. Action mode of PPO, PDS and HPPD in plants.

toquinone, eventually leaf bleaching of the plant leaves.[23, 24] The results show that leaves albinism occurred when HPPD and PPO inhibitors are applied, further affecting weed growth by reducing the content of chlorophyll.

Compared with traditional single-target drug design, multi-target drug acts on multiple targets in the same body at the same time, producing synergistic effects on each target.[25] If a certain target is mutated, the drug will maintain therapeutic efficacy by inhibiting other targets, and avoiding drug resistance caused by single-target mutations. Sorafenib is a multi-target drug that has been marketed for the treatment of cancer by acting on metallothionein 1G(MT1G), DNA methyltransferase 1 (NMT1), Krüpple-like Factor 4(KLF4), and Carbonic anhydrase 9(CA9) in hepatocellular carcinoma.[26] Virtual screening of the dual FMS-like tyrosine kinase 3 (FLT3) and mitogen-activated protein kinase (MAPK)-interacting kinases 2 (MNK2) inhibitor in the treatment of acute myeloid leukemia was conducted by molecular docking methods and cell experiments, the results showed that the obtained candidate K783-0308 exhibited inhibitory effect for the target FLT3 and MNK2.[27] Novel dual-target of HPPD and PDS inhibitors were screened using pharmacophore models, molecular docking and structure optimization.[5]

Pharmacophore models are collections of spatial and electronic features, in continuous of our study on multi-target albino herbicides, HPPD and PPO multi-target pharmacophore models were constructed and 1024513 small molecules were screened. Pharmacophore models based on common characteristics of molecules (Hiphop)

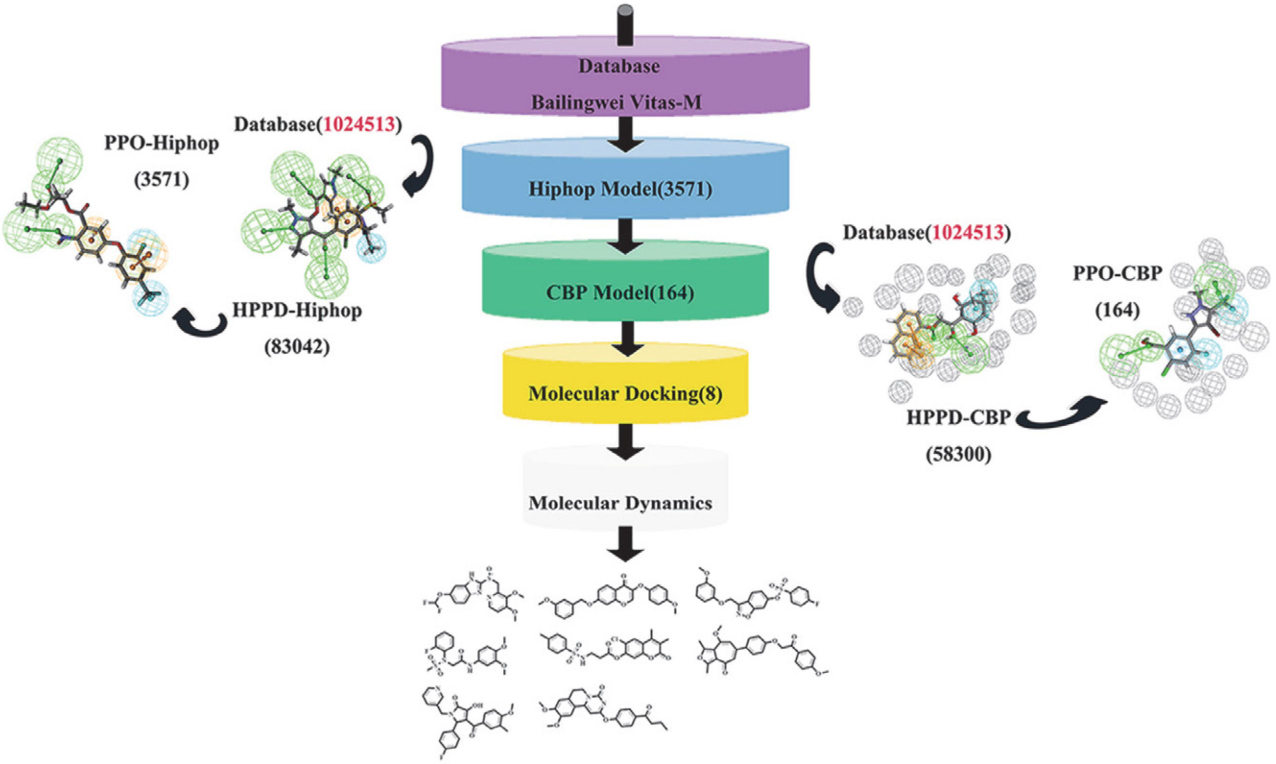

Figure 2. The workflow of multi virtual screening base on dual herbicide target.

and complex-based pharmacophore models (CBP) were constructed respectively, molecular docking and molecular dynamics (MD) simulation were performed on candidate compounds. Finally, 8 potential compounds with inhibitory effects on HPPD and PPO were obtained. The workflow of virtual screening based on the pharmacophore model is shown in Figure 2.

2. Experimental

2. 1. Database Collection and Preparation

1024513 Compounds were extracted from Bailingwei and Vitas-M (https://vitasmlab.biz) databases, and screened according the Lipinski rules compounds. Compounds were conformational optimized with Discovery Studio (DS, Biovia Inc. San Diego, CA, USA, 2020), the 3D database was built with the "Build 3D Database" module, the conformation number was set to 200, and the BEST method was selected for conformation generation.

2. 2. Generation and Verification of Hiphop Pharmacophore Model and Virtual Screening

The Hiphop pharmacophore was established in "Common Feature Pharmacophore Generation model of DS. According to the common characteristics of active compounds, pharmacophore models were generated based on the overlap of these common characteristics and subsequently applied to virtual screening. Regarding HPPD, six commercial HPPD herbicides topramezone, pyrasulfotole, cypyrafluone, tolpyralate, fenpyrazone and tripyrasulfone were collected as the training set to construct HPPD-Hiphop pharmacophore models, the physicochemical properties are listed in Table S1. All ligands were set the MaxOmitFeat feature with 0 and Principal feature with 2. Compound feature elements were selected using the "Edit and Cluster Features" tool. The characteristic elements of hydrogen bond donor (HBD), hydrogen bond acceptor (HBA), aromatic ring (AR) and hydrophobic (HY) were selected to produce pharmacophore. Hiphop pharmacophore was constructed using the "Common Feature Pharmacophore Generation" function in the "Create Pharmacophores Automatically" module. The BEST was selected to produce 10 pharmacophore and 200 conformations with a cut-off value of 10 kcal·mol^{-1}. To test the reliability of the pharmacophore model, the compounds reported in literature on HPPD inhibitors and structures that have no effect on HPPD were collected. 16 Active compounds and 10 inactive compounds (Figure S1) were collected as a testing set, the "Search, Screen and Profile" module was used to evaluate the constructed Hiphop pharmacophore match with the test set. Input File Pharmacophores were loaded, and 10 pharmacophore models were input. The Maximum Conformation number was set to 200 and the Energy Threshold was set to 10.

In the same way as the construction process of the pharmacophore model of HPPD, 6 commercial PPO herbicides fluroximin, fomesafen, fluoroglycofen, lactofen, acifluorfen and ethhoxyfen-ethyl were used as the training set to construct the PPO-Hiphop pharmacophore model, the physicochemical properties of six commercial PPO inhibitors were shown in Table S2. The PPO pharmacophore construction and validation were the same as that for HPPD pharmacophore model. The PPO testing set consisted of 13 active compounds and 12 inactive compounds (Figure S2).

HPPD-Hiphop pharmacophore model was used to screen the 3D database, and the remaining compounds were screened by PPO-Hiphop pharmacophore model.

2. 3. Generation and Verification of CBP Pharmacophore Model and Virtual Screening

Different from the Hiphop model, the construction of the CBP model was based on single receptor-ligand crystal complex interaction, the number of training set was fixed. To ensure the accuracy of the constructed CBP model, a diverse set of active and inactive compounds must be collected for rigorous validation. Arabidopsis thaliana HPPD (*At*HPPD) (PDB ID: 7X5Y) (resolution 1.50 Å)[19] and crystalline small compound were defined as receptor and ligand, and the "Interaction Pharmacophore Generation" module of DS was used to generate a CBP pharmacophore model. Through a literature search, 47 Active compounds and 68 inactive compounds were collected to validate the CBP pharmacophore model (Figure S3). Validation was set to True, Active Ligands were set to All, Inactive Ligands were set to All and other parameters were set to default. Commercial HPPD inhibitors included triketone and pyrazole structure, and the active compounds in the validation set were mainly composed of these two structures. To examine the relationship between the collected active compounds and inactive compounds, principal component analysis (PCA) was employed to analyze the chemical space. The molecular weight, number of hydrogen bond donors and receptors, number of rotatable bonds and log p descriptors of the collected compounds were used as input value.[28]

The PPO-CBP pharmacophore model was constructed using the same protocol as for HPPD. Nicotiana tabacum PPO (*Nt*PPO, PDB ID: 1SEZ, resolution 2.90 Å)[29] was selected to establish the CBP pharmacophore model. The validation set of the PPO pharmacophore model consisted of 19 active compounds and 43 inactive compounds (Figure S4). The active compounds were dominated by diphenyl ether structures.

2. 4. Molecular Docking

In order to ensure the accuracy of molecular docking results, complex structures of plant origin with resolution less than 2.0 Å were selected for study. Mesotrione and oxyfluofen were used as positive controls, the *At*HPPD (PDB ID: 1TFZ) (resolution 1.8 Å)[30] and *Nt*PPO crystal structure were downloaded from the PDB database for molecular docking with compounds. Sequence information for 1TFZ and 1SEZ is provided in Table S3. Proteins and ligands were treated with DS and SYBYL-X 2.0. The unnecessary water molecules and side chains of the Protein were removed, the Protein was treated with "Prepare Protein" under the "Molecular" module in DS, the lost residues were supplemented, and the position of the protein was added with the CHARMm force field.[5,31,32] The Sketch module in SYBYL-X 2.0 was used to process compounds. Under the Tripos force field, Gasteiger-Huckel charge was used to optimize the molecules, the maximum iteration coefficient was selected as 1000, and the energy convergence was 0.005 kcal mol^{-1}.

CDOCKER in DS "Receptor-Ligand Interactions" module was used for molecular docking. The high temperature dynamic rotation method was used to generate the random ligand configuration, and then the lattice based simulated annealing algorithm was used to optimize the ligand configuration, using the "From Current Selection" under the "Define and Edit Binding Site" module to define the binding site of the protein around the ligand. The binding site size was set to 10Å, other settings were default.[33] The *At*HPPD binding site information was x: 45.937, y: 38.936, z: 51.499, and the *Nt*PPO binding site information was x: –39.832, y: –6.094, z: 28.669. Set the Dock Ligands (CDOCKER) parameter to define the coordinates and radius of the docking site, and adjust the Pose Cluster Radius parameter to 0.5 to maximize diversity in the docking conformations. After docking, the interactions between ligands and proteins were analyzed and the top 10 conformational combinations with higher –CDOCKER_ENERGY values were preserved.

2. 5. MD Simulation

MD simulation was commonly used to aid in the study of dynamic atomic details, reveal the dynamics of receptor-ligand interactions and explain the molecular mechanisms behind them, allowing for a more accurate and convenient assessment of the binding affinity of selected compounds.[34–36] In order to verify the stability of binding between the screening results and proteins, MD simulation was further tested by using Desmond module of Schrodinger software. Biological macromolecules mostly used the water model, after the structure of the complex was optimized, the system was constructed by a simple point charge (SPC) water model and the ligand-protein complex was placed in a regular hexahedral box filled with water molecules.[37–39] To ensure the simulation system was neutral, appropriate counterbalance ion neutralization was added. With the parameters set under the Molecular Dynamics module, the complex was simulated for 100 ns at 298 K temperature and 1.01 bar pressure. In addition, the maximum interaction was set to 2000, the convergence threshold was set to 1.0 kcal mol^{-1} A^{-1}, and the OPLS_2005 force field was used to minimize the energy of the complex system.[40] The steepest descent and limited memory Broyden Fletcher Goldfarb Shanno algorithm minimize system energy with 5000 steps until it reached the gradient threshold of 25 kcal mol^{-1} Å^{-1}. Mesotrione and oxyfluofen were used as positive control groups in MD simulation. After the simulation, RMSD of protein skeleton, residues around ligands and binding pockets, and ligand heavy atoms were analyzed for the equilibrium state and stability of the complex. RMSD of the backbone was the main index to evaluate the stability of the system.

The Desmond module of Schrödinger software was selected to calculate the molecular mechanics/generalized born surface area (MM/GBSA) for the compounds, the binding free energy (ΔG_{bind}) was divided into molecular mechanical terms and solvation energy, respectively, reflecting the degree of binding between compounds and proteins.[41, 42]

3. Results and Discussion

3. 1. Hiphop Pharmacophore for Virtual Screening

All of the ten pharmacophore models generated according to the HPPD training set had six characteristic elements and ranked above 85, which proved the reliability of the pharmacophore models, as shown in Table 1. By matching the HPPD-Hiphop pharmacophore models with the training set, the hydrogen bond receptors were nearby the oxygen and nitrogen atoms of the training set, the aromatic ring center was formed at the benzene ring, and the hydrophobic characteristics could be found at the methyl of the compounds (Figure S5). To ensure the accuracy of the pharmacophore models, the Hiphop pharmacophore models were verified through the testing set (Figure 3(a)). The pharmacophore models could well recognize the active and inactive compounds, and HPPD-Hiphop pharmacophore models-02, 03 and 05 were more effective than other models. The Hiphop pharmacophore model-02 had a score of 89.143, was selected for further screening (Figure 3(b)). The pharmacophore signature elements included 1 aromatic ring center, 1 hydrophobic feature, and 4 hydrogen bond receptors.

Table 1 Result parameters of HPPD-Hiphop pharmacophore model.

Number	Features	Rank	Direct Hit	Partial Hit	Max Fit
01	RHAAAA	91.10	111111	000000	6
02	RHAAAA	89.14	111111	000000	6
03	RHAAAA	89.14	111111	000000	6
04	RHAAAA	88.67	111111	000000	6
05	RHAAAA	88.42	111111	000000	6
06	RHAAAA	88.26	111111	000000	6
07	RHAAAA	88.25	111111	000000	6
08	RHAAAA	87.84	111111	000000	6
09	RHAAAA	87.84	111111	000000	6
10	RHAAAA	87.83	111111	000000	6

Rank: Indicates the fit values of the pharmacophore.
Direct Hit: indicates the match between the pharmacophore and the training set molecule.
Partial Hit: indicates the number of pharmacophore features that match the training set molecule.
Max Fit: indicates the matching of pharmacophore features.

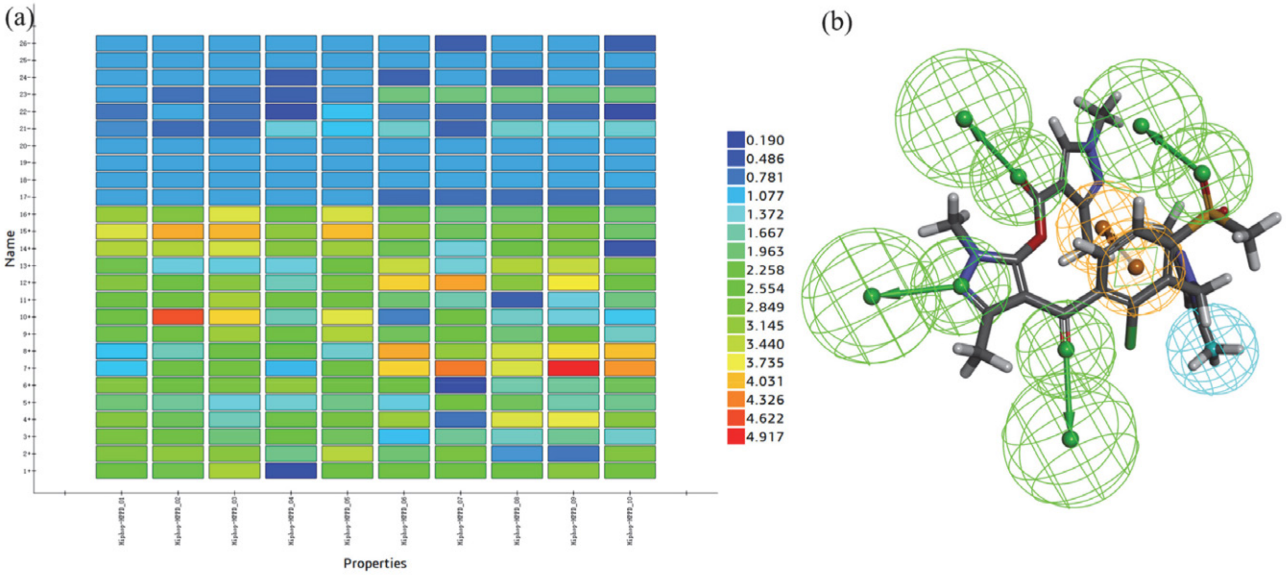

Figure 3. HPPD-Hiphop pharmacophore. (a) The heat map of the 10 hypotheses in the test; (b) The matching of pharmacophore model-02 with tripyrasulfone, the color of pharmacophore features RA, HY and HBA are represented by orange, blue and green, respectively. RA: The aromatic ring needs to be defined by two parameters: one parameter was the spatial position of the aromatic ring and the other parameter was the direction of the aromatic ring plane vector. HY: The hydrophobic center need not be represented by a vector. HBA: Hydrogen bond interaction has a clear directivity, and two points are used to describe hydrogen bond characteristics. One point represents the spatial position of the heavy atom in the hydrogen bond feature, and the other point represents the vector direction of the hydrogen bond acceptor.

Ten PPO pharmacophore models were generated ranking above 95 and had six characteristic elements, 2 aromatic ring centers, 2 hydrophobic characteristics and 2 hydrogen bond receptors, as shown in Table 2. The matching between the training set and the PPO-Hiohop pharmacophore models showed that the benzene ring in the compound produced the aromatic ring center, and the hydrogen bond receptor was formed nearby the oxygen atom. The hydrophobic features were observed between methyl and fluorine atom (Figure S6). Consistent with the test method of HPPD, according to the rank and the matching between the testing set and pharmacophore (Figure 4(a)), Hiphop pharmacophore model-01 was finally selected for subsequent screening, which included 2 aromatic ring centers, 2 hydrophobic features and 2 hydrogen bond receptors (Figure 4(b)).

Table 2 Result parameters of PPO-Hiphop pharmacophore model.

Number	Features	Rank	Direct Hit	Partial Hit	Max Fit
01	RRHHAA	96.17	111111	000000	6
02	RRHHAA	96.17	111111	000000	6
03	RRHHAA	96.16	111111	000000	6
04	RRHHAA	96.16	111111	000000	6
05	RRHHAA	96.15	111111	000000	6
06	RRHHAA	96.12	111111	000000	6
07	RRHHAA	95.96	111111	000000	6
08	RRHHAA	95.96	111111	000000	6
09	RRHHAA	95.40	111111	000000	6
10	RRHHAA	95.40	111111	000000	6

Rank: Indicates the fit values of the pharmacophore.
Direct Hit: indicates the match between the pharmacophore and the training set molecule.
Partial Hit: indicates the number of pharmacophore features that match the training set molecule.
Max Fit: indicates the matching of pharmacophore features.

3. 2. CBP Pharmacophore for Virtual Screening

As for the PCA of compounds (Figure 5(a)), the data of active compounds and inactive compounds was distributed widely. There was a clear separation between the two groups, which could be used to validate the model. The ten generated HPPD pharmacophore models have more than five characteristic elements and the area under the curve (AUC) value was above 0.7, as shown in Table 3. According to the AUC value, the HPPD-CBP-01 model (AUC = 0.976) was selected for virtual screening. The HPPD-CBP-01 contained aromatic ring centers, the hydrogen bond receptor and the hydrophobic group. Hydrogen bond acceptor was located at the oxygen atom, the six-membered ring center and the methyl group generated the hydrophobic feature (Figure 5(b)). The receiver operating characteristic curve (ROC) was used to verify the ability of the HPPD-CBP pharmacophore model to distinguish between active and inactive compounds, the accuracy of the CBP pharmacophore model was evaluated by AUC value, and ROC curves of ten CBP pharmacophore models were shown in Figure S7(a).

PCA was performed for PPO active compounds and inactive compounds, as shown in Figure 6(a), the spatial distribution of compounds was wide, active compounds and inactive compounds were distributed on two sides, with a clear demarcation line, the constructed model was verified by a test set. In ten PPO-CBP pharmacophore models, PPO-CBP-01 and PPO-CBP-02 included six characteristic elements, and the remaining models included five characteristic elements. According to the AUC values (Table 4), CBP pharmacophore models was selected for virtual screening. PPO-CBP-04 contained 2 hydrogen bond receptors, 2 hydrophobic features and 1 Harom (Figure 6(b)). Figure S7(b) shows the ROC of ten CBP pharmacophore models.

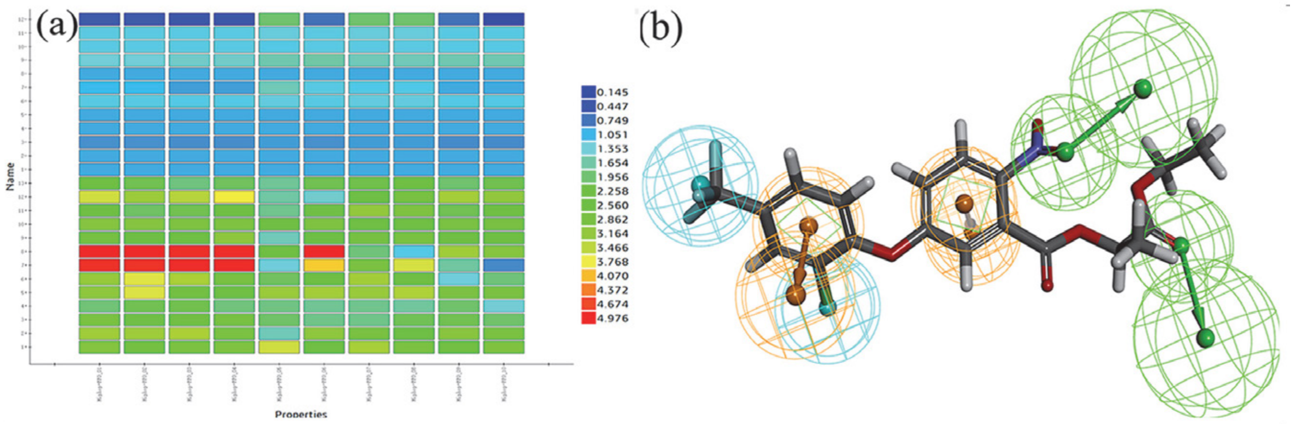

Figure 4. PPO-Hiphop pharmacophore. (a) The heat map of the 10 hypotheses in the test; (b) The matching of pharmacophore model-01 with lactofen, the color of pharmacophore features RA, HY and HBA are represented by orange, blue and green, respectively. RA: The aromatic ring needs to be defined by two parameters: one parameter was the spatial position of the aromatic ring and the other parameter was the direction of the aromatic ring plane vector. HY: The hydrophobic center need not be represented by a vector. HBA: Hydrogen bond interaction has a clear directivity, and two points are used to describe hydrogen bond characteristics. One point represents the spatial position of the heavy atom in the hydrogen bond feature, and the other point represents the vector direction of the hydrogen bond acceptor.

Table 3 Result parameters of HPPD-CBP pharmacophore model.

Number	TP	TN	FP	FN	SE	SP	AUC	Features
01	45	68	1	2	0.96	0.98	0.98	AAHHRR
02	42	66	3	5	0.89	0.96	0.94	AAHHRR
03	45	68	1	2	0.96	0.98	0.98	AAHHRR
04	43	66	3	4	0.91	0.96	0.95	AAHHRR
05	47	52	17	0	1.00	0.75	0.91	AAHHHaromR
06	45	53	16	2	0.96	0.77	0.89	AAHHHaromR
07	47	53	16	0	1.00	0.77	0.89	AAHHHaromR
08	46	54	15	1	0.98	0.78	0.90	AAHHHaromR
09	32	59	10	15	0.68	0.86	0.75	DHHRR
10	32	59	10	15	0.68	0.86	0.75	DHHRR

TP: true positive; TN: true negative; FP: false positive; FN: false negative; SE: sensitivity; SP: specificity.

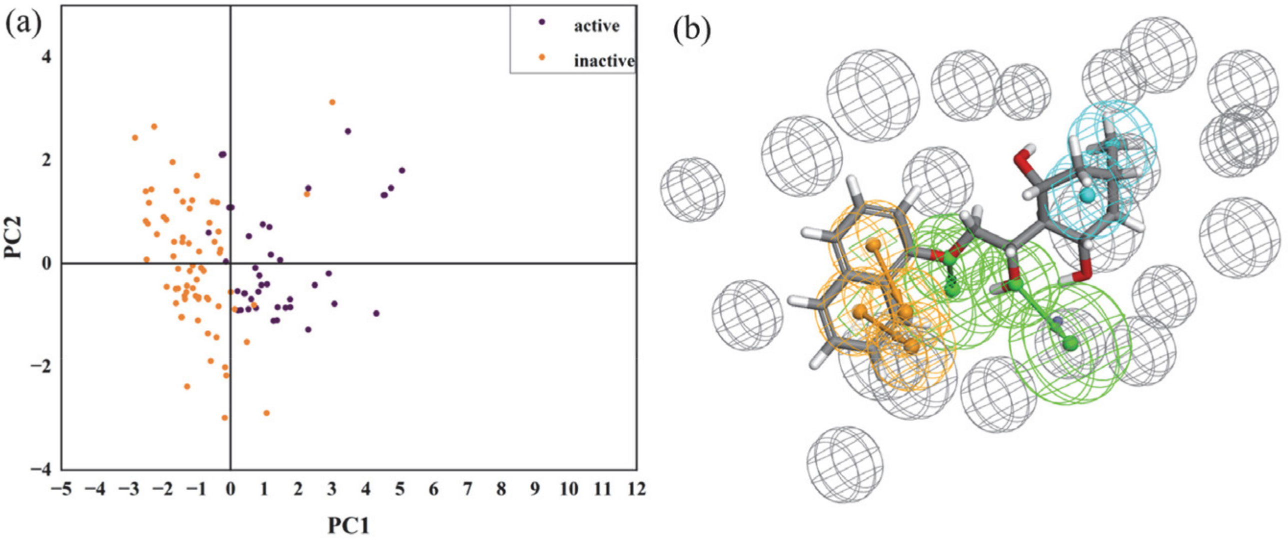

Figure 5. (a) PCA of active compounds and inactive compounds of HPPD; (b) The matching of pharmacophore model-01 with crystalline small compound.

Table 4 Result parameters of PPO-CBP pharmacophore model.

Number	TP	TN	FP	FN	SE	SP	AUC	Features
1	15	43	0	4	0.79	1.00	0.89	AAFFHalHarom
2	17	43	0	2	0.89	1.00	0.95	AAFFHalHarom
3	17	43	0	2	0.89	1.00	0.95	AAFFHal
4	18	43	0	1	0.95	1.00	0.97	AAFFHarom
5	18	42	1	1	0.95	0.98	0.97	AAFFHalHarom
6	18	42	1	1	0.96	0.98	0.97	AAFFHalHarom
7	17	43	0	2	0.89	1.00	0.95	AAFFHal
8	18	43	0	1	0.96	1.00	0.97	AAFFHarom
9	18	43	0	1	0.96	1.00	0.97	AAFFHalHarom
10	18	43	0	1	0.96	1.00	0.97	AAFFHalHarom

TP: true positive; TN: true negative; FP: false positive; FN: false negative; SE: sensitivity; SP: specificity

3. 3. Pharmacophore Virtual Screening

Before the virtual screening, the database was pre-processed. 1024513 Compounds, extracted from Bailingwei and Vitas-M databases, were screened according to the Lipinski principle: $MW \le 500$, $HBD < 5$, $HBA < 10$, $\log p < 5$, $RB \le 10$. 498843 screened compounds were used to create a 3D database for the future investigations. HipHop pharmacophore model and CBP pharmacophore model were used to screen the compounds, and the intersection compounds of the two models were selected for further study.

83042 Compounds were screened through the Hiphop pharmacophore of HPPD-02, and the hit compounds were

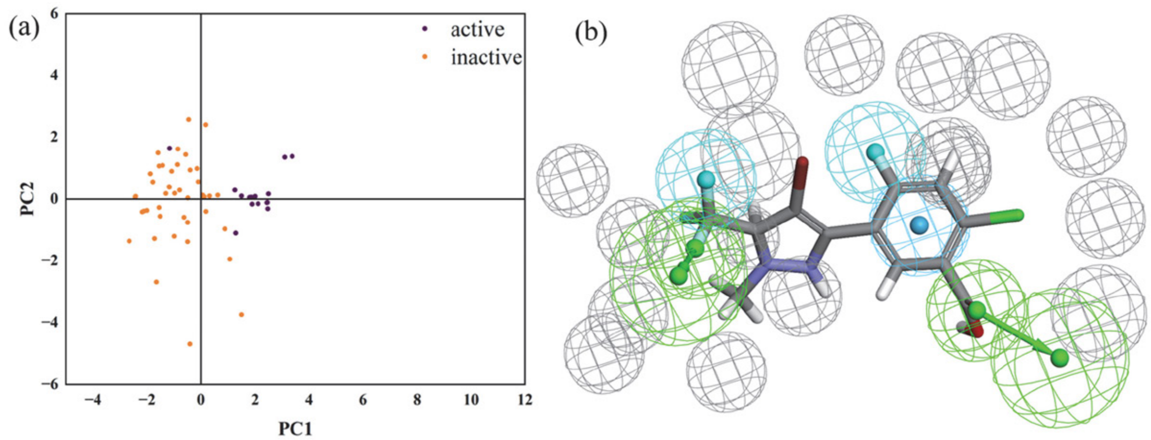

Figure 6. (a) PCA of active compounds and inactive compounds of PPO; (b) The matching of pharmacophore model-04 with crystalline small compound.

Table 5 FitValues of compounds and pharmacophore model.

Name	Structure	FitValue^a	FitValue^b	FitValue^c	FitValue^d
Compound49317	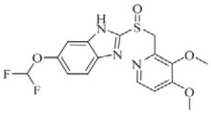	3.29	3.73	3.28	2.91
Compound10674	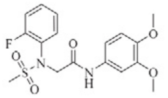	3.01	3.62	3.01	2.57
Compound35215	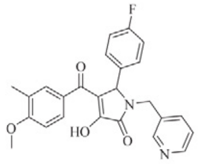	3.11	3.36	2.89	2.50
Compound1555	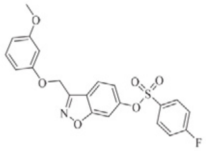	3.15	3.49	3.47	2.12
STOCK1N-41398	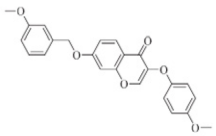	3.15	3.1491	3.35	2.64
STOCK1N-67214	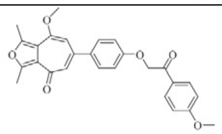	3.06	3.69	3.18	2.64
STOCK1N-57851	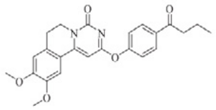	3.19	3.25	2.52	2.58
STOCK1N-40313	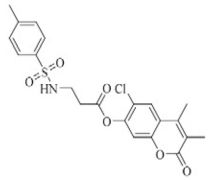	3.59	3.36	3.55	2.51

a: Hiphop-HPPD FitValue; b: Hiphop-PPO FitValue; c: CBP-HPPD FitValue; d: CBP-FitValue sent to the PPO-01 pharmacophore model, finally, 3571 compounds were obtained with the FitValue greater than 2. The CBP pharmacophore virtual screening was similar to Hiphop model. HPPD-01 was employed to screen 498843 compounds, 58300 compounds could hit the pharmacophore model, the hit compounds were filtered the PPO-04 model, 164 compounds were matched to the model. Finally, 8 cross-compounds were obtained by Hiphop model and CBP model, the FitValues were shown in Table 5.

ADMET properties play a crucial role in drug discovery for the druggability and safety. ADMET predictions were performed to evaluate the solubility and safety profiles of the selected compounds. The DS "Calculate Molecular Properties" module under the "ADMET Descriptors" function was used for ADMET prediction, set evaluation option while maintaining default other Settings. The molecular properties (Table S4) and ADMET predictions (Table S5) of the selected compounds showed satisfactory results. It was evident from the predictions that all compounds exhibited good solubility. In addition, based on the CYP2D6 binding value, none of the 8 compounds showed inhibition CYP2D6, indicating their potential to avoid ab-

Table 6 The structure and evaluation of the potential compounds.

Compound	Structure	–CDOCKER ENERGY-HPPD (kcal/mol)	–CDOCKER ENERGY-PPO (kcal/mol)
Natural ligand		15.61	4.72
Negative compound	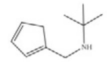	5.49	3.84
Mesotrione	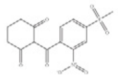	19.70	–
Oxyfluofen	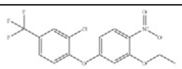	–	18.52
Compound49317	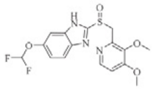	32.75	19.07
Compound10674	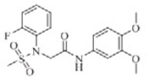	34.14	25.48
Compound35215	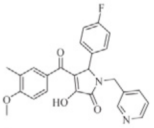	14.54	14.39
Compound1555	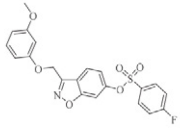	36.73	25.58
STOCK1N-41398	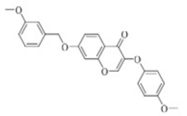	24.87	24.15
STOCK1N-67214	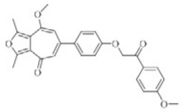	32.21	14.48
STOCK1N-57851	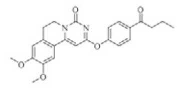	34.61	34.81
STOCK1N-40313	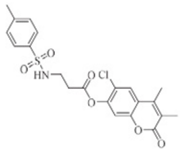	43.74	36.63

normal blood concentration due to CYP2D6 inhibition. Additionally, the binding form and stability of these 8 compounds were conducted.

3. 4. Molecular Docking

To test the binding mode of the 8 hit compounds to the target, the CDOCKER program in DS was carried out, retenting the result of a high CDOCKER ENERGY value. Before the molecular docking, the natural ligand was redocked to protein to verify the reliability of the docking procedure, and the natural ligand was extracted for hydrogenation and energy minimization. As shown in Figure S8, the redocking ligand (brown) and the natural ligand (blue) almost completely overlapped, the RMSD values between HPPD, PPO and the natural ligand were 0.599 and 0.892, indicating that the CDOCKER procedure was reliable.

Eight compounds were docked with 1TFZ and 1SEZ, the results were analyzed according to the -CDOCKER ENERGY value. As shown in Table 6, for HPPD, the –CDOCKER ENERGY was higher than that the natural ligand except Compound35215. In PPO, the results of all

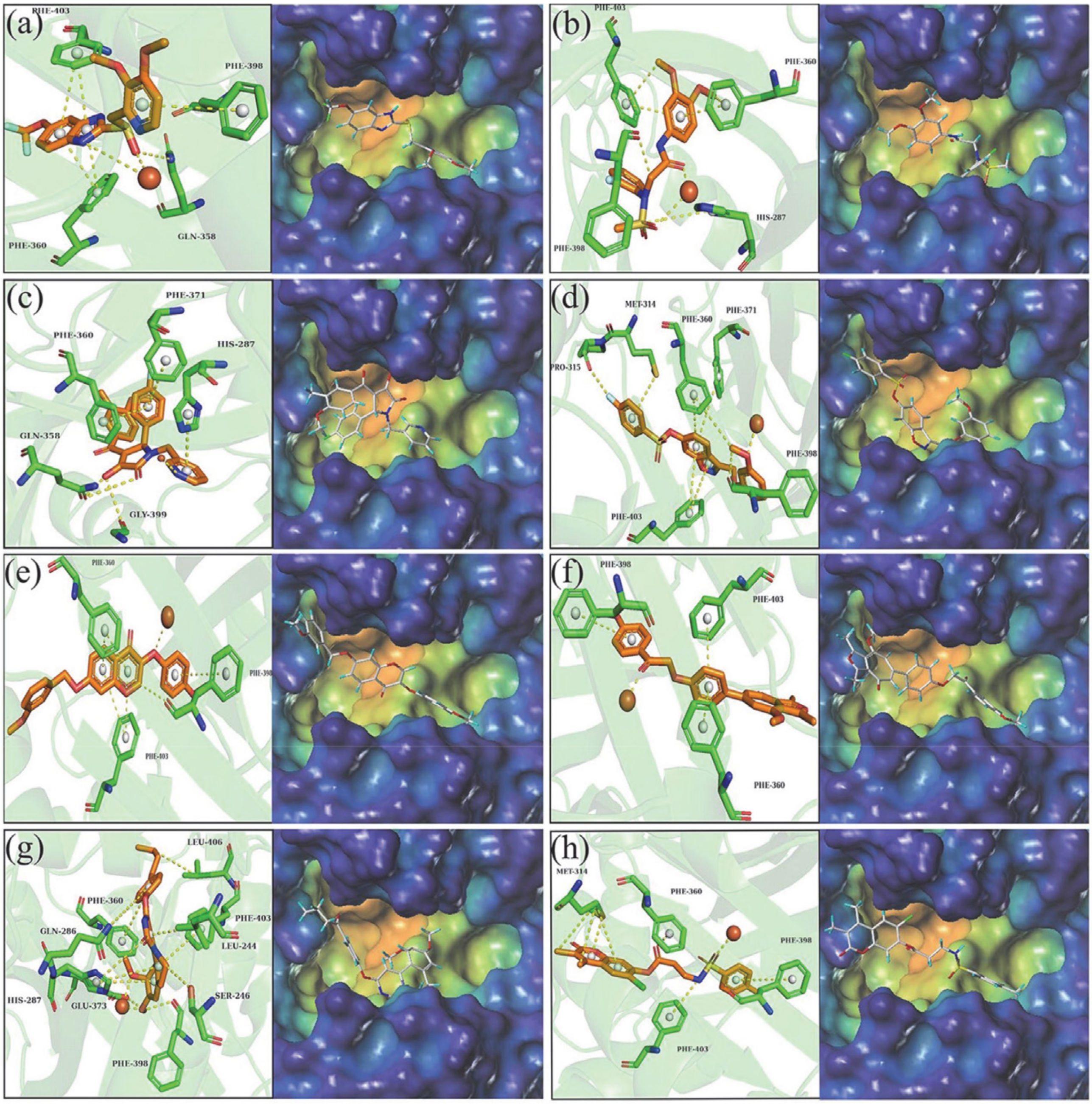

Figure 7. CDOCKER docking results of *At*HPPD. (a) Compound49317; (b) Compound10674; (c) Compound35215; (d) Compound1555; (e) STOCK1N-41398; (f) STOCK1N-67214; (g) STOCK1N-57851; (h) STOCK1N-40313 interact with receptor-ligand at the active site of *At*HPPD.

compounds were superior to the natural ligand. The commercial herbicides mesotrione and oxyfluofen were selected for molecular docking with *At*HPPD and *Nt*PPO, and it was found that except Compound35215, the –CDOCKER_ENERGY of the other 7 compounds were superior to the commercial herbicides. The docking results of negative compound showed that all compounds had good docking results, which were higher than negative compound.

The interactions between HPPD and ligands were shown in Figure 7. All the 8 compounds could chelate with the metal Fe(II). Compound49317, Compound10674, and STOCK1N-57851 formed bidentate combination. The hot spot residues Phe403 and Phe360 binded to the benzene ring via π-π interaction. Phe398 binded to ligands in two ways, one was the π-π interaction with the aromatic rings of Compound49317, STOCK1N-41398, STOCK1N-67214 and STOCK1N-40313, another way of binding was to hydrogen bond interactions with the hydrogen atoms of Compound10674, Compound1555, STOCK1N-41398, STOCK1N-57851, and STOCK1N-40313. In addition to a metal ligand, Phe403, Phe398, and Phe360, the formation of interactions between ligands and other residues (His287,

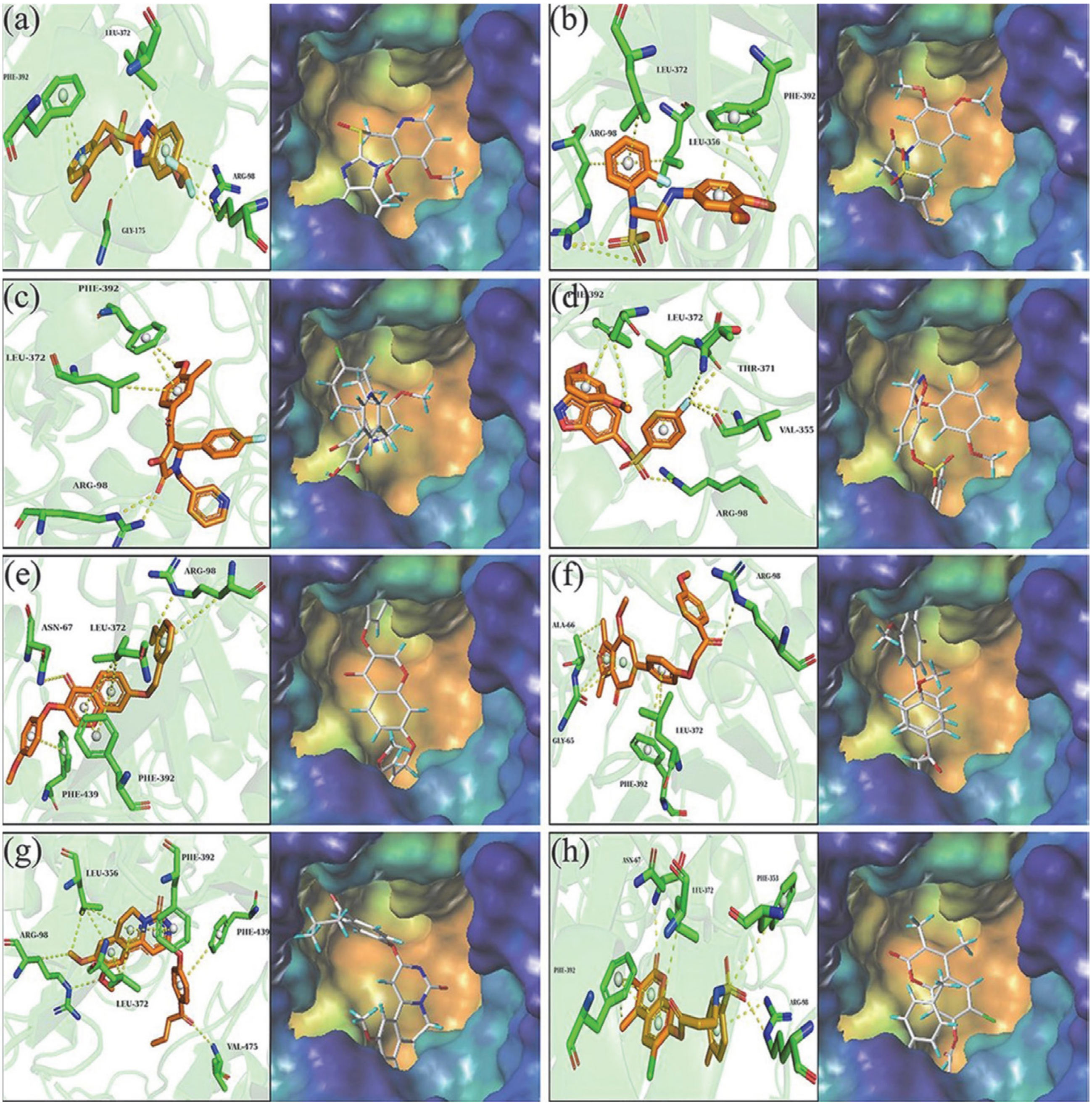

Figure 8. CDOCKER docking results of *Nt*PPO. (a) Compound49317; (b) Compound10674; (c) Compound35215; (d) Compound1555; (e) STOCK1N-41398; (f) STOCK1N-67214; (g) STOCK1N-57851; (h) STOCK1N-40313 interact with receptor-ligand at the active site of *Nt*PPO.

Phe360, Phe371, Met314) was also beneficial to improve the binding stability of the compound to the target, which enhanced the inhibition effect.

The interactions between PPO and ligands were shown in Figure 8. There were hydrogen bond interactions with Arg98 and oxygen atoms in 8 ligands, and π-π interactions with Phe392 and aromatic rings, all ligands produced π-alkyl interactions with Leu372. The π-π interaction was observed in STOCK1N-41398 and STOCK1N-57851 with Phe439, and the π-alkyl interaction was identified in Compound10674, Compound35215, STOCK1N-67214 and STOCK1N-40313 with Phe439. By molecular docking analysis with *At*HPPD and *Nt*PPO, it was found that all compounds could bind to the key residues of two targets, and obtained similar docking scores with commercial herbicides.

3. 4. MD Simulation

The MD simulation was employed to verify the stability of the binding of the compound to the protein. The simulation time was set at 100 ns, and a stable system was obtained. The results were expressed using the root-mean-square deviation (RMSD), which included the Cα atom of the protein backbone, the heavy atom of the ligand, and the active pocket of the residues around the ligand. As shown in Figure 9(a)(b)(c), in the process of binding with HPPD, Compound35215 fluctuated at the first 10 ns and stabilized after 20 ns. Compound49317, Compound10674 and STOCKIN-57851 did not fluctuate significantly after 15 ns. Compared with the natural ligand in 1TFZ, the RMSD of STOCKIN-40313, STOCKIN-41398 and Compound35215 were similar as the native ligand. The RMSD values for Compound10674, Compound35215, Compound49317, STOCKIN-57851, and STOCKIN-67214 were comparable to those of commercial herbicides. In contrast, the RMSD values for Compound1555, Compound40313, and Compound41398 were lower than those observed for mesotrione. 8 Compounds maintained good stability during MD simulation. As shown in Figure 9(d)(e)(f), STOCKIN-57851, STOCKIN-41398 and STOCKIN-40313 kept stable after 15 ns with the PPO protein. 3 Compounds showed lower RMSD than natural ligand. Compound10674 and STOCKIN-67214 began to level off after 40 ns. Exception of Compound 35215, the RMSD values for the other seven compounds were comparable to those of the commercial herbicide oxyfluofen. All compounds tended to stabilize after a certain period of time, which proved that the screened compounds could stably bind to the target. In HPPD and PPO targets, the screened compounds showed good stability in MD simulation, which further indicated that the screened compounds could form stable structures with the targets.

As shown in Figure S9, the residues Phe403, Glu373, Phe398, His287, Phe360 and His205 in HPPD contributed significantly to the protein binding process of the natural ligand, Compound49317, Compound10674 and STOCKIN-57851. Similar to HPPD analysis, in the binding process of PPO to ligand, Phe392, Leu372, Leu356 and Arg98 contributed greatly, these residues were the key residues of

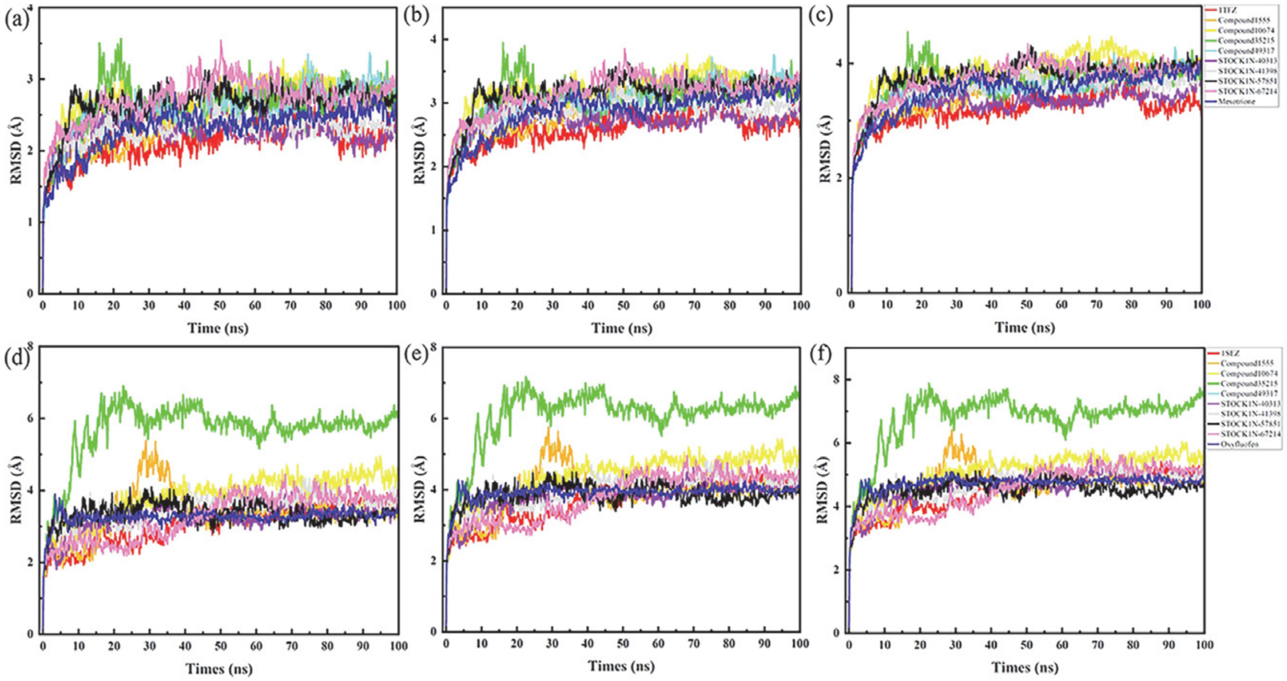

Figure 9 (a) *At*HPPD-RMSD of skeleton Cα atom; (b) *At*HPPD-RMSD of the heavy atom of the ligand; (c) *At*HPPD-RMSD of the protein active pocket with 5 Å residues around the ligand. (e) *Nt*PPO-RMSD of skeleton Cα atom; (f) RMSD of the heavy atom of the ligand; (g) RMSD of the protein active pocket with 5 Å residues around the ligand.

PPO protein. In addition to key residues, Thr68 and Phe439 also played key roles in MD simulation.

The acceptor-ligand binding free energy (ΔG_{bind}) was calculated using the MM/GBSA method. Table 7 gave the parameters of ΔG_{bind}, ΔG_{bind} *coulomb*, ΔG_{bind} *Hbond*, *ΔGbind Lipo* and ΔG_{bind} *vdW*. The ΔG_{bind} value reflected the degree of binding between the compound and HPPD. Among the 8 compounds, ΔG_{bind} *Covalent* was positive values, indicating that ΔG_{bind} *Covalent* formed negative effect on protein binding, and the calculated values of ΔG_{bind} *Lipo* and ΔG_{bind} *vdW* were both negative, according to the parameters, it was concluded that ΔG_{bind} *Lipo* and ΔG_{bind} *vdW* were the main contributors of binding free energy. The ΔG_{bind} values of STOCK1N-57851, STOCK1N-40313 and STOCK1N-67214 were –41.03 kcal mol^{-1}, –26.14 kcal mol^{-1} and –24.75 kcal mol^{-1}, respectively. STOCK1N-57851 showed the greatest binding force with the protein. ΔG_{bind} *Coulomb* was –38.37 kcal mol^{-1}, ΔG_{bind} *Hbond* was –0.75 kcal mol^{-1} and ΔG_{bind} *Lipo* was –24.87 kcal mol^{-1}, ΔG_{bind} *vdW* was –48.05 kcal mol^{-1}. According to the residue contribution degree and binding free energy, the compound had the potential to be an inhibitor of HPPD.

As shown in Table 8, similar as the HPPD complex, most of the ΔG_{bind} Covalent in 8 compounds were mostly positive, which had a negative effect on protein binding. G_{bind} *Lipo* and ΔG_{bind} *vdW* were major contributors to binding free energy. The ΔG_{bind} values of STOCK1N-57851, STOCK1N-40313 and STOCK1N-41398 were –73.20 kcal mol^{-1}, –52.53 kcal mol^{-1} and –57.40 kcal mol^{-1}, respectively. The ΔG_{bind} *vdW* of STOCK1N-57851 and STOCK1N-40313 were –48.05 kcal mol^{-1} and –46.54 kcal mol^{-1}, respectively. The results confirmed that STOCK1N-57851 had good binding ability for both HPPD and PPO.

4. Conclusion

In summary, based on commercial inhibitors and crystalline complexes of two herbicide targets enzyme (HPPD and PPO), Hiphop pharmacophore and CBP pharmacophore models were constructed for screening, respectively. Eight potential molecules were obtained for further molecular docking, ADMET prediction, dynamics studies and binding free energy calculation. All the eight compounds matched with *At*HPPD and *Nt*PPO well. The selected ligands were in line with drug formation and had the advantages of low toxicity and no pollution, which were in accord with the current concept of developing green pesticides and had the potential to become double target herbicides. STOCK1N-57851 interacted with the key residues Arg98, Phe392, Leu372 and Phe439 in PPO active site, blocking the synthesis of chlorophyll. For HPPD receptor, in addition to interacting with the key residues, it also formed bidentate combination with Fe(II), by occupying the active site. This compound prevented HPPD from participating in the biosynthesis of plastoquinone and tocopherol in plants, thereby inhibiting photosynthesis. In general, STOCK1N-57851 was regarded as a promising potential dual-target inhibitor of HPPD and PPO, providing valuable insights for the design of novel molecular frameworks.

Table 7 HPPD-Contribution of various energy components to binding free energy (kcal mol^{-1}).

Compound	ΔG_{bind}	ΔG_{bind} *Coulomb*	ΔG_{bind} *Covalent*	ΔG_{bind} H_{bond}	ΔG_{bind} *Lipo*	ΔG_{bind} *vdW*
STOCK1N-57851	–41.03	–38.37	8.82	–0.75	–24.87	–48.05
Compound35215	–19.21	–9.06	9.32	–0.68	–24.62	–44.61
Compound49317	–6.13	–25.56	1.18	–0.04	–15.09	–49.95
Compound10674	–18.48	–49.48	7.58	0.06	–18.40	–41.38
STOCK1N-40313	–26.14	–18.88	8.60	0.015	–23.12	–46.54
STOCK1N-41398	–13.17	–38.47	11.75	–1.21	–21.46	–40.97
Compound1555	–14.74	–24.75	4.95	–0.04	–22.91	–45.11
STOCK1N-67214	–24.75	–46.54	9.074	–1.64	–23.89	–45.37

Table 8 PPO-Contribution of various energy components to binding free energy (kcal mol^{-1}).

Compound	ΔG_{bind}	ΔG_{bind} Coulomb	ΔG_{bind} Covalent	ΔG_{bind} H_{bond}	ΔG_{bind} Lipo	ΔG_{bind} vdW
STOCK1N-57851	–73.20	–9.00	6.64	–1.09	–28.73	–55.94
Compound35215	–62.33	–19.49	–1.63	–1.62	–20.46	–46.59
Compound49317	–64.99	10.45	3.92	–0.62	–14.752	–56.75
Compound10674	–46.15	–12.52	2.96	–2.11	–10.45	–44.71
STOCK1N-40313	–52.53	–0.477	10.04	–1.09	–18.77	–54.96
STOCK1N-41398	–57.40	–12.99	6.15	–0.99	–21.82	–49.68
Compound1555	–57.64	–12.06	1.58	–2.19	–19.085	–49.53
STOCK1N-67214	–64.28	–8.26	8.64	–0.02	–25.80	–60.66

Acknowledgment

This work was supported by the National Nature Science Foundation of China (No. 22077014, No. 32372589, No. 32311530764) and Natural Science Foundation of Heilongjiang Province (ZD2022C003). The authors are grateful to Prof. Jian Wang (Shenyang Pharmaceutical University) for helping in the application of SYBYL and Schrödinger software.

6. References

1. Y. Fu, T. Ye, Y. X. Liu, J. Wang, F. Ye, *Int. J. Mol. Sci.* **2020**, *21,* 5546. **DOI:**10.3390/ijms21155546
2. X. Y. Leng, S. Gao, Y. F. Ma, L. X. Zhao, M. Wang, F. Ye, Y. Fu, *Pestic. Biochem Physiol.* **2023**, *192,* 105390. **DOI:**10.1016/j.pestbp.2023.105390
3. P. E. Hulme, *Field. Crops. Res.* **2023**, *292,* 108819. **DOI:**10.1016/j.fcr.2023.108819
4. Y. Fu, M. Wang, L. X. Zhao, S. Q. Zhang, Y. X. Liu, Y. Y. Guo, D. Zhang, S. Gao, F. Ye, *Pestic. Biochem. And. Physiol1.* **2021**, *74,* 104811.
5. J. Shi, H. F. Cao, C. F. Wang, S. Gao, J. Y. Wang, L. X. Zhao, F. Ye, Y. Fu, *J. Taiwan. Inst. Chem. Eng.* **2023**, *143,* 104711. **DOI:**10.1016/j.jtice.2023.104711
6. E. A. Borgato, A. Thiagarayaselvam, D. E. Peterson, M. M. Hay, J. A. Dille, M. Jugulam, *J. Agric. Food. Chem.* **2024**, *72,* 5122–5132. **DOI:**10.1021/acs.jafc.3c05333
7. B. F. Zheng, Y. Zuo, G. Y. Huang, Z. Z. Wang, J. Y. Ma, Q. Y. Wu, G. F. Yang, *J. Agric. Food. Chem.* **2023**, *21,* 14221–14231. **DOI:**10.1021/acs.jafc.3c03593
8. W. Zhang, J. H. Zhang, C. H. Yan, X. H. Gan, *J. Agric. Food. Chem.* **2024**, *72,* 12946–12955. **DOI:**10.1021/acs.jafc.4c00272
9. W. Geng, Q. Zhang, L. Liu, G.Y. Tai, X. H. Gan, *J. Agric. Food. Chem.* **2024**, *72,* 17191–17199. **DOI:**10.1021/acs.jafc.4c01389
10. N. Alnafta, R. Beffa, G. Bojack, B. Bollenbach-Wahl, N. Z. Brant, C. Dörnbrack, N. J. Dorn, Freigang, E. Gatzweiler, R. Getachew, C. Hartfiel, I. Heinemann, H. Helmke, S. Hohmann, H. Jakobi, G. Lange, P. Lümmen, L. Willms, J. Frackenpohl, *J. Agric. Food. Chem.* **2023**, *71,* 18270–18284. **DOI:**10.1021/acs.jafc.3c01420
11. D. W. Wang, H. Zhang, S. Y. Yu, R. B. Zhang, L. Liang, X. Wang, H. Z. Yang, Z. Xi, J. *Agric. Food Chem.* **2021**, *69,* 14115–14125. **DOI:**10.1021/acs.jafc.1c05665
12. H.Y. Liu, L. K. Yu, S. N. Qin, H. Z. Yang, D. W. Wang, Z. Xi, *J. Agric. Food. Chem.* **2023,** *71,* 3225–3238. **DOI:**10.1021/acs.jafc.2c09082
13. E. Ivantsova, I. Konig, V. Lopez-Scarim, C. English, S. R. Charnas, C. L. Souders, C. J. Martyniuk, *Environ. Toxicol. Pharmacol.* **2023**, *98,* 104084. **DOI:**10.1016/j.etap.2023.104084
14. H. Lu, Q. Yu, H. Han, M. J. Owen, S. B. Powles, *Pest. Manag. Sci.* **2020**, *76,* 2015–2020. **DOI:**10.1002/ps.5733
15. L. Yang, D. Wang, D. Ma, D. Zhang, N. Zhou, J. Wang, H. Xu, Z. Xi, *Molecules.* **2021**, *26*, 6979. **DOI:**10.3390/molecules26226979
16. C. Chen, Q. Lei, W. Geng, D. Wang, X. Gan, *Food. Chem.* **2024**, *72,* 12425–12433. **DOI:**10.1021/acs.jafc.3c09350
17. R. Dreesen, A. Capt, R. Oberdoerfer, I. Coats, K.E. Pallett, *Regul. Toxicol. Pharm.* **2018**, *97,* 170–185. **DOI:**10.1016/j.yrtph.2018.06.002
18. X. L. Sun, Z. M. Ji, S. P. Wei, Z. Q. Ji, *J. Agric. Food. Chem.* **2020**, *68,* 15107–15114.
19. J. Dong, J. Q. Dong, X. H. Yu, Y. C. Yan, J. X. Nan, B. Q. Ye, W.C. Yang, H. Y. Lin, G. F. Yang, *J. Agric. Food. Chem.* **2023**, *71,* 1170–1177. **DOI:**10.1021/acs.jafc.2c06727
20. Z. B. Jiang, S. Gao, W. Hu, B. R. Sheng, J. Shi, F. Ye, Y. Fu, Design, *Pestic. Biochem. Physiol.* **2023**, *194,* 105493. **DOI:**10.1016/j.pestbp.2023.105493
21. H. Y. Lin, J. Dong, J. Dong, W. C. Yang, G. F. Yang, *Trends. Biochem. Sci.* **2023**, *48,* 568–584. **DOI:**10.1016/j.tibs.2023.02.006
22. X. Gong, G. Zhao, W. Shan, H. Guo, C. Wang, Q. Liu, B. Xu, Y. Wang, X. Guo, *Pestic. Biochem. Physiol.* **2022**, *184,* 105110. **DOI:**10.1016/j.pestbp.2022.105110
23. J. P. Sun, J. W. Zan, X. N. Zang, *Int. J. Mol. Sci.* **2022**, *23,* 3122. **DOI:**10.3390/ijms23063122
24. M. Zhang, H. Cai, D. Ling, C. Pang, J. Chang, Z. Jin, Y. R. Chi, *J. Agric. Food. Chem.* **2023**, *71,* 16972–16983.
25. W. Zhang, J. Pei, L. Lai, *J. Chem. Inf. Model.* **2017**, *57,* 403–412. **DOI:**10.1021/acs.jcim.6b00491
26. T. Wei, R. Lin, X. Fu, Y Lu, W. Zhang, Z. Li, J. Zhang, H. Wang, *Pharmacol. Res.* **2022**, *180,* 106244. **DOI:**10.1016/j.phrs.2022.106244
27. S. C. Yen, L. C. Chen, H. L. Huang, W. C. Huangfu, Y. Y. Chen, T. Eight Lin, S. T. Lien, H. J. Tseng, T. Y. Sung, J. H. Hsieh, W. J. Huang, S. L. Pan, K. C. Hsu, *Bioorg. Chem.* **2022**, *21,* 105675.
28. S. Liu, H. H. Qin, X. R. Ji, J. W. Gan, M. J. Sun, J. Tao, Z. Q. Tao, G. N. Zhao, B. X. Ma, *J. Agric. Food. Chem.* **2023**, *71,* 8038–8049. **DOI:**10.1021/acs.jafc.3c00867
29. M. Koch, C. Breithaupt, R. Kiefersauer, J. Freigang, R. Huber, A. Messerschmidt, *EMBO. J.* **2004**, *23,* 1720–1728. **DOI:**10.1038/sj.emboj.7600189
30. C. Yang, J. W. Pflugrath, D. L. Camper, M. L. Foster, D. J. Pernich, T. A. Walsh, *Biochemistry.* **2004**, *43,* 10414–10423. **DOI:**10.1021/bi049323o
31. A. Ilic, N. Djokovic, T. Djikic, K. Nikolic, *Comput. Biol. Chem.* **2024**, *113,* 108242. **DOI:**10.1016/j.compbiolchem.2024.108242
32. T. Zhang, Y. Hua, C. Zhou, Y. Xiong, D. Pan, Z. Liu, Y. Dang, *Food. Chem.* **2022**, *394,* 133504. **DOI:**10.1016/j.foodchem.2022.133504
33. Y. X. Liu, S. Gao, T. Ye, J. Z. Li, F. Ye, Y. Fu, *Future. Med. Chem.* **2020**, *12,* 795–811. **DOI:**10.4155/fmc-2019-0349
34. Y. Sun, Y. Jiao, C. Shi, Y. Zhang, *Biotechnol. J.* **2022**, *20,* 5014–5027. **DOI:**10.1016/j.csbj.2022.09.002
35. S. Rajasekhar, S. Das, R. Karuppasamy, M. B. Musuvathi, K. Chanda, *J Comput. Chem.* **2022**, *43,* 619–630. **DOI:**10.1002/jcc.26823
36. S. Rajasekhar, R. Karuppasamy, K. Chanda, *J. Comput. Chem.* **2021**, *42,* 1736–1749. **DOI:**10.1002/jcc.26712

37. G. Borhan, M. Sahihi, *J. Mol. Model.* **2024***, 133,* 108882. **DOI:**10.1016/j.jmgm.2024.108882
38. I. Kucuk, Ö. B. Küçükşahin, M. Yildirim, M. Z. Kabir, H. Silah, I. Celik, *Spectrochim. Acta. A.* **2024***, 326,* 125246. **DOI:**10.1016/j.saa.2024.125246
39. X. Li, Y. J. Liu, B. B. Nian, X. Y. Cao, C. P. Tan, Y.F. Liu, Y. J. Xu, *Food. Chem.* **2022***, 373,* 131285. **DOI:**10.1016/j.foodchem.2021.131285
40. J. Y. Wang, L. X. Zhao, J. Shi, S. Gao, F. Ye, Y. Fu, *J. Mol. Liq.* **2022***, 362,* 119683. **DOI:**10.1016/j.molliq.2022.119683
41. J. Shi, L.X. Zhao, J. Y. Wang, T. Ye, M. Wang, S. Gao, F. Ye, Y. Fu, *Arab. J. Chem.* **2022***, 15,* 103919. **DOI:**10.1016/j.arabjc.2022.103919
42. G. Poli, C. Granchi, F. Rizzolio, T. Tuccinardi, *Molecules.* **2020***, 25,* 1971. **DOI:**10.3390/molecules25081971

Povzetek

Razvoj in identifikacija herbicidov z dvojno tarčo je eden izmed glavnih pristopov za reševanje problema odpornosti plevela. Protoporfirinogen oksidaza (PPO) in p-hidroksifenilpiruvat dioksigenaza (HPPD) sta dve pomembni tarči v fotosintezi rastlin. V nasprotju s tradicionalnim načrtovanjem zdravil, ki temeljijo na eni sami tarči, se ta študija osredotoča na oblikovanje zdravil z dvojnim učinkom na HPPD in PPO. Hiphop farmakoforni modeli za tarči HPPD in PPO so bili izdelani z uporabo komercialnih pesticidov, farmakoforni modeli CBP pa so bili napravljeni na podlagi proteinskih kompleksov. Z uporabo farmakofornih modelov smo pregledali več milijonov molekul, izmed katerih smo jih izbrali 8. Kandidatne spojine so tvorile kelate z železom (Fe II) v HPPD in vypostavile stabilne π-π interakcije s ključnimi ostanki v aktivnem mestu HPPD. Večina spojin je tvorila vodikove vezi in π-π interakcije z ostanki v PPO. V kombinaciji z večstopenjskim vizualnim presejalnim postopkom smo pridobili potencialne spojine z zaviralnim učinkom na obe tarči.

Scientific paper

Optimization of The Bleaching Process of Sunflower Oil

Nebojša Vasiljević*,[1,2], Suzana Yusup[3], Vladan Mićić[1], Goran Tadić[1], Dragica Lazić[1], Duško Kostić[1]

[1] *University of East Sarajevo, Faculty of Technology, 75400 Zvornik, Republic of Srpska, Bosnia and Herzegovina*

[2] *University of Novi Sad, Faculty of Technology, 21000 Novi Sad, Serbia*

[3] *Fuel Combustion Section, Generation Unit, Department of Generation and Environment, TNBResearch Sdn Bhd, No1, Lorong Ayer Itam, Kawasan Instituisi Penyelidikan, 43000, Kajang, Selangor, Malaysia.*

** Corresponding author: E-mail: nebojsa.vasiljevic@tfzv.ues.rs.ba*
Tel: +387 66647692; Fax: +387 56260190

Received: 05-21-2024

Abstract

Bleaching is a crucial step in oil refining that removes unwanted pigments and oxidative products, which degrade oil quality. This study evaluated the effects of temperature (75–115 °C), adsorbent concentration (1–3 wt%), and time (20–40 minutes) on sunflower oil bleaching using a Box-Behnken factorial design in Minitab 21. Responses were divided into two groups: (I) peroxide value and spectroradiometric-based chroma and hue-angle, and (II) peroxide value and spectrophotometric-based bleaching efficiency. Under optimal conditions (approximately 78 °C, 2.95 wt% adsorbent, and 20 minutes), peroxide value decreased from 1.8 meq/kg to 0.398 meq/kg, chroma reduced from 45.89 to 9.61, hue-angle increased from 92.69 to 105.55, and bleaching efficiency reached 71.86%. Composite desirability was higher in the first group (0.97 vs 0.89), primarily due to the more objective nature of spectroradiometric parameters (hue-angle and chroma).

Keywords: Oil bleaching, Optimization, Response Surface Method, Sunflower oil

1. Introduction

Global consumption of sunflower oil exceeds 20 million tons per year; therefore, there is a growing demand for high-quality oil products.[1] Bleaching is a crucial step in the edible oil refining process, as it removes unwanted pigments and oxidation products that deteriorate the oil's quality.[2,3] Crude sunflower oil contains various components such as phospholipids, metals, phytosterols, carotene, tocopherols, and tocotrienols. As a result,, a refining process is necessary to transform crude oil into an edible product that is odorless, tasteless, and oxidatively stable, which is preferred by consumers.[5,6,7]

Adsorption processes are particularly important in refining because they effectively remove most of the contaminants found in crude edible oil.[8,9] Suitable adsorbents can sequester oxidation products, pigments, the trace metals, and residues of phospholipids and soaps, which greatly improve the oxidation stability and sensory quality of the oil.[10] The color improvement results from the removal of organic compounds such as carotenoids, particularly β-carotene and their derivatives, xanthophylls, chlorophylls, pheophytins, tocopherols, gossypol, and their degradation products. These compounds can contribute to an undesirable color to oil.[11]

In the process of removing unwanted pigments and oxidative compounds from neutralized oil, various adsorbents-such as bleaching earth, activated carbon, zeolites, silica gel, and activated alumina-are used due to their neutral effect on the beneficial properties of the oil.[12,13,14] Among these, bleaching earth is preferred because of its high adsorption capacity for color pigments and low initial cost.[15] In industrial conditions, edible oil is most often bleached with commercial bentonite or montmorillonite adsorbents (bleaching earth) in concentrations of 0.5–3.0 wt% of the oil mass, at temperatures between 90 °C and 120 °C and at a contact time of 15–60 min, depending on whether it is a batch or continuous flow.[12,15]

Bleaching earth physically adsorbs some pigments, while others are chemically bound via covalent or ionic bonds. The acidity of the bleaching earth correlates with its pigment adsorption capability. Acid-activated bleaching earth serves multiple functions, such as a solid catalyst, adsorbent, cation exchanger, and filter, whereas neutral bleaching earth primarily serves as an adsorbent.[16] In addition to the adsorption characteristic of the bleaching earth, temperature and contact time are also critical process parameters throughout the bleaching process.

Recently, Response Surface Methodology (RSM) has emerged as an effective tool for process optimization.[5,17] The main objective of the RSM is to identify optimal process conditions. The application of statistical design techniques can increase efficiency and bring output closer to nominal values, minimizing variation, modification time, and overall cost.[12,18] Digital tools such as real-time process monitoring and machine learning algorithms for predictive control are also being used to optimize processes.[19,20,21] For the bleaching of edible oils, ultrasonically assisted bleaching and microwave activation of adsorbents have been explored. In addition, nanostructured or modified bioadsorbents are used in continuous process, enabling faster diffusion of undesirable compounds and reducing adsorbent consumption while maintaining high oil quality.[22,23] Recently, waste shells, rich in calcium carbonate, have emerged as a promising low-cost biomaterial for neutralizing and potentially bleaching vegetable oils.[24]

The aim of this research is to optimize the process parameters in the sunflower oil bleaching process using a Box-Behnken factorial design. The effect of temperature, adsorbent concentration, and contact time on the oil's chroma, hue-angle, bleaching efficiency, and peroxide value will be evaluated. The responses are divided into two main assessment groups: (I) hue-angle, chroma and peroxide value, and (II) bleaching efficiency and peroxide value. Response variables in previous oil-bleaching studies have included chroma, hue angle and peroxide value, or bleaching efficiency and peroxide value, but none have directly compared these two groups. The primary goal of the study is to determine which group of responses give more reliable and objective results. The findings of this research have a practical application in the industry because they enable more rational use of adsorbents and energy, ultimately reducing production costs and improving the quality of the final product.

2. Experimental

2. 1. Materials

In this work, degummed and neutralized unrefined sunflower oil was used, which was obtained from the oil refinery "Bimal" d.d. Brčko (Bosnia and Herzegovina). To prevent unwanted oxidation prior, the oil was stored in a plastic bottle wrapped with aluminum foil and kept in a dark place. Commercial bleaching earth (Bimal, Brčko, Bosnia and Herzegovina) was used as an adsorbent for oil bleaching.

To enhance the adsorption capacity of the bleaching earth, a two-step pretreatment process was employed:

- **Sieving**: The bleaching earth was sieved using a 36 μm sieve to eliminate dust particles, which could form stable emulsions with oil.
- **Acid activation**: The sieved earth was treated with sulfuric acid (Gram-mol, Zagreb, Croatia) in a 1:3 ratio (w/w) for 3 hours at 85 °C under continuous stirring. The activation process was performed in a digester, which was a closed system, without evaporation, line with laboratory safety protocols. The goal of the acid activation was to increase the specific surface area and porosity of the adsorbent, thereby improving its adsorption properties.[15,25]

2. 2. Sunflower Oil Bleaching

The neutralized sunflower oil was initially heated to the desired temperature (Factor A, Table 1). The temperature was maintained at a constant level throughout the process using a magnetic stirrer (uniSTIRRER 3) with an integrated heater and automatic temperature controller (LLG Labware, Meckenheim, Germany). Following this, the acid-activated bleaching earth (Factor B) was added. A mixing speed of 450 min^{-1} was chosen based on preliminary tests and literature, as it ensured sufficient dispersion of the bleaching earth particles within the oil matrix without the formation of emulsions or phase separation.[26] Bleaching was carried out for the predeterminated contant time (Factor C), after which the mixture was cooled to room temperature. The oil was then separated from the residual bleaching earth using a Centric 322A centrifuge (Domel, Železniki, Slovenia) at 5000 rpm for 10 minutes. To further minimize oxidative degradation, the bleached oil was packaged in tightly sealed bottles lined with aluminum foil to reduce exposure to air (oxygen). To further limit oxidative degradation, storage was maintained at room temperature and sources of heat and light were avoided.

2. 3. Methods

The following methods were used to characterize the oil: determination of peroxide value, spectrophotometric determination of bleaching efficiency and spectroradiometric determination of hue-angle and chroma.

The peroxide value represents the primary oxidation status of the oil, and the standard method ISO 3960:2017 was used for its determination.[27] The method is based on the titration of oil sample, which was previously diluted with a mixture of acetic acid (Lachner, Neratovice, Czech Republic) and chloroform (Macron Fine Chemicals, Radnor, Pennsylvania, US), followed by the addition of potassium iodide (Gram-mol, Zagreb, Croatia). The liberated iodine was then titrated with a standardized sodium thiosulfate solution (Semikem, Sarajevo, Bosnia and Herzegovina). The results are expressed as milliequivalents per kg of oil (meq/kg).

The bleaching efficiency was determined following the method by Nwabanne and Ekwu.[12] The oil samples were first poured into a 10 mm cuvette and the absorbance was measured at a wavelength of 450 nm on a Shimadzu 1800 spectrophotometer (Agilient Technologies, Santa Clara, California, United States) with hexane as a blank. The sensitivity of the device was ±0.001 AU (absorbance unit), and the calibration was performed using certified reference standards in the UV-VIS range (Starna Scientific, Ilford, UK). The efficiency of bleaching was calculated according to the following formula:

$$Bleaching\ efficiency\,(\%) = \frac{(A_0 - A)}{A_0} \cdot 100 \tag{1}$$

where:

A_0 – absorbance of the raw, neutralized sunflower oil and
A – absorbance of bleached sunflower oil.

Spectroradiometry was used to measure the color of the samples. Compared to spectrophotometry, spectroradiometry captures the entire visible spectrum, making it more efficient for the analysis of cloudier samples and provides non-subjective measurements.[28] Oil analysis was performed in cuvettes (10 mm·10 mm·50 mm) using a Conica Minolta CM-5 (Conica Minolta, Tokyo, Japan), which measured the entire visible color spectrum. From the spectral measurements, the CIELAB color coordinates: a* and b*, and the psychometric light index L were derived. The parameter a* has a positive value for reddish samples and a negative value for greenish samples, while b* has a positive value for yellowish samples and a negative value for bluish samples. L is an estimate of relative brightness (luminosity) and according to this parameter, each color can be considered equivalent to a member of the grayscale, ranging from black (L = 0) to white (L = 100). The hue-angle (h) and chroma (C*) parameters can be derived from the values of a* and b* via the following equations, respectively:

$$h = \tan^{-1}\left(\frac{b^*}{a^*}\right) \tag{2}$$

$$C^* = \sqrt{\left(a^*\right)^2 + \left(b^*\right)^2} \tag{3}$$

Hue-angle is the value according to which colors are traditionally categorized into red, green, yellow and others. The chroma value is related to a quantitative attribute of a color and allows for each hue-angle to determine the degree of difference compared to gray color with the same lightness.

2. 4. Experimental Design

Experimental design and statistical analysis were performed in MINITAB 21 (software version 21.1.1.0) with the Response Surface Method (RSM).

A Box-Behnken experimental design (BBD), a form of Response Surface Method, was applied to determine the influence of three experimental factors: temperature (A), bleaching earth concentration (B), and contact time (C) on the output variables (Responses) (Table 1).

Table 1. Coded and actual levels of independent variables used in the RSM design for bleaching sunflower oil.

Symbol	Independent variables	Levels		
		–1	0	1
A	Temperature [°C]	75	95	115
B	Bleaching earth concentration [wt%]	1	2	3
C	Time [min]	20	30	40

The Box-Behnken design was selected because it avoids extreme experimental conditions, unlike the Central Composite Design (CCD). The selected process parameters were chosen to resemble industrial conditions, so there was no need to include extremes as in CCD. Additionally, the BBD factorial design uses fewer experiments than the CCD, while still providing enough data to develop a reliable second-order polynomial model.[29] A second-order polynomial model was employed due to its ability to be validated using ANOVA analysis, allowing for an assessment of the data's reliability.[30] The main disadvantage of BBD compared to CCD is the existence of only a mid-level without axial points. This can lead to a high fitted R^2 but a low Predicted R^2 indicating that the model "remember" the sample but not the general curvature. Due to the limited number of experiments, extrapolating the results beyond the specific process parameters becomes problematic.[31] In this study, there were three experimental factors, each with three levels, resulting in 13 experimental runs. Two two replicates were carried out at the design center point to estimate pure error and to calculate the repeatability of the method. This allows validation of the model's adequacy of the model and separation of lack-of-fit from experimental error. As a results, a total of 15 experimental runs were performed.

The responses in this study were chroma, hue value, bleaching efficiency and peroxide value of the bleached oil.

The experimental data were fitted to a second-order polynomial model to obtain the regression coefficients. The generalized second-order polynomial model used in the response surface method is as follows:

$$Y = a_0 + \sum a_i X_i + \sum a_{ii} X_i^2 + \sum a_{ij} X_i X_j \tag{4}$$

where Y represents the experimental response, a_0 is a constant, a_i, a_{ii} and a_{ij} are coefficients of linear, quadratic and interactive regression models, and X_i and X_j are independent variables in coded values.

Lack of fit, coefficient of determination (*R^2*) and p-value obtained ANOVA were used to assess the adequacy of the developed model. Regression analysis and contour plots were generated to explain the effects of independent variables on responses. Finally, parameters were optimized using the RSM optimization procedure.

3. Results and Discusion

According to the Box-Behnken factorial design with three factors, 15 experimental runs were performed, and the output variables are shown in Table 2. The bleaching process not only affects the color removal but also contributes to the decomposition of unwanted oxidation products. Therefore, in addition to the chroma value, the hue-angle and bleaching efficiency (which are direct indicators of the degree of removal of colored pigments) and the peroxide number were used as the responses in this study.

The L, a^*, and b^* values of the starting, unbleached oil were 91.49, –2.15, and 45.84, respectively. These values indicate that the oil is yellowish in color, with a high concentration of carotenoids.[32] The value of L increased after bleaching, which resulted in the oil samples becoming lighter and slightly more transparent. As mentioned, more positive b^* values meant the presence of yellow color in the sample. The parameter b^* exhibited the greatest change, decreasing from starting value of 45.84 to a range of 8.94–14.22, depending on the process conditions. This decrease in the b^* value of the samples with the addition of bleaching earth indicated that most of the carotenoid pigments (which are mostly yellow-brown in color) have been removed. The negative value of a^* value for each sample indicated that the greenish color predominates in the samples.

To determine the influence of process parameters on product quality, ANOVA analysis and evaluation of the obtained models were performed.

The experimental data of each measured variable were fitted into a complete quadratic model. Polynomial coefficients for the response surface model were calculated through multiple regressions. An F-value and a p-value were calculated for each term in the regression model. The F-value represents the ratio between the variance explained by the model and the error variance – the higher it is, the better the model explains the data. On the other hand, the p-value shows how much chance the F-value of that size would have if there was no real effect. A confidence level of 95% was chosen and a p-value greater than 0.05 were not considered statistically significant. The Adjusted R^2 and Predicted R^2 were evaluated to determine whether the model was adequate after eliminating non-significant parameters, i.e. whether the model can accurately predict responses under different process conditions. Table 3 shows the ANOVA results for the response surface quadratic model for responses of bleached sunflower oil.

The R^2 values for chroma, hue-angle, bleaching efficiency and peroxide value in bleached oil were 0.993, 0.9789, 0.952 and 0.9701, respectively. These values indicate that the response variability was well explained in the generated model. The models could explain 99.3% of the variation in chroma, 97.89% of the variation in hue-angle, 95.52% of the variation in bleaching efficiency and 97.01% of the variation in peroxide value. The R^2 value for all four responses were close to unity, indicating a good correlation between the independent variables and the responses.

Adjusted R^2 is the corrected value for R^2 after eliminating non-significant terms in the model. Adjusted R^2 values for chroma, hue angle and peroxide value in bleached oil were 0.981, 0.941, and 0.916, respectively. These values

Table 2. Measured values for the response variables.

Number of rafination	Process condition			Color			Chroma (C^*)	Hue-angle (h)	Bleaching efficiency [%]	Peroxide value [meq/kg]
	Temp [°C]	Bleaching earth conc. [wt%]	Time [min]	L	a^*	b^*				
Int. sample	–	–	–	91.49	–2.15	45.84	45.89	92.69	–	1.80
1	75	1	30	93.37	–2.46	10.62	10.90	103.03	68.27	1.30
2	115	1	30	94.02	–3.30	14.22	14.60	103.06	74.18	1.70
3	75	3	30	91.49	–2.72	9.90	10.27	105.37	61.71	0.50
4	115	3	30	91.22	–3.40	13.30	13.73	104.32	59.52	0.59
5	75	2	20	93.14	–2.32	8.94	9.24	104.55	72.43	0.60
6	115	2	20	92.51	–2.98	11.65	12.02	104.37	69.15	0.70
7	75	2	40	92.32	–2.50	9.58	9.90	104.62	68.27	0.50
8	115	2	40	91.64	–3.43	13.91	14.33	103.85	67.30	0.70
9	95	1	20	94.00	–2.68	11.36	11.67	103.26	69.37	1.30
10	95	3	20	92.67	–2.90	10.37	10.77	105.61	68.71	0.40
11	95	1	40	93.85	–2.75	11.84	12.16	103.05	76.81	0.90
12	95	3	40	90.37	–3.12	11.80	12.21	104.82	53.39	0.50
13	95	2	30	91.84	–2.81	10.94	11.29	104.41	64.99	0.52
14	95	2	30	90.16	–2.78	11.21	11.55	104.93	64.55	0.59
15	95	2	30	92.42	–2.93	11.16	11.53	104.69	65.86	0.60

Table 3. ANOVA results for the response surface quadratic model for all responses of bleached sunflower oil.

Source	DF[a]	Chroma F-Value[b]	Chroma P-Value[c]	Hue angle F-Value	Hue angle P-Value	Bleaching efficiency F-Value	Bleaching efficiency P-Value	Peroxide value F-Value	Peroxide value P-Value
Model	9	79.22	<0.0001	25.76	0.0011	11.01	0.0083	18.01	0.0027
Linear	3	213.62	<0.0001	65.78	0.0002	21.30	0.0028	38.70	0.0007
Temperature (A)	1	560.67	<0.0001	11.68	0.0189	0.73	0.4327	6.58	0.0503
Adsorbent conc. (B)	1	14.99	0.0117	179.35	<0.0001	54.07	0.0007	107.81	<0.0001
Time (C)	1	65.19	0.0005	6.33	0.0535	9.12	0.0294	1.70	0.2490
Square	3	17.37	0.0045	7.79	0.0248	1.38	0.3510	12.83	0.0088
AA	1	6.94	0.0463	7.20	0.0437	0.76	0.4246	7.12	0.0444
BB	1	31.24	0.0025	17.77	0.0084	0.00	0.9643	28.12	0.0032
CC	1	11.48	0.0195	0.18	0.6917	3.54	0.1184	2.90	0.1494
2-Way Interaction	3	6.67	0.0337	3.71	0.0959	10.36	0.0138	2.49	0.1749
AB	1	0.31	0.6001	7.02	0.0455	3.45	0.1222	1.90	0.2265
AC	1	14.78	0.0121	2.10	0.2074	0.31	0.6042	0.20	0.6706
BC	1	4.90	0.0777	2.02	0.2140	27.31	0.0034	5.37	0.0684
Lack-of-Fit	3	3.00	0.2600	0.36	0.7949	9.61	0.0957	8.05	0.1126
Coefficients of determinations		$R^2 = 0.993$; Adjusted $R^2 = 0.981$; Predicted $R^2 = 0.906$		$R^2 = 0.9789$; Adjusted $R^2 = 0.941$; Predicted $R^2 = 0.852$		$R^2 = 0.952$; Adjusted $R^2 = 0.866$; Predicted $R^2 = 0.274$		$R^2 = 0.970$; Adjusted $R^2 = 0.916$; Predicted $R^2 = 0.553$	

[a] – Degree of Freedom [b] – ANOVA test statistic (variance ratio) [c] – $p < 0.05$ indicates statistical significance.

were very close to the R^2 values, which meant that the proposed models remain valid after eliminating members whose p-value is greater than 0.05. The Adjusted R^2 value for bleaching efficiency was 0.866, slightly lower but still reliable enough that the abbreviated regression model can validly represent the responses.

Predicted R^2 is used to determine how well a regression model makes predictions. It is extremely high for chroma and hue angle (0.906 and 0.852), confirming valid predictions for new data. On the other hand, Predicted R^2 is significantly lower (0.274 and 0.553) for bleaching efficiency and peroxide value, which means that the model fits the original data, but the predictions are not accurate enough. This indicates that the model is complicated and begins to model noise in the data (a condition known as "overfitting the model").[33] This may be due to a small number of samples, an overly complex model, or the inclusion of variables that have no real impact.

Lack of fit can be used to confirm the validity of the model. By ANOVA analysis for lack-of-fit values of all responses, it was determined that the p-value was significantly higher than 0.05, which indicated that the models were adequately adapted to the experimental data.

3. 1. The Influence of Process Parameters on the Value of Chroma

Chroma refers to the degree of color purity. A color with a high chroma value does not have a significant presence of black, white or gray. A high chroma value means that the color contains little to no presence of black, white or gray, distinctly different from neutral gray at the given brightness.

Table 4 shows the coefficients of the regression equation and p-values for the terms in the proposed quadratic

Table 4. Regression coefficients and p-values for all responses.

Variables	Chroma Regression coeff.	Chroma p-Value	Hue angle Regression coeff.	Hue angle p-Value	Bleaching efficiency Regression coeff.	Bleaching efficiency p-Value	Peroxide value Regression coeff.	Peroxide value p-Value
Constant	14.14	<0.0001	90.31	<0.0001	65.70	<0.0001	5.20	0.0003
Temperature (A)	−0.1058	<0.0001	0.1720	0.0189	−0.208	0.4327	−0.0632	0.0503
Adsorbent conc. (B)	−3.218	0.0117	4.471	<0.0001	21.24	0.0007	−1.627	<0.0001
Time (C)	0.0448	0.0005	0.1077	0.0535	−0.089	0.0294	0.016	0.2490
AA	0.000735	0.0463	−0.000711	0.0437	0.00246	0.4246	0.000379	0.0444
BB	0.624	0.0025	−0.447	0.0084	−0.05	0.9643	0.3012	0.0032
CC	−0.00378	0.0195	−0.00045	0.6917	0.0213	0.1184	−0.000967	0.1494
AB	−0.003	0.6001	−0.0135	0.0455	−0.1012	0.1222	−0.00376	0.2265
AC	0.002063	0.0121	−0.000738	0.2074	−0.00301	0.6042	0.000123	0.6706
BC	0.0238	0.0777	−0.0145	0.2140	−0.569	0.0034	0.01264	0.0684

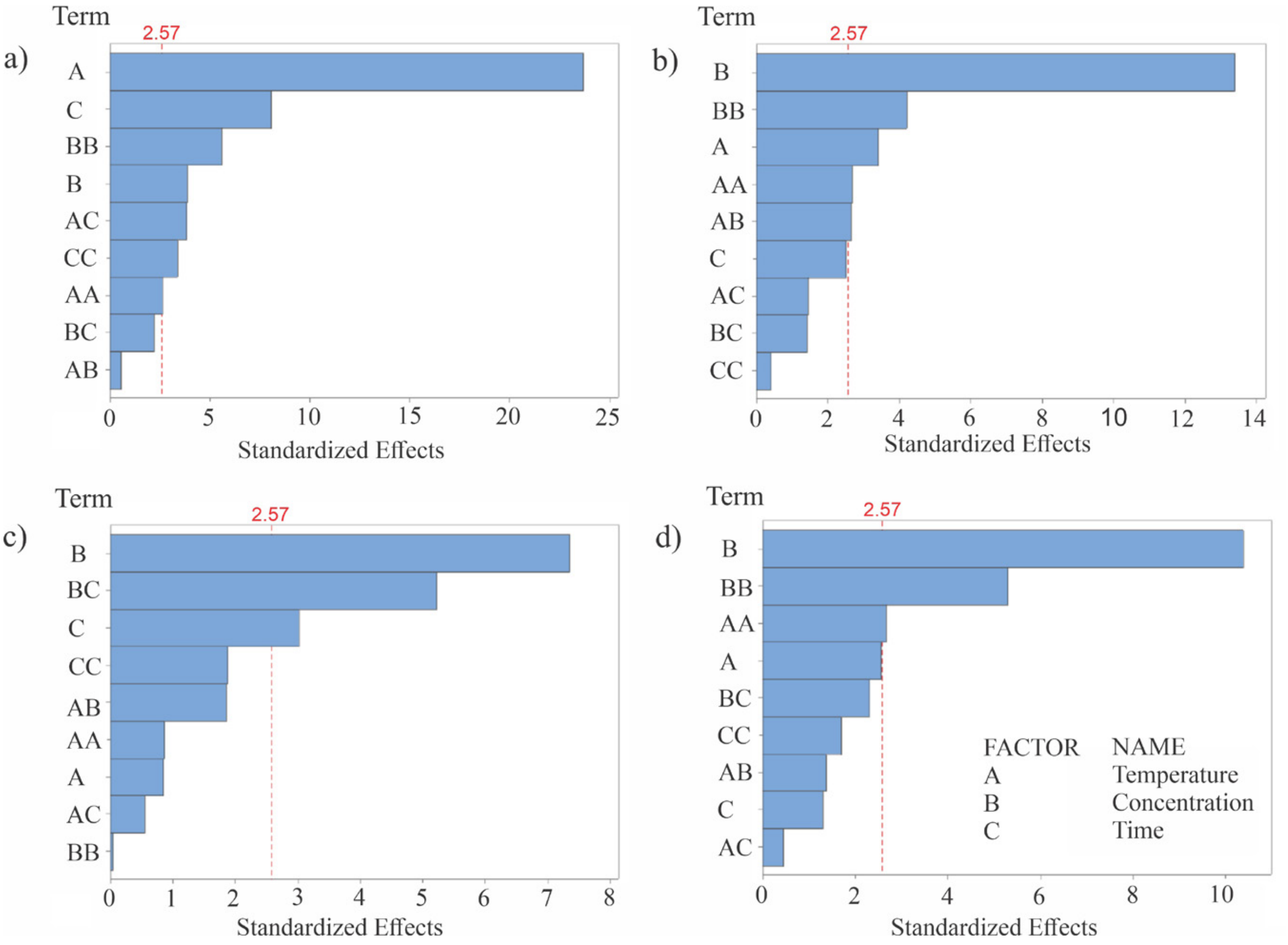

Figure 1. Pareto Chart of the Standardized Effect for a) chroma, b) hue angle, c) bleaching efficiency and d) peroxide value.

model for chroma in bleached oils, while Figure 1a shows the corresponding Pareto diagram. Among the parameters, temperature (A) has a very significant effect ($p < 0.0001$) on the chroma value.

The following parameters have an influence on chroma ($p < 0.05$): time (C), square of concentration (BB), concentration (B), cross product of temperature and time (AC), square of time (CC) and square of temperature (AA). The mutual interaction of concentration and time (BC) and temperature and concentration (AB) did not have significant effects ($p > 0.05$), and can be excluded from the regression model.

By discarding members that do not have a large impact, the regression equation in uncoded units has the following form:

$$C^* = 14.14 - 0.106 \cdot A - 3.218 \cdot B + 0.0448 \cdot C + 0.000735 \cdot \\ \cdot AA + 0.624 \cdot BB - 0.00378 \cdot CC + 0.002063 \cdot AC \quad (5)$$

In order to assess the influence of bleaching earth concentration (B) and temperature (A) on the chroma value, a contour diagram was constructed based on the mean level (0) of time (30 min). Based on Figure 2a, it is observed that the chroma value decreased with decreasing temperature. Also, it was noticed that the lowest value of chroma was at the addition of 2–2.5 wt% of bleaching earth, at a temperature of about 75 °C.

Figure 2b shows the influence of time and temperature at a constant concentration of added earth (2 wt%). The chroma value was low for the entire covered time interval of 20 to 40 minutes at temperatures of 75–80 °C. As the temperature increased, the response value gradually increased. The contour diagram showing the effect of time and concentration on the chroma value of the bleached oil that was not processed, because based on the number of degrees of freedom, it is dependent on the previous two diagrams.

The lowest chroma values (9.24–9.90) were achieved at the lowest temperature in the study (75 °C) and moderate adsorbent concentration (2 wt%) regardless of time. At 75 °C, molecular diffusion in the pores of the adsorbent is fast enough, while further increase in temperature, although leading to even faster diffusion, also leads to thermal damage, which causes the chroma value to deteriorate. A dose of 2 wt% of adsorbent provides an optimal surface area for adsorption, while further increase in dose leads to the occurrence of particle agglomeration and pore block-

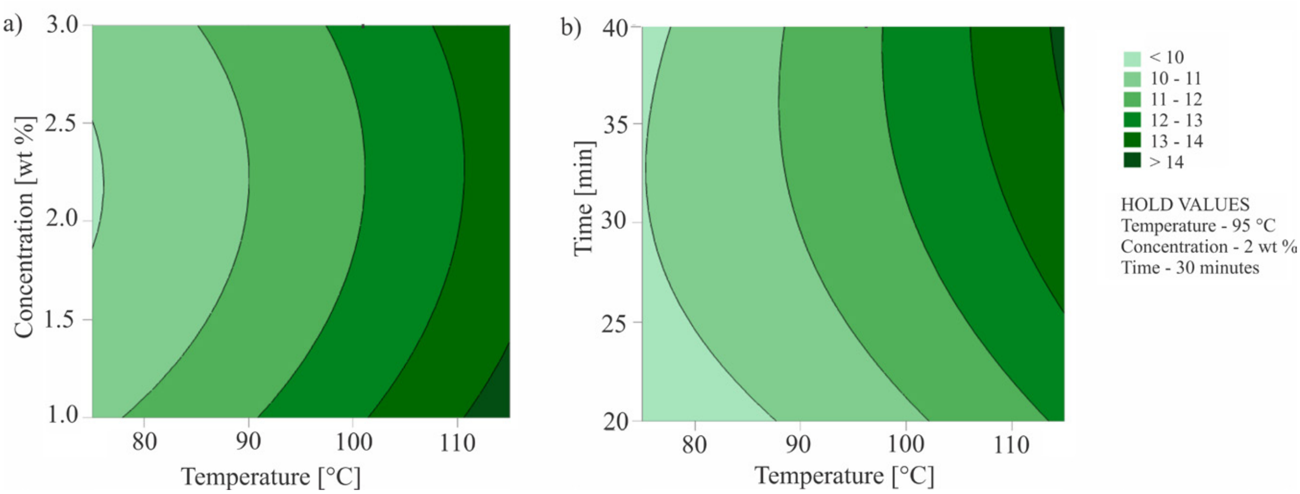

Figure 2. Contour diagrams to show the influence of a) concentration and temperature, b) time and temperature on the chroma value of bleached oil.

ing.[34] Similar trends are present in the work of Marrakchi et. al.[35]

3. 2. Influence of Process Parameters on the Value of Hue-angle

At the beginning of the interpretation of the results, an individual explanation of the CIELAB parameters a* and b* was provided. These parameters can be combined via Equation 2 to obtain the value of the hue-angle, which indicates the dominant color type of the sample (e.g., yellow, green, red...) and its shades. The hue-angle is crucial for assessing the purity and freshness of the oil, as it helps identity the presence of residual yellow and green pigments. Conceptually, the hue angle is graphically represented as an RGB CMY circle or a hue hexagon (Figure 3).

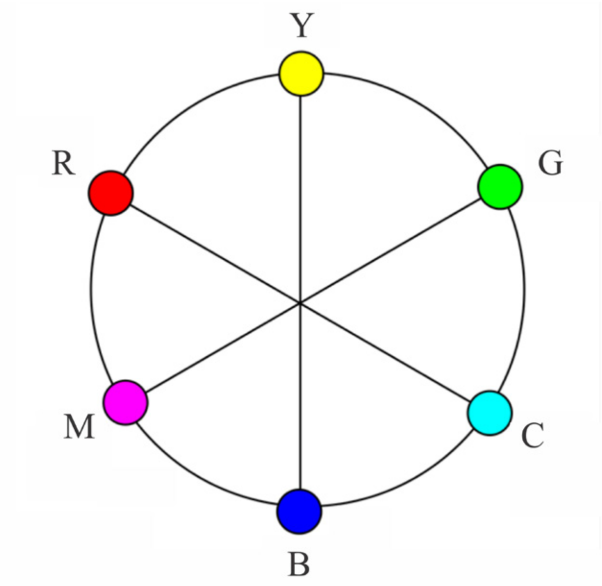

Figure 3. RGB CMY circle.[36]

The three primary screen colors-R (scarlet or orange-red), G (yellowish green), and B (deep violet-blue)- are arbitrarily placed at 120° angles to each other. Their additive complementaries Y (yellow), M (magenta or red-violet), and C (cyan or blue green)-are positioned opposite them.[36]

Table 4 shows the coded coefficients of the regression equation and p-values for members in the proposed quadratic model for the hue angle of bleached oils, while Figure 1b shows the corresponding Pareto diagram. Among the parameters, the concentration (B) has a very significant effect ($p < 0.0001$) on the hue angle value. Coefficient B has a high positive value, which indicates a favorable influence of concentration on the response.

The following parameters have a significant influence ($p < 0.05$): square of concentration (BB), temperature (A), square of temperature (AA) and mutual interaction of temperature and concentration (AB). The coded coefficient with these parameters has a negative value, which meant that increasing them decreased the value of the hue angle. The p-value of time (C) was 0.0535, slightly higher than allowed, but this term was kept in the reduced regression model to maintain the hierarchy of the model. The interactions of temperature and time (AC), concentration and time (BC) and time squared (CC) were dropped from the regression model because the p-value was far higher than 0.05.

By discarding terms that do not have a large impact, the regression equation in uncoded units for hue angle has the following form:

$$\begin{gathered} h = 90.31 + 0.172 \cdot A + 4.471 \cdot B + 0.108 \cdot C0 - \\ 0.000711 \cdot AA - 0.447 \cdot BB - 0.01350 \cdot AB \end{gathered} \tag{6}$$

In order to assess the influence of temperature (A), bleaching earth concentration (B) and time (C) on the hue angle value, contour diagrams were constructed showing the interaction of concentration and temperature (Figure 4a) and time and concentration (Figure 4b).

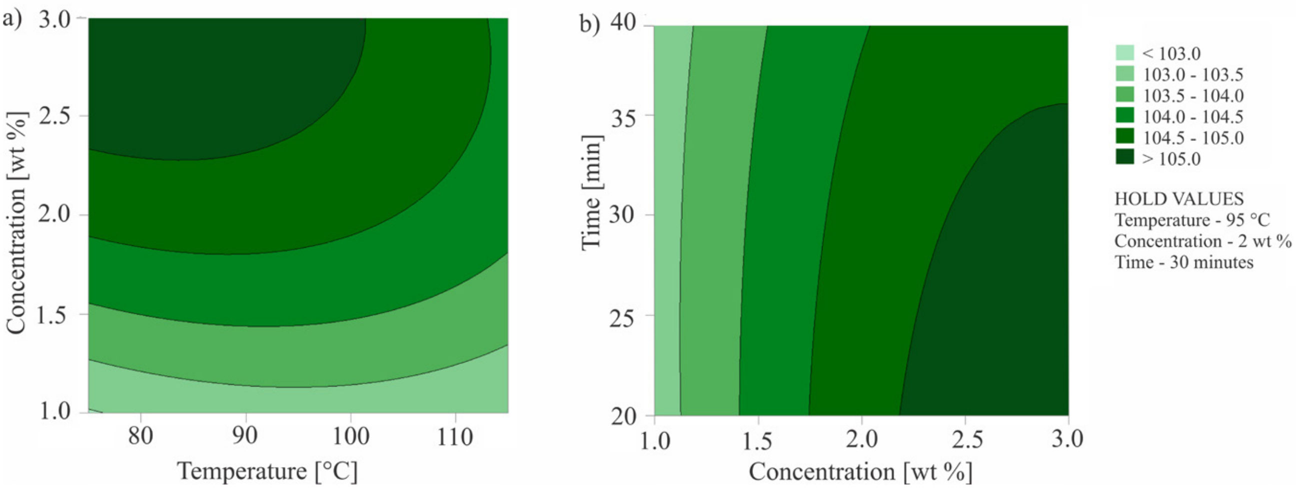

Figure 4. Contour diagrams to show the influence of a) concentration and temperature and b) time and concentration of adsorbent on the hue angle value of bleached oil.

By observing Figure 4, it is clear that concentration is the dominant factor, thus confirming the results of the ANOVA analysis and p-value. Addition of 2.4–3% of adsorbent, at temperatures of 75–102 °C lead to the maximum response value (h > 105) (Figure 4a). Hue-angle values are extremely high even when adding 1.8 wt% adsorbent in the entire temperature interval. A further decrease in the amount of added adsorbent led to a decrease in the value of hue angle which was independent of temperature.

A similar interaction between the variables can be seen in Figure 4b. The value of hue – angle was the highest in the first thirty minutes with the addition of 2.2–3% adsorbent, and with further extension of the process it decreased slightly. A sufficiently high response value was also achieved with the addition of 1.8% adsorbent, while further reduction of the added bleaching earth reduced the response value in the entire temperature interval.

By comparing chroma and hue-angle, it is observed that both the reduction of chroma and the increase of hue-angle are favored by lower temperatures, because further increase in temperature can lead to thermal decomposition. Higher doses of adsorbent (2.5–3 wt%) favor the increase of hue-angle, because for the shift of tone-angle to higher values (from 92.69 to 105.61) (less pure yellow, more yellow-green), carotenoids (yellow, brown colors) that bind more weakly at lower doses should be removed.[34,35]

3. 3. Influence of Process Parameters on Bleaching Efficiency Value

Table 4 and Figure 1c show the coded coefficients of the regression equation and p-values, i.e. the Pareto diagram for the proposed quadratic model for bleaching efficiency of bleached oils. As for the value of the hue angle, the concentration (B) has a very significant effect ($p < 0.001$) on the response.

In addition to concentration (B), the efficiency of bleached oil removal was significantly influenced ($p < 0.05$) by two other factors: time (C) and the interaction of concentration and time (BC). The coded coefficients with these parameters had negative values, which meant that increasing them decreased the value of bleaching efficiency.

ANOVA analysis also found that all other parameters have a p-value greater than 0.05, and can be discarded from the regression model while still maintaining a high degree of precision.

The abbreviated regression equation for the bleaching efficiency response has the following form:

$$Bleaching\ efficiency = 65.7 + 21.24 \cdot B - 0.089 \cdot C - 0.569 \cdot BC \qquad (7)$$

By observing Figure 5a, it can be figured out that the bleaching efficiency did not change significantly with temperature, thus confirming the results of the ANOVA analysis. On the other hand, looking at the same figure, it was clear that the degree of bleaching depended on the amount of added adsorbent. Efficiency is highest with the addition of only 1 wt% of adsorbent for the entire temperature range, and the same efficiency can be achieved with the addition of up to 1.4 wt% of adsorbent at temperatures of 105–115 °C (bleaching efficiency >75%). By increasing the amount of added adsorbent, the degree of bleaching decreases almost linearly, and the lowest value of bleaching efficiency (bleaching efficiency <55%) is achieved with 3 wt%of adsorbent and temperatures higher than 90 °C.

It is noticed from the contour diagram 5b that at a time between 20–25 minutes, regardless of the amount of added adsorbent, almost the same bleaching efficiency is achieved. By prolonging the adsorption time, significant differences in bleaching efficiency are observed with the change in concentration. Thus, with smaller amounts of added adsorbent and time between 35 and 40 minutes, the highest degree of removal of pigments from the un-

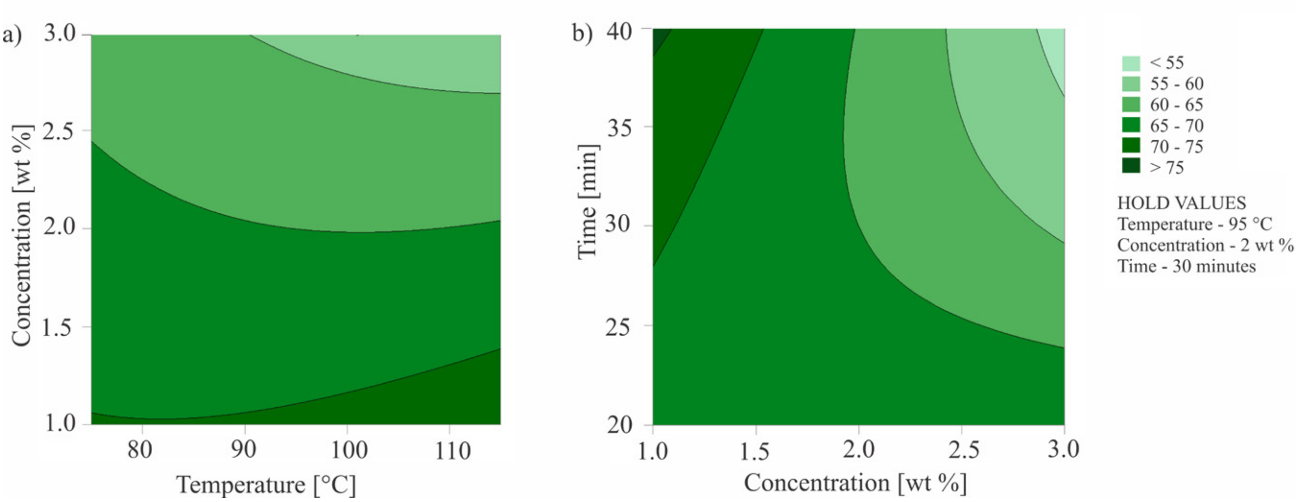

Figure 5. Contour diagrams to show the influence of a) concentration and temperature and b) time and concentration on the value of bleaching efficiency of bleached oil.

bleached oil (>70%) was achieved. On the contrary, at the same time interval and with the addition of larger amounts of adsorbent, a drastic decrease in the value of the degree of bleaching was observed.

Thus, the key influence of adsorbent concentration (factor B) and its interaction with contact time (BC). The highest efficiency (> 75%) was achieved at a low dose of 1 wt% adsorbent because at that concentration the ratio of active sites on the surface of the adsorbent and pigment distribution in the oil is the best, while the interaction of BC is most instructive at longer times (35–40 minutes), because at low doses of adsorbent additional time enhances the binding of pigments.[37] A similar trend is present in other works.[38,39]

3. 4. Influence of Process Parameters on Peroxide Value

Although some studies use the TOTOX index (peroxide value combined with anisidine value) to determine the content of primary and secondary oxidation products, in our research only the peroxide value was analyzed. Preliminary analysis found that the PV values were low for unrefined oil, and it was considered unnecessary to include the anisidine value. However, this approach has certain limitations because it is possible that certain secondary oxidation products were formed during refining that cannot be detected using the peroxide value.

Table 4 shows the coded coefficients of the regression equation and p-values for the members in the proposed quadratic model for peroxide value of bleached oils, while Figure 1d shows the corresponding Pareto diagram. Among the parameters, the concentration of the added adsorbent (B) has a very significant effect ($p < 0.0001$) on the peroxide value. A negative regression coefficient indicates that increasing the concentration decreases the value of the responses.

The following parameters have an influence on the peroxide value ($p < 0.05$): the square of the concentration (BB) and the square of the temperature (AA). The p-value of temperature (A) is slightly higher than the allowed value (0.0503), but since it is a linear variable, it will not be removed from the regression model. Other factors do not greatly affect the value of the responses and can be excluded from the regression model.

A shortened regression model for the peroxide value is given by the relation (8):

$$\mathit{Peroxide\ value} = 5.20 - 0.0632 \cdot A - 1.627 \cdot B + 0.000379 \cdot AA + 0.3012 \cdot BB \tag{8}$$

Although the previous shortened regression model does not have many terms, the same predictive accuracy is still maintained. At the same time, it enables a clearer interpretation, reduces the risk of over-adjustment, and facilitates practical application.

Figures 6a and 6b show that the amount of added adsorbent is the key variable that affects the value of the peroxide value, which confirms the results of the ANOVA analysis. The response value is the highest at a temperature of 110 °C, with the addition of 1 wt% adsorbent in the initial 30 minutes of adsorption (>1.5 meq/kg). Also, with the addition of the same amount of adsorbent, but at lower temperatures and longer adsorption time, the value of response decreases (1.25–1.5 meq/kg). By increasing the concentration, almost independently of temperature and time, the value of the peroxide value decreases.

By observing Figure 6a, it can be concluded that at concentrations of 2.5–3 wt% adsorbent and temperatures of 80–105 °C, resulted in the lowest value of the peroxide number (< 0.5 meq/kg), and that range of conditions is considered optimal. The reason for the pronounced decrease in peroxide value with increasing adsorbent concentration is that its abundant porous structure and surface functional

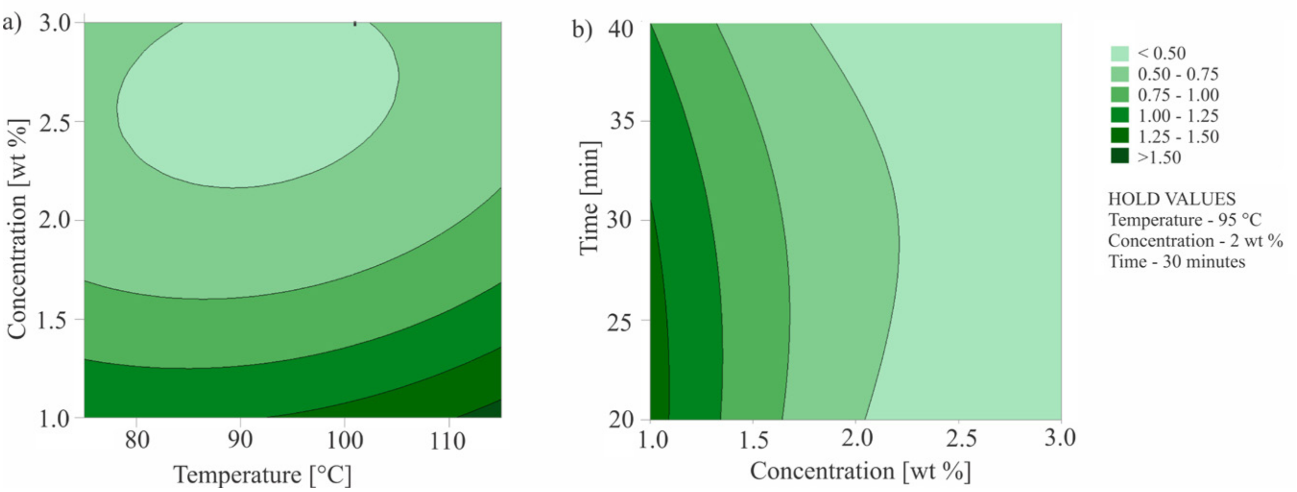

Figure 6. Contour diagrams to show the influence of a) concentration and temperature and b) time and concentration on the Peroxide value of bleached oil.

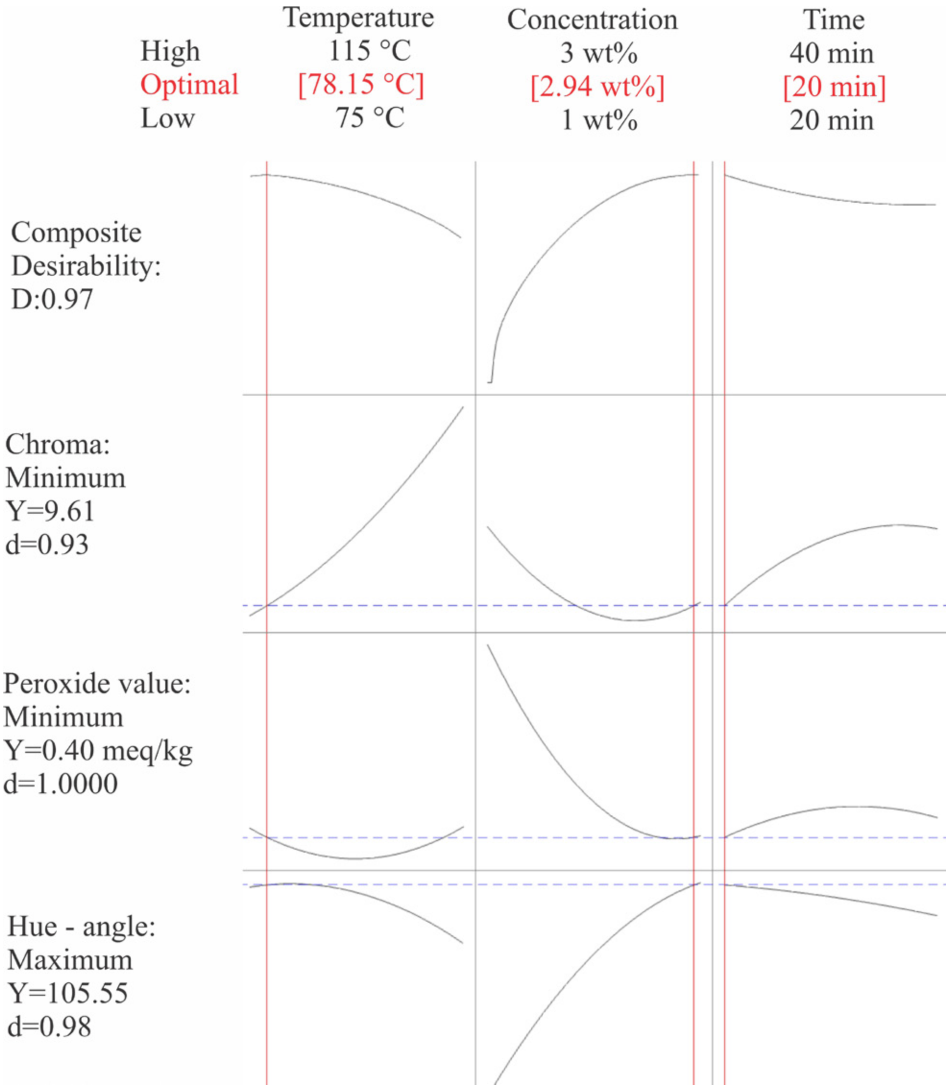

Figure 7. Optimization plot for three responses: chroma, peroxide value and hue-angle.

groups actively adsorb hydroperoxide species.[12] Also, these surface sites catalyze the decomposition of trapped hydroperoxides into non-oxidizing substances.[40] These effects are consistent with a similar study by Chew et al., where kenaf seed oil was bleached under different bleaching conditions.[5]

3. 5. Optimization

The input parameters (temperature, time and amount of added adsorbent) affect the output variables (chroma, hue angle, peroxide value and bleaching efficiency) differently. An optimal combination of input parameters must be found for each response. The goal of color quality optimization is to maximize the hue-angle to obtain lighter oils, and minimize the chroma value to reduce the intensity of the color.[34] Also, a minimum peroxide value is required, in order to obtain refined oil free from oxidative compounds while also maximizing bleaching efficiency.

Given the existence of four responses and the complex optimization, the responses were grouped into two categories.

In the first group, the process conditions were optimized for the following responses: chroma, hue angle and peroxide value. On one hand, there is chroma and hue angle serve asindicators of the color quality of refined oils, on the other hand, the peroxide value serves as an indicator of the presence of unwanted oxidative compounds. For this optimization, the goal is to minimize both chroma value and peroxide value, and to maximize the hue-angle value.

Figure 7 shows the optimization plot for the first group of responses. Since there is no specific target value, only a minimum or maximum values are considered for each response, leading to one optimal solution. The optimal process parameters are: temperature of 78.15 °C, adsorbent concentration of 2.94 wt% and time of 20 minutes, at which the value of chroma is minimized (9.61), the peroxide value is minimized (0.40 meq/kg), and the hue-angle is maximized (105.56). Composite desirability (0.97) is close to unity, indicating that the chosen settings achieve favorable results for all responses overall. Individual desirability indicates that the set settings most strongly affect the peroxide value (1.00), followed by the the hue-angle (0.98) and the least on the chroma (0.93).

In the second group, two responses were contrasted: peroxide value, as a measure of the chemical quality of the oil, and bleaching efficiency, as a value that shows the percentage of colored pigments removed. As in the first group, the goal is to minimize the value of the peroxide number, while on the other hand the value of bleaching efficiency is maximized.

Figure 8 shows the optimization plot for the second group of responses. The obtained results are similar to the first group; the minimum value of the peroxide value (0.41 meq/kg), i.e. the maximum value of the bleaching efficiency (71.87%) is achieved at a temperature of 77.83 °C, a concentration of the added adsorbent of 2.96 wt% and a time of 20 minutes.

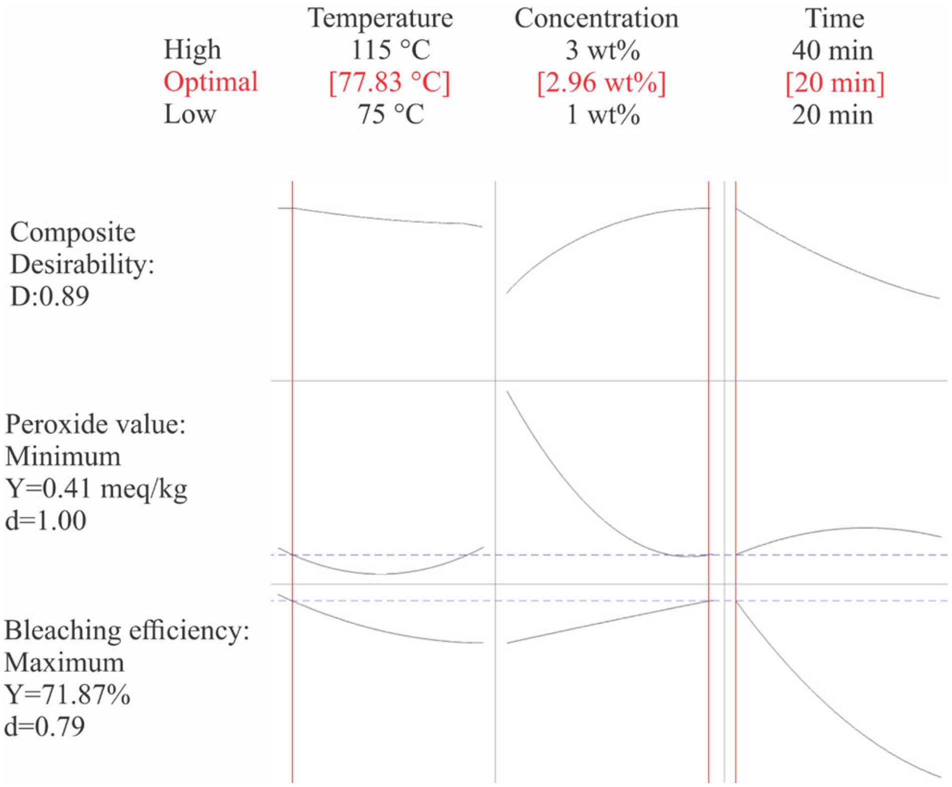

Figure 8. Optimization plot for two Responses: bleaching efficiency and peroxide value.

Composite desirability is slightly lower compared to the first optimization (0.89), which indicates that the settings achieve slightly weaker results when both responses are observed simultaneously. When the responses are considered separately, it is concluded that the settings have a far greater effect on the peroxide value (1.00) than on the bleaching efficiency (0.79).

Observing the optimal conditions for both groups of responses, it is clear that similar results are obtained: in both cases, the minimum time (20 min) is optimal for obtaining the best quality oil, the temperature ranges between 77.83–78.15 °C, and the concentration of the added adsorbent 2.94–2.96 wt%. When performing the optimization, either the first or the second group of responses can be examined because similar results are obtained. Nevertheless, the first group has a higher composite desirability (0.97) compared to the second (0.89), on the basis of which it was concluded that spectroradiometry, which was used to determine chroma and hue-angle, was far more reliable than spectrophotometry that was used to determine bleaching efficiency, because it covered the entire visible color spectrum, not just the 450 nm wavelength.

Minimum time (20 min) and lower temperatures (78 °C) have a favorable effect on the oxidative properties (peroxide value) and the color of the sample. By prolonging the adsorption time and increasing the temperature, the oxidative stability of edible oils decreases.[40] On the other hand, the unfavorable influence of increasing the time and increasing the temperature on the color of the oil is reflected in the destruction of the active sites on the adsorbent.[41] Moderate temperatures were required to obtain an optimum color for the bleached oil. This can be explained by the fact that working in this range of temperature, the following phenomena may occur: (I) a better activation, in terms of pigments removal, of the acid-activated earth employed, (II) a reduction in the oxidation of colorless components which cause alteration in the oil color, and (III) a less pronounced fixing of the existing color pigments.[42] In some studies, it was found that high temperatures (100–110 °C) have a favorable effect on the removal of colored pigment because the viscosity decreases with temperature, and therefore the dispersion of particles and the interaction of the oil with the adsorbent is better.[12] However, this is not the case in this paper. A possible reason for this is that the adsorbent particles were small enough (d50 = 45 μm), thus viscosity is not a limiting factor.

The addition of high concentrations of bleaching earth resulted in the removal of undesirable compounds in the oil. The catalytic properties of acid-activated bleaching earth lead to the decomposition of hydroperoxides into secondary oxidation products, which decrease the peroxide value with increasing concentration.[43] High adsorbent concentrations also have a favorable effect on color reduction, because there are more active sites where the adsorption of colored pigments takes place.[5]

4. Conclusion

The Box–Behnken factorial design proved to be an effective tool for optimizing temperature, adsorbent concentration, and time in the sunflower oil bleaching process. Significant p-values (<0.05), along with high R^2 (>0.95) and Adjusted R^2 confirmed that the model provides a strong fit to the experimental data. The composite desirability for the group containing chroma and hue-angle (determined by spectroradiometry) along with peroxide value is 0.97, compared to 0.89 for the group containing bleaching efficiency (determined by spectrophotometry) and peroxide value. This indicates that full-spectrum coverage by spectroradiometry provides a more reliable assessment of oil quality. The optimal conditions identified in the study can be to bleach bleaching sunflower oil in industrial conditions with minimal resource use. Future studies should explore the use of other adsorbents, such as bio-based or modified adsorbents, in oil bleaching. Additionally,the adsorbent used in this study could be applied to bleach other vegetable oils, such as soybean or palm oil.

5. References

1. Consumer Goods & FMCG, Consumption of vegetable oils worldwide from 2013/14 to 2024/2025, by oil type, https://www.statista.com/statistics/263937/vegetable-oils-global-consumption, (assessed: July 3, 2025)
2. M. Hatami, M. Sabour, A. Amiri, *Global J. Environ. Sci. Manage.* **2018**, *4*, pp. 9–18.
3. L. M. Serrano-Bermudez, C. A. Monroy-Pena, D. Moreno, A. Abril, A. D. Imbachi Nino, C. A. Martinez Riascos, G. B. Hurtado, P. C. Narvaez Rincon, *Food Bioprod. Process.* **2021**, *129*, pp. 75–83. **DOI:**10.1016/j.fbp.2021.07.005
4. I. Mukasa-Tebandeke, P. Ssebuwufu, S. Nyanzi, A. Schumann, G. Nyakairu, F. Lugolobi, *Am. J. Anal. Chem.* **2014**, *5*, pp. 1302–1312. **DOI:**10.4236/ajac.2014.517136
5. S. Chew, C. Tan, K. Nyam, *J. Food Sci.* **2017**, *82*(7), pp. 1622–1630. **DOI:**10.1111/1750-3841.13758
6. I. Kim, E. Choe, *J. Food Sci.* **2006**, *70*, pp. C48–C52. **DOI:**10.1111/j.1365-2621.2005.tb09019.x
7. Y. Liu, R. Mo, D. Zhong, D. Shen, Z. Ni, F. Tang, *J. Food Sci.* **2015**, *80*(8), pp. 1926–1932. **DOI:**10.1111/1750-3841.12951
8. J. Huang, S. Sathivel, *J. Food Eng.* **2010**, *96*, pp. 51–58. **DOI:**10.1016/j.jfoodeng.2009.06.042
9. M. M. Strieder, C. P. Pinheiro, V. S. Borba, R. S. Pohndorf, T. R. Cavalaj Jr, L. A. Pinto, *Sep. Purif. Technol.* **2017**, *175*, pp. 72–78. **DOI:**10.1016/j.seppur.2016.11.026
10. S. Sathivel, W. Prinyawiwatkul, *J. Am. Oil Chem. Soc.* **2004**, *81*(4), pp. 493–496. **DOI:**10.1007/s11746-004-0929-0
11. J. Okolo, B. Adejumo, *J. Eng. (IOSRJEN)* **2014**, *4*(12), pp. 25–28. **DOI:**10.9790/3021-041203025028
12. J. Nwabanne, F. Ekwu, *Int. J. Appl. Sci.* **2013**, *3*(4), pp. 69–77.
13. T. M. Soylu, C. Özel, B. K. Ikizler, A. C. Özarslan, P. Terzioğlu, Y. B. Elalmis, S. Yücel, *J. Sol-gel Sci. Techn.* **2024**, *115*, pp.

327–348. **DOI:**10.1007/s10971-024-06395-9

14. Y. Wang, C. Yang, X. Wang, S. Zhang, S. Wang, D. Wu, K. Rakariyatham, J. Hu, Q. Zhao, *Food Chem.* **2024**, *443*, pp. 138561. **DOI:**10.1016/j.foodchem.2024.138561
15. F. Hussin, M. Kheireddine Aroua, W. Wan Daud, *Chem. Eng. J.* **2011**, *170*, pp. 90–106. **DOI:**10.1016/j.cej.2011.03.065
16. S. Silva, K. Sampaio, R. Ceriani, R. Verhe, C. Stevens, W. De Greyt, A. Meirelles, *LWT-Food Sci. Technol.* **2014**, *59*(2), pp. 1258–1264. **DOI:**10.1016/j.lwt.2014.05.028
17. T. Hu, Y. Guo, Q. Zhou, X. Zhong, L. Zhu, J. Piao, J. Chen, J. Jiang, *J. Food Sci.* **2012,** *77*(9), pp. 975–982.
18. A. Merikhy, A. Heydari, H. Eskandari, F. Ghahraman-Rozegar, *Chem. Eng. Process.* **2020**, *158*, p. 108167. **DOI:**10.1016/j.cep.2020.108167
19. S. Huang, Y. Hu, W. Jin, D. Huang, *LWT* **2023**, *185*, pp. 115139. **DOI:**10.1016/j.lwt.2023.115139
20. Ş. S. Seçilmiş, D. K. Yanik, S. Fadiloğlu, F. Göğüş, *Food Chem.* **2021**, *365*, pp. 130488. **DOI:**10.1016/j.foodchem.2021.130488
21. M. Mousavifard, E. Abedi, K. Alirezalu, *LWT* **2024**, *198*, pp. 115983. **DOI:**10.1016/j.lwt.2024.115983
22. L. Ifa, T. Syarif, S. Sartia, J. Juliani, N. Nurdjannah, H. S. Kusuma, *Helyon* **2022**, *8*, pp. e09146. **DOI:**10.1016/j.heliyon.2022.e09146
23. M. Y. Nassar, E. A. Abdelrahman, A. A. Aly, T. Y. Mohamed, *J. Mol. Liq.* **2017**, *248*, pp. 302–313. **DOI:**10.1016/j.molliq.2017.10.061
24. Ş. S. Seçilmiş, *Food Biosci.* **2024**, *60*, pp. 104430. **DOI:**10.1016/j.fbio.2024.104430
25. H. Bayram, G. Ustunisik, M. Önal, Y. Sarikaya, *Clay Miner.* **2021**, *56*(2), pp. 1–22. **DOI:**10.1180/clm.2021.28
26. E. S. Almeida, A. C. B. Carvalho, I. O. Soares, L. F. Valadares, A. R. Mendonca, I. J. Silva Jr, *Food Res. Int.* **2019**, *121*, pp. 785–797. **DOI:**10.1016/j.foodres.2018.12.061
27. International Organization for Standardization, Animal and vegetable fats and oils – Determination of peroxide value – Iodometric (visual) endpoint determination, **2017**.
28. M. Melgosa, L. Gómez-Robledo, R. Huertas, L. Capitán-Vallvey, M. Moyano, F. Heredia, *J. Am. Oil Chem. Soc.* **2009**, *86*(7), pp. 627–636. **DOI:**10.1007/s11746-009-1387-2
29. L. Sedaghat Boroujeni, M. Ghavami, Z. Piravi Vanak and A. Ghasemi Pirbalouti, *J. Food Sci. Technol.* **2020**, *40*, pp. 322–330. **DOI:**10.1590/fst.10919
30. M. S. Huda, P. Wilson, N. C. Sarker, E. Monono, *LWT* **2024**, *212*, pp. 116991. **DOI:**10.1016/j.lwt.2024.116991
31. S. Narukulla, S. Bogadi, V. Tallapaneni, B. K. Sanapalli, S. Sanju, A. Khan, A. Malik, H. Barai, T. K. Mondal, V. V. Karri, A. Alexiou, S. K. Pindiprolu, G. Kuppusamy, V. Subramaniyan, M. R. Islam, M. Papadakis, *Microchem. J.* **2024**, *207*, pp. 111875. **DOI:**10.1016/j.microc.2024.111875
32. W. Indrasena, C. Barrow, in C. Alasalvar, F. Shahidi, K. Miyashita, U. Wanasundara (Ed.): Handbook of Seafood Quality, Safety and Health Applications, West Sussex, John Wiley & Sons Ltd, **2010**, pp. 317–322.
33. X. Ying, *J. Phys. Conf. Ser.* **2019**, *1168*(2), p. 022022. **DOI:**10.1088/1742-6596/1168/2/022022
34. P. García-Moreno, A. Guadix, L. Gómez-Robledo, M. Melgosa and E. Guadix, *J. Food Eng.* **2013**, *116*(2), pp. 606–612. **DOI:**10.1016/j.jfoodeng.2012.12.040
35. F. Marrakchi, K. Kriaa, B. Hadrich, N. Kechaou, *Food. Bioprod. Process.* **2015**, *94*, pp. 124–135. **DOI:**10.1016/j.fbp.2015.02.002
36. D. Briggs, The dimensions of color: Hue circles based on additive complementaries, http://www.huevaluechroma.com/074.php, (assessed: March 10, 2023)
37. M. Saneei, S. A. Goli, J. Keramat, *Clay Miner.* **2015**, *50*, pp. 639–648. **DOI:**10.1180/claymin.2015.050.5.07
38. S. H. Siregar, W. Irma, F. Perdana, A. Jusnita, O. Syahbella, *ICCELST-ST* **2019**, *190*, pp. 86–91.
39. W. A. Raji, R. U. Azike, F. W. Ngubi, *OJOp* **2019**, *8*, pp. 38–46.
40. D. Škevin, T. Domijan, K. Kraljić, J. Gajdoš Kljusurić, S. Neđeral, M. Obranović, *Food Technol. Biotechnol.* **2012**, *50*(2), pp. 199–207.
41. O. James, M. Mesubi, F. Adekola, E. Odebumni, J. Adekeye, R. Bale, *Lat. Am. Appl. Res.* **2008**, *38*, pp. 45–49.
42. V. Crexi, M. Monte, L. Soares, L. Pinto, *Food Chem.* **2010**, *119*(3), pp. 945–950. **DOI:**10.1016/j.foodchem.2009.07.050
43. S. Chew, C. Tan, K. Long, K. Nyam, *Ind. Crops Prod.* **2016**, *89*, pp. 59–65. **DOI:**10.1016/j.indcrop.2016.05.002

Povzetek

Beljenje je ključni korak v rafiniranju olja, ki odstranjuje nezaželene pigmente in oksidacijske produkte, ki poslabšajo kakovost olja. Ta študija je ocenila učinke temperature (75–115 °C), koncentracije adsorbenta (1–3 wt%) in časa (20–40 minut) na beljenje sončničnega olja z uporabo Box-Behnken faktorske analize v Minitab 21. Odgovori so bili razdeljeni v dve skupini: (I) vrednost peroksida in spektrometrična metoda ter barvni kot, in (II) vrednost peroksida in spektrofotometrično merjena učinkovitost beljenja. Pod optimalnimi pogoji (približno 78 °C, 2,95 wt% adsorbenta in 20 minut), se je vrednost peroksida zmanjšala z 1,8 meq/kg na 0,398 meq/kg, kromatska vrednost se je zmanjšala s 45,89 na 9,61, kot obarvanosti se je povečal s 92,69 na 105,55, učinkovitost beljenja pa je dosegla 71,86%. »Composite desirability« je bila višja v prvi skupini (0.97 proti 0.89), predvsem zaradi bolj objektivne narave spektrometričnih parametrov.

DOI: 10.17344/acsi.2025.9352 Acta Chim. Slov. 2025, 72, 491–502

Scientific paper

Copper(I/II) and Palladium(II) Complexes Containing Carbothioamide and Triphenylphosphine Ligands: Synthesis, Characterization, and Theoretical Studies

Karwan Omer Ali[1,2*], Nabil Adil Fakhre[1,3], Salim Najm Aldain Saber[1]

[1] *Department of Chemistry, College of Education, Salahaddin University-Erbil, Erbil 44001, Iraq*

[2] *Department of General Science, College of Basic Education, University of Halabja, Halabja 46018, Iraq.*

[3] *Tishk International University, Erbil 44001, Iraq*

** Corresponding author: E-mail: karwan.ali@uoh.edu.iq*
Phone No. 009647503849284

Received: 06-02-2025

Abstract

A carbothioamide ligand, 4,5-dihydro-5-(4-methoxyphenyl)-3-phenylpyrazole-1-carbothioamide, [$C_{17}H_{17}N_3OS$], has been synthesized from the condensation of 4-methoxychalcone with thiosemicarbazide. The carbothioamide (L) ligand and triphenylphosphine (Ph_3P) as co-ligand, was coordinated with Cu(I), Cu(II), and Pd(II) metal ions to synthesis the corresponding complexes: [$CuCl_2$(L)] **1**, [CuCl(L)(Ph_3P)] **2**, [$PdCl_2$(L)] **3**, and [PdCl(L)(Ph_3P)]Cl **4**. The ligand and all complexes were collected in solid form after the reactions and characterized by magnetic susceptibility, elemental analysis, molar conductivity, FT-IR, UV-Vis, and ^{1}H, ^{13}C, ^{31}P-NMR techniques. The molar conductance values in DMSO (5.8–16.3 Ω^{-1} cm^2 mol^{-1}) confirmed all the complexes to be non-electrolytic except for the Pd(II) complex **4** (32.6 Ω^{-1}cm^2 mol^{-1}) that behaves as a 1:1 electrolyte. According to spectroscopic evidence, the carbothioamide ligand behaves as an N, S donor and chelating agent. Magnetic susceptibility measurements combined with electronic spectral data suggest that the Cu(II) and Pd(II) complexes have square planar geometry, whereas the Cu(I) complex **2** has a tetrahedral geometry. Elemental analysis and ^{1}H-NMR spectroscopy confirmed the mononuclear structure of all complexes. DFT calculations showed that the synthesized complexes **1**, **3**, and **4** exhibit higher thermodynamic stability than the free ligand (L), with ΔE values of 1.4695, 2.1116 eV, 1.9076 eV, and 1.2980 eV, respectively. In contrast, complex **2** has ΔE = 0.5385 eV, indicating lower thermodynamic stability. Among the complexes, complex **2** (S = 3.7140 eV) exhibited the highest softness, and all complexes were observed to be softer than the triphenylphosphine ligand. According to the results, electron transitions are easier in certain complexes than in their ligands, which suggests that the prepared complexes could be used in the photocell in future studies.

Keywords: Carbothioamide, Cu(I/II) complexes, Pd(II) complexes, NBO analysis, DFT calculations, MEP surfaces

1. Introduction

Thioamides, such as thiosemicarbazone and carbothioamide, are an important class of compounds that have attracted considerable attention due to their remarkable pharmacological and biological properties.[1] The complexes of carbothioamide with transition metals have received significant attention because of their biological behaviors, including antitumor, antibacterial, antifungal, and anticarcinogenic activities.[2,3] In particular, when chalcone derivatives are combined with thiosemicarbazide, novel carbothioamides are often synthesized with better pharmacological activities.[4] In addition, carbothioamide ligands possess multiple donor atoms, enabling them to coordinate with metal ions through either N or S atoms.[5] Typically, these ligands act as chelating ligands for transition metal ions, ligated via sulfur (=S) and pyrazoline nitrogen (=N–). However, in certain cases, they exhibit monodentate behavior, binding entirely through the sulfur (=S) atom.[6,7] A previous study reported that the carbothioamide ligand coordinates with the Cu(II) center via its nitrogen and sulfur donor atoms, forming a five-membered chelated ring in the resulting copper complex.[8] In this study, Cu(I/II) and Pd(II) were selected as metal centers.

Copper(I/II) complexes exhibit a wide range of biological activity, including antiviral, antitumor, and anti-inflammatory properties.[9] Furthermore, Pd complexes, particularly with sulfur and nitrogen donor ligands, have demonstrated significant *in vitro* cytotoxicity against different cancer cell lines.[10] The addition of triphenylphosphine, an organophosphorus substance, as a co-ligand also plays a critical role in coordination chemistry.[11] Because it has strong sigma-donor and pi-acceptor abilities, it can form stable complexes with a variety of metal ions.[12] In palladium chemistry, mixed ligand complexes containing Ph_3P are commonly used as homogeneous catalysts in necessary organic transformations, such as Suzuki-Miyaura and Sonogashira coupling reactions, which play a crucial role in pharmaceutical and material science.[13] Similarly, mixed ligand copper complexes based on triphenylphosphine have demonstrated promising catalytic activity in azide-alkyne cycloadditions as well as in oxidation reactions.[14] There are a few studies that reported metal complexes that combine both carbothioamide and triphenylphosphine ligands; however, researchers have thoroughly studied carbothioamide metal complexes separately. An X-ray structure of a distorted tetrahedral copper(I) complex containing both 4-benzoylpyridinethiosemicarbazone and triphenylphosphine ligands has been reported.[15] Additionally, a square planar palladium complex containing a thioamide ligand was synthesized, and its cytotoxic activity was evaluated against colorectal (HT-29), human colon (Caco-2), and human cervical (HeLa) cancer cell lines using the MTT assay.[16] The current study describes the synthesis, characterization, and geometrical structure of new Cu(I) and Pd(II) complexes containing 4,5-dihydro-5-(4-methoxyphenyl)-3-phenylpyrazole-1-carbothioamide (L) and triphenylphosphine as co-ligands. These complexes were characterized by magnetic susceptibility, elemental analysis, molar conductivity, FT-IR, ^{31}P, ^{1}H, ^{13}C-NMR, and UV-Vis techniques. In addition, theoretical studies, including FMO (Frontier Molecular Orbital), NBO (Natural Bond Orbital), and MEP (Molecular Electrostatic Potential), were conducted on the synthesized complexes.

2. Experimental

2. 1. Materials, General Methods, and Instrumentation

$PdCl_2$ (59% Pd) was purchased from Sigma Aldrich and $CuCl_2·2H_2O$ (99%) was purchased from BDH. Triphenylphosphine was purchased from Carl Roth. Methanol (99%), dimethyl sulfoxide (99%), and dimethylformamide (99.5%) were supplied by Chem-Lab Company and used directly without further purification. A Shimadzu FT-IR Affinity-1 spectrophotometer was used to record FT-IR spectra within the range 400-4000 cm^{-1} using KBr discs. The far–infrared spectra were obtained using a Shimadzu Affinity-ICE FTIR 800 cm^{-1} spectrophotometer using CsI discs in the 200-600 cm^{-1} frequency range. UV-Vis spectra were measured utilizing a Jenway 7205 UV-Visible spectrophotometer with DMSO as the solvent. ^{1}H, ^{13}C, and ^{31}P-NMR spectra were recorded on a Bruker 400 MHz Ultra-shield in DMSO-d_6 solvent at the University of Isfahan, Iran. In order to determine the carbon, hydrogen, and nitrogen content of the synthesized ligand and its complexes, ECS 4010 at the University of Isfahan, Iran was utilized. The conductivity measurement was taken in a 1×10^{-3} mol dm^{-3} solution at 25 °C by using the Jenway 4200 conductivity/TDS meter. Magnetic susceptibility measurements were performed with the auto magnetic susceptibility Sherwood Scientific device. In order to determine the melting point, a melting device, model DMP-800, manufactured by A&E Lab UK CO., LTD, was used.

2. 2. Synthesis Procedures

2. 2. 1. Synthesis of 4,5-dihydro-5-(4-methoxyphenyl)-3-phenylpyrazole-1-carbothioamide (L) ligand

A mixture of thiosemicarbazide (0.006 mmol, 0.5468 g) and 4-methoxychalcone (0.006 mmol, 1.4296 g) was refluxed in 50 mL of methanol at 70 °C. Upon complete dissolution of the reactants, 10 mL of NaOH (1.2 mol/L) was added dropwise. The reaction mixture was further refluxed for 3 hours. Subsequently, the mixture was cooled in an ice bath, and the resulting precipitate was filtered, washed with cold ethanol/water (50:50%), and recrystallized in a mixture of chloroform-ethanol (4:1).

The synthesis route of Ligand (L) is displayed in Scheme 1.

Color: Light yellow powder, Melting point: 145-147 °C, Yield: 1.3304 g (71.21%); Elemental analysis for [$C_{17}H_{17}N_3OS$]: M.W. 311.40 g mol^{-1}; Calculated (%): C, 65.57; H, 5.50; N, 13.49. Found (%): C, 65.36; H, 5.19; N, 13.29; FT-IR spectral peak (ν/cm^{-1}): 3406, 3255 (NH_2), 3147–3062 (ArC-H), 2960, 2837 (C-H of CH_3), 1654 (C=N), 1597-1481 (ArC=C), 1255 (C-O), 835 (C=S); ^{1}H NMR (DMSO-d_6) δ/ppm: 8.08 (s, 2H, NH_2), 7.89 (d. 2H, $H_{9,13}$), 7.47 (t, 1H, H_{11}), 7.44 (t, 2H, $H_{10,12}$), 7.07 (d, 2H, $H_{4,6}$), 6.86 (d, 2H, $H_{1,3}$), 5.88 (dd, 1H, H_c), 3.90 (dd, 1H, H_b), 3.70 (s, 3H, OCH_3), 3.14 (dd, 1H, Ha). ^{13}C NMR (DMSO) δ/ppm: 176.07 (C=S), 158.18 (C-2), 154.95 (C-18), 135.02 (C-8), 130.93 (C-5), 130.53 (C-11), 128.68 (C-10,12), 127.08 (C-9,13), 126.64 (C-4,6), 113.80 (C-1,3), 62.35 (C-7), 55.02 (C-22), 42.39 (C-17). UV-Vis. (λ_{max}/nm): 288, 358.

2. 2. 2. Synthesis of [$CuCl_2(L)$] 1

A solution of ligand (L) (2.40 mmol, 0.7473 g) in 20 mL of ethanol was added dropwise to a stirred solution of $CuCl_2·2H_2O$ (2.40 mmol, 0.4091 g) in 20 mL of ethanol. The reaction mixture was then stirred at 50 °C for 3

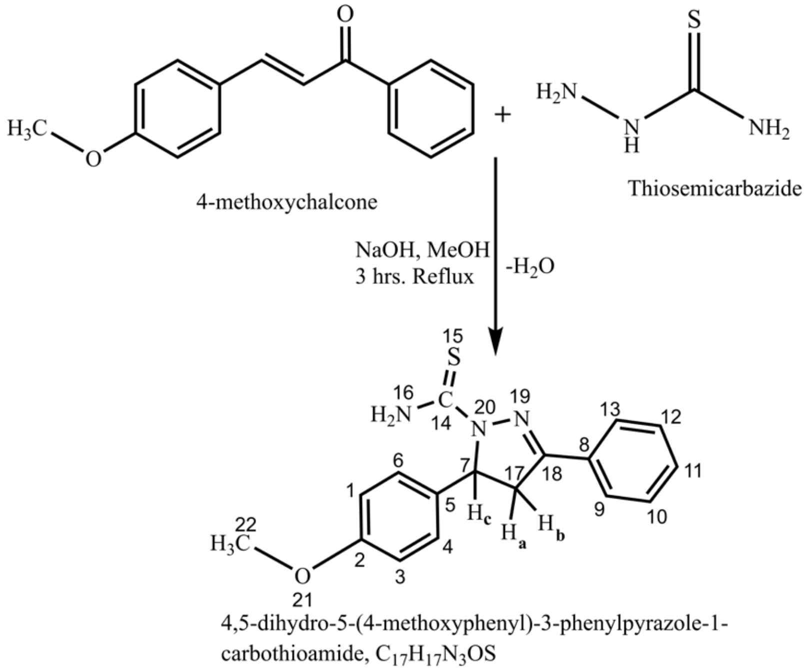

Scheme 1. Synthetic route of carbothioamide ligand.

hours, resulting in the formation of a brown precipitate. The precipitate was filtered, washed with ethanol/diethyl ether mixture, and dried in air. Color: brown powder, Melting point: 160-161.5 °C, Yield: 0.7811 g (73%); Elemental analysis for [$C_{17}H_{17}Cl_2CuN_3OS$]: M.W. 445.85 g mol^{-1}; Calculated (%): C, 45.80; H, 3.84; N, 9.42. Found (%): C, 46.22; H, 3.50; N, 9.17; IR spectral peak (ν/cm^{-1}): 3446, 3244 (NH_2), 3147-3062 (ArC-H), 2956, 2835 (CH_3), 1608 (C=N), 1585–1444 (ArC=C), 1249 (C-O), 829 (C=S), 578 (Cu-N), 487 (Cu-S), 322 (Cu-Cl); ^{1}H NMR (DMSO-d$_6$) δ/ppm: 9.11 (s, 2H, NH_2), 8.13 (d. 2H, $H_{9,13}$), 7.78 (t, 1H, H_{11}), 7.45 (t, 2H, $H_{10,12}$), 6.80 (d, 2H, $H_{4,6}$), 6.65 (d, 2H, $H_{1,3}$), 5.74 (dd, 1H, H_c), 3.95 (dd, 1H, H_b), 3.70 (s, 3H, OCH_3), 2.87 (dd, 1H, H_a); Molar conductance (Λ_m/ Ω^{-1}cm^2 mol^{-1}): 5.8; Magnetic moment (μ_{eff} / B.M.): 1.83; UV-Vis. (λ_{max} /nm): 292, 317, 363, 579.

2. 2. 3. Synthesis of [CuCl(L)(Ph_3P)] 2

To a solution of $CuCl_2{\cdot}2H_2O$ (1.440 mmol, 0.2455 g) in 10 ml of ethanol, a solution of ligand (L) (1.440 mmol, 0.4484 g) in 10 ml ethanol was added, followed by stirring for one hour at room temperature. To the brown precipitates formed, solid Ph_3P (0.3778 g, 1.440 mmol) was added and the contents were stirred for an additional 4 hours, the precipitate color was changed to white. The precipitate formed was isolated by filtration, washed with methanol, and dried in air. Color: white powder, Melting point: 197–199 °C, Yield: 0.4785 g (69%); Elemental analysis for [$C_{35}H_{32}ClCuN_3OPS$]: M.W. 672.69 g mol^{-1}; Calculated (%): C, 62.49; H, 4.80; N, 6.25. Found (%): C, 63.13; H, 4.45; N, 5.81; IR spectral peak (ν/cm^{-1}): 3441, 3244 (NH_2), 3142-3055 (ArC-H), 2953, 2833 (CH_3), 1602 (C=N), 1587, 1489 (ArC=C), 1435 (P-Ph), 1249 (C-O), 1097 (P-C), 831 (C=S), 565 (Cu-N), 476 (Cu-S), 384 (Cu-P), 338 (Cu-Cl); ^{1}H NMR (DMSO-d$_6$) δ/ppm: 8.91 (s, 2H, NH_2), 8.39 (d. 2H, $H_{9,13}$), 7.91 (t, 1H, H_{11}), 7.66 (t, 2H, $H_{10,12}$), 7.54-7.28 (m, 15H, Ph_3P), 7.08 (d, 2H, $H_{4,6}$), 6.89 (d, 2H, $H_{1,3}$), 5.55 (dd, 1H, H_c), 3.82 (dd, 1H, H_b), 3.72 (s, 3H, OCH_3), 2.77 (dd, 1H, H_a); ^{31}P-NMR (DMSO-d$_6$) δ/ppm: δ = –1.18; Molar conductance (Λ_m/ Ω^{-1}cm^2 mol^{-1}): 8.6; Magnetic moment (μ_{eff} / B.M.): < 1.0; UV-Vis. (λ_{max}/nm): 301, 369.

2. 2. 4. Synthesis of [$PdCl_2$(L)] 3

$PdCl_2$ (1.1280 mmol, 0.200 g) was added to a stirred solution of ligand (L) (1.1280 mmol, 0.3513 g) in 20 mL of ethanol and stirred for 6 hours at 60 °C, during stirring a red-brown precipitate was formed. After completing the reaction, the product was filtered, washed with ethanol/diethyl ether mixture, and dried in air. Color: red-brown powder, Melting point: 183–185 °C, Yield: 0.3647 g (66%); Elemental analysis for [$C_{17}H_{17}Cl_2N_3OPdS$]: M.W. 488.72 g mol^{-1}; Calculated (%): C, 41.78; H, 3.51; N, 8.60. Found (%): C, 42.09; H, 3.29; N, 8.47; IR spectral peak (ν/cm^{-1}): 3414, 3250 (NH_2), 3145-3061 (ArC–H), 2956, 2833 (CH_3), 1608 (C=N), 1587-1446 (ArC=C), 1247 (C-O), 829 (C=S), 480 (Pd-N), 320 (Pd-S), 296 (Pd-Cl); ^{1}H NMR (DMSO-d$_6$) δ/ppm: 9.03 (s, 2H, NH_2), 8.08 (d. 2H, $H_{9,13}$), 7.74 (t, 1H, H_{11}), 7.46 (t, 2H, $H_{10,12}$), 7.03 (d, 2H, $H_{4,6}$), 6.89 (d, 2H, $H_{1,3}$), 5.89 (dd, 1H, H_c), 4.00 (dd, 1H, H_b), 3.73 (s, 3H, OCH_3), 3.33 (dd, 1H, H_a). Molar conductance (Λ_m/ Ω^{-1}cm^2 mol^{-1}): 16.3; Magnetic moment (μ_{eff} / B.M.): < 1.0; UV-Vis. (λ_{max}/nm): 299, 346, 390, 476.

2. 2. 5. Synthesis of [PdCl(L)(Ph_3P)]Cl 4

$PdCl_2$ (1.410 mmol, 0.2500 g) was added to a solution of Ph_3P (1.410 mmol, 0.3698 g) in ethanol (15 mL) and stirred for 2 hours at 60 °C. Subsequently, a solution of ligand (L) (1.410 mmol, 0.4390 g) in ethanol (10 mL) was added to the reaction mixture, and stirring was continued for an additional 8 hours. The resulting orange-yellow precipitate was collected by filtration, washed with methanol, and dried in air. Color: Orange-Yellow powder, Melting point: 216–218 °C, Yield: 0.8577 g (81%); Elemental analysis for [$C_{35}H_{32}Cl_2N_3OPPdS$]: M.W. 751.01 g mol^{-1}; Calculated (%): C, 55.98; H, 4.29; N, 5.60. Found (%): C, 56.40; H, 4.09; N, 5.11; IR spectral peak (ν/cm^{-1}): 3392, 3253 (NH_2), 3155-3055 (ArC-H), 2954, 2833 (CH_3), 1606 (C=N), 1583-1492 (ArC=C), 1435 (P-Ph), 1247 (C-O), 1095 (P-C), 827 (C=S), 457 (Pd-N), 364 (Pd-P), 321 (Pd-S), 297 (Pd-Cl); ^{1}H NMR (DMSO-d_6) δ/ppm: 8.84 (s, 2H, NH_2), 8.34 (d. 2H, $H_{9,13}$), 7.94 (t, 1H, H_{11}), 7.72 (t, 2H, $H_{10,12}$), 7.66-7.37 (m, 15H, Ph_3P), 7.27 (d, 2H, $H_{4,6}$), 7.06 (d, 2H, $H_{1,3}$), 5.84 (dd, 1H, H_c), 3.90 (dd, 1H, H_b), 3.69 (s, 3H, OCH_3), 3.32 (dd, 1H, H_a); ^{31}P-NMR (DMSO-d_6) δ/ppm: δ = 25.58; Molar conductance ($\Lambda_m/\Omega^{-1}\ cm^2\ mol^{-1}$): 32.6; Magnetic moment (μ_{eff} /B.M.): < 1.0; UV-Vis. (λ_{max}/nm): 294, 310, 360, 418.

2. 3. DFT Calculation

Density functional theory (DFT) calculations were carried out using the Gaussian 09 software package to gain better insights into the structural characteristics of the copper and palladium complexes. The Gauss View 6.0 software, with the B3LYP level of theory was utilized to analyze the frontier molecular orbitals of the 4,5-dihydro-5-(4-methoxyphenyl)-3-phenylpyrazole-1-carbothioamide (L) ligand, Cu(I), Cu(II) and Pd(II) complexes. The 6-311G basis set was employed for non-metal elements such as C, H, N, O, S, P, and Cl, while the LANL2DZ basis set was utilized for copper and palladium metal centers.[17] The molecular electrostatic potential (MEP) and natural bond orbital (NBO) calculations of the ligands and their complexes were carried out using the same Gaussian software.[18]

3. Results and Discussions

Triphenylphosphine (Ph_3P) and 4,5-dihydro-5-(4-methoxyphenyl)-3-phenylpyrazole-1-carbothioamide (L) were employed as ligands for the coordination of copper and palladium ions as displayed in Scheme 2.

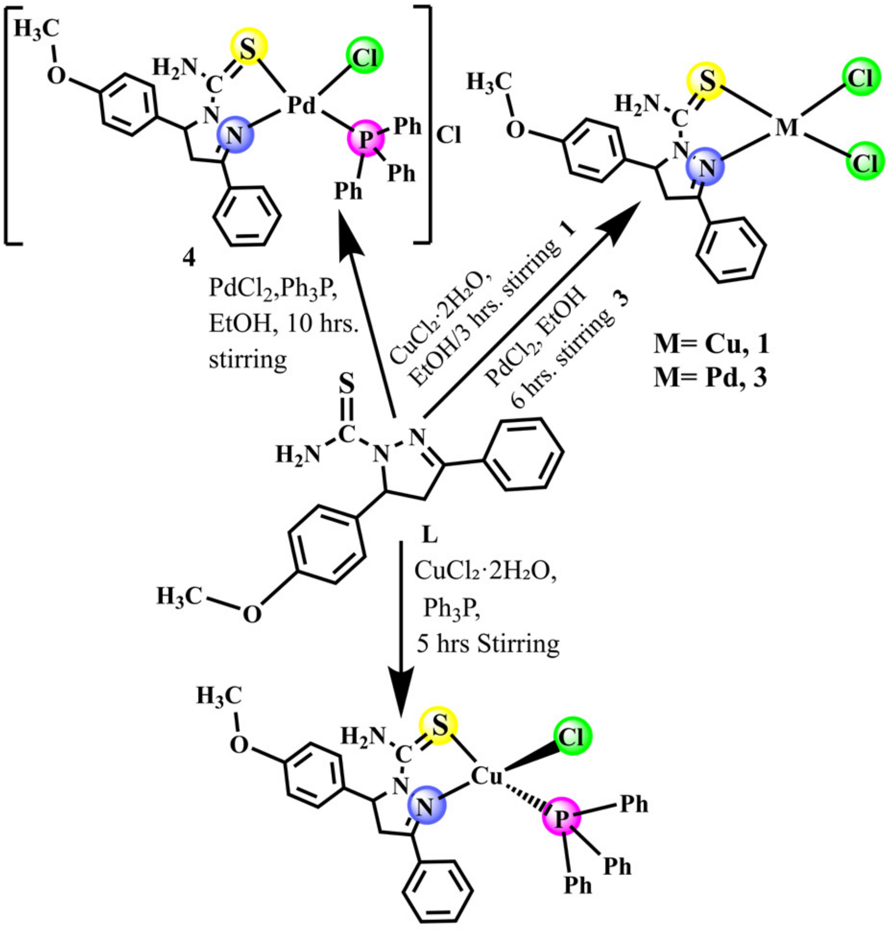

Scheme 2. Synthetic routes for complexes **1**, **2**, **3**, and **4**

One mole equivalent of $CuCl_2{\cdot}2H_2O$ reacts with one mole equivalent of carbothioamide (L) in ethanol to yield Cu(II) complex **1**, while the mixed ligand complex **2** results from the reaction of $CuCl_2{\cdot}2H_2O$ with equimolar amounts of Ph_3P and L ligands in ethanol. During the synthesis of complex **2**, the spontaneous reduction of Cu(II) to Cu(I) is caused by triphenylphosphine, which serves as a reducing agent. In addition, sterically demanding ligands containing sulfur also led to the reduction reaction, resulting in a color change from blue to white, indicative of the copper d^{10} electron configuration. Similarly, the reaction of anhydrous $PdCl_2$ salt with carbothioamide (L) under certain experimental conditions led to the synthesis of complex **3**, while the mixed ligand complex **4** was formed from the reaction of $PdCl_2$ with equimolar amounts of Ph_3P and L ligands in ethanol. The structural composition of the prepared complexes was confirmed by elemental analysis, magnetic susceptibility, molar conductivity, UV-Vis, FT-IR, and ^1H, ^{13}C, ^{31}P-NMR spectroscopy. In addition, the complexes were soluble in some organic solvents, such as dimethyl sulfoxide and dimethylformamide, at ambient temperatures; however, they were insoluble in ethanol, chloroform, acetone, diethyl ether, methanol, and water.

3. 1. IR Spectral Studies

The metal complexes were identified by studying their infrared spectra and comparing them with the FT–IR spectra of the free ligands used in their synthesis. The IR spectrum of free 4,5-dihydro-5-(4-methoxyphenyl)-3-phenylpyrazole-1-carbothioamide (L) (Figure S1) exhibits medium bands of the NH_2 group at 3406 and 3255 cm^{-1}, whereas the complex spectra of **1**, **2**, **3**, and **4** show medium bands of the -NH_2 group at (3446, 3244 cm^{-1}), (3441, 3244 cm^{-1}), (3414, 3250 cm^{-1}), and (3392, 3253 cm^{-1}), respectively.[19] In the solid state, NH_2 peaks are observed in complexes spectra, suggesting that the ligand remains in its thione tautomeric form.[20] The free ligand has a characteristic ν(C=N) band at 1654 cm^{-1}, but upon complexation, it was shifted to 1608, 1602, 1608, and 1606 cm^{-1} in **1**, **2**, **3**, and **4**, respectively, indicating the participation of pyrazoline nitrogen (C=N) in coordination with the corresponding metal ions. This is also supported by the appearance of new bands in the range of 578–565 cm^{-1} and 480–457 cm^{-1}, which have been assigned to ν(Cu-N) and ν(Pd-N), respectively.[21,22] The band observed at 835 cm^{-1} is related to ν(C=S) in the IR spectrum of the ligand (L) and is shifted towards a lower wave number in the IR spectra of the complexes (Figure S3–6). It suggests that thione sulfur is ligated to metal ions. Therefore, it can be concluded that the ligand acts as a bidentate chelating agent coordinated via pyrazoline nitrogen and thione sulfur.[23] The diagnostic of the ν(P-Ph) band at 1435 cm^{-1} supports the presence of coordinated triphenylphosphine.[24] Another definitive evidence is the appearance of weak new low-frequency absorption bands in the range of 384–364 cm^{-1} and 296–338 cm^{-1} that are assigned the ν(M-P) and ν(M-Cl) frequencies, respectively (Figure S7–10).[25]

3. 2. ^{13}C, ^1H, and ^{31}P–NMR Studies

The ^{13}C NMR spectrum of the ligand (L) showed a characteristic peak at δ = 176.07 ppm attributed to the thione carbon (C=S), whereas the carbon (C-2) appeared at δ = 158.18 ppm. The imine carbon (C-18) appeared at δ = 154.95 ppm. The aromatic carbons (C-8), (C-5), (C-11), (C-10,12), (C-9,13), (C-4,6), (C-1,3), (C-7), and (C-17) showed signals at δ = 135.02, 130.93, 130.53, 128.68, 127.08, 126.64, 113.80, 62.35, and 42.39 ppm, respectively. Additionally, the signal at δ = 55.02 ppm (C-22) was assigned to the methyl group (Figure S11).[26] The ^1H-NMR spectrum of the free ligand (L) showed a singlet at δ = 8.08 ppm, corresponding to the (NH_2) proton. The methoxy (OCH_3) protons appeared at δ = 3.70 ppm. In the ^1H-NMR spectrum of free ligand L, C-17 (Ha), C-17 (Hb), and C-7 (Hc) protons of the pyrazoline ring resonated as three doublets of doublets at δ 3.14–3.09, 3.90–3.82, and 5.88–5.84 ppm, respectively. These splittings arise from vicinal coupling with the two magnetically inequivalent C-17 methylene protons (Figure S12).[27] A signal was observed at δ = 3.34 ppm in the ^1H-NMR spectrum of the free ligand (L), attributed to trace amounts of water in the DMSO solvent.[28] The spectra of metal complexes (**1**-**4**) showed signals at δ 9.11, 8.91, 9.03, and 8.84 ppm, respectively, corresponding to the NH_2 group, although this signal is slightly downfield shifted from that of the free ligand; these observations are taken as evidence for coordination through the thione (C=S) group and chelate formation (Figures S13-16).[29] The ^{31}P-NMR spectra for complexes **2** and **4** (Figures S17 and S18) showed a single peak at δP = –1.18 and 25.58 ppm, respectively, which means there is only one type of isomer for each complex and confirms that they are pure.[30]

3. 3. Electronic Spectra, Magnetic Susceptibility and Molar Conductivity Studies

The UV-visible spectra of triphenylphosphine (Ph_3P), carbothioamide (L) ligands, and their corresponding complexes (**1**, **2**, **3**, and **4**) were recorded at room temperature in DMSO solution (10^{-3} mol. L^{-1}), as shown in (Figure 1). The Ph_3P and Carbothioamide (L) ligands exhibited electronic absorption bands at 34013 cm^{-1} (294 nm) and 34722 cm^{-1} (288 nm), attributed to $\pi\to\pi^*$ transitions, respectively. Also, the (L) ligand displayed an absorption band at 27932 cm^{-1} (358 nm), which is associated with $n\to\pi^*$ transition.[31] Complexes **1** and **2** exhibited absorption bands at 34246 cm^{-1} (292 nm), 33222 cm^{-1} (301 nm), 31545 cm^{-1} (317 nm), 27548 cm^{-1} (363 nm), and 27100 cm^{-1} (369 nm), attributed to intra–ligand transitions.[32] The observed bathochromic shifts in these bands are due to the coordination of the ligands with the metal centers. Additionally, a weak absorption band was observed at

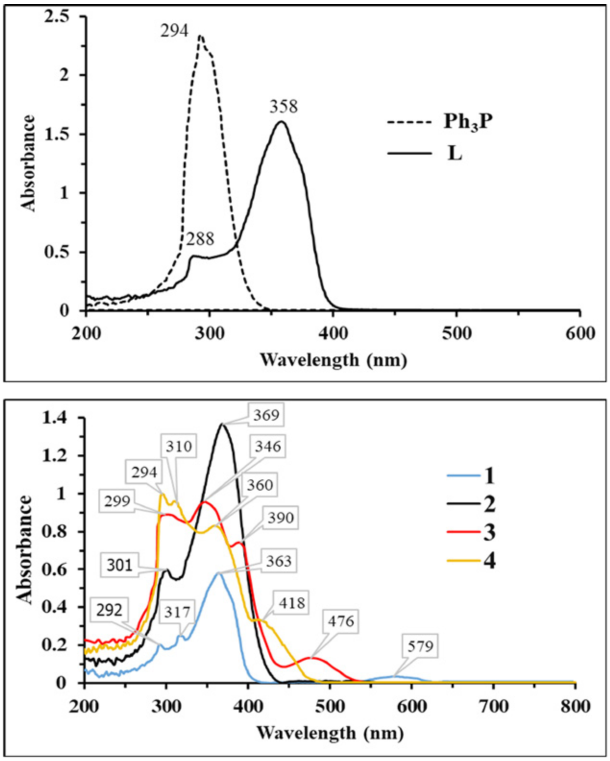

Figure 1. The UV-Vis spectra of Ph$_3$P, (L) ligands and their complexes

17271 cm^{-1} (579 nm) in complex **1**, which is assigned to the $^2B_{1g}$→$^2A_{1g}$ transition, which is typical of a square planar Cu(II) complex.[33] The electronic spectra of complexes **3** and **4**, displayed two d–d transition bands in the ultraviolet and visible regions. The two d–d transition bands were observed in the ranges of 27777–25641 cm^{-1} (360-390 nm) and 23923–21008 cm^{-1} (418–476 nm) and have been attributed to the $^1A_{1g}$→^1E_g and $^1A_{1g}$→$^1B_{1g}$ transitions, respectively. Furthermore, in the spectra of complexes **3** and **4**, the transitions situated within the spectral range of 34013–33444 cm^{-1} (294–299 nm) and 32258–28901 cm^{-1} (310–346 nm) are related to intra-ligand transitions.[34] The complexes **1**, **2**, and **3** exhibited molar conductivity values in DMSO at 5.8, 8.6, and 16.3 Ω^{-1}cm^2 mol^{-1}, respectively, indicating that they are non–ionic and have chlorine inside the coordination sphere.[35] In contrast, the complex **4** [PdCl(L)(Ph$_3$P)]Cl showed a molar conductivity value of 32.6 Ω^{-1}cm^2 mol^{-1}, suggesting the presence of only one chloride ion outside the coordination sphere, and the complex is ionic at a ratio equal to 1:1.[36] Complex **1** has (μ_{eff} = 1.83 B.M.), which confirms that the Cu(II) complex is square planar and paramagnetic due to a 3d^9 electron configuration. In contrast, complexes **2**, **3**, and **4** show (μ_{eff} < 1.0 B.M.), confirming that these complexes are diamagnetic.[37]

3. 4. Theoretical Studies

Frontier molecular orbitals (FMOs) and their energy gaps are crucial parameters in quantum chemistry computations. FMO analysis demonstrates chemical reactivity and stability. The negative values of E_{HOMO} and E_{LUMO} are indicators of a molecule's chemical stability. Higher E_{HOMO} values indicate that the molecule is an

Table 1. Quantum chemical parameters (eV) and NBO Charges (e).

Parameter	Ph$_3$P	L	1	2	3	4
EHOMO	−5.7176	−1.4544	−2.4735, −3.2762	−1.5517	−2.6014	−2.5932
E_{LUMO}	−0.7055	−0.4655	−1.004, −1.1646	−1.0132	−0.6938	−1.2952
ΔE	5.0121	0.9889	1.4695, 2.1116	0.5385	1.9076	1.2980
I	5.7176	1.4544	2.4735, 3.2762	1.5517	2.6014	2.5932
A	0.7055	0.4655	1.004, 1.1646	1.0132	0.6938	1.2952
η	2.5061	0.4944	0.73475, 1.0558	0.2693	0.9538	0.6490
S	0.3990	2.0224	1.3610, 0.9471	3.7140	1.0484	1.5408
χ	3.2116	0.9600	1.73875, 2.2204	1.2825	1.6476	1.9442
μ	−3.2116	−0.9600	−1.73875, −2.2204	−1.2825	−1.6476	−1.9442
ω	2.0578	0.9318	2.0573, 2.3348	3.0542	1.4230	2.9121
The NBO charge of Ph$_3$P, L ligands and their complexes						
Atom	**Ph$_3$P**	**L**	**1**	**2**	**3**	**4**
Cu	–	–	−0.419, −0.393	−0.221	–	–
Pd	–	–	–	–	−0.214	−0.459
Cl	–	–	−0.304	–	−0.456	−0.515
Cl	–	–	−0.179	−0.514	−0.354	–
N	–	−0.098	0.254	−0.091	0.014	0.171
S	–	0.114	0.726	0.399	0.270	0.495
P	0.7610	–	–	1.040	–	1.126

Ionization potential ($I = -E_{HOMO}$); Electron affinity ($A = -E_{LUMO}$); Hardness ($\eta = (I - A)/2$); Softness ($S = 1/\eta$); Electronegativity ($\chi = (I + A)/2$); Chemical potential ($\mu = -(I + A)/2$); Electrophilicity ($\omega = \mu^2/2\eta$).

electron donor crucial for forming a charge-transfer complex between it and the biological target. Low E_{HOMO} values, in contrast, suggest that a molecule's ability to donate electrons is weak, whereas E_{LUMO} values indicate a molecule's capacity to accept an electron.[38] The chemical hardness of compounds can be used to determine their chemical stability. In general, soft molecules tend to be more polarizable since they require less energy to excite electrons from the HOMO to the LUMO. Hard molecules have a large energy gap, whereas soft molecules have a small energy gap.[39] In this study, we computed the electronic properties of the Ph_3P, 4,5-dihydro-5-(4-methoxyphenyl)-3-phenylpyrazole-1-carbothioamide (L) ligands, and complexes **1**, **2**, **3**, and **4** using the B3LYP method and the 6-311G and LANL2DZ basis sets, respectively. The Ph_3P, L ligands, and complexes **1**, **2**, **3**, and **4** E_{HOMO}, E_{LUMO}, and $\boldsymbol{\Delta E}$ energy gaps are presented in (Figures 2, 3) along with their positive and negative areas. Positive and negative phases are indicated by green and red, respectively. The quantum chemical parameters of the ligands and complexes are listed in Table 1. Each of the ligands and complexes has a singlet spin, except complex **1**, which has a doublet spin. The free Ph_3P and (L) ligands have an energy gap ($\boldsymbol{\Delta E}$) of 5.0121 and 0.9889 eV, while complexes **1**, **2**, **3**, and **4** have a $\boldsymbol{\Delta E}$ of (1.4695, 2.1116), (0.5385), (1.9076), and (1.2980) eV, respectively. The results show that complex **2** is softer (S= 3.7140 eV) than the other complexes because it has the smallest energy gap ($\boldsymbol{\Delta E}$= (0.5385 eV). Therefore, the synthesized Cu(I) complex **2** is more reactive and less stable than the other complexes. Based on ΔE, the stability trend was in the following order: Ph_3P > Cu(II) complex **1** > Pd(II) complex **3** > Pd(II) complex **4** > ligand (L) > Cu(I) complex **2**. The chemical potential values for the synthesized complexes are negative, revealing that they are stable and do not decompose into their components.[40]

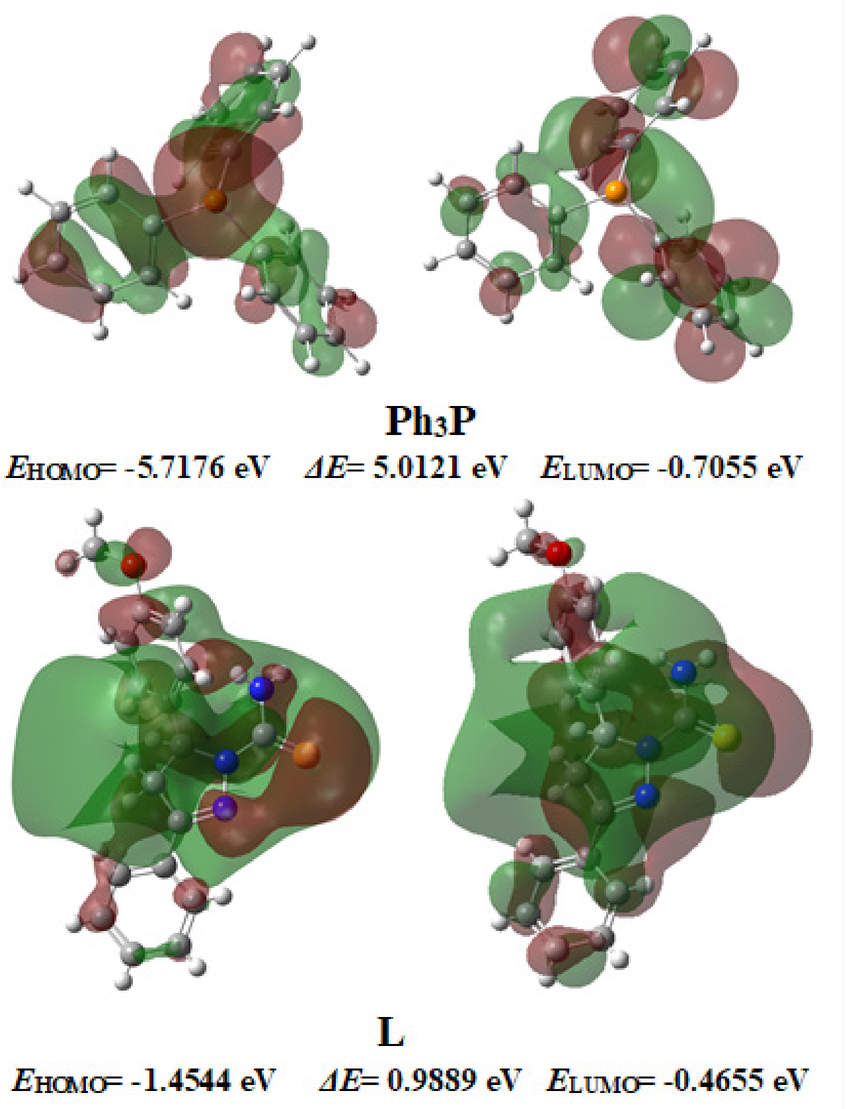

Figure 2. Surface plots of HOMO-LUMO orbitals of Ph_3P and L ligands

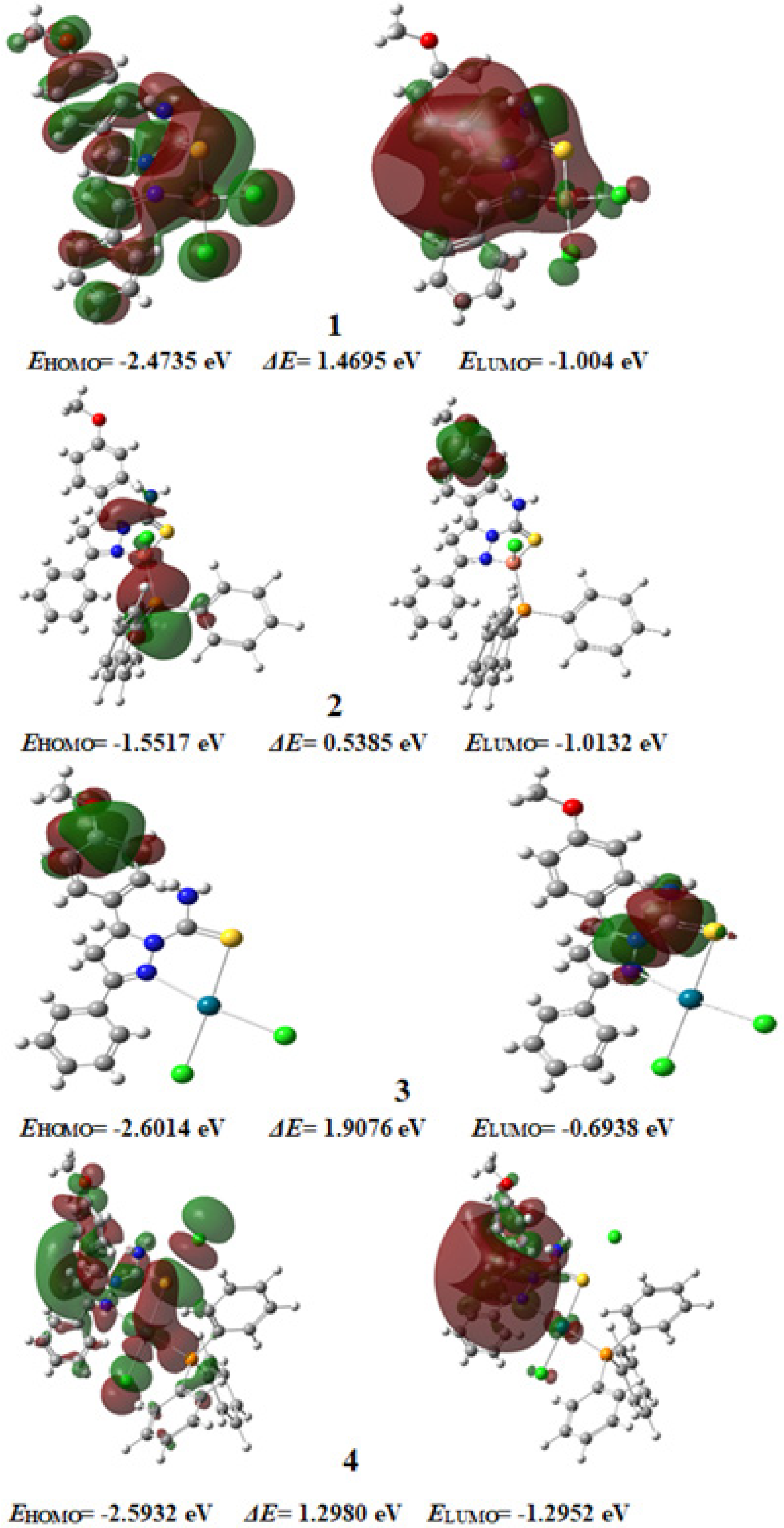

1

E_{HOMO}= -2.4735 eV ΔE= 1.4695 eV E_{LUMO}= -1.004 eV

2

E_{HOMO}= -1.5517 eV ΔE= 0.5385 eV E_{LUMO}= -1.0132 eV

3

E_{HOMO}= -2.6014 eV ΔE= 1.9076 eV E_{LUMO}= -0.6938 eV

4

E_{HOMO}= -2.5932 eV ΔE= 1.2980 eV E_{LUMO}= -1.2952 eV

Figure 3. Surface plots of HOMO-LUMO orbitals of complexes **1**, **2**, **3**, and **4**

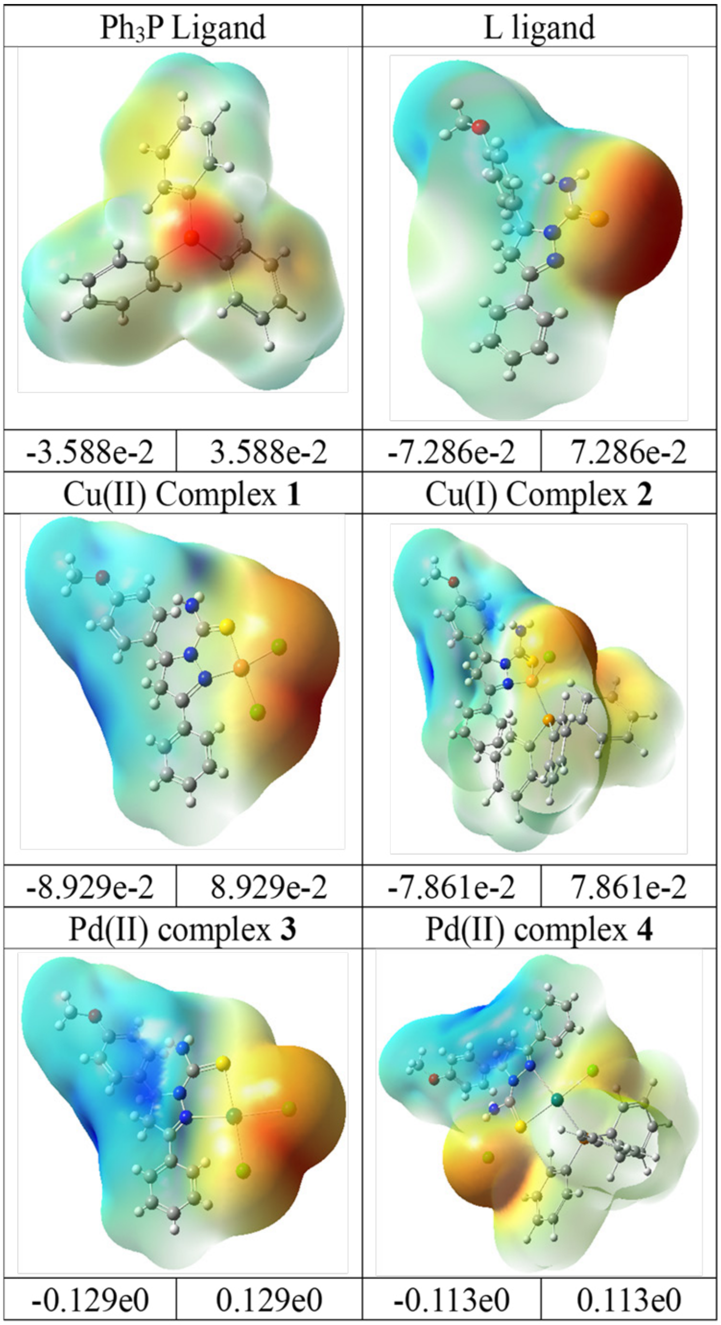

Figure 4. MEP surfaces of the target compounds

Analysis of natural bond orbitals (NBOs) can be used to investigate intermolecular and intramolecular bonding, interactions between donors (ligands) and acceptors (metal centers), as well as charge transfer in molecular structures.[41] According to NBO analysis, the natural electron configuration (NEC) of Cu metal in mononuclear complex **1** is $[Ar]4S^{0.46}\ 3d^{9.59}\ 4P^{1.00}\ 5S^{0.18}\ 4d^{0.03}\ 5P^{0.16}$ and $[Ar]4S^{0.49}\ 3d^{9.55}\ 4P^{0.97}\ 5S^{0.21}\ 4d^{0.05}\ 5P^{0.20}$, containing 11.04974, 11.13174 valence electrons and 0.37680, 0.33826 Rydberg electrons. The natural charge of Cu atom in complex **1** is -0.419 and -0.393e supporting ligand–to–metal charge transfer. The occupancies of the Cu 3d orbitals are $d_{xy}^{1.7362}\ d_{xz}^{1.9904}\ d_{yz}^{1.9819}\ d_{X^2-Y^2}^{\ 1.900}\ d_{z^2}^{\ 1.9790}$ and $d_{xy}^{1.7505}\ d_{xz}^{1.9802}\ d_{yz}^{1.9801}\ d_{X^2-Y^2}^{\ 1.8600}\ d_{z^2}^{\ 1.9792}$. Natural electron configuration (NEC) of Cu atom in complex **2** is $[Ar]4S^{0.01}\ 3d^{9.63}\ 4P^{0.02}\ 5S^{0.45}\ 4d^{0.01}\ 5P^{1.13}$ containing 11.20146 valence electrons and 0.04595 Rydberg electrons. The Cu atom's natural charge is -0.221e, which validates electron transfer to copper metal. The occupancy of the Cu 3d orbitals are $d_{xy}^{1.90008}\ d_{xz}^{1.9693}\ d_{yz}^{1.9243}\ d_{X^2-Y^2}^{\ 1.8774}\ d_{z^2}^{\ 1.9546}$. The NEC of the Pd atom in complex **3** is $[Ar]5S^{0.48}\ 4d^{9.13}\ 5P^{0.18}\ 5d^{0.01}\ 6P^{0.42}$, containing 10.18715 valence electrons and 0.03024 Rydberg electrons.[42] The natural charge of the Pd atom is –0.214e, confirming electron transport to palladium metal. The occupancy of the Pd 4d orbitals is $d_{xy}{}^{1.30797}\ d_{xz}{}^{1.95286}\ d_{yz}{}^{1.93445}\ d_{X^2-Y^2}{}^{1.98573}\ d_{z^2}{}^{1.94596}$. Also, the NEC of the Pd atom in complex **4** is $[Ar]5S^{0.51}\ 4d^{9.39}\ 5P^{0.34}\ 5d^{0.01}\ 6P^{0.23}$, containing 10.4485 valence electrons and 0.0214 Rydberg electrons. The Pd atom's natural charge is -0.459e, indicating electron transfer to palladium metal. The occupancy of the Pd 4d orbitals is $d_{xy}{}^{1.70578}\ d_{xz}{}^{1.96137}\ d_{yz}{}^{1.97689}\ d_{X^2-Y^2}{}^{1.81095}\ d_{z^2}{}^{1.93072}$. The NBO data indicates that the positive charge on the P (0.7610) atom in the free ligand increases in complexes **2** and **4** due to the transfer of electron density from the filled p orbital of the phosphorus atom to the vacant metal d orbitals (p-d sigma-bonding).[43]

The molecular electrostatic potential (MEP) surfaces for the ligands and their corresponding complexes were calculated and are shown in (Figure 4). In MEP surfaces, red areas signify electrophilic reactivity, whereas blue areas indicate nucleophilic reactivity.[44] The phosphorus atom in Ph_3P and the sulfur atom in the (L) ligand, with their red regions, are identified as reactive sites for electrophilic attack due to the high electronegativity of these atoms. In all complexes, the chlorine atoms located at the negative electrostatic region represented by the red color is a good target for an electrophilic attack.[45]

4. Conclusions

In this research paper, we describe the synthesis and spectral characterization of the complexes $[CuCl_2(L)]$ **1**; $[CuCl(L)(Ph_3P)]$ **2**; $[PdCl_2(L)]$ **3**; and $[PdCl(L)(Ph_3P)]Cl$ **4,** which contain carbothioamide (L) and triphenylphosphine ligands. Spectroscopic studies have shown that carbothioamide (L) acts as an SN-donor bidentate ligand. Magnetic moment, elemental analysis, and electronic spectral data indicate that all synthesized complexes are mononuclear. Moreover, structural analysis suggests that complexes **1**, **3**, and **4** display a square planar geometry, while complex **2** shows a tetrahedral geometry. The magnetic susceptibility measurements indicated that the Pd(II) and Cu(I) complexes are diamagnetic, related to their d^8 and d^{10} electron configurations, respectively. In contrast, the Cu(II) complex demonstrates paramagnetic behaviour, in agreement with the d^9 configuration. UV-Vis spectral analysis detected the ${}^2B_{1g} \rightarrow {}^2A_{1g}$ transition at 579 nm in complex **1**. Also, d-d transitions were observed at (390–360 nm) and (476–418 nm), which were attributed to the ${}^1A_{1g} \rightarrow {}^1E_g$ and ${}^1A_{1g} \rightarrow {}^1B_{1g}$ transitions in complexes **3** and **4**, respectively. NBO analysis showed that the charges on the copper and palladium metal centres, coordinated to the sulfur, nitrogen, and phosphorus atoms of the ligands, were computed as Cu= –0.419, –0.393 e **1**, Cu = –0.221 e **2**, Pd= –0.214 e **3**, and Pd= –0.459 e **4**. These values are less than the formal charge of the $Cu^{+1}/^{+2}$ and Pd^{+2}, supporting electron density transfer from the ligands to the metal ions. MEP surface analysis indicated that electrophilic sites are mainly localized on chlorine atoms in all complexes.

Acknowledgments

The authors are grateful to the Chemistry Department of the College of Education at Salahaddin University for their assistance in the accomplishment of this study. The authors are also thankful to the Department of General Science, College of Basic Education, Halabja University, for offering the laboratory equipment to complete this study.

Funding

The authors did not receive any support from any organization for the submitted study.

5. References

1. S. Chandra, S. Bargujar, R. Nirwal, N. Yadav, Spectrochim. *Acta A Mol. Biomol. Spectrosc.* **2013**, *106*, 91–98. **DOI:**10.1016/j.saa.2012.12.014
2. D. Varna, E. Geromichalou, A. G. Hatzidimitriou, R. Papi, G. Psomas, P. Dalezis, P. Aslanidis, T. Choli–Papadopoulou, D. T. Trafalis, P. A. Angaridis, *Dalton Trans.* **2022**, *51*, 9412–9431. **DOI:**10.1039/D2DT00793B
3. M. K. Vekariya, D. B. Patel, P. A. Pandya, R. H. Vekariya, P. U. Shah, D. P. Rajani, N. K. Shah, *J. Mol. Struct.* **2019**, *1175*, 551–565. **DOI:**10.1016/j.molstruc.2018.08.018
4. E. P. Mendes, C. M. Goulart, O. A. Chaves, V. D. S. Faiões, M. M. Canto-Carvalho, G. C. Machado, E. C. Torres–Santos, A. Echevarria, *Biomol.* **2019**, *9*, 643–662. **DOI:**10.3390/biom9110643
5. T. S. Lobana, A. K. Sandhu, R. Sultana, A. Castineiras, R. J. Butcher, J. P. Jasinski, *RSC Adv.* **2014**, *4*, 30511–30522. **DOI:**10.1039/C4RA02748E
6. A. M. Abu-Dief, L. H. Abdel-Rahman, M. R. Shehata, A. A. H. Abdel-Mawgoud, *J. Phys. Org. Chem.* **2019**, *32*, e4009. **DOI:**10.1002/poc.4009
7. L. Walczak–Nowicka, A. Biernasiuk, W. Ziemichód, Z. Karczmarzyk, M. Kwaśnik, P. Kozyra, W. Wysocki, A. Stenzel–Bembenek, D. Kowalczuk, M. Herbet, M. Pitucha, *Pharm.* **2023**, *16*, 1706–1734. **DOI:**10.3390/ph16121706
8. N. I. Vorozhtsov, D. D. Korablina, E. I. Kalenikova, L. A. Sviridova, A. I. Petkova, A. A. Moiseeva, V. A. Tafeenko, A. N. Ataeva, B. V. Makhmudova, A. A. Markova, A. A. Shtil, *Results Chem.* **2024**, *9*, 101632. **DOI:**10.1016/j.rechem.2024.101632
9. P. L. Hegde, S. S. Bhat, V. K. Revankar, S. A. Shaikh, K. Kumara, L. NK, *J. Mol. Struct.* **2022**. *1257*, 132589. **DOI:**10.1016/j.molstruc.2022.132589
10. M. A. Arafath, F. Adam, M. R. Razali, L. E. A. Hassan, M. B. K. Ahamed, A. M. S. Majid, *J. Mol. Struct.* **2017**, *1130*, 791–798. **DOI:**10.1016/j.molstruc.2016.10.099

11. J. Pann, H. Roithmeyer, W. Viertl, R. Pehn, M. Bendig, J. Dutzler, B. Kriesche, P. Brüggeller, *Sustain. Energy Fuels*. **2019**, *3*, 2926–2953. **DOI:**10.1039/C9SE00320G
12. R. E. Brooner, T. J. Brown, R. A. Widenhoefer, *Chem. Eur*. **2013**, *19*, 8276–8284. **DOI:**10.1002/chem.201204564
13. K. Hong, M. Sajjadi, J. M. Suh, K. Zhang, M. Nasrollahzadeh, H. W. Jang, R. S. Varma, M. Shokouhimehr, *ACS Appl. Nano Mater*. **2020**, *3*, 2070–2103. **DOI:**10.1021/acsanm.9b02017
14. E. Haldón, M. C. Nicasio, P. J. Pérez, *Org. Biomol. Chem*. **2015**. *13*, 9528–9550. **DOI:**10.1039/C5OB01457C
15. T. S. Lobana, M. Kaushal, R. Bala, I. Garcia–Santos, J. P. Jasinski, *J. Indian Chem. Soc*. **2022**, *99*, 100298. **DOI:**10.1016/j.jics.2021.100298
16. W. O. Misigo, L. W. Njenga, R. A. Odhiambo, M. Meyer, L. Julius, N. Sibuyi, R. A. Lalancette, M. O. Onani, *Inorg. Chim. Acta*. **2023**, *558*, 121746. **DOI:**10.1016/j.ica.2023.121746
17. U. Solmaz, H. Arslan, *J. Mol. Struct.* **2022**, *1269*, 133839. **DOI:**10.1016/j.molstruc.2022.133839
18. K, Sayin, *J. Coord. Chem*. **2018**, *71*, 3292–3303. **DOI:**10.1080/00958972.2018.1511050
19. K. Alomar, M. A. Khan, M. Allain, G. Bouet, *Polyhedron*, **2009**, *28*, 1273–1280. **DOI:**10.1016/j.poly.2009.02.042
20. P. Goel, D. Kumar, S. Chandra, *Iran. J. Sci. Technol. Trans. A Sci.* **2019**, *43*, 477–487. **DOI:**10.1007/s40995-018-0573-1
21. N. Özdemir, R. Fırıncı, M. E. Günay, *Croat. Chem. Acta*. **2023**, *96*, 1–8. **DOI:**10.5562/cca3933
22. S. A Sadeek, A. A. Mohamed, W. A. Zordok, H. M. Awad, S. M. Abd El–Hamid, *Egypt. J. Chem*. **2021**, *64*, 4197–4208.
23. A. A. Aly, E. M. Abdallah, S. A. Ahmed, M. M. Rabee, E. S. M. Abdelhafez, *J. Mol. Struct*. **2022**, *1265*, 133480. **DOI:**10.1016/j.molstruc.2022.133480
24. L. A. Al–Doori, A. A. Irzoqi, H. M. Jirjes, A. H. AL–Obaidi, M. A. Alheety, *Inorg. Chem. Commun.* **2022**, *140*, 109454. **DOI:**10.1016/j.inoche.2022.109454
25. G. A. El-Inany, H. S. Seleem, H. F. El-Shafiy, B. A. El-Shetary, A. I. Nabeel, A. Madyan, M. Shebl, *Appl. Organomet. Chem*. **2024**, *38*, e7367. **DOI:**10.1002/aoc.7367
26. A. A. Al–Amiery, W. K. Al–Azzawi, W. N. R. W. Isahak, *Sci. Rep*. **2022**, *12*, 17773–17791. **DOI:**10.1038/s41598-022-22611-4
27. A. Ahmad, M. Y. Wani, M. Patel, A. J. Sobral, A. G. Duse, F. M. Aqlan, A. S. Al–Bogami, *Med. Chem. Comm.* **2017**, *8*, 2195–2207. **DOI:**10.1039/C7MD00440K
28. S. A. Ross, G. Lowe, *Tetrahedron Lett.* **2000**, *41*, 3225–3227. **DOI:**10.1016/S0040-4039(00)00355-5
29. W. Hernández, J. Paz, F. Carrasco, A. Vaisberg, E. Spodine, J. Manzur, L. Hennig, J. Sieler, S. Blaurock, L. Beyer, *Bioinorg. Chem. Appl.* **2013**, *2013*, 524701. **DOI:**10.1155/2013/524701
30. T. Chivers, C. Fedorchuk, M. Krahn, M. Parvez, G. Schatte, *Inorg. Chem.* **2001**, *40*, 1936–1942. **DOI:**10.1021/ic001173s
31. S. A. Shaker, *J. Chem*. **2010**. *7*, S594–S600.
32. K. O. Ali, *Acta Chim. Slov*. **2023**, *70*, 611–619. **DOI:**10.17344/acsi.2023.8416
33. G. A. El-Inany, H. S. Seleem, B. A. El-Shetary, H. F. El-Shafiy, A. I. Nabeel, A. Madyan, M. Shebl, *Appl. Organomet. Chem*. **2023**, *37*, e7233. **DOI:**10.1002/aoc.7233
34. H. A. Mohamad, W. T. Al–Kattan, Z. M. Al–Daly, A. N. Najim, *Orient. J. Chem*. **2020**, *36*, 903. **DOI:**10.13005/ojc/360515
35. H. Kargar, M. Fallah–Mehrjardi, N. Dege, M. Ashfaq, K. S. Munawar, M. N. Tahir, M. A. Bajgirani, M. Sahihi, *J. Iran. Chem. Soc*. **2024**, *21*, 1561–1572. **DOI:**10.1007/s13738-024-03016-8
36. M. Saeidifar, H. Mirzaei, N. A. Nasab, H. Mansouri–Torshizi, *J. Mol. Struct*. **2017**, *1148*, 339–346. **DOI:**10.1016/j.molstruc.2017.06.139
37. S. Bharti, M. Choudhary, B. Mohan, S. P. Rawat, S. R. Sharma, K. Ahmad, *J. Mol. Struct*. **2018**, *1164*, 137–154. **DOI:**10.1016/j.molstruc.2018.03.041
38. G. A. El-Inany, H. S. Seleem, B. A. El-Shetary, H. F. El-Shafiy, A. I. Nabeel, A. Madyan, A, M. Shebl, *Inorg. Chem. Commun*. **2024**, *160*, 111888. **DOI:**10.1016/j.inoche.2023.111888
39. H. S. Seleem, G. A. El-Inany, B. A. El-Shetary, H. F. El-Shafiy, F. I. Hanafy, A. I. Nabeel, A. Madyan, M. Shebl, M, *Inorg. Chem. Commun*. **2025**, *179*, 114847. **DOI:**10.1016/j.inoche.2025.114847
40. M. A. Arafath, F. Adam, M. B. K. Ahamed, M. R. Karim, M. N. Uddin, B. M. Yamin, A. Abdou, *J. Mol. Struct*. **2023**, *1278*, 134887. **DOI:**10.1016/j.molstruc.2022.134887
41. M. Guin, S. Halder, S. Chatterjee, S. Konar, *J. Mol. Struct*. **2022**, *1270*, 133949. **DOI:**10.1016/j.molstruc.2022.133949
42. D. Milenković, E. Avdović, D. Dimić, S. Sudha, D. Ramarajan, Z. Milanović, S. Trifunović, Z. S. Marković, *J. Mol. Struct*. **2020**, *1209*, 127935. **DOI:**10.1016/j.molstruc.2020.127935
43. L. Saghatforoush, K. Moeini, S. A. Hosseini–Yazdi, Z. Mardani, A. Hajabbas–Farshchi, H. T. Jameson, S. G. Telfer, J. D. Woollins, *RSC Adv*. **2018**, *8*, 35625–35639. **DOI:**10.1039/C8RA07463A
44. M. A. I. Al–Gaber, H. M. Abd El–Lateef, M. M. Khalaf, S. Shaaban, M. Shawky, G. G. Mohamed, A. Abdou, M. Gouda, A. M. Abu–Dief, *Materials*, **2023**, *16*, 897. **DOI:**10.3390/ma16030897
45. H. M. Abd El–Lateef, A. M. Ali, M. M. Khalaf, A. Abdou, *Bull. Chem. Soc. Ethiop*. **2024**, *38*, 397–416. **DOI:**10.4314/bcse.v38i2.9

Povzetek

S kondenzacijo 4-metoksihalkona s tiosemikarbazidom smo sintetizirali karbotioamidni ligand, 4,5-dihidro-5-(4-metoksifenil)-3-fenilpirazol-1-karbotioamid [$C_{17}H_{17}N_3OS$]. Karbotioamidni ligand (L) in trifenilfosfin (Ph_3P) kot koligand sta se vezala na ione kovin Cu(I), Cu(II) in Pd(II) za sintezo ustreznih kompleksov: [$CuCl_2$(L)] (**1**), [CuCl(L)(Ph_3P)] (**2**), [$PdCl_2$(L)] (**3**) in [PdCl(L)(Ph_3P)]Cl (**4**). Ligand in vse komplekse smo izolirali v trdni obliki ter karakterizirali z magnetno susceptibilnostjo, elementno analizo, molsko prevodnostjo, FT-IR, UV-Vis in NMR spektroskopijami (^{1}H, ^{13}C, ^{31}P). Vrednosti molske prevodnosti v DMSO (5,8–16,3 Ω^{-1} cm^2 mol^{-1}) potrjujejo, da so vsi kompleksi neelektrolitski, razen Pd(II) kompleksa **4**, ki se obnaša kot 1:1 elektrolit (32,6 Ω^{-1} cm^2 mol^{-1}). Spektroskopski podatki kažejo, da se karbotioamidni ligand koordinira kot N,S-donor in kelatni ligand. Meritve magnetne susceptibilnosti skupaj z elektronsko spektroskopijo nakazujejo, da imajo kompleksi Cu(II) in Pd(II) kvadratno planarno geometrijo, medtem ko ima Cu(I) kompleks **2** tetraedrično strukturo. Elementna analiza in ^{1}H NMR spektroskopija potrjujeta enojedrno strukturo vseh kompleksov. DFT-računi kažejo, da imajo sintetizirani kompleksi **1**, **3** in **4** večjo termodinamsko stabilnost kot prosti ligand (L), s pripadajočimi vrednostmi ΔE (1,4695; 2,1116 eV), (1,9076 eV) in (1,2980 eV). V nasprotju s tem ima kompleks **2** nižjo termodinamsko stabilnost (ΔE = 0,5385 eV). Med sintetiziranimi kompleksi je največjo mehkobo pokazal kompleks **2** (S = 3,7140 eV), sicer pa so bili vsi kompleksi mehkejši od trifenilfosfinskega liganda. Rezultati kažejo, da v določenih kompleksih elektronski prehodi potekajo lažje kot v njihovih ligandih, kar nakazuje možnost njihove uporabe v fotocelicah v prihodnjih raziskavah.

DOI: 10.17344/acsi.2025.9327 *Acta Chim. Slov.* **2025,** *72,* 503–513

Scientific paper

Synthesis and Antimicrobial Efficacy of Novel 1,3,4-Thiadiazole Derivatives Against Key Bacterial and Fungal Strains

Mohamed M. Eleribi,[1,*] **Fakhri A. Elabbar,**[2] **and Basma Saad Baaiu**[2]

[1] *Department of Chemistry, Faculty of Art and Science, Alabyar Branch, University of Benghazi, P. O. Box 1308, Benghazi, Libya.*

[2] *Department of Chemistry, Faculty of Science, Benghazi, University of Benghazi, P. O. Box 1308, Benghazi, Libya.*

[*] *Corresponding author: E-mail: mohamed.eribi@uob.edu.ly*

Received: 05-14-2025

Abstract

Two series of new 1,3,4-thiadiazole derivatives were synthesized through heterocyclization of methyl 2-(3,5-dibromo-2-hydroxybenzylidene)hydrazine-1-carbodithioate (**4**) and methyl (*E*)-2-(1-(5,7-dibromobenzofuran-2-yl)ethylidene)hydrazine-1-carbodithioate (**5**) with various hydrazonoyl chlorides, respectively. The structures of the newly synthesized products were elucidated through elemental analysis and spectral data. Eight new compounds from the first series (i.e. containing dibromohydroxybenzene moiety) were evaluated for their antimicrobial activity against *Staphylococcus aureus* ATCC 6538-P as the Gram-positive bacteria, *Escherichia coli* ATCC 25933 as the Gram-negative bacteria, *Candida albicans* ATCC 10231 as a yeast, and the filamentous fungus *Aspergillus niger* NRRL-A326 in comparison with neomycin as a reference drug in the case of *S. aureus, E. coli* and *C. albicans* whereas cyclohexamide was used as a reference for filamentous fungi. The results showed that some of the novel compounds have promising antimicrobial activity.

Keywords: 1,3,4-thiadiazole, carbodithioate, hydrazonoyl chloride, antimicrobial activity.

1. Introduction

Heterocyclic compounds have garnered significant interest among organic chemists, medical researchers, and those involved in drug discovery. Thiadiazole is a prominent class of heterocyclic compounds characterized by a five-membered ring containing two nitrogen atoms, one sulfur atom, and two carbon atoms. Thiadiazoles are categorized into four types: 1,3,4-thiadiazole, 1,2,4-thiadiazole, 1,2,5-thiadiazole, and 1,2,3-thiadiazole (Figure 1), with 1,2,4-thiadiazole and 1,3,4-thiadiazole being the most extensively studied.[1]

Compounds containing the 1,3,4-thiadiazole moiety have been shown to exhibit a broad spectrum of biological activities, including antimicrobial,[2,3] antituberculosis,[4] antiinflammatory,[5–7] anticonvulsant,[4,8,9] antihypertensive,[10] local anesthetic,[11] and anticancer activities,[12,13] 1,3,4-thiadiazole scaffold has been utilized in several FDA-approved[14] drugs such as desaglybuzole, acetazolamide, sulfamethizole, litronesib, filanesib, and methazolamide[15] (Figure 2).

Various synthetic routes including cyclization reactions involving thioketones, hydrazines and various carbonyl compounds are utilized to synthesis thiadiazole. In this work, we aim to synthesize a new series of 1,3,4-thiadiazole derivatives which are expected to exhibit antimicrobial activity.

Figure 1. Structures of thiadiazoles

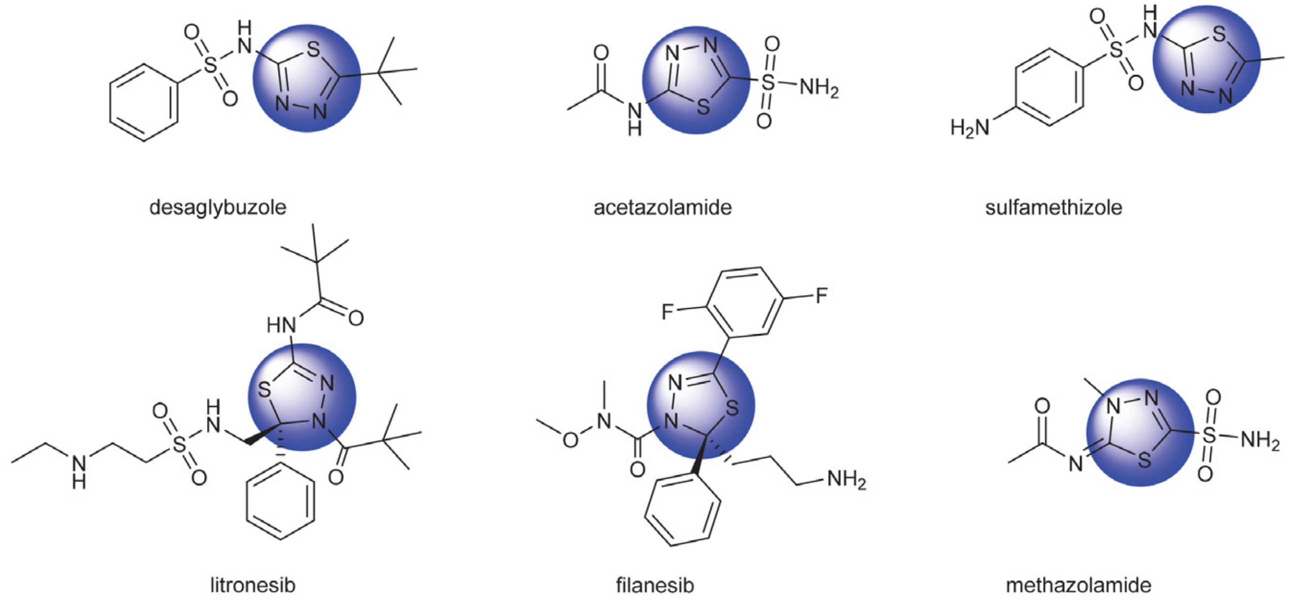

Figure 2. FDA-approved drugs contain thiadiazole

2. Experimental

Melting points were measured on an electrothermal digital apparatus. IR spectra (KBr disks) were recorded on a Shimadzu FT-IR 8201 PC Infrared spectrophotometer. ^{1}H NMR spectra were recorded in DMSO-d_6 solutions on a Bruker spectrometer operating at 400 MHz, ^{13}C NMR were recorded on a Bruker spectrometer at 100 MHz, and chemical shifts were referenced to that of the solvent. Mass spectra were recorded on a GCMS QP1000 EX Shimadzu. Elemental analyses were carried out by the Microanalytical Research Centre, Faculty of Science, Cairo University. Analytical C, H, N, and S results were within ±0.4% of the calculated values, hydrazonoyl halides **6a–h**[16–19] were prepared as reported in the literature.

2. 1. Chemistry

Synthesis of 3,5-Dibromo-2-hydroxybenzaldehyde (2)

Bromine 16 g (5 mL), 0.1 mol was added step-wise to salicylaldehyde (**1**) (22.12 g, 0.18 mol) in acetic acid (150 mL), while stirring for 1 hour in an ice bath. The reaction mixture was then poured on ice-cold water (1000 mL).[20,21] The resulting solid residue compound **2** was collected and recrystallized from ethanol to give white crystals, yield 43.353 g (85%). M.p. 81–83 °C (ethanol); IR (KBr) ν 3347 (OH), 3176, 3067 (CH, aromatic), 1680 (C=O) cm^{-1}; ^{1}H NMR (400 MHz, DMSO-d_6) δ 11.25 (s, 1H, CHO), 10.01 (s, 1H, OH), 7.95 (d, J = 2.4 Hz, 1H, Ar-H), 7.83 (d, J = 2.4 Hz, 1H, Ar-H); MS m/z (%): 281.87 ([M+4]$^+$, 22.64), 279.61 ([M+2]$^+$, 33.78), 278.08 (M$^+$, 100). Anal. Calcd. for $C_7H_4Br_2O_2$ (279.96): C, 30.04; H, 1.44. Found: C, 29.83; H, 1.42 %.

Synthesis of 1-(5,7-Dibromobenzofuran-2-yl)ethan-1-one (3)

A total of 28 g (0.1 mol) of compound **2** was refluxed for 2 hours in a solution of potassium hydroxide (5.6 g, 0.1 mol) in ethanol. After cooling the reaction mixture to room temperature, 10 g (0.1 mol) of chloroacetone was added. The mixture was then refluxed for an additional 2 hours. Following this, the reaction mixture was filtered, and the resulting solution was allowed to cool at room temperature. Light green crystals of compound **3** were obtained with a yield 19.76 g (60%). M.p. 147–151 °C (ethanol); IR (KBr) ν 3117, 3094, 3091 (=C–H, aromatic), 1692 (C=O) cm^{-1}; ^{1}H NMR (400 MHz, DMSO-d_6) δ 8.07 (d, J = 1.7 Hz, 1H, Ar-H), 7.97 (d, J = 1.7 Hz, 1H, Ar-H), 7.92 (s, 1H, Ar-H), 2.58 (s, 3H, CH$_3$); ^{13}C NMR (101 MHz, DMSO-d_6) δ 188.15 (C=O), 153.83, 151.55, 133.11, 130.21, 126.08, 116.86, 114.54, 105.73, 27.06; MS m/z (%): 319.65 ([M+4]$^+$, 77.01), 317.50 ([M+2]$^+$, 19.42), 315.05 (M$^+$, 25.53). Anal. Calcd for $C_{10}H_6Br_2O_2$ (317.96): C, 37.78; H, 1.89. Found C, 37.58; H, 1.88 %.

Synthesis of Methyl (*E*)-2-(3,5-Dibromo-2-hydroxybenzylidene)hydrazine-1-carbodithioate (4)

To a solution of 3,5-dibromo-2-hydroxybenzaldehyde (2.79 g, 10 mmol) in 20 mL of 2-propanol, 1.22 g (10 mmol) of methylhydrazinecarbodithioate was added. The mixture was warmed gently and stirred for 1 hour. The solid product was filtered off and recrystallized from dioxane to afford compound **4** as a pale yellow solid in yield 3.341 g (87%). M.p. 187–189 °C (dioxane); IR (KBr) ν 3575 (OH), 3428 (NH), 3219, 3127, 3091 (C–H, aromatic), 1628 (C=N), 1605 (C=C) cm^{-1}; ^{1}H NMR (400 MHz, DMSO-d_6) δ 13.46 (s, 1H, NH), 11.83 (s, 1H, OH), 8.56 (d, J = 1.7 Hz, 1H, Ar-H), 8.55 (s, 1H, CH=N), 8.18 (d, *J* = 1.7 Hz, 1H, Ar-H), 2.56 (s, 3H, S-CH_3); ^{13}C NMR (101 MHz, DMSO-d_6) δ 199.01 (C=S), 165 (C–OH), 141.41 (C=N), 140.51, 127.66, 122.20, 120.80, 117.48, 17.30 (CH_3).

Synthesis of Methyl (*E*)-2-(1-(5,7-Dibromobenzofuran-2-yl)ethylidene)hydrazine-1-carbodithioate (5)

To a solution of 1-(5,7-dibromobenzofuran-2-yl) ethan-1-one (**3**) (3.17 g, 10 mmol) in 2-propanol (20 mL), methyl hydrazinecarbodithioate (1.22 g, 10 mmol) was added. The mixture was heated under reflux for 1 hour. The precipitated product was filtered off, recrystallized from dioxane to afford compound **5** as a white solid, yield 3.503 g (83%). M.p. 210 °C (acetic acid); FT-IR (KBr) ν 3199 (NH), 3065 (C–H, aromatic), 2955, 2856 (CH), 1645 (C=C), 1598 (C=N), 1238 (C=S), 704 (C–S) cm^{-1}; ^{1}H NMR (400 MHz, DMSO-d_6) δ 12.63 (s, 1H, NH), 7.97 (d, *J* = 1.7 Hz, 1H, Ar-H), 7.85 (d, *J* = 1.7 Hz, 1H, Ar-H), 7.55 (s, 1H, Ar-H), 2.54 (s, 3H, S–CH_3), 2.41 (s, 3H, CH_3); MS *m/z* (%): 423.17 ([M+4]$^+$, 7.45), 421.18 ([M+2]$^+$, 22.46), 419.19 (M$^+$, 23.59), 402.7 (100), 390.08 (22.44). Anal. Calcd for $C_{12}H_{10}Br_2N_2OS_2$ (422.15): C, 34.14; H, 2.37; N, 6.64; S, 15.19. Found: C, 34.06; H, 2.36; N, 6.62; S, 15.16%.

General Procedure for the Synthesis of 1,3,4-Thiadiazole Derivatives 10a–g

To a mixture of appropriate hydrazonoyl halides **6a–g** (1 mmol) and hydrazine-1-carbodithioate derivative (**4**) (0.384 g, 1 mmol) in ethanol (20 mL), triethylamine (0.5 mL) was added, the mixture was warmed gently and stirred at room temperature for 1 hour.[22] The resulting solid product was collected and recrystallized from the appropriate solvent to give the corresponding 1,3,4-thiadiazole derivatives **10a–g**. The physical constants of products **10a–g** are listed below.

4-(4-Chlorophenyl)-5-(((*E*)-3,5-dibromo-2-hydroxybenzylidene)hydrazineylidene)-*N*-phenyl-4,5-dihydro-1,3,4-thiadiazole-2-carboxamide (10a)

Yellow solid, yield 0.534 g (88%). M.p. 230–232 °C (dioxane); FT-IR (KBr) ν 3382 (OH), 3310 (NH), 3070 (CH, aromatic), 2925 (CH), 1667 (C=O), 1601 (C=N), 1544 (C=N, thiadiazole) cm^{-1}; ^{1}H NMR (400 MHz, DMSO-d_6) δ 10.83 (s, 1H, OH), 8.70 (s, 1H, NH), 8.65 (s, 1H, CH=N), 8.24 (d, *J* = 8.9 Hz, 2H, Ar-H), 8.17 (d, *J* = 8.9 Hz, 2H, Ar-H), 7.86 (d, *J* = 2.3 Hz, 1H, Ar-H), 7.82 (d, *J* = 2.3 Hz, 1H, Ar-H), 7.76 (d, *J* = 7.9 Hz, 2H, Ar-H), 7.40 (t, *J* = 7.9 Hz, 2H, Ar-H), 7.18 (t, *J* = 7.4 Hz, 1H, Ar-H); MS *m/z* (%): 609.32 ([M+4]$^+$, 23.14), 607.21 ([M+2]$^+$, 20.78), 604.90 (M$^+$, 60.81), 446.51 (100), 405.70 (52). Anal. Calcd. for $C_{22}H_{14}Br_2ClN_5O_2S$ (607.71): C, 43.48; H, 2.32;N, 11.52; S, 5.28. Found: C, 43.36; H, 2.29; N, 11.48; S, 5.26%.

2,4-Dibromo-6-((1*E*)-((5-(furan-2-yl)-3-(4-nitrophenyl)-1,3,4-thiadiazol-2(3*H*)-ylidene)hydrazineylidene)methyl)phenol (10b)

Brown solid, yield 0.468 g (83%). M.p. 295–298 °C (dioxane); FT-IR (KBr) ν 3384 (OH), 3112, 3071 (CH, aromatic), 2923 (CH), 1743 (C=C, furan ring), 1605 (C=N), 1590 (C=N, thiadiazole), 693 (C–S) cm^{-1}; ^{1}H NMR (400 MHz, DMSO-d_6) *δ* 11.38 (s, 1H, OH), 8.81 (s, 1H, CH=N), 8.43 (s, 2H, Ar-H), 8.06 (d, *J* = 1.6 Hz, 1H, furan-H), 7.91 (d, *J* = 2.3 Hz, 1H, Ar-H), 7.89 (d, *J* = 2.3 Hz, 1H, Ar-H), 7.90 (d, *J* = 8.12 Hz, 2H, Ar-H), 7.46 (d, *J* = 3.6 Hz, 1H, furan-H), 6.82 (dd, *J* = 3.6, 1.6 Hz, 1H, furan-H); MS *m/z* (%): 566.53 ([M+4]$^+$, 5.00), 564.17 ([M+2]$^+$, 28.24), 562.97 (M$^+$, 15.01), 440.47 (100), 429.35 (45.58). Anal. Calcd for $C_{19}H_{11}Br_2N_5O_4S$ (565.20): C, 40.38; H, 1.96; N, 12.39; S, 5.67. Found: C, 40.33; H, 1.94; N, 12.37; S, 5.66%.

5-(((*E*)-3,5-Dibromo-2-hydroxybenzylidene)hydrazineylidene)-*N*,4-diphenyl-4,5-dihydro-1,3,4-thiadiazole-2-carboxamide (10c)

Pale yellow solid, yield 0.441 g (77%). M.p. 187 °C (dioxane); FT-IR (KBr) ν 3382 (OH), 3310 (NH), 3070 (CH, aromatic), 2925 (CH), 1667 (C=O), 1601 (C=N), 1544 (C=N, thiadiazole) cm^{-1}; ^{1}H NMR (400 MHz, DMSO-d_6) δ 10.75 (s, 1H, OH), 8.66 (s, 1H, NH), 8.62 (s, 1H, CH=N), 8.07 (d, *J* = 7.9 Hz, 2H, Ar-H), 8.01 (d, *J* = 7.9 Hz, 2H, Ar-H), 7.83 (d, *J* = 2.3 Hz, 1H, Ar-H), 7.82 (d, *J* = 2.3 Hz, 1H, Ar-H), 7.56 (d, *J* = 6.8 Hz, 2H, Ar-H), 7.47–7.33 (m, 3H, Ar-H), 6.92 (d, *J* = 7.8 Hz, 1H, ArH); MS *m/z* (%): 574.16 ([M+4]$^+$, 5.04), 572.46 ([M+2]$^+$, 22.09), 570.61 (M$^+$, 13.02), 273.67 (100), 260.89 (58.38). Anal. Calcd for $C_{22}H_{15}Br_2N_5O_2S$ (573.93): C, 46.09; H, 2.64; N, 12.22;S, 5.59. Found: C, 46.10; H, 2.62; N, 12.22; S, 5.59%.

2,4-Dibromo-6-((1*E*)-((3-(4-nitrophenyl)-5-(thiophen-2-yl)-1,3,4-thiadiazol-2(3*H*)-ylidene)hydrazineylidene)methyl)phenol (10d)

Orange solid, yield 0.447 g (77%). M.p. >300 °C (acetic acid); FT-IR (KBr) ν 3444 (OH), 3108, 3065 (C–H aromatic), 2913 (CH), 1608 (C=N), 1589 (C=N thiadiazole), 1491 (C=C), 695 (C–S–C) cm^{-1}; ^{1}H NMR (400 MHz, DMSO-d_6) δ 11.37 (s, 1H, OH), 8.80 (s, 1H, CH=N), 8.41 (d, *J* = 9.2 Hz, 2H, Ar-H), 7.94 (d, *J* = 5.1 Hz, 1H, thiophene-H), 7.93 (d, *J* = 1.8 Hz, 1H, thiophene-H), 7.92 (d, *J* = 9.2 Hz, 2H, Ar-H), 7.90 (d, *J* = 3.0 Hz, 1H, Ar-H), 7.89 (d, *J* = 3.0 Hz, 1H, Ar-H), 7.28 (t, *J* = 5.1 Hz 1H, thiophene-H); MS *m/z* (%): 582.57 ([M+4]$^+$, 28.40), 580.90 ([M+2]$^+$, 23.47), 578.48 (M$^+$, 32.64), 327.52 (61.54), 307.76 (24.94). Anal. Calcd for $C_{19}H_{11}Br_2N_5O_3S_2$ (581.26): C, 39.26; H, 1.91; N, 12.05; S, 11.03. Found: C, 39.05; H, 1.88; N, 11.98; S, 10.98%.

Ethyl 5-(((*E*)-3,5-Dibromo-2-hydroxybenzylidene)hydrazineylidene)-4-phenyl-4,5-dihydro-1,3,4-thiadiazole-2-carboxylate (10e)

Yellow solid, yield 0.447 g (85%). M.p. 205–207 °C (acetic acid); FT-IR (KBr) ν 3423 (OH), 3110, 3071 (C–H aromatic), 2991, 2922 (CH), 1746 (C=O), 1604 (C=N), 1555 (C=N thiadiazole), 687 (C–S–C) cm^{-1}; ^{1}H NMR (400 MHz, DMSO-d_6) δ 10.89 (s, 1H, OH), 8.65 (s, 1H, CH=N), 7.86 (d, *J* = 8.6 Hz, 2H, Ar-H), 7.80 (d, *J* = 2.2 Hz, 1H, Ar-H), 7.78 (d, *J* = 2.2 Hz, 1H, Ar-H), 7.57 (t, *J* = 7.8 Hz, 2H, Ar-H), 7.46 (t, *J* = 7.4 Hz, 1H, Ar-H), 4.41 (q, *J* = 7.1 Hz, 2H, CH$_2$), 1.34 (t, *J* = 7.1 Hz, 3H, CH$_3$); MS *m/z* (%): 528.22 ([M+4]$^+$, 13.73), 526.46 ([M+2]$^+$, 10.12), 523.90 (M$^+$, 8.77), 362.13 (53.28), 317.37 (100), 298.08 (43.31). Anal. Calcd for $C_{18}H_{14}Br_2N_4O_3S$ (526.20): C, 41.09; H, 2.68; N, 10.65; S, 6.09. Found: C, 41.07; H, 2.66; N, 10.64; S, 6.09%.

1-(5-(((*E*)-3,5-Dibromo-2-hydroxybenzylidene)hydrazineylidene)-4-(*para*-tolyl)-4,5-dihydro-1,3,4-thiadiazol-2-yl)ethan-1-one (10f)

Pale yellow solid, yield 0.405 g (75%). M.p. 220 °C (dioxane); FT-IR (KBr) ν 3423 (OH), 3110, 3071 (C–H aromatic), 2991, 2922 (CH), 1746 (C=O), 1604 (C=N), 1555 (C=N thiadiazole), 687 (C–S–C) cm^{-1}; ^{1}H NMR (400 MHz, DMSO-d_6) δ 10.68 (s, 1H, OH), 8.65 (s, 1H, CH=N), 7.87 (d, *J* = 2.3 Hz, 1H, Ar-H), 7.80 (d, *J* = 2.3 Hz, 1H, Ar-H), 7.72 (d, *J* = 8.3 Hz, 2H, Ar-H), 7.38 (d, *J* = 8.3 Hz, 2H, Ar-H), 4.41 (q, *J* = 7.0 Hz, 2H, CH$_2$), 2.39 (s, 3H, CH$_3$), 1.34 (t, *J* = 7.1 Hz, 3H, CH$_3$); MS *m/z* (%): 541.88 ([M+4]$^+$, 18.7), 539.78 ([M+2]$^+$, 14.33), 537.68 (M$^+$, 28.74), 213.9 (100), 207.93 (43.55). Anal. Calcd for $C_{19}H_{16}Br_2N_4O_3S$ (540.23): C, 42.24; H, 2.99; N, 10.37; S, 5.93. Found C, 42.13; H, 2.95; N, 10.34; S, 5.92%.

1-(5-(((*E*)-3,5-Dibromo-2-hydroxybenzylidene)hydrazineylidene)-4-(*para*-tolyl)-4,5-dihydro-1,3,4-thiadiazol-2-yl)ethan-1-one (10g)

Orange solid, yield 0.459 g (90%). M.p. 285 °C (dioxane); FT-IR (KBr) ν 3422 (OH), 3083 (C–H aromatic), 2920 (CH), 1681 (C=O), 1601 (C=N), 1555 (C=N thiadiazole), 687 (C–S–C) cm^{-1}; ^{1}H NMR (400 MHz, DMSO-d_6) δ 10.71 (s, 1H, OH), 8.67 (s, 1H, CH=N), 7.87 (d, *J* = 2.3 Hz, 1H, Ar-H), 7.80 (d, *J* = 2.3 Hz, 1H, Ar-H), 7.79 (d, *J* = 8.4 Hz, 2H, Ar-H), 7.40 (d, *J* = 8.4 Hz, 2H, Ar-H), 2.59 (s, 3H, CH$_3$), 2.40 (s, 3H, CH$_3$); MS *m/z* (%): 511.29 ([M+4]$^+$, 5.97), 509.52 ([M+2]$^+$, 10.03), 507.33 (M$^+$, 14.58), 467.31 (86.40), 419.28 (100). Anal. Calcd for $C_{18}H_{14}Br_2N_4O_2S$ (510.20): C, 42.37; H, 2.77; N, 10.98; S, 6.28. Found: C, 42.28; H, 2.74; N, 10.96; S, 6.27%.

Synthesis of 6,6'-((1*E*,1'*E*)-((1,4-Phenylenebis(3-phenyl-1,3,4-thiadiazole-5(3*H*)-yl-2(3*H*)-ylidene))bis(hydrazine-2,1-diylidene))bis(methaneylylidene))bis(2,4-dibromophenol) (10h)

To a mixture of appropriate hydrazonoyl halide **6h** (1 mmol), and hydrazine-1-carbodithioate derivative compound **4** (0.768 g, 2 mmol) in ethanol (20 mL), triethylamine (0.5 mL) was added, the mixture was warmed gently and stirred at room temperature for 1 hour.[22] The resulting solid product was collected and recrystallized from dioxane to give the corresponding 1,3,4-thiadiazole derivative **10h**. The physical constants of product **10h** are listed below.

Yellow solid, yield 1.37 g (70%). M.p. >300 °C (dioxane); FT-IR (KBr) ν 3420 (OH), 3064 (C–H aromatic), 2921 (CH), 1603 (C=N), 1554 (C=N thiadiazole), 692 (C–S–C) cm^{-1}; ^{1}H NMR (400 MHz, DMSO-d_6) δ 10.12 (s, 1H, OH), 8.69 (s, 1H, CH=N), 7.95 (s, 2H, Ar-H), 7.86 (d, *J* = 1.5 Hz, 1H, Ar-H), 7.81 (d, *J* = 1.4 Hz, 1H, Ar-H), 7.58 (t, *J* = 7.7 Hz, 2H, Ar-H), 7.39 (d, *J* = 8.0 Hz, 2H, Ar-H), 7.31 (t, *J* = 6.0 Hz, 1H, Ar-H); MS *m/z* (%): 985.85 ([M+8]$^+$, 37.87), 982.66 ([M+4]$^+$, 53.24), 386.73 (100), 339.25 (73.62). Anal. Calcd for $C_{36}H_{22}Br_4N_8O_2S_2$ (982.36): C, 44.02; H, 2.26 ; N, 11.41; S, 6.53. Found: C, 43.86; H, 2.23; N, 11.37; S, 6.51%.

General Procedure for the Synthesis of 1,3,4-Thiadiazole Derivatives 11a–e

To a mixture of appropriate hydrazonoyl halides **6a–e** (1 mmol) and hydrazine-1-carbodithioate derivative compound **5** (0.422 g, 1 mmol) in ethanol (20 mL), triethylamine (0.5 mL) was added, the mixture was warmed gently and stirred at room temperature for 1 hour.[22] The resulting solid product was collected and recrystallized from the appropriate solvent to give the corresponding 1,3,4-thiadiazoles **11a–e**. The physical constants of products **11a–e** are listed below.

((*E*)-5-(((*E*)-1-(5,7-Dibromobenzofuran-2-yl)ethylidene)hydrazineylidene)-4-phenyl-4,5-dihydro-1,3,4-thiadiazol-2-yl)(phenyl)methanone (11a)

Brown solid, yield 0.524 g (88%). M.p. 145–146 °C (acetic acid); FT-IR (KBr) ν 3066, 3024 (C–H Ar), 2918, 2852 (C–H), 1728 (C=O), 1599 (C=N), 1582 (C=N thiadiazole), 686 (C–S) cm^{-1}; ^{1}H NMR (400 MHz, DMSO-d_6) δ 8.10 (d, *J* = 1.7 Hz, 1H, Ar-H), 8.01 (d, *J* = 1.7 Hz, 1H, Ar-H), 7.95 (s, 2H, Ar-H), 7.78 (d, *J* = 6.0 Hz, 2H, Ar-H), 7.63–7.58 (m, 3H, Ar-H), 7.54 (s, 1H, Ar-H), 7.43–7.37 (m, 3H, Ar-H), 2.43 (s, 3H, CH$_3$); MS *m/z* (%): 597.94 ([M+4]$^+$, 18.05), 596.39 ([M+2]$^+$, 24.62), 594.17 (M$^+$, 24.75), 300.17 (100), 277.25 (57.98). Anal. Calcd for $C_{25}H_{16}Br_2N_4O_2S$ (596.30): C, 50.36; H, 2.70; N, 9.40; S, 5.38. Found C, 50.22; H, 2.68; N, 9.37; S, 5.36%.

(*Z*)-4-(4-Chlorophenyl)-5-(((*E*)-1-(5,7-dibromobenzofuran-2-yl)ethylidene)hydrazineylidene)-*N*-phenyl-4,5-dihydro-1,3,4-thiadiazole-2-carboxamide (11b)

Green solid, yield 0.497 g (77%). M.p. 200–203 °C (acetic acid); FT-IR (KBr) ν 3390 (NH), 3106, 3073 (C–H aromatic), 2954, 2922 (C–H), 1691 (C=O), 1598 (C=N), 1578 (C=N thiadiazole), 686 (C–S) cm^{-1}; ^{1}H NMR (400 MHz, DMSO-d_6) δ 10.75 (s, 1H, NH), 8.29 (d, *J* = 9.0 Hz, 2H, Ar-H), 7.92 (d, *J* = 1.7 Hz, 1H, Ar-H), 7.80 (d, *J* = 1.7 Hz, 1H, Ar-H), 7.76 (d, *J* = 7.4 Hz, 2H, Ar-H), 7.65 (d, *J* = 9.0 Hz, 2H, Ar-H), 7.53 (s, 1H, Ar-H), 7.40 (t, *J* = 7.8 Hz, 2H, Ar-H), 7.18 (t, *J* = 7.4 Hz, 1H, Ar-H), 2.43 (s, 3H, CH$_3$); MS *m/z* (%): 646.95 ([M+4]$^+$, 19.56), 643.51 ([M+2]$^+$, 8.54), 642.61 (M$^+$, 34.29), 334.94 (100), 263.22

(44.32). Anal. Calcd for $C_{25}H_{16}Br_2ClN_5O_2S$ (645.75): C, 46.50; H, 2.50; N, 10.85; S, 4.96. Found: C, 46.41; H, 2.47; N, 10.83; S, 4.96%.

2-(((*E*)-1-(5,7-Dibromobenzofuran-2-yl)ethylidene) hydrazineylidene)-3-phenyl-5-(*para*-tolyl)-2,3-dihydro-1,3,4-thiadiazole (11c)

Yellow solid, yield 0.454 g (78%). M.p. >300 °C (dioxane); FT-IR (KBr) ν 3066, 3024 (C–H aromatic), 2918, 2852 (C–H), 1599 (C=N), 1582 (C=N thiadiazole), 683 (C–S) cm^{-1}; ^1H NMR (400 MHz, DMSO-d_6) δ 8.15 (d, *J* = 8.4 Hz, 2H, Ar-H), 8.04 (d, *J* = 8.4 Hz, 2H, Ar-H), 7.87 (d, *J* = 1.8 Hz, 1H, Ar-H), 7.83 (d, *J* = 1.8 Hz, 1H, Ar-H), 7.79 (d, *J* = 7.9 Hz, 2H, Ar-H), 7.70 (t, *J* = 7.9 Hz, 2H, Ar-H), 7.58 (t, *J* = 7.9 Hz, 1H, Ar-H), 7.51 (s, 1H, Ar-H), 2.44 (s, 3H, CH_3), 2.39 (s, 3H, CH_3); MS *m/z* (%): 584.98 ($[M+4]^+$, 24.67), 582.97 ($[M+2]^+$, 18.12), 580.05 (M^+, 25.19), 264.08 (100), 190.92 (64.69). Anal. Calcd for $C_{25}H_{18}Br_2N_4O_2S$ (582.31): C, 51.57; H, 3.12; N, 9.62; S, 5.51. Found: C, 51.33; H, 3.08; N, 9.58; S, 5.48 %.

(*E*)-2-(((*E*)-1-(5,7-Dibromobenzofuran-2-yl) ethylidene)hydrazineylidene)-5-(furan-2-yl)-3-(4-nitrophenyl)-2,3-dihydro-1,3,4-thiadiazole (11d)

Brown solid, yield 0.464 g (77%). M.p. >300 °C (dioxane); FT-IR (KBr) ν 3114, 3070 (C–H aromatic), 2920 (C–H), 1604 (C=N), 1593 (C=N thiadiazole), 683 (C–S) cm^{-1}; ^1H NMR (400 MHz, DMSO-d_6) δ 8.53 (d, *J* = 9.2 Hz, 2H, Ar-H), 8.44 (d, *J* = 9.3 Hz, 2H, Ar-H), 8.10 (d, *J* = 1.7 Hz, 1H, Ar-H), 8.01 (d, *J* = 1.7 Hz, 1H, Ar-H), 7.95 (dd, *J* = 3.5, 1.7 Hz, 1H, furan-H), 7.83 (d, *J* = 1.7 Hz, 1H, furan-H), 7.57 (s, 1H, Ar-H), 7.35 (d, *J* = 3.5 Hz, 1H, furan-H), 2.58 (s, 3H, CH_3); MS *m/z* (%): 604.78 ($[M+4]^+$, 22.44), 602.98 ($[M+2]^+$, 18.11), 600.15 (M^+, 26.02), 436.93 (98.87), 391.31 (52.40). Anal.Calcd for $C_{22}H_{13}Br_2N_5O_4S$ (603.25): C, 43.80; H, 2.17; N, 11.61; S, 5.31. Found: C, 43.75; H, 2.15; N, 11.60; S, 5.31%.

4-((*E*)-5-(((*E*)-1-(5,7-Dibromobenzofuran-2-yl) ethylidene)hydrazineylidene)-4-phenyl-4,5-dihydro-1,3,4-thiadiazol-2-yl)-*N*-phenylbenzohydrazonoyl Chloride (11e)

Orange solid, yield 0.540 g (75%). M.p. 220 °C (chloroform); FT-IR (KBr) ν 3317 (NH), 3078, 3052 (C–H aromatic), 2918 (C–H), 1600 (C=N), 1573 (C=N thiadiazole), 692 (C–S) cm^{-1}; ^1H NMR (400 MHz, DMSO-d_6) δ 10.02 (s, 1H, NH), 8.10 (d, *J* = 8.7 Hz, 2H, Ar-H), 8.05 (d, *J* = 8.7 Hz, 2H, Ar-H), 7.86 (d, *J* = 1.7 Hz, 1H, Ar-H), 7.83 (d, *J* = 1.7 Hz, 1H, Ar-H), 7.53 (s, 1H, Ar-H), 7.38 (d, *J* = 7.8 Hz, 4H, Ar-H), 7.29 (t, *J* = 7.9 Hz, 4H, Ar-H), 6.89 (t, *J* = 7.2 Hz, 2H, Ar-H), 2.40 (s, 3H, CH_3); MS *m/z* (%): 721.27 ($[M+4]^+$, 17.82), 718.83 ($[M+2]^+$, 15.17), 717.99 (M^+, 39.38), 618.66 (65.29), 84.21 (100). Anal.Calcd for $C_{31}H_{21}Br_2ClN_6OS$ (720.87): C, 51.65; H, 2.94; N, 11.66; S, 4.45. Found: C, 51.62; H, 2.91; N, 11.65; S, 4.45%.

2. 2. Antimicrobial Activity Assay

The newly synthesized compounds were tested *in vitro* for antimicrobial activity against strains of pathogenic microorganisms, namely *Staphylococcus aureus* ATCC 6538-P (Gram-positive bacterium), *Escherichia coli* ATCC 25933 (Gram-negative bacterium), *Candida albicans* ATCC 10231 and *Aspergillus niger* NRRL-A326 (unicellular and multicellular fungi) using an agar well diffusion method.[23] Neomycin and cycloheximide were used as the standard antimicrobial drugs. Nutrient agar (NA) plates were inoculated deeply with 0.1 mL of 10^5–10^6 cells/mL for bacteria and yeast. Potato dextrose agar (PDA) plates were densely seeded with 0.1 mL (10^6 cells/mL) of fungal inoculum to assess antifungal activities. Compounds were prepared by dissolving 10 mg of the compound in 2 mL of dimethyl sulfoxide (DMSO).[24] The plates were desiccated, and a sterilized cork borer (7 mm in diameter) was used for punching the wells (2 wells) in agar medium. Wells were filled with 100 µL of each compound and allowed to diffuse at room temperature for 1 hour, then the plates were placed in an incubator at 37 °C for 24 hours in the case of bacteria and at 27 °C for 48–72 hours in the case of fungi. After the incubation, the plates were observed for the formation of a clear inhibition zone around the well indicating the presence of antimicrobial activity. The absence of a clear zone around the well was taken as inactivity. The DMSO solvent was used as a negative control. The resulting diameters of zones of inhibition, including the diameter of the well, were measured using a ruler and reported in millimeters. To maintain the consistency of measurements, each zone of inhibition was measured twice (one vertical and one horizontal measurement), and the average value was taken. The experiment was performed in triplicate.[25]

2. 3. Determination of Minimal Inhibitory Concentration (MIC) and Minimum Bactericidal/Fungicidal Concentration (MBC/MFC)

Test Microbes

Three pathogenic microbial strains: *Staphylococcus aureus* ATCC 6538, *Escherichia coli* ATCC 25933 and *Candida albicans* ATCC 10231. The tested microbes are grown on Mueller Hinton Agar (MHA) and Sabouraud Dextrose Agar (SDA).

Preparation of Microbial Culture

Clean microbial cells were prepared by cultivated test microbes in 100 mL bottles capped and incubated at 37 °C for 24 hours in the case of bacteria and 48 hours in the case of yeast. Cells were obtained under sterile conditions, in a cooling centrifuge at 4000 rpm for 15 min. The cells were washed using 20 mL of sterile normal saline until the supernatant was clear. The optical density of the microbial suspension was measured at 500 nm, and serial dilutions were carried out with appropriate aseptic techniques until the optical density was in the range of 0.5–1.0. The actual number of colony-forming units was carried out to obtain a concentration of $5 \cdot 10^6$ cfu/mL.

Preparation of Resazurin Solution

The resazurin solution was prepared by dissolving a 270 mg tablet in 40 mL of sterile distilled water and shaken well with vortex mixer and sterilized by filtration through a membrane filter (pore size of 0.22–0.45 μm).

Preparation of the Plates

Microplates with 96 wells were prepared and labeled under aseptic conditions. A volume of 500 μL of test material in DMSO (a stock concentration of 5 mg/mL for purified compounds) was pipetted into the first row of the plate. To all other wells 50 μL of broth medium was added. Serial dilutions were performed. To each well 10 μL of resazurin indicator solution was added, and 10 μL of microbial suspension ($5 \cdot 10^6$ cfu/mL) was added to each well. Each plate was wrapped loosely with parafilm to ensure that microbes did not become dehydrated. The plates were placed in an incubator at 37 °C for 24 hours in the case of bacteria and for 48 hours in the case of yeast. The color change was then assessed visually. Any color changes from purple to pink or colorless were recorded as positive. The lowest concentration at which color change occurred was taken as the MIC.[26]

Determination of Minimum Bactericidal Concentrations (MBC) of Each Compound

Streaks were taken from the two concentrations higher than MIC and the plates exhibiting no growth were considered as MB.[27,28]

Determination of Minimum Fungicidal Concentrations (MFC)

Minimal fungicidal concentrations were determined according to the reported literature.[29] Briefly, MFC was evaluated by transporting 100 μL from all clear MIC wells (no growth seen in microdilution trays) onto Sabouraud agar (SDA) plates. The MFC was the lowest sample concentration that killed ≥ 99.9% of *Candida* cells.

3. Results and Discussion

3. 1. Chemistry

The objective of this research was to synthesize novel heterocyclic compounds derived from 3,5-dibromosalicylaldehyde compound **2**. This compound was prepared by reacting salicylaldehyde with an equivalent amount of liquid bromine in the presence of acetic acid, as illustrated in Scheme 1. The structure of compound **2** was confirmed through spectral data analysis; thus, the IR spectrum displayed a broad absorption band at 3347 cm^{-1} which corresponds to the OH group, a strong band at 1680 cm^{-1} which is attributable to the carbonyl group. ^{1}H NMR spectrum data showed two doublets at δ 7.95 and 7.83 ppm with J_{meta} = 2.4 Hz, each one integrating for one proton; mass spectrum data confirmed molecular weight with a molecular ion peak at 278.08 (M$^+$), 281.87 (M+4) and 279.61 (M+2) peaks which are attributed to bromine isotopes 81 and 79, respectively. Chloroacetone was added to a mixture of compound **2** and ethanolic potassium hydroxide solution to afford compound **3**. The IR spectrum displayed no absorption bands in the region corresponding to the OH group, a strong band at 1692 cm^{-1} which is attributable to the carbonyl group. ^{1}H NMR spectrum data showed a singlet at δ 7.92 ppm which corresponds to one aromatic proton of the furan ring; also one singlet appeared at δ 2.58 ppm integrated for three protons of the ketonic methyl group; ^{13}C NMR showed a ketonic carbonyl signal at 188 ppm and methyl group at 27 ppm; mass spectrum data

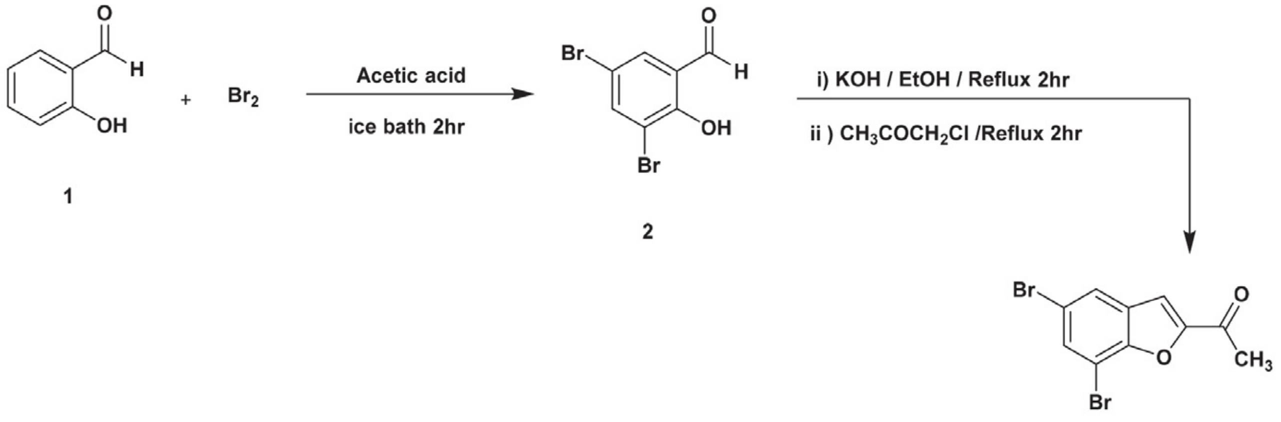

3

Scheme 1. Synthesis of 3,5-dibromo-2-hydroxybenzaldehyde (**2**) and 1-(5,7-dibromobenzofuran-2-yl) ethan-1-one (**3**) confirmed molecular weight with a molecular ion peak at 315 (M^+), 319 (M+4) and 317 (M+2) peaks which are attributed to bromine isotopes 81 and 79, respectively

Compound **2** was reacted with alkyl carbodithioate in 2-propanol to yield the corresponding methyl (*E*)-2-(3,5-dibromo-2-hydroxybenzylidene)hydrazine-1-carbodithioate **4**. Treatment of this compound with the appropriate hydrazonoyl chlorides **6a**–**h** in ethanolic triethylamine produced 1,3,4-thiadiazole derivatives **10a**–**h** (Scheme 2). The reaction mechanism outlined in Scheme 3 involves three steps: first, 1,3-addition of the C=S thiol tautomer to the nitrilimine **7** produces the thiohydrazonate ester **8** which subsequently undergoes nucleophilic cyclization to afford compound **9**. The latter compound is readily converted to final products **10,11**[30] through the elimination of alkylthiol. Structures **10a**–**h** were elucidated on the basis of spectral data: IR spectrum displayed absorption bands in the range of 3382–3444 cm^{-1}, corresponding to OH groups, strong bands at 1601–16081 cm^{-1} suggesting the presence of a C=N bond. Additionally, bands at 1544–1590 cm^{-1} were attributed to C=N in the thiadiazole ring. ^1H NMR spectral data showed singlet for the OH proton in the range δ 10.68–11.38 ppm for compounds **10a**–**h**. OH proton of compounds **10b** and **10d** exhibited a downfield signal at δ 11.38 and 11.37 ppm, respectively. Another singlet appeared in the range of δ 8.65–8.80 ppm, attributable to the sp^2 proton (H–C=N). Compounds **10a** and **10c** showed singlets at δ 8.70 ppm and δ 8.66 ppm, respectively, corresponding to the H–N proton. Mass spectra confirmed the molecular weight with molecular ionic peak (M^+), (M+4) and (M+2) peaks attributed to bromine isotopes 81 and 79, respectively.

Analogously, treatment of compound **3** with the appropriate hydrazonoyl chlorides **6a**–**e** in ethanolic triethylamine at room temperature afforded 1,3,4-thiadiazole derivatives **11a**–**e**, respectively (Scheme 4).

Structures **11a**–**e** were elucidated on the basis of their spectral data. The IR spectra showed no absorption bands in the region corresponding to carbonyl groups, while strong absorption bands in the range 1604–1599 cm^{-1} confirmed the presence of a C=N group, and bands at 1582–1598 cm^{-1} were attributed to C=N in thiadiazole ring. The ^1H NMR spectra displayed clear singlets in the range of δ 2.40–2.58 ppm for CH_3 protons, along with another singlet in the range of δ 7.50–7.57ppm corresponding to the benzofuran ring. Additionally, compounds **11b** and **11e** exhibited singlets at δ 10.75 and 10.02 ppm for NH proton. Mass spectra showed ion peaks (M+4) and

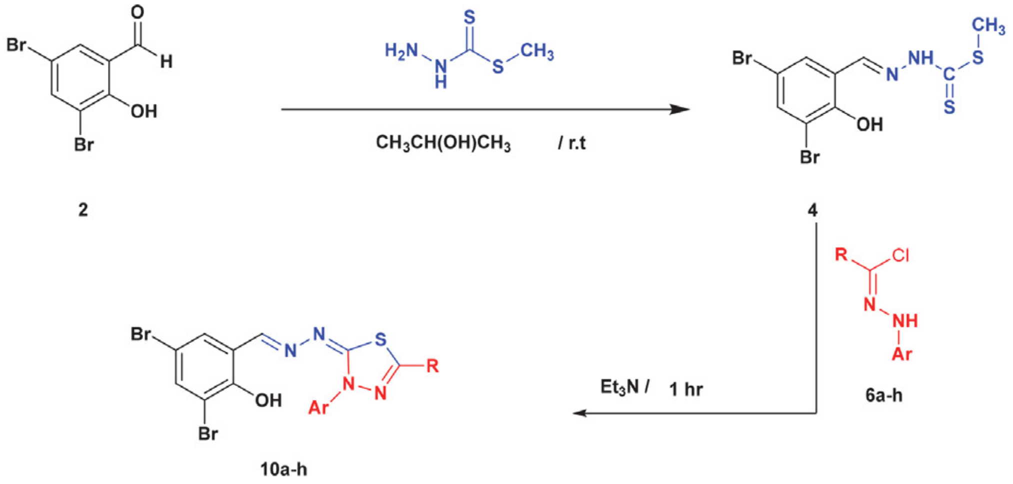

Compound 6,10	R	Ar
a	$CONHC_6H_5$	$4\text{-}ClC_6H_4$
b	C_4H_3O	$4\text{-}NO_2C_6H_4$
c	$CONHC_6H_5$	C_6H_5
d	C_4H_3S	$4\text{-}NO_2C_6H_4$
e	$COOC_2H_5$	C_6H_5
f	$COOC_2H_5$	$4\text{-}CH_3C_6H_4$
g	$COCH_3$	$4\text{-}CH_3C_6H_4$
h	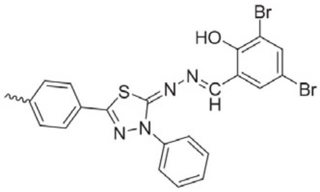	C_6H_5

Scheme 2. Synthesis of 1,3,4-thiadiazoles **10a**–**h**

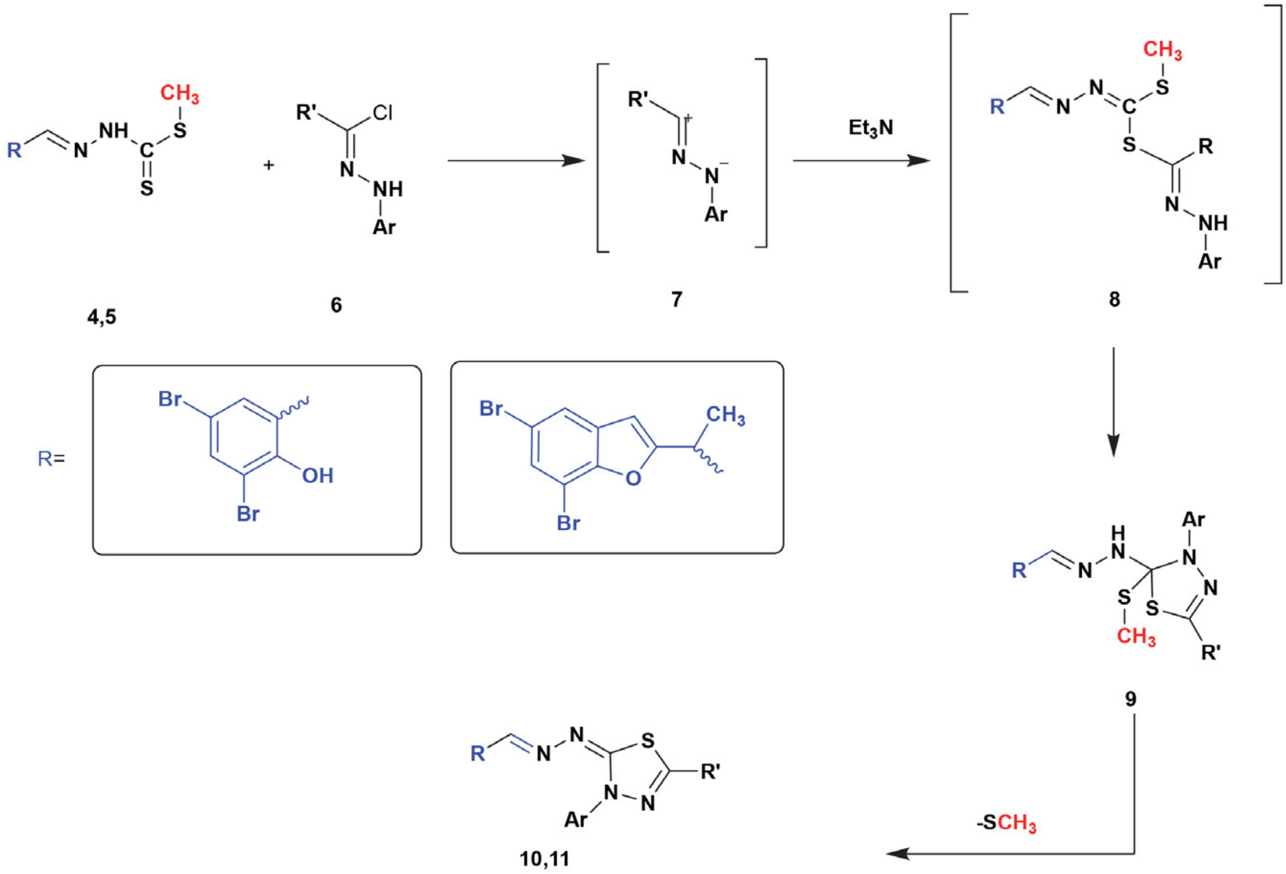

Scheme 3. Proposed mechanistic pathway for the formation of 1,3,4-thiadiazoles **10,11**

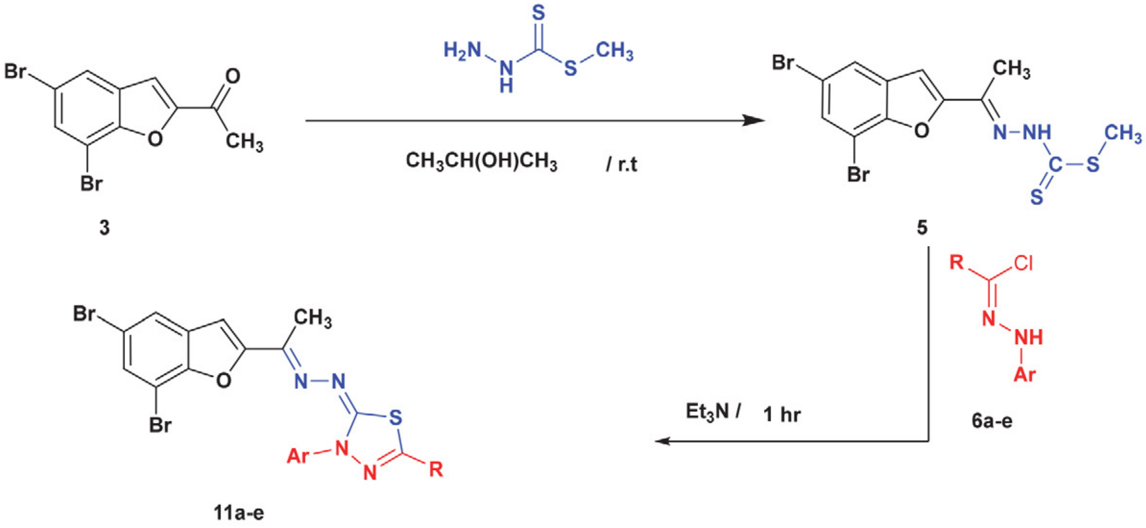

Compounds 6,11	R	Ar
a	COC_6H_5	C_6H_5
b	$CONHC_6H_5$	$4\text{-}ClC_6H_4$
c	$4\text{-}CH_3C_6H_4$	C_6H_5
d	C_4H_3O	$4\text{-}NO_2C_6H_4$
e	$4\text{-}C_6H_4NHNCClC_6H_5$	C_6H_5

Scheme 4. Synthesis of 1,3,4-thiadiazoles **11a–e**

(M+2) which are attributed to bromine isotopes 81 and 79, respectively.

3. 2. Biological Evaluation

In vitro Antimicrobial Activity

Using an agar well diffusion method, the newly synthesized 1,3,4-thiadiazole derivatives were investigated to evaluate their antimicrobial activity against *S. aureus* ATCC 6538-P, *E. coli* ATCC 25933, *C. albicans* ATCC 10231, and *A. niger* NRRL-A326. The inhibition zone diameter was observed for the synthesized compounds and the positive control, but not for the negative control. Evaluation of the antimicrobial activity of these newly synthesized compounds is presented in Table 1 and shown in Figure 3. It has been found that compound **10e** exhibited the highest activity against all tested microbial strains: *S. aureus* ATCC 6538-P, *E. coli* ATCC 25933, *C. albicans* ATCC 10231, and *A. niger* NRRL-A326, with inhibition zone diameters (IZDs) of 29, 28, 27, and 25 mm, respectively (Supplementary Information, Figure **52**). Compounds **10a**, **10f**, and **10h** showed moderate activity against all tested microbial strains; the IZDs were 18, 17, and 18 mm on *S. aureus* ATCC 6538-P, and 17, 19, and 21 mm on *E. coli* ATCC 25933, while the IZDs were 21, 16, and 20 mm on *C. albicans* ATCC 10231, and 11, 16, and 12 mm on *A. niger* NRRL-A326. Additionally, it was found that compound **10c** showed activity only against the tested bacterial strains but showed no inhibitory effect against the tested fungal strains. Compound **10d** showed low activity against *S. aureus* ATCC 6538-P and *C. albicans* ATCC 10231 with IZDs of 8 and 9 mm, but showed no inhibitory effect against *E. coli* ATCC 25933 and *A. niger* NRRL-A326. On the other hand, compounds **10b** and **10g** showed no activity against any of the tested microbial strains. Compound **10e** was more potent than the selected standard antibiotics, while other compounds were less effective.

The results listed in Table 1 show that compounds **10a**, **10e**, **10f**, and **10h** were the most effective against three tested microbial strains (*S. aureus* ATCC 6538-P, *E. coli* ATCC 25933, and *C. albicans* ATCC 10231); therefore, to determine the minimum inhibitory concentration (MIC) and minimum bactericidal/fungicidal concentration (MBC/MFC) against these microbial strains, experiments on these four compounds (**10a**, **10e**, **10f**, and **10h**) were conducted.

The MIC and MBC/MFC results are reported in Table 2 and in the Figure 4. The MIC values for compounds **10a**, **10e**, **10f**, and **10h** were 78.28, 2.58, 77.43, and 313.47 μg/mL, respectively, against *S. aureus* ATCC 6538-P, and 156.30, 4.88, 155.87, and 313.16 μg/mL against *E. coli* ATCC 25933, while they reached 39.14, 2.56, 78.30, and 156.25 μg/mL, respectively, against *C. albicans* ATCC 10231.

The MBC values for compounds **10a**, **10e**, **10f**, and **10h** were 313.68, 4.03, 158.33, and 627.11 μg/mL, respec-

Table 1. Zones of inhibition of the synthesized 1,3,4-thiadiazole derivatives, neomycin and cyclohexamide against tested microbial strains.

	Inhibition zone measured in millimeters			
Compound no.	***S. aureus* ATCC 6538-P**	***E. coli* ATCC 25933**	***C. albicans* ATCC 10231**	***A. niger* NRRL-A326**
10a	18.50 ± 0.50	17.33 ± 0.58	21.33 ± 0.58	11.00 ± 1.00
10b	00.00 ± 0.00	00.00 ± 0.00	00.00 ± 0.00	00.00 ± 0.00
10c	15.75 ± 0.66	12.67 ± 0.58	00.00 ± 0.00	00.00 ± 0.00
10d	08.33 ± 0.58	00.00 ± 0.00	09.33 ± 0.58	00.00 ± 0.00
10e	29.00 ± 1.00	28.17 ± 0.29	27.33 ± 0.58	25.67 ± 0.00
10f	17.67 ± 0.58	19.00 ± 1.00	16.67 ± 0.58	16.33 ± 0.58
10g	00.00 ± 0.00	00.00 ± 0.00	00.00 ± 0.00	00.00 ± 0.00
10h	18.67 ± 0.58	21.67 ± 0.58	20.00 ± 0.00	12.67 ± 0.58
C$^+$ Neomycin[17] *Cycloheximid^{e1}8	27	25	28	*22
C$^-$ DMSO	0	0	0	0

C$^+$: Positive control, C$^-$: Negative control.

Table 2. MIC and MBC/MFC of the synthesized 1,3,4-thiadiazole derivatives against highly susceptible microbial strains.

Compounds	***S. aureus* ATCC 6538-P**		***E. coli* ATCC 25933**		***C. albicans* ATCC 10231**	
	MIC (μg/mL)	**MBC (μg/mL)**	**MIC (μg/mL)**	**MBC (μg/mL)**	**MIC (μg/mL)**	**MFC (μg/mL)**
10a	78.28 ± 1.07	313.68 ± 0.89	156.30 ± 0.96	314.08 ± 0.84	39.14 ± 0.93	156.46 ± 0.77
10e	2.58 ± 0.51	4.03 ± 0.55	4.88 ± 1.10	8.86 ± 0.98	2.567 ± 0.53	19.49 ± 1.07
10f	77.43 ± 1.08	158.33 ± 1.05	155.87 ± 1.47	311.68 ± 1.68	78.30 ± 1.08	156.36 ± 0.96
10h	313.47 ± 0.86	627.11 ± 1.61	313.16 ± 2.55	314.68 ± 1.07	156.25 ± 1.00	312.66 ± 1.09

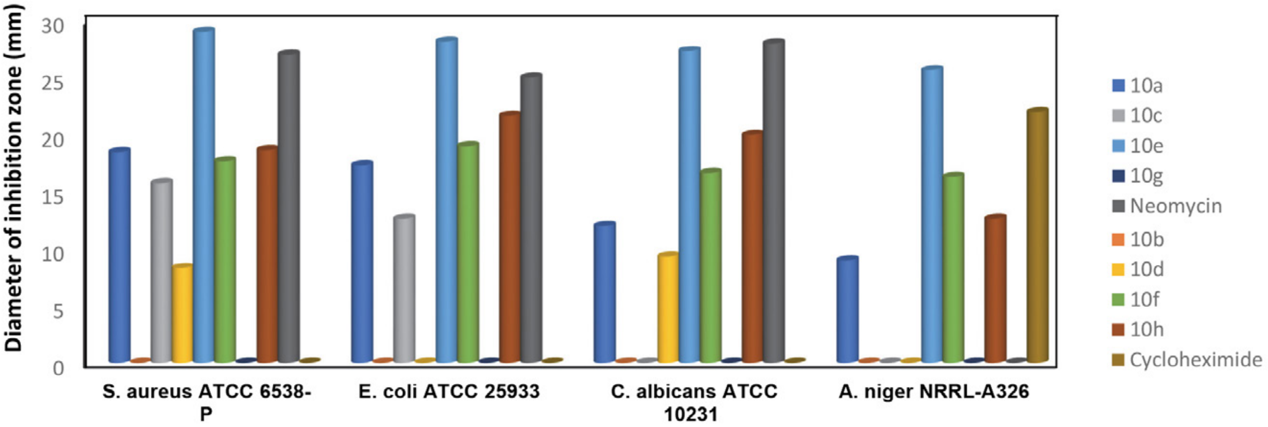

Figure 3. Effect of the synthesized 1,3,4-thiadiazole derivatives, neomycin and cyclohexamide against tested microbial strains.

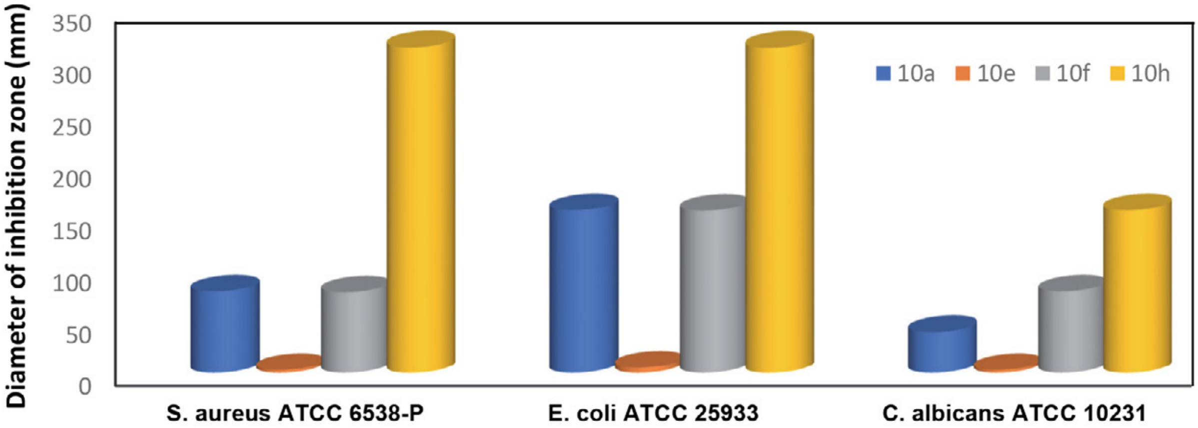

Figure 4. MIC of the synthesized 1,3,4-thiadiazole derivatives against highly susceptible microbial strains.

tively, against *S. aureus* ATCC 6538-P, and 314.08, 8.86, 311.68, and 314.68 µg/mL, respectively, against *E. coli* ATCC 25933. The MFC values for compounds **10a**, **10e**, **10f**, and **10h** were 156.46, 19.49, 156.36, and 312.66 µg/mL, respectively, against *C. albicans* ATCC 10231.

4. References

1. Y. Li, J. Geng, Y. Liu, S. Yu, G. Zhao, *Chem. Med. Chem*. **2013**, *8*, 27–41. **DOI:**10.1002/cmdc.201200355
2. M. N. Noolvi, H. M. Patel, S. Kamboj, S. S. Cameotra, *Arabian J. Chem*. **2016**, *9*, S1283–S1289. **DOI:**10.1016/j.arabjc.2012.02.003
3. G. de Andrade Danin Barbosa, A. P. de Aguiar, *Rev. Virtual Quim*. **2019**, *11*, 806–848. **DOI:**10.21577/1984-6835.20190058
4. C. B. Chapleo, P. L. Myers, A. C. B. Smith, I. F. Tulloch, D. S. Walter, *J. Med. Chem*. **1987**, *30*, 951–954. **DOI:**10.1021/jm00388a038
5. Y. Song, D. T. Connor, A. D. Sercel, R. J. Sorenson, R. Doubleday, P. C. Unangst, B. D. Roth, V. G. Beylin, R. B. Gilbertsen, K. Chan, D. J. Schrier, A. Guglietta, D. A. Bornemeier, R. D. Dyer, *J. Med. Chem*. **1999**, *42*, 1161–1169. **DOI:**10.1134/S1070428008060158
6. M. D. Mullican, M. W. Wilson, D. T. Connor, C. R. Kostlan, D. J. Schrier, R. D. Dyer, *J. Med. Chem*. **1993**, *36*, 1090–1099. **DOI:**10.1021/jm00060a017
7. L. Labanauskas, V. Kalcas, E. Udrenaite, P. Gaidelis, A. Brukstus, V. Dauksas, *Pharmazie*. **2001**, *56*, 617—619. **DOI:**10.3390/12010103
8. C. B. Chapleo, P. L. Myers, J. F. Saville, A. C. B. Smith, M. R. Stillings, I. F. Tulloch, D. S. Walter, A. P. Welbourn, M. Myers, *J. Med. Chem*. **1986**, *29*, 2273–2280. **DOI:**10.1021/jm00161a024
9. Y. Murti, T. Agrawal, D. Pathak, *Indian Drugs*. **2010**, *47*, 19–27. **DOI:**10.1007/s13312-010-0036-z
10. S. Turner, M. Myers, B. Gadie, A. J. Nelson, R. Pape, J. F. Seville, J. C. Doxey, T. L. Berridge, *J. Med. Chem*. **1988**, *31*, 902–906. **DOI:**10.1021/jm00212a014
11. G. Mazzone, R. Pignatello, S. Mazzone, A. Panico, G. Pennisi, R. Castana, P. Mazzone, *Farmaco*. **1993**, *48*, 1207–1224. **DOI:**10.1016/0014-827X(93)90007-4
12. J. Zhao, L. Xuan, H. Zhao, J. Cheng, X. Fu, S. Li, F. Jing, Y. Liu,

B. Chen, *Chem. Res. Chin. Univ*. **2014**, *30*, 764–769. **DOI:**10.1007/s40242-014-4080-4

13. D. Kumar, N. Maruthi Kumar, K. H. Chang, K. Shah, *Eur. J. Med. Chem*. **2010**, *45*, 4664–4668. **DOI:**10.1016/j.bmcl.2011.07.089
14. G. Serban, *Molecules*. **2020**, *25*, 942. **DOI:**10.3390/molecules25040942
15. M. Haroon, M. Khalid, T. Akhtar, M. N. Tahir, M. U. Khan, S. Muhammad, A. G. Al-Sehemi, S. Hameed, *J. Mol. Struct*. **2020**, *1202*, 127354. **DOI:**10.1016/j.molstruc.2019.127354
16. P. Wolko, *Can. J. Chem.***1975**, *53*, 1–23. **DOI:**10.1139/v75-183
17. A. R. Sayed, S. S. Al-Shihry, M. A.-M. Gomaa, *Eur. J. Chem*. **2014**, *5*, 267–271. **DOI:**10.5155/eurjchem.5.2.267-271.913
18. A. S. A. S. Shawali, A. Osman, *Tetrahedron*. **1971**, *27*, 2517–2528. **DOI:**10.1016/S0040-4020(01)90753-7
19. A. S. Shawali, A. O. Abdelhamid, *Bull. Chem. Soc. Jpn*. **1976**, *49*, 321–324. **DOI:**10.3390/molecules21070929
20. C. M. Brewster, *J. Am. Chem. Soc*. **1964**, *277*, 2463–2468.
21. Ng. Ph. Buu-Hoï, Ng. Hoán, M. R. Khenissi, *J. Chem. Soc.* **1951**, 2307–2309. **DOI:**10.1039/JR9510002307
22. A. O. Abdelhamid, S. M. Gomha, N. A. Abdelrehem, A. M. Shalaby, S. M. Kandeel, *Synth. Commun*. **2018**, *48*, 677–684. **DOI:**10.3390/molecules27206977
23. B. Athanassiadis, P. V Abbott, N. George, L. J. Walsh, *Aust. Dent. J.* **2009**, *54*, 141–146. **DOI:**10.1111/j.1834-7819.2009.01107.x
24. E. Tamam, A. A. Fadda, E. R. El-Sawy, M. S. Abdel-Aziz, E. H. Tawfik, *ChemistrySelect*. **2023**, *8*, e202302468. **DOI:**10.1002/slct.202302468
25. M. M. Miloud, N. A. Senussi, *Acad. J. Microbiol. Res.* **2020**, *9*, 13–20. **DOI**:10.15413/ajmr.2020.1101
26. N. Ryad, A. A. Elmaaty, S. Selim, M. S. Almuhayawi, S. K. Al Jaouni, M. S. Abdel-Aziz, A. S. Alqahtani, I. Zaki, L. M. A. Abdel Ghany, *RSC Adv.* **2024**, *14*, 34005–34026. **DOI:**10.1039/D4RA06712F
27. H. M. Abo-Salem, H. A. Abd El Salam, A. M. Abdel-Aziem, M. S. Abdel-Aziz, E. R. El-Sawy, *Molecules*. **2021**, *26*, 4112. **DOI:**10.3390/molecules26144112
28. S. D. Sarker, L. Nahar, Y. Kumarasamy, *Methods*. **2007**, *42*, 321–324. **DOI:**10.1016/j.ymeth.2007.01.006
29. E. Cantón, J. Pemán, M. Gobernado, A. Viudes, A. Espinel-Ingroff, *Antimicrob. Agents. Chemother*. **2004**, *48*, 2477–2482. **DOI:**10.1128/AAC.48.7.2477-2482.2004
30. A. O. Abdelhamid, S. M. Gomha, N. A. Abdelrehem, A. M. Shalaby, S. M. Kandeel, *Synth. Commun*. **2018**, *48*, 677–684. **DOI:**10.3390/molecules27206977

Povzetek

S pomočjo heterociklizacije metil 2-(3,5-dibromo-2-hidroksibenziliden)hidrazin-1-karboditioata (**4**) oz. metil (*E*)-2-(1-(5,7-dibromobenzofuran-2-il)etiliden)hidrazin-1-karboditioata (**5**) z različnimi hidrazonoil kloridi smo pripravili dve seriji novih 1,3,4-tiadiazolskih derivatov. Strukture novih produktov smo določili s pomočjo elementne analize in spektroskopskih podatkov. Osmim novim spojinam iz prve serije (ki vsebuje dibromohidroksibenzenski fragment) smo določili antimikrobno delovanje proti: *Staphylococcus aureus* ATCC 6538-P (kot primer Gram-pozitivne bakterije), *Escherichia coli* ATCC 25933 (Gram-negativna bakterija), *Candida albicans* ATCC 10231 (kvasovka) in glivi *Aspergillus niger* NRRL-A326 ter dobljene rezultate primerjali z vrednostmi za standardno referenčno učinkovino neomicin (v primeru *S. aureus, E. coli* and *C. albicans*) oz. cikloheksamid (v primeru glive *A. niger*). Rezultati kažejo, da imajo nekatere izmed novih spojin obetavne antimikrobne lastnosti.

DOI: 10.17344/acsi.2025.9331

Scientific paper

Evaluating the Cytotoxic Effects of Some Chlorinated Substituted 2-Amino-3-carbonitrile Chromene Derivatives on 3T3 and MCF-7 Cell Lines

**Mehdi Abaszadeh,[1] Arghavan Arjomand Kermani,[1,2,a] Ali Armin,[1,2,a]
Yasaman Abolhassani,[1,a] Fatemeh Haghani,[1,3] Salehe Sabouri,[3,4]
Bagher Amirheidari,[3,4] Behzad Behnam[5,6,*]**

[1] *Pharmaceutics Research Center, Institute of Neuropharmacology, Kerman University of Medical Sciences, Kerman, Iran.*

[2] *Students Research Committee, Faculty of pharmacy, Kerman University of Medical Sciences, Kerman, Iran*

[3] *Extremophile and Productive Microorganisms Research Center Kerman University of Medical Sciences, Kerman, Iran.*

[4] *Department of Pharmaceutical Biotechnology, Faculty of Pharmacy Kerman University of Medical Sciences, Kerman, Iran*

[5] *Herbal and Traditional Medicines Research Center, Kerman University of Medical Sciences, Kerman, Iran*

[6] *Pharmaceutical Sciences and Cosmetic Products Research Center, Kerman University of Medical Sciences, Kerman, Iran*

[a] *These authors contributed equally to this work as the second authors.*

* *Corresponding author: E-mail: behnamb@kmu.ac.ir, or Behzad.bp@gmail.com*

Received: 05-21-2025

Abstract

Cancer remains a leading cause of death worldwide, necessitating novel therapeutic approaches. In this study we synthesized and characterized 2-amino-3-carbonitrile chromene derivatives and evaluated their cytotoxic effects on 3T3 and MCF-7 cell lines. Characterization included melting point, IR, NMR, and *elemental analysis***.** Cytotoxicity was assessed via MTT assay, with IC_{50} values calculated, while apoptosis induction was confirmed by flow cytometry using annexin V/propidium iodide staining. Compounds 4f and 4h demonstrated significant cytotoxicity against breast cancer cells, with IC_{50} values of 4.74 and 21.97 μg/mL and selectivity indices of 3.83 and 2.80, respectively. Increased apoptotic cell populations support their pro-apoptotic potential. These findings indicate that the chromene derivatives, synthesized via a one-pot method, may serve as promising candidates for further anticancer drug development.

Keyword: Chromene derivatives, Anticancer, Breast cancer**,** 3T3, MCF-7.

1. Introduction

The global economic burden of cancer is rapidly increasing as populations continue to grow, age, and adopt certain lifestyle behaviors.[1] Current estimates indicate that approximately 20% of the global population may develop cancer over the course of their lives. Moreover, cancer-related mortality affects about one in nine men and one in twelve women. Projections suggest that by the year 2050, the number of newly diagnosed cancer cases worldwide may surpass 35 million annually.[2] Breast cancer remains the most prevalent cancer in women, both in terms of incidence and mortality rates.[3] These incidence rates vary widely across different regions, with certain Asian and African countries reporting rates below 40 per 100,000 women, while in countries like Australia/New Zealand, North America, and parts of Europe, rates exceed 80 per 100,000.[4]

The primary treatment approaches for cancer include surgery, radiation therapy, chemotherapy, and radiotherapy.[5–7] Modern therapeutic strategies additionally encompass hormonal interventions, anti-angiogenesis approaches, stem cell-based therapies, and immunotherapeutic techniques utilizing dendritic cells.[8] In recent years, nanotechnology-based therapies, gene editing approaches, and tumor microenvironment-modifying agents have emerged as promising modalities to enhance treatment precision and reduce toxicity.[9–11]

Chemotherapy is commonly used to treat various types of cancer, but its toxic side effects lead to a range of complications, such as gastrointestinal problems, immune system suppression, nausea, hair loss, anemia, and damage to organs like the liver and kidneys.[12] A major challenge in cancer therapy lies in the harmful effects of chemotherapeutic agents on normal tissues, which can greatly compromise the effectiveness of treatment.[13,14] Moreover, the development of resistance to chemotherapy agents is a major barrier in cancer therapy. This resistance leads to the treatment becoming ineffective, forcing doctors to increase the drug dosage, which consequently raises toxicity levels and worsens side effects.[15,16]

Several mechanisms have been identified as contributing to drug resistance, with one of the primary causes being the overexpression of ATP-dependent membrane proteins, which are part of the large family of ABC membrane transporters. These transporters play a key role in drug resistance by efficiently transferring drugs out of cancer cells, making them one of the most significant obstacles in cancer treatment.[17] Additionally, tumor heterogeneity, metabolic reprogramming, and ferroptosis resistance also contribute significantly to therapeutic failure.[18]

Thus, the use of novel medications is prompted by the rise of tumor cells that are resistant to traditional chemotherapeutic drugs. A class of organic compounds known as chromenes from the flavonoid family exhibits biological activities, including anti-tumor, anti-leishmanial, and antibacterial effects.[19,20] Recent research on plant-derived flavonoids, including those extracted from hawthorn, highlights their potential in modulating oxidative stress and cancer pathways.[20] These findings have led to the consideration of these substances for evaluation as potential novel medicinal agents.[21,22]

These substances prevent the polymerization of microtubules, resulting in cell cycle arrest and ultimately apoptosis by suppressing cell proliferation and interacting with the colchicine site in tubulin B.[23] These compounds can benefit cancer patients with resistance to conventional antitumor drugs, as they are effective against certain drug-resistant cell types.[24] Some chromene derivatives may also induce ferroptosis or modulate immune responses in the tumor microenvironment.[25–28]

Considering that the anticancer properties of these compounds have been demonstrated through the induction of apoptosis, attempts have been made to synthesize various chromene derivatives.[29,30] The objective of this research was to examine the cytotoxic impact of chlorinated 2-amino-3-carbonitrile chromene derivatives on 3T3 and MCF-7 cell lines. These dihydropyrano chromene derivatives had been synthesized in previous investigations[31–33] and are modified in this study to reach to the novel structures (Scheme 1).

2. Experimental

2. 1. Chemical Synthesis and Structural Characterization

All materials and reagents utilized in this investigation were obtained from commercial suppliers and em-

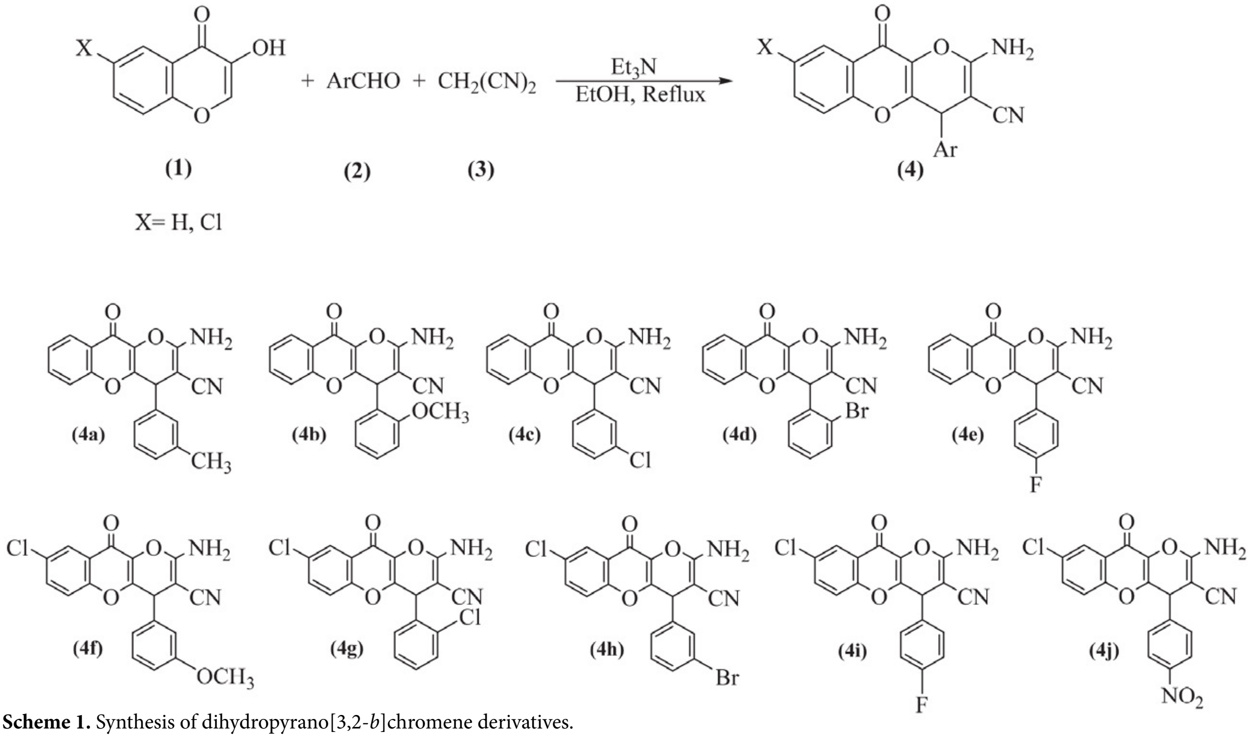

Scheme 1. Synthesis of dihydropyrano[3,2-*b*]chromene derivatives.

ployed without any further purification. Melting point measurements were carried out using an Electrothermal 9100 apparatus, without applying any correction. Infrared (IR) spectra were recorded on a Bruker Alpha FTIR spectrometer using potassium bromide (KBr) pellets. ^{13}C NMR (75 MHz) and ^{1}H NMR (300 MHz) spectra were obtained on a Bruker AVANCE III 300 MHz spectrometer in dimethyl sulfoxide (DMSO)-d_6, with tetramethylsilane (TMS) as the internal reference. Coupling constants (J) are denoted in hertz (Hz), and chemical shifts (δ) are expressed in parts per million (ppm). Reaction progress was tracked via thin-layer chromatography (TLC) using silica gel GF254 plates on aluminum backing, and spots were visualized under 254 nm UV light. Elemental composition was analyzed using a Heraeus CHN-O-Rapid elemental analyzer.

2. 2. Materials and Methods

Sodium citrate and dimethyl sulfoxide (DMSO) were obtained from Sigma-Aldrich (USA), while DMEM and RPMI were sourced from Biosera (France). Fetal bovine serum (FBS) was acquired from Gibco (USA), and MTT was provided by Melford (UK).

2. 3. General Procedure for the Preparation of Dihydropyrano[3,2-*b*]chromene Derivatives (4a-j)

A 50 mL round-bottom flask fitted with a magnetic stir bar and a reflux condenser was charged with 3-hydroxychromone or 6-chloro-3-hydroxychromone **1** (2 mmol), an aromatic aldehyde **2** (2 mmol), malononitrile **3** (2.1 mmol), and a few drops of triethylamine, all dissolved in 10 mL of ethanol. The reaction mixture was stirred and heated under reflux for one hour. Progress of the reaction was assessed by thin-layer chromatography (TLC), employing a hexane/ethyl acetate mixture as the mobile phase. After completion, the reaction mixture was cooled to room temperature, and the resulting solid was collected by filtration, washed with ethanol, and purified by recrystallization from ethanol to afford the desired product in solid form for further characterization.

2. 4. Cell Lines and Cell Culture

MCF-7 human breast cancer cells and 3T3 mouse embryonic fibroblasts were sourced from the Pasteur Institute of Iran (Tehran, Iran). These cells were cultured in either Roswell Park Memorial Institute (RPMI) 1640 medium or Dulbecco's Modified Eagle's Medium (DMEM), both supplemented with 10% fetal bovine serum (FBS) and 1% penicillin-streptomycin antibiotics. The cultures were maintained at 37 °C in a humidified incubator with 5% CO_2.

2. 5. Assessment of Cytotoxicity Using MTT assay

The cells were plated into 96-well culture plates at a density of 10,000 cells per well for both cell lines and incubated in a CO_2-controlled environment. Treatment was applied the following day in accordance with the experimental protocol. At the specified time intervals, 10 μL of MTT solution (5 mg/mL) was added to each well, and the cells were incubated in the dark for 4 hours. Subsequently, the medium was removed, and the resulting formazan crystals were solubilized in 100 μL of DMSO. Absorbance was recorded at 570 nm using a multi-well plate reader.[34–37] MTT assays were performed in triplicate across three independent biological experiments, and each condition was tested in three technical replicates. Data are presented as mean ± SD. The selectivity index (SI) for chromene compounds against cancer cells was calculated as follows:

2. 6. Apoptosis Analysis Using Flow Cytometry

An annexin V-FITC/PI double staining assay was performed to evaluate apoptosis in MCF-7 cells. The cells were exposed to **4f** and **4h** at concentrations of 4 μg/mL and 21 μg/mL, respectively, for a duration of 24 hours. The FITC-Annexin V apoptosis detection kit (XBIO, Czech Republic) was used according to the manufacturer's instructions. The samples were then analyzed using a BD FACSCalibur flow cytometer to measure the fluorescence intensity.

2. 7. Statistical Analyses

A one-way analysis of variance (ANOVA) was used to compare the results among different experimental groups, followed by Tukey's post hoc test for multiple comparisons. Data are presented as the mean ± standard deviation (mean ± SD), and statistical significance was accepted at $P < 0.05$. All experiments were performed in triplicate.

3. Results and Discussion

In this work, a novel one-pot, three-component synthetic strategy was developed for producing dihydropyrano[3,2-*b*]chromene derivatives (**4a–j**) by reacting 3-hydroxychromones or 6-chloro-3-hydroxychromones (**1**), various aromatic aldehydes (**2**), and malononitrile (**3**) in ethanol using triethylamine (Et_3N) as a catalyst under reflux conditions. The crude products were purified by recrystallization, yielding a series of 2-amino-10-oxo-4,10-dihydropyrano[3,2-*b*]chromene-3-carbonitrile derivatives (**4a–j**) with yields ranging from 81% to 92% (Scheme 1). The structures of the synthesized compounds were confirmed by elemental analysis, ^{1}H and ^{13}C NMR, and IR spectroscopy.

2-Amino-10-oxo-4-(*m*-tolyl)-4,10-dihydropyrano[3,2-*b*]chromene-3-carbonitrile (4a)

This compound was obtained as a white solid in 88% yield, with a melting point of 268–269 °C. The IR spectrum (KBr, cm^{-1}) showed characteristic bands at 3399 and 3308 (NH_2), 3016 (aromatic C–H), 2196 ($C\equiv N$), 1650 (C=O), and 1626 (C=C). ^{1}H NMR (300 MHz, DMSO-d_6, δ ppm): 8.00 (dd, *J* = 6, 3 Hz, 1H, ArH), 7.79–7.74 (m, 1H, ArH), 7.54–7.46 (m, 2H, ArH), 7.33–7.14 (m, 6H, ArH and NH_2), 4.91 (s, 1H, CH), 2.32 (s, 3H, CH_3). ^{13}C NMR (75 MHz, DMSO-d_6, δ ppm): 169.04 (C=O), 159.70 (C-2), 155.01, 150.55, 141.47, 138.72, 134.93, 133.74, 129.30, 128.77, 125.88, 125.76, 125.59, 123.60, 119.85 (CN), 118.71, 56.26 (C-3), 41.47 (C-4), 21.48 (CH_3). Elemental analysis calculated for $C_{20}H_{14}N_2O_3$: C, 72.72%; H, 4.27%; N, 8.48%. Found: C, 72.57%; H, 4.08%; N, 8.11%.

2-Amino-4-(2-methoxyphenyl)-10-oxo-4,10-dihydropyrano[3,2-*b*]chromene-3-carbonitrile (4b)

This compound was obtained as a cream-colored powder in 83% yield, with a melting point of 266.5–267 °C. The IR spectrum (KBr, cm^{-1}) showed characteristic bands at 3389 and 3327 (NH_2), 3021 (aromatic C–H), 2187 ($C\equiv N$), 1667 (C=O), and 1648 (C=C). ^{1}H NMR (300 MHz, DMSO-d_6, δ ppm): 8.13 (dd, *J* = 6, 3 Hz, 1H, ArH), 7.79–7.73 (m, 1H, ArH), 7.53–7.47 (m, 2H, ArH), 7.36–7.30 (m, 1H, ArH), 7.26–7.23 (m, 1H, ArH), 7.16 (s, 2H, NH_2), 7.09 (d, *J* = 6 Hz, 1H, ArH), 6.98 (t, *J* = 6 Hz, 1H, ArH), 5.19 (s, 1H, CH), 3.80 (s, 3H, OCH_3). ^{13}C NMR (75 MHz, DMSO-d_6, δ ppm): 168.89 (C=O), 160.17 (C-2), 157.59, 154.96, 150.92, 134.82, 134.30, 129.89, 129.81, 129.05, 125.82, 125.75, 123.66, 121.46, 119.91 (CN), 118.72, 112.47, 56.35 (C-3), 55.54 (OCH_3), 36.48 (C-4). Elemental analysis calculated for $C_{20}H_{14}N_2O_4$: C, 69.36%; H, 4.07%; N, 8.09%. Found: C, 69.09%; H, 3.93%; N, 7.79%.

2-Amino-4-(3-chlorophenyl)-10-oxo-4,10-dihydropyrano[3,2-*b*]chromene-3-carbonitrile (4c)

This compound was obtained as a white powder with a yield of 91%, and a melting point of 244–244.5 °C. The IR spectrum (KBr, cm^{-1}) displayed prominent bands at 3396 and 3308 (NH_2), 3071 (aromatic C–H), 2197 ($C\equiv N$), 1648 (C=O), and 1627 (C=C). ^{1}H NMR (300 MHz, DMSO-d_6, δ ppm): 8.12 (dd, *J* = 6, 3 Hz, 1H, ArH), 7.80–7.74 (m, 1H, ArH), 7.75–7.35 (m, 8H, NH_2, ArH), 5.05 (s, 1H, CH). ^{13}C NMR (75 MHz, DMSO-d_6, δ ppm): 169.08 (C=O), 159.81 (C-2), 157.04, 155.02, 149.53, 143.78, 134.99, 134.00, 131.37, 128.47, 128.32, 127.30, 125.92, 125.77, 123.63, 119.67 (CN), 118.69, 55.63 (C-3), 40.99 (C-4). Elemental analysis calculated for $C_{19}H_{11}ClN_2O_3$: C, 65.06%; H, 3.16%; N, 7.99%. Found: C, 64.79%; H, 3.02%; N, 7.77%.

2-Amino-4-(2-bromophenyl)-10-oxo-4,10-dihydropyrano[3,2-*b*]chromene-3-carbonitrile (4d)

This compound was obtained as a white powder with a yield of 86%, and a melting point ranging from 281–282 °C. The IR spectrum (KBr, cm^{-1}) displayed absorption bands at 3394 and 3331 (NH_2), 3046 (aromatic C-H), 2184 ($C\equiv N$), 1653 (C=O), and 1626 (C=C). ^{1}H NMR (300 MHz, DMSO-d_6, δ ppm): 8.11 (dd, J = 6, 3 Hz, 1H, ArH), 7.77–7.68 (m, 2H, ArH), 7.50–7.26 (m, 7H, NH_2, ArH), 5.45 (s, 1H, CH). ^{13}C NMR (75 MHz, DMSO-d_6, δ ppm): 168.95 (C=O), 159.94 (C-2), 154.91, 149.47, 139.85, 134.98, 134.23, 133.74, 131.68, 130.52, 129.23, 125.92, 125.76, 123.61, 123.49, 119.42 (CN), 118.66, 55.18 (C-3), 41.44 (C-4). Elemental analysis calculated for $C_{19}H_{11}BrN_2O_3$: C, 57.74%; H, 2.81%; N, 7.09%. Found: C, 57.46%; H, 2.57%; N, 6.80%.

2-Amino-4-(4-fluorophenyl)-10-oxo-4,10-dihydropyrano[3,2-*b*]chromene-3-carbonitrile (4e)

The compound was obtained as a white powder with an 83% yield, and its melting point was observed between 228 and 229 °C. The IR spectrum (KBr, cm^{-1}) exhibited the following characteristic peaks: 3378 and 3304 (NH_2), 3068 (aromatic C-H), 2201 ($C\equiv N$), 1654 (C=O), and 1602 (C=C). ^{1}H NMR (300 MHz, DMSO-d_6, δ ppm): 8.11 (d, *J* = 6 Hz, 1H, ArH), 7.76 (t, *J* = 6 Hz, 1H, ArH), 7.53–7.44 (m, 4H, ArH), 7.33–7.22 (m, 4H, NH_2, ArH), 5.03 (s, 1H, CH). ^{13}C NMR (75 MHz, DMSO-d_6, δ ppm): 169.04 (C=O), 163.77 (C-2), 160.54, 159.74, 154.99, 150.09, 137.62, 137.58, 134.93, 133.75, 130.55, 130.44, 125.87, 125.76, 123.59, 119.77 (CN), 118.65, 116.37, 116.09, 55.99 (C-3), 40.67 (C-4). Elemental analysis calculated for $C_{19}H_{11}FN_2O_3$: C, 68.26%; H, 3.32%; N, 8.38%. Found: C, 68.01%; H, 3.29%; N, 8.11%.

2-Amino-8-chloro-4-(3-methoxyphenyl)-10-oxo-4,10-dihydropyrano[3,2-*b*]chromene-3-carbonitrile (4f)

The compound was obtained as a white powder with an 88% yield and a melting point of 242–243 °C. The IR spectrum (KBr, cm^{-1}) exhibited prominent peaks at: 3395 and 3313 (NH_2), 3061 (aromatic C-H), 2197 ($C\equiv N$), 1645 (C=O), and 1629 (C=C). ^{1}H NMR (300 MHz, DMSO-d_6, δ ppm): 8.01 (d, *J* = 6 Hz, 1H, ArH), 7.76 (dd, *J* = 6 Hz, 3 Hz, 1H, ArH), 7.58 (d, *J* = 6 Hz, 1H, ArH), 7.33 (t, *J* = 6 Hz, 3H, NH_2, ArH), 6.95-6.89 (m, 3H, ArH), 4.93 (s, 1H, CH), 3.77 (s, 3H, OCH_3). ^{13}C NMR (75 MHz, DMSO-d_6, δ ppm): 168.00 (C=O), 160.04, 159.70 (C-2), 153.54, 150.64, 142.75, 134.70, 133.84, 130.59, 130.39, 124.80, 124.64, 121.15, 120.49, 119.73 ($C\equiv N$), 114.47, 113.48, 55.97, 55.58 (C-3), 41.39 (C-4). Elemental analysis calculated for $C_{20}H_{13}ClN_2O_4$: C, 63.09%; H, 3.44%; N, 7.36%. Found: C, 62.89%; H, 3.12%; N, 7.19%.

2-Amino-8-chloro-4-(2-chlorophenyl)-10-oxo-4,10-dihydropyrano[3,2-*b*]chromene-3-carbonitrile (4g)

The compound was isolated as a cream powder with a yield of 92% and a melting point of 262–262.5 °C. The IR spectrum (KBr, cm^{-1}) displayed the following significant bands: 3389 and 3335 (NH$_2$), 3075 (aromatic C-H), 2187 (C≡N), 1654 (C=O), and 1633 (C=C). ^{1}H NMR (300 MHz, DMSO-d_6, δ ppm): 8.01 (d, J = 3 Hz, 1H, ArH), 7.73 (dd, J = 6 Hz, 3 Hz, 1H, ArH), 7.54-7.35 (m, 7H, NH$_2$, ArH), 5.43 (s, 1H, CH). ^{13}C NMR (75 MHz, DMSO-d_6, δ ppm): 167.88 (C=O), 159.90 (C-2), 153.46, 149.78, 137.95, 134.77, 134.37, 133.15, 131.57, 130.49, 130.32, 128.63, 124.76, 124.63, 121.11, 119.37 (C≡N), 54.94 (C-3), 40.82 (C-4). Elemental analysis calculated for $C_{19}H_{10}Cl_2N_2O_3$: C, 59.24%; H, 2.62%; N, 7.27%. Found: C, 59.00%; H, 2.39%; N, 7.07%.

2-Amino-4-(3-bromophenyl)-8-chloro-10-oxo-4,10-dihydropyrano[3,2-*b*]chromene-3-carbonitrile (4h)

The compound was obtained as a cream powder with a yield of 84%, and it melted at 242.5–244 °C. The IR spectrum (KBr, cm^{-1}) showed the following key bands: 3389, 3312 (NH$_2$), 3057 (aromatic C-H), 2196 (C≡N), 1650 (C=O), and 1632 (C=C). ^{1}H NMR (300 MHz, DMSO-d_6, δ ppm): 8.01 (d, J = 3 Hz, 1H, ArH), 7.76 (dd, J = 6 Hz, 3 Hz, 1H, ArH), 7.64-7.53 (m, 3H, NH$_2$, ArH), 7.44-7.36 (m, 4H, ArH), 5.05 (s, 1H, CH). ^{13}C NMR (75 MHz, DMSO-d_6, δ ppm): 168.05 (C=O), 159.71 (C-2), 153.57, 149.83, 143.83, 134.72, 134.07, 131.63, 131.42, 131.20, 130.41, 127.76, 124.86, 124.64, 122.65, 121.15, 119.59 (C≡N), 55.62 (C-3), 40.93 (C-4). Elemental analysis calculated for $C_{19}H_{10}BrClN_2O_3$: C, 53.11%; H, 2.35%; N, 6.52%. Found: C, 53.04%; H, 2.11%; N, 6.54%.

2-Amino-8-chloro-4-(4-fluorophenyl)-10-oxo-4,10-dihydropyrano[3,2-*b*]chromene-3-carbonitrile (4i)

The compound was obtained as a white powder with a yield of 82%, and it melted at 253–255 °C. The IR spectrum (KBr, cm^{-1}) exhibited the following prominent bands: 3378, 3306 (NH$_2$), 3071 (aromatic C-H), 2200 (C≡N), 1655 (C=O), and 1603 (C=C). ^{1}H NMR (300 MHz, DMSO-d_6, δ ppm): 8.02 (d, J = 3 Hz, 1H, ArH), 7.77 (dd, J = 6 Hz, 3 Hz, 1H, ArH), 7.59 (d, J = 6 Hz, 1H, ArH), 7.48-7.43 (m, 2H, ArH), 7.35 (s, 2H, NH$_2$), 7.28-7.21 (m, 2H, ArH), 5.02 (s, 1H, CH). ^{13}C NMR (75 MHz, DMSO-d_6, δ ppm): 168.03 (C=O), 163.80, 160.57 (C-2), 159.64, 153.56, 150.44, 137.42, 137.38, 134.74, 133.86, 130.60, 130.49, 130.41, 124.80, 124.64, 121.14, 119.66 (C≡N), 116.38, 116.10, 55.95 (C-3), 40.62 (C-4). Elemental analysis calculated for $C_{19}H_{10}ClFN_2O_3$: C, 61.89%; H, 2.73%; N, 7.60%. Found: C, 61.66%; H, 2.56%; N, 7.39%.

2-Amino-8-chloro-4-(4-nitrophenyl)-10-oxo-4,10-dihydropyrano[3,2-*b*]chromene-3-carbonitrile (4j)

The compound was obtained as a cream powder with a yield of 81%, and it melted at 250–251.5 °C. The IR spectrum (KBr, cm^{-1}) showed prominent bands at 3370, 3321 (NH$_2$), 3071 (aromatic C-H), 2206 (C≡N), 1659 (C=O), 1602 (C=C), 1517, and 1351 (NO$_2$). ^{1}H NMR (300 MHz, DMSO-d_6, δ ppm): 8.27 (d, J = 6 Hz, 2H, ArH), 8.02 (d, J = 3 Hz, 1H, ArH), 7.79-7.72 (m, 3H, ArH), 7.58 (d, 1H, ArH), 7.48 (s, 2H, NH$_2$), 5.26 (s, 1H, CH). ^{13}C NMR (75 MHz, DMSO-d_6, δ ppm): 168.05 (C=O), 159.79 (C-2), 153.59, 149.36, 148.29, 147.66, 134.81, 134.21, 130.49, 130.03, 124.83, 124.65, 124.60, 121.14, 119.44 (C≡N), 55.08 (C-3), 41.00 (C-4). Elemental analysis calculated for $C_{19}H_{10}ClN_3O_5$: C, 57.66%; H, 2.55%; N, 10.62%. Found: C, 57.31%; H, 2.19%; N, 10.43%.

3. 1. *In vitro* Cytotoxicity Assessment of Synthesized Chromene Derivatives

The toxicity of the chromene compounds was evaluated using the MTT assay on MCF-7 (breast cancer) and 3T3 (normal) cell lines. Approximately all of the synthesized compounds displayed high levels of toxicity, resulting in IC$_{50}$ values below 50 μg/mL for all compounds, except in three cases. The selectivity index of chromene compounds on cancerous and non-cancerous cell lines were calculated and reported in Table. 1. Among the tested compounds, **4f** and **4h** exhibited the highest toxicity. Compound **4f**, which had an IC$_{50}$ of approximately 4 μg/mL in MCF-7 cells and an IC$_{50}$ of nearly 20 μg/mL in normal 3T3 cells, had the highest cytotoxic effect among these samples. Additionally,

Table. 1 Summary of molecular features, IC$_{50}$ values, and selectivity index of synthesized compounds in 3T3 and MCF-7 cells.

Compounds	Chemical Formula	Molecular Weight	3T3 (μg/ml)	3T3 (μM)	MCF-7 (μg/ml)	MCF-7 (μM)	Selectivity Index (SI)
4a	$C_{20}H_{14}N_2O_3$	330.34	>125	–	>125	–	–
4b	$C_{20}H_{14}N_2O_4$	346.34	>125	–	>125	–	–
4c	$C_{19}H_{11}ClN_2O_3$	350.76	48.40	137.98	79	225.22	0.612
4d	$C_{19}H_{11}BrN_2O_3$	395.21	>125	–	>125	–	–
4e	$C_{19}H_{11}FN_2O_3$	334.31	47	140.58	125.20	374.50	0.375
4f	$C_{20}H_{13}ClN_2O_4$	380.78	18.170	47.71	4.740	12.44	3.83
4g	$C_{19}H_{10}Cl_2N_2O_3$	385.20	32.450	84.24	42.000	109.03	0.772
4h	$C_{19}H_{10}BrClN_2O_3$	429.65	61.550	143.25	21.970	51.13	2.80
4i	$C_{19}H_{10}ClFN_2O_3$	368.75	32.780	88.89	30.870	83.71	1.061
4j	$C_{19}H_{10}ClN_3O_5$	395.76	34.123	86.22	43.800	110.67	0.779

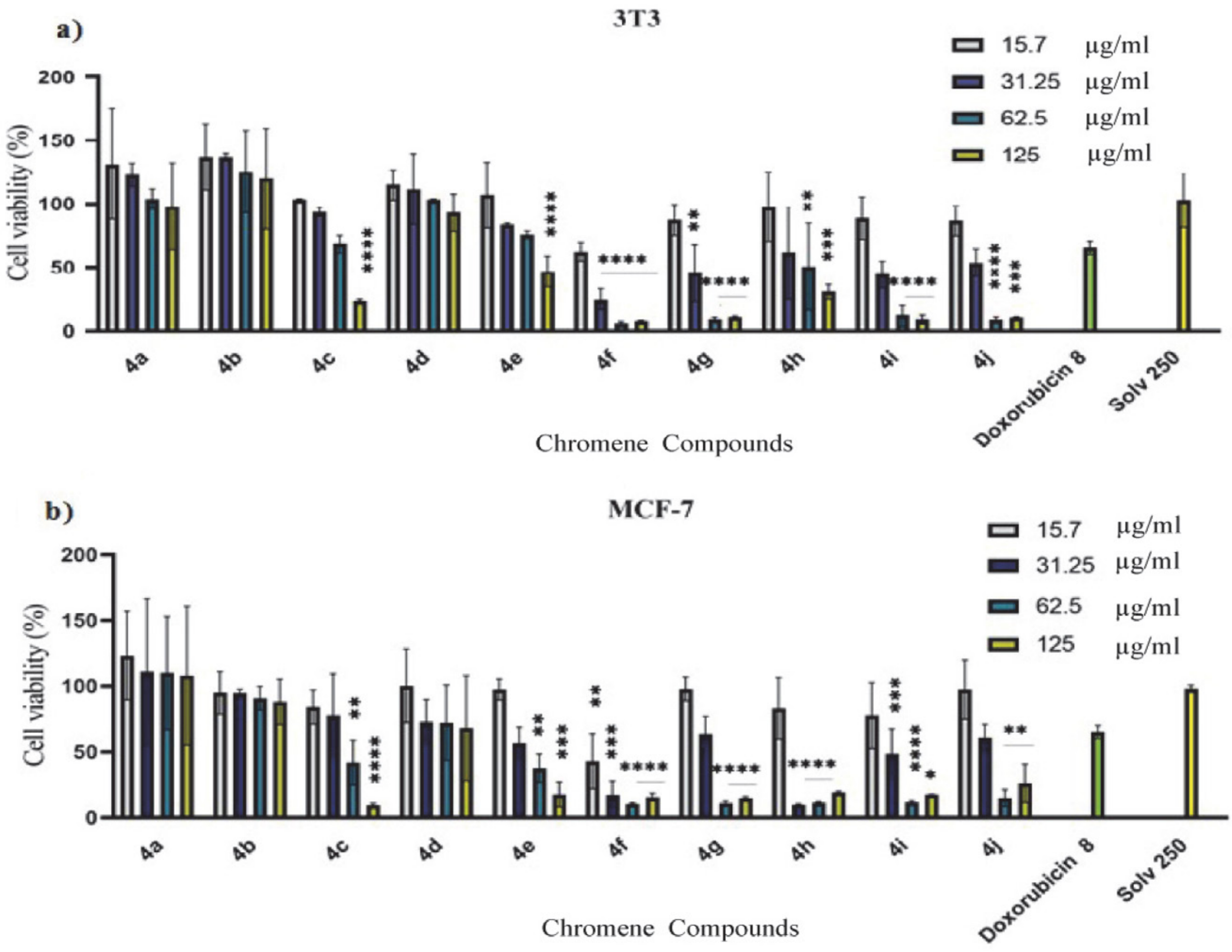

Figure 1. (a, b) The cytotoxic effects of chromene compounds at concentrations of 15.7–125 μg/mL were evaluated on 3T3 and MCF-7 cells after 24 hours of exposure. Doxorubicin (8 μg/mL) was used as a positive control. *Solv 250* refers to the solvent control containing 0.25% DMSO used to dissolve the test compounds. Data are expressed as mean ± SD (n = 3). Statistical significance was assessed by one-way ANOVA with Tukey's post hoc test (*P < 0.05, **P < 0.01, ***P < 0.001, **P < 0.0001).

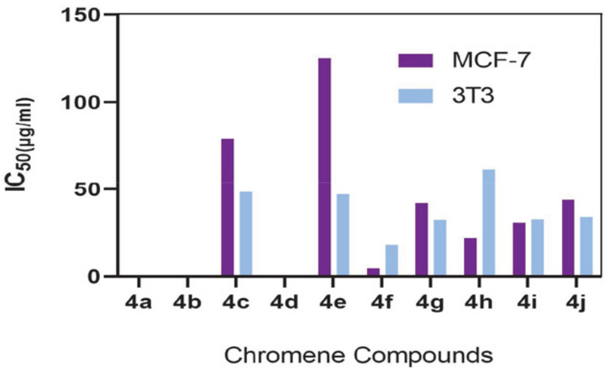

Figure 2. Bar chart showing IC_{50} values (μg/mL) of synthesized chromene derivatives against MCF-7 and 3T3 cell lines. Values were calculated from mean viability data (n = 3); error bars are not shown as IC_{50}s were derived from averaged curves. Corresponding numerical data are listed in Table 1

compound **4h** has an acceptable level of cytotoxicity, with an IC_{50} of about 21 μg/mL in MCF-7 cells and 61 μg/mL in 3T3 cells (Fig. 2). Interestingly, *in vitro* potential of chromene compounds was promising with selectivity index of 3.83 and 2.80 for **4f** and **4h**, respectively. These results highlight the potential of chromene derivatives as selective anticancer agents.

3. 2. Flow Cytometric Analysis of Apoptosis Using Annexin V/PI Staining

To further elucidate the cytotoxic mechanisms, flow cytometry analysis was performed on MCF-7 cells treated with compounds **4f** and **4h**. Flow cytometry analysis revealed that treatment with compound **4h** resulted in 13.57% viable cells, 6.2% early apoptotic cells, and 76% late apoptotic cells. For compound **4f**, 44.53% of the cells remained viable, while 4.04% and 25.83% underwent early and late apoptosis, respectively. Figure 4 depicts the morphology of MCF-7 cells treated with compounds **4f** and **4h**, which corresponds to the findings from the MTT and flow cytometry assays. These findings confirm that the cytotoxicity of these compounds is primarily mediated via induction of apopto-

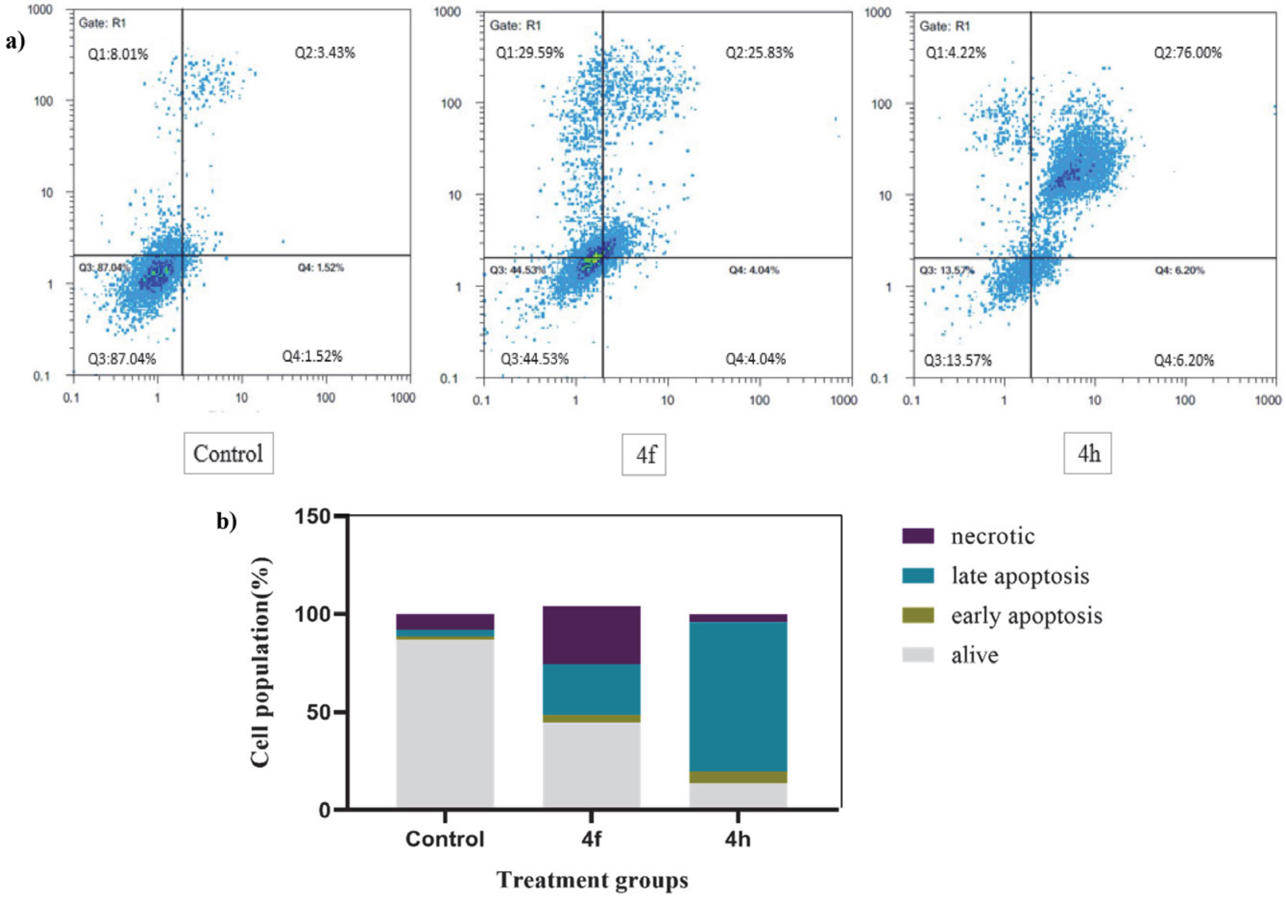

Figure 3. (a) Dot-plot flow cytometry histograms showing the distribution of MCF-7 cell populations after treatment with compounds **4f** (5 µg/mL) and **4h** (25 µg/mL) for 24 h. Cells were stained with Annexin V-FITC and propidium iodide (PI). The quadrants represent: viable cells (lower left, Annexin V– / PI–), early apoptotic (lower right, Annexin V+ / PI–), late apoptotic (upper right, Annexin V+ / PI+), and necrotic cells (upper left, Annexin V– / PI+). (b) Bar chart showing the percentage distribution of viable, early apoptotic, late apoptotic, and necrotic cells in each treatment group.

sis, consistent with previous studies on chromene derivatives demonstrating their ability to induce programmed cell death through mitochondrial pathways and regulation of apoptosis-related genes such as Bax, caspase-3, and Bcl-2.[31,34,38–40]

3. 3. Biological Significance of Chromene Derivatives

Chromenes are a class of naturally occurring oxygen-containing heterocycles, known for their simple

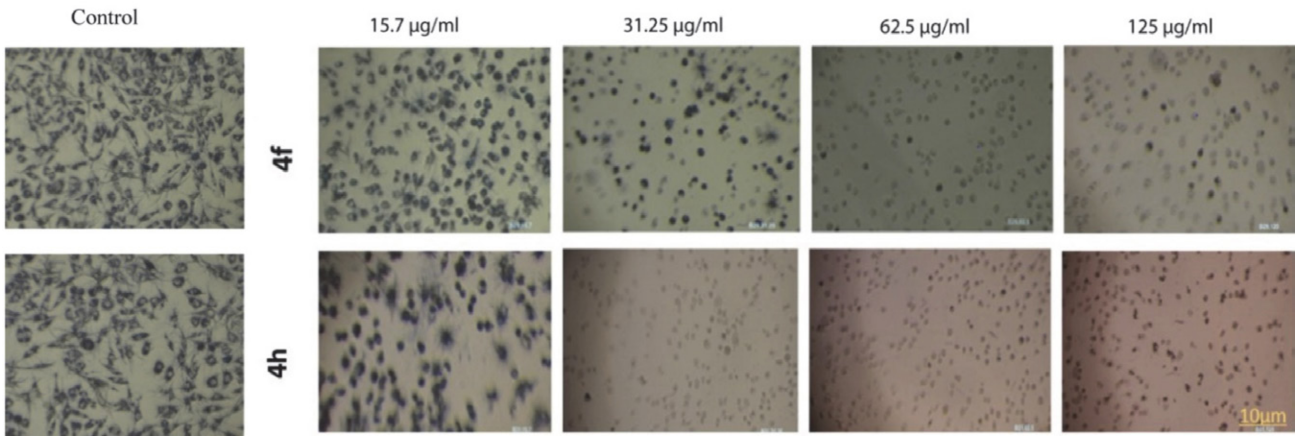

Figure 4. Phase-contrast images showing morphological changes in MCF-7 cells after 24-hour treatment with compounds **4f** and **4h** at increasing concentrations (15.7, 31.25, 62.5, and 125 µg/mL, left to right. Images were captured using phase-contrast microscopy at 40× magnification. Control: untreated MCF-7 cells. Cell shrinkage and death were more pronounced at higher concentrations, consistent with MTT and apoptosis assay results.

structure and minimal adverse effects, making them attractive for drug development.[41,42] They form the core of many flavonoids and possess a broad range of biological activities including anticancer, antimicrobial, neuroprotective, and anti-HIV effects.[41–47] Several chromene derivatives have shown significant cytotoxicity by binding to the colchicine-binding site of tubulin, inhibiting polymerization, and causing cell cycle arrest leading to apoptosis.[23,24] Gourdeau et al. demonstrated the anti-vascular and anticancer properties of certain chromene derivatives, highlighting their potential in clinical cancer therapy, particularly due to their anti-angiogenic effects and synergy with chemotherapeutic agents.[24]

3. 4. Structure–activity Relationship Analysis of Chromene Derivatives Based on Cytotoxicity Results

Structure–activity relationship (SAR) analysis revealed that substitution patterns on the chromene core significantly influence activity. In particular, compounds **4f** and **4h** contain *meta*-positioned substituents on the 4-aryl phenyl ring, a methoxy (-OCH_3) group in **4f** and a bromine (-Br) atom in **4h**, which may explain their higher potency.[48] Previous studies have also noted that electron-donating groups at the 7th position of the chromene scaffold enhance pharmacological effects, while electron-withdrawing groups tend to reduce activity.[48] Zhang et al. reported anticancer effects of chromene derivatives via modulation of the p53 pathway and downregulation of VEGF, ICAM1, and MMP-2, supporting their antitumor potential.[49]

4. Conclusion

In summary, we successfully synthesized and characterized a series of chromene-based derivatives via a one-pot, three-component reaction. The structures of the synthesized compounds were confirmed by spectroscopic methods, including IR and NMR (^{1}H and ^{13}C NMR), and elemental analysis. Biological evaluations revealed that several of these compounds, particularly **4f** and **4h**, exhibit potent cytotoxic effects against MCF-7 breast cancer cells, with IC_{50} values of 4.74 µg/mL and 21.97 µg/mL, and favorable selectivity indexes of 3.83 and 2.80, respectively. Flow cytometry analysis confirmed their ability to induce apoptosis, further supporting their anticancer potential. These findings underscore the value of chromene scaffolds as promising leads for breast cancer therapy.

Nevertheless, to fully elucidate their therapeutic potential, further research is warranted, including evaluations across diverse cancer cell lines, *in vivo* toxicity and efficacy assessments, and deeper mechanistic investigations such as gene expression profiling and protease interaction studies. Such efforts may lead to the development of more effective chromene-based agents for overcoming chemo-resistance in cancer therapy.

Declarations

Data availability statement

The original contributions made in this study are part of the article/supplementary material. For additional questions, please contact the corresponding author.

Author contributions

BB, SS, BA and MA designed and supervised the project, supplied all reagents; and edited the manuscript. YA, BB, and MA wrote the original draft and collaborated with AAK, AA, and FH to carry out the experiments and analysis of the results. All authors participated in the interpretation, and analysis of the data and review of the manuscript.

Conflict of interest

The authors confirm that the research was carried out without any commercial or financial relationships that could be perceived as a potential conflict of interest.

Funding

This work is the report of the results of Pharm D thesis (KUMS_1394) of AAK and AA.

Ethics approval and consent to participate

The study did not involve human participants or animals.

Acknowledgement

We are extremely grateful to the Vice-Chancellor for Research and Technology, Kerman University of Medical Sciences, Kerman, Iran.

5. References

1. L. A. Torre, R. L. Siegel, E. M. Ward and A. Jemal, *Cancer Epidemiol. Biomarkers Prev.* **2016**, *25*, 16–27. **DOI:**10.1158/1055-9965.EPI-15-0578
2. F. Bray, M. Laversanne, H. Sung, J. Ferlay, R. L. Siegel, I. Soerjomataram and A. Jemal, *CA Cancer J. Clin.* **2024**, *74*, 229–263. **DOI:**10.3322/caac.21834
3. M. Anjomshoa, B. Amirheidari, J. Janczak, M. Sahihi, Y. Abolhassani, A. Farsinejad and H. Forootanfar, *Sci. Rep.* **2024**, *14*, 29138. **DOI:**10.1038/s41598-024-79644-0
4. M. Arnold, E. Morgan, H. Rumgay, A. Mafra, D. Singh, M. Laversanne, J. Vignat, J. R. Gralow, F. Cardoso, S. Siesling and I. Soerjomataram, *Breast* **2022**, *66*, 15–23. **DOI:**10.1016/j.breast.2022.08.010
5. A. G. Waks and E. P. Winer, *JAMA* **2019**, *321*, 288–300. **DOI:**10.1001/jama.2018.19323
6. L. Guo, Z. Fu, H. Li, R. Wei, J. Guo, H. Wang and J. Qi, *Adv. Colloid Interface Sci.* **2025**, 103470.

DOI:10.1016/j.cis.2025.103470

7. A. Bemidinezhad, Y. Abolhassani, A. S. Tabrizi, M. Noroozi-Karimabad, M. Parsa-Kondelaji, R. Roshani and F. Gheybi, *Iran. J. Biotechnol.* **2025**, *23*, e4032.
8. K. D. Miller, L. Nogueira, A. B. Mariotto, J. H. Rowland, K. R. Yabroff, C. M. Alfano, A. Jemal, J. L. Kramer and R. L. Siegel, *CA Cancer J. Clin.* **2019**, *69*, 363–385. **DOI:**10.3322/caac.21565
9. K. Wang, S. Ning, S. Zhang, M. Jiang, Y. Huang, H. Pei, M. Li and F. Tan, *J. Exp. Clin. Cancer Re.s* **2025**, *44*, 30. **DOI:**10.1186/s13046-025-03297-8
10. F. Luan, Y. Cui, R. Huang, Z. Yang and S. Qiao, *Sci. Rep.* **2025**, *15*, 3223. **DOI:**10.1038/s41598-025-85444-x
11. M. Anjomshoa, B. Amirheidari, M. Sahihi, J. Janczak, H. Forootanfar, A. Farsinejad, Y. Abolhassani and S. Karami-Mohajeri, *J. Biol. Inorg. Chem.* **2025**, 1–21. **DOI:**10.1007/s00775-025-02114-z
12. M. E. Robson, N. Tung, P. Conte, S. A. Im, E. Senkus, B. Xu, N. Masuda, S. Delaloge, W. Li, A. Armstrong, W. Wu, C. Goessl, S. Runswick and S. M. Domchek, *Ann. Oncol.* **2019**, *30*, 558–566. **DOI:**10.1093/annonc/mdz012
13. J. Wang, B. Chen, J. Chen, X. Cai, G. Xia, R. Liu, P. Chen, Y. Zhang and X. Wang, *Int. J. Nanomedicine* **2011**, *6*, 203–211. **DOI:**10.2147/IJN.S16165
14. M. E. Larsen, J. Rowntree, A. M. Young, S. Pearson, J. Smith, O. J. Gibson, A. Weaver and L. Tarassenko: 2008 30th Annual International Conference of the IEEE Engineering in Medicine and Biology Society, IEEE, 2008, pp. 5152–5155. **DOI:**10.1109/IEMBS.2008.4650374
15. T. Makovec, *Radiol. Oncol.* **2019**, *53*, 148–158. **DOI:**10.2478/raon-2019-0018
16. Y. Abolhassani, S. Mirzaei, M. Nejabat, S. Talebian, H. Gholamhosseinian, M. Iranshahi, F. B. Rassouli and K. Jamialahmadi, *Mol. Biol. Rep.* **2023**, *50*, 5709–5717. **DOI:**10.1007/s11033-023-08439-9
17. D. B. Longley and P. G. Johnston, *J. Pathol.* **2005**, *205*, 275–292. **DOI:**10.1002/path.1706
18. S. Chen, S. Long, Y. Liu, S. Wang, Q. Hu, L. Fu and D. Luo, *Front. Oncol.* **2024**, *14*, 1432869. **DOI:**10.3389/fonc.2024.1432869
19. M. Mamaghani, R. H. Nia, F. Tavakoli and P. Jahanshahi, *Curr. Org. Chem.* **2018**, *22*, 1704–1769. **DOI:**10.2174/1385272822666180530104302
20. Z. Han, C. Li and G. Liu, *J. Food Compos. Anal.* **2025**, 107372. **DOI:**10.1016/j.jfca.2025.107372
21. M. Sairafianpour, O. Kayser, J. Christensen, M. Asfa, M. Witt, D. Stærk and J. W. Jaroszewski, *J. Nat. Prod.* **2002**, *65*, 1754–1758. **DOI:**10.1021/np020244s
22. K. Y. Lee, D. H. Nam, C. S. Moon, S. H. Seo, J. Y. Lee and Y. S. Lee, *Eur. J. Med. Chem.* **2006**, *41*, 991–996. **DOI:**10.1016/j.ejmech.2006.04.008
23. H. Aryapour, G. H. Riazi, S. Ahmadian, A. Foroumadi, M. Mahdavi and S. Emami, *Pharm. Biol.* **2012**, *50*, 1551–1560. **DOI:**10.3109/13880209.2012.695799
24. H. Gourdeau, L. Leblond, B. Hamelin, C. Desputeau, K. Dong, I. Kianicka, D. Custeau, C. Boudreau, L. Geerts and S.-X. Cai, *Mol. Cancer Ther.* **2004**, *3*, 1375–1384 **DOI:**10.1158/1535-7163.1375.3.11
25. C. Zhao, W. Song, J. Wang, X. Tang and Z. Jiang, *Chem. Commun.* **2025**, *61*, 1962–1977. **DOI:**10.1039/D4CC06510G
26. X. Li, J.-Q. Luo, X.-Q. Liao, S. Zhang, L.-F. Yang, T. Wu, L. Wang, Q. Xu, B.-S. He and Z. Guo, *Neoplasma* **2024**, *71*, 243–254. **DOI:**10.4149/neo_2024_240108N8
27. D. Sun, X. Li, S. Nie, J. Liu and S. Wang, *Biomed. Pharmacother.* **2023**, *157*, 113993. **DOI:**10.1016/j.biopha.2022.113993
28. Y. F. Zeng, J. Y. Li, X. Y. Wei, S. Q. Ma, Q. G. Wang, Z. Qi, Z. C. Duan, L. Tan and H. Tang, *Front. Pharmacol.* **2023**, *14*, 1310023. **DOI:** 10.3389/fphar.2023.1310023
29. W. Kemnitzer, J. Drewe, S. Jiang, H. Zhang, C. Crogan-Grundy, D. Labreque, M. Bubenick, G. Attardo, R. Denis and S. Lamothe, *J. Med. Chem.* **2008**, *51*, 417–423. **DOI:**10.1021/jm7010657
30. W. Kemnitzer, J. Drewe, S. Jiang, H. Zhang, Y. Wang, J. Zhao, S. Jia, J. Herich, D. Labreque and R. Storer, *J. Med. Chem.* **2004**, *47*, 6299–6310. **DOI:**10.1021/jm049640t
31. T. Eslaminejad, E. Faghih Mirzaei and M. Abaszadeh, *Iran J. Pharm. Res.* **2023**, *22*, e132932. **DOI:**10.5812/ijpr-132932
32. S. Sabouri and M. Abaszadeh, *Polycyclic Aromat. Compd.* **2021**, *41*, 467–477. **DOI:**10.1080/10406638.2019.1597381
33. M. Abaszadeh, A. Ebrahimi and S. Sabouri, *Biointerface Res. Appl. Chem.* **2021**, *11*, 10987–10995. **DOI:**10.33263/BRIAC113.1098710995
34. M. Ohadi, P. Rezaei, M. Mehrabani, B. Behnam and M. Ansari, *J. Cluster Sci.* **2022**, *33*, 975–984. **DOI:**10.1007/s10876-021-02026-3
35. M. Moballegh-Nasery, A. Mandegary, T. Eslaminejad, M. Zeinali, A. Pardakhti, B. Behnam and M. Mohammadi, *J. Liposome Res.* **2021**, *31*, 189–194. **DOI:**10.1080/08982104.2020.1755981
36. B. Behnam, M. Rezazadehkermani, S. Ahmadzadeh, A. Mokhtarzadeh, S. N. Nematollahi-Mahani and A. Pardakhty, *Artif. Cells Nanomed. Biotechnol.* **2018**, *46*, 118–125. **DOI:**10.1080/21691401.2017.1296850
37. R. Mohammadinejad, A. Dehshahri, H. Sassan, B. Behnam, M. Ashrafizadeh, A. Samareh Gholami, A. Pardakhty and A. Mandegary, *Minerva Biotecnol.* **2020**, *32*, 106–113. **DOI:**10.23736/S1120-4826.20.02618-X
38. L. M. Al-Harbi, E. A. Al-Harbi, R. M. Okasha, R. A. El-Eisawy, M. A. A. El-Nassag, H. M. Mohamed, A. M. Fouda, A. A. Elhenawy, A. Mora, A. M. El-Agrody and H. K. A. El-Mawgoud, *J. Enzyme Inhib. Med. Chem.* **2023**, *38*, 2155814. **DOI:**10.1080/14756366.2022.2155814
39. F. F. Albalawi, M. A. El-Nassag, R. A. El-Eisawy, M. B. I. Mohamed, A. M. Fouda, T. H. Afifi, A. A. Elhenawy, A. Mora, A. M. El-Agrody and H. K. El-Mawgoud, *Int. J. Mol. Sci.* **2022**, *24*, 49. **DOI:**10.3390/ijms24010049
40. R. A. Ardeshir and K. Moarefvand, *Sci. Rep.* **2025**, *15*, 15061. **DOI:**10.1038/s41598-025-97906-3
41. N. Vasan, J. Baselga and D. M. Hyman, *Nature* **2019**, *575*, 299–309. **DOI:**10.1038/s41586-019-1730-1
42. M. K. Hussain, M. F. Khan, S. Khatoon, A. G. Al-Sehemi and M. Saquib: Plant-derived Bioactives, Springer, **2020**, pp. 185–

204. **DOI:**10.1007/978-981-15-2361-8_8

43. M. Puppala, X. Zhao, D. Casemore, B. Zhou, G. Aridoss, S. Narayanapillai and C. Xing, *Bioorg. Med. Chem*. **2016**, *24*, 1292–1297. **DOI:**10.1016/j.bmc.2016.01.056
44. H. H. Jardosh and M. P. Patel, *Med. Chem. Res.* **2013**, *22*, 2954–2963. **DOI:**10.1007/s00044-012-0301-x
45. N. K. Shah, N. M. Shah, M. P. Patel and R. G. Patel, *J. Chem. Sci.* **2013**, *125*, 525–530. **DOI:**10.1007/s12039-013-0421-y
46. M. Friden-Saxin, T. Seifert, M. R. Landergren, T. Suuronen, M. Lahtela-Kakkonen, E. M. Jarho and K. Luthman, *J. Med. Chem.* **2012**, *55*, 7104–7113. **DOI:**10.1021/jm3005288
47. Y. Kang, Y. Mei, Y. Du and Z. Jin, *Org. Lett.* **2003**, *5*, 4481–4484. **DOI:**10.1021/ol030109m
48. A. Chaudhary, K. Singh, N. Verma, S. Kumar, D. Kumar and P. P. Sharma, *Mini-Rev. Med. Chem.* **2022**, *22*, 2736–2751. **DOI:**10.2174/1389557522666220331161636
49. W. H. Zhang, S. Chen, X. L. Liu, L. Bing, X. W. Liu and Y. Zhou, *Bioorg. Med. Chem. Lett.* **2020**, *30*, 127410. **DOI:**10.1016/j.bmcl.2020.127410

Povzetek

Rak ostaja vodilni vzrok smrti po vsem svetu, zato so potrebni novi terapevtski pristopi. V tej študiji so avtorji sintetizirali in karakterizirali derivate 2-amino-3-karbonitril kromena in ocenili njihove citotoksične učinke na celične linije 3T3 in MCF-7. Karakterizacija je vključevala tališče, IR, NMR in elementno analizo. Citotoksičnost je bila ocenjena z MTT testom, pri čemer so bile izračunane vrednosti IC_{50}, indukcija apoptoze pa je bila potrjena s pretočno citometrijo z barvanjem z anexinom V/propidijevim jodidom. Spojine **4f** in **4h** so pokazale znatno citotoksičnost proti celicam raka dojke, z vrednostmi IC_{50} 4,74 in 21,97 µg/ml ter indeksi selektivnosti 3,83 in 2,80. Povečana populacija apoptičnih celic podpira njihov proapoptični potencial. Ti rezultati kažejo, da derivati kromena, sintetizirani z enostopenjsko metodo, predstavljajo obetavne kandidate za nadaljnji razvoj zdravil proti raku.

DOI: 10.17344/acsi.2024.9007 *Acta Chim. Slov.* **2025,** *72,* 524–531

Scientific paper

Design, Synthesis and Anticonvulsant Activity of 2 and 5-disubstituted 1,3-dioxoisoindoline

Asghar Davood[1,*], Maryam Yadavar Nikravesh[1], Mahsa Hadipour Jahromy[2], Sepideh Taghizad[1]

[1] *Department of Medicinal Chemistry, TeMS.C., Islamic Azad University, Tehran, Iran.*

[2] *Department of Pharmacology, Herbal Pharmacology Research Center, TeMS.C., Islamic Azad University, Tehran, Iran.*

** Corresponding author: E-mail: adavood@iaups.ac.ir ; adavood2001@yahoo.com*
Tel: +98 21 22609043, Fax: +98 21 22602059

Received: 10-02-2024

Abstract

The isoindoline scaffold, a rigid analogue of ameltolide, exhibits notable antiepileptic properties. Here we describe the design, synthesis, and evaluation of nine new isoindoline derivatives prepared by condensation of trimellitic anhydride with various arylamines. Anticonvulsant activity of prepared compounds was assessed in maximal electroshock (MES; tonic seizure) and pentylenetetrazole (PTZ; clonic seizure) seizure models. All compounds significantly attenuated both tonic and clonic seizures; in MES they reduced seizure-induced mortality, while in PTZ they improved seizure frequency and latency. Compounds **3** and **4** showed the highest efficacy, surpassing phenytoin. Structure–activity analysis indicates that bulky *ortho*-substituents on the *N*-aryl group, combined with a *meta*-nitro substituent, enhance anticonvulsant potency.

Keywords: Isoindoline, MES, PTZ, Docking, Anticonvulsant, Sodium channel

1. Introduction

Epilepsy, also known as a seizure disorder, is a chronic non-communicable neurological disease that affects people of all ages. With an estimated 50 million people affected worldwide, it is one of the most common neurological disorders. About 80% of people with epilepsy live in low- and middle-income countries. With an accurate diagnosis and appropriate treatment, up to 70% of patients can control their seizures and live seizure-free.[1] Treatment usually includes antiepileptic drugs (AEDs) and, in some cases, surgery.

Many widely used AEDs, particularly those that block sodium channels, are associated with a variety of side effects and limited efficacy in drug-resistant cases.[2,3] Therefore, the development of new agents with improved safety profiles and higher therapeutic indices remains an important research priority.

Phenytoin, one of the most commonly prescribed AEDs, contains a hydantoin moiety that has been associated with various adverse effects.[4] Ameltolide, an antiepileptic drug with phenytoin-like activity, lacks a hydantoin ring and has a more favorable profile.[5,6] In addition, phthalimide–the rigid analog of ameltolide–has similar receptor binding properties to phenytoin and has demonstrated potent anticonvulsant activity in various models.[7]

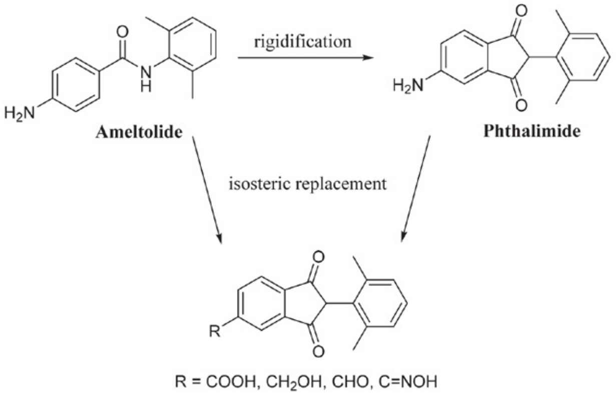

Figure 1. Design of phthalimide analogues based on isosteric replacement.

In our previous work, we reported several novel and more potent phthalimide derivatives with promising anticonvulsant activity.[8–15] Continuing this line of research, we now present the design and synthesis of a new series of phthalimide analogs based on isosteric replacement. In particular, the hydrogen at position 4 of the phthalimide ring was replaced by various functional groups, including –COOH, $-CH_2OH$, –CHO, and –C=NOH (Figure 1), with the aim of improving biological activity and selectivity.

2. Materials and Methods

2. 1. Chemistry

All reagents and solvents were purchased from Sigma-Aldrich and EXIR and used without further purification. Melting points were determined using an Electrothermal IA 9100MK2 capillary melting point apparatus. Infrared (IR) spectra were recorded with a Shimadzu 8400-S FT-IR spectrometer using KBr pellets. ^1H NMR spectra were recorded using a Varian INOVA FT-500 MHz instrument. Chemical shifts (δ) are expressed in parts per million (ppm) relative to tetramethylsilane (TMS) as an internal standard, in $CDCl_3$ or DMSO-d_6. The signal multiplicities are labelled as follows: s (singlet), brs (broad singlet), d (doublet), t (triplet), and m (multiplet).

Compounds **1–6** were synthesized by condensation of trimellitic anhydride with the corresponding arylamines, as previously described.[8–15] Compounds **7–9** were prepared from compound **1** by successive reduction, oxidation,[16] and reaction with hydroxylamine.[17–18] The synthetic pathway for compounds **1**–**9** is shown in Scheme 1.

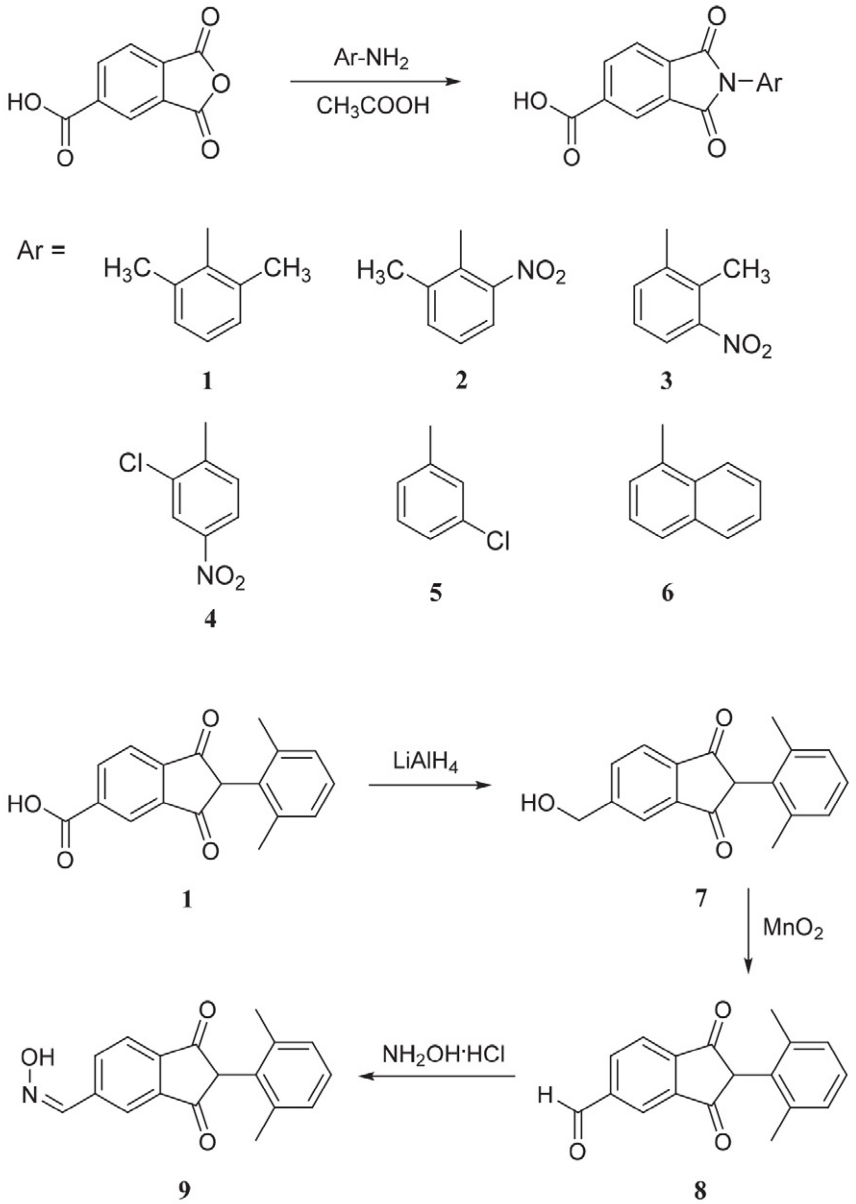

Scheme 1. The synthetic pathway for designed compounds **1–9**.

Synthesis of 2-(2,6-dimethylphenyl)-1,3-dioxoisoindoline-5-carboxylic acid (1)

A solution of trimellitic anhydride (1 mmol) and 2,6-dimethylaniline (1 mmol) in glacial acetic acid (2.5 mL) was heated under reflux for 48 h. The reaction mixture was then cooled to room temperature, and water (5 mL) was added. The resulting precipitate was filtered off, washed with water and dried to obtain the desired compound as gray crystals. Yield: 50%; m.p. 225 °C. IR (KBr, cm^{-1}) ν 1691, 1750, 1775 (C=O), 2400–3400 (O–H). ^1H NMR (500 MHz, DMSO-d_6) δ 8.44 (dd, *J* = 1.26, 7.92 Hz, 1H, H-6-isoindoline), 8.34 (s, 1H, H-4-isoindoline), 8.10 (d, *J* = 7.65 Hz, 1H, H-7-isoindoline), 7.15–7.42 (m, 3H, H-3,4,5-phenyl), 2.10 (s, 6H, CH_3).

Synthesis of 2-(2-methyl-6-nitrophenyl)-1,3-dioxoisoindoline-5-carboxylic acid (2)

Trimellitic anhydride (1 mmol) and 2-methyl-6-nitroaniline (1 mmol) were refluxed in glacial acetic acid (2.5 mL) for 72 h using the same procedure as described for compound **1**. The crude product was isolated by filtration and recrystallized from methanol to give the desired compound as yellow crystals. Yield: 51%; m.p. 230 °C. IR (KBr, cm^{-1}) ν 1340, 1386, 1533 (NO_2), 1706, 1737, 1780 (C=O), 2812–3462 (O–H). ^1H NMR (250 MHz, DMSO-d_6) δ 8.40 (d, *J* = 8.0 Hz, 1H, H-5-phenyl), 8.30 (s, 1H, H-4-isoindoiline), 8.08 (d, *J* = 7.75 Hz, 1H, H-6-isoindoline), 8.00 (d, *J* = 7.75 Hz, 1H, H-7-isoindoline), 7.80 (d, *J* = 8.10 Hz, 1H, H-3-phenyl), 7.65 (t, *J* = 7.50 Hz, H-4-phenyl), 2.23 (s, 3H, CH_3). ^{13}C NMR (62.5 MHz, DMSO-d_6) δ 17.91 (CH_3), 123.95 (C-5-phenyl), 124.57 (C-7-isoindoline), 125.07 (C-4-isoindoline), 131.07 (C-4-phenyl), 132.12 (C-1-phenyl), 134.82 (C-9-isoindoline), 136.62 (C-5,6-isoindoline), 137.01 (C-2-phenyl), 137.62 (C-3-phenyl), 140.36 (C-8-isoindoline), 146.85 (C-6-phenyl), 165.87, 166.04 (C=O).

Synthesis of 2-(2-methyl-3-nitrophenyl)-1,3-dioxoisoindoline-5-carboxylic acid (3)

Following the same procedure as for compound **1**, trimellitic anhydride (1 mmol) and 2-methyl-3-nitroaniline (1 mmol) were refluxed for 3 h in glacial acetic acid (2.5 mL). After completion, the solvent was removed under reduced pressure. The resulting crude product was washed with diethyl ether and recrystallized from chloroform to give the desired compound as light brown crystals. Yield: 75%; m.p. 290 °C. IR (KBr, cm^{-1}) ν 1354, 1365, 1479, 1526 (NO_2), 1697, 1742, 1782 (C=O), 2350–3300 (O–H). ^1H NMR (250 MHz, DMSO-d_6) δ 8.35 (d, *J* = 7.75 Hz, 1H, H-6-isoindoline), 8.25 (s, 1H, H-4-isoindoline), 8.02 (d, *J* = 8.00 Hz, 1H, H-6-phenyl), 7.98 (d, *J* = 7.75 Hz, H-7-isoindoline), 7.71 (d, *J* = 7.5 Hz, H-4-phenyl), 7.54 (t, *J* = 8.00 Hz, 1H, H-5-phenyl), 2.16 (s, 3H, CH_3). ^{13}C NMR (62.5 MHz, DMSO-d_6) δ 14.42 (CH_3), 124.10 (C-4-phenyl), 124.56 (C-7-isoindoline), 125.47 (C-2-phenyl), 127.96 (C-4-isoindoline), 131.62 (C-5-phenyl), 132.56 (C-9-isoindoline), 133.02 (C-5,6-isoindoline), 134.44 (C-6-phenyl), 135.38 (C-3-phenyl), 136.05 (C-1-phenyl), 136.97 (C-8-isoindoline), 151.10 (C-3-phenyl), 166.23, 166.42 (C=O).

Synthesis of 2-(2-chloro-4-nitrophenyl)-1,3-dioxoisoindoline-5-carboxylic acid (4)

Following the same procedure as for compound **1**, trimellitic anhydride (1 mmol) and 2-chloro-4-nitroaniline (1 mmol) were refluxed for 52 h in glacial acetic acid (2.5 mL). The crude product was isolated by filtration and recrystallized from methanol to give the desired compound as light brown crystals. Yield: 35%; m.p. 220 °C. IR (KBr, cm^{-1}) ν 1364, 1371, 1485, 1525 (NO_2), 1692, 1731, 1757 (C=O), 2352–3309 (O–H). ^1H NMR (250 MHz, DMSO-d_6) δ 8.57 (s, 1H, H-3-phenyl), 8.48 (d, *J* = 7.75Hz, 1H, H-6-isoindoline), 8.42 (d, *J* = 8.5Hz, 1H, H-5-phenyl), 8.39 (s, 1H, H-4-isoindoline), 8.17 (d, *J* = 7.5 Hz, 1H, H-7-isoindoline), 7.97 (d, *J* = 8.5 Hz, 1H, H-6-phenyl). ^{13}C NMR (62.5 MHz, DMSO-d_6) δ 123.59 (C-5-phenyl), 124.21 (C-7-isoindoline), 124.72 (C-6-phenyl), 125.38 (C-3-phenyl), 132.13 (C-4-isoindoline), 132.61 (C-2-phenyl), 133.56 (C-9-isoindoline), 134.87 (C-5-isoindoline), 135.49 (C-6-isoindoline), 136.24 (C-8-isoindoline), 137.27 (C-1-phenyl), 148.69 (C-4-phenyl), 165.22, 165.89 (C=O).

Synthesis of 2-(3-chlorophenyl)-1,3-dioxoisoindoline-5-carboxylic acid (5)

Following the same procedure as for compound **1**, trimellitic anhydride (1 mmol) and 3-chloroaniline (1 mmol) were refluxed for 4 h in glacial acetic acid (2.5 mL). The crude product was recrystallized from methanol and washed with diethyl ether to give the desired compound as yellow crystals. Yield: 54%; m.p. 290 °C. IR (KBr, cm^{-1}) ν 1692, 1683, 1724, 1784 (C=O), 2352–3309 (O–H). ^1H NMR (250 MHz, DMSO-d_6) δ 8.34 (d, *J* = 7.5Hz, 1H, H-6-isoindoline), 8.24 (s, 1H, H-4-isoindoline), 8.01 (d, 1H, *J* = 7.75Hz, 1H, H-7-isoindoline), 7.40-7.60 (m, 3H, H-2,5,6-phenyl), 7.39 (d, *J* = 7.25Hz, 1H, H-4-phenyl). ^{13}C NMR (62.5 MHz, DMSO-d_6) δ 123.88 (C-7-isoindoline), 124.36(C-4-isoindoline), 126.51 (C-6-phenyl), 127.58 (C-4-phenyl), 128.64 (C-5-phenyl), 130.99 (C-9-isoindoline), 132.40 (C-2-phenyl), 133.35 (C-5-isoindoline), 133.52 (C-6-isoindoline), 135.25 (C-1-phenyl), 135.99 (C-3-phenyl), 136.93 (C-8-isoindoline), 166.22, 166.38 (C=O).

Synthesis of 2-(naphthalen-1-yl)-1,3-dioxoisoindoline-5-carboxylic acid (6)

Following the same procedure as for compound **1**, trimellitic anhydride (1 mmol) and 1-naphthylamine (1 mmol) were heated in glacial acetic acid (2.5 mL) for 25 h under reflux. The crude product was recrystallized from methanol to give the desired compound as yellow crystals.

Yield: 68%; m.p. 230 °C. IR (KBr, cm^{-1}) ν 1667, 1697, 1780 (C=O), 2534–3483 (O–H). ^1H NMR (250 MHz, DMSO-d_6) δ 8.38 (d, *J* = 7.75 Hz, 1H, H-6-isoindoline), 8.28 (s, 1H, H-4-isoindoline), 7.97-8.06 (m, 3H, aromatic), 7.74 (d, 1H, *J* = 8Hz, H-7-isoindoline), 7.57-7.59 (m, 2H, aromatic), 7.44-7.52 (m, 2H, aromatic). ^{13}C NMR (62.5 MHz, DMSO-d_6) δ 123.36 (C-2-naphthyl), 124.00 (C-4-naphthyl), 124.43 (C-8-naphthyl), 126.06 (C-7-isoindoline), 127.09 (C-9-naphthyl), 127.59 (C-4-isoindoline), 127.83 (C-7-naphthyl), 128.71 (C-6-naphthyl), 128.78 (C-3-naphthyl), 130.04 (C-5-naphthyl), 130.51 (C-9-isoindoline), 132.81 (C-5-isoindoline), 134.15 (C-6-isoindoline), 135.64 (C-10-naphthyl), 135.96 (C-8-isoindoline), 136.95 (C-1-naphthyl), 166.36, 166.37 (C=O).

Synthesis of 2-(2,6-dimethylphenyl)-5-(hydroxymethyl) isoindoline-1,3-dione (7)

To a stirred solution of compound **1** (1.06 mmol, 312 mg) in dry tetrahydrofuran (THF, 5 mL), BH_3-THF (4.5 mL) was added dropwise over 30 min at 0 °C. The reaction mixture was stirred for 48 h at the same temperature. Then a saturated aqueous solution of K_2CO_3 (5 mL) was added and stirred for 30 min. The organic phase was separated, washed with saturated $NaHCO_3$ solution and dried over anhydrous $MgSO_4$. The solvent was removed under reduced pressure and the crude product was purified by column chromatography (stationary phase: silica gel; mobile phase: $CHCl_3$-methanol, 1:0.8) to obtain compound **7** as a yellow oil. Yield: 45%. IR (KBr, cm^{-1}) ν 1477, 1438, 1718 (C=O), 2951 (CH aliphatic), 3030 (CH-aromatic), 3000 (O–H). ^{1}H NMR (500 MHz, $CDCl_3$) δ 7.97 (s, 1H, H-4-isoindoline), 7.92 (d, *J* = 7.67 Hz, 1H, H-6-isoindoline), 7.77 (d , *J* = 7.79 Hz, 1H, H-7-isoindoline), 7.26 (t, *J* = 7.61 Hz, 1H, H-4-phenyl), 7.17 (d, *J* = 7.59 Hz, 2H, H-3,5-phenyl), 4.86 (s, 2H, CH_2), 2.14 (s, 6H, CH_3), 2.01 (s, 1H, OH). ^{13}C NMR (125 MHz, $CDCl_3$) δ 18.48 (CH_3), 64.68 (CH_2), 122.24 (C-4-isoindoline), 124.36 (C-4-phenyl), 128.92 (C-3,5- phenyl), 129.93 (C-7-isoindoline), 130.20 (C-8-isoindoline), 131.41 (C-9-isoindoline), 132.85 (C-6- isoindoline), 132.66, 132.85 (C-2,6-phenyl), 137.27 (C-1-phenyl), 148.92 (C-5-isoindoline), 167.59, 167.69 (C=O).

Synthesis of 2-(2,6-dimethylphenyl)-1,3-dioxoisoindoline-5-carbaldehyde (8)

A mixture of compound **7** (0.18 mmol) and MnO_2 (1.44 mmol) in dichloromethane (5 mL) was refluxed for 8 hours. The warm reaction mixture was filtered and the residue was washed with hot acetonitrile. The combined filtrates were concentrated under reduced pressure and the crude product was purified by thin layer chromatography (silica gel; $CHCl_3$-methanol, 1:0.027) to afford compound **8** as a yellow oil. Yield: 80%. IR (KBr, cm^{-1}) ν 1699, 1700, 1778 (C=O), 2853 (CH-aldehyde), 2922 (CH aliphatic), 2957(CH-aromatic). ^{1}H NMR (500 MHz, $CDCl_3$) δ 10.20 (s, 1H, H-aldehyde), 8.449 (s, 1H, H-4-isoindoline), 8.33 (dd, *J* = 7.62 and 1.08 Hz, 1H, H-6-isoindoline), 8.13 (d, *J* = 7.61 Hz, H-7-isoindoline), 7.29 (t, *J* = 7.76, 7.43 Hz, 1H, H-4-phenyl), 7.19 (d, *J* = 7.61 Hz, 2H, H-3,5-phenyl), 2.149 (s, 6H, CH_3). ^{13}C NMR (125 MHz, $CDCl_3$) δ 18.49 (CH_3), 124.97 (C-7-isoindoline), 125.01 (C-4-phenyl), 129.03 (C-3,5-phenyl), 129.84 (C-4-isoindoline), 130.173 (C-9-isoindoline), 133.24 (C-6-isoindoline), 135.91 (C-2,6-phenyl), 136.61 (C-8-isoindoline), 137.07 (C-5-isoindoline), 141.40 (C-1-phenyl), 166.37, 166.47 (C=O), 190.47 (C=O, aldehyde).

Synthesis of 2-(2,6-dimethylphenyl)-1,3-dioxoisoindoline-5-carbaldehyde oxime (9)

A solution of compound **8** (0.17 mmol) and hydroxylamine hydrochloride (0.68 mmol) in methanol (5 mL) was stirred at room temperature for 13 hours. Water (3 mL) was then added and stirring continued for 30 minutes. The mixture was extracted with dichloromethane and the organic phase was dried over anhydrous Na_2SO_4. The solvent was removed under reduced pressure and the crude product was purified by thin layer chromatography (silica gel; $CHCl_3$-methanol, 3:1) to give compound **9** as a yellow oil. Yield: 50%. IR (KBr, cm^{-1}) ν 1616, 1722, 1774 (C=O, C=N), 2922 (CH-aliphatic), 3067 (CH-aromatic), 3000-3650 (N-OH). ^{1}H NMR (250 MHz, CD_3COCD_3) δ 11.1 (s, 1H, N-OH), 8.43 and 8.40 (s,1H, CH=N), 8.20 (s, 1H, H-4-isoindoline), 8.17 (d, *J* = 8Hz, 1H, H-6-isoindoline), 8.01 (d, *J* = 7.5 Hz, 1H, H-7-isoindoline), 7.31 (t, *J* = 5.75 Hz, 1H, H-4-phenyl), 7.24 (d, *J* = 5.75 Hz, 2H, H-3,5-phenyl), 2.15 (s, 6H, CH_3).

3. Methods

3. 1. Pharmacology

The anticonvulsant effects of compounds **1–9** were investigated using maximal electroshock (MES) and pentylenetetrazole (PTZ) models as previously described.[8–15] Male NMRI mice (Balb/c, 8–9 weeks old, 20–25 g) were used in accordance with the Tehran Islamic Azad Medical Sciences University and the *National Institutes of Health (NIH) Guide for the Care and Use of Laboratory Animals.*

The test substances were dissolved in dimethyl sulfoxide and administered intraperitoneally 30 minutes before inducing seizures (groups of 5–6 mice). For the MES test, the conditions that induced tonic seizures in ≥90% of the animals were determined in preliminary experiments. The following parameters were used for all experiments: 0.2 s duration, 50 mA current and 50 Hz frequency. The mortality protection rates and the effects of compounds **1–9** at doses of 5, 10 and 20 mg/kg were determined and compared with phenytoin-treated controls.

In the PTZ test, PTZ (80 mg/kg, i.p.) was used to induce minimal clonic seizures. The latency and frequency of clonic seizures were recorded for each group.

3. 2. Statistical Analysis

The data were analyzed using SPSS 16.0. One-way ANOVA followed by Tukey–Kramer post hoc test was performed, and results were expressed as mean ± SEM. Differences were considered statistically significant at $P < 0.05$.

3. 3. Docking

Molecular modeling and docking of compounds 3 and 4 were performed using HyperChem and AutoDock according to the known procedures.[6–15] Docking results were analyzed with MGL Tools and LigPlot+.[19–20]

4. Results and Discussion

4. 1. Chemistry

Nine new isoindoline derivatives were synthesized with yields between 35 % and 80 % according to the procedure shown in Figure 1. All compounds were characterized by FT IR, ^{1}H NMR and ^{13}C NMR spectroscopy. The reduction of the carboxylic acid group in compound **1** to the corresponding alcohol (compound **7**) was achieved with BH_3, while the oxidation of the alcohol to the aldehyde (compound **8**) was carried out with MnO_2.

4. 2. Pharmacology

PTZ test (clonic seizure)

The PTZ-induced seizure threshold model was used to assess the ability of compounds **1**–**9** to inhibit clonic seizures. The results are summarized in Table 1. All compounds tested showed strong protection against PTZ-induced seizures, with most showing a stronger effect than the reference drug phenytoin. At a dose of 5 mg/kg, all compounds were more potent than phenytoin, with compounds **3** and **4** showing the highest activity. At a dose of 10 mg/kg, all compounds except **8** and **9** were more potent than phenytoin; compounds **1** and **3** were the most active in this group. At a dose of 20 mg/kg, all compounds tested exceeded the potency of phenytoin, with compounds **1**, **3**, 4, **6** and 9 being the most active. All compounds significantly reduced the frequency of clonic seizures at all doses tested compared to vehicle controls. In particular, compounds **1**, **2**, **3**, **4**, **6** and **8** reduced the frequency of seizures more than phenytoin. Of the ligands tested, compounds **3** and **4** showed outstanding activity at all doses and exhibited significant differences compared to both the vehicle-treated and phenytoin-treated groups.

Structure–activity relationship analysis of the PTZ assay results showed that reduction of the carboxylic acid moiety in compound **1** to $-CH_2OH$ (compound **7**), followed by oxidation to an aldehyde (compound **8**) and condensation to an imine (compound **9**), resulted in decreased potency. Thus, compound **1** containing a carboxylic acid was the most active, while compound **9** with the imine moiety was the least active.

Comparing compounds **1**–**6**, compounds **3** and **4** were the most active, which can be attributed to the pres-

Table 1. The ability of isoindoline derivatives (**1-9**) to protect against PTZ- and MES-induced seizures.

No.	**PTZ latency in clonic seizure (mg/kg)**			**PTZ frequency in clonic seizure (mg/kg)**			**Protection of mortality (%) in MES**			**Protection of tonic seizure in MES (%)**		
	20	10	5	20	10	5	20	10	5	20	10	5
1	NS[a]	NS	110.25 ± 8.70^c	0.00 ± 0.00^b	0.00 ± 0.00^b	2.25 ± 8.70	100	100	100	50	50	25
2	584.25 ± 15.33^b	283.15 ± 11.00^b	295.00 ± 10.25^b	0.00 ± 0.00^b	0.00 ± 0.00^b	2.25 ± 0.23	100	100	60	100	50	25
3	NS	NS	NS	0.00 ± 0.00^b	0.00 ± 0.00^b	0.00 ± 0.00^b	100	100	100	90	80	80
4	NS	639.00 ± 10.80^b	410.50 ± 7.07^b	0.00 ± 0.00^b	0.00 ± 0.00^b	1.50 ± 0.07	100	100	100	100	50	75
5	260.77 ± 48.33^b	780.50 ± 35.70^b	188.25 ± 12.50^c	5.77 ± 0.33	4.50 ± 0.70	4.25 ± 0.50	100	100	80	–	80	30
6	NS	245.35 ± 17.19^b	304.67 ± 12.06^b	0.00 ± 0.00^b	4.35 ± 0.19	2.17 ± 0.16	100	80	60	90	80	–
7	280.25 ± 15.00^b	886.15 ± 25.82^b	290.00 ± 17.33^b	4.25 ± 1.00	2.15 ± 0.45	6.24 ± 0.83	60	75	75	15	30	50
8	NS	105.00 ± 29.11^c	126.40 ± 28.25^c	0.00 ± 0.00^b	1.85 ± 0.20	1.40 ± 0.25	100	100	100	75	60	50
9	220.14 ± 17.90^b	95.15 ± 17.21	105.00 ± 8.22^d	6.35 ± 0.90	4.50 ± 0.21	4.11 ± 0.22	100	75	75	20	50	75
PHE	142.15 ± 18.00^c	118.00 ± 6.08	71.70 ± 6.10	1.58 ± 0.30	2.12 ± 1.08	2.85 ± 0.20	100	100	100	100	80	25
DMSO		75.50 ± 5.71			4.60 ± 3.75			0			0	

[a] NS: No seizure; [b] $p < 0.001$, [c] $p < 0.01$, [d] $p < 0.05$. Compared to the DMSO (vehicle) group.

ence of a bulky substituent at one of the ortho positions of the *N*-aryl group, which promotes a perpendicular orientation of the phenyl ring with respect to the isoindoline moiety. Furthermore, the comparison between compounds **2** to **4** showed that a nitro substituent in the meta position of the phenyl ring confers higher activity than substitutions in the ortho or para position.

Overall, these results emphasize that the carboxylic acid moiety has higher anticonvulsant activity compared to alcohol, aldehyde or imine functions, with compound **1** identified as the most potent ligand.

MES test (tonic seizure)

The protective effect of compounds **1**–**9** against tonic seizures induced by maximal electroshock (MES) is also shown in Table 1. Most of the prepared compounds showed significant protection over the entire dose range tested. Compounds **1**, **3**, **4** and **8** provided 100% protection against mortality at all doses and showed efficacy comparable to phenytoin.

4. 3. Docking

In silico studies to evaluate compaunds **3** and **4** as active ligands during in vivo evaluation were performed with the voltage-sensitive sodium channel receptor. The MGL tools and Ligplus were used to study the receptor profile of the drug. The drug-receptor interaction profile of compounds **3** and **4** is shown in Figure 2. Minimum energy, Ki and crowded cluster were used to evaluate the drug-receptor interactions.

In compound **3**, the nitrophenyl ring was located in a hydrophobic pocket formed by residues Phe84, Val 87 and Val 88 of the H-chains and residues Phe91 and Ile95 of the E-chain, where the phenyl ring of compound **3** had a charge transfer interaction with the phenyl ring of Phe84. The carboxyl group at position 4 of the isoindoline component of compound **3** forms a hydrogen bond interaction with residue Ser 84 of chain G (Figure 2A).

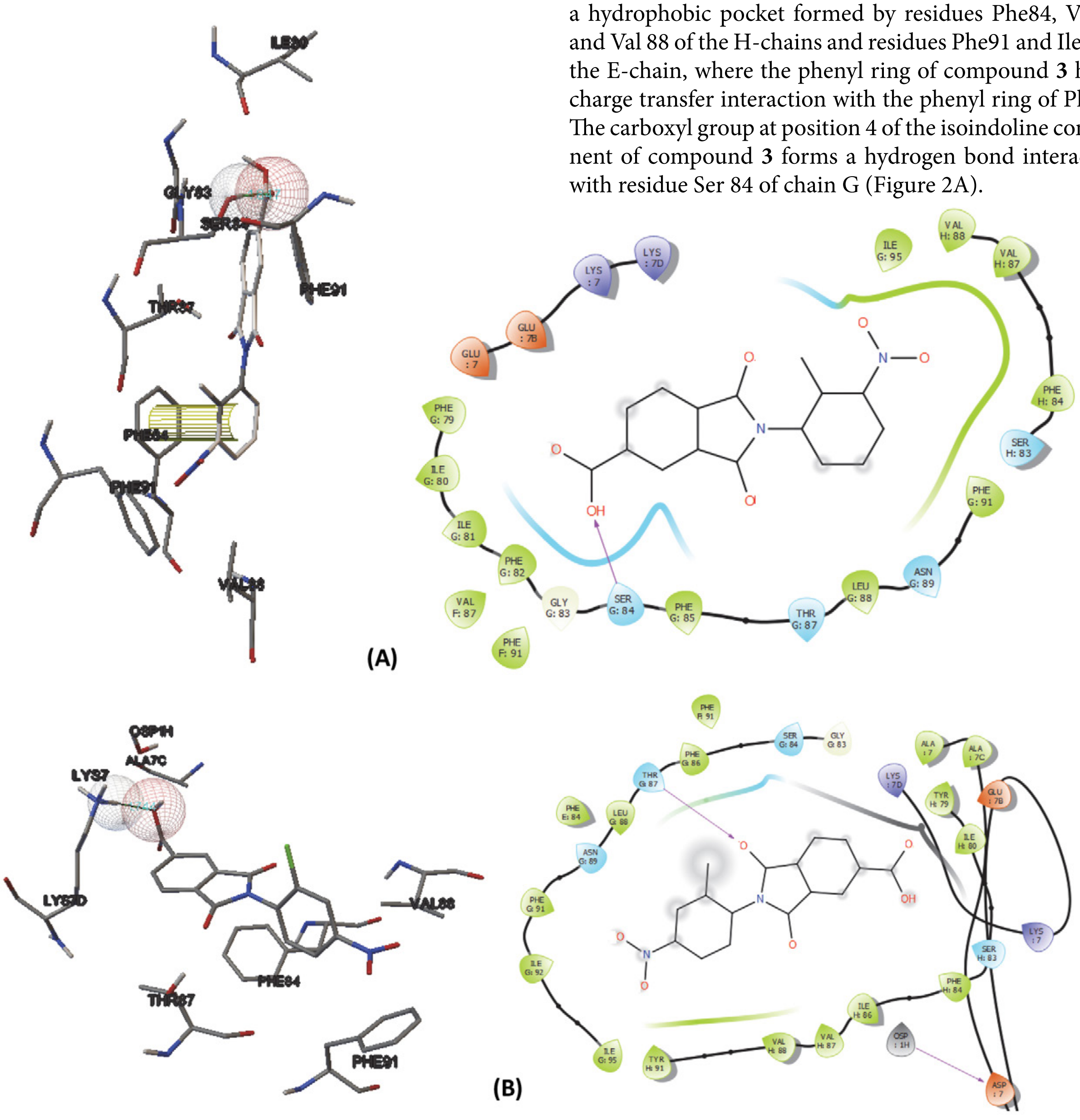

Figure 2. Docked structure of compounds **3** (A) and **4** (B) in the sodium channel model.

In compound **4**, the oxygen of the imide of compound **4** forms a hydrogen bond interaction with residue Thr87 of chain G (Figure 2B). In addition, the *N*-phenyl moiety was aligned with a hydrophobic pocket formed by the hydrophobic residues Phe91, Ile92 and Ile95 of the G chain and Tyr91, Val87 and Val88 of the H chain.

5. Conclusions

Nine new isoindoline derivatives were synthesized and characterized by FT IR, ^{1}H NMR and ^{13}C NMR spectroscopy. Their anticonvulsant activities were investigated using PTZ (clonic seizure) and MES (tonic seizure) models. All compounds showed a pronounced ability to prolong seizure latency, reduce the frequency of clonic seizures and protect against MES-induced tonic seizures. Structure–activity relationship analysis showed that 4-carboxyl derivatives exhibited greater efficacy than 4-hydroxymethyl, 4-carboxaldehyde and 4-hydroxyimine analogs. Compounds **3** and **4** showed the highest potency among all compounds tested, outperforming phenytoin in the PTZ model and showing comparable potency to phenytoin in the MES model.

The results also suggest that the anticonvulsant activity, especially in the PTZ model, is enhanced by the presence of a bulky ortho substituent and by the positioning of the nitro group in the meta position of the phenyl ring instead of the para position. These findings will be useful for the design and synthesis of new isoindoline derivatives with improved anticonvulsant properties.

Ethics Approval and Consent to Participate

No human participants were involved in this study. All animal experiments were performed in accordance with the *National Institutes of Health (NIH) Guide for the Care and Use of Laboratory Animals* and the current regulations of the Medical Sciences Research Center, Tehran Medical Sciences Branch, Islamic Azad University, Tehran, Iran (Approval No. IR.IAU.PS.REC.1399.007).

Conflict of interest

The authors declare no conflict of interest.

Acknowledgements

We thank Professors A. J. Olson and A. Fozzard for their generosity in providing the AutoDock software and the homology model of the sodium channel.

6. References

1. Epilepsy - https://www.who.int/news-room/fact-sheets/detail/epilepsy, 7 February 2024.
2. W. Loscher, P. Klein, *CNS Drugs* **2021**, *35*, 935–963. **DOI:**10.1007/s40263-021-00827-8
3. M. J. Brodie, F. Besag, A. B. Ettinger, M. Mula, G. Gobbi, S. Comai, A. P. Aldenkamp, B. J. Steinhoff, *Pharmacol. Rev.* **2016**, *68*, 563–602. **DOI:**10.1124/pr.115.012021
4. Phenytoin, https://www.accessdata.fda.gov/drugsatfda_docs/label/2009/084349s060lbl.pdf
5. D. W. Robertson, E. E. Beedle, J. H. Krushinski, R. R. Lawson, C. J. Parli, B. Potts, J. D. Leander, *J. Med. Chem.* **1991**, *34*, 1253–1257. **DOI:**10.1021/jm00108a003
6. M. Iman, A. Saadabadi, A. Davood, *Turk. J. Chem.* **2015**, *39*, 306–316. **DOI:**10.3906/kim-1402-37
7. M. Iman, A. Saadabadi, A. Davood, *Iran. J. Basic Med. Sci.* **2013**, *16*, 1016–1021. **PMID**:24171082
8. A. Davood, H. Shafaroudi, M. Amini, A. Nematollahi, A. Shirazi, M. Iman, *Med. Chem.* **2012**, *8*, 953–963. **DOI:**10.2174/157340612802084289
9. A. Davood, M. Amini, L. Azimidoost, S. Rahmatpour, A. Nikbakht, M. Iman, H. Shafaroodi, A. Ansari, *Med. Chem. Res.* **2013**, *22*, 3177–3184. **DOI:**10.1007/s00044-012-0256-y
10. A. Davood, L. Azimidoost, H. Shafaroodi, M. Amini, M. Iman, A. Ansari, A. Nikbakht, M. Iman, S. Rahmatpour, A. R. Nematollahi, *Pharm. Chem. J.* **2014**, *48*, 175–180. **DOI:**10.1007/s11094-014-1073-z
11. M. Iman, A. Saadabadi, A. Davood, H. Shafaroodi, A. Nikbakht, A. Ansarican, M. Abedini, *Iran. J. Pharm. Res.* **2017**, *16*, 586–595.
12. A. Davood, M. Iman, H. Pouriaiee, H. Shafaroodi, S. Akhbari, L. Azimidoost, E. Imani, S. Rahmatpour, *Iran. J. Basic Med. Sci.*, **2017**, *20*, 430–437. **DOI**:10.22038/IJBMS.2017.8586
13. M. Iman, S. Fakhari, M. Jahanpanah, N. Naderi, A. Davood, *Iran. J. Pharm. Res.* **2018**, *17*, 896–905.
14. A. Saadabadi, B. Kohen, M. Irandost, H. Shafaroodi, T. Mohammadpour, M. Rezayat, A. Davood, *Curr. Comput. Aided Drug Des.* **2018**, *14*, 310–321. **DOI:**10.2174/1573409914666180516115450
15. S. Taghizad, K. Behbahaninia, M. H. Jahromy, A. Davood, *Curr. Comput. Aided Drug Des.* **2022**, *18*, 159–167. **DOI:**10.2174/1573409918666220512000247
16. C. Shinji, S. Maeda, K. Imai, M. Yoshida, Y. Hashimoto, H. Miyachi, *Bioorg. Med. Chem.* **2006**, *14*, 7625–7651. **DOI:**10.1016/j.bmc.2006.07.008
17. A. Davood, A. Rahimi, M. Iman, P. Azerang, S. Sardari, A. Mahboubi, *Curr. Comput. Aided Drug Des.* **2021**, *17*, 235–243. **DOI:**10.2174/1573409916666200217090855
18. A. Davood, Y. EbrahimiNassimi, S. Sardari, Y. F. Farahani, *Curr. Pharm. Des.* **2023**, *29*, 1875–1881. **DOI:**10.2174/1381612829666230807120704
19. G. M. Morris, R. H. W. Lindstorm, M. F. Sanner, R. K. Belew, D. S. Goodsell, A. J. Olson, *J. Comput. Chem.* **2009**, *30*, 2785–2791. **DOI:**10.1002/jcc.21256
20. A. C. Wallace, R. A. Laskowski, J. M. Thornton, *Protein Eng.* **1995**, 8, 127–134. **DOI:**10.1093/protein/8.2.127

Povzetek

Izoindolinsko ogrodje, togi analog ameltolida, kaže pomembne antiepileptične lastnosti. V prispevku je opisana zasnova, sinteza in vrednotenje devetih novih izoindolinskih derivatov, pripravljenih s kondenzacijo anhidrida benzen-1,2,4-trikarboksilne (trimelitne) kisline z različnimi arilamini. Antikonvulzivno aktivnost pripravljenih spojin je ocenjena z modelom maksimalnega elektrošoka (MES; toniči napad) in pentilentetrazolom (PTZ; klonični napad). Vse pripravljene spojine so znatno oslabile tako tonične kot tudi klonične napade; pri MES so zmanjšale umrljivost zaradi napadov, medtem ko so pri PTZ pomembno zmanjšale pogostost in latenco napadov. Spojini 3 in 4 sta pokazali najvišjo učinkovitost in presegli fenitoin kot standard. Analiza strukture in aktivnosti spojin kaže, da sterično veliki orto-substituenti na N-arilni skupini v kombinaciji z meta-nitro substituentom povečajo antikonvulzivno učinkovitost.

DOI: 10.17344/acsi.2025.9244 *Acta Chim. Slov.* **2025,** *72,* 532–544

Scientific paper

Therapeutic Potential and *In silico* Evaluation of Phytochemicals in the Leaves of *Eucalyptus Globulus*, *Jasminum Officinale* and *Solanum Nigrum*

Imran Ali[1ⴕ*], Afshan Kaleem[2ⴕ*], Farah Akram[2], Muhammad Talal[1], Roheena Abdullah[2], Mehwish Iqtedar[2], Irfana Iqbal[1], Xiaoming Chen[1]

[1] *'College of Life Sciences and Agri-forestry, Southwest University of Science and Technology. 621010, China*

[2] *Department of Biotechnology, Lahore College for Women University, Lahore, Pakistan*

* *Corresponding author: E-mail: imranalisheik@gmail.com; afshan.kaleem@lcwu.edu.pk*
Call: +86-13088107801

ⴕ *Both authors contributed equally as principal authors*

Received: 03-12-2025

Abstract

In this study, the plants *Eucalyptus globulus* (*E. globulus*), *Jasminum officinale* (*J. officinale*), and *Solanum nigrum* (*S. nigrum*) are investigated for their antibacterial, antioxidant, and therapeutic properties. The extraction solvents (aqueous, methanol, ethanol, and butanol) were used for phytochemical screening, antibacterial activity while aqueous extracts were specifically used for antioxidant analysis. The quantitative determination showed that the highest phenolic and tannin content was found in *J. officinale*, while highest flavonoid and alkaloids levels were found in *E. globulus* among the tested species. The disc diffusion method was followed for assessing the antibacterial activity against *Escherichia coli* (*E. coli*) and *Staphylococcus aureus* (*S. aureus*). All extracts of *E. globulus* leaves showed antibacterial activity against *E. coli* and *S. aureus*. The aqueous extracts on FTIR showed quercetin, benzoic, salicylic, gallic, ferulic, and ascorbic acid. Furthermore, *in silico* analysis to assess the interaction of selected bioactive compounds, quercetin and benzoic acid, found in *E. globulus*, were docked with haemagglutinin and neuraminidase, as these influenza virus surface proteins play an important role in the virus's ability to infect host cells. Salicylic, gallic, ferulic, and ascorbic acid from *J. officinale* and *S. nigrum,* were docked with GABA receptor-associated proteins, which are important in synaptic transmission and plasticity.

Keywords: Disc diffusion method; anti-bacterial; DPPH radical scavenging assay; haemagglutinin; neuraminidase; GABA receptor-associated protein.

1. Introduction

Plants provide the basis of intricate, conventional medical systems that have been used for many years, and scientists are still developing innovative remedies for humanity today. Plants are commonly used to treat infections and other conditions.[1] Nearly two-thirds of people worldwide utilize medicinal plants for primary healthcare. When compared to conventional medications, medicinal plants have fewer side effects, are readily available, and cost less.[2]

Antibiotic resistance has been created in microorganisms due to the haphazard usage of antimicrobial drugs. Several antimicrobial drugs are needed to treat infectious diseases. One strategy is to examine the potential antibacterial properties of local herbal remedies. Medicinal plants serve as a substantial reservoir of new antifungal and antibacterial chemotherapeutic drugs.[3] Medicinal plants are good antioxidants, anti-diabetic agents, antibacterial agents, anti-cancer agents, detoxifying agents, antifungal agents, and neuro-pharmacological agents.[4]

Jasmine belongs to the olive family and is a genus of shrubs/vines in this family.[5] *J. officinale* stems have been used to treat chronic inflammatory conditions like colitis, ulceration, angiitis, and enteritis, as well as for the alleviation of insomnia.[6] The entire plant is traditionally used to treat skin conditions, tumors, and chronic ulcers. The alkaloids, salicylic acid, ascorbic acid, and resin found in the entire plant are used to cure fevers, skin conditions, and ulcers[7]. *Eucalyptus* is a genus that possesses various shrubs and flowering trees. Eucalyptus leaves possess antioxidant, anti-inflammatory, and antibacterial properties. *Eucalyptus* is used to treat ailments such as rheumatism, skin diseases, upper respiratory tract infections, diabetes, snakebites, and diarrhea.[8,9] *S. nigrum* is an annual herbaceous herb.[10] Whole plants are used for coughs, burns, snake bites, rabies, wound healing, and enhancing sleep.[11,12]

The discovery of new therapeutic agents has been based on medicinal plants. Based on their reported pharmacological characteristics and documented traditional uses, this study investigates the bioactive potential of *J. officinale*, *E. globulus,* and *S. nigrum*. They have been traditionally used to treat respiratory diseases and sleep disturbances. Although several phytochemicals from these plants have demonstrated preliminary antiviral and sedative effects, more research is needed to confirm their relevance to illnesses such as influenza and insomnia [13,14]

2. Materials and Methods

2. 1. Plant Collection

Fresh and disease-free plant samples of *E. globulus*, *J. officinale,* and *S. nigrum* were collected from dry and shady areas of GCU botanical garden, Lahore, Pakistan.

2. 2. Plant Extract Preparation

The plant extract preparation was started by washing the leaves 2–3 times with running tap water and drying them completely under shade. The plant leaves were dried and grounded to a fine powder. 20 g of powdered leaves from each plant species (*E. globulus*, *J. officinale,* and *S. nigrum)* were soaked in 200 mL of each solvent (ethanol, methanol, butanol, and distilled water). The mixtures with a concentration of 0.1 g/ml were periodically stirred, while being stored at room temperature (25 ± 2 °C) for 72 hours followed by filtration using Whatman No. 1 filter paper. The dried extracts were kept at 4 °C in sterile, labelled containers for phytochemical, antioxidant, and antibacterial analysis.[16–18]

2. 3. Phytochemical analysis

Both qualitative and quantitative tests were performed for phytochemical analysis.

(a) Qualitative analysis

For the determination of bioactive components present in plant leaves, different tests were performed, including alkaloids, flavonoids, phenolics, terpenoids, anthraquinones, carbohydrates, proteins, coumarins, emodins, saponins, steroids, tannins, anthocyanins, leucoanthocyanin, quinones, cardiac glycosides, and phlobotannins.[19,20]

(b) Quantitative Analysis

The total phenolics, flavonoids, tannins, alkaloids, and antioxidant activity were quantified using standard spectrophotometric methods. Measurements were taken in triplicates. Total Phenolic Content (TPC) was measured using the Folin-Ciocalteu method with gallic acid as a reference. 0.5 mL of extract was wixed with 0.6 mL of Folin-Ciocalteu reagent, then 1.5 mL of 20% Na_2CO_3 was added and incubated for 90 minutes in the dark. The absorbance was measured at 765 nm.[21]

Total Tannin Content (TTC) was calculated using the Folin-Ciocalteu method with a tannic acid standard. 0.1 mL of extract which was treated with 0.5 mL Folin reagent and 1 mL of 35% Na_2CO_3.The absorbance was measured at 725 nm after 30 minutes.[22]

Total Flavanoid Content (TFC) was calculated using the aluminium chloride method with quercetin standard. To 0.5 mL of extract, 1 mL water, 75 μL of 5% $NaNO_2$, 75 μL of 10% $AlCl_3$, and 0.5 mL of 1M NaOH was added, and incubated for 15 minutes. The absorbance at 510 nm was measured.[22]

Alkaloid content was determined by extracting 1.25 g of powder in 50 mL of 10% acetic acid in ethanol for 4 hours. The filtrate was concentrated to 1/4 and precipitated with NH_4OH. The residue was filtered, dried, weighed, and the alkaloid content was determined.[23]

The *in vitro* approach was used to measure the antioxidant activity (DPPH free radical scavenging assay) 100–200 μL extract was mixed with 1 mL of 0.4 mM DPPH. Incubated for 30 minutes in the dark. The absorbance was measured at 517 nm.[24]

2. 4. Antibacterial Activity

To determine antibacterial activity against *S. aureus* and *E. coli,* the disc diffusion method was used. Sterile 6 mm filter paper discs were impregnated with plant extracts at doses of 25, 50, 75, and 100 μL. 50 μl broth was spread on nutrient agar plates. The discs that had been impregnated with various extracts quantities were incubated at 37 °C for 24 hours. The inhibition zones were recorded.[25] As positive control the antibiotics Tetracycline was used, which zone of inhibition was 15 mm.

2. 5. Bioinformatic Analysis

The aqueous extracts of *E. globulus*, *J. officinale,* and *S. nigrum* were used to identify different functional groups of bioactive compounds by FTIR.[26] The compounds were found using the Pubchem database (https://pubchem.ncbi.nlm.nih.gov/). The bioactive compounds in *E. globulus* found by FTIR were used for *in silico* investigation by molecular docking against the target proteins influenza virus hemagglutinin (PDB ID: 4WE5) and neuraminidase (PDB ID: 7U4F) and bioactive compounds in *J. officinale* and *S. nigrum* against GABA receptors associated protein

(1KOT). The Galaxy web (https://galaxy.seoklab.org/) was used for the determination of ligand and protein interaction. The protein structure was retrieved from the Protein Data Bank (PDB) (https://www.rcsb.org/)

2. 6. Statistical Analysis

All analyses were analyzed as triplicates, and for statistical analysis, SPSS (version 32) was used, and the one-way ANOVA test was performed to check the significance ($p < 0.01$) of the results.

3. Results and Discussion

There is a dire need to develop novel antibacterial medicines, as the excessive usage of antibiotics leads to antibiotic resistance.[27] Plants are a big source of phytochemicals and possess numerous biological properties.[28] The use of solvents also plays a crucial role in the extraction process of phytochemicals.[30] Different types and content of secondary metabolites that are recovered from plants are influenced by the solvents employed in the extraction process.[31] Phenols, flavonoids, and tannins are polar phytochemicals that dissolve easily in polar or semi-polar solvents, making them more effective for extracting these components from dried plant materials.[33]

3. 1. Antimicrobial Activity of Extracts

The leaf extracts of *E. globulus* showed antibacterial activity against both *E. coli* and *S. aureus* (Fig. 1–3). All extracts of *J. officinale* leaves showed zones of inhibition against *E. coli* and *S. aureus*, while the leaf extracts of *S. nigrum* showed no activity against *E. coli* and *S. aureus*. *S. nigrum* methanol extracts showed the highest activity against *E. coli* (Fig. 1–3).

With the increase in concentration, an increase in inhibition zones was observed that has been reported.[34] Butanol extracts proved to be the most effective due to their intermediate polarity.[35] This enables it to extract a diverse spectrum of bioactive components, including moderately polar phytochemicals, which may contribute to the observed antibacterial properties. As an organic solvent, it enhances the dissolving of both polar and non-polar molecules, hence improving the extraction of a wide range of active components.[36] Methanol and butanol extracts of *E. globulus* leaves showed more inhibition zones against *S.*

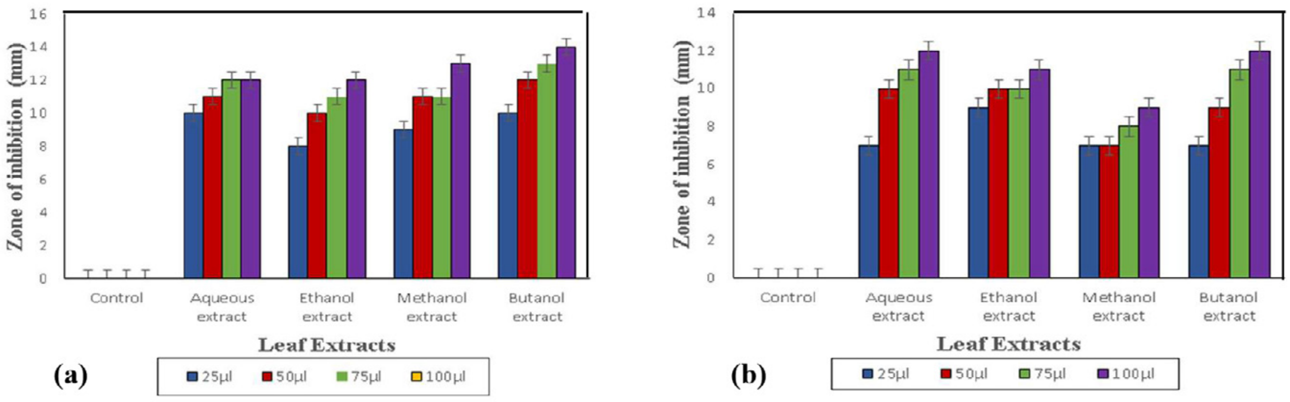

Fig. 1. (a) Antibacterial activity of *E. globulus* leaf extracts against *E. coli* **(b)** Antibacterial activity of *E. globulus* leaf extracts against *S. aureus*.

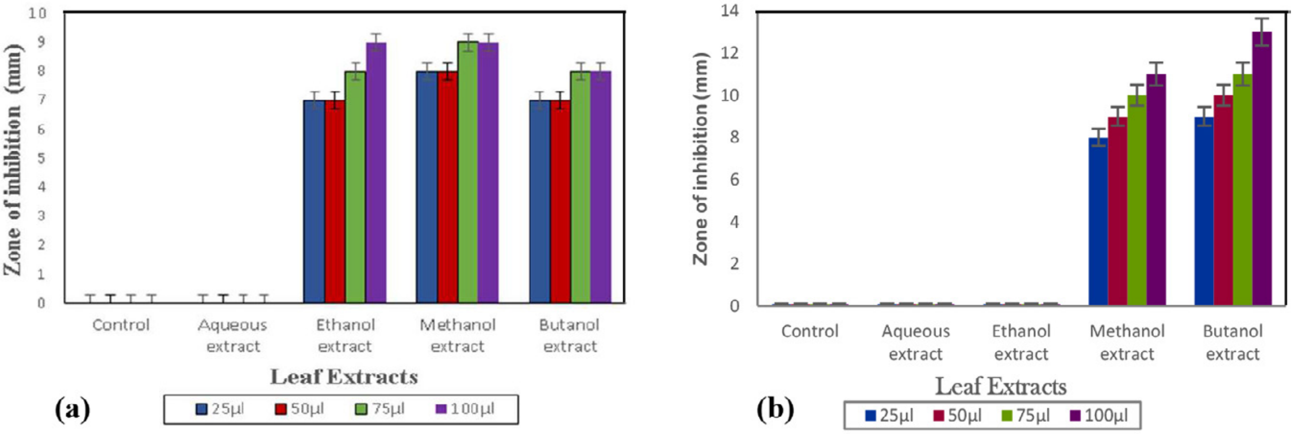

Fig. 2. (a) Antibacterial activity of *J. officinale* leaf extracts against *E. coli* **(b)** Antibacterial activity of *J. officinale* leaf extracts against *S. aureus*.

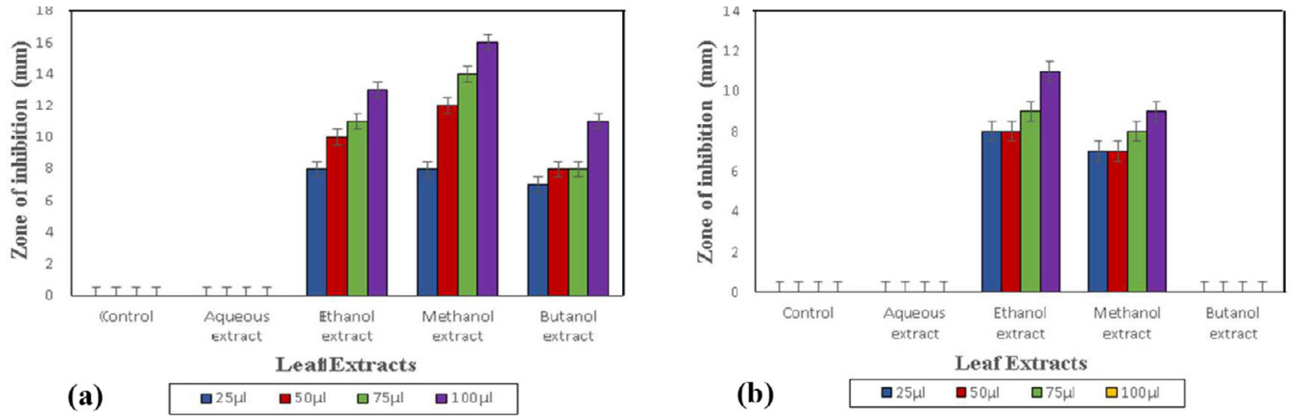

Fig. 3. (a) Antibacterial activity of *S. nigrum* leaf extracts against *E. coli* **(b)** Antibacterial activity of *S. nigrum* leaf extracts against *S. aureus.*

aureus and *E. coli,* which has been reported in different publications.[8,18,37] It was also reported that similar leave- and root- aqueous extracts showed higher activity against *E. coli* and *S. aureus* as compared ethanol extract.[38] The highest zones in butanol might be due to its high polarity as compared to other solvents.[39] Ethanol extract of *J. officinale* inhibited both strains, similar to the results of[7] and,[40] which reported that DCM and methanol extract of *J. officinale* whole plant showed the higher inhibition zones as compared to aqueous, ethanol, methanol and butanol extracts of leaves. The results of this study follow the work of different research groups,[41, 42] who reported that aqueous extract of *S. nigrum* leaves showed no inhibition zones, while methanol extracts showed high inhibition zones against *E. coli* and *S. aureus*. Our results are contradictory to the work of,[11] who reported that aqueous extract showed inhibitory activity against both *E. coli* and *S. aureus*. Butanol extract from leaves of *S. nigrum* did not show activity against *S. aureus*.

3. 2. Qualitative Analysis of Extracts

Qualitative phytochemical analysis of leaf extracts of *E. globulus*, *J. officinale* and *S. nigrum* was performed for the identification of secondary metabolites present in them. Extracts showed that alkaloids, flavonoids, saponins, steroids, carbohydrates and tannins are present in these extracts, while phlobotannins, emodins, anthocyanins and leucoanthocyanins were not found.[43–45] Qualitative analysis of different solvent extracts of *E. globulus*, *J. officinale* and *S. nigrum* was performed. Phytochemical tests showed that alkaloids, carbohydrates, coumarins, cardiac glycosides, steroids, phenol, protein, tannin, quinones and terpenoids were the bioactive components identified in all plant extracts.[46–48] The results of this work correlate with the work of different research groups.[18,49] Furthermore, it has been reported that anthocyanins, anthraquinones, phlobtinins and leucoanthocyanins are not present in any parts of *E. globulus, J. officinale* and *S. nigrum*. These phytochemicals make plants good antioxidants, enhancing antibacterial, anti-inflammatory, anti-influenza, anti-diabetic, and anti-sedative properties.[50,51]

3. 3. Quantitative Analysis of Extracts

Quantitative phytochemical analysis of the leaf extracts of *E. globulus*, *J. officinale*, and *S. nigrum* were performed (Fig. 4). Total phenol content, flavonoid content, tannin content, alkaloids, and antioxidant activity of each extract were calculated. The results showed that maximum alkaloid content (60%) was present in *E. globulus* as compared to other extracts; maximum tannin content (0.38 mg TAE/mL) was found in *J. officinale*, max. phenolic content was found in *J. officinale* (0.64 mg GAE/mL), and the highest flavonoid (11.39 mg QAE/mL) content was present in *E. globulus* leaves.

The highest amount of flavonoid was found in the leaves of *E. globulus* (11.39 mg/mL) and the least in *S. nigrum* (1.725 mg/mL). Total phenolic content and tannin content were highest in *J. officinale* (0.64 mg/mL, 0.38 mg/mL) and least in *S. nigrum* leaves (0.15 mg/mL, 0.209 mg/mL). Alkaloid content was found to be highest in *E. globulus* (60%) and least in *S. nigrum* (46%). These results are compatible with the results of,[37] which showed similar values of the total flavonoids and phenolic content in the leaves of *E. globulus*. The aqueous extract of *E. globulus* showed higher flavonoid, phenol, tannin, and alkaloid content as compared to the methanol extract, which has been reported.[8,52] Methanol extract of *J. officinale* leaves showed lower flavonoid, phenol, and tannin content that has already been reported by[53] and is in agreement with.[54] Methanol extract of *S. nigrum* leaves showed more flavonoid, phenol, tannin, and alkaloid content as compared to aqueous extract.[41]

2,2-Diphenyl-1-picrylhydrazyl (DPPH) assay was used to measure the antioxidant activity of aqueous extracts. Aqueous extracts were chosen to assess antioxidant activity since they are commonly used in traditional medicine and contain polar phytochemicals such as phenols and flavonoids, both of which contribute considerably to antioxidant activity. Furthermore, aqueous extracts are

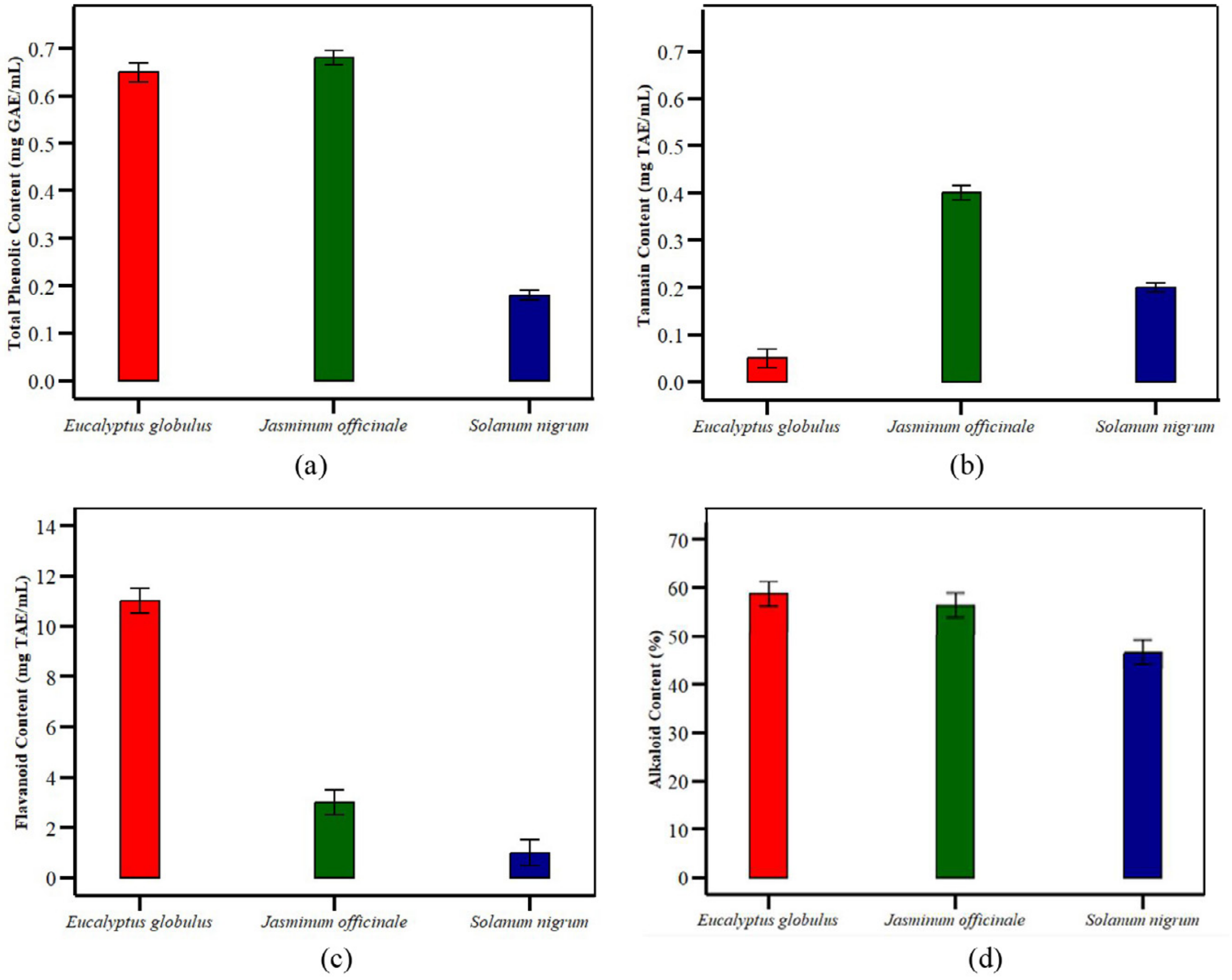

Fig. 4. (a) Determination of total phenolic content in aqueous leaf extracts of *E. globulus, J. offcinale* and *S. nigrum* **(b)** Tannin content in aqueous extracts leaves of *E. globulus, J. offcinale* and *S. nigrum.* **(c)** Flavonoid content in aqueous extracts of leaves of *E. globulus, J. offcinale* and *S. nigrum.* **(d)** Alkaloid content in leaves of *E. globulus, J. offcinale* and *S. nigrum.*

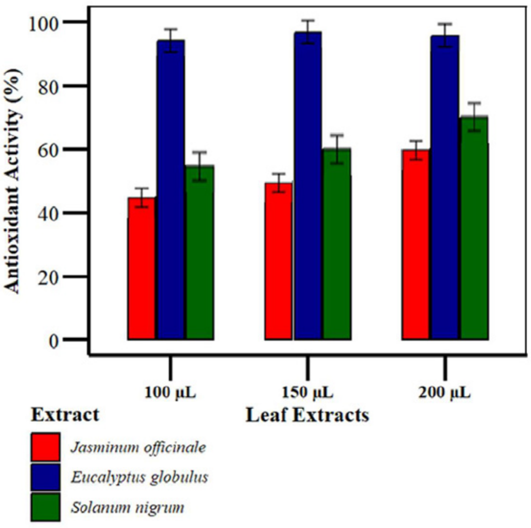

Fig. 5. Determination of the antioxidant activity of *J. offcinale*, *E. globulus* and *S. nigrum* leaves.

easier to use in the DPPH assay since they do not require organic solvents or evaporation stages, making them ideal for early antioxidant screening. An increase in radical scavenging activity shows a low absorbance value.[55] The antioxidant activity increased with the increase in concentration.[56] The results of this study are consistent with previous findings, which reported that the antioxidant activity was lower in leaves than in stems of *E. globulus*.[52] Another study found higher antioxidant activity in methanol extract of *E. globulus* leaves, when compared with its aqueous extract. For *J. officinale*, the leaves exhibited the highest antioxidant activity, as previously reported.[53] (Fig. 5). Comparative evaluation of solvent extracts is a promising subject for future research.

3. 4. FTIR Analysis

The aqueous extracts of *E. globulus*, *J. officinale,* and *S. nigrum* were used for FTIR analysis to determine dis-

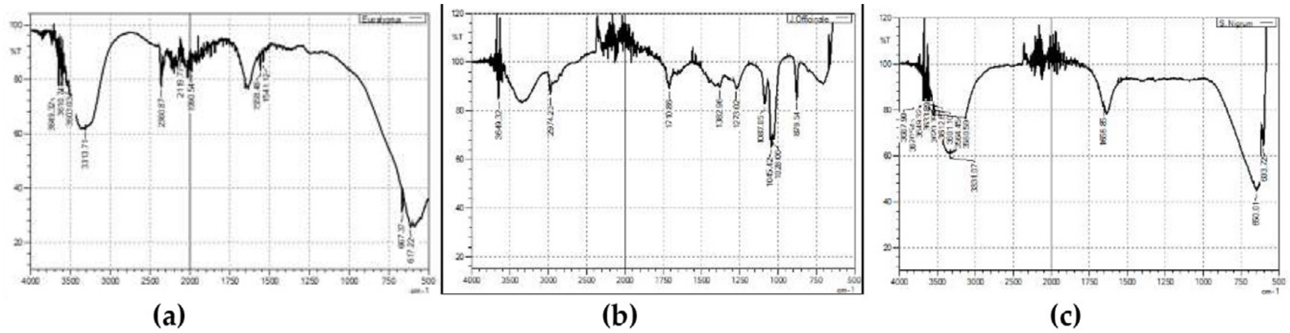

Fig. 6. FTIR spectrum of *E. globulus* leaves (a), *J. officinale* leaves (b), and *S. nigrum* leaves (c)

tinctive functional groups in the phytochemical profile (Fig. 6, Table 1). This analysis revealed functional groups such as C=C, COO⁻, C=O, C–N, and N–H, recognized through distinctive absorption peaks. These groups are frequently found in classes of bioactive chemicals such as flavonoids, phenolics, and carboxylic acids. These functional groups are found in many beneficial substances, including quercetin, benzoic acid, salicylic acid, rutin, and ascorbic acid. While FTIR cannot determine the specific identity of these compounds, spectrum similarities indicate their possible presence, backed up by literature and bioinformatic analysis on known phytochemicals in these plants.[57] This guided the selection of quercetin, benzoic acid, salicylic acid, and ascorbic acid for molecular docking investigations. Thus, FTIR gave functional proof of their presence, but compound-level validation is outside the purview of this investigation.

Table 1. Functional groups detected by FTIR analysis found *Eucalyptus globulus*, *Jasminum officinale* and *Solanum nigrum*

Plants extracts	Frequency range	Functional group
Eucalyptus globulus	1541 cm^{-1}	Carboxyl group (COO^-) and
	637 cm^{-1}	C=C stretching C–H stretch and C≡C–H bend
Jasminum officinale	1273 cm^{-1}	C–N stretch
	1382 cm^{-1}	C–N stretch
	1636 cm^{-1}	C=O stretch
	3313 cm^{-1}	N-H functional group
Solanum nigrum	667 cm^{-1}	C–H stretch and C≡C–H bend
	1656 cm^{-1}	C=C stretching
	3313 cm^{-1}	N–H functional group

3. 5. Bioinformatic Analysis of Bioactive Compounds

Molecular docking studies were conducted against specific protein targets that correspond with the traditional or pharmacological use of the plants in order to offer a deeper understanding of the therapeutic relevance of the phytochemicals found. The antiviral properties of *E. globulus* are well known, particularly in relation to respiratory tract infections. Thus, the Influenza A virus's surface glycoproteins, haemagglutinin and neuraminidase, were selected to investigate possible antiviral interactions. On the other hand, *S. nigrum* and *J. officinale* have ethnomedical significance in neurological conditions like anxiety and insomnia. In order to study neuropharmacological interactions, GABA receptor-associated protein, a protein that regulates neurotransmitters in the central nervous system was chosen. In order to guarantee that the docking simulations represent therapeutic pathways that are biologically plausible, these choices were made.

Molecular docking was performed of the determined bioactive components against the two proteins haemagglutinin and neuraminidase in *E. globulus*, and GABA receptor associated protein in *J. officinale* and *S. nigrum* against.

Molecular docking studies were conducted to evaluate the interactions of quercetin and benzoic acid ligands with neuraminidase (PDB ID: 7U4F) and haemagglutinin (PDB ID: 4WE5). The analysis revealed various hydrophobic interactions and hydrogen bonds between the ligands and target proteins. The best docking models, which displayed hydrogen bonding patterns, hydrophobic contacts, ligand-binding sites, and overall protein–ligand interactions, were selected (Tables 2–3; Figs. 7–9). *In silico* screening was performed to identify potential new drug leads and elucidate possible mechanisms of action. Additional docking of identified bioactive compounds was carried out with haemagglutinin (4WE5), neuraminidase (7U4F), and the GABA receptor-associated protein (1KOT), revealing hydrogen bonding and hydrophobic interactions within the receptor binding pockets.[58] An increase in negative binding energy indicated greater stability of the protein–ligand complexes.[59]

The Influenza A virus is an infectious respiratory disease.[60] Hemagglutinin and neuraminidase are surface glycoproteins of the Influenza A virus[61] and functional targets for anti-influenza therapy.[62] FTIR spectra confirmed the presence of quercetin, methane and benzoic acid in *E. globulus*. These bioactive components were docked with 4WE5 and 7U4f. Methane did not bind with 4WE5 and 7U45, while quercetin and benzoic acid actively bind with the proteins, as reported by.[63] Quercetin is a compound which belongs to the flavonoids class.[64] It possesses antimicrobial and anti-inflammatory properties.[65] Benzoic acid is a compound composed of a benzene ring along with carboxylic acid. It possesses antibacterial, antiviral and food preservation properties. Compounds of benzoic acid have anti-influenza virus properties.[66] Quercetin binds with neuraminidase via hydrogen bonding and hydrophobic interaction with Glu 413, Trp 87, Arg 85, Cys 124, Phe 410, Glu 229, Cys 280 and Ser 228 (Table 2), which are the amino acids that bind with the head of neuraminidase ranging from 91–469. Whereas benzoic acid did not show hydrogen bonding and hydrophobic interactions with Neuraminidase. Quercetin binds with haemagglutinin via hydrogen bonding with Thr 65 and Tyr 100 and hydrophobic interaction with Tyr 105, Arg 109 and Ile 67 (Table 3). Whereas, benzoic acid binds with haemagglutinin via hydrogen bonding with Arg 109 and hydrophobic interactions with Ile 67, Tyr 100, Tyr 105 and Val 102 (Table 3), which are the amino acids present in the topological domain extending from 17–530.[67] Neuraminidase cleaves terminal sialic acids and prevents the escape of the virus from host cells.[61] Haemagglutinin binds with sialic acids, attaches the virus on the cell surface and penetrates the virus into host cells.[68] Benzoic acid and quercetin prevent the virus from penetrating and escaping from its host cell.[69] The result showed that benzoic acid and quercetin bind with the active catalytic site of the domain and suppresses the neuraminidase and haemagglutinin activity.[70,71] Quercetin showed strong binding abilities with haemagglutinin and neuraminidase. As Quercetin bound with both surface proteins of the Influenza A virus, it could be a potent anti-influenza compound.

Interactions of ligands salicylic acid, gallic acid, ferulic acid and ascorbic acid with protein GABA receptor associated protein (PDB ID: 1KOT). Different hydrogen bonds and hydrophobic interactions were formed between the protein and ligands. The best model was chosen that shows the hydrogen bonding, hydrophobic interaction, ligand binding sites and protein ligand interaction (Table 4 and Fig. 10–13).

Table 2. Binding of Quercetin with Neuraminidase

Ligand	7U4F AA	Types of bonds	Length (A)	Ligand AA binding sites
Quercetin	Glu 413	HB	3.35	OE1-O7
	Trp 87	HI		
	Arg 85	HI		
	Cys 124	HI		
	Phe 410	HI		
	Glu 229	HI		
	Cys 280	HI		
	Ser 228	HI		

Table 3. Binding of quercetin and benzoic acid with haemagglutinin protein

Ligand	Haemagglutinin AA	Types of bonds	Length (A)	Ligand AA binding sites
Quercetin	Thr 65	HB	2.95	OG1–O6
	Tyr 100	HB	2.87	OH–O6
	Tyr 105	HI		
	Arg 109	HI		
	Ile 67	HI		
		HI		
		HI		
		HI		
Benzoic aicd	Arg 109	HB	3.15	NH2–O2
	Ile 67	HI		
	Tyr 100	HI		
	Tyr 105	HI		
	Val 102	HI		

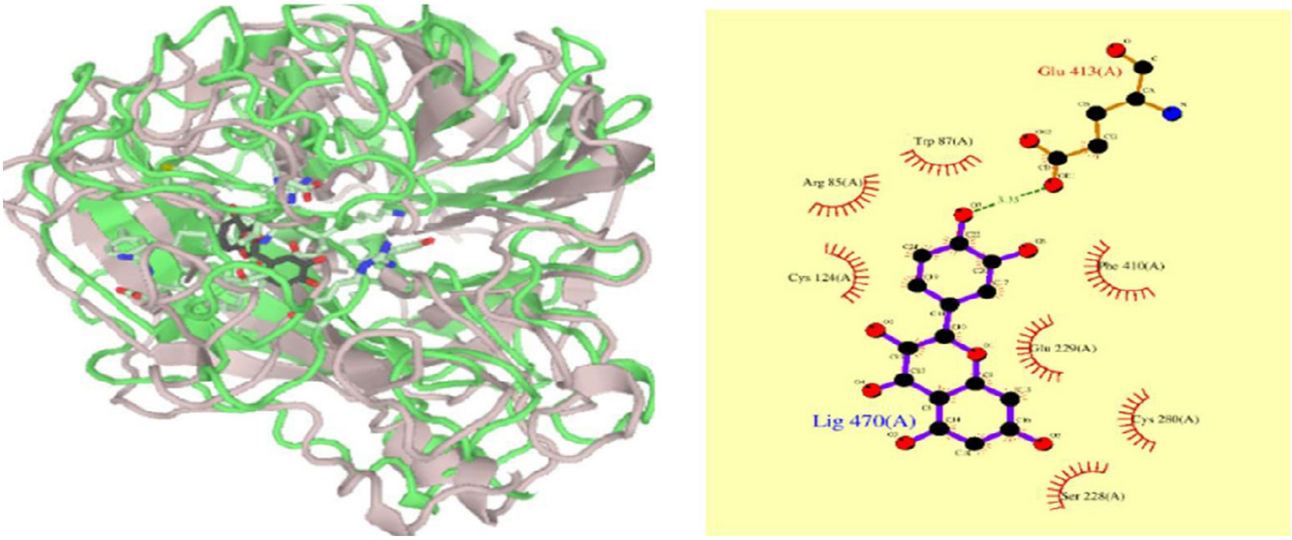

Fig. 7. Results of docking of quercetin ligand with neuraminidase

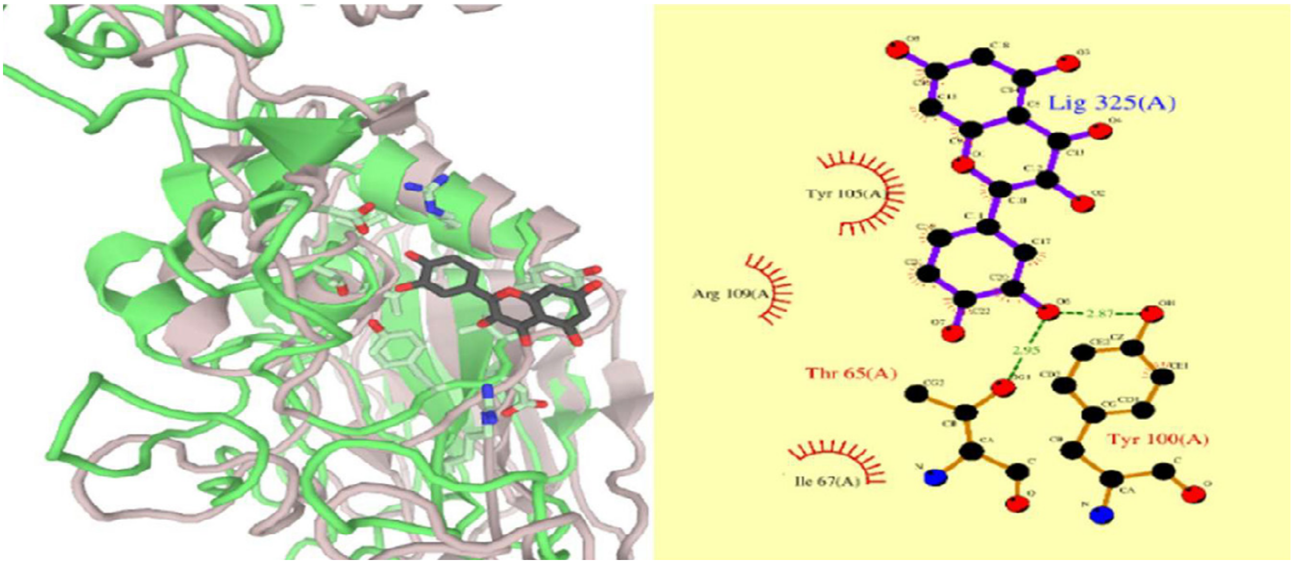

Fig. 8. Results of docking of quercetin ligand with haemagglutinin

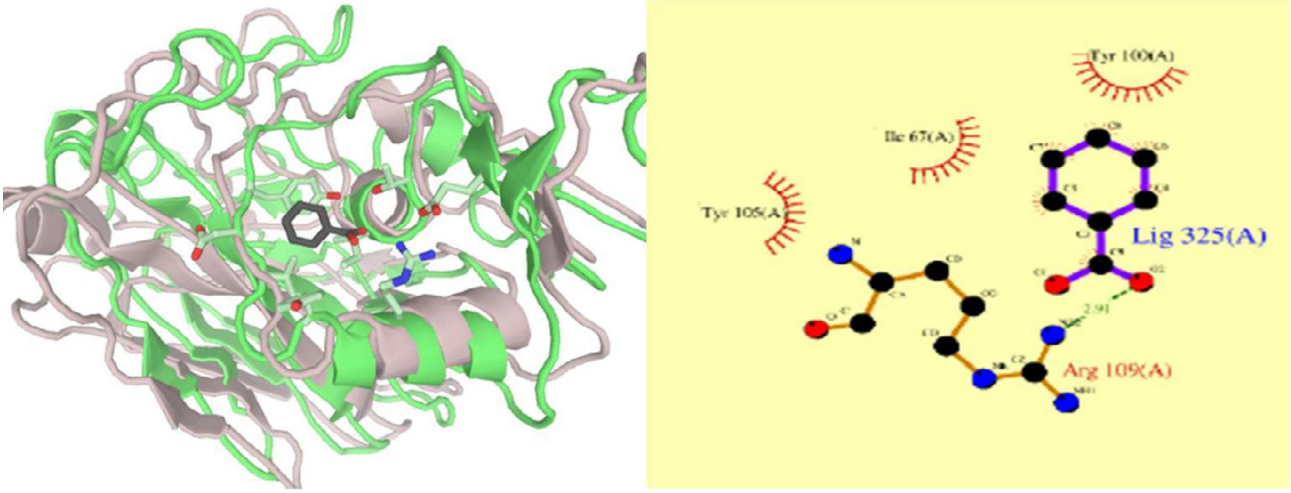

Fig. 9. Results of docking of benzoic acid with haemagglutinin

Table 4. Binding of different salicylic acid, ferulic acid, gallic acid and sscorbic acid with GABA receptor associated protein

Ligand	GABA receptor associated protein (AA)	Types of bonds	Length (A)	Ligand AA binding sites
Salicylic acid	Asn 84	HB	3.11	ND2–O1
	Val 85	HI		
	Ile 86	HI		
Ferulic acid	Lys 40	HB	2.86	NZ–O1
	Ser 112	HB	2.84	
	Glu 114	HI		
	Val 116	HI		
	Gly 118	HI		OG–O3
Gallic acid	Asp 113	HB	2.86	OD2–O1
	Lys 40	HI		
	Glu 114	HI		
	Val 116	HI		
Ascorbic acid	Lys 238	HB	3.05	NZ–O3
	Ile 236	HI		
	Ile 260	HI		
	Leu 111	HI		
	Leu 177	HI		
	Ser 115	HI		

GABA receptor-associated proteins are neurotransmitters that play a role in the regulation of the sleep cycle.[72] A new method of pharmacologically influencing receptor activation and neurotransmitter action at the synaptic junction is the modification of GABA receptor-associated protein binding to its interacting partners.[73] FTIR spectra of *J. officinale* confirmed the presence of salicylic acid, gallic acid, ferulic acid, epicatechin and rutin.

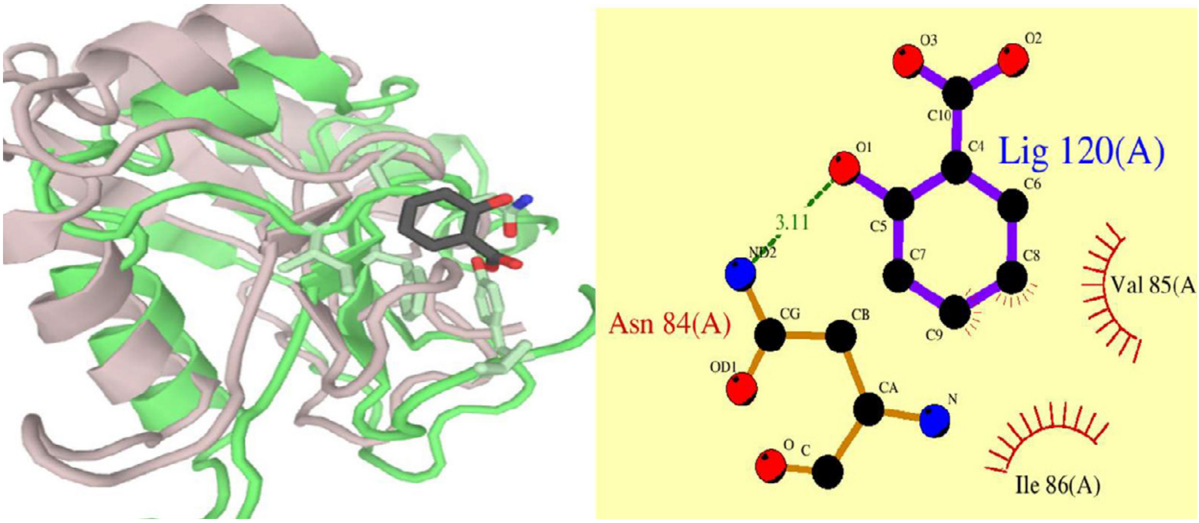

Fig. 10. Results of docking of salicylic acid ligand with GABA receptor associated protein

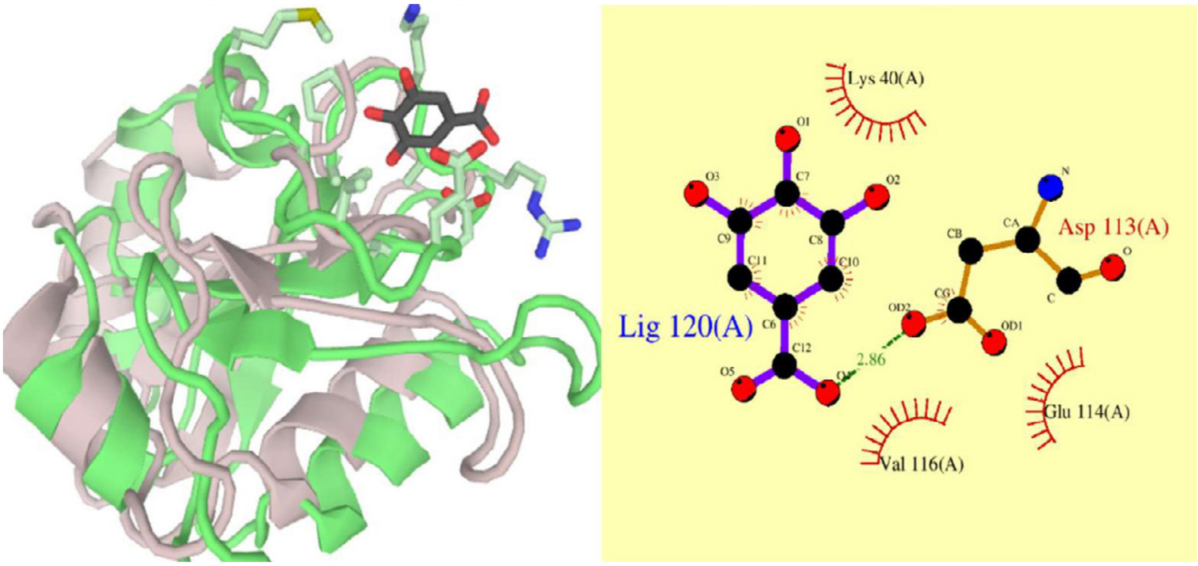

Fig. 11. Results of docking of gallic acid ligand with GABA receptor associated protein

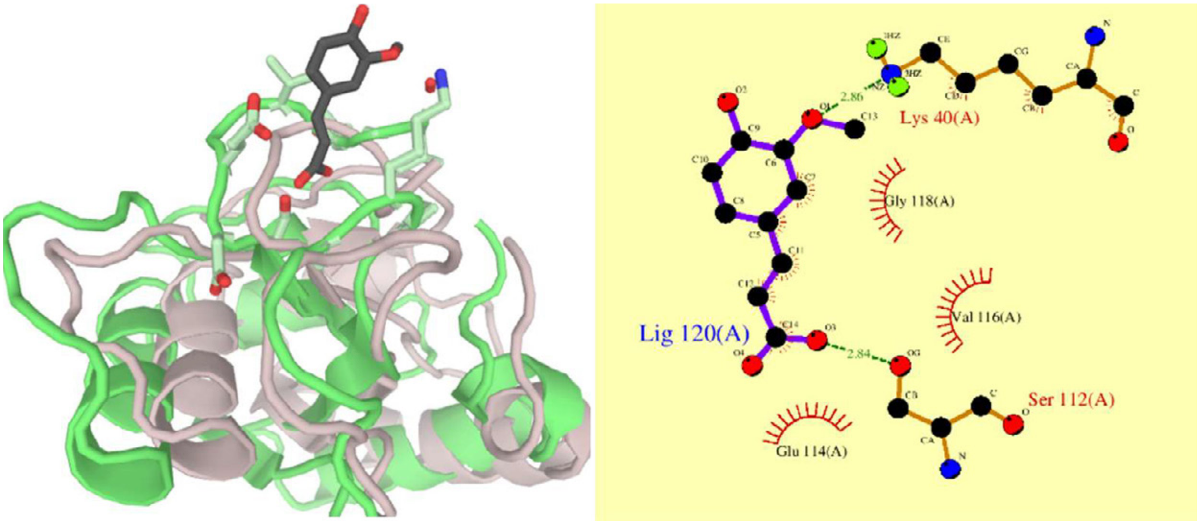

Fig. 12. Results of docking of ferulic acid ligand with GABA receptor associated protein

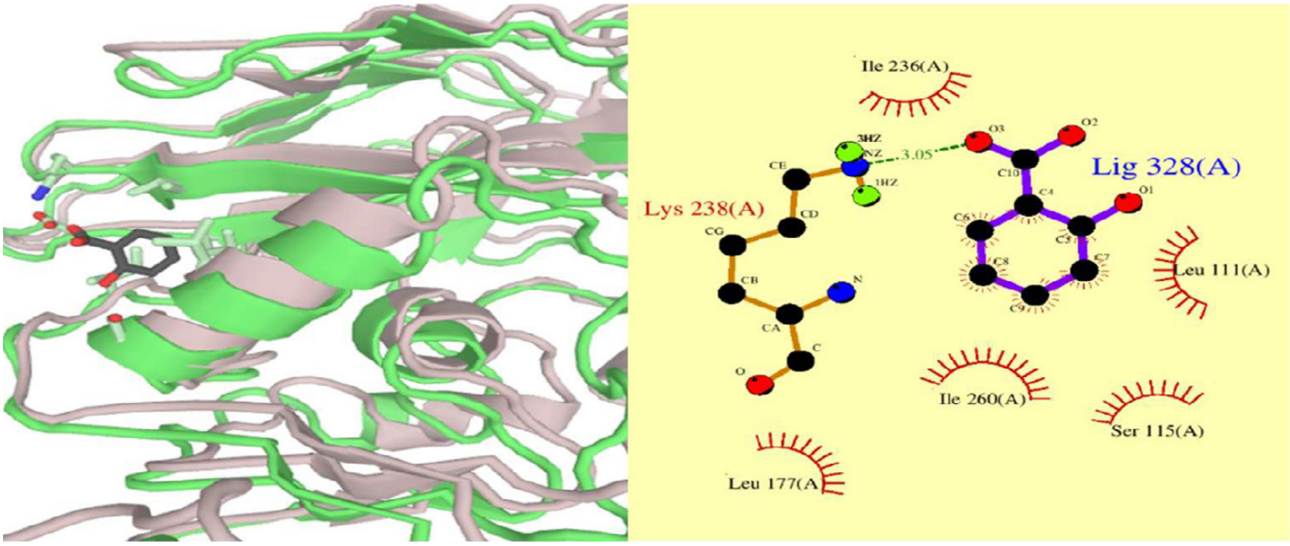

Fig. 13. Results of docking of ascorbic acid ligand with GABA receptor associated protein

Spectrum of *S. nigrum* supported the existence of ascorbic acid, rutin, *p*-cymene and 3,4-dihydroxybenzoic acid. These bioactive components were docked with GABA receptor-associated protein. Epicatechin, rutin, *p*-cymene, and 3,4-dihydroxybenzoic acid did not bind with the GABA receptor-associated protein. While ferulic acid, salicylic acid, gallic acid and ascorbic acid bind via hydrogen bonding and hydrophobic interactions. Ferulic acid and salicylic acid are compounds belonging to the phenol family. Gallic acid belongs to the hydrolysable tannins family. Ascorbic acid, also known as vitamin C, is a potent antioxidant agent. They possess anti-bacterial, anti-inflammatory and hypnotic properties. Studies have shown that a low intake of vitamin C can lead to sleep disorders. One may be able to prolong sleep and lessen sleep disturbances by increasing the consumption of this antioxidant.[74] Salicylic acid binds via hydrogen bonding with Asn 84 and hydrophobic interaction with Val 85 and Ile 86 with GABA receptor associated protein (Table 4), which the amino acids that bind with gephyrin *E* domain are ranging from 36–117. GABA receptor-associated protein and gephyrin are dependent on each other, as if one of the proteins is down-regulated, the other one is also down-regulated.[75] Gallic acid binds via hydrogen bonding with Asp 113 and hydrophobic interaction with Lys 40, Glu 114 and Val 116 with GABA receptor associated protein (Table 4), which are the amino acids that bind with gephyrin *E* domain ranging from 36–117. Ferulic acid binds with protein via hydrogen bonding (Lys 40, Ser 112) and hydrophobic interaction (Glu 114, Val 116 and Gly 118) (Table 4), which are the amino acids that bind with *C*-terminal domain of GABA receptor gamma 2 domain and gephyrin *E* domain ranging from 36–68 and 36–117, respectively. Ascorbic acid binds via hydrogen bonding with Lys 238, and hydrophobic interaction with Ile 236, Ile260, Leu 111, Leu 177 and Ser 115 (Table 4), which are the amino acids that bind with *N*-terminal domain of tubulin, *C*-terminal domain of GABA receptor gamma 2 and gephyrin *E* domain ranging from 1–22, 36–68 and 36–117, respectively. The result showed that salicylic, gallic, ferulic and ascorbic acid bind with the agonist binding site of domains and will stimulate the release of GABA receptors and inhibit the catabolism of GABA receptor associated protein. Ferulic acid showed more hydrogen bonds as compared to gallic acid and salicylic acid. Ascorbic acid also formed more than one hydrogen bond. These bioactive components bind with neurotransmitter receptors and strengthen the GABAergic system, which increases the efficacy of hypnotic activity.[76] Models that show good binding energy are suggested to interact with the enzyme active sites, indicating better stability with the GABA receptor-associated protein. These bioactive compounds showed good affinity by forming hydrogen bonds and hydrophobic interactions, and they could be a good alternative to medicines to treat influenza and regulate the sleep cycle.

4. Conclusions

In this work, biological activities of medicinal plants were assessed, which demonstrates the potential use of isolated components from plants as alternative therapies or as models for the synthesis of novel compounds. Furthermore, it was concluded that these plant extracts possess an appreciable content of phytochemicals as well as good antioxidant and antibacterial potential. The butanol extract of these plants showed the highest antibacterial potential. The findings show that the bioactive components found in these plants may have the potential to treat influenza-related symptoms and sleep disruptions, indicating that they are worth further exploration as complementary therapies. The combined *in silico* and *in vitro* approach brings up new possibilities for developing novel therapies to treat various illnesses. This study can be a guideline for researchers in the field of pharmacology and pharma industries to develop novel therapeutic agents.

Acknowledgements

The authors are grateful for all the lab staff who helped in this research.

Ethical statements

All the research was approved by the ethical committee of Lahore College for Women University and no human or animal was involved in this research.

Conflict of interest statement

The authors declare that they have no conflicts of interest.

5. References

1. H. Siddique, B. Pendry, M. A. Rashid and M. M. Rahman, *J. Herb. Med.* **2021**, *29*, 100484. **DOI:**10.1016/j.hermed.2021.100484
2. F. Ur Rehman, M. Kalsoom, M. Adnan, B. Fazeli-Nasab, N. Naz, H. Ilahi, M. F. Ali, M. Ilyas, G. Yousaf and M. D. Toor, *Int. J. Pharm. Biomed. Res* **2021**, *8*, 1–11.
3. I. Ahmad, Z. Mehmood and F. Mohammad, *J. Ethnopharmacol.* **1998**, *62*, 183–193. **DOI:**10.1016/S0378-8741(98)00055-5
4. H. U. Ugboko, O. C. Nwinyi, S. U. Oranusi, T. H. Fatoki and C. A. Omonhinmin, *Sci. World J.* **2020**, *2020*. **DOI:**10.1155/2020/7059323
5. A. E. Al-Snafi, *Indo Am. J. Pharm. Sci.* **2018**, *5*, 2191–2197.
6. A. W. Khan, A.-u. Khan, S. M. M. Shah, A. Ullah, M. Faheem and M. Saleem, *Evid.-Based Complement. Altern. Med.* **2019**, *2019*. **DOI:**10.1155/2019/6191505
7. S. M. Al-Khazraji, *IOSR J. Pharm. Biol. Sci.* **2015**, *10*, 121–124.
8. N. Dwivedi, A. Tiwari, R. Singh and I. Tripathi, *Int. J. Curr. Microbial. App. Sci.* **2018**, *7*, 4517–4527.
9. S. Kaur, S. Gupta and P. B. Gautam, *J. Pharmacogn. Phytochem.* **2019**, *8*, 2442–2446.
10. I. Akubugwo, A. Obasi and S. Ginika, *Pak. J. Nutr.* **2007**, *6*, 323–326. **DOI:**10.3923/pjn.2007.323.326
11. K. B. Dar, A. H. Bhat, S. Amin, M. Zargar, A. Masood, A. Malik and S. Ganie, *Biochem. Anal. Biochem* **2017,** *6,* 309. **DOI:**10.4172/2161-1009.1000309
12. F. Muhammad, *Curr. Res. J. Biol. Sci.* **2014**, *6*, 183–190.
13. C. Baglioni, K. Spiegelhalder, C. Lombardo and D. Riemann, *Sleep Med. Rev.* **2010**, *14*, 227–238. **DOI:**10.1016/j.smrv.2009.10.007
14. E. Sigel and M. E. Steinmann, *J. Biol. Chem.* **2012**, *287*, 40224–40231. **DOI:**10.1074/jbc.R112.386664
15. S. Mardaninejad, M. Janghorban and M. Vazirpour, *J. Herb. Med.* **2013,** *1,* 23–32.
16. J. R. Shaikh and M. Patil, *Int. J. Chem. Stud.* **2020**, *8*, 603–608. **DOI:**10.22271/chemi.2020.v8.i2i.8834
17. M. M. Bhaldar, S. R. Kane, H. S. Mali and H. S. Kandle, *IJSRST,* **2021,** *4,* 637–645. **DOI:**10.32628/IJSRST218499
18. T. Mahmood, P. Bagga, M. H. Siddiqui and S. Fareed, *Nat. Prod. Commun.* **2011**, *7*, 171–3.
19. O. U. Shirazi, M. M. A. K. Khattak and N. A. M. Shukri, *J. Pharmacogn. Phytochem.* **2014**, *3*, 104–108.
20. N. P. Sapra and H. A. Pandya, *IJRAT.* **2019**, *7*, 1392. **DOI:**10.32622/ijrat.732019115
21. G. B. Devi, K. Ramya, P. Josthna and C. Naidu, *JETIR.* **2021**, *8*, 12.
22. M. Zaidan, A. Noor Rain, A. Badrul, A. Adlin, A. Norazah and I. Zakiah, *Trop. Biomed.* **2005**, *22*, 165–170. **DOI:**10.1175/JTECH-1683.1
23. M. S. Blois, *Nature* **1958**, *181*, 1199–1200. **DOI:**10.1038/1811199a0
24. U. Theuretzbacher, K. Bush, S. Harbarth, M. Paul, J. H. Rex, E. Tacconelli and G. E. Thwaites, *Nat. Rev. Microbiol.* **2020**, *18*, 286–298. **DOI:**10.1038/s41579-020-0340-0
25. V. M. Koistinen, M. Tuomainen, P. Lehtinen, P. Peltola, S. Auriola, K. Jonsson and K. Hanhineva, *npj. Sci. Food.* **2020**, *4*, 21. **DOI:**10.1038/s41538-020-00081-0
26. S. Afrin, F. Giampieri, M. Gasparrini, T. Y. Forbes-Hernandez, D. Cianciosi, P. Reboredo-Rodriguez, J. Zhang, P. P. Manna, M. Daglia and A. G. Atanasov, *Biotechnol. Adv.* **2020**, *38*, 107322. **DOI:**10.1016/j.biotechadv.2018.11.011
27. M. Manzoor, J. Singh, A. Gani and N. Noor, *Food Chem.* **2021**, *362*, 130141. **DOI:**10.1016/j.foodchem.2021.130141
28. D. Alwazeer, *Phytochem. Anal.* **2024**, *35*, 203–219. **DOI:**10.1002/pca.3304
29. M. Barbouchi, K. Elamrani and M. El Idrissi, *J. King Saud Univ.-Sci.* **2020**, *32*, 302–306. **DOI:**10.1016/j.jksus.2018.05.010
30. Z. X. Ng, S. N. Samsuri and P. H. Yong, *J. Food Process. Preserv.* **2020**, *44*, e14680.
31. D. Bencheikh, A. Gueddah, K. Soualat, H. Ben-aissi, A. Benslama, A. Harrar and S. Khennouf, *J. Appl. Biol. Sci.* **2021**, *15*, 53–63.
32. K. A. Motghare, D. Z. Shende and K. L. Wasewar, *J. Chem. Tech. Biotechnol.* **2022**, *97*, 873-884. **DOI:**10.1002/jctb.6970
33. Z. Liu, T. Xu, X. Meng, Y. Zhao, Q. Lan, Y. Liu, Z. Song, J. Qin and H. Zhan, *Batter. Supercaps.* **2023**, *6*, e202200436. **DOI:**10.1002/batt.202200436
34. P. Singh, R. Mathur and T. Khan, *J.Clin. Exp. Pathol.* **2018**, *8*, 2161-0681.1000351.
35. A. D. Sharma, M. Chahal, I. Kaur and N. Singh, *Life Sci. J.* **2020**, *17*, 896. **DOI:**10.3390/plants10061089
36. A. Balkrishna, A. Rohela, A. Kumar, A. Kumar, V. Arya, P. Thakur, P. Oleksak, O. Krejcar, R. Verma and D. Kumar, *Plants* **2021**, *10*, 1089.
37. W. Liu, F. Wang, P. Meng and S.-Q. Zang, *Catalysts* **2020**, *10*, 1271. **DOI:**10.3390/catal10111271
38. M. Hussain, H. Bakhsh, A. Aziz, A. Majeed, I. A. Khan, A. Mujeeb and U. Farooq, *J. Pharm. Alter. Med.* **2013**, *2*, 33–43.
39. E. Gębarowska, J. Łyczko, M. Rdzanek, B. Wiatrak,

E. Pląskowska, H. Gołębiowska, A. Kuźniarski and T. Gębarowski, *Appl. Sci.* **2022**, *12*, 6845. **DOI:**10.3390/app12146845

40. S. Ramya, G. Krishnasamy, R. Jayakumararaj, N. Periathambi and A. Devaraj, *Asian J. Biomed. Pharma. Sci.* **2012**, *2*, 65.
41. M. M. Rahman, M. S. Rahaman, M. R. Islam, M. E. Hossain, F. Mannan Mithi, M. Ahmed, M. Saldías, E. K. Akkol and E. Sobarzo-Sánchez, *Antibiotics* **2021**, *10*, 1076. **DOI:**10.3390/antibiotics10091076
42. T. Momoh, J. Appah, G. Onwumere and V. Dan, *J. Appl. Sci. Environ. Manage.* **2024**, *28*, 3917–3922.
43. S. Shoukat, S. Kamal, I. Bibi, N. Akhter, S. Rehman and M. Khalid: Essentials of Medicinal and Aromatic Crops, Springer, **2023**, pp. 909–934. **DOI:**10.1007/978-3-031-35403-8_35
44. M. G. Agidew, *Bull. Natl. Res. Cen.* **2022**, *46*, 87. **DOI:**10.1186/s42269-022-00770-8
45. L. Maheshwaran, L. Nadarajah, S. Senadeera, C. Ranaweera, A. Chandana and R. Pathirana, *Asian Plant Res. J.* **2024**, *12*, 11–38. **DOI:**10.9734/aprj/2024/v12i5267
46. O. S. Khade, K. Sruthi, R. M. Sonkar, P. S. Gade and P. Bhatt, *Inter. J. Herb. Med.* **2023**, *11*, 01–17. **DOI:**10.22271/flora.2023.v11.i2a.855
47. K. Patil, V. Patil, S. Patil and A. Bhuktar, *Trends Life Sci.* **2012**, *1*, 43–45. **DOI:**10.1016/j.measurement.2011.12.012
48. A. Y. Shala and M. A. Gururani, *Horticulturae* **2021**, *7*, 450. **DOI:**10.3390/horticulturae7110450
49. R. Sahu, V. Arya, R. Joshi, P. Kaushik and M. Chauhan, *Indian J. Ecol.* **2022**, *49*, 1122–1128.
50. V. Pathak and S. Kumar, *J. Pharmacogn. Phytochem.* **2015**, *4*, 136–139.
51. S. S. El-Hawary, H. M. El-Hefnawy, S. M. Osman, M. A. El-Raey and F. A. Mokhtar Ali, *Nat. Prod. Res.* **2021**, *35*, 4663–4668. **DOI:**10.1080/14786419.2019.1700508
52. I. Gbadamosi and A. Afolayan, *J. Appl. Biosci.* **2016**, *98*, 9240–9251. **DOI:**10.4314/jab.v98i1.1
53. S. Baliyan, R. Mukherjee, A. Priyadarshini, A. Vibhuti, A. Gupta, R. P. Pandey and C.-M. Chang, *Molecules* **2022**, *27*, 1326. **DOI:**10.3390/molecules27041326
54. G. Celiz, M. Renfige and M. Finetti, *Chem. Pap.* **2020**, *74*, 3101–3109. **DOI:**10.1007/s11696-020-01110-8
55. P. Ragavendran, D. Sophia, C. Arul Raj and V. Gopalakrishnan, *Pharmacologyonline* **2011**, *1*, 358–364.
56. V. K. Bhardwaj, R. Purohit and S. Kumar, *Food Chem.* **2021**, *347*, 128932. **DOI:**10.1016/j.foodchem.2020.128932
57. M. Majewski and X. Barril, *J. Chem. Inf. Model.* **2020**, *60*, 1644–1651. **DOI:**10.1021/acs.jcim.9b01062
58. K. Shimizu, C. Kawakami, Y. Matsuzaki, S. Fujisaki, S. Nagata, H. Morita, K. Watanabe, H. Miura, T. Momoki and M. Saikusa, *Influenza Other Respir. Viruses* **2024**, *18*, e13345. **DOI:**10.1111/irv.13345
59. E. de Vries, W. Du, H. Guo and C. A. de Haan, *Trends Microbiol.* **2020**, *28*, 57–67. **DOI:**10.1016/j.tim.2019.08.010
60. Y. Arai, E. M. Elgendy, T. Daidoji, M. S. Ibrahim, T. Ono, N. Sriwilaijaroen, Y. Suzuki, T. Nakaya, K. Matsumoto and Y. Watanabe, *J. Virol.* **2020**, *94*, 10.1128/jvi. 01210–20. **DOI:**10.1128/JVI.01210-20
61. D. Bešlo, G. Došlić, D. Agić, V. Rastija, M. Šperanda, V. Gantner and B. Lučić, *Antioxidants* **2022**, *11*, 970. **DOI:**10.3390/antiox11050970
62. P. Singh, Y. Arif, A. Bajguz and S. Hayat, *Plant Physiol. Biochem.* **2021**, *166*, 10–19. **DOI:**10.1016/j.plaphy.2021.05.023
63. S. Dhanaraj, *Arab. J. Chem.* **2023**, *16*, 104881. **DOI:**10.1016/j.arabjc.2023.104881
64. J. R. Chipley: Antimicrobials in food, CRC Press, **2020**, pp. 41–88. **DOI:**10.1201/9780429058196-3
65. J. Xie and L. Lai, *Curr. Opin. Struct. Biol.* **2020**, *62*, 158–165. **DOI:**10.1016/j.sbi.2020.01.011
66. M. S. Borau and S. Stertz, *Curr. Opin. Virol.* **2021**, *48*, 23–29. **DOI:**10.1016/j.coviro.2021.03.001
67. Z. J. Zhang, S. L. Morris-Natschke, Y. Y. Cheng, K. H. Lee and R. T. Li, *Med. Res. Rev.* **2020**, *40*, 2290–2338. **DOI:**10.1002/med.21707
68. M. Guo, J. Ni, J. Yu, J. Jin, L. Ma, H. Zhang, D. Wang, X. Zhang, J. Dou and C. Zhou, *Int. J. Mol. Sci.* **2019**, *20*, 6261. **DOI:**10.3390/ijms20246261
69. P. Mehrbod, D. Hudy, D. Shyntum, J. Markowski, M. J. Łos and S. Ghavami, *Biomolecules* **2020**, *11*, 10. **DOI:**10.3390/biom11010010
70. Y. Oishi, Y. C. Saito and T. Sakurai, *Pharmacol. Ther.* **2023**, *249*, 108505. **DOI:**10.1016/j.pharmthera.2023.108505
71. D. M. Lovinger, Y. Mateo, K. A. Johnson, S. A. Engi, M. Antonazzo and J. F. Cheer, *Nat. Rev. Neurosci.* **2022**, *23*, 191-203. **DOI:**10.1038/s41583-022-00561-0
72. A. Otocka-Kmiecik and A. Król, *Nutrients* **2020**, *12*, 3908. **DOI:**10.3390/nu12123908
73. V. Tretter, J. Mukherjee, H.-M. Maric, H. Schindelin, W. Sieghart and S. J. Moss, *Front. Cell. Neurosci.* **2012**, *6*, 23. **DOI:**10.3389/fncel.2012.00023
74. M. Ghasemzadeh Rahbardar and H. Hosseinzadeh, *Phytother. Res.* **2024**, *38*, 3037–3059. **DOI:**10.1002/ptr.8201
75. J. Chen, H. Zhao, M. Liu and L. Chen, *Mol. Cell. Biochem.* **2024**, *6*, 1415–41. **DOI:**10.1007/s11010-023-04800-5
76. O. Bruni, L. Ferini-Strambi, E. Giacomoni and P. Pellegrino, *Nutrients* **2021**, *13*, 530. **DOI:**10.3390/nu13020530

Povzetek

Rastlinam in njihovim ekstraktom *Eucalyptus globu*lus (*E. globulus*), *Jasminum officinale* (*J. officinal*e) in *Solanum nigrum* (*S. nigrum*) so določilie njihovo protibakterijsko, antioksidativno aktivnost in terapevtske lastnosti. Za fitokemijsko presejanje in protibakterijsko aktivnost so bila uporabljena ekstrakcijska topila (voda, metanol, etanol in butanol), medtem ko so bili za analizo antioksidativne aktivnosti uporabljeni izključno vodni izvlečki. Kvantitativna določitev je pokazala, da je imel *J. officinale* najvišjo vsebnost fenolov in taninov, medtem ko je imel *E. globulus* najvišje ravni flavonoidov in alkaloidov med preizkušenimi vrstami. Za oceno protibakterijske aktivnosti proti *Escherichia coli* (*E. coli*) in *Staphylococcus aureus* (*S. aureus*) je bila uporabljena metoda difuzije po disku. Vsi izvlečki listov *E. globulus* so pokazali protibakterijsko delovanje proti *E. coli* in *S. aureus*. FTIR analiza vodnih izvlečkov je pokazala prisotnost kvercetina, benzojske, salicilne, galne, ferulne in askorbinske kisline. Poleg tega je bila izvedena *in silico* analiza za oceno interakcije izbranih bioaktivnih spojin: kvercetina in benzojske kisline iz *E. globulus* sta bila sidrana v hemaglutinin in nevraminidazo, saj imata ti površinski beljakovini virusa influence ključno vlogo pri zmožnosti virusa, da okuži gostiteljske celice. Salicilna, galna, ferulna in askorbinska kislina iz *J. officinale* in S. nigrum so bile sidrane na proteine, povezane z GABA receptorji, ki so pomembni pri sinaptičnem prenosu in plastičnosti.

DOI: 10.17344/acsi.2025.9250 *Acta Chim. Slov.* **2025,** *72,* 545–552

Scientific paper

Preparation and Characterization of Ionic Liquid Supported on Fe_3O_4-Lignin and Investigation of Its Catalytic Activity in the Synthesis of Dihydropyrano[3,2-*c*] chromene Derivatives

Majidreza Gerami and Mahnaz Farahi*

Department of Chemistry, Yasouj University, P. O. Box 353, Yasouj 75918-74831, Iran

** Corresponding author: E-mail: farahimb@yu.ac.ir*

Received: 03-15-2025

Abstract

To extend the use of supported ionic liquids as effective heterogeneous catalysts, in this research, the ionic liquid immobilized on magnetic lignin (Fe_3O_4-lignin-SO_3/IL) was used as an environmentally friendly, and recyclable catalyst for the synthesis of dihydropyrano[3,2-*c*]chromene derivatives via a one-pot reaction between aromatic aldehydes, malononitrile, and 4-hydroxycoumarin. This method offers the benefits of high yield, short reaction times, straightforward processing, and its potential for green applications in pharmaceutical and chemical sectors. Furthermore, the detailed role of Fe_3O_4-lignin-SO_3/IL as a catalyst in chemical reactions was examined, providing insights into its mechanism and potential uses in organic synthesis and other chemical processes.

Keywords: Lignin, Ionic liquid, Nanocatalyst, Dihydropyrano[3,2-*c*]chromene

1. Introduction

Catalysts are generally divided into two major classes: homogeneous and heterogeneous.[1] In the context of liquid-phase organic synthesis, homogeneous catalysts are widely used due to their high activity and well-defined active sites. However, they often pose challenges in separation and recycling, which can limit their practical applications, especially in sustainable and green chemistry approaches.[2] In contrast, heterogeneous catalysts offer the advantage of easy separation from reaction mixtures, typically via simple filtration or magnetic recovery (when applicable), making them highly attractive for reuse in organic transformations. Many heterogeneous catalytic systems have been developed by dispersing metal nanoparticles or organometallic complexes onto solid supports such as carbon, silica, metal oxides, polymers, reduced graphene oxide, or mesoporous materials through covalent or non-covalent interactions.[3–5] A common limitation of conventional heterogeneous catalysts is the loss of catalyst during recovery and the time-consuming separation processes, which can reduce their overall efficiency. To address these issues, magnetic nanocatalysts (particularly those based on magnetite (Fe_3O_4) have emerged as promising alternatives. Their superparamagnetic properties enable rapid and efficient separation using external magnetic fields, minimizing catalyst loss and eliminating the need for expensive and labor-intensive workup procedures. Fe_3O_4 nanoparticles also provide an excellent platform for further functionalization with biocompatible and biodegradable materials, enhancing catalytic performance, stability, and selectivity.[6,7] They are often coated with mesoporous silica, polymers, carbon-based materials (e.g., carbon nanotubes, graphene oxide, biochar), or boehmite to create core–shell nanostructures. These modifications extend their applicability in areas such as catalysis, biomedicine, and nanotechnology.[8,9]

Lignin, a complex aromatic compound, is abundant in plant biomass and exhibits unique physical properties that can enhance catalyst performance.[10] Also, lignin and its derivatives have been used in the manufacture of adsorbents, catalyst supports, flame retardants, adhesives, carbon fibers, bioplastics, dispersants, reinforcement, etc. Lignin as an amorphous polymer, has advantages such as low cost, biocompatibility, high thermal stability, and abundance.[11] Heterogeneous catalysts supported on lignin as natural substrates offer an eco-friendly approach to catalysis, leveraging renewable biomass-derived materials as supports.[12] This biopolymer offers abundant functional groups (e.g., hydroxyl, carboxyl, and aromatic structures) that facilitate strong interactions with catalytic metal nanoparticles or active species, enhancing their dispersion and stability. By anchoring heterogeneous catalysts to this natural substrate, the surface area and accessibility for reactants are maximized, improving catalytic efficiency. The natural porous structures of lignin can increase the surface area available for catalysis, enhancing reaction rates and selectivity. Furthermore, their three-dimensional interpenetrating network architecture allows for the incorporation of a wide range of catalytic metals, including noble metals and transition metals, enabling various catalytic applications. Its unique physicochemical properties could synergize with metal complexes to enhance catalytic activity or improve the selectivity of the reaction.[13–15]

Ionic liquids (ILs) are salts that remain in liquid form at or near room temperature and have received significant attention due to their exceptional properties such as low vapor pressure, low toxicity, high chemical and thermal stability, and the ability to dissolve a wide range of organic, inorganic, and polymeric materials.[16] ILs have various applications in electrochemistry, water treatment, polymerization, engineering, and biological uses, and are applied as efficient solvents and catalysts in different organic reactions.[17] In the field of catalysis, ILs can be applied as homogeneous or heterogeneous catalysts. ILs can act as both catalysts and reaction media, enhancing reaction rates while minimizing side reactions.[18] Recently, several research teams have reported the ability of ILs immobilized on the surfaces of nanomaterials to catalyze many chemical reactions.[19,20] In such systems, the catalytic activity typically arises from Brønsted-acidic functional groups, such as sulfonic acid ($-SO_3H$). These groups release protons, which help to facilitate acid-catalyzed transformations. They play a crucial role in activating electrophilic centers, such as carbonyl or nitrile groups, thereby accelerating nucleophilic addition steps. Their ionic nature enables them to stabilize transition states and reactive intermediates, making them particularly useful in acid-base catalysis, enzymatic reactions, and metal-catalyzed processes. In heterogeneous IL-based systems, the IL is usually immobilized on a solid support to improve stability and reusability while maintaining its Brønsted or Lewis acidic properties. Consequently, the active sites primarily come from the acidic groups of the IL instead of the support itself. The integration of ILs with natural substrates, such as cellulose and lignin, offers a compelling approach to enhance the catalytic efficiency and sustainability of chemical processes.[21] Immobilizing ILs on natural substrates helps reduce the challenges of catalyst separation and recycling while maintaining or improving catalytic performance, especially in processes like biomass conversion, green chemistry, and renewable energy production. The interaction between ILs and these biopolymers can also enhance the dispersal of the IL, creating more active sites for catalysis and improving overall reaction efficiency.[22,23]

Pyrano[3,2-*c*]chromene derivatives are an important class of O-containing heterocyclic compounds that find widespread use in the pharmaceutical and agrochemical industries.[24] These heterocycles are known to possess a wide variety of biological activities, including spasmolytic, diuretic, anticoagulant, anti-cancer, and anti-anaphylactic effects.[25] Pyranochromenes also form components of many natural products such as calanolides, calophyllolide, and calanone.[26] Moreover, some pyrano[3,2-*c*]chromenes also serve as valuable photoactive agents. Many drugs contain the pyranochromene structure, including acetylcholinesterase[27] and Novobicin.[28] Although these compounds hold significant pharmacological, industrial, and synthetic value, there are relatively few methods available for synthesizing pyrano[3,2-*c*]chromene derivatives. The main method for their preparation is the one-pot three-component reaction of 4-hydroxycoumarin with aldehyde and malononitrile in the presence of a catalyst. Recent advances have focused on developing greener and more efficient synthetic routes to overcome limitations in traditional methods. Furthermore, exploring novel catalytic systems could enhance the yield and selectivity of pyrano[3,2-*c*]chromene derivatives in pharmaceutical applications.[29,30] Acid-catalyzed multicomponent reactions particularly benefit from catalysts that can activate carbonyl groups while stabilizing intermediates. Consequently, a Brønsted-acidic IL immobilized on a biopolymeric magnetic support is well-suited for these transformations.[31]

In continuation of our research on the introduction of recoverable catalysts in organic synthesis,[30–37] herein, lignin-based nanocomposite containing high contents of Fe_3O_4 nanoparticles (Fe_3O_4–Lignin-SO_3/IL) was used as a catalyst in the condensation reaction between aromatic aldehydes, malononitrile, and 4-hydroxycoumarin to prepare dihydropyrano[3,2-*c*]chromene derivatives in good to excellent yields. The main catalytic activity in this system is due to the sulfonic acid groups in the ionic liquid component, which act as Bronsted acid sites to facilitate the critical steps of the multicomponent reaction.

2. Experimental

All solvents, chemicals, and reagents were sourced from suppliers such as Fluka, Merck, and Sigma-Aldrich. Structural characterization of the samples was carried out using X-ray diffraction (XRD) on a Rigaku Ultima IV diffractometer. The magnetic properties of the synthesized materials were measured with a vibrating sample magnetometer (VSM) model MDK VSM. Additionally, Fourier-transform infrared (FT-IR) spectra covering the range of 400–4000 cm^{-1} were obtained using an FT-IR JASCO-Model 680 spectrometer.

2. 1. Preparation of Zwitterionic Salts $[(CH_2)_4SO_3TEA]$

The zwitterionic compound was synthesized through a simple one-step process by reacting 1 mmol of triethylamine with 1 mmol of 1,4-butane sultone, under solvent-free conditions, with continuous stirring at ambient temperature for 18 h. The produced solid salt was extensively washed with diethyl ether and then dried under vacuum at 75 °C to obtain the final product.[38]

2. 2. Synthesis of Fe_3O_4 Nanoparticles

Initially, $FeCl_2{\cdot}4H_2O$ (0.5 g, 2.5 mmol) and $FeCl_3{\cdot}6H_2O$ (1.35 g, 5 mmol) were dissolved in deionized water (30 mL) under a nitrogen atmosphere at 80 °C. Next, a sodium hydroxide solution (10 M, 5 mL) was gradually added dropwise over 60 min. After the reaction was completed, the magnetic solid was collected using a magnet and washed with water and ethanol. The obtained solid was then dried in an oven at 80 °C for 2 h to yield Fe_3O_4 nanoparticles.[39]

2. 3. Preparation of Fe_3O_4-Lignin Composite

To prepare the Fe_3O_4-lignin composite, lignin (0.5 g) was dissolved in deionized water (30 mL) with continuous stirring for 1 h until fully dissolved. The mixture was then filtered to remove any particulate impurities. Next, Fe_3O_4 nanoparticles (0.15 g) were added to the lignin solution and sonicated for 50 min. The mixture was stirred for 12 h at room temperature. The resultant Fe_3O_4-lignin composite was separated using a magnet, washed with ethanol, and dried.[40]

2. 4. Synthesis of Fe_3O_4-Lignin-SO_3H

In the following, Fe_3O_4-lignin (0.3 g) was dispersed in CH_2Cl_2 (10 mL) by sonication for 20 min. Then, chlorosulfonic acid (0.1 mL) was added dropwise to the reaction mixture for 20 min at room temperature and it was stirred for 2 h. The resulting solid was separated using an external magnet and dried in an oven at 90 °C for 2 h to obtain Fe_3O_4-lignin-SO_3H.[41]

2. 5. Preparation of Fe_3O_4-Lignin-SO_3/IL

In the final step, Fe_3O_4-lignin-SO_3H (1.5 g) was dispersed in toluene (30 mL) using sonication for 20 min. Subsequently, a solution of the zwitterionic salt $[(CH_2)_4SO_3TEA]$ (0.8 g) in 1,4-dioxane (20 mL) was added to the mixture at room temperature. The reaction temperature was then raised to 85 °C and maintained for 3 h with continuous stirring. Following this, the solvent was removed under vacuum at 80 °C. The Fe_3O_4-lignin-SO_3/IL catalyst obtained was washed with ethanol and subsequently dried under vacuum at 70 °C.[42]

2. 6. General Procedure for the Synthesis of Dihydropyrano[3,2-*c*]chromene Derivatives

In a 25 mL round-bottom flask equipped with a magnetic stirrer and reflux condenser, a mixture of the desired aromatic aldehyde (1 mmol), malononitrile (1.2 mmol), 4-hydroxycoumarin (1 mmol), and Fe_3O_4-lignin-SO_3H/IL nanocatalyst (0.025 g) was added to 4 mL of a 1:1 ethanol-water mixture. The reaction mixture was heated under reflux conditions with constant stirring. The progress of the reaction was monitored by thin-layer chromatography (TLC) using ethyl acetate/*n*-hexane (2:1) as the eluent. Reaction completion was confirmed by the disappearance of the aldehyde spot on TLC, usually within 30–90 minutes, depending on the substrate. After the reaction was complete, the mixture was cooled to room temperature, and the catalyst was separated using a magnet. The crude product was filtered, washed with cold ethanol, and recrystallized from methanol to obtain the pure dihydropyrano[3,2-*c*]chromene derivative.

2. 7. Catalyst Recovery and Reusability

To assess the reusability of the Fe_3O_4-lignin-SO_3H/IL nanocatalyst, the catalyst was magnetically separated from the reaction mixture after product isolation, thoroughly washed with methanol to remove any adsorbed organic residues, and dried at 70 °C under vacuum. The recovered catalyst was reused directly in subsequent runs of the model reaction (benzaldehyde, malononitrile, and 4-hydroxycoumarin under identical reaction conditions as described in Section 2.6). The catalytic activity remained consistent over five consecutive cycles with minimal loss in product yield, demonstrating the excellent stability and recyclability of the nanocatalyst.

3. Results and Discussion

3.1. Synthesis of the Catalyst

This study describes the method for synthesizing Fe_3O_4-lignin-SO_3H/IL, with the steps illustrated in Scheme 1. The process began with the synthesis of Fe_3O_4 nanoparticles, which were then coated with lignin to produce Fe_3O_4-lignin. Next, Fe_3O_4-lignin reacted with chlorosulfonic acid to form Fe_3O_4-lignin-SO_3H. The ionic liquid (IL) was created by the reaction of triethylamine with 1,4-butane sultone. The final step was electrostatically stabilizing the IL onto Fe_3O_4-lignin-SO_3H to obtain the Fe_3O_4-lignin-SO_3H/IL nanocatalyst. This immobilization strategy ensured that the Brønsted-acidic $–SO_3H$ functional groups of the ionic liquid (IL) were retained on the heterogeneous support, making them accessible as active sites during catalysis. The IL component introduces a strong proton-donating capacity to the composite, which is responsible for the acid-catalyzed activation of electrophilic centers, such as aldehydes, and for stabilizing reactive intermediates.

Meanwhile, the Fe_3O_4-lignin framework provides a high surface area and allows for magnetic recoverability without significantly contributing to catalytic activity. The synthesis and structural features of the catalyst were previously reported and characterized using XRD, FT-IR, FE-SEM, EDS, VSM, TGA, and TEM techniques [42].

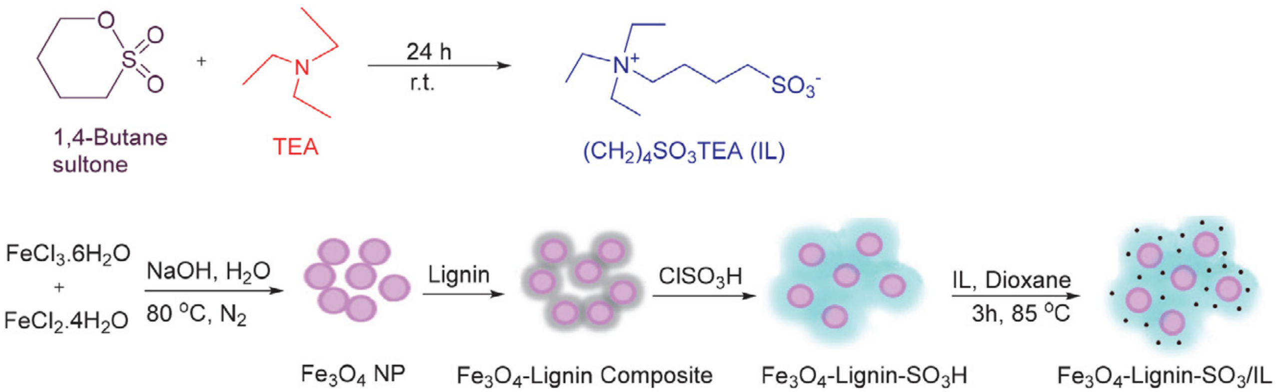

Scheme 1. Preparation of Fe_3O_4-lignin-SO_3/IL nanocatalyst.

3.2. Synthesis of Dihydropyrano[3,2-*c*] chromenes Derivatives 4

Following the successful characterization of the Fe_3O_4-lignin-SO_3H/IL nanocatalyst, its catalytic potential was explored in the synthesis of dihydropyrano[3,2-*c*] chromenes through the reaction between aromatic aldehydes, malononitrile, and 4-hydroxycoumarin (Scheme 2).

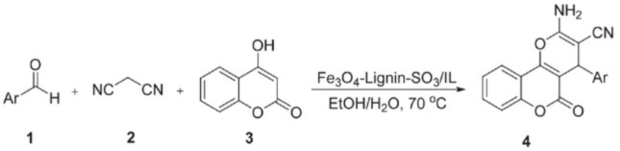

Scheme 2. Synthesis of dihydropyrano[3,2-*c*]chromenes **4** using Fe_3O_4-lignin-SO_3/IL nanocatalyst.

To determine the optimal reaction conditions, a one-pot reaction involving benzaldehyde, malononitrile, and 4-hydroxycoumarin was chosen as the model reaction. By screening loading of the catalyst and considering the effect of the solvent and temperature on the reaction, it was found that as little as 0.025 g of Fe_3O_4-lignin-SO_3/IL nanocatalyst was sufficient to produce the desired product **4a** at 70 °C in EtOH/H_2O as the solvent (Table 1). Following this, the various aryl aldehydes were used to synthesize dihydropyrano[3,2-*c*] chromene derivatives. As indicated in Table 2, the products were prepared in yields ranging from good to excellent. Subsequently, the effectiveness of the Fe_3O_4-lignin-SO_3/IL catalyst was compared with other catalysts reported for the synthesis of dihydropyrano[3,2-*c*] chromene derivatives. As illustrated in Table 3, the Fe_3O_4-lignin-SO_3/IL catalyst shows better performance than other catalysts in terms of catalyst amount, reaction temperature, reaction time, and yield.

Scheme 3 illustrates the proposed mechanism for the formation of dihydropyrano[3,2-*c*]chromene derivatives in the presence of Fe_3O_4-lignin-SO_3/IL nanocatalyst. Initially, the carbonyl group of the aldehyde is activated by the acid catalyst, which accelerates the condensation step.

Table 1. Optimization of the reaction conditions for the synthesis of **4a**.[a]

Entry	Catalyst loading (g)	Solvent	Temp. (°C)	Yield (%)[b]
1	0.01	–	70	60
2	0.015	–	70	64
3	0.025	–	70	73
4	0.035	–	70	70
5	0.025	CH_3CN	70	75
6	0.025	EtOH	70	85
7	0.025	EtOH/H_2O (1:1)	70	92
8	0.025	MeOH	reflux	80
9	0.025	Toluene	70	70
10	0.025	EtOH/H_2O (1:1)	r.t.	40
11	0.025	EtOH/H_2O (1:1)	40	55
12	0.025	EtOH/H_2O (1:1)	60	85

[a] Reaction conditions: benzaldehyde (1 mmol), malononitrile (1.2 mmol), 4-hydroxycoumarin (1 mmol). time: 30 min. [b] Isolated yields.

Table 2. Synthesis of derivatives **4** using Fe_3O_4-lignin-SO_3/IL nanocatalyst.[a]

Entry	Product 4	M.p. (°C)	Yield (%)[b]
4a	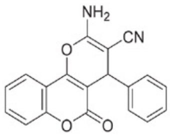	252–254[43]	92
4b	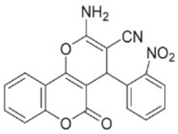	258–260[44]	95
4c	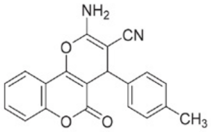	258–260[45]	94
4d	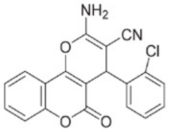	267–269[46]	92
4e	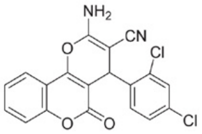	257–259[47]	98
4f	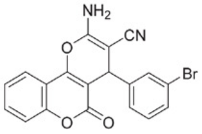	249–251[48]	96
4g	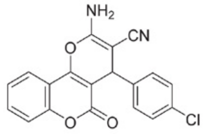	256–258[47]	95
4h	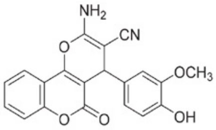	255–257[49]	93
4i	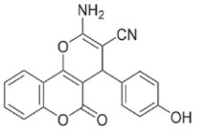	259–261[47]	95
4j	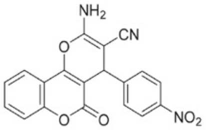	260–262[47]	97
4k	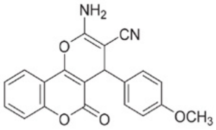	246–248[47]	94

[a] Reaction conditions: Aldehyde (1 mmol), malononitrile (1.2 mmol), 4-hydroxycoumarin (1 mmol), Fe_3O_4-lignin-SO_3/IL (0.025 g), 70 °C, EtOH/H_2O (5 mL), time: 20–60 min. [b] Isolated yields.

Table 3. The comparison study between the efficiency of the present catalyst and that of other catalysts in the synthesis of **4a**.

Entry	Catalyst	Conditions	Time (min)	Yield (%)[a]
1	Zinc hydroxyapatite (0.1 g)	DMF, 120 °C	720	78 (ref. 50)
2	Amberlite IRA 400-Cl resin	H_2O/EtOH, 80 °C	180	95 (ref. 51)
3	Na_2SeO_4	EtOH/H_2O, Reflux	60	95 (ref. 52)
4	Yb(PFO)$_3$	DMF, 60 °C	300	92 (ref. 53)
5	Zn/Al hydrotalcite (0.1 g)	DMF, 120 °C	720	84 (ref. 54)
6	$H_3PW_{12}O_{40}$	EtOH/reflux	300	93 (ref. 55)
7	Fe_3O_4-lignin-SO_3/IL	Cat. (0.025 g), EtOH/H_2O, 85 °C	20	92[b]

[a] Isolated yields. [b] This work.

In this system, the Brønsted acid sites (coming from the sulfonic acid groups (-SO_3H) present in the ionic liquid) mainly protonate the carbonyl oxygen, making the aldehyde group more electrophilic. Subsequently, the activated aldehyde is attacked by the active methylene of malononitrile to give α,β-unsaturated intermediate **I** via the Knoevenagel condensation, and elimination of a water molecule. Next, a Michael addition reaction between 4-hydroxycoumarin and the activated intermediate **I** leads to the formation of intermediate **II**. Finally, the intramolecular cyclization of intermediate **II** to intermediate **III** and its tautomerization gives the corresponding products. Throughout this cascade process, the IL's acidic sites facilitate both the initial condensation and the subsequent cyclization steps, while the magnetic lignin support offering a stable, reusable heterogeneous platform that guarantees high catalyst dispersion and recoverability. Similar IL-functionalized systems have been shown in the literature to operate through analogous acid-catalyzed mechanisms in multicomponent transformations.[31]

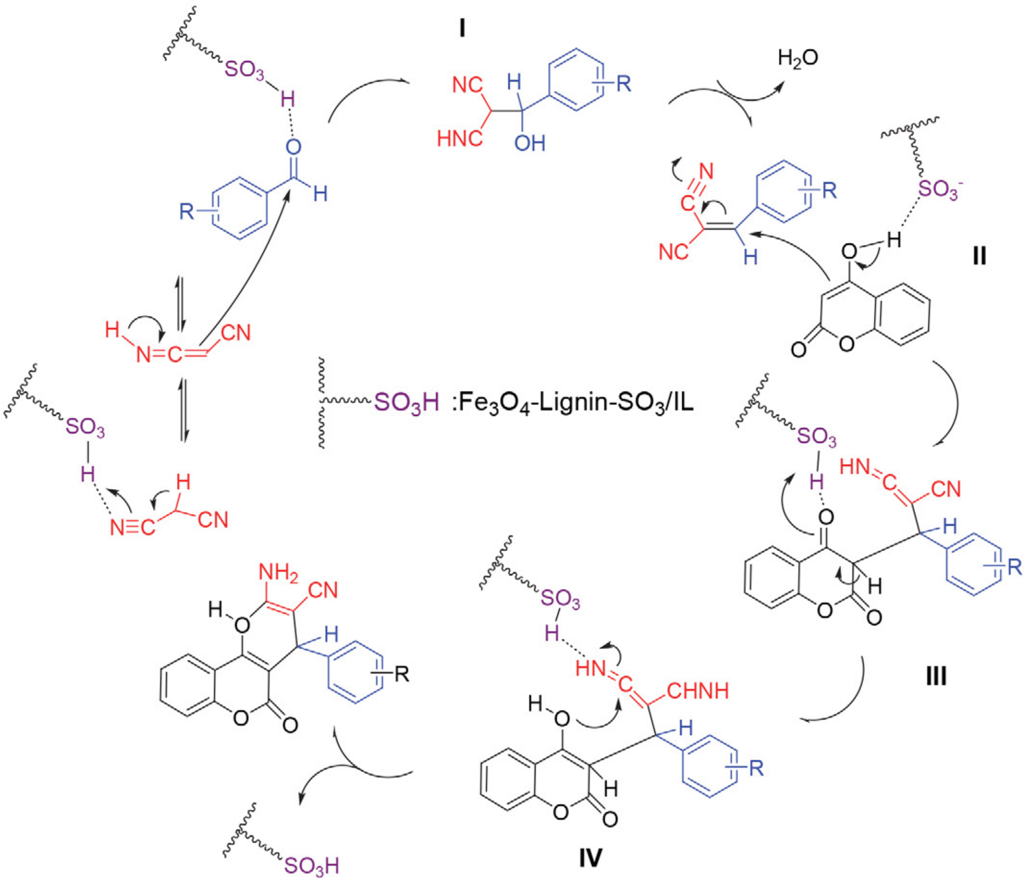

Scheme 3. The suggested mechanism for the formation of compound **4**.

3. 3. Efficiency of the Catalyst

The leaching test was conducted to confirm the heterogeneous nature of the Fe_3O_4-lignin-SO_3/IL catalyst during the synthesis of dihydropyrano[3,2-*c*]chromene derivatives. Based on this, the model reaction was investigated using the optimized reaction conditions. After the progress of approximately 50%, the catalyst was removed from the reaction. Next, the residue of the reaction was stirred under optimal conditions without the presence of the catalyst. However, no significant increase in product conversion was observed, which confirms that the catalyst performance varies heterogeneously. The reusability of the catalyst was investigated in the model reaction under optimal reaction conditions. After completion of the reaction, the heterogeneous catalyst was magnetically separated, washed with MeOH, and dried for use in the next run. As shown in Figure 1, the recycled catalyst was used for five runs with no significant loss in performance.

The FT-IR spectrum of the recovered Fe_3O_4-lignin-SO_3/IL nanocatalyst is presented in Figure 2. This analysis demonstrates the high stability of the catalyst's struc-

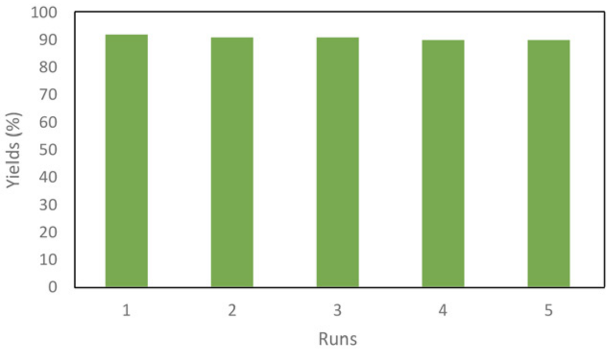

Figure 1. Reusability of Fe_3O_4-lignin-SO_3/IL in the synthesis of **4a**.

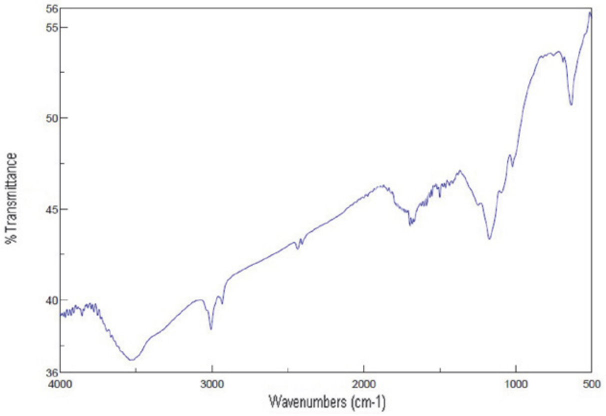

Figure 2. FT-IR spectrum of the recycled Fe_3O_4-lignin-SO_3/IL catalyst.

ture after reuse. In addition, the structural properties of the recovered catalyst have been examined using XRD diffraction patterns (Figure 3). As shown, the relative intensity and position of all the peaks confirm the stability of the catalyst. The VSM analysis of the reused catalyst was conducted, revealing that the magnetic properties of the catalyst remained consistent after multiple cycles (Figure 4).

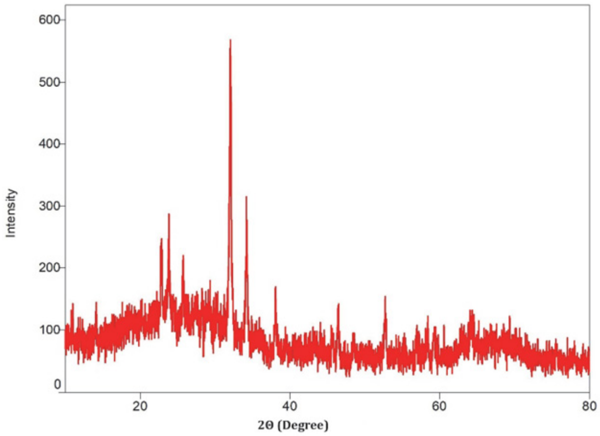

Figure 3. XRD pattern of the recycled Fe_3O_4-lignin-SO_3/IL catalyst.

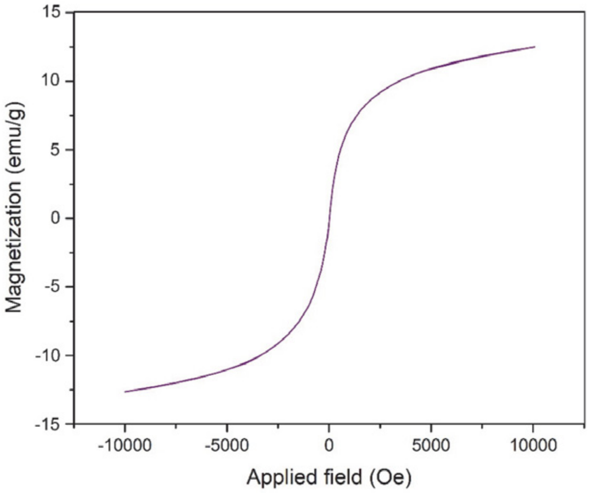

Figure 4. VSM curves of the recycled Fe_3O_4-lignin-SO_3/IL catalyst.

4. Conclusions

In this study, an ionic liquid was effectively immobilized on magnetic lignin to create a heterogeneous catalytic system (Fe_3O_4-lignin-SO_3/IL nanocatalyst), providing a green, efficient, and recyclable platform for chemical reactions. Its catalytic performance was tested in the synthesis of dihydropyrano[3,2-*c*]chromene derivatives, demonstrating excellent activity and selectivity. Notably, the catalyst's heterogeneous nature enabled easy magnetic recovery and reuse for at least five consecutive cycles with minimal activity loss, highlighting its potential for sustainable and practical use in organic synthesis.

5. References

1. D. Astruc, F. Lu, J. R. Aranzaes, *Angew. Chem. Int. Ed.* **2005**, *44*, 7852–7872. **DOI:**10.1002/anie.200500766
2. I. Fechete, Y. Wang, J. C. Védrine, *Catal. Today,* **2012**, *189*, 2–27. **DOI:**10.1016/j.cattod.2012.04.003
3. V. I. Parvulescu, H. Garcia, *Catal. Sci. Technol.* **2018**, *8*, 4834–4857. **DOI:**10.1039/C8CY01295D
4. F. Zaera, *Chem. Rev.* **2022**, *122*, 8594–8757. **DOI:**10.1021/acs.chemrev.1c00905
5. C. A. McNamara, M. J. Dixon, M. Bradley, *Chem. Rev.* **2002**, *102*, 3275–3300. **DOI:**10.1021/cr0103571
6. M. B. Gawande, P. S. Brancoa, R. S. Varma, *Chem. Soc. Rev.* **2013**, *42*, 3371–3393. **DOI:**10.1039/c3cs35480f
7. M. Liu, Y. Ye, J. Ye, T. Gao, D. Wang, G. Chen, Z. Song, *Magnetochemistry* **2023**, *9*, 110. **DOI:**10.3390/magnetochemistry9040110
8. T. B. Mbuyazi, P. A. Ajibade, *Discover Nano* **2024**, *19*, 158. **DOI:**10.1186/s11671-024-04102-9
9. R. Dubadi, S. D. Huang, M. Jaroniec, *Materials* **2023**, *16*, 1460. **DOI:**10.3390/ma16041460
10. G. Haiwei, Q. I. Zaojuan, L. Yuxuan, X. Haian, L. Lin, H. Q. Huang, A. Wang, L. Changzhi, *Catal. Sci. Technol.* **2019**, *9*, 2144. **DOI:**10.1039/C9CY00251K
11. C. Vasile, M. Baican, *Polymers* **2023**, *15*, 3177. **DOI:**10.3390/polym15153177
12. P. K. Sarangi, A. K. Singh, S. V. Ganachari, D. P. G. Mohanakrishna, T. M. Aminabhavi, *Environ. Res.* **2024**, *261*, 119745. **DOI:**10.1016/j.envres.2024.119745
13. S. Laurichesse, L. Averous, *Prog. Polym. Sci.* **2014**, *39*, 1266–1290. **DOI:**10.1016/j.progpolymsci.2013.11.004
14. H. Zhang, S. Fu, X. Du, Y. Deng, *ChemSusChem* **2021**, *14*, 2268–2294. **DOI:**10.1002/cssc.202100067
15. A. Moreno, M. H. Sipponen, *Mater. Horiz.* **2020**, *7*, 2237. **DOI:**10.1039/D0MH00798F
16. S. K. Singh, A. W. Savoy, *J. Mol. Liq.* **2020**, *297*, 112038. **DOI:**10.1039/D0MH00798F
17. R. L. Vekariya, *J. Mol. Liq.* **2017**, *227*, 44–60. **DOI:**10.1016/j.molliq.2016.11.123
18. D. Xu, X. N. Wang, L. Wang, L. Dai, C. Yang, *Molecules* **2024**, *29*, 23. **DOI:**10.3390/molecules29235661
19. H. Liu, J. Lu, X. Zhao, T. Xu, *Synth. Commun.* **2021**, *51*, 2265–2286. **DOI:**10.1080/00397911.2021.1936057
20. B. Xin, J. Hao, *Chem. Soc. Rev.* **2014**, *43*, 7171–7187. **DOI:**10.1039/C4CS00172A
21. R. Liu, P. Zhang, S. Zhang, T. Yan, J. Xin, X. Zhang, *Rev. Chem. Eng.* **2016**, *32*, 587–609. **DOI:**10.1515/revce-2015-0078
22. M. G. Adsul, A. P. Terwadkar, A. J. Varma, D. V. Gokhale, *BioResources* **2009**, *4*, 1670–1681. **DOI:**10.15376/biores.4.4.1670-1681
23. I. A. Ansari, R. Gree, *Org. Lett.* **2002**, *4*, 1507–1509. **DOI:**10.1021/ol025721c

24. D. C. Mungra, M. P. Patel, D. P. Rajani, R. G. Patel, *Eur. J. Med. Chem.* **2011**, *46*, 4192–4200. **DOI:**10.1016/j.ejmech.2011.06.022
25. A. Rajmane, R. Bandal, S. Shirke, U. More, S. Patil, A. Kumbhar, *J. Mol. Liq.* **2023**, *391*, 123247. **DOI:**10.1016/j.molliq.2023.123247
26. M. Shunmughanathan, N. Madankumar, K. Pitchumani, *ChemistrySelect* **2018**, *48*, 13743–13750. **DOI:**10.1002/slct.201803483
27. J. Zheng, M. He, B. Xie, L. Yang, Z. Hu, H. B. Zhou, C. Dong, *Org. Biomol. Chem.* **2018**, *16*, 472–479. **DOI:**10.1039/C7OB02794J
28. K. Chand, A. N. Shirazi, P. Yadav, R. K. Tiwari, M. Kumari, K. Parang, S. K. Sharma, *Can. J. Chem.* **2013**, *91*, 741–754. **DOI:**10.1139/cjc-2013-0053
29. K. Tangdenpaisal, P. Songthammawat, K. Akkarasereenon, K. Chuayboonsong, S. Ruchirawat, P. Ploypradith, *J. Org. Chem.* **2019**, *84*, 13410–13429. **DOI:**10.1021/acs.joc.9b01596
30. S. Abdolmohammadi, S. Balalaie, *Tetrahedron Lett.* **2007**, *48*, 3299–3303. **DOI:**10.1016/j.tetlet.2007.02.135
31. A. Jahanbakhshi, M. Farahi, *RSC Adv.* **2024**, *14*, 16401–16410. **DOI:**10.1039/D4RA01381F
32. A. Jahanbakhshi, M. Farahi, *Arab. J. Chem.* **2022**, *15*, 104311. **DOI:**10.1016/j.arabjc.2022.104311
33. A. Jahanbakhshi, S. Eskandari, M. Farahi, *New J. Chem.* **2024**, *48*, 1381–1389. **DOI:**10.1039/D3NJ04796B
34. A. Jahanbakhshi, M. Farahi, *RSC Adv.* **2023**, *13*, 31252–31262. **DOI:**10.1039/D3RA04953A
35. M. Farahi, B. Karami, R. Keshavarz, F. Khosravian, *RSC Adv.* **2017**, *7*, 46644–46650. **DOI:**10.1039/C7RA08253C
36. S. Khodabakhshi, B. Karami, M. Baghernejad, *Monatsh. Chem.* **2014**, *145*, 1839–1843. **DOI:**10.1007/s00706-014-1240-7
37. I. Sedighimehr, B. Karami, M. Farahi, M. Keshavarz, *Mol. Divers.* **2022**, *26*, 3325–3336. **DOI:**10.1007/s11030-022-10393-w
38. J. E. Gholtash, M. Farahi, *RSC Adv.* **2018**, *8*, 40962–40967. **DOI:**10.1039/C8RA06886K
39. S. V. Salihov, Y. A. Ivanenkov, S. P. Krechetov, M. S. Veselov, N. V. Sviridenkova, A. G. Savchenko, A. G. Majouga, *J. Magn. Magn. Mater.* **2015**, *394*, 173–178. **DOI:**10.1016/j.jmmm.2015.06.012
40. T. A. Revathy, K. Dhanapal, S. Dhanavel, *J. Alloys Compd.* **2018**, *735*, 1703–1711. **DOI:**10.1016/j.jallcom.2017.11.264
41. S. Hashemi-Uderji, M. Abdollahi-Alibeik, R. Ranjbar-Karimi, *J. Porous Mater.* **2019**, *26*, 467–480. **DOI:**10.1007/s10934-018-0628-x
42. M. Gerami, M. Farahi, B. Karami, *J. Mol. Struct.* **2025**, *1328*, 141246. **DOI:**10.1016/j.molstruc.2024.141246
43. K. Niknam, A. Jamali, *Chin. J. Catal.* **2012**, 33, 1840–1849. **DOI:**10.1016/S1872-2067(11)60457-9
44. I. Clark, R. L. Gomes, C. Crawshaw, L. Neve, R. Lodge, M. Fay, C. Winkler, M. Hull, E. Lester, *React. Chem. Eng.* **2019**, *4*, 663–666. **DOI:**10.1039/C8RE00241J
45. J. Wang, D. Q. Shi, Q. Y. Zhuang, X. S. Wang, H. W. Hu, *J. Chem. Res.* **2004**, *12*, 818–820. **DOI:**10.3184/0308234043431221
46. M. Rostami, S. Momeni, R. Ghorbani, *J. Mol. Struct.* **2024**, *1312*, 138527. **DOI:**10.1016/j.molstruc.2024.138527
47. H. Mehrabi, H. Abusaidi, *J. Iran. Chem. Soc.* **2010**, *7*, 890–894. **DOI:**10.1007/BF03246084
48. M. G. Dekamin, M. Eslami, A. Maleki, *Tetrahedron* **2013**, *69*, 1074–1085. **DOI:**10.1016/j.tet.2012.11.068
49. M. Ahmadian, K. Rad-Moghadam, Z. Gholami, *J. Mol. Liq.* **2022**, *367*, 120501. **DOI:**10.1016/j.molliq.2022.120501
50. M. L. Kantam, V. Balasubrahmanyam, K. B. S. Kumar, *Synth. Commun.* **2006**, *36*, 1809–1814. **DOI:**10.1080/00397910600619630
51. I. Clark, R. L. Gomes, C. Crawshaw, L. Neve, R. Lodge, M. Fay, C. Winkler, M. Hull, E. Lester, *React. Chem. Eng.* **2019**, *4*, 663–666. **DOI:**10.1039/C8RE00241J
52. X. G. Si, Y. P. Zhao, Q. L. Song, J. P. Cao, R. Y. Wang, X. Y. Wei, *React. Chem. Eng.* **2020**, *5*, 886–895. **DOI:**10.1039/D0RE00071J
53. K. Nikoofar, H. Heidari, Y. Shahedi, *Res. Chem. Intermed.* **2018**, *44*, 4533–4546. **DOI:**10.1007/s11164-018-3402-4
54. M. L. Kantam, K. B. S. Kumar, K. P. Raja, *J. Mol. Catal. A Chem.* **2006**, *247*, 186–188. **DOI:**10.1016/j.molcata.2005.11.043
55. A. M. Alsalme, P. V. Wiper, Y. Z. Khimyak, E. F. Kozhevnikova, I. V. Kozhevnikov, *J. Catal.* **2010**, *276*, 181–189. **DOI:**10.1016/j.jcat.2010.09.014

Povzetek

Z namenom razširiti uporabnost imobiliziranih ionskih tekočin kot učinkovitih heterogenih katalizatorjev, smo ionsko tekočino imobilizirali na magnetni lignin (Fe_3O_4-lignin-SO_3/IL) ter tako pripravljeno snov uporabili kot okolju prijazen, obnovljiv katalizator v enolončni reakciji med aromatskimi aldehidi, malononitrilom in 4-hidroksikumarinom s katero smo sintetizirali serijo dihidropirano[3,2-*c*]kromenskih derivatov. Naš pristop se odlikuje z visokimi izkoristki, kratkimi reakcijskimi časi, enostavnostjo izolacije in je potencialno uporaben pri različnih okolju prijaznih procesih na področju farmacevtske kemije. Dodatno smo mehanistično razjasnili vlogo Fe_3O_4-lignin-SO_3/IL kot katalizatorja v izvedeni sintezi in s tem pokazali na njegovo potencialno uporabnost v organski sintezi in pri drugih kemijskih procesih.

DOI: 10.17344/acsi.2025.9289 *Acta Chim. Slov.* **2025,** *72,* 553–561

Scientific paper

Adsorption and Corrosion Inhibition Effect of Expired Prednisolone on AISI 1020 Carbon Steel: Electrochemical, Gravimetric, and Surface Studies

Sihem Kherraf*,[1,2], Malika Foudia[3], Zohra Djetoui[2], Leila Kherraf [4], Nour El Houda Sobhi[3,5]

[1] *Laboratory of Chemical Engineering and Environment of Skikda, University of 20 August 1955-Skikda, Algeria.*

[2] *Departement of Petrochemicals, Faculty of Technology, University of 20 August 1955-Skikda, Skikda, Algeria*

[3] *Laboratory of Energy and Electrochemistry of Solids, Faculty of Technology, Ferhat Abbas University Setif-1, Setif 19000, Algeria.*

[4] *Department of Civil Engineering, University of 20 Août 1955-Skikda, Algeria.*

[5] *Department of chemistry, Water and Environment Science and Technology Laboratory, Mohamed Cherif Messaadia University, Souk-Ahras, Algeria.*

** Corresponding author: E-mail: s.kherraf@univ-skikda.dz*

Received: 04-21-2025

Abstract

The present study evaluated the inhibition performance of expired prednisolone against the corrosion of AISI 1020 carbon steel in a 3.5% sodium chloride medium. The inhibition effectiveness was evaluated using electrochemical impedance spectroscopy, potentiodynamic polarization, gravimetric measurements, and surface characterization techniques. Data obtained from the polarization studies indicated that prednisolone acted as mixed-type inhibitor. Electrochemical impedance spectroscopy results revealed an increase in charge transfer resistance with rising inhibitor concentration. The inhibitor showed a maximum inhibition efficiency of 90% at 298 K. The interaction between the steel surface and the inhibitor was determined to be physisorption, consistent with the Langmuir adsorption isotherm model. The corrosion inhibition performance of prednisolone decreased with increasing temperature, reaching 79.42% at 328 K. Surface characterization showed that the inhibitor significantly reduced the corrosion on the metal surface.

Keywords : Corrosion, drug inhibitors, sodium chloride medium, electrochemical methods, weight loss method.

1. Introduction

Seawater is widely used across various industries due to its economic benefits and ecological availability. However, its corrosive nature poses a significant challenge, leading to material degradation, equipment failure, and increased maintenance costs. The corrosion of metals and other materials in marine environments is a complex process influenced by several factors, with salinity being one of the most important.[1] Halide ions, particularly chloride ions, play a critical role in metal corrosion. These ions have an autocatalytic effect on localized corrosion and the propagation of pits on metal surfaces, which leads to the deterioration of steel performance and causes significant economic losses.[2–4]

AISI 1020, a low-carbon steel, is widely used in industrial applications, particularly in marine environments, due to its cost-effectiveness, excellent weldability, and favorable mechanical properties.[5,6] However, its corrosion resistance in seawater and chloride-rich environments remains a persistent concern, attracting growing interest from researchers and industrial communities.

Rios et al.[7] demonstrated the corrosion behavior of AISI 1020 steel in seawater. Their findings showed that, during the early stages of exposure, the steel primarily underwent localized corrosion, characterized by pitting and intergranular attack. After 14 hours of immersion, the corrosion progressed into a more uniform form. In another study, Cáceres et al.[8] investigated the corrosion behavior of

AISI 1020 carbon steel in sodium chloride (NaCl) solutions and found that the corrosion kinetics depended on both immersion time and the dissolved oxygen concentration in the electrolyte.

To address the corrosion challenges associated with AISI 1020 steel and prevent premature equipment failure, the use of corrosion inhibitors is widely recognized as a practical and cost-effective strategy.[9] These inhibitors are chemical compounds added in low concentrations to corrosive environments to significantly reduce the rate of the electrochemical reactions responsible for corrosion.[10] These inhibitors can be added directly into circulating systems to protect internal metal surfaces or incorporated into protective coatings to serve as a barrier against chloride-induced degradation.

In industrial applications, the most effective inhibitors are heteroatomic organic compounds containing oxygen, sulfur, phosphorus, nitrogen, π-electrons in double or triple bonds, and/or aromatic rings.[11,12] The effectiveness of these inhibitors mainly depends on their adsorption onto the metal surface.[13] Metal-inhibitor interactions can be formed through van der Waals forces between the charged metal and charged inhibitor molecules (physisorption), and/or by the creation of coordinate covalent bonds (chemisorption).

Among traditional organic inhibitors, many compounds are recognized as toxic and non-biodegradable.[14] As a result, the development of eco-friendly, protective, and cost-effective corrosion inhibitors has become a major research priority.[15–17] Drugs have emerged as promising alternatives to conventional toxic organic corrosion inhibitors, as they are rich in various polar substituents such as –C=N, –C=O, and –OH, and are both biodegradable and non-toxic.[18,13]

Using expired drugs as corrosion inhibitors offer multiple benefits: reducing environmental pollution caused by active pharmaceutical ingredients, preventing harm to human health, addressing disposal and treatment challenges of expired drugs, and lowering the economic costs associated with traditional corrosion inhibitors.[19–21] Several pharmaceuticals, such as miglitol,[22] amoxicillin,[23] hexamine,[24] ceftin,[25] oxazepam,[26] clonazepam,[27] and imidazole,[28] have been reported to effectively protect carbon steels in neutral chloride environments.

For AISI 1020 steel, Schneider et al.[29] investigated the anti-corrosion properties of tetracycline hydrochloride in various corrosive media, including sulfuric acid (1 M), hydrochloric acid (1 M), nitric acid (1 M), and sodium chloride solution (0.05 M). The evaluation, conducted using electrochemical impedance spectroscopy (EIS), weight loss measurements, and metallographic analysis, revealed that tetracycline hydrochloride significantly reduced the corrosion rate of AISI 1020 steel in hydrochloric acid and sodium chloride media, achieving maximum inhibition efficiencies of 74.10% and 72.58%, respectively.

Similarly, Swetha et al.[30] evaluated the corrosion inhibition performance of Seroquel on AISI 1020 steel in 3.5% NaCl solution over a temperature range of 303–333 K, using weight loss, EIS, and potentiodynamic polarization techniques. EIS results showed that inhibition efficiency increased with both inhibitor concentration and temperature, reaching a maximum of 83% at 333 K. Polarization studies further revealed that Seroquel functioned as a mixed-type inhibitor, effectively reducing both anodic and cathodic reactions involved in the corrosion process.

Prednisolone is a corticosteroid drug widely used to treat a variety of metabolic diseases, including inflammation, allergies, asthma, and vision problems.[31,32] The molecular formula of prednisolone is $C_{21}H_{28}O_5$ (Fig. 1).[33] The presence of oxygen atoms with π-electrons in conjugated double bonds provides active sites for adsorption onto metal surfaces, enhancing its potential as a corrosion inhibitor.

Notably, no prior research has explored the use of prednisolone as a corrosion inhibitor. In this study, the corrosion inhibition performance of prednisolone was investigated for the first time as a novel anticorrosion compound for AISI 1020 steel in 3.5% sodium chloride solutions. The inhibitory performance was evaluated using the weight loss method, electrochemical measurements, and surface characterization via scanning electron microscopy (SEM).

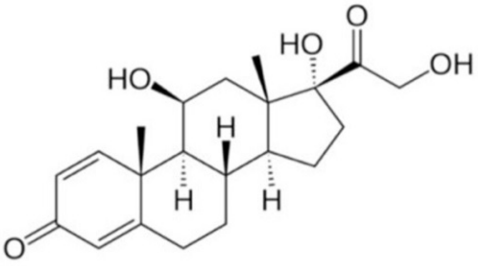

Figure 1. Molecular structure of prednisolone.[33]

2. Experimental

2. 1. Materials.

AISI 1020 low-carbon steel, supplied by Shaanxi Shew-E Steel Pipe Co., Ltd, was used in this study. The chemical composition of the steel, expressed in weight percent (wt.%), was as follows: 0.16% C, 0.012% P, 0.63% Mn, 0.031% S, 0.012% Si, 0.01% Cu, 0.03% Cr, 0.01% Ni, with the remainder being iron. The corrosive solution (3.5% NaCl) was prepared using high-purity sodium chloride (99.5%) and distilled water.

2. 2. Electrochemical Techniques

An electrochemical cell equipped with a three-electrode setup and a potentiostat/galvanostat (Voltalab

PGZ301) was used for the electrochemical measurements. The working electrode was AISI 1020 steel with a surface area of 1 cm^2. A platinum electrode served as the counter electrode, and a saturated calomel electrode was used as the reference electrode. Prior to measurements, the working electrodes were abraded using abrasive paper with progressively finer grit sizes (240–2000), degreased with acetone, and rinsed with distilled water. Once the open circuit potential stabilized, potentiodynamic polarization and electrochemical impedance spectroscopy (EIS) measurements were carried out. Polarization curves were recorded at a sweep rate of 1 mV/s. EIS measurements were performed over a frequency range of 100 kHz to 10 mHz, using a sinusoidal excitation signal of ±10 mV.

2. 3. Weight Loss Method

Weight loss measurements were performed at various temperatures ranging from 298 K to 328 K. The steel sample dimensions were 4 cm × 2 cm × 0.3 cm. Prior to the experiments, the carbon steel samples were gradually abraded using different grades of emery paper, degreased with acetone, cleaned with distilled water, dried, and then weighed. The polished and pre-weighed samples were subsequently immersed in a 3.5% NaCl solution, both with and without varying concentrations of the inhibitor. After 24 hours of immersion, the AISI 1020 samples were removed from the electrolyte, cleaned with acetone and distilled water, dried, and reweighed.

2. 4. Surface Studies

The alloy specimens, measuring 1 cm × 1 cm × 1 cm, were polished to a smooth finish using different grades of abrasive paper. The alloys were then immersed in 3.5% NaCl solutions, both with and without the inhibitor, at room temperature. After 24 hours of immersion, the carbon steel samples were rinsed with distilled water, dried, and analyzed using scanning electron microscopy (Euromex) to evaluate their surface morphology.

3. Results and Discussion

3. 1. Polarization Curves

Fig. 2 presents the polarization curves for carbon steel in aerated 3.5% NaCl solutions, both with and without various concentrations of prednisolone at 298 K. The polarization curves for the inhibited solutions closely resembled those of the blank solution, suggesting that the inhibitor did not alter the underlying corrosion mechanism. This indicates that the corrosion inhibition of steel by prednisolone occurred primarily through a geometric blocking effect.[34]

Electrochemical parameters, including current density (i_{corr}), corrosion potential (E_{corr}), anodic Tafel slope (β_a), cathodic Tafel slope ($-\beta_c$), and inhibition efficiency (IE_p), are presented in Table 1. The inhibition efficiency was calculated from the extrapolated corrosion current densities using Eq. (1):[35]

$$IE_p\,\% = \frac{i^0_{corr} - i_{corr}}{i^0_{corr}} \times 100 \qquad (1)$$

where, i^0_{corr} and i_{corr} refer to the corrosion current densities of carbon steel without and with the inhibitor, respectively.

The results in Table 1 indicate that the addition of prednisolone to the corrosive media reduced the corrosion current density, with the lowest value observed in the solution containing 5.25 g L^{-1} of the inhibitor. Correspondingly, the inhibition efficiency increased with inhibitor concentration, reaching a maximum value of 89.54%. The decrease in i_{corr} in the presence of prednisolone was attributed to the adsorption of inhibitor molecules onto the steel surface, forming a protective layer that slowed down the kinetics of the corrosion reactions.[36,37]

The results also showed that the corrosion potential (E_{corr}) shifted anodically with increasing inhibitor concentrations. According to the literature, if the shift in E_{corr} exceeds 85 mV relative to the E_{corr} of the blank solution, the inhibitor can be classified as either anodic or cathodic. However, if the shift is less than 85 mV, the inhibitor is considered a mixed-type inhibitor.[30,31]

In this study, the largest shift in E_{corr} was 48.7 mV, which is below the 85 mV threshold, indicating that prednisolone acted as a mixed-type inhibitor with a predominant anodic effect. Additionally, the anodic and cathodic Tafel slope values for the inhibited solutions differed significantly from those of the blank solution, further supporting the classification of prednisolone as a mixed-type inhibitor.

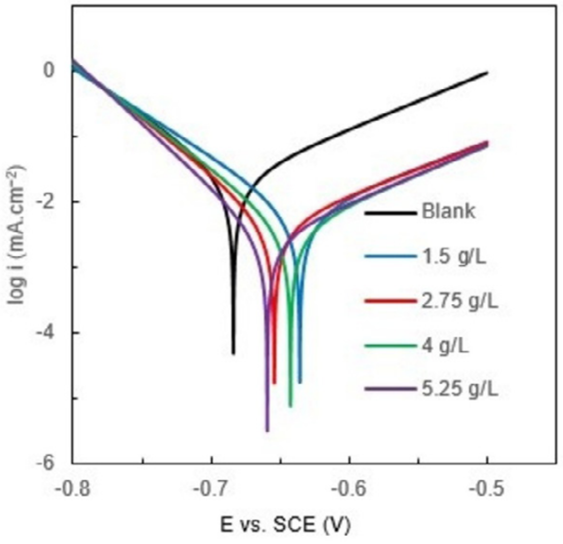

Figure. 2 Polarization curves for AISI 1020 steel in 3.5% NaCl solution containing different concentrations of prednisolone at 298K

Table 1. Polarization parameters and the corresponding inhibition efficiency for the corrosion of AISI 1020 steel in a 3.5% NaCl solution containing different concentrations of prednisolone at 298 K

C_{inh} (g.L^{-1})	E_{corr} (mV)	i_{corr} (μA.cm^{-2})	β_a (mV.dec^{-1})	$-\beta_c$ (mV.dec^{-1})	IE$_{pol}$ (%)
Blank	–683.7	24.3	115.3	69	
1.5	–635.6	7.53	126.4	74.1	69.01
2.75	–654.1	4.5	123.1	59.4	81.48
4	–642.4	3.7	112.9	62.7	84.77
5.25	–659,2	2.54	111.8	51.7	89.54

3. 2. Impedance Measurements

Fig. 3 (a) and (b) show the Nyquist and Bode plots, respectively, recorded for AISI 1020 carbon steel in 3.5% NaCl solutions, both with and without various concentrations of prednisolone. The Nyquist plots (Fig. 3a) exhibited a depressed semicircular shape. The diameter of the semicircle in the inhibited solutions was larger than that of the blank electrolyte and increased with rising drug concentration. Similarly, the impedance modulus |*Z*| (Fig. 3b) increased with increasing drug concentration, suggesting the adsorption of inhibitor molecules onto the steel surface.[3,40]

All phase angle plots exhibited values below 90°, which could be attributed to surface roughness, the adsorption behavior of the inhibitor molecules, or the formation of corrosion products.[41] Therefore, in the EIS analysis, a constant phase element (*CPE*) was more appropriate for fitting the data than a pure capacitance.

The electrochemical equivalent circuit used to model the metal/solution interface consisted of two relaxation constants, as illustrated in Fig. 4. In this model, R_s represented the solution resistance, R_f denoted the resistance of the protective film, and R_{ct} was the charge transfer resistance between the steel surface and the outer Helmholtz plane. CPE_f and CPE_{dl} were the constant phase elements associated with the protective film and the double layer at the metal/solution interface, respectively.

The impedance of a *CPE* is described by Eq. (2):[42]

$$Z_{CPE} = Q^{-1}(j\omega)^{-n} \tag{2}$$

where *Q* is the magnitude of the *CPE* ,[43] ω is the angular frequency, *j* is the imaginary number, and *n* is the *CPE* exponent. The exponent *n* provided insight into the degree of surface inhomogeneity, which could result from surface roughness or the adsorption of inhibitor molecules.[44,45]

The inhibition efficiency (IE$_{EIS}$) for the impedance data was calculated using the charge transfer resistance values of the uninhibited and inhibited solutions, as shown in Eq. (3):[46]

$$IE_{EIS}(\%) = \frac{R_{ct}-R^0_{ct}}{R_{ct}} \times 100 \tag{3}$$

Where R^0_{ct} and R_{ct} were the charge transfer resistances in 3.5% NaCl solution without and with different concentrations of prednisolone, respectively.

The impedance parameters and inhibition efficiency values are listed in Table 2. It was evident that the values of R_{ct} and R_f increased with increasing inhibitor concentration, while Q_f and Q_{dl} decreased. The most pronounced effect was observed at the highest concentration. The increase in R_{ct} values was attributed to the adsorption of inhibitor molecules onto the metal surface, forming a barrier that hindered mass and charge transfer processes.[47,48]

Meanwhile, the decrease in Q_{dl} was likely related to a reduction in the local dielectric constant and/or an increase in the thickness of the double electric layer. The adsorption of drug molecules on the electrode surface displaced water molecules and other ions, thereby lowering the dielectric constant.[49,50]

Furthermore, the addition of prednisolone to the test electrolyte increased the *n* value, indicating a decrease in surface inhomogeneity. The inhibition efficiency also increased with inhibitor concentration, reaching a maximum of 89.59% at 5.25 g L^{-1} of inhibitor. The enhancement in inhibition performance was likely due to increased

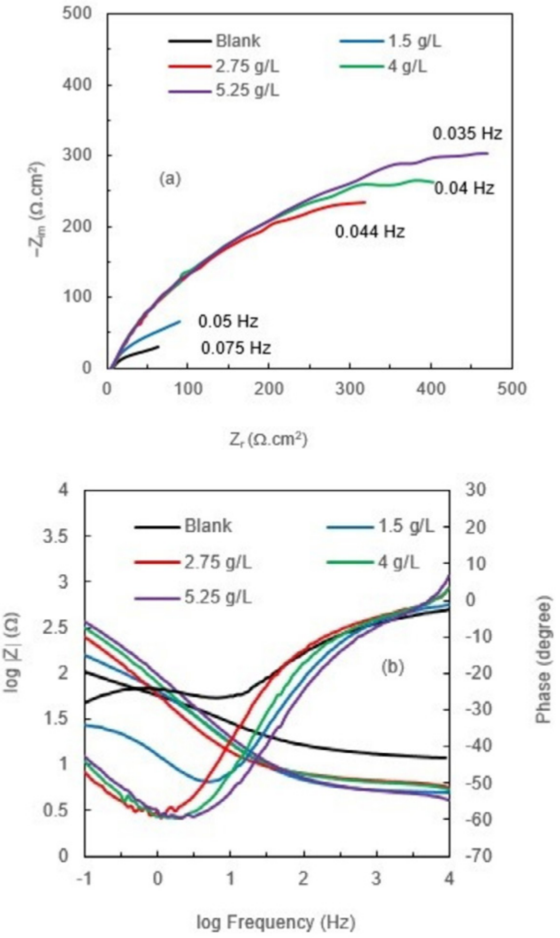

Figure 3. Nyquist diagrams (a) and Bode plots (b) recoprded for AISI 1020 carbon steel in blank and inhibited solutions.

Table 2. Impedance data for the steel electrode in uninhibited and inhibited solutions.

		CPE_f			**CPE_{dl}**			
C_{inh} (g.L^{-1})	**R_s (Ω.cm^2)**	**Q_f (mF.cm^{-2})**	**n_f**	**R_f (Ω.cm^2)**	**Q_{dl} (mF.cm^{-2})**	**n_{dl}**	**R_{tc} (Ω.cm^2)**	**IE_{EIS} (%)**
Blank	4.95	7.96	0.64	22.9	8.56	0.61	119.6	
1.5	4.99	6.64	0.68	51.6	6.87	0.64	389.8	69.31
2.75	4.33	6.24	0.73	66.2	5.61	0.72	658.9	81.84
4	6.51	4.60	0.75	84.5	4.42	0.76	801.1	85.07
5.25	6.64	3.90	0.84	100.5	3.3	0.80	1 149	89.59

surface coverage.[51] As the drug concentration increased, more inhibitor molecules were adsorbed onto the active sites of the metal surface, resulting in a reduced dissolution rate of carbon steel.

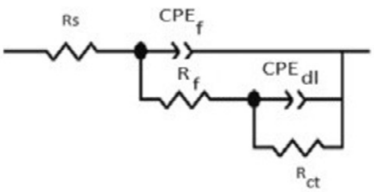

Figure 4. The equivalent circuit used to fit the EIS data

The effect of temperature on the inhibition performance of prednisolone was assessed using the gravimetric method. The corrosion rate (C_R) and inhibition efficiency (IE_{WL}) were calculated using Eqs. (4) and (5).[52,53] The calculated values are summarized in Table 3.

$$C_R(mmy^{-1}) = \frac{\Delta W \times 8.76 \times 10^4}{S \times t \times d} \tag{4}$$

$$IE_{WL}\,(\%) = \frac{C_R^0 - C_R}{C_R^0} \times 100 \tag{5}$$

In these equations, ΔW represents the average weight loss in grams, S is the total area of the specimen in cm^2, t is the immersion time in hours, d is the density of the carbon steel samples used (7.87 g cm^{-3}). C^0_R and C_R refer to the corrosion rates without and with the addition of the inhibitor, respectively.

As shown in Table 3, increasing the temperature of the electrolyte led to a decrease in the inhibition performance of prednisolone. When the temperature rose from 298 K to 328 K, the inhibition efficiency decreased from 90% to 79.42%. This behavior could be attributed to the desorption of inhibitor molecules from the metal surface. As the temperature of the corrosive medium increased, the adsorbed inhibitor molecules became more mobile and tended to detach from the surface, leaving the metal exposed to corrosive species and thereby accelerating the corrosion rate.[54,55]

3. 3. 1. Thermodynamic Calculations

To investigate the corrosion kinetic parameters of prednisolone adsorbed at the metal/solution interface, thermodynamic parameters such as activation energy (E_a), activation enthalpy (ΔH_a), and activation entropy (ΔS_a) were calculated using the Arrhenius and transition state equations, shown in Eqs. (6) and (7).[56]

$$C_R = A \exp\left(\frac{-E_a}{RT}\right) \tag{6}$$

$$C_R = \frac{RT}{Nh} \exp\left(\frac{\Delta H_a}{R}\right) \exp\left(\frac{-\Delta S_a}{RT}\right) \tag{7}$$

where A is the Arrhenius pre-exponential factor, N is Avogadro's number, h is Planck's constant, R is the universal gas constant, and T is the absolute temperature.

Fig. 5(a) and (b) show the linear fit of the Arrhenius and transition state equations, respectively. The values of E_a, ΔH_a, and ΔS_a for different concentrations of prednisolone were calculated from the slopes and intercepts of the straight lines and are reported in Table 4.

It was observed that the E_a values of the inhibited solutions were higher than that of the blank solution, sug-

Table 3. Effect of temperature on the corrosion rate of AISI 1020 steel in 3.5% NaCl solutions containing different concentrations of prednisolone

	Temperature (K)							
	298		**308**		**318**		**328**	
C_{inh} (g.L^{-1})	**C_R (mmy^{-1})**	**IE_G (%)**	**C_R (mmy^{-1})**	**IE_G (%)**	**C_R (mmy^{-1})**	**IE_G (%)**	**C_R (mmy^{-1})**	**IE_G (%)**
Blank	0.0025		0.0027		0.0031		0.0035	
1.5	0.00077	69.2	0.0009	66.66	0.0011	64.51	0.0014	60
2.75	0.00045	82	0.00056	79.25	0.00075	75.80	0.00099	71.71
4	0.00036	85.32	0.00048	82.22	0.00064	79.35	0.00087	75.14
5.25	0.00025	90	0.00036	86.66	0.0005	83.87	0.00072	79.42

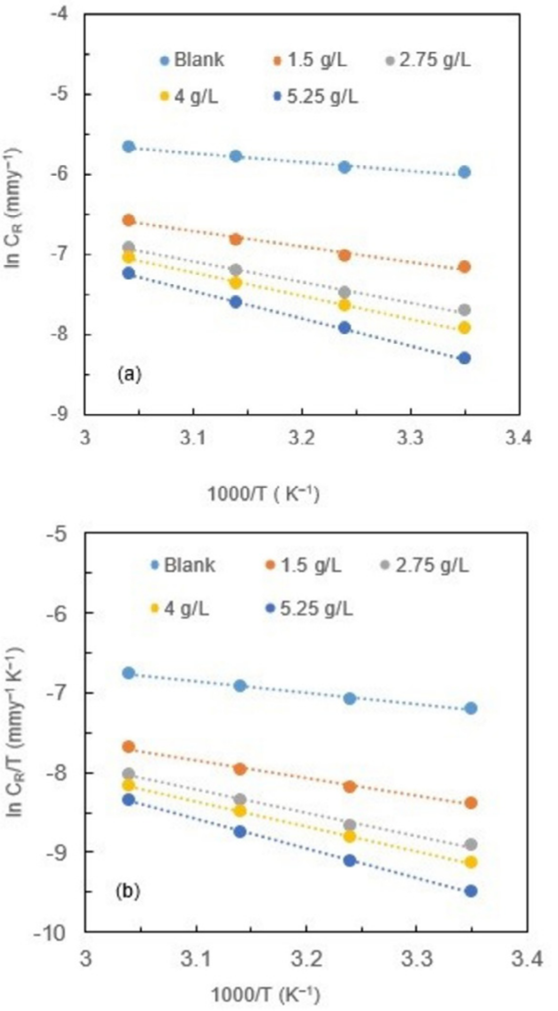

Figure 5. Arrhenius (a) and Transition state (b) plots of AISI 1020 steel in 3.5% NaCl solutions containing various concentration of prednisolone

Table 4. Kinetic parameters for the corrosion of carbon steel in uninhibited and inhibited solutions

C_{inh} (g.L^{-1})	E_a (kJ.mol^{-1})	ΔH_a (kJ.mol^{-1})	ΔS_a (J.mol^{-1}K^{-1})
Blank	9.24	11.84	−217.3
1.5	16.03	18.64	−204.3
2.75	21.40	24.01	−190.8
4	23.39	26.26	−185
5.25	28.24	30.83	−172.7

gesting that the substitution process between the inhibitor molecules and the pre-adsorbed water molecules required more energy.[57] Additionally, the activation energy increased with rising inhibitor concentration, confirming the increased thickness of the adsorbed layer formed on the metal surface.

The ΔH_a values of both uninhibited and inhibited solutions were positive, indicating the endothermic nature of the metal dissolution and adsorption processes.[58,59] Moreover, the negative values of the activation entropy (ΔS_a) suggested an increase in order as the reactants formed an activated complex.[60,61]

3. 4. Adsorption Isotherm

The interaction between the inhibitor and the metal surface was typically attributed to several factors, including the chemical structure of the organic compound, the type of electrolyte, and the charge and nature of the metal. Adsorption isotherms served as important tools for describing this interaction. To gain insight into the adsorption behavior of prednisolone on the AISI 1020 steel surface, the degree of surface coverage (θ) values, calculated using Eq. (8), were fitted to various adsorption isotherm models, including Langmuir, Temkin, Frumkin, and Freundlich, to determine the best-fitting model.

Based on the correlation coefficient (R^2), the Langmuir isotherm provided the best fit, as shown in Fig. 6, and was defined by Eq. (9).[62] This result suggested that the adsorption of prednisolone molecules on the metal surface occurred through the formation of monolayers without lateral interactions between the adsorbed molecules.[63,64]

The degree of surface coverage (θ) was calculated using Eq. (8):

$$\theta = \frac{C_R^0 - C_R}{C_R^0} \tag{8}$$

The Langmuir adsorption isotherm was expressed by Eq. (9):

$$\frac{C_{inh}}{\theta} = \frac{1}{K_{ads}} + C_{inh} \tag{9}$$

Here, K_{ads} was the equilibrium constant of the adsorption-desorption process and was related to the standard free energy of adsorption ($\Delta G^0{}_{ads}$) by Eq. (10):[65]

$$\Delta G^0_{ads} = -RT \ln{(1000K_{ads})} \tag{10}$$

From the Langmuir plots, adsorption parameters such as K_{ads} and $\Delta G^0{}_{ads}$ were obtained and are presented in Table 5. The K_{ads} values decreased from 1.48 to 1.2 L g^{-1} as the electrolyte temperature increased from 298 K to 328 K. This decrease in K_{ads} suggested that the adsorption strength of prednisolone weakened with rising temperature.[52,66]

Generally, when $\Delta G^0{}_{ads}$ was greater than −20 kJ mol^{-1}, it indicated physical adsorption involving electrostatic interactions, while values smaller than −40 kJ mol^{-1} were associated with chemisorption.[67,68] As shown in Table 5, the $\Delta G^0{}_{ads}$ values for prednisolone at different temperatures ranged from −18.07 kJ mol^{-1} to −19.32 kJ mol^{-1}, indicating that the adsorption of the inhibitor on the metal surface was spontaneous and occurred through a physical adsorption process. Furthermore, as the electrolyte temperature increased, the $\Delta G^0{}_{ads}$ values became less negative, further supporting the reduction in the adsorption capacity of prednisolone at higher temperatures.

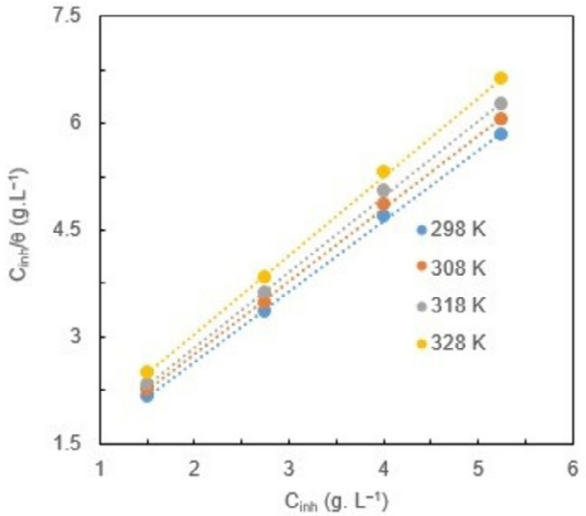

Figure 6. Langmuir adsorption isotherms for the adsorption of prednisolone on carbon steel at different temperatures.

Table 5. Thermodynamic parameters of the adsorption of prednisolone on the metal surface at different temperatures

Temperature (K)	***R***^{2}	***K***$_{ads}$ **(L.g**$^{-1}$**)**	ΔG^0_{ads} **(kJ. mol**$^{-1}$**)**
298	0.999	1.48	−18.07
308	0.999	1.43	−18.59
318	0.999	1.36	−19.06
328	0.999	1.2	−19.32

3. 5. Surface Characterization

Fig. 7(a) and (b) illustrate the SEM images of the AISI 1020 steel surface after 24 hours of exposure to 3.5% NaCl solutions, both in the absence and presence of the maximum concentration (5.25 g L^{-1}) of prednisolone. In the uninhibited solution (Fig. 7a), significant corrosion damage was visible on the steel surface. In contrast, in the presence of the inhibitor (Fig. 7b), steel dissolution was notably reduced, and the surface exhibited significantly less damage. This improvement was attributed to the adsorption of prednisolone molecules onto the steel surface, forming a protective barrier that prevented direct contact between the metal and the corrosive medium, thereby mitigating corrosion.

4. Conclusion

In this study, expired prednisolone was evaluated as a novel corrosion inhibitor for AISI 1020 carbon steel in a 3.5% sodium chloride solution. Electrochemical and gravimetric analyses demonstrated that prednisolone effectively reduced the corrosion rate of carbon steel in neutral chloride environments. The inhibition efficiency depended on both the inhibitor concentration and the temperature of the corrosive medium. This inhibitory performance was primarily attributed to the adsorption of prednisolone molecules onto the steel surface through electrostatic interactions. Surface characterization confirmed the formation of a protective layer on the inhibited steel surface. Therefore, expired prednisolone offered a sustainable solution for mitigating corrosion of carbon steel in marine and saline environments.

Funding

This research received no external funding.

5. References

1. S. Mandal, S. Bej, P. Banerjee, *J. Mol. Liq.* **2023**, *381*, 121789. **DOI:**10.1016/j.molliq.2023.121789

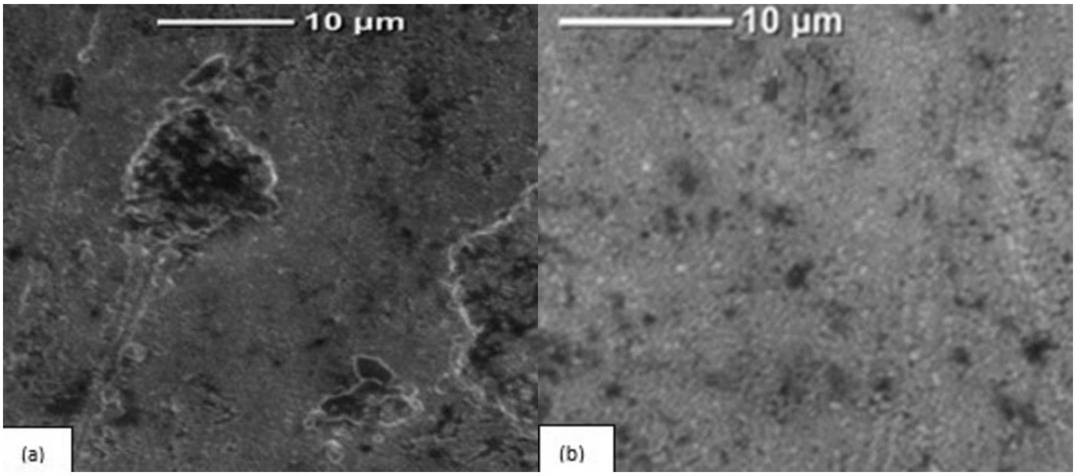

Figure 7. SEM for the exposed carbon steel in (a) blank solution, (b) 3.5% NaCl solution containing 5.25 g. L^{-1} of inhibitor

2. O. R. Wamba-Tchio, M. Pengou, A. L. Teillout, C. Baumier, I. M. Mbomekallé, P. De Oliveira, C. P Nanseu-Njiki, E. Ngameni, *J. Electroanal. Chem.* **2022**, *919*, 116553. **DOI:**10.1016/j.jelechem.2022.116553
3. M. Al-Noaimi, S. Benabid, H. Hamani, Q. F. Salman, M. Binsabt, F. F. Awwadi, K. Douadi, T. Douadi, *Chem. Data Collect.* **2022**, *40*, 100877. **DOI:**10.1016/j.cdc.2022.100877
4. E. Li, S. Liu, F. Luo, P. Yao, *J. Electroanal. Chem.* **2023**, *944*, 117650. **DOI:**10.1016/j.jelechem.2023.117650
5. L. Cáceres, A. Soliz, F. Galleguillos, *Metals* **2022**, 12, 1980. **DOI:**10.3390/met12111980
6. T. A. Wiradinata, A. A. Daryus, D. Sugiyanto, M. Ikhsan, *J. Konv. Energi Manufaktur.* **2025**, 10, 44–52. **DOI:**10.21009/JKEM.10.1.5
7. E. C. Rios, A. M. Zimer, E. C. Pereira, L. H. Mascaro, *Electrochim. Acta* **2014**, 124, 211–217. **DOI:**10.1016/j.electacta.2013.10.059
8. L. Cáceres, L. Herrera, T. Vargas, *Corrosion.* **2007**, 63, 722–730. **DOI:**10.5006/1.3278421
9. N. Ferraa, M. Ouakki, H. El Harmouchi, M. Cherkaoui, M. B. Ziatni, *Inorg. Chem. Commun.* **2023**, *157*, 111343. **DOI:**10.1016/j.inoche.2023.111343
10. U. Mamudu, J. H. Santos, S. A. Umoren, M. S. Alnarabiji, R. C. Lim, *Corros. Commun.* **2024**, *15*, 52–62. **DOI:**10.1016/j.corcom.2023.10.005
11. A. H. Al-Moubaraki, E. A. Noor, A. M. Khayaya, J. M. Al-Ahmari, A. A. Al-Ghamdi, F. M. Al Hayazi, Y. G. Ko, *J. Indian Chem. Soc.* **2025**, 102, 101547. **DOI:**10.1016/j.jics.2024.101547
12. X. Huang, H. Jiang, K. Cao, W. Huang, J. Liu, B. Liu, H. Wang, *Int. J. Electrochem. Sci.* **2024**, *19*, 100824. **DOI:**10.1016/j.ijoes.2024.100824
13. M. S. Bejandi, M. H. Behroozi, M. R. Khalili, R. Sharifi, A. A. Javidparvar, E. Oguzie, *J. Ind. Eng. Chem.* **2024**, *131*, 662–675. **DOI:**10.1016/j.jiec.2023.11.003
14. X. An, J. Dai, S. Wang, W. Zou, *Int. J. Electrochem. Sci.* **2024**, *19*, 100677. **DOI**:1016/j.ijoes.2024.100677
15. A. Royani, V. S. Aigbodion, M. Hanafi, N. M. Mubarak, C. Verma, A. Alfantazi, A. Manaf, *Appl. Surf. Sci. Adv.* **2023**, *18*, 100465. **DOI:**10.1016/j.apsadv.2023.100465
16. R. K. Mehta, M. Yadav, *Mater. Sci. Eng.* B **2023**, *295*, 116566. **DOI:**10.1016/j.mseb.2023.116566
17. E. De Ketelaere, D. Moed, M. Vanoppen, A. R. D. Verliefde, K. Verbeken, T. Depover, *Corros. Sci.* **2023**, *217*, 111119. **DOI:**10.1016/j.corsci.2023.111119
18. X. Wang, H. Guo, S. Cai, X. Xu, *J. Mol. Struct.* **2023**, *1294*, 136555. **DOI:**10.1016/j.molstruc.2023.136555
19. A. I. Ikeuba, F. O. Faithpraise, K. I. Nwokolo, F. E. Umo, O. C. Echem, A. T. Ibrahim, H. O. Edet, B. I. Ita, P. C. Okafor, F. C. Asogwa, J. Amajama, P. C. Iwuji, *Results Mater.* **2024**, *21*, 100542. **DOI:**10.1016/j.rinma.2024.100542
20. A. S. K. Zadeh, M. S. Zandi, M. Kazemipour, *J. Indian Chem. Soc.* **2022**, *99*, 100522. **DOI:**10.1016/j.jics.2022.100522
21. V. C. Anadebe, P. C. Nnaji, O. D. Onukwuli, N. A. Okafor, F. E. Abeng, V. I. Chukwuike, C. C. Okoye, I. I. Udoh, M. A. Chidiebere, L. Guo, R. C. Barik, *J. Mol. Liq.* **2022**, *349*, 118482. **DOI:**10.1016/j.molliq.2022.118482
22. R. G. Sundaram, G. Vengatesh, M. Sundaravadivelu, *Surf. Interfaces* **2021**, *22*, 100841. **DOI:**10.1016/j.surfin.2020.100841
23. Z. S. Mahmoud, A. K. Shams, T. A. Salman, *Baghdad Sci. J.* **2022**, *19*, 121–131. **DOI:**10.21123/bsj.2022.19.1.0121
24. F. H. Ebrahim, M. Ghorbani, *Mater. Prot.* **2023**, *64*, 134–152 **DOI:**10.5937/zasmat2302134F
25. N. Raghavendra, *Iran. J. Energy Environ.* **2018**, *9*, 295–298.
26. N. Raghavendra, *Front. Chem. Res.* **2019**, *1*, 1-4.
27. F. E. Abeng, B. I. Ita, V. C. Anadebe, V. I. Chukwuike, K. M. Etiowo, P. Y. Nkom, O. O. Ekerenam, N. B. Iroha, I. J. Ikot, *Results Eng.* **2023**, *17*, 100924. **DOI:**10.1016/j.rineng.2023.100924
28. M. Mahdavian, M. M. Attar, *Prog. Color Colorants Coat.* **2015**, 8, 177–196
29. E. V. Schneider, R. D. Balboni, R. M. Lemos, L. U. Krüger, T. Poletti, B. V. Lopes, B. V. Lopes, R. Camaratta, S. M. M. Tamborim, N. L. V. Carreno , C. O. Avellaneda, C. M. Cholant, *J. Build. Eng.* **2024**, 97, 110708. **DOI:**10.1016/j.jobe.2024.110708
30. G. A. Swetha, H. P. Sachin, A. M. Guruprasad, B. M. Prasanna, K. H. Sudheer Kumar, *J. Bio- Tribo-Corros.* **2018**, 4, 57. **DOI:**10.1007/s40735-018-0173-9
31. Z. Wu, X. Du, J. Zhang, *Alexandria Eng. J.* **2024**, *96*, 93–98. **DOI:**10.1016/j.aej.2024.03.098
32. A. Szegedi, I. Trendafilova, J. Mihaly, K. Lazar, P. Nemeth, G. Momekov, L. Marinov, I. Nikolova, M. Popova, *J. Drug Deliv. Sci. Technol.* **2020**, *60*, 102092. **DOI:**10.1016/j.jddst.2020.102092
33. I. A. Ionita, D. M. Fast, F. Akhlaghi, *J. Chromatogr. B.* **2009**, *877*, 765–772. **DOI:**10.1016/j.jchromb.2009.02.019
34. J. He, Q. Xu, G. Li, Q. Li, R. Marzouki, W. Li, *J. Ind. Eng. Chem.* **2021**, *102*, 260-270. **DOI:**10.1016/j.jiec.2021.07.007
35. A. Singh, K. R. Ansari, I. H. Ali, M. Younas, A. K. Alanazi, A. H. Alamri, Y. LinInorg, *Chem. Commun.* **2023**, *158*, 111684. **DOI:**10.1016/j.inoche.2023.111684
36. Q. Wang, R. Wang, J. Zhao, Z. Zou, Q. Huang, Y. Sui, J. Shi, R. Aslam, Y. Sun, Z. Yan, *Microchem. J.* **2024**, 207, 111957. **DOI:**10.1016/j.microc.2024.111957
37. E. Ech-chihbi, B. Es-Sounni, C. Kerdoune, A. Mouhib, M. Bakhouch, R. Salim, R. Salghi, B. Hammouti, N. Mazoir, M. Chafiq, A. Chaouiki, Y. G. Ko, *Colloids Surf. A Physicochem. Eng. Asp.* **2024**, 702, 135073. **DOI:**10.1016/j.colsurfa.2024.135073
38. S. A. Raji, A. P. I. Popoola, O. L. Akanji, *J. Mol. Struct.* **2024**, *1312*, 138414. **DOI:**10.1016/j.molstruc.2024.138414
39. T. Zheng, J. Liu, M. Wang, Q. Liu, J. Wang, Y. Chong, G. Jia, *Corros. Sci.* **2022**, *199*, 110199. **DOI:**10.1016/j.corsci.2022.110199
40. N. Hassan, A. M. Ramadan, S. Khalil, N. A. A. Ghany, A. M. Asiri, R.M. El-Shishtawy, *Colloids Surf. A: Physicochem. Eng. Asp.* **2020**, *607*, 125454. **DOI:**10.1016/j.colsurfa.2020.125454
41. A. Soliz, P. P. Zamora, J. P. Muena, K. Bieger, J. Haribabu, E. Landaeta, A. Arulraj, R. V. Mangalaraja, *Colloids Surf. A Physicochem. Eng. Asp.* **2024**, 703, 135283. **DOI:**10.1016/j.colsurfa.2024.135283

42. M. A. Belayachi, O. Kharbouch, K. Dahmani, A. El Magri, N. Er-rahmany, I. Saber, F. El hajri, G. Mouhsine , S. Abdelillah, Z. Benzekri, S. Boukhris, R. Almeer, A. Chaouiki, *Int. J. Electrochem. Sci.* **2025**, 20, 100951. **DOI:**10.1016/j.ijoes.2025.100951
43. S. Thakur, A. K. Singh, *Inorg. Chem. Commun.* **2024**, 166, 112602. **DOI:**10.1016/j.inoche.2024.112602
44. I. Lakikza, H. Ghodbane, A. Boublia, S. I. Aouni, A. Zouaoui, K. S. A. A. Al-Qasim, M. Albrahim, Y. Benguerba, *J. Mol. Liq.* **2024**, *414*, 126219. **DOI:**10.1016/j.molliq.2024.126219
45. X. X. Li, Q. H. Chen, T. Zhang, B. X. Wei, B. K. Liao, X. P. Guo, *Colloids Surf. A: Physicochem. Eng. Asp.* **2024**, *703*, 135422. **DOI:**10.1016/j.colsurfa.2024.135422
46. Y. G. Devi, S. Adhikari, A. K. Pulikkal, P. V. Rajaraman, *Surf. Interfaces.* **2024**, *45*, 103796. **DOI:**10.1016/j.surfin.2023.103796
47. J. Tang, Y. Shi, S. He, J. Luo, Y. Liu, K. Zhai, D. Ming , H. Wang, J. Xie, *Int. J. Electrochem. Sci.* **2024**, *19*, 100547. **DOI:**10.1016/j.ijoes.2024.100547
48. F. Z. Eddahhaoui, A. Najem, M. Elhawary, M. Boudalia, O. S. Campos, M. Tabyaoui, A. J. Garcia, A. Bellaouchou, H. M. Amin, *J. Alloys Compd.* **2024**, *977*, 173307. **DOI:**10.1016/j.jallcom.2023.173307
49. R. Khanna, M. Dudi, B. Mangla, V. Kalia, A. Sihmar, H. Tanwar, H. Dahiya, *J. Mol. Struct.* **2024**, *1317*, 139066. **DOI:**10.1016/j.molstruc.2024.139066
50. H. S. Gadow, A. Fawzy, M. Khairy, M. M. Sanad, A. Toghan, *Int. J. Electrochem. Sci.* **2023**, *18*, 100174. **DOI:**10.1016/j.ijoes.2023.100174
51. A. Salhi, A. Elyoussfi, I. Azghay, A. El Aatiaoui, H. Amhamdi, M. El Massaoudi, M. Ahari, A. Abdelhamid Bouyanzer, S. Radi, S. El barkany, *Inorg. Chem. Commun.* **2023**, *152*, 110684. **DOI:**10.1016/j.inoche.2023.110684
52. K. Haruna, T. A. Saleh, *Mater. Today Commun.* **2024**, 40, 109978. **DOI:**10.1016/j.mtcomm.2024.109978
53. S. Wang, Z. Liang, Y. Wang, J. Li, H. Jin, *Mater. Today Commun.* **2024**, 40, 109980. **DOI:**10.1016/j.mtcomm.2024.109980
54. N. N. Hau, D. Q. Huong, *J. Mol. Struct.* **2023**, 1277, 134884. **DOI:**10.1016/j.molstruc.2022.134884
55. C. Merimi, B. Hammouti, K. Zaidi, B. Hafez, H. Elmsellem, R. Touzani, S. Kaya, *J. Mol. Struct.* **2023**, 1278, 134883. **DOI:**10.1016/j.molstruc.2022.134883
56. K. Rasheeda, N. P. Swathi, V. D. Alva, S. Samshuddin, T. A. Aljohani, I. Baig, F. Y Alomari, A. H. Alamri, S. Afr. *J. Chem. Eng.* **2024**, *48*, 80-94. **DOI:**10.1016/j.sajce.2024.01.006
57. J. Pan, X. He, K. Cao, *Int. J. Electrochem. Sci.* **2025**, 20, 100916. **DOI:**10.1016/j.ijoes.2024.100916
58. A. Belkheiri, K. Dahmani, K. Mzioud, M. Rbaa, M. Galai, A. Hmada, S. Erdo gan , B. Tüzün, M. Ebn Touhami, H. El-Serehy, B. M. Al-Maswari, *Int. J. Electrochem. Sci.* **2024**, *19*, 100772. **DOI:**10.1016/j.ijoes.2024.100772
59. M. Kemel, *J. Ind. Eng. Chem.* **2024**, *140*, 617–630. **DOI:**10.1016/j.jiec.2024.08.038
60. Z. Aribou, M. Ouakki, F. El Hajri, E. Ech-chihbi, I. Saber, Z. Benzekri, S. Boukhris, M. K. Al-Sadoon, M. Galai, J. Charafeddine, M. E. Touhami, *Int. J. Electrochem. Sci.* **2024**, *19*, 100788. **DOI:**10.1016/j.ijoes.2024.100788
61. M. Ouakki, Z. Aribou, F. El Hajri, E. Ech-chihbi, Z. Benzekri, R. Lachhab, B. Srhir, M. Patrick, R. Almeer, M. Galai, S. Boukhris, M. Cherkaoui, *Int. J. Electrochem. Sci.* **2024**, *19*, 100795. **DOI:**10.1016/j.ijoes.2024.100795
62. M. Rezaeivala, M. Bozorg, N. Rafiee, K. Sayin, B. Tuzun, *Inorg. Chem. Commun.* **2023**, *148*, 110323. **DOI:**10.1016/j.inoche.2022.110323
63. R. Salim, E. Ech-chihbi, Y. Fernine, M. Koudad, L. Guo, E. Berdimurodov, M. Azam, Z. Rais, M. Taleb, *J. Mol. Liq.* **2024**, *393*, 123579. **DOI:**10.1016/j.molliq.2023.123579
64. M. O. Danyliak, I. M. Zin, S. A. Korniy, *J. Ind. Eng. Chem.* **2024**, *129*, 267–277. **DOI:**10.1016/j.jiec.2023.08.039
65. X. Yang, G. He, W. Dong, L. Yu, X. Li, *J. Environ. Chem. Eng.* **2023**, *11*, 109846. **DOI:**10.1016/j.jece.2023.109846
66. P. Du, S. Deng, G. Du, D. Shao, D. Xu, X. Li, *Corros. Sci.* **2023**, *220*, 111296. **DOI:**10.1016/j.corsci.2023.111296
67. R. Sehrawat, R. Pundeer, S. Yadav, P. Vashishth, H. Bairagi, S. K. Shukla, B. Mangla, *J. Mol. Struct.* **2024**, *1316*, 139017. **DOI:**10.1016/j.molstruc.2024.139017
68. S. Ravi, S. Peters, *J. Taiwan Inst. Chem. Eng.* **2024**, *165*, 105726. **DOI:**10.1016/j.jtice.2024.105726

Povzetek

V študiji smo preučevali inhibicijsko učinkovitost pretečenega prednizolona pri preprečevanju korozije ogljikovega jekla AISI 1020 v 3,5-odstotni raztopini natrijevega klorida. Učinkovitost inhibicije smo ovrednotili z elektrokemijsko impedančno spektroskopijo, potenciodinamično polarizacijo, gravimetričnimi meritvami in karakterizacijo površine. Polarizacijske študije so pokazale, da prednizolon deluje kot inhibitor mešanega tipa, medtem ko so rezultati impedančne spektroskopije razkrili povečanje upora prenosa naboja z naraščajočo koncentracijo inhibitorja. Največja učinkovitost inhibicije, 90 %, je bila dosežena pri temperaturi 298 K. Interakcija med površino jekla in inhibitorjem ustreza fizisorpciji, skladno z Langmuirjevim modelom adsorpcijske izoterme. Pri višjih temperaturah se je učinkovitost inhibicije zmanjšala in pri 328 K znašala 79,42 %. Karakterizacija površine je potrdila, da inhibitor bistveno zmanjša korozijo na kovinski površini.

Scientific paper

Synthesis, DFT, and Molecular Docking Studies of Anti-cancer Imidazolidine-2,4-dione and Thiazolidine-2,4-dione Derivatives

Osama Alharbi

[1] *Department of Chemistry, College of Science, Taibah University, Al-Madinah Al-Munawwarah, 30002, Saudi Arabia*

* *Corresponding author: E-mail: oamharbi@taibahu.edu.sa*

Received: 05-14-2025

Abstract

Novel families of thiazolidine-2,4-dione and imidazolidine-2,4-dione derivatives were synthesized. Thiazolidine-2,4-dione **3** was prepared using chloroacetic acid and thiourea, followed by condensation with terephthalaldehyde to form 4-((2,4-dioxothiazolidine-5-ylidene)methyl)benzaldehyde **4**. This compound reacted with 2-aryloxyacetohydrazides **8a-b** to yield Schiff bases **9a-b**. Imidazolidine-2,4-diones **13a-c** were synthesized via cyclizing of anilines **10a-c**, urea **11**, and chloroacetic acid **12**. The compounds **9a-b** and **13a-c** were evaluated for antitumor activity against the Caco-2 cell line, compounds **13b** and **13c** exhibiting the highest potency (IC_{50} values of 41.30 ± 0.07 μM and 109.2 ± 0.027 μM, respectively). DFT calculations, including HOMO-LUMO analysis, energy gap estimation, and molecular docking, were conducted to evaluate and optimize the molecular properties of the target compounds.

Keywords: Imidazolidine-2,4-dione; thiazolidine-2,4-dione; molecular docking; DFT; anti-cancer.

1. Introduction

Tumors are a category of intricate disorders described by the rapid, unregulated, and serious cell proliferation, which disrupts the process of normal cell division.[1] It is considered one of the gravest diseases threatening human health. Improved recognition of the complicated nature of cancer biology has been critical in the advancement of cancer therapies. Recent research has focused on developing novel cancer therapies using non-toxic therapeutic approaches.[2] Chemotherapy, a widely used cancer treatment, works by interfering with the mechanisms regulating cell division. Its goal is to prevent metastasis and invasion by inhibiting tumor growth. However, chemotherapy can cause adverse side effects due to its impact on healthy cells. Key challenges in cancer treatment include drug resistance and adverse off-target effects, driving the development of new anti-cancer agents with minimal toxicity and high efficacy.[3] Heterocyclic scaffolds are valued in medicinal and synthetic organic chemistry for their diverse biological activities and chemical versatility.[4,5] These compounds, derived from natural sources or synthetic methods, have significant potential in overcoming drug resistance and improving treatment efficacy. Notably, thiazolidine-2,4-diones, commonly known as glitazones, are a class of heterocyclic compounds exemplified by the archetypal medication ciglitazone. These compounds are used in the management of type 2 diabetes mellitus, introduced in the late 1990s.[6] In addition to their antidiabetic efficacy, thiazolidine-2,4-diones inhibit the proliferation of various cancer cell lines, including colon, breast, and prostate, both *in vivo* and *in vitro.*[7,8] Thiazolidine-2,4-dione is a highly selective oral agonist of peroxisome proliferator-activated receptor gamma (PPARγ), which shown potential in stabilizing disease progression in patients with metastatic colorectal cancer (mCRC), along with demonstrating favourable safety and pharmacokinetic stability.[9] Imidazolidine-2,4-dione and thiazolidine-2,4-dione are significant five-membered heterocycles characterized by two carbonyl groups. These groups impart unique electronic and steric properties, making them valuable synthetic intermediates and pharmacophores in medicinal chemistry. The incorporation of nitrogen and sulfur in these frameworks significantly affects their nucleophilic, electrophilic, and tautomeric properties, thus regulating their reactivity and applications. The imidazolidine-2,4-dione ring is a key pharmacophore with diverse biological properties.[10] Its derivatives are well-known for anticonvulsant, antiarrhythmic, antibacterial, skeletal muscle relaxant, and non-steroidal antiandrogen properties. Imidazolidine-2,4-dione and its analogues are found in some naturally occurring compounds, such as certain alkaloids. Numerous alkaloids containing an imidazolidine-2,4-dione ring, such as the aplysinopsins, have been isolated from sponges or corals and demonstrate potent biological activity, including antimicrobial and cytotoxic effects.[10] Building on the diverse therapeutic potential of imidazolidine-2,4-dione and thiazolidine-2,4-dione derivatives, this study investigates novel approaches to enhance cancer treatment by synthesizing and evaluating new derivatives for their anti-cancer activity.[11]

2. Experimental

2. 1. Materials and Methods

All chemical reagents were of analytical grade and purchased from Accela ChemBio Co., Ltd. (Shanghai, China). Melting points have been determined using an XT-4 melting point instrument (Beijing Tech Instrument Co., China). ^{1}H and ^{13}C NMR were recorded on an AVANCE III HD 400 MHz NMR spectrometer (Bruker Corporation, Switzerland.) or JEOL ECX 500 MHz NMR spectrometer (JEOL Ltd., Japan) operating at room temperature, using DMSO-d_6 or $CDCl_3$ as solvents. Reaction progress was monitored by thin-layer chromatography (TLC). FT-IR spectra were recorded on a Nicolet iS5 FTIR spectrophotometer (Thermo Fisher Scientific, USA) using KBr pellets.

2. 2. Synthesis of Thiazolidin-2,4-dione (3)[12]

The established procedure was followed to synthesize compound **3**. Chloroacetic acid (9.45 g, 0.1 mol) and thiourea (7.61 g, 0.1 mol) were dissolved in 10 mL of H_2O and stirred for 15 minutes until a white precipitate formed. The mixture was cooled, and 10 mL of concentrated HCl was slowly added. The flask was then attached to a reflux condenser, and the mixture was refluxed with stirring at 100–110 °C for 8–10 hours. The product was cooled, filtered, washed, dried at room temperature, and recrystallized from water to yield a white solid. Melting point: 115 °C; yield: 11.11 g (95%).

2. 3. Synthesis of 4-((2,4-dioxothiazolidine-5-ylidene)methyl)benzaldehyde (4)[13]

A mixture containing compound **1** (0.03 mol), terephthalaldehyde (0.03 mol), and 45 mL of ethanol was prepared. Piperidine (3 mL, 0.0188 mol) was added, and the solution was stirred and refluxed for 12 hours. The reaction mixture was then poured onto ice and acidified using glacial acetic acid. This process yielded a yellow substance identified as compound **4,** which was subsequently filtered, dried, and purified through recrystallization using ethanol.

2. 4. Synthesis of Ethyl 2-substituted-oxyacetate 7a–b[13,14]

In 65 mL of anhydrous acetone, hydroxy aromatic compounds (**5a–b**, 0.034 mol), anhydrous K_2CO_3 (4.72 g, 0.034 mol), and chloroethyl acetate (2, 4.2 g, 0.034 mol) were refluxed for 8–10 h. After completion, the solvent was removed under reduced pressure, and the residue was dissolved in dichloromethane (DCM, 20 mL) and washed with water. The organic layer was evaporated to yield compounds **7a** and **7b** as solids, with yields of 84% (**7a**) and 92% (**7b**), respectively.

2. 5. Synthesis of 2-(substituted-2-yloxy) acetohydrazide 8a–b[13–15]

The hydrazine hydrate (0.75 g; 0.015 mol) was added dropwise to solution of **7a** or **7b** (0.015 mol) in ethanol (25 mL). The resulting mixture was subjected to ultrasonic irradiation at ambient temperature for 0.5 h. The solid was filtered and dried to produce compounds **8a**, Yield: 45%; m.p. 220–222 °C; **8b**, Yield: 60%; m.p. 242–243 °C.

2. 6. Synthesis of Compounds (9a-b)

Using a catalytic quantity of glacial acetic acid, substituted hydrazides **8a** or **8b** (0.01 mol) were added to a solution of compound **4** (0.01 mol) in methanol (50 mL), and the obtained mixture was refluxed for 4–18 h. The final compounds (**9a-b**) were obtained by recrystallizing the reaction mixture from methanol after it had cooled.

Synthesis of 2-((3,6-dioxocyclohexa-1,4-dien-1-yl)oxy)-*N'*-(4-(-(2,4-dioxothiazolidin-5-ylidene)methyl)benzylidene)acetohydrazide (9a)

Brown solid; Yield: 45%; m.p. 220–224 °C.; FT-IR υ_{max} (KBr)/cm^{-1} 3367, 3186 (NH), 1774, 1716, 1678 (C=O); ^{1}H NMR (DMSO-d_6): δ 4.57 (s, 2H, CH_2), 7.27–8.02 (m, 9H, CH=C, H-Ar), 11.71, 11.76 (s, 2H, NH). ^{13}C NMR (DMSO-d_6): δ 52.10, 116.22, 129.68,131.50, 143.82, 146.87, 162.91, 163.51, 165.14, 165.43; Anal. Calcd. for $C_{19}H_{13}N_3O_6S$ (411.05): C, 55.47; H, 3.19; N, 10.21; Found: C, 55.52; H, 3.09; N, 10.29%.

Synthesis of *N'*-(4-(-(2,4-dioxothiazolidin-5-ylidene) methyl)benzylidene)-2-(naphthalen-1-yloxy)acetohydrazide (9b).

Pale brown solid; Yield: 60%; m.p. 243 °C; FT-IR υ_{max} (KBr)/cm^{-1} 3323–3257(N-H), 3098–3021 (C-HAr), 2967–2911 (C-HAliph), 1709–1619 (C=O), 1651–1624 (C=N) 1645–1625 (C=C); ^{1}H NMR (DMSO-d_6): δ 4.98 (s, 1H, NH), 5.30 (s, 2H, CH_2), 6.40–7.95 (m, 13H, C=CH, H-Ar), 11.73 (s, 1H, NH). ^{13}C NMR (DMSO-d_6): δ 62.54, 105.99, 121.21, 125.76, 125.95, 126.46, 126.55, 127.89, 127.94, 134.56, 154.11, 162.86, 172.54; Anal. Calcd. for $C_{23}H_{17}N_3O_4S$ (431.09): C, 64.03; H, 3.90; N, 9.74; Found: C, 64.13; H, 3.99; N, 9.94%.

2. 7. Synthesis of 3-phenyl-2-(phenylimino) imidazolidin-4-one derivatives (13a-c)

A mixture of phenylamine (0.01 mol, 0.94 g), urea (0.01 mol, 0.69 g), and chloroacetic acid (0.01 mmol, 0.95 g was stirred for 30 minutes. The resulting mixture underwent trituration with hot, diluted methanol solution in distilled water. After cooling, the precipitated solid was separated through filtration, subjected to drying, and subsequently recrystallized using ethanol as solvent, producing buff-coloured crystalline material identified as compound **13a-c**.

Synthesis of 2-((4-chlorophenyl)imino)-3-phenylimidazolidin-4-one (13a)

Pale brown solid; Yield: 53%; m.p. 277–280 °C; FT-IR υ_{max}(KBr)/cm^{-1} 3310–3277 (N-H), 3100–3001 (C-H, Ar), 2997–2941 (C-H, Aliph), 1733–1649 (C=O), 1649–1627 (C=N), 1635–1619 (C=C); ^{1}H NMR (DMSO-d_6): δ 3.90 (s, 2H, CH$_2$), 6.17–7.62 (m, 9H, H-Ar). ^{13}C NMR (DMSO-d_6): δ 52.09, 114.00, 115.70, 120.13, 120.20, 121.32, 129.01, 138.17, 147.50, 172.04; Anal. Calcd. for $C_{15}H_{12}ClN_3O$ (285.07): C, 63.05; H, 4.23; N, 14.71; Found: C, 63.12; H, 4.16; N, 14.63%.

Synthesis of 2-((4-bromophenyl)imino)-3-phenylimidazolidin-4-one (13b)

Pale brown solid; Yield: 66%; m.p 281–285°C; FT-IR υ_{max}(KBr)/cm^{-1} 3301–3282 (N-H), 3099–3001(C-H, Ar), 2997–2941(C-H, Aliph), 1731–1656 (C=O), 1649–1627 (C=N), 1625–1619 (C=C); ^{1}H NMR (DMSO-d_6): δ 3.90 (s, 2H, CH$_2$), 6.20–7.57 (m, 9H, H-Ar) . ^{13}C NMR (DMSO-d_6): δ 52.10, 107.50, 114.58, 114.60, 114.41, 114.74, 116.27, 121.70, 131.78, 131.83, 132.01, 132.67, 138.59, 147.87, 172.00; Anal. Calcd. for $C_{15}H_{12}BrN_3O$ (329.02): C, 54.56; H, 3.66, N, 12.73; Found: C, 54.66; H, 3.78, N, 12.85%.

Synthesis of 2-((4-acetylphenyl)imino)-3-phenylimidazolidin-4-one (13c)

Pale brown solid; Yield: 43%; m.p. 279–284 °C; FT-IR υ_{max}(KBr)/cm^{-1}; 3313–3267 (N-H), 3108–3021(C-H, Ar), 2977–2921 (C-H, Aliph), 1713–1619 (C=O), 1654–1619 (C=N) 1645–1625 (C=C; ^{1}H NMR (DMSO-d_6): δ 1.65 (s, 3H, CH$_3$), 4.40 (s, 2H, CH$_2$), 7.47–8.21 (m, 9H, C=CH, H-Ar), 11.71(s, 1H, NH). ^{13}C NMR (DMSO-d_6): δ 22.49, 50.85, 128.54, 129.04, 129.38, 133.34, 133.37, 134.50, 134.86, 143.00, 146.43, 169.34, 171.25; Anal. Calcd. for $C_{17}H_{15}N_3O_2$ (293.12): C, 69.61; H, 5.15; N, 14.33; Found: C,-70.11; H, 5.45; N, 14.67%.

2 .8. Biological Evaluation

2. 8. 1. Cell Culture

Human splenic fibroblast (HSF) and human colonic epithelial (Caco-2) cell lines, obtained from the National Cancer Institute in Egypt, were cultivated in RPMI 1640 or DMEM media (Gibco, USA) with a 10% fetal bovine serum added (Hyclone, USA). At 70–80% confluence, cells were harvested using a 0.25% trypsin/EDTA cocktail and planted into a fresh culture flask containing DMEM-LG with 10% FBS and 0.1 mg/mL primocin. Flask were then incubated at 37 °C with 5% CO$_2$. Cells were passaged every 5–6 days, and the media was replaced every 48 hours.[13,15]

2. 8. 2. MTT Assay

Using the MTT assay, recently synthesized compounds (**9a**-**b**, **13a–c**) were evaluated for cytotoxicity against normal human skin fibroblasts (HSF) and malignant Caco-2 cell lines, the latter derived from human colorectal adenocarcinoma and serving as a standard *in vitro* model for colorectal cancer. These compounds had not previously been tested against Caco-2 in this context, making this study novel in assessing their anticancer activity in a colorectal cancer model. The results, particularly for **13b** and **13c**, demonstrated significant cytotoxicity and selectivity, supporting their potential as anticancer agents.

The MTT assay was used to assess the cytotoxicity of compounds **9a-b** and **13a–c** by measuring cell viability via mitochondrial reduction of yellow tetrazolium salt to purple formazan crystals. Cells were plated at a density of 1 × 10^4 cells/well in 96-well plates and incubated at 37 °C with 5% CO$_2$. They were then exposed to test compounds at concentrations of 0–500 μM for 48 hours. After incubation with 10 μL of MTT solution for 4 hours, 100 μL of solubilization solution (e.g., DMSO) was added to dissolve the formazan, and absorbance was measured at 490 nm. Experiments were conducted in biological triplicate, with untreated control cells set as 100% viability. IC$_{50}$ values were analyzed using GraphPad Prism 5.0.

2. 9. Docking Simulation

AutoDockTools-1.5.6rc3 (ADT4),[16] was adopted for *in silico* molecular docking toward calculate the compelling modes of potent **13b** through selected proteins. ADT4 has been widely reported as one of the best docking tools for structure-based drug design and virtual screening of drug-like molecules through the prediction of how the ligands can interact with protein targets to obtain the possible effective interactions between them.[17–19] In the current docking, we have used Bcl-2 protein (PDBID: 4IEH) which is recognized as a target for anti-cancer compounds, especially with colorectal cancer.[19–21] The 3D structure data of Bcl-2 protein target proteins were obtained in pdb, format from RCSB- PDB internet site (http://www.rcsb.org/pdb/). Besides, the compound **13b** was built and refined in 3D-Chem Draw Ultra 12.0 and minimized energetically by MM2 force field before saving in pdb. file. Prior of the docking, the target protein has been prepared by deleting all water, co-crystal ligand and co-factors. As well, ADT4 was utilized to set polar hydrogens, charge deactivations and rotatable bonds. The computer simulation of ligand-protein was achieved under Lamarckian Genetic Algorithm (LGA) technique.[22] The docking grid box [110 × 110 × 110 Å^3] was run at the active site pocket of the Bcl-2 protein. The prediction analysis of docking results was carefully done under strict settings with RMSD ≤ 2.0Å. This effects for modern docking exposed possible H-bonds as well as binding energy interactions of our compound with the Bcl-2 protein. The parameters of five orientations are recorded in **Table 2**. Along with ADT4, both PyMOL and BIOVIA software were also used for the analysis and visualization of the results.[22–24]

2. 10. Density Functional Theory (DFT)

The computational function within the current test was done through using DFT-B3LYP efficient under 6-311++G(d,p) bases organized which is considered as one of the best computational quantum models used with organic compounds.[25,26] DFT-B3LYP/6-311++G(d,p) combination has proven high degree of accuracy in the geometric optimization, energies, electronic structure and correlated molecular characteristics.[26–28] Owing to the relation between the reactivity features and biological behaviours of the compound, DFT-B3LYP/6-311++G(d,p) was employed to calculate the verves of lowest- unoccupied/highest employed molecular orbitals (LUMO-HOMO) which are recognized as (FMOs = frontier molecular orbitals). Based on the FMOs, we have also computed the energy gap (ΔE_{gap}) and other parameters of chemical reactivities like; international electrophilicity index ψ, global hardness η, electronegativity χ, electronic chemical potential μ and global softness ζ. Moreover, the molecular electrostatic potential (MEP) of the computed compound was also explored under the same computational combination. All the DFT studies, in the present work, were executed in Gaussian 09 program.[29] While the construction of structure input file and figure visualizations have been done using GaussView5 program.[13,30]

3. Results and Discussion

3. 1. Rationale of the Study

This study builds on the well-documented pharmacological potential of thiazolidine-2,4-dione and imidazolidine-2,4-dione scaffolds, both recognized for their broad spectrum of biological activities, particularly in cancer therapy (Figure 1). Previous research by El-Adl et al. described the development of thiazolidine-2,4-dione-based compound **A**, which demonstrated superior anticancer efficacy compared to a reference drug against HepG2, HCT-116, and MCF-7 cell lines.[30] Similarly, Mahmoud et al. reported the synthesis of novel imidazolidine-2,4-dione derivatives, derivative **B**, which exhibited significant cytotoxicity against MCF-7 and A549 cell lines, surpassing the activity of the standard treatment. Inspired by the robust anticancer profiles of these scaffolds, the present study introduced strategic modifications to enhance their therapeutic performance. This approach successfully yielded compounds **13b** and **13c**, both showing notable inhibitory activity *in vitro*.

3. 2. Chemistry

In this study, we synthesized novel imidazolidine-2,4-dione as well as thiazolidine-2,4-dione derivatives via synthetic pathway shown in Schemes 1. The production of thiazolidine-2,4-dione **3** has been accomplished by an established literature procedure using chloro-acetic acid and thiourea in the presence of HCl as catalyst.[31] Consequently, Knoevenagel condensation of thiazoli-

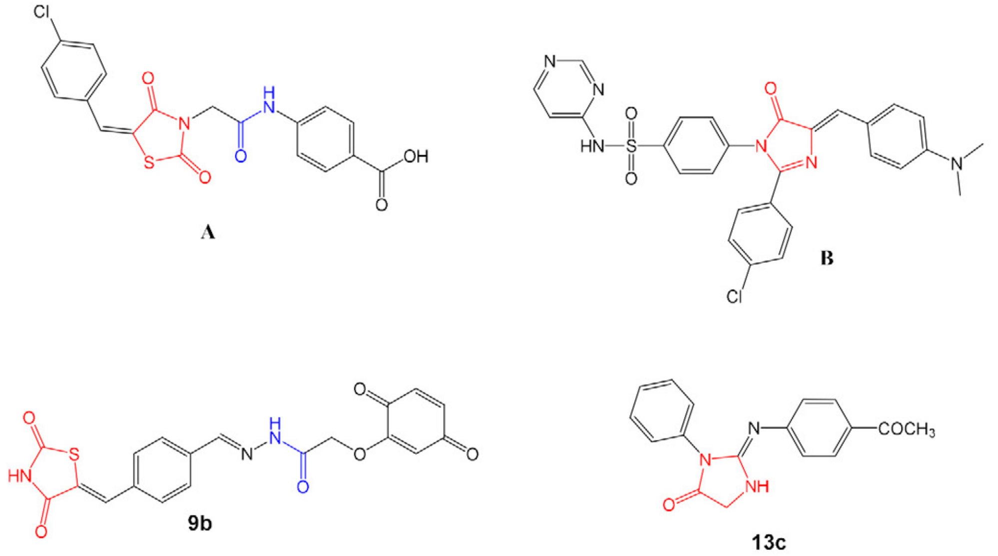

Figure 1. Examples of the well-documented pharmacological potential of thiazolidine-2,4-dione and imidazolidine-2,4-dione scaffolds.

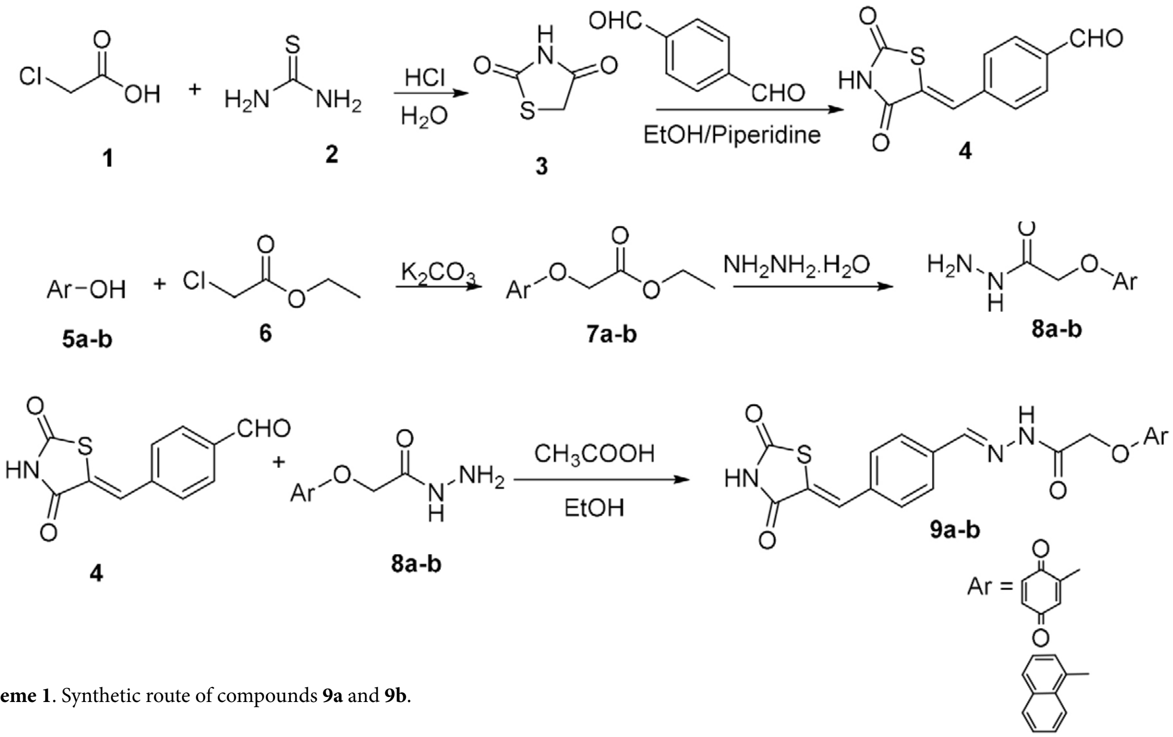

Scheme 1. Synthetic route of compounds **9a** and **9b**.

din-2,4-dione **3** with equivalent amount of terephthalaldehyde was performed resulting in the formation of 4-((2,4-dioxothiazolidine-5-ylidene)-methyl)-benzaldehyde **4** in the presence of piperidine.[31]

In this study, the key intermediate compounds, substituted ethyl 2-aryloxyacetates **(7a-b)**, were synthesized efficiently with good yields by reacting ethyl 2-chloroacetate **(6)** with substituted hydroxy compounds (**5a-b**, as detailed in Scheme 1) using anhydrous potassium carbonate in dry acetone. These intermediates were then reacted with hydrazine hydrate in ethanol to yield substituted 2-aryloxyacetohydrazides **(8a-b)** with yields of 84 and 92%.[32,33] In the final step, 4-((2,4-dioxothiazolidin-5-ylidene)methyl)benzaldehyde **(4)** was refluxed with 2-aryloxyacetohydrazides (**8a-b**) in absolute ethanol with a catalytic amount of acetic acid for 4–5 hours, forming Schiff bases **(9a-b)**, as illustrated in Scheme 1.

In Scheme 2, the target molecules **13a-c** were synthesized by one-pot condensation reaction of aniline derivatives **10a-c**, urea **11**, and chloro-acetic acid **12** which undergo cyclization without solvent to produce *N*-phenylimidazole, followed by condensation with another molecule of aniline to furnish 3-phenyl-2-(phenylimino)imidazolidin-4-one **13a-c**.

All the target compounds were structurally confirmed through IR, ^{1}H and ^{13}C NMR spectroscopy. The formation of Schiff base compound **9a** was confirmed by IR spectroscopy, which revealed a C=N stretching band at 1649 cm^{-1} and two carbonyl stretching bands at 1626 and 1635 cm^{-1}, consistent with conjugated carbonyl groups. The ^{1}H NMR spectrum showed signals at 11.71 and 11.76 ppm, assigned to two NH proton Additionally, new signals were observed in the range of 7.27–8.02 ppm, attributed to C=CH and aromatic protons. The IR spectrum of compound **13a** revealed bands at 3282 and 3292 cm^{-1} assigned to NH stretching and a band at 1639 cm^{-1} assigned to C=N stretching. The ^{1}H NMR spectrum displayed a signal at 3.90 ppm attributed to the CH_2 group and signals in the

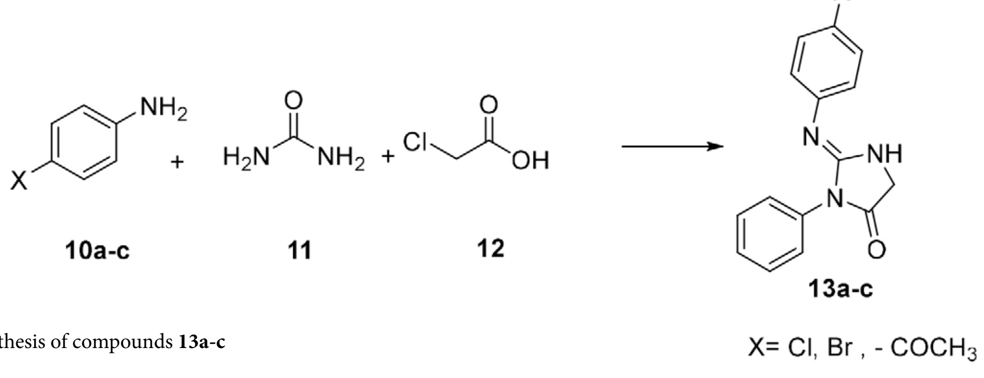

Scheme 2. Synthesis of compounds **13a-c**

range of 6.20–7.57 ppm corresponding to aromatic protons, consistent with the proposed structure.[32,33]

3. 3. Biological Assays

3. 3. 1. Cytotoxicity Assay

This study investigated the *in vitro* cytotoxic activity of all selected compounds (**9a-b** and **13a-c**) against normal (HSF) and cancer (Caco-2) cell lines. All tested compounds exhibited cytotoxicity against Caco-2 cells, with IC_{50} values ranging from 40.67 ± 0.09 to 109.2 ± 0.027 μM (Table 1). Compounds **13b** and **13c** showed higher cytotoxicity, with IC_{50} values of 41.30 ± 0.07 μM and 109.2 ± 0.027 μM, respectively. Compounds **13a** and **9a** displayed moderate cytotoxicity, with IC_{50} values of 40.67 ± 0.09 μM and 66.68 ± 0.068 μM, respectively, while compound **9b** exhibited less potent cytotoxicity, with an IC_{50} value of 73.91 ± 0.03 μM. To address IC_{50} values exceeding 500 μM, particularly for HSF cells, compounds **9a-b** and **13a-c** were tested using a two-fold serial dilution from 15.625 to 1000 μM. Compounds with low cytotoxicity against HSF cells (e.g., **13b**, **13c**) were evaluated at higher concentrations, despite initial screening up to 500 μM. IC_{50} values were calculated using GraphPad Prism 5.0 based on full dose-response curves, with data points up to 1000 μM ensuring accurate determination for compounds like **13c**, which showed low inhibition below 500 μM. All compounds were soluble in culture medium with ≤0.5% DMSO, showing no precipitation or turbidity, ensuring no vehicle-related cytotoxicity. Caco-2 and HSF cell lines were treated under identical conditions (seeding density, incubation time, medium composition, assay procedures) to ensure data consistency and comparability, validating the reported IC_{50} and selectivity index values.

Table 1. *In vitro* cytotoxicity (IC_{50}) of compounds **9a-b** and **13a-c** against HSF and Caco-2 cell lines using the MTS assay.

Compound	IC_{50} ± SD* (μM)		SI for Caco-2
	HSF	Caco-2	
9a	187.3±0.014	66.68±0.068	2.81
9b	102.1±0.11	73.91±0.036	1.38
13a	143.4±0.022	40.67±0.09	3.52
13b	496.8±0.041	41.30±0.07	12.03
13c	805.9±0.05	109.2±0.027	7.38

*IC_{50}: Concentration of the compound resulting in 50% suppression of cell growth ± standard deviation.

The selectivity index (SI), defined as the ratio of IC_{50} values for normal (HSF) to cancer (Caco-2) cell lines, was calculated and presented in Figure 2 and Table 1. SI values greater than 2.0 indicate higher selectivity for cancer cells.[34] According to the results, compound **9b** with SI of 1.38 suggests that it has comparable effects on malignant and healthy cells, which limits its usefulness as a selective anticancer agent. Because cancer cells do not exhibit a markedly increased cytotoxicity, the use of this compound in therapy may result in significant toxicity to normal cells, raising the possibility of adverse effects. On the other hand, compound **9a** demonstrates moderate selectivity (SI = 2.81), indicating that although the chemical is more harmful to cancerous cells than cells that are normal, the difference is not very large. This indicates that the possibility of cytotoxic effects on healthy cells remains at therapeutic dosages. Compound **13a**, with an SI of 3.52, demonstrated moderate selectivity for Caco-2 cells over HSF cells, making it a promising candidate for further preclinical anticancer studies. According to this, the compound is substantially more cytotoxic to cancer cells than healthy cells, which makes it an attractive option for more preclinical study in anticancer investigations. Compounds **13b** and **13c** exhibited SI values of 12.02 and 7.38, respectively, for Caco-2 cells relative to HSF cells, indicating higher selectivity with significantly greater cytotoxicity toward cancer cells than normal cells (Figure 2). These results position both compounds as promising candidates for further anticancer drug development.[35]

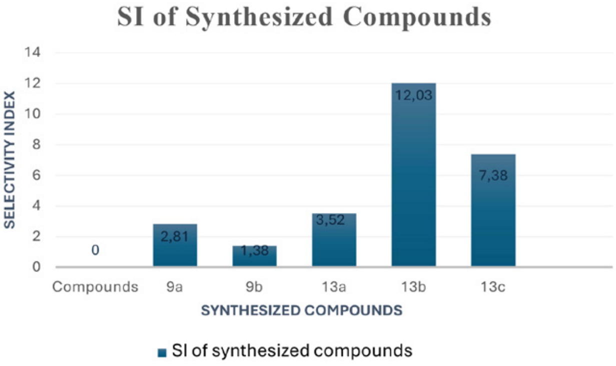

Figure 2. SI of synthesized compounds.

3. 3. 2. Docking Simulation

The molecular docking study was aimed to check the possible effective interactions of potent molecule compound **13b** with the Bcl-2 protein receptors. Based on the co-crystal ligand, the typical modes for inhibition binding positions were identified within the Bcl-2 active site, which comprise the interaction of cocrystal ligand (1E9) with ARG66 and GLY104 residues.[20] The outcomes of recent docking exposed rational H-bond connections with our ligand with the effective amino acids of Bcl-2 as listed in Table 2. The greatest binding energy reached (–7.77 kcal/mol) through three H-bond interaction formed as single bond of GLY104 with N14 atom at distance 1.78 Å, as well as double H-bonds linked over-coordinated O29 atom of our ligand with two N atoms of ARG66 residue at distances of 1.78, 1.82 and 2.14 Å forming R^2_1 ring motif which strengthens the interaction and bond stabilization of protein-ligand. Additionally, this conformation exhibited pi-pi stacking between HIS432 and the phenyl ring of compound **13b**, as shown in Figures 3 and 4. Other conformations (2 and 3) showed hydrogen bonds with ARG66 and PHE63 via the O29 atom (2.17 Å and 2.28 Å, binding energies of –7.71 and –7.69 kcal/mol, respectively). Moreover, the conformations 2 and 3 showed H-bond interactions of AGR66 and PHE63 a with the O29 atom at distances 2.17 and 2.28 Å and B.E of –7.71 and –7.69 kcal/mol. Likewise, TYR161 and GLY104 residues in conformations 4 and 5 shaped H-bonds with N14 atom at distances of 2.15, and 1.97 Å (see Figure **S1** in Supplementary Material). Thus, the bond interactions in our current docking are observed to be parallel to that of co-crystal ligand and reported literature which reflects the perfect settlement of our potent molecule in Bcl-2 active site pocket.[20,21,36] Figure 3 depicts 2D plot of ligand-**Bcl2** interactions, while Figure 4 illustrates the enfoldment of ligand inside Bcl-2 active site cleft with zoom view in ribbon and 3D models. Consistently, the computer docking predicted the better B.E values and strong bonding interactions of our potent compound **13b**, that might be a favourable candidate for anticancer drugs development.

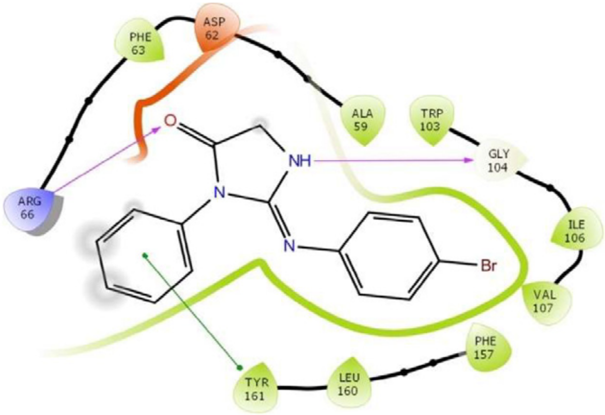

Figure 3. 2-D interaction plot of the potent molecule compound **13b** docked with 4IEH showing hydrogen bond and pi interactions.

3. 4. Density Functional Theory (DFT)

3. 4. 1. Geometry Optimization

The structure geometry of compound **13b** has been prudently enhanced at stationary point of ground state energy level, which is adopted in all other computations. Furthermore, the stability of optimized geometry has been examined and confirmed by implementing the ˮsta-

Table 2. Docking results of the potent molecule **13b** compound docked with 4IEH.

Conf	B.E (kcal/mol)	L.E	I. C, µM T = 298.15 K	vdW-Hb-des-energy kcal/mol	H-bonds of amino acids with ligand	B.L (Å)	π–Interaction (Å)
1	–7.77	–0.39	2.03	–7.82	AGR66NH:O	1.82 2.14	TYR161…*Cg*1
2	–7.71	–0.39	2.23	–7.76	AGR66NH:O	1.47	-----------------
3	–7.69	–0.38	2.31	–7.47	PHE63NH:O	2.28	TYR161…*Cg*2
4	–7.21	–0.36	5.22	–7.55	TYR161O:HN	1.45	-----------------
5	–7.07	–0.35	6.56	–7.52	GLY104O:HN	1.42	TYR161…*Cg*1

Conf: Conformation, **B.E**: Binding Energy, **L.E**: Ligand Efficiency, **I.C**: Inhibition Constant, **vdW**: Vander Walls energy, **Hb**: Hydrogen bond energy, **des**: desolv energy, and **B.L**: Bond length. ***Cg*1** and ***Cg*2** are the centroids of phenyl and bromophenyl rings, respectively.

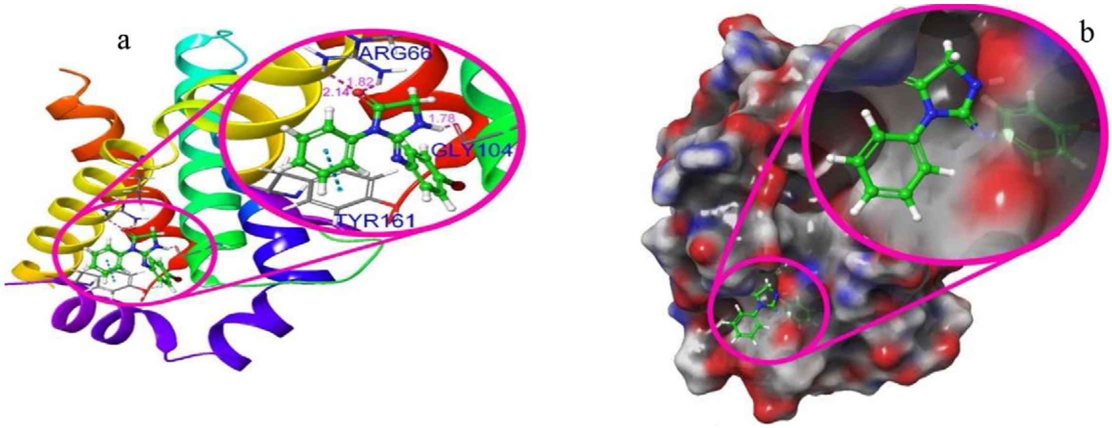

Figure 4. Visualization of whole and close view of the potent molecule compound **13b** docked at the active site groove of the protein target a) Ribbon and b) 3D model.

bile" keyword and validated by the nonappearance of negative frequencies, which specified the stationary point computed structure at the ground state.[37,38] The DFT optimized tested form of compound **13b** through atoms enumeration is given in Figure 5. The selected computed geometries are recorded in Tables 3–5. Full geometry parameters are given in Tables 3–5 of Supplementary Material. The DFT computed structure of compound **13b** exhibited coplanarity conformation between phenyl rings, while the mean plane of imidazole ring is nearly perpendicular to the both phenyl rings as depicted in Figure 5. The torsion angle usually describes the steric connection across the bonds and ring geometries. The imidazole ring is an anti-clinal conformity by point to the phenyl ring, as specified by the rotation angle degree of −125.72° (C28–N13–C17–C18). While the imidazole ring exhibited in +anti-clinal with respect to bromophenyl ring according to the torsion angle of C4–C3–N12–C15 (121.24°). The optimized geometry of compound **13b** is in good agreement with the similar reported phenyl-imidazole compounds.[39]

3. 3. 2. Frontier Molecular Orbitals (FMOs)

The reactivity, stability, and electronic transport properties are significantly associated with the values of E_H, E_L and ΔE_{gap} which empowers us to explore chemical hardness, softness, and kinetic stability for tested molecules.[40,41] Typically, the small data for ΔE_{ga} reflects the softness which lead toward the easy electronic transportations from HOMO toward LUMO of the molecules, which points to the significant bio-activity of the molecules. Because the biomedical system possess well interaction with soft molecules compared to hard ones.[42] The illustration of LUMO and HOMO populations of **13b** are depicted in Figure 6, as (−ve &+ve) stages are introduced in red as well as green, individually. The computed values all reactivity parameters are enumerated in Table 6. The E_H value of HOMO orbital is found to be −3.514 eV with electronic distribution of π character appears over the bromophenyl ring which predictable to involve in pi-pi stacking interaction. In addition, the σ electronic density covered the imidazole ring and bromine moiety, while the other phenyl ring has no electron density. In contrast, the LUMO orbital revealed the main π electronic distribution over the entire molecular system with $E_L = -1.060$ eV. The DFT values of ΔE_{gap} and softness are 2.453 eV and 0.815, respectively. The lower ΔE_{gap} value, highest softness degree and main dose of electronic intensity for LUMO compared to LUMO signifies the easiest of electronic transportation and good reactivity of the molecule in comparison of similar reported compounds.[43,44]

Table 3. Selected bond lengths(å) of potent compound **13b** computed at dft-b3lyp/6-311++g(d,p)

Atoms	Length (Å)	Atoms	Length (Å)
C1–C2	1.3927	N14–H16	1.008
C1–C6	1.3911	N14–C30	1.4511
C3–N12	1.4054	C19–C22	1.3925
C4–C5	1.3918	C19–H23	1.0822
C4–H9	1.0836	C20–C24	1.394
C6–Br11	1.9195	C22–H26	1.0839
N12–C15	1.2726	C24–H27	1.084
N14–C15	1.3792	C30–H32	1.093

3. 3. 3. Molecular Electrostatic Potential MEP

The diagram of 3D-MEP illustration at different orientations of our potent molecule is shown in Figure 7. It portrayed in colour system ranging from highest +ve potential (dark blue) to highest −ve potential (deepest red). The highest nucleophilic site (i.e., −ve site) seems round the oxygen atom, so it exists an attractive object for the electrophilic attack to shape acceptor hydrogen bonds. The average −ve sites represented by orange colour and appear over bromine Br11 and nitrogen bridge atom N12 with middling opportunity to construct H-bonds with electrophilic sites. On the other hand, the maximum electrophilic site (i.e., +ve site) appears over the nitrogen atom in imidazole ring N14, so it tends to build donor hydrogen bond during the interaction with nucleophilic substrate-protein interactions, (see docking part).

Besides, the carbon atom in imidazole ring C30 exhibited average +ve site which may also act as hydrogen donor in the interaction with nucleophilic sites. The light green (zero potential) is broadly covering phenyl rings, which tend to shape pi-bonding interactions as demonstrated in docking study.

Table 4. Selected bond angles (°) of potent compound **13b** computed at dft-b3lyp/6-311++g(d,p)

Atoms	Angle (°)	Atoms	Angle (°)	Atoms	Angle (°)	Atoms	Angle (°)
C2–C1–C6	119.46	C6–C5–H10	120.36	N13–C17–C18	120.23	C24–C22–H26	120.22
C2–C1–H7	120.16	C1–C6–C5	120.75	N13–C17–C19	119.21	C20–C24–C22	119.81
C2–C3–C4	118.34	C15–N13–C28	111.52	C17–C19–C22	119.57	O29–C28–C30	126.58
C2–C3–N12	122.24	C17–N13–C28	123.91	C17–C19–H23	119.9	N14–C30–C28	102.71
C3–C4–H9	118.9	H16–N14–C30	122.49	C18–C20–H25	119.51	C28–C30–H31	109.08
C4–C5–C6	119.43	N12–C15–N14	130.23	C19–C22–C24	120.24	H31–C30–H32	108.59

Table 5. Selected torsion angles (°) of potent compound **13b** computed at dft-b3lyp/6-311++g(d,p)

Atoms	Angle (°)	Atoms	Angle (°)	Atoms	Angle (°)
C6–C1–C2–C3	−0.05	C3–N12–C15–N14	−3.26	N13–C17– C19–C22	−179.01
C2–C1–C6–Br11	−179.94	C15–N13–C17–C18	55.4	C17- C18- C20- H25	179.59
H7–C1–C6–C5	−178.99	C15–N13–C17–C19	−125.58	H21–C18–C20–C24	−179.59
H7–C1–C6–Br11	0.5	C28– N13–C17–C18	−125.72	H21–C18–C20–H25	0.64
C2–C3–C4–C5	1.23	C17–N13–C28– C30	−179.65	C18–C20–C24–C22	0.22
N12–C3–C4–C5	176.95	H16–N14–C15–N13	160.69	H25–C20–C24–C22	179.99
C4–C3–N12–C15	121.24	C15–N14–C30–C28	−9.11	C19–C22–C24–H27	−179.72
H9–C4–C5–C6	178.88	H16–N14–C30–C28	−159.56	N13–C28–C30–N14	5.66
C4–C5–C6–Br11	−179.68	N13–C17–C18–C20	179.53	O29–C28–C30–N14	−174.5

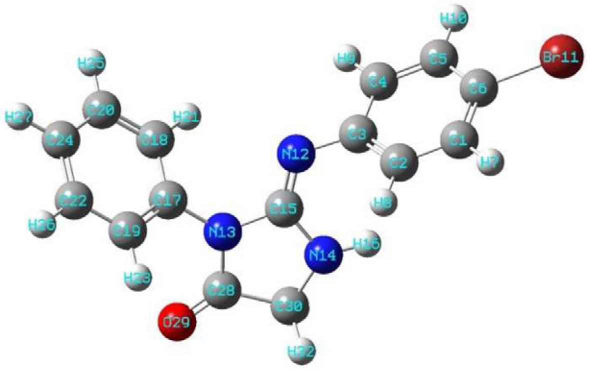

Figure 5. Optimized structure of the potent compound **13b** DFT-B3LYP/6-311++G(d,p).

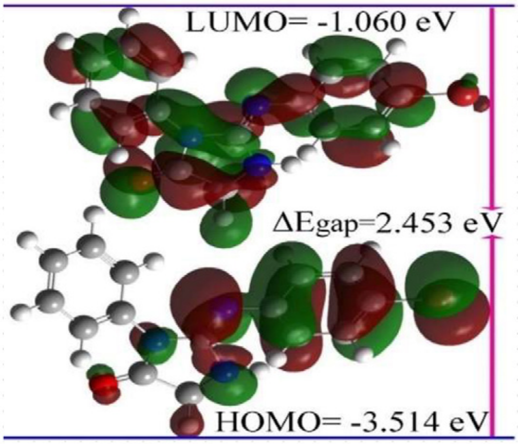

Figure 6. HOMO-LUMO surfaces with $\Delta E_{ga}$of the potent **13b** computed at DFT-B3LYP/6-311++G(d,p) combination.

Table 6. Values of homo-lumo, δe_{gap} and reactivity parameters of potent compound **13b** computed at dft-b3lyp/6-311++g(d,p)

Property	Formula	Value
LUMO energy	E_L (eV)	−1.060
HOMO energy	E_H (eV)	-3.514
Energy gap	$\Delta E_{gap} = E_L - E_H$ (eV)	2.453
hardness	$\eta = (E_L - E_H)/2$ (eV)	1.227
Softness	$\zeta = 1/\eta$ (eV^{-1})	0.815
Chemical potential	$\mu = (E_L + E_H)/2$ (eV)	−2.287
Electronegativity	$\chi = -\mu$ (eV)	2.287
Electrophilicity	$\psi = \mu^2/2\eta$ (eV)	2.132

4. Conclusions

To summarize, our work involved design and synthesis of two compound series featuring imidazolidine-2,4-dione as well as thiazolidine-2,4-dione structural elements. The synthesized compounds have demonstrated notable cytotoxicity against the tested cancer (Caco-2) cell lines. The two most potent compounds were compound **13b** and compound **13c**. The activity values of these compounds against the Caco-2 cell line were 41.30 ± 0.07 µM and 109.2 ± 0.027 µM, respectively. The compounds **13b** and **13c**, which exhibited the highest activity, had selective index values of 12.03 and 7.38, respectively. This indicates that the compounds had a good therapeutic window and significant anticancer selectivity. To validate its promise as a clinically effective anticancer treatment, more mechanis-

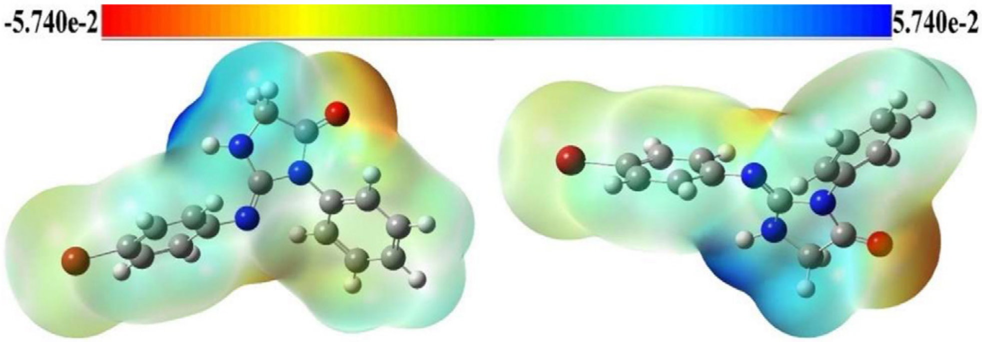

Figure 7. MEP of the potent molecule1 obtained by DFT-B3LYP/6-311++G(d.p) level

tic research, *in vivo* validation, and drug formulation improvement are required.

5. References

1. Z. Tarhini, J. Magne, P. Preux, A. Parenté, M. Mathonnet, N. Christou, J. Jost, *Biomed. Pharmacother*. **2024**, *170*, 115950. **DOI:**10.1016/j.biopha.2023.115950
2. D. Sonkin, A. Thomas, B. A. Teicher, *Cancer Genet*. **2024**, 286–287, 1–11. **DOI:**10.1016/j.cancergen.2024.06.001
3. K. Bukowski, M. Kciuk, R. Kontek, *Int. J. Mol. Sci*. **2020**, *21*(9), 3233. **DOI:**10.3390/ijms21093233
4. N. Kumar, N. Goel, *Anti-Cancer Agents Med. Chem*. **2022**, *22*(20), 3196–3207. **DOI:**10.2174/1871520622666220404082648
5. Y. Wan, G. Fang, H. Chen, X. Deng, Z. Tang, Eur. *J. Med. Chem*. **2021**, *226*, 113837. **DOI:**10.1016/j.ejmech.2021.113837
6. A. Jaromin, A. Czopek, S. Parapini, N. Basilico, E. Misiak, J. Gubernator, A. Zagórska, *Biomolecules* **2020**, *11*(1), 33. **DOI:**10.3390/biom11010033
7. D. Bialonska, J. K. Zjawiony, *Mar. Drugs* **2009**, *7*(2), 166–183. **DOI:**10.3390/md7020166
8. G. Bansal, S. Singh, V. Monga, P. V. Thanikachalam, P. Chawla, *Bioorg. Chem*. **2019**, *92*, 103271. **DOI:**10.1016/j.bioorg.2019.103271
9. Y. Komatsu, T. Yoshino, K. Yamazaki, S. Yuki, N. Machida, T. Sasaki, I. Hyodo, Y. Yachi, H. Onuma, A. Ohtsu, *Invest. New Drugs* **2014**, *32*(3), 473–480. **DOI:**10.1007/s10637-013-0056-3
10. M. Azizmohammadi, M. Khoobi, A. Ramazani, S. Emami, A. Zarrin, O. Firuzi, R. Miri, A. Shafiee, *Eur. J. Med. Chem*. **2013**, *59*, 15–22. **DOI:**10.1016/j.ejmech.2012.10.036
11. S. Chandrappa, C. V. Kavitha, M. S. Shahabuddin, K. Vinaya, C. A. Kumar, S. R. Ranganatha, S. C. Raghavan, K. S. Rangappa, *Bioorg. Med. Chem*. **2009**, *17*(6), 2576–2584. **DOI:**10.1016/j.bmc.2009.01.066
12. F. Damkaci, A. A. Szymaniak, J. P. Biasini, R. Cotroneo, *Compounds* **2022**, *2* (3), 182–190. **DOI:**10.3390/compounds2030015
13. H. Kumar, A. Deep, R. K. Marwaha, *BMC Chem*. **2020**, *14*, 25. **DOI:**10.1186/s13065-020-00678-2
14. M. Al-Ghorbani, M. A. Gouda, M. Baashen, O. Alharbi, F. A. Almalki, L. V. Ranganatha, *Pharm. Chem. J*. **2022**, *56*(1), 29–37. **DOI:**10.1007/s11094-022-02597-z
15. E. S. Tantawy, A. M. Amer, E. K. Mohamed, M. M. Abd Alla, M. S. Nafie, *J. Mol. Struct*. **2020**, *1210*, 128013. **DOI:**10.1016/j.molstruc.2020.128013
16. G. M. Morris, R. Huey, W. Lindstrom, M. F. Sanner, R. K. Belew, D. S. Goodsell, A. J. Olson, *J. Comput. Chem*. **2009**, *30*(16), 2785–2791. **DOI:**10.1002/jcc.21256
17. M. N. Khadri, H. A. Khamees, S. Kouser, S. A. Khanum, *J. Mol. Struct*. **2023**, *1272*, 134240. **DOI:**10.1016/j.molstruc.2022.134240
18. F. H. Al-Ostoot, H. A. Khamees, N. Prasad, F. Zameer, S. A. Khanum, *J. Mol. Struct.* **2022**, *1270*, 133963. **DOI:**10.1016/j.molstruc.2022.133963
19. M. Jyothi, H. A. Khamees, S. M. Patil, R. Ramu, S. A. Khanum, *J. Iran. Chem. Soc*. **2022**, *19*, 3919–3933. **DOI:**10.1007/s13738-022-02574-z
20. B. B. Touré, K. Miller-Moslin, N. Yusuff, L. Perez, M. Doré, C. Joud, W. Michael, L. DiPietro, S. Van Der Plas, M. McEwan, F. Lenoir, M. Hoe, R. Karki, C. Springer, J. Sullivan, K. Levine, C. Fiorilla, X. Xie, R. Kulathila, K. Herlihy, D. Porter, M. Visser, *ACS Med. Chem. Lett*. **2013**, *4*, 186–190. **DOI:**10.1021/ml300321d
21. Y. Gu, M. Chen, B. H. May, X. Liao, J. Liu, L. Tao, D. M. Sze, A. L. Zhang, S. Mo, *Phytomedicine* **2018**, *51*, 214–225. **DOI:**10.1016/j.phymed.2018.10.004
22. G. M. Morris, D. S. Goodsell, R. S. Halliday, R. Huey, W. E. Hart, R. K. Belew, A. J. Olson, *J. Comput. Chem*. **1998**, *19*, 1639–1662. **DOI:**10.1002/(SICI)1096-987X(19981115)19:14<1639::AID-JCC10>3.0.CO;2-B
23. L. L. C. Schrodinger, The PyMOL Molecular Graphics System, Version 1.8, **2015**.
24. D. S. Biovia, Discovery Studio Visualizer, **2017**.
25. P. Hohenberg, W. Kohn, *Phys. Rev*. **1964**, 136, B864–B871. **DOI:**10.1103/PhysRev.136.B864
26. V. L. Ranganatha, C. Mallikarjunaswamy, R. Ramu, P. S. Shirahatti, N. Kumar, B. P. Sowmya, H. A. Khamees, M. Madegowda, S. A. Khanum, *Bioinformation* **2021**, *17*, 393.
27. G. Naray-Szabo, M. R. Peterson, *J. Mol. Struct.: Theochem* **1981**, *85*, 249–255. **DOI:**10.1016/0166-1280(81)85023-3
28. H. A. Khamees, M. Jyothi, S. A. Khanum, M. Madegowda, *J. Mol. Struct.* **2018**, *1161*, 199–217. **DOI:**10.1016/j.molstruc.2018.02.045
29. M. Frisch, Gaussian 09, Revision D.01, **2009**.
30. K. El-Adl, H. Sakr, S. S. A. El-Hddad, A. A. El-Helby, M. Nasser, H. S. Abulkhair, *Arch. Pharm*. **2021**, *354*, 2000491. **DOI:**10.1002/ardp.202000491
31. M. R. Mohamed, W. R. Mahmoud, R. H. Refaey, R. F. George, H. H. Georgey, *ACS Med. Chem. Lett*. **2024**, *15*, 892–898. **DOI:**10.1021/acsmedchemlett.4c00095
32. N. S. Hanafy, N. A. A. M. Aziz, S. S. A. El-Hddad, M. A. Abdelgawad, M. M. Ghoneim, A. F. Dawood, S. Mohamady, K. El-Adl, S. Ahmed, *Arch. Pharm.* **2023**, *356*, 2300137. **DOI:**10.1002/ardp.202300137
33. M. Al-Ghorbani, Russ. *J. Org. Chem*. **2022**, *58*, 1272–1279. **DOI:**10.1134/S1070428022090123
34. O. Alharbi, K. A. Al-Mutairi, M. M. Ibrahim, R. Ramu, M. Al-Ghorbani, *Chem. Biodivers*. **2025**, e202402104. **DOI:**10.1002/cbdv.202402104
35. H. Boulebd, *J. Biomol. Struct. Dyn*. **2022**, *40*, 10373–10382. **DOI:**10.1080/07391102.2021.1943529
36. T. Mosmann, *J. Immunol. Methods* **1983**, *65*, 55–63. **DOI:**10.1016/0022-1759(83)90303-4
37. M. Türkmenoğlu, S. T. Yıldırım, A. Altay, B. Türkmenoğlu, *ChemistrySelect* **2024**, 9, e202303519. **DOI:**10.1002/slct.202303519
38. A. Tomberg, Gaussian 09W Tutorial: An Introduction to Computational Chemistry Using G09W and Avogadro Soft-

ware, **2013**, 1–36.

39. Ł. Balewski, M. Gdaniec, A. Hering, C. Furman, A. Ghinet, J. Kokoszka, A. Ordyszewska, A. Kornicka, *Int. J. Mol. Sci.* **2024**, *25*, 11495. **DOI:**10.3390/ijms252111495
40. N. T. A. Ghani, A. M. Mansour, *Eur. J. Med. Chem*. **2012**, *47*, 399–411. **DOI:**10.1016/j.ejmech.2011.11.008
41. T. Prashanth, V. Lakshmi Ranganatha, M. Al-Ghorbani, S. Girish, H. A. Khamees, S. A. Khanum, *Discov. Chem*. **2025**, *2*, 19. **DOI:**10.1007/s44371-025-00089-z
42. Y. Wang, Y. Zhong, Y. Wang, Y. Ma, X. Gao, L. Xu, J. He, K. Yung, X. Li, L. Wu, W. Wong, *CCS Chem*. **2024**, 1–13. **DOI:**10.31635/ccschem.024.202404867
43. R. I. Al-Wabli, K. S. Resmi, Y. S. Mary, C. Y. Panicker, M. I. Attia, A. A. El-Emam, C. Van Alsenoy, *J. Mol. Struct*. **2016**, 1123, 375–383. **DOI:**10.1016/j.molstruc.2016.07.044
44. Y. Erdogdu, D. Manimaran, M. T. Güllüoğlu, M. Amalanathan, I. Hubert Joe, S. Yurdakul, *Opt. Spectrosc*. **2013**, *114*, 525–536. **DOI:**10.1134/S0030400X13040073

Povzetek

Sintetizirali smo derivate tiazolidin-2,4-diona in imidazolidin-2,4-diona. Tiazolidin-2,4-dion **3** je bil pripravljen z uporabo kloroocetne kisline in tiouree, nato pa kondenziran s tereftalaldehidom za tvorbo 4-((2,4-dioksotiazolidin-5-ilidensko)metil)benzaldehida **4**. Ta spojina je reagirala z 2-ariloksiacetohidrazidi **8a** in **8b** in dala Schiffove baze **9a-b**. Imidazolidin-2,4-dioni **13a-c** so bili sintetizirani s ciklizacijo anilinov **10a-c**, sečnine **11** in kloroocetne kisline **12**. Spojine **9a-b** in **13a-c** so bile ovrednotene glede protitumorske aktivnosti proti celični liniji Caco-2, pri *čemer* sta spojini **13b** in **13c** izkazali najmočnejšo jakost (vrednosti IC_{50} 41,30 ± 0,07 μM in 109,2 ± 0,027 μM). Izvedeni so bili DFT-izračuni, vključno z analizo HOMO-LUMO, oceno energijske vrzeli in molekularnim dokovanjem, z namenim ovrednotenja in optimizcije molekulskih lastnosti ciljnih spojin.

DOI: 10.17344/acsi.2025.9384 *Acta Chim. Slov.* **2025,** *72,* 573–580

Scientific paper

Synthesis, Characterization, and Theoretical Calculation of a Copper Complex of 3-Hydroxy-2-methylquinolin-4-carboxylate and 1,10-Phenanthroline

Yan-Hua Li,[1] Xing-Jian Liu,[1] Jian Huang,[1] Yu Xie,[1] Fei Deng,[1*] Xiu-Guang Yi[1,2,3*]

[1] *School of Chemistry and Chemical Engineering, Jinggangshan University, Ji'an 343009, PR China*

[2] *State Key Laboratory of High-Efficiency Utilization of Coal and Green Chemical Engineering, Yinchuan 750021, PR China*

[3] *Jiangxi Hongjing Pharmaceutical Co., Ltd, Ji'an 343009, PR China*

** Corresponding author: E-mail: 9920190013@jgsu.edu.cn and jayxgggchem@163.com*

Received: 06-29-2025

Abstract

A copper complex containing mixed ligands [Cu(MCA)(Phen)·3H_2O)] (HMCA = 3-hydroxy-2-methylquinoline-4-carboxylic acid, Phen = 1,10-phenanthroline) was prepared by the hydrothermal method. Structure was characterized by single crystal X-ray diffraction. Solid state fluorescence photoluminescence measurement shows a strong emission peak at 620 nm, which is attributed to the characteristic electronic transitions and molecular stacking effects within the ligand. CIE color difference analysis indicates that the title complex exhibits red photoluminescence (chromaticity coordinates of 0.1256, 0.2418). In addition, solid-state UV-Vis diffuse reflectance experiments revealed that the titled complex has an energy band gap of 1.578 eV.

Keywords: Copper, crystal structure, photoluminescence, band gap.

1. Introduction

Metal organic frameworks (MOFs), as a novel coordination polymer, are formed through self-assembly of multidentate organic ligands (such as aromatic polyacids and polybasic bases) with transition metal ions. Their performance regulation is influenced by multiple factors such as the stability of the composite, ligand metal spacing, and intrinsic properties of the metal.[1] Among ligands, organic carboxylic acids stand out due to their strong coordination ability, diverse coordination modes, and moderate balance between rigidity and flexibility. The coordination between the oxygen atom of carboxylic acid ligands and metal ions not only stabilizes the metal center, but also forms hydrogen bonds through deprotonation, thereby enhancing the structural integrity and stability of materials,[2] In addition, the multidentate nature of carboxylic acid ligands enables them to form chelating structures with multiple metal ions, further enhancing the stability of the complex.[3] Nitrogen containing heterocyclic carboxylic acid ligands (such as quinoline carboxylic acid) can coordinate with metal ions through various ways such as monodentate, bidentate, or bridging, forming coordination polymers with different geometric configurations. For example, quinoline carboxylic acids can form 1D, 2D, and 3D structures through monodentate or bidentate coordination.[4,5] The rigid plane of the quinoline ring endows the complex with excellent structural stability, and the introduction of nitrogen-containing heterocyclic carboxylic acid ligands can significantly improve the thermal and mechanical stability of the coordination polymer.[6,7] The coordination between transition metals (such as Cu^{2+}, Fe^{3+}, etc.) and nitrogen-containing heterocyclic carboxylic acid ligands further enhances the functionality of the material. The synergistic effect of these metal ions with nitrogen atoms and carboxylic acid groups can form stable multi-core supramolecular structures.[8–10]

Quinolinecarboxylic acid-based MOFs, due to their high porosity and tunable chemical structure, can efficiently adsorb pollutants in water, such as heavy metal ions (such as mercury, lead, cadmium, etc.), and have high selectivity and sensitivity. For example, certain MOFs can efficiently capture heavy metal ions and exhibit excellent selectivity through size exclusion, adsorption, and photocatalytic mechanisms.[11] In addition, fluorescence sensors based on MOFs have shown significant advantages in detecting heavy metal ions, such as sensitivity to mercury ions reaching ppb levels.[12] Quinolinecarboxylic acid-based MOFs have shown transformative potential in cutting-edge fields such as lithium battery energy storage, anti-cancer drug carriers, and solar energy conversion, fully demonstrating the core advantages of designability and functional diversity of metal organic complexes.[13–17]

Based on this, we are interested in the crystal engineering of transition metal Cu^{2+} compounds containing 3-hydroxy-2-methylquinoline-4-carboxylic acid (HMCA) as ligand. [18] We report the solvothermal synthesis, X-ray crystal structure, photoluminescence and UV Vis diffuse reflectance spectral properties of a novel structural copper complex, and time-dependent density functional theory (TDDFT) calculations.

2. Experiment

2. 1. Experimental Materials and Instruments

All reagents and consumables used in the experiment are commercially available and can be used directly without purification. Infrared spectroscopy was measured using KBr tablets on a PE Spectrum One FT-IR instrument. Solid state UV-visible diffuse reflectance spectroscopy was performed using a computer-controlled TU1901 UV-visible spectrometer to measure diffuse reflectance. Fine ground powder samples are coated on $BaSO_4$ to achieve 100% reflectance. The photoluminescence performance was measured on the F97XP photoluminescence spectrometer.

2. 2. Synthesis of Title Complexes

Ligand HMCA (0.0304 g, 1.5 mmol), auxiliary ligand Phen (0.0099 g, 0.5 mmol), and $CuSO_4 \cdot 5H_2O$ (0.0125g, 0.5mmol) were added into a 25 mL stainless steel high-pressure vessel lined with polytetrafluoroethylene. Then, 10 mL of ethanol and 5 mL of water, and finally 0.15 mL of NaOH aqueous solution (1 mol/L) were added. The high-pressure reactor was heated to 120 °C in an oven and maintained for four days, then slowly cooled down to room temperature to obtain black block crystals, which are collected for single crystal X-ray diffraction testing. IR (KBr, cm^{-1}): 3434(s), 2925(w), 1633(w), 1586(m), 1520(w), 1436(m), 1396(w), 1339(w), 1237(w), 1174(w), 1147(w), 1112(w), 876(w), 846(w), 815(w), 776(w), 747(w), 721(w), 618(w).

2. 3. Collection and Refinement of Crystal Data for Title Complexes

A suitable single crystal (0.3 mm × 0.2 mm × 0.13 mm) was selected for measurement, and the structure of the complex was determined by X-ray single crystal diffractometer (SuperNova charge coupled device) at room temperature of 293 K. The structure was analyzed using the ShelXT plugin in Olex2 software, and the structure was refined using the ShelXL plugin in Olex2 software.[19–22] All non-hydrogen atoms were refined anisotropically, while hydrogen atoms were refined using riding model. The crystallographic data of the title complex are presented in Table 1.

Table 1. The main crystallographic data of the title complex

Empirical formula	$C_{23}H_{21}CuN_3O_6$
Formula weight	498.97
Temperature/K	293
Crystal system	triclinic
Space group	*P*–1
a/Å	6.9583(5)
b/Å	12.1607(8)
c/Å	12.7196(9)
α/°	77.027(6)
β/°	78.035(6)
γ/°	88.947(6)
V/Å^3	1025.60(13)
Z	2
ρ_{calc}/g cm^{-3}	1.616
μ/mm^{-1}	1.114
F(000)	514.0
Reflections collected	8185
Independent reflections (R_{int})	3759 (0.0197)
Data/restraints/parameters	3759/4/311
GOOF on F^2	1.036
R_1, wR_2 ($I \geq 2\sigma(I)$)	0.0571, 0.1404
R_1, wR_2 (all data)	0.0711, 0.1519
$\Delta\rho_{max}$, $\Delta\rho_{min}$ / e Å^{-3}	1.60/–0.38

3. Results and Discussion

3. 1. Crystal Structure

Single crystal X-ray diffraction measurements show that the title complex belongs to the triclinic *P*–1 space group with a Z value of 2. Its unconformity unit is mainly composed of a neutral molecule composed of one Cu^{2+} ion, one MCA^- ion, one Phen molecule, and three free water molecules. Cu^{2+} is four coordinated and the complex has a square-planar structure. The coordination sphere is composed of O1 and O2 of the HMCA and N2 and N3 of the auxiliary ligand Phen, as shown in Figure 1. The bond distances of Cu–O1, Cu–O2, Cu–N2, and Cu–N3 are 1.863(3), 1.892(3), 1.991(3), and 2.004(3) Å, respectively, as shown in Table 2. The C–H···O hydrogen bonding interaction enables the construction of a three-dimensional supramolecular skeleton; intramolecular hydrogen bonding: C8–H8···O3; C12–H12···O1; C23–H23···O2, intermolecular hydrogen bonds: O4–H4A···O3; O4–H4B···O5; O5–H5D···O6; O5–H5E···O2; O6–H6A···O4; O6–H6B···N1; C20–H20···

O4; C21–H21···O5), see Table 3 and Figure 2 for details. In addition to a large number of hydrogen bonds, this structure also shows abundant π···π stacking interactions (Cg1···Cg2; Cg1·····Cg2; Cg1···Cg5; Cg2···Cg3; Cg3···Cg5), as shown in Table 4 and Figure 3, forming a three-dimensional supramolecular structure, as shown in Figure 4.

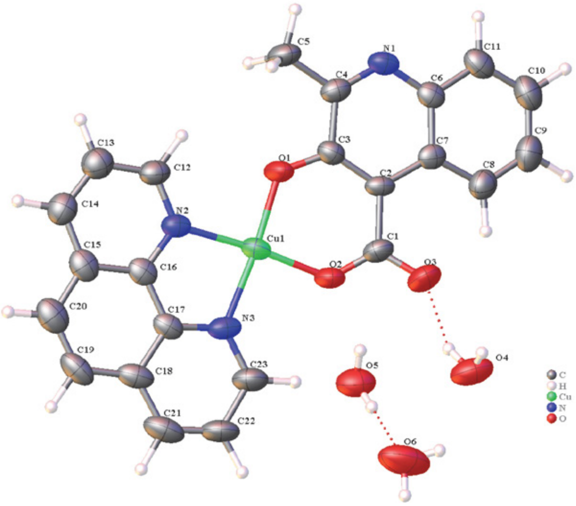

Figure 1. The molecular structure diagram of the title compound with 50% thermal ellipsoids.

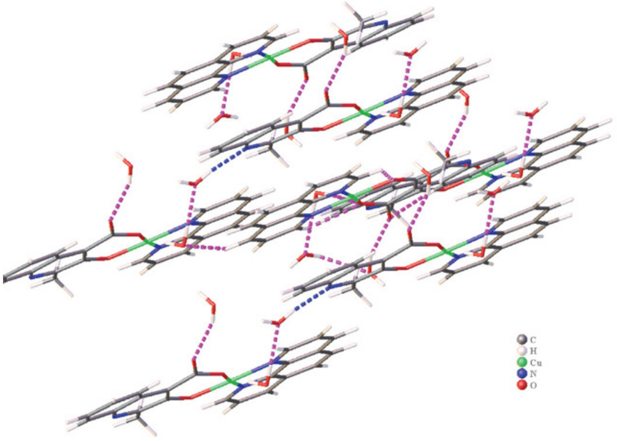

Figure 2. The hydrogen bonds diagram of the title compound (pink dotted line)

Table 2. The main bond lengths (Å) and bond angles (°) of the title complex

Bond	Distance [Å]	Bond	Distance [Å]
Cu–O1	1.869(3)	Cu–N2	1.994(3)
Cu–O2	1.891(3)	Cu–N3	2.004(3)
Angle	Angle [°]	Angle	Angle [°]
O1–Cu–O2	93.39(12)	C3–O1–Cu	126.7(3)
O1–Cu–N2	92.12(13)	C1–O2–Cu	128.8(3)
O1–Cu–N3	173.47(13)	C12–N2–Cu	127.4(3)
O2–Cu–N2	173.44(12)	C16–N2–Cu	112.5(3)
O2–Cu–N3	92.65(13)	C17–N3–Cu	111.9(3)
N2–Cu–N3	81.81(13)	C23–N3–Cu	130.0(3)

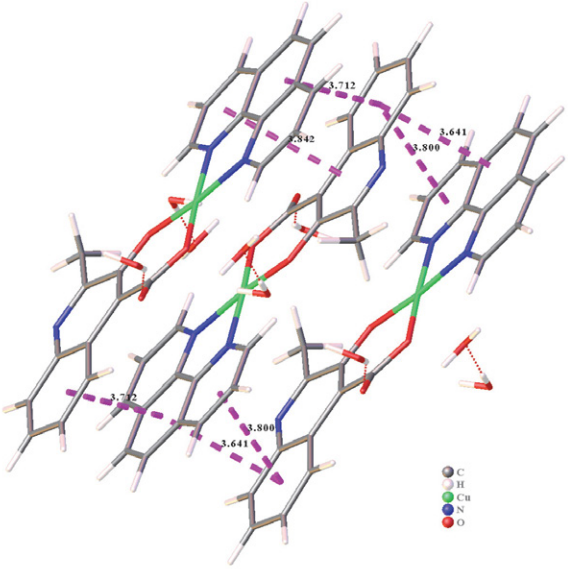

Figure 3. The π···π interaction diagram of the title complex (pink dotted line)

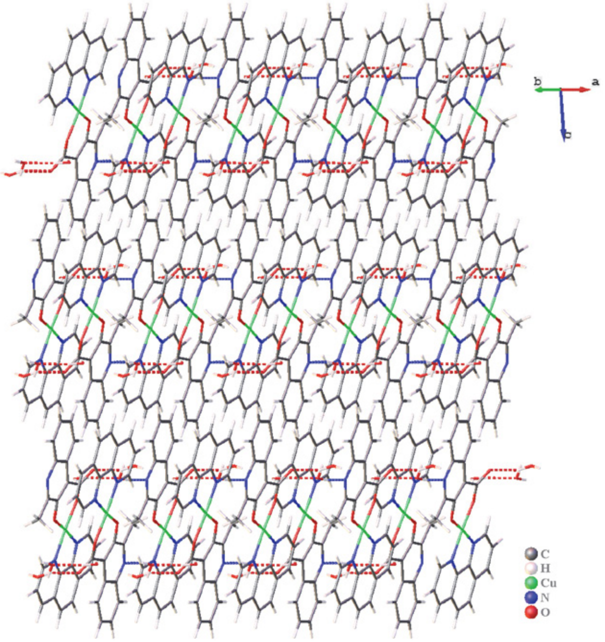

Figure 4. Stacking diagram

3. 2. Hirshfeld Surface Analysis

Hirshfeld surface analysis is an important tool for quantifying and visualizing weak intermolecular interactions in molecular crystals. By analyzing the size and shape of Hirshfeld surface, it can reflect the interactions between different atoms and the contact of molecules in the crystal. This analytical method can systematically characterize the weak interactions between molecules, reveal which parts of the molecules contribute mainly to the interactions, and the proportion of these interactions in the entire molecular crystal.[23–25] The weak intermolecular interactions were

Table 4. π···π stacking interactions of the title complex

Cg···Cg	Symmetry codes	Centroid-centroid distance (Å)	Slippage distance (Å)	Dihedral angle (Å)
Cg1···Cg2	$-x, 1-y, 1-z$	3.712	1.725	5.506
Cg1···Cg2	$1-x, 1-y, 1-z$	3.641	0.994	5.506
Cg1···Cg5	$-x, 1-y, 1-z$	3.568	1.056	2.131
Cg2···Cg3	$1-x, 1-y, 1-z$	3.800	1.485	5.989
Cg3···Cg5	$-x, 1-y, 1-z$	3.842	1.762	2.626

Table 3. The main hydrogen bond lengths (Å) and bond angles (°) of the title complex

D–H···A	Symmetry codes	D–A (Å)	H···A (Å)	D···A (Å)	D–H···A(°)
O4–H4A···O3	$1+x, y, z$	0.85	1.99	2.789(6)	157
O4–H4B···O5	$1+x, y, z$	0.85	2.23	2.997(6)	151
O5–H5D···O6	$1+x, y, z$	0.86(5)	1.96(5)	2.819(6)	176(8)
O5–H5E···O2	$1+x, y, z$	0.86(4)	2.26(5)	3.057(5)	153(5)
C6–H6A···O4	$1+x, y, z$	0.85	2.38	2.882(7)	118
O6–H6B···N1	$x, -1+y, z$	0.85	2.14	2.976(6)	169
C8–H8···O3	x, y, z	1.08	2.08	2.782(6)	120
C12–H12···O1	x, y, z	1.08	2.46	2.984(5)	109
C20–H20···O4	$-1+x, y, 1+z$	1.08	2.49	3.543(7)	163
C21–H21···O5	$-x, -y, 1-z$	1.08	2.58	3.330(6)	126
C23–H23···O2	x, y, z	1.08	2.57	3.075(6)	107

systematically characterized using the Crystal Explorer 3.1 program. The results showed that the d_{norm} shape index and curvature range of the complex were −0.5727~1.3606, −0.9872~0.9963, and −3.7005~0.3254, respectively, as shown in Figure 5.

The two-dimensional fingerprint image supplements the Hirshfeld surface and quantitatively summarizes the properties and types of intermolecular contacts experienced by molecules in the crystal.[26] The five main modes of action are H···H, C···C, C···H, O···H, and N···C, as shown in Figure 6. Among them, the H···H interaction shows a symmetrical distribution in the central region of the fingerprint spectrum, with a contribution rate of 46.3%, becoming the dominant mode of intermolecular interaction. Next are C···C, C···H, O···H, and N···C, with contribution rates of 13.5%, 7.5%, 5.9%, and 2.8%, respectively. C···H and O···H are common intramolecular hydrogen bonds, distributed in a single wing shape in the two-dimensional fingerprint region.

3. 3. Solid-state Photoluminescence

At room temperature, photoluminescence measurements were conducted on the solid powder sample of the title complex, and the results are shown in Figure 7. From Figure 7, it can be clearly seen that the photoluminescence spectrum of the title complex exhibits effective energy absorption in the wavelength range of 525–675 nm. When excited at a wavelength of 397 nm, its emission spectrum shows a sharp band at 620 nm in the blue region. From this, it can be inferred that the title complex is a typical blue luminescent material. The emission band is located in the blue region, with CIE1931 chromaticity coordinates of (0.1256, 0.2418), as shown in Figure 8.

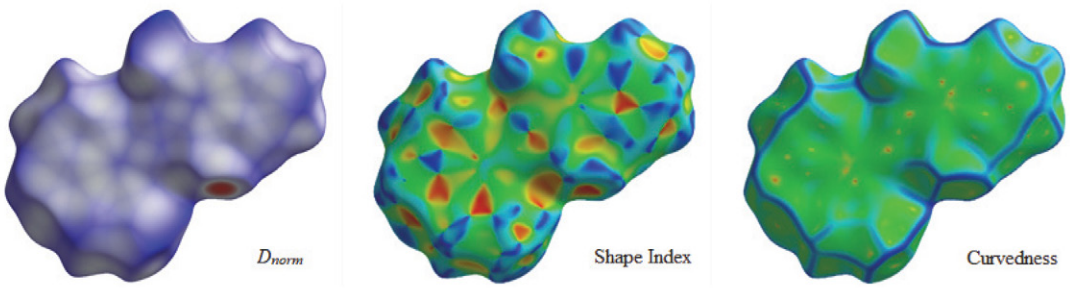

Figure 5. The Hirshfeld surface picture of the title complex

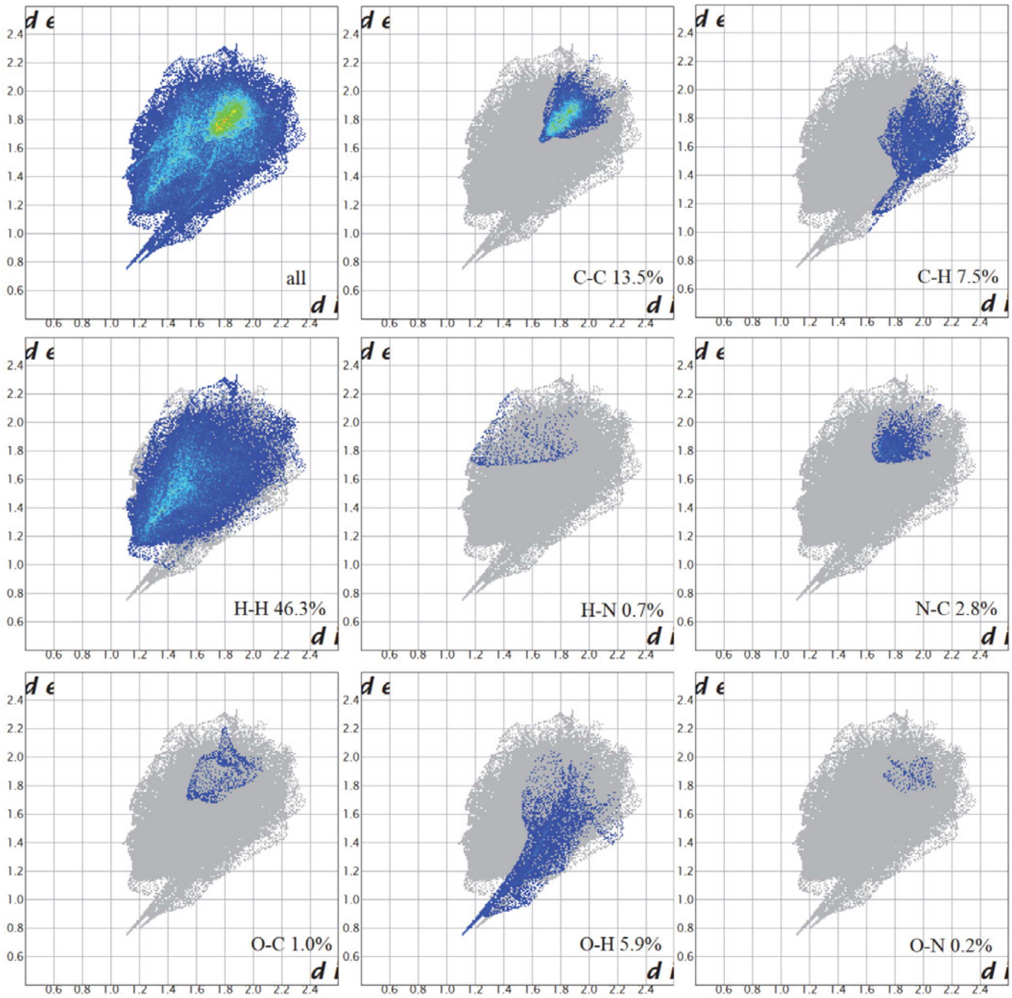

Figure 6. 2D fingerprint of the title complex (global 2D fingerprint and fingerprint of different molecular connections)

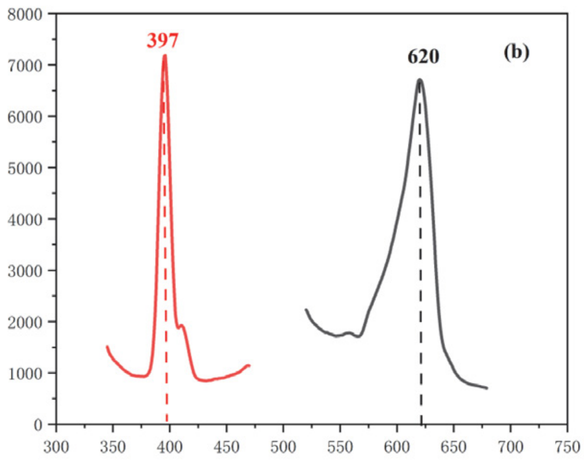

Figure 7. Solid state photoluminescence spectra of the title complex

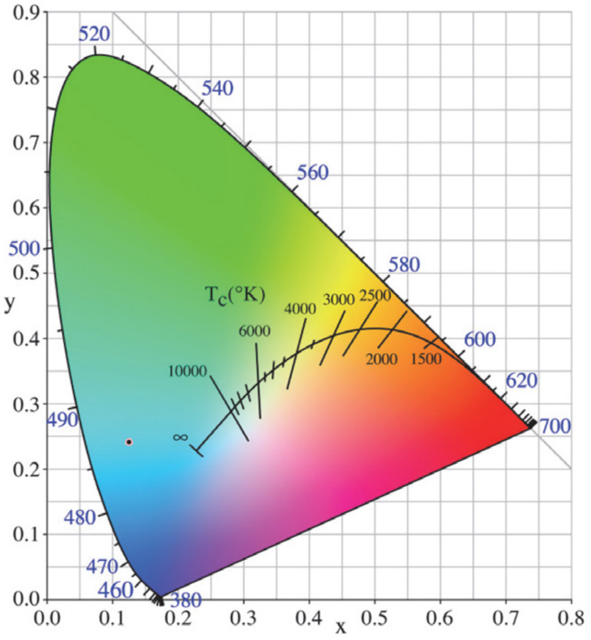

Figure 8. CIE chromaticity diagram and chromaticity coordinates of the emission spectrum of the title complex

3. 4. Solid State Diffuse Reflectance Spectroscopy (DRS)

In order to gain a deeper understanding of the conductivity of composites, solid-state UV Vis diffuse reflec-

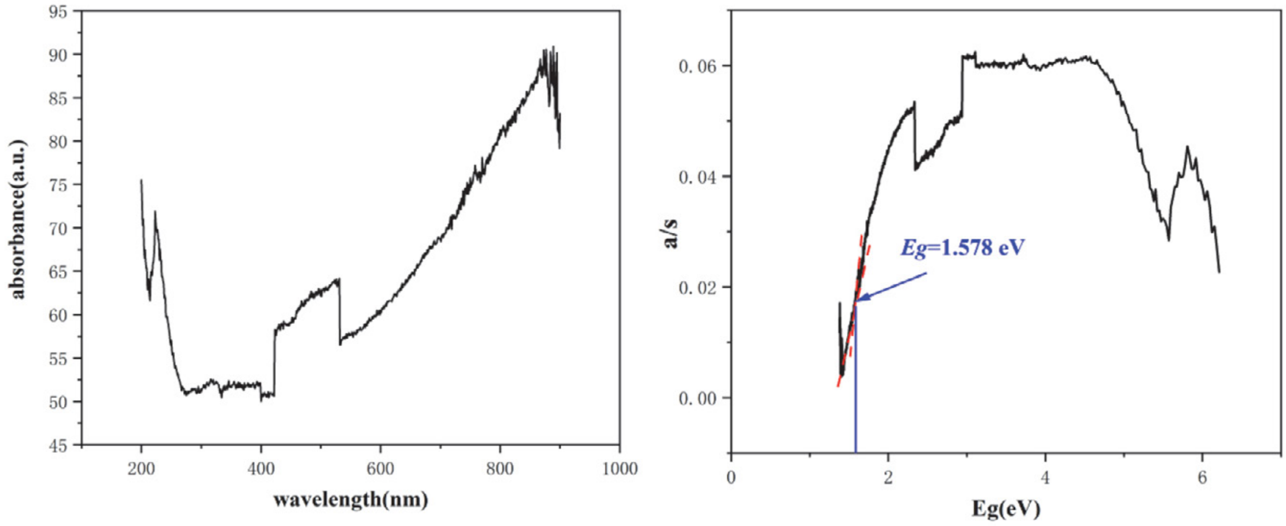

Figure 9. The UV-Vis spectra and the solid-state UV-Vis diffuse reflectance spectrum of the complex

tance technology has gradually become an important research tool. Under ultraviolet excitation, electrons in the complex absorb energy, transition from the ground state to the excited state, and exhibit absorption phenomena in the ultraviolet region. Through this process, relevant information about the conductivity of the material can be obtained.[27] Solid state samples of the title complex were measured by UV Vis DRS at room temperature using Ba_2SO_4 as the 100% reflective surface. The data processing is mainly based on the formulas proposed by Tauc, Davis, and Mott, commonly referred to as Tauc graphs.[28] The formula is $(ahv)^{1/n} = C(hv - E_g)$, where a represents the absorbance index, h is Planck's constant, v is frequency, C is constant, and E_g represents the semiconductor band gap width.[29,30] The measurement results show that the title complex belongs to a narrow band gap semiconductor with an energy band gap of 1.578 eV, as shown in Figure 9.

3. 5. Theoretical Calculation

The HOMO and LUMO of the title complex (HOMO: highest occupied molecular orbital; LUMO: lowest unoccupied molecular orbital) are shown in Figure 10. HOMO is the highest energy level orbital occupied by electrons in a molecule, with strong electron donating ability, mainly related to the π bond structure of the ligand, and the electron density is highly concentrated on the π orbital of the ligand,[31] The energy is –0.189668 a.u. In contrast, LUMO, as an electron acceptor, has lower energy and stronger electron acceptance ability, which is related to the π orbital of the ligand, and the electron density is concentrated on the aromatic ring or other π orbitals of the ligand. The energy is –0.123450 a.u. The energy difference between LUMO and HOMO is 0.066218 a.u., which is sufficient to allow charge transfer from HOMO to LUMO. Based on this observation, it is proposed that the photoluminescence of the title complex can be attributed to the charge transfer between ligands (LLCT: from the HOMO of the ligand HMCA π orbital to the LUMO of the ligand Phen π orbital). The calculation result is consistent with the experimental observation result.

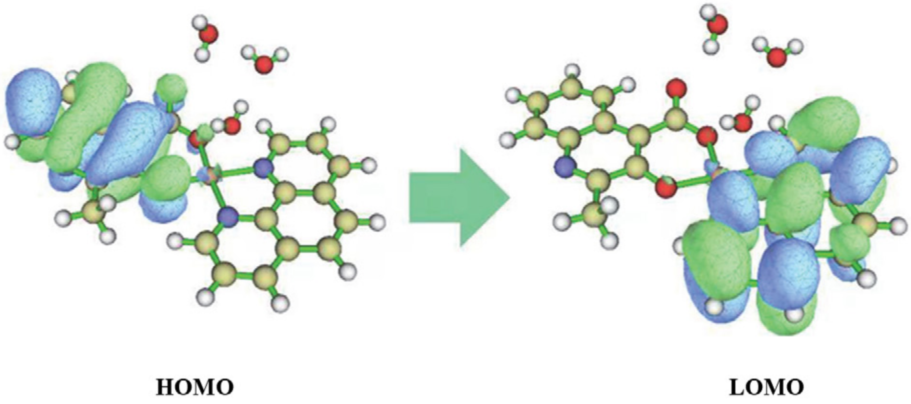

Figure 10. HOMO (left) and LUMO (right) of the complex

4. Conclusion

In summary, a novel Cu(II) mononuclear complex with excellent luminescent properties was successfully prepared by hydrothermal method, and its crystal structure was determined by single crystal X-ray diffraction. The structure is mainly constructed by hydrogen bonding and π···π interactions to form a three-dimensional supramolecular complex. The solid-state photoluminescence measurement results show that the complex exhibits a blue emission band at 620 nm, with CIE chromaticity coordinates of (0.1256, 0.2418). Solid state DRS measurements indicate that the complex is a high-performance semiconductor material with a band gap E_g of 1.578 eV.

Supplementary Materials and Data Availability

Crystallographic data have been deposited with the Cambridge Crystallographic Data Center, CCDC 2468160. Copies of the data can be obtained free of charge from the Director, CCDC, 12 Union Road, Cambridge, CBZ, 1 EZ, UK; email: deposit@ccdc.cam.ac.uk or http://www.ccdc.cam.ac.uk.

Acknowledgements

The authors thank the National Natural Science Foundation of China (22168018), the National Natural Science Foundation of Jiangxi, China (20232BAB203048), the National Natural Science Foundation of Jiangxi Ji'an, China (20244-018539) and the Open Project of State Key Laboratory for Efficient Utilization of Coal and Green Chemical Industry (2025-KF07) for supporting this work.

Declaration of Competing Interest

The authors declare that they have no known competing financial interests or personal relationships that could have appeared to influence the work reported in this paper.

Data availability

Data will be made available on request.

5. References

1. R. Wang, J. Gao, M. Vijayalakshmi, H. Tang, K. Chen, C. V. Reddy, R. R. Kakarla, P. M. Anjana, M. Rezakazemi, B. Cheolho, J. Shim, T. M. Aminabhavi, *Chem. Eng. J.* **2024**, 496, 154294. **DOI:**10.1016/j.cej.2024.154294
2. T. R. Cook, Y. R. Zheng, P. J. Stang, *Chem. Rev.* **2013**, 113, 734–777. **DOI:**10.1021/cr3002824
3. A. Byrne, N. J. English, U. Schwingenschlögl, D. F. Coker, *J. Phys. Chem. C* **2015**, 120, 21–30. **DOI:**10.1021/acs.jpcc.5b08964
4. C. B. Liu, Y. Cong, H. Y. Sun, *Acta Crystallogr. Sect. E: Struct. Rep.* **2012**, 68, m1177. **DOI:**10.1107/S1600536812035209
5. X. L. Li, G. Z. Liu, *Z. Kristallogr. NCS.* **2010**, 225, 761–762. **DOI:**10.1524/ncrs.2010.0335
6. H. H. Chen, R.Y. Kuang, Y. Wu, H. Y. Guo, S. H. Xie, D. H. Chen, X. G. Yi, *J. Chem. Crystallogr.* **2021**, 51, 516-522. **DOI:**10.1007/s10870-020-00874-x
7. X. X. Wang, J. J. Zhao, J. J. Zhang, N. Ren, S. K. Shi, *J. Therm. Anal. Calorim.* **2022**, 147, 10337–10349. **DOI:**10.1007/s10973-022-11281-z
8. M. Selvaganapathy, N. Raman, *J. Chem. Biol. Ther.* **2016**, *1*, 108. **DOI:**10.4172/2572-0406.1000108
9. J. D. Rolfes, M. Van Gastel, F. Neese, *Inorg. Chem.* **2020**, 59, 1556–1565. **DOI:**10.1021/acs.inorgchem.9b03474
10. J. C. Ott, D. Bürgy, H. Guan, L. H. Gade, *Acc. Chem. Res.* **2022**, *55*, 857–868. **DOI:**10.1021/acs.accounts.1c00737
11. S. Essalmi, S. Lotfi, A. BaQais, M. Saadi, M. Arab, H. A. Ahsaine, *RSC Adv.* **2024**, *14*, 9365–9390. **DOI:**10.1039/D3RA08815D
12. P. Samanta, S. Let, W. Mandal, S. Dutta, S.K. Ghosh, *Inorg. Chem. Front.* **2020**, *7*, 1801–1821. **DOI:**10.1039/D0QI00167H
13. N. Javed, T. Noor, N. Iqbal, S. R. Naqvi, *RSC Adv.* **2023**, *13*, 1137–1161. **DOI:**10.1039/D2RA06741B
14. N. Singh, J. Kim, J. Kim, K. Lee, Z. Zunbul, I. Lee, E. Kim, S. G. Chi, J. S. Kim, *Bioact. Mater.* **2023**, *21*, 358–380. **DOI:**10.1016/j.bioactmat.2022.08.016
15. I. Tibbetts, G. E. Kostakis, *Molecules* **2020**, *25*, 1291. **DOI:**10.3390/molecules25061291
16. Y. Xu, H. Xue, X. Li, X. Fan, P. Li, T. Zhang, K. Chang, T. Wang, J. He, *Nano Res. Energy* **2023**, *2*, e9120052. **DOI:**10.26599/NRE.2023.9120052
17. O. Yildirim, M. Bonomo, N. Barbero, C. Atzori, B. Civalleri, F. Bonino, G. Viscardi, C. Barolo, *Energies* **2020**, *13*, 5602. **DOI:**10.3390/en13215602
18. X. G. Yi, X. N. Fang, J. Guo, J. Li, Z. P. Xie, *Acta Chim. Slov.* **2020**, *67*, 507–515. **DOI:**10.1107/S1600536812035209
19. Y. Kenzhebayeva, I. Gorbunova, A. Dolgopolov, M. V. Dmitriev, T. S. Atabaev, E. A. Stepanidenko, A. S. Efimova, A. S. Novikov, S. Shipilovskikh, V. A. Milichko, *Adv. Photon. Res.* **2024**, *5*, 2300173. **DOI:**10.1002/adpr.202300173
20. G. M. Sheldrick, *Acta Crystallogr. A* **2008**, A*64*, 112–122. **DOI:**10.1107/S0108767307043930
21. G. M. Sheldrick, *Acta Crystallogr. C* **2015**, *C71*, 3–8. **DOI:**10.1107/S2053229614024218
22. O. V. Dolomanov, L. J. Bourhis, R. J. Gildea, J. A. K. Howard, H. Puschmann, *J. Appl. Crystallogr.* **2009**, *42*, 339–341. **DOI:**10.1107/S0021889808042726
23. S. L. Tan, M. M. Jotani, E. R. T. Tiekink, *Acta Crystallogr. Sect. E.* **2019**, *75*, 308–318. **DOI:**10.1107/S2056989019001129
24. S. Suda, A. Tateno, D. Nakane, T. Akitsu, Akitsu T. *J. Org. Chem.* **2023**, *13*, 57–85. **DOI:**10.4236/ijoc.2023.132006
25. G.Shabir, H. Ghulam, A. Saeed, H. Tasawwar, T. Hökelek, M. F. Erben, U. Flörke, *J. Mol. Model.* **2021**, *27,* 296. **DOI:**10.1007/s00894-021-04910-1
26. D. F. Mertsalov, V. P. Zaytsev, K. M. Pokazeev, M. S. Grigoriev, A. V. Bachinsky, S. T. Çelikesir, M. Akkurt, S. Mlowe, *Acta Crystallogr. Sect. E* **2021**, *77*, 255–259. **DOI:**10.1107/S2056989021001481
27. X. G. Yi, F. P. Lai, Y. Y. Yan, C. Zhang, W. P. Li, *J. Chem. Res.*

2020, *45*, 295–304. **DOI:**10.1177/1747519820948363

28. T. Peng, X. Y. Chen, T. Q. Qiu, J. L. Fan, *Rev. Roum. Chim.* **2024**, *69* ,49–56. **DOI:**10.33224/rrch.2024.69.1-2.06
29. W. Li, Q. Wang, F. Cui, G. Jiang, *RSC Adv.* **2022**, *12*, 17984–17989. **DOI:**10.1039/D2RA02660K
30. J. Li, P. Tu, Q. Yang, *Sci. Rep.* **2024**, *14*, 10643. **DOI:**10.1038/s41598-024-60250-z
31. K. E. Srikanth, A. Veeraiah, T. Pooventhiran, R. Thomas, K. A. Solomon, Ch. J. Soma Raju, J. N. L. Latha, *Heliyon* **2020**, *6*, e04106. **DOI:**10.1016/j.heliyon.2020.e04106

Povzetek

Bakrov kompleks [Cu(MCA)(Phen)·3H_2O)] (HMCA = 3-hidroksi-2-metilkinolin-4-karboksilna kislina, Phen = 1,10-fenantrolin) smo pripravili s hidrotermalno metodo. Struktura je bila določena z monokristalno rentgensko difrakcijo. Meritve fluorescenčne fotoluminiscence v trdnem stanju kažejo močan emisijski vrh pri 620 nm, ki se pripisuje značilnim elektronskim prehodom in molekularnim učinkom zlaganja znotraj liganda. Analiza barvne razlike CIE kaže, da kompleks izkazuje rdečo fotoluminiscenco (kromatične koordinate 0,1256, 0,2418). Poleg tega so eksperimenti UV-Vis difuzne reflektance v trdnem stanju pokazali, da ima kompleks energijsko vrzel 1,578 eV.

Review

How to Expedite Drug Discovery: Integrating Innovative Approaches to Accelerate Modern Drug Development

Nail Besli[1*], Nilufer Ercin[1*], Ulkan Celik[1,2], Yusuf Tutar[3,4]**

[1] *Department of Medical Biology, Hamidiye School of Medicine, University of Health Sciences, Istanbul, Türkiye*

[2] *Department of Medical Biology, Institute of Health Sciences, University of Health Sciences, Istanbul, Türkiye*

[3] University of Health Sciences, Faculty of Pharmacy, Division of Biochemistry, Istanbul, Türkiye

[4] Recep Tayyip Erdogan University, Faculty of Medicine, Division of Biochemistry, Rize, Türkiye

* *These authors contributed equally to this study*

** *Corresponding author: E-mail: yusuf.tutar@erdogan.edu.tr*

Received: 04-14-2025

Abstract

The drug discovery process, traditionally a lengthy and costly endeavor, is being revolutionized by integrating innovative approaches. This review delves into how modern techniques accelerate drug discovery and development, significantly reducing costs. We focus on the robust synergy of bioinformatics, artificial intelligence (AI), and high-throughput screening (HTS). Bioinformatics aids in the identification and validation of drug targets by analyzing vast genomic and proteomic datasets. AI enhances lead compound identification and optimization through predictive modeling and machine learning (ML) algorithms, slashing the time required for these stages. HTS facilitates the rapid screening of vast compound libraries to pinpoint potential drug candidates. AI-based approaches, such as HTS and predictive modeling, enhance early-stage decision-making, minimize trial-and-error experimentation, and contribute to cost-efficiency across the pipeline. Moreover, advancements in computational chemistry and molecular dynamics simulations provide deeper insights into drug-target interactions, further accelerating the design of effective and selective drugs. In drug discovery, drug candidates are tested in laboratory and live animal settings to assess their effectiveness, pharmacokinetics, and safety. By integrating these preclinical methods, the efficiency and success of drug discovery can be significantly improved, leading to more effective and safer drugs. This review underscores the important role of these technologies in contemporary drug development and explores their promising implications for future research and clinical applications.

Keywords: Artificial Intelligence (AI), Drug Development Pipeline, Drug Discovery, Bioinformatics, AI-Driven Drug Discovery

1. Introduction

Drug development is a complex process encompassing several stages, each essential for ensuring the efficacy and safety of new therapeutics. These phases, from disease-related genomic analysis to clinical testing, are the backbone of the pharmaceutical industry, driving innovation and improving patient outcomes.[1] The drug development process is generally categorized into two primary stages: discovery and development, which are crucial for advancing medicine.[2] Artificial intelligence (AI) has transformed the early phases of drug development, from disease understanding to compound optimization. Drug discovery refers to the early stages of identifying potential drug targets and compounds, whereas drug development includes preclinical and clinical testing phases aimed at bringing a drug to market. This manuscript adopts this distinction consistently throughout. Figure 1 illustrates the integration of AI across key stages of drug development, from disease characterization and target identification to lead compound optimization, preclinical evaluation, and clinical trials.

Drug screening and target identification are not simple tasks but pivotal aspects of drug development. They are aimed at resolving challenges such as insufficient efficacy and substantial adverse effects, which are common hurdles

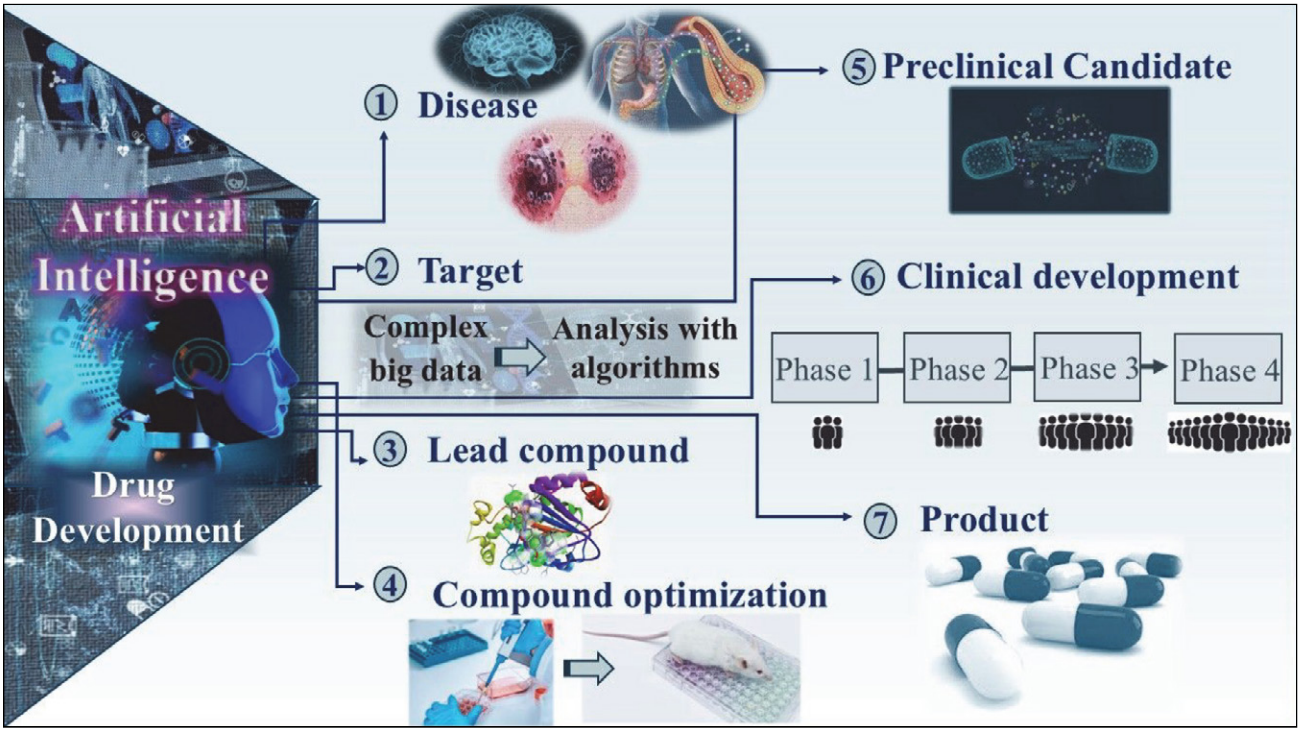

Fig 1. Ilustration of the AI-driven drug development pipeline from disease identification to final product. The schematic outlines key stages, including target selection via analysis of complex big data (Step 2), lead compound identification (Step 3), compound optimization (Step 4), preclinical candidate selection (Step 5), and progression through clinical development phases (Step 6), culminating in an approved therapeutic product (Step 7). This framework highlights how artificial intelligence streamlines the entire pipeline by enhancing data interpretation and decision-making at each stage.

in the process.[3] The drug discovery and development process has become increasingly lengthy and costly over the past decades[4], with current estimates suggesting an average duration of 10–15 years and capitalized R&D costs ranging from $1 to $4.5 billion per approved drug.[5,6] The final stage in the drug development process is not a mere formality but a critical step in product marketing.[7] To reduce the likelihood of failure during drug development, new methodologies have been developed to evaluate absorption, distribution, metabolism, excretion, and toxicity (ADMET) profiles at early stages of the pipeline.[8] Early ADMET profiling helps identify pharmacokinetic and toxicity issues before clinical testing, thereby improving decision-making and reducing the risk of costly late-stage failures.[9,10]

Despite the increasing urgency in minimizing drug resistance, the drug development pipeline incurs significant time and budget costs, with a high failure rate for most drug candidates during the clinical stages.[11] In this regard, drug design and development aspire to acquire a drug that effectively modulates the drug targets while maintaining an optimal balance of physicochemical properties and minimal toxicity.[12] Clinically approved medications, which have completed multiple phases of the drug development process, generally contain extensive information regarding dosage, interactions with other drugs, safety, adverse effects, potential harm, drug movement within the body, and the effects of the drug on the body's functions. The drug discovery and development process has become lengthier and costlier over time, necessitating strategies to reduce attrition rates during drug discovery and development.[13] In this concept, efficient computational methods for the identification of drug targets can help mitigate the high costs associated with experiments, making them crucial for successful drug development.[14]

The swift advancement of computer technologies has led to a notable increase in the screening of compounds using high-throughput methods, the application of combinatorial chemistry, and the ability to synthesize compounds. Additionally, there is an increasing need for ADMET data on lead compounds, and the methods for assessing ADMET *in vitro* are steadily expanding. Numerous effective *in silico* methods have been utilized for the *in vitro* prediction of ADMET, and *in silico* models have been devised to substitute *in vivo* models for forecasting pharmacokinetics, toxicity, and other parameters.[15,16]

Likewise, ADMET, various techniques such as QSAR (Quantitative Structure–Activity Relationship), which models the relationship between a compound's chemical structure and its biological activity using statistical or machine machine learning (ML), pharmacophore modeling, which identifies the essential chemical features required for a molecule to interact with a specific biological target, molecular docking, and molecular dynamics simulations have proven effective at different stages of drug development, resulting in significant cost and time savings compared to traditional methods.[17] Collaborations and mergers in pharmaceutical research are strategic moves that enhance research and development initiatives. Furthermore, they have been observed to enhance the availability of pharmaceutical products in the market, particularly when these partnerships are forged at the outset of the drug development process.[18]

Integrating innovative approaches is a well-established strategy to enhance the efficiency of drug discovery. The success of utilizing organic synthesis methods compatible with biomacromolecules, machine-assisted synthesis planning, and artificial intelligence (AI) in expediting drug discovery is a testament to their effectiveness.

Computer-aided drug design (CADD) techniques have been instrumental in expediting drug discovery, reducing costs, minimizing failures, and laying a solid foundation for future endeavors. Moreover, advancements in computational methodologies, such as generative chemistry and deep learning models, are promising and showing tangible results in hastening drug discovery. Strategies like repurposing existing therapeutics, leveraging traditional medicines, and employing large-scale data analytics and AI can enrich and revolutionize contemporary drug development. These multidimensional approaches, encompassing target identification, structure-based virtual screening, and *in vitro* assays, have proven to be the drivers of drug discovery, leading to more effective and successful outcomes. Figure 2 presents a conceptual framework of drug design, depicting the interplay among computational and experimental strategies, such as CADD, bioassays, and AI/ML, in identifying and refining drug candidates.

2. Identification of Drug Target: How to Get from DNA to Drug?

The journey from DNA to drugs in the drug discovery process is a complex and multi-stage process that begins with genomic information and culminates in the development of effective therapeutic molecules. The initial and crucial step in this process is identifying the correct target. In drug discovery, a 'target' refers to a specific biomolecule, often a protein, that is involved in a disease and can be modified by a drug to treat the disease. The design of drugs to target these specific molecules can lead to better therapeutic outcomes by directly influencing the function of the target. This approach can be more effective and less harmful to other cells or organ systems, potentially increasing the success rate in clinical trials.[19,20]

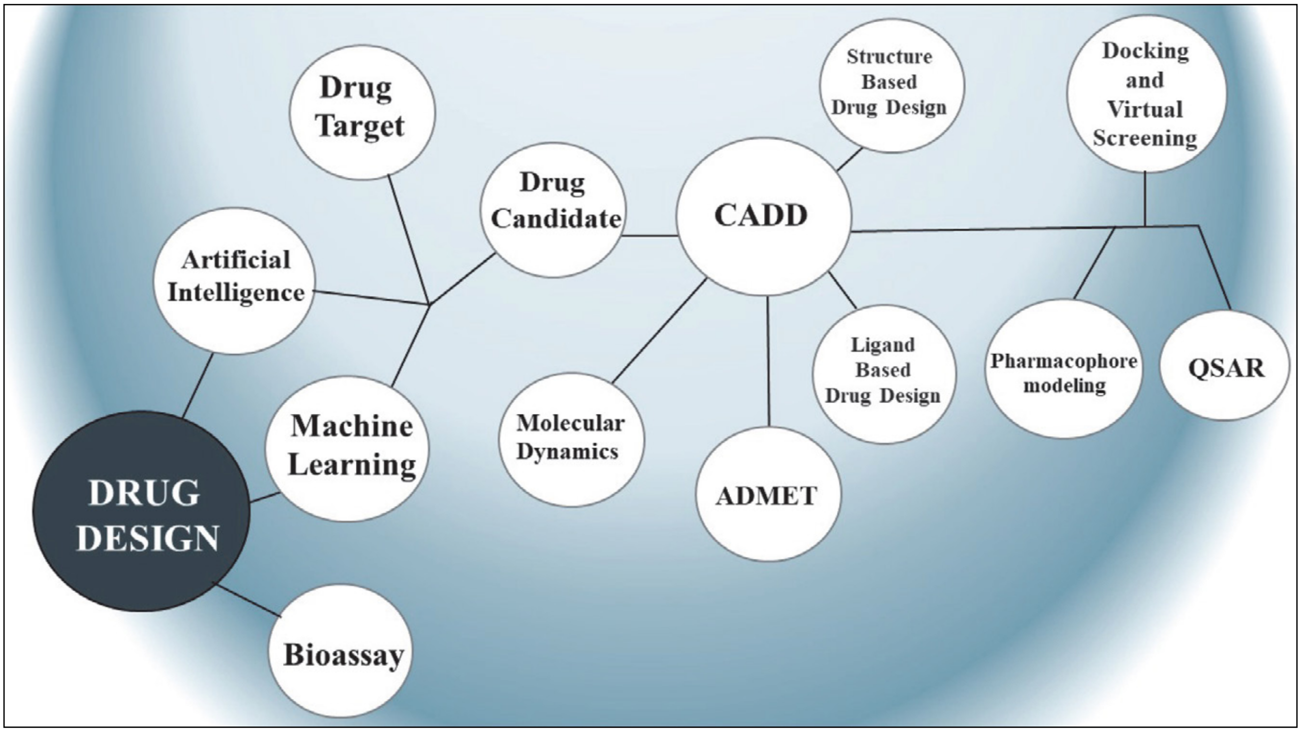

Fig 2. Conceptual map illustrating the interconnected components of modern drug design. The diagram illustrates the integration of artificial intelligence (AI), machine learning (ML), and computer-aided drug design (CADD) tools, including structure-based and ligand-based design, molecular dynamics, and ADMET prediction, to generate drug candidates. Additional elements, such as pharmacophore modeling, QSAR analysis, and bioassay validation, are also shown to be essential parts of the iterative drug discovery process.

In drug discovery, the pivotal role of data mining through bioinformatics approaches using sources such as genomic methods like Genome-Wide Association Studies (GWAS) and gene expression profiling, proteomic analyses, transgenic phenotyping, and compound profiling data is of paramount importance. This process is integral to the target identification process, providing crucial information for further analysis. Conducting mutation and polymorphism analysis to examine disease-associated mutations and genetic changes, as well as functional genomic analysis to investigate the function of specific genes and their impact on the disease, is a targeted approach in this process.[21]

With the striking progress in computer systems, integrating AI/ML in genomics has become increasingly essential. This is primarily due to the vast amount of data generated by advanced technologies in biomedicine. In clinical genomics, deep learning algorithms process large and complex genomic datasets, enabling more efficient analysis and interpretation of genetic information.[22] AI/ML algorithms, such as convolutional neural networks (CNNs), have been widely employed to interpret complex genomic data. Tools like DeepVariant utilize deep learning to accurately call genetic variants,[23] while AlphaFold leverages AI to predict protein 3D structures with unprecedented accuracy,[24] significantly aiding in structure-based target identification and validation. The systematic analysis of genomic data using AI/ML technologies has led to measurable advancements in precision medicine, particularly in chronic airway diseases such as asthma and COPD.[25] For instance, convolutional neural networks and ensemble models have been successfully applied to predict asthma exacerbations from electronic health records with high accuracy (AUC ≈ 0.85),[26] while AI-driven biomarker discovery has facilitated the stratification of asthma endotypes to support individualized treatment strategies.[27]

The application of AI in genomics is still in its nascent stages, but its potential impact is already significant. With the rapid growth of biomedical data facilitated by advanced experimental technologies, AI/ML have emerged as indispensable tools for drawing meaningful insights and improving decision-making processes in various areas, including drug discovery.[28] In the context of cancer genomics, the development of AI-based platforms capable of integrated analyses of large-scale multiomics data is pivotal for enhancing the diagnosis and therapy of cancer patients.[29] Furthermore, the use of AI/ML in cancer genomics is seen as a key component in integrating genomic analysis for precision cancer care, underscoring the importance of these technologies in advancing personalized medicine.[30] Yet, using AI/ML in genomics is not without challenges. Before AI/ML applications can be widely adopted in clinical care, rigorous studies are needed to test the safety and effectiveness of these technologies in real-world settings.[31] Efforts must be made to overcome these challenges, harness the potential benefits of AI/ML in genomics, and firmly ensure their successful integration into clinical practice.

The application of AI-powered spatial analysis in microenvironments, particularly in the context of cancer drug identification, represents a paradigm shift in research. This innovative study area significantly uses ML and AI techniques to enhance drug discovery processes. The tumor microenvironment (TME) is a complex ecosystem comprising various cell types, signaling molecules, and extracellular matrix components that interact dynamically to influence tumor growth, progression, and response to therapy.[32] Understanding the intricate interactions within the TME is crucial for developing effective cancer treatments. Recent technological advancements, such as AI-supported spatial analysis and multiplex assays, have significantly enhanced our ability to dissect the tumor microenvironment (TME) with high precision and resolution.[33] By integrating deep learning techniques with spatial omics data modeling methods like SOTIP[34], researchers can gain insights into spatial heterogeneity and differential microenvironments within tumors. This approach provides a comprehensive understanding of the tumor microenvironment, identifying potential drug targets and responses to treatment.[35]

The advent of multiplexed methodologies has opened doors for the simultaneous examination of different components of the TME, providing insights into the biological cross-talk occurring at the tumor-host interface.[36] By harnessing digital analysis tools, researchers can scrutinize paraffin tumor tissues at subcellular and cell population levels, illuminating the complex interactions within the TME.[36] These approaches enable identifying biomarker-positive cells and their spatial colocalization within tumor regions, offering valuable information for predicting treatment outcomes.[37] Furthermore, AI-powered spatial analysis tools, such as Lunit SCOPE IO, have been developed to automate the segmentation and quantification of histologic components in hematoxylin and eosin-stained whole-slide images (WSI).[33] These tools enhance the characterization of tumor-infiltrating lymphocytes (TILs) and serve as complementary biomarkers for immune checkpoint inhibition in non-small-cell lung cancer.[33]Additionally, ML and AI-driven spatial analysis techniques applied to pathology slides have facilitated a deeper understanding of the tumor immune microenvironment.[38]

This collaborative effort underscores the importance of our collective work in characterizing the molecular, cellular, and spatial properties of tumor microenvironments across different cancer types.[39] By combining image analysis algorithms with multiplex staining, researchers can conduct in-depth quantitative and spatial analyses of the broader TME, enhancing our comprehension of tumor-immune interactions.[40] These advancements underscore the potential of automated methodologies in characterizing tumor microenvironments' molecular, cellular, and spatial properties across different cancer types, ultimately leading to improved patient outcomes.[41] These in-

Table 1: Pharmaceutical companies that are using AI-supported spatial analysis in their drug development processes

Pharmaceutical Company	AI Provider/ Tool	Application	Description
AstraZeneca	DeepMind	Drug discovery, tissue analysis	Utilizing AI for spatial analysis of tissue samples to understand disease mechanisms and identify new drug targets.
Pfizer	IBM Watson	Oncology research	Applying AI-supported spatial analysis to study tumor microenvironments and improve cancer treatment strategies.
Novartis	PathAI	Pathology, diagnostic advancements	Using AI to analyze spatial patterns in tissue samples for better diagnostics and treatment planning.
Sanofi	Insilico Medicine	Biomarker discovery	Leveraging spatial analysis to identify biomarkers and understand disease progression.
Roche	Genentech	Personalized medicine	Implementing AI for spatial analysis to tailor treatments based on individual tissue profiles.
Merck	NVIDIA	Immunotherapy research	Using spatial analysis to study immune cell interactions within tissues to enhance immunotherapy approaches.
Johnson & Johnson	Atomwise	Drug target identification	Applying AI-supported spatial analysis to identify and validate new drug targets.
GlaxoSmithKline	BenevolentAI	Drug discovery	Utilizing spatial analysis to understand disease mechanisms at the cellular level and identify potential drug candidates.
Eli Lilly	Flatiron Health	Clinical trials	Using spatial analysis in clinical trial data to improve patient stratification and treatment efficacy.
Bristol-Myers Squibb	GNS Healthcare	Drug development	Implementing AI-supported spatial analysis to enhance understanding of tissue responses to treatments.

novative approaches highlight the importance of advanced imaging and analysis techniques in unraveling the complexities of the TME. In parallel with these developments, some pharmaceutical companies (see Table 1) use AI-supported spatial techniques.

Several pharmaceutical companies listed in Table 1 are actively applying AI-supported spatial analysis to address complex biomedical questions. For instance, AstraZeneca collaborates with DeepMind to analyze tissue samples for elucidating disease mechanisms and identifying targets. Pfizer uses IBM Watson's AI to study tumor microenvironments in oncology research. Novartis, through PathAI, advances diagnostic accuracy by identifying spatial patterns in tissue. Companies like Roche (via Genentech) and Sanofi (via Insilico Medicine) apply spatial tools for personalized medicine and biomarker discovery, respectively. These applications demonstrate how AI is enabling a precise, spatially resolved understanding of tissue pathology, thereby enhancing decision-making in both the early discovery and clinical phases.

2. 1. Computer Aided Drug Discovery (CADD)

CADD is a crucial approach that utilizes computer models, data analyses, and artificial intelligence (AI) techniques to improve the efficiency and effectiveness of drug development processes. The integration of ML algorithms, deep learning technologies, and AI-driven solutions has transformed various stages of drug discovery and development.[42,43] These technologies are essential for tasks such as structure- and ligand-based virtual screening, de novo drug design, physicochemical property prediction, and drug repurposing.[42] Pharmaceutical companies and research groups increasingly rely on computer-aided drug discovery techniques.[44]

CADD is recognised as a cutting-edge strategy with numerous advantages, including cost and time savings, high efficiency and success rates, better alignment and selectivity to the target, rational drug design, ADMET prediction, environmentally friendly approaches and ethical benefits, such as reduced reliance on animal testing. Structure-based drug discovery (SBDD) and ligand-based drug discovery (LBDD) are the two primary methods used in CADD.[45]

2. 1. 1. Structure-based Drug Design (SBDD)

SBDD, a method that comes into play when the three-dimensional structure of the target molecule is known or can be predicted, is a testament to precision in drug design and optimization. It strives to create and enhance drug candidates that will bind specifically to the target, thereby exhibiting biological activity. This is achieved by leveraging the structural information of the target protein or nucleic acid.[46]

SBDD is the method of choice when the crystal structure of the target protein has been resolved, a feat accomplished through techniques like X-ray crystallography or Cryo-EM (electron microscopy). These methods provide high-resolution structural data, offering a clear view of the binding sites of ligands and the active regions of the target. Similarly, it is employed when the three-dimensional structure of the target protein in solution is determined using NMR spectroscopy, a particularly valuable tool for small proteins and protein complexes. If the structure of the target protein is unknown, homology modeling steps in, creating a predicted structure based on a known structure. This process involves using the structure of a closely related protein as a reference.[47] In this regard, researchers access approximately 1 million Computed Structure Models (CSMs) from AlphaFoldDB and RoseTTAFold (from the Model Archive) and ~200,000 empirically determined PDB structures at https://www.rcsb.org/.

Docking and virtual screening:

Finding and improving therapeutic compounds requires understanding the binding mechanism between proteins and small molecules.[48] Molecular docking is a widely used SBDD method. Molecular docking estimates the optimal position, orientation, and conformation of a drug candidate (small molecule) when binding to a protein. Most docking systems currently in use achieve success rates between 70% and 80% in terms of accurately reproducing known ligand binding poses, typically within a root mean square deviation (RMSD) of 1.5 to 2 Å when compared to crystallographic reference structures.[49] A virtual screening computational technique evaluates a vast library of compounds to determine if they can bind to specific locations on target molecules, such as proteins and, well-compounds examined.[50] It focuses on rapidly searching enormous chemical structure libraries using computers to find those structures most likely to bind to a therapeutic target, usually an enzyme or protein receptor.

Structure-based virtual screening (SBVS): SBVS is a computer-aided drug discovery method that uses the three-dimensional structure of a target molecule (usually a protein) to identify potential drug candidates.[51] SBVS screens an extensive library of chemical compounds, predicting how these compounds might bind to the target molecule and identifying the most promising candidates.[48] Docking techniques are frequently employed in SBVS on extensive chemical libraries due to their rapidity in scanning millions of molecules with a simplified scoring function. Scoring functions are utilized by docking tools like DOCK, AutoDock, Glide, FRED, GOLD, and Surflex-Dock to assess protein–ligand binding.[48]

Ligand-based virtual screening (LBVS): LBVS is a computer-aided drug discovery method that uses the properties of known active ligands to predict the binding potential of chemical compounds to specific biological targets. LBVS uses the molecular similarity concept to analyze the structural details and physicochemical characteristics of the chemical scaffold of known active and inactive compounds. Accordingly, similarity measurements utilizing appropriate chemical descriptors are used to investigate the links between compounds in a particular library and one or more known actives.[51] These measurements can be carried out using 3D descriptors related to molecular fields, shape, and volume as well as pharmacophores, as well as 1D and 2D descriptors that often include information on the chemical nature of compounds and their topological properties. The following circumstances make LBVS a better choice: (a) when little is known about the molecular target's structure. Additionally, it is used to enhance the database for SBVS experiments; (b) LBVS methods are generally superior to SBVS methods for targets with a large amount of available experimental data or where the drug-binding site is not well defined; (c) using both approaches simultaneously can improve the accuracy of the VS by removing some false-positive compounds that the SBVS technique identified as promising, increasing the likelihood of obtaining positive results.[52] When information on the structure of ligand-target complexes and similarity relationships to active compounds are available, combining the methods of SBVS and LBVS may be a viable approach that can result in a comprehensive framework that can improve the success of drug discovery efforts.[51]

Despite their widespread use, both SBVS and LBVS come with notable limitations. SBVS often suffers from high false-positive rates due to inaccuracies in scoring functions, may fail to rank active compounds over decoys reliably. Additionally, the quality and resolution of protein structures especially for flexible or disordered regions can significantly affect docking results. LBVS, on the other hand, is inherently limited by its dependence on the availability of well-characterized ligands with known activity. This restricts its application to targets with rich ligand databases, making it unsuitable for novel or poorly studied targets. Both approaches also entail substantial computational costs, especially in large-scale screenings, and are sensitive to the quality of input data, which can impact the robustness of the outcomes.

2. 1. 2. Ligand-based Drug Design (LBDD)

To anticipate the properties of a novel compound, LBDD examines current activities using techniques such as pharmacophore modeling, QSAR models, and 3D shape matching.[48]

Pharmacophore modeling: An abstract representation of the structural characteristics needed by a biological macromolecule to identify a ligand is called a pharmacophore. To develop a pharmacophore model, an initial set of compounds is chosen with a variety of structural features. Compatibility analysis is performed to make a list of low-energy conformations for each chosen molecule, including the likely bioactive conformation. The low-energy conformations of molecules in every possible combination are stacked. Functional groups (such as carboxylic acid groups or phenyl rings) that are common to all the compounds in the collection can be added. It is thought that the collection of conformations that yields the best fit is the active conformation. Molecules are stacked and repre-

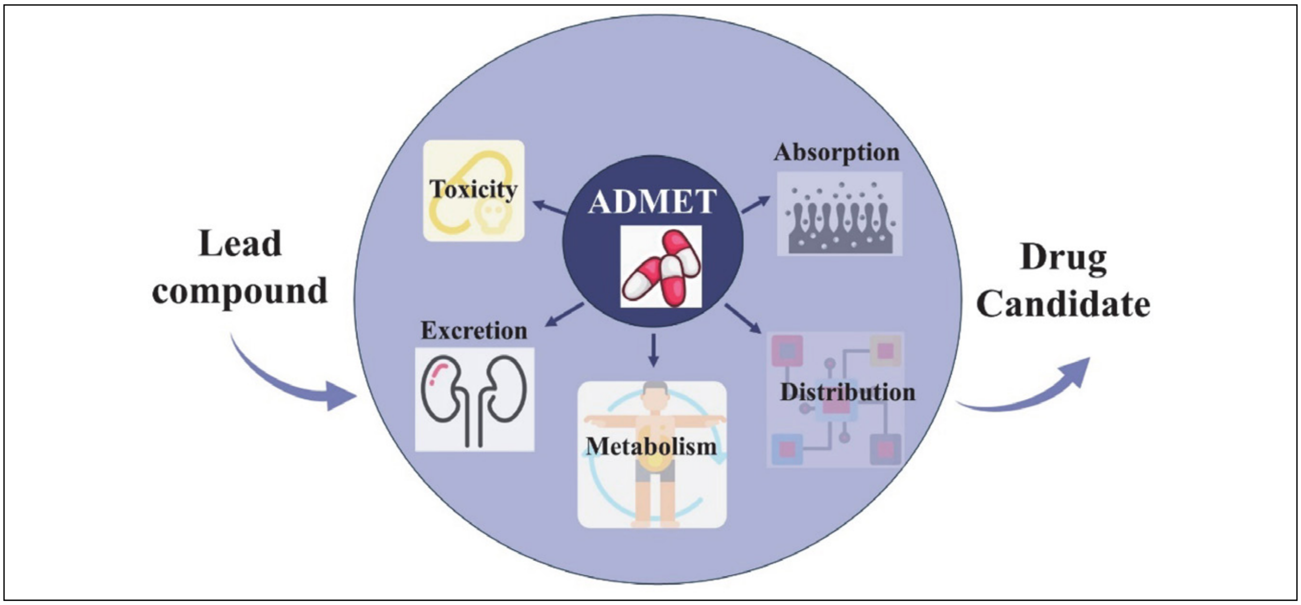

Fig 3. Schematic representation of ADMET evaluation in the drug development pipeline. The diagram outlines how absorption, distribution, metabolism, excretion, and toxicity assessments are used to screen lead compounds before selecting viable drug candidates. These properties collectively determine the pharmacokinetic and safety profile of a compound, significantly influencing its success in preclinical and clinical stages.

sented abstractly. The pharmacological effects of a collection of substances that bind to the same biological target are evaluated.[53]

Quantitative structure-activity relationships (QSAR): One of the traditional uses of ML techniques in drug discovery is QSAR.[54] Building prediction models of biological activities based on the structural and molecular details of a compound library is known as quantitative structure-activity relationship, or QSAR, modeling. The idea of quantitative structure-property relationship, or QSAR, was first applied in drug discovery and development. Since then, it has found widespread use in the correlation of molecular data with various physicochemical properties as well as biological activities.[50] In QSAR, the selection of molecular descriptors and the evaluation of molecular similarity are crucial. It is important to note that, regardless of the field of study, comparing object representations, similarity metrics, and the interactions between related attributes and relationships among objects are generally relevant for data modeling.[55] Important pharmacological characteristics, like ADMET, have been thoroughly modeled using QSAR techniques. To develop novel and safe medications, it is imperative to minimize toxicity and optimize pharmacokinetics; inaccurate assessment of these factors may cause unfavorable side effects and impair in vivo efficacy, which could ultimately lead to a drug candidate's failure.[55]

Moreover, AI–driven virtual screening, particularly through deep learning and ultra-large compound library docking, has significantly accelerated early-stage drug discovery. These approaches reduce the number of false positives and eliminate resource-intensive failures during hit-to-lead stages.[56,57] For instance, deep docking strategies can rapidly screen over a billion compounds, drastically decreasing both time and experimental cost compared to traditional *in vitro* methods. A landmark example is the discovery of Halicin, a novel broad-spectrum antibiotic, identified using a deep learning model trained on molecular structures an achievement that conventional screening pipelines had missed.[58] This case illustrates the practical application of AI in streamlining discovery pipelines and alleviating the economic burden of early-stage drug development.

2. 1. 3. ADMET Prediction

Drugs that are both safe and effective have precisely calibrated pharmacokinetics and pharmacodynamics, which include sufficient absorption, distribution, metabolism, excretion, and acceptable toxicity (ADMET), as well as high potency, affinity, and selectivity against the molecular target.[59] It was observed that the inadequacies in ADMET characteristics cause a lot of clinical trials to fail. Although it is ideal to profile ADMET early in the drug discovery process, there is a lack of data and a high expense associated with experimentally evaluating ADMET characteristics. Additionally, computational analyses of ADMET during the clinical trial phase can be a useful design approach that enables researchers to focus more on the most promising drugs.[60] Today, there is a large range of tools available for ADMET prediction, including ADMETlab[61], QikProp[62], MetaTox, SwissADME, pKCMS[63], DataWarrior[64], MetaSite and StarDrop[65] to mention a few. By easily excluding inappropriate compounds, ADMET prediction tools can cut down on the amount of costly late-stage failures and synthesis-evaluation cycles.[59] Figure 3 exhibits the ADMET evaluation process, highlighting how absorption, distribution, metabolism, excretion, and toxicity profiling are employed to refine lead compounds into viable drug candidates.

Furthermore, AI-powered predictive toxicology and ADMET modeling enable early elimination of compounds with poor safety profiles, thus lowering attrition rates in later phases and saving substantial R&D resources. Machine learning techniques have been shown to outperform conventional rule-based methods in predicting toxic effects.[66] In addition, Kelleci Çelik and Karaduman[67] employed a one-vs-all QSTR (OvA-QSTR) approach to accurately predict drug-induced hepatotoxicity using structural and molecular descriptors, reinforcing the utility of AI in early-stage toxicological assessments.

2. 1. 4. Incorporated Artificial Intelligence and Molecular Dynamics (AI-MD)

AI and MD methods have demonstrated significant potential in various scientific fields, particularly drug design, chemistry, and materials science. The integration of AI with MD simulations not only enables the development of innovative computational workflows but also underscores the significance of combining AI with mechanistic insights from MD, a crucial aspect of this integration. Elend et al.[68] present a computational drug design work-

Table 2A: AI Applications in Drug Discovery Phase

Application	Description	AI Techniques Used	Tools
Target Identification	Identifying biological targets linked to diseases	ML, NLP	IBM Watson, DeepMind
Lead Compound Identification	Screening large compound libraries	VS, Deep Learning	Atomwise, Schrödinger, DeepChem
Lead Optimization	Improving efficacy and reducing toxicity	QSAR, Generative Models	MOE, ChemDraw, ADMET Predictor
ADMET Predictions	Early profiling of pharmacokinetics and toxicity	ML, Predictive Modeling	ADMET Predictor, pkCSM
Drug Repurposing	New uses for existing drugs	ML, Network Analysis	IBM Watson
Protein Structure Prediction	Predict 3D structures for interaction studies	Deep Learning	AlphaFold
Genomic Data Analysis	Disease-related genetic profiling	ML, Data Mining	GATK, DeepVariant
Biomarker Discovery	Identifying biomarkers that predict response to therapies	ML, Data Mining	BenevolentAI, GNS Healthcare
Virtual Screening and Docking	Simulating molecular docking to predict how drugs bind to their targets	VS, Molecular Docking	AutoDock, Schrödinger Suite

Table 2B. AI Applications in Drug Development Phase

Application	Description	AI Techniques Used	Tools
Preclinical Testing	Evaluating efficacy & safety pre-clinically	Image Analysis, ML	Insilico Medicine, PathAI
Clinical Trial Design	Patient recruitment, protocol optimization	AI Analytics, Predictive Modeling	Medidata, REDCap
Predictive Toxicology	Forecasting toxicity and safety issues	ML, Neural Networks	DeepTox, Tox21 Challenge
Molecular Dynamics Simulations	Atomistic simulations of drug-target interactions	Molecular Dynamics	GROMACS, NAMD
Chemical Synthesis Optimization	Improving synthesis yield and routes	AI-driven Planning	ChemPlanner, Reaxys
Synthetic Biology	Designing novel biological systems	ML, Synthetic Biology	Benchling
Patient Stratification	Subgrouping based on genetic/clinical data	Clustering, ML	Illumina BaseSpace, Synthego
Personalized Medicine	Individualized therapy planning	ML, Data Analytics	23andMe, Foundation Medicine
Image Analysis	Tissue/pathology image evaluation	AI Diagnostic Systems	ImageJ, PathAI
Data Mining	Identifying patterns from large datasets	ML, Data Mining	RapidMiner, Weka

Abbreviations: ML: Machine Learning, NLP: Natural Language Processing, VS: Virtual Screening, QSAR: Quantitative Structure–Activity Relationship, ADMET: Absorption, Distribution, Metabolism, Excretion, and Toxicity, AI: Artificial Intelligence.

flow that merges AI methods and MD simulations to create potential drug candidates, showcasing the effectiveness of AI-MD integration in drug discovery. Baum et al.[69] discuss the impact of AI implementations in chemistry, highlighting their role in reducing experimental effort and optimizing reaction conditions, underscoring the transformative potential of AI in scientific research. Tran et al.[70] utilize MD simulations to gain insights into AI-generated cell-penetrating peptides, stressing the significance of combining AI with mechanistic insights from MD. Terayama et al.[71] underscore the importance of integrating ML techniques with simulations and experiments in research. Meuwly[72] explores the application of ML techniques in chemical reactions, illustrating the historical use of AI in chemistry research. Zhang et al.[73] focus on enhancing molecular simulations with AI, emphasizing the computational intensity of such applications and the necessity for advanced methodologies. Xu et al.[74] combine chemical descriptors with AI/ML tools to predict synthesis reactions, demonstrating the potential of AI in predicting chemical outcomes. Elbaz et al.[75] investigate the use of MD simulations to study diffusion mechanisms, highlighting the importance of detailed simulations in understanding molecular processes. In conclusion, the amalgamation of AI and MD methods provides a robust tool for expediting scientific discovery, streamlining experimental processes, and designing innovative materials and drugs. Researchers can unlock new frontiers in various scientific disciplines by leveraging AI's strengths in data analysis and prediction with detailed insights from MD simulations.

Table 2A summarizes AI-driven tools and methods employed in the drug discovery phase, including target identification, virtual screening, and biomarker discovery. Table 2B, on the other hand, outlines applications in the drug development phase, such as preclinical testing, clinical trial design, and predictive toxicology. This separation facilitates a clearer understanding of the sequential use of AI technologies across the whole drug development pipeline.

2. 1. 5. Key Takeaways in AI-Aided Drug Development in CADD

AI has significantly impacted drug development processes by offering various benefits. AI plays a crucial role in rational drug design, decision-making support, personalized therapies, clinical data management, and expediting drug development.[76] AI/ML platforms are instrumental in determining the correct dosage form, optimizing it, and facilitating quick decision-making for efficient manufacturing of high-quality products.[77] Advances in AI-powered Language Models (LMs) have shown the potential to enhance drug discovery and development processes.[78] CADD techniques are essential for accelerating drug discovery, reducing costs, and minimizing failures in the final stages of development.[44]

AI is involved in every drug design and development stage, from target identification to trial design and post-market product monitoring.[79] Pharmaceutical companies have utilized AI to speed up drug discovery processes, automate target identification, and enhance development speed.[80] AI assists in developing treatment regimens, prevention strategies, and drug/vaccine development, particularly crucial during health crises like the COVID-19 pandemic.

AI algorithms enable the design of advanced drug development pipelines, reducing time and costs in the drug discovery process.[81] AI advancements in radiotherapy show promise in improving treatment efficiency and effectiveness.[82] AI has been extensively used in computer-aided drug design, including repurposing existing drugs against specific targets like COVID-19 receptor proteins.[83] Open data sharing and model development are crucial for the progress of drug discovery with AI.[84]

The application of AI/ML in synthetic drug substance process development presents significant untapped opportunities.[85] AI's role in drug discovery spans from compound screening to clinical trial conduct and repurposing, enhancing various phases of drug development.[86] AI/ML trends impact clinical pharmacology by aiding target identification, generative chemistry, and clinical trial outcome evaluation.[87] Effective multimodal approaches integrating big data, chemistry, biology, and medicine with AI capabilities optimize drug discovery.[87]

2. 1. 6. AI/ML in Drug Development

Artificial intelligence (AI) and machine learning (ML) have become indispensable tools in drug development, offering advanced capabilities across both discovery and development stages. Their unique contributions are particularly pronounced in clinical trial optimization, post-market surveillance, and biomarker-driven drug repositioning areas less emphasized in earlier sections of this review.

AI algorithms are now extensively used to enhance clinical trial design by predicting patient enrollment dynamics, optimizing inclusion/exclusion criteria, and estimating dropout risks, thus improving efficiency and reducing costs.[88] In the post-marketing phase, AI-powered pharmacovigilance systems can detect adverse drug events faster and more reliably than traditional methods by analyzing real-world data from electronic health records and patient forums.[89]

In preclinical development, AI models support compound screening, molecular property prediction, and de novo drug design through deep learning techniques that handle complex datasets, expediting lead optimization and safety profiling.[90,91] These tools are especially valuable in oncology and rare diseases, where patient stratification and precision targeting are essential.

Table 3 summarizes real-world implementations of AI/ML by leading pharmaceutical companies. For in-

Table 3: Pharmaceutical Companies Using AI For Drug Development

Pharmaceutical Company	Collaboration Focus	AI Provider/Tool	Year Started
Pfizer	Drug discovery and development using AI-driven data analysis	IBM Watson, Atomwise	2016
Novartis	Drug discovery, personalized medicine, drug discovery, and clinical trial design	Microsoft, PathAI	2017
Sanofi	Drug discovery and design, biomarker development	Exscientia, Insilico Medicine	2019
AstraZeneca	Discovery of new drug targets and develop therapies	BenevolentAI, DeepMind	2018
GlaxoSmithKline	Drug discovery, clinical trials, and biomarker development	Insilico Medicine, GNS Healthcare	2019
Johnson& Johnson	Pathology, diagnostic advancements	Atomwise, PathAI	2016
Merck	Drug discovery, predictive toxicology	PathAI, DeepTox	2017
Roche	Personalized medicine, drug development	Genentech, Flatiron Health	2018
Bristol-Myers Squibb	Drug discovery, immunotherapy research	NVIDIA, Flatiron Health	2019
Eli Lilly	Drug discovery, lead optimization	Atomwise, BioSymetrics	2017
Takeda	Drug discovery, clinical trials	Atomwise, BioSymetrics	2018
AbbVie	Drug discovery, target validation	IBM Watson, BioSymetrics	2019
Amgen	Drug discovery, biologics development	GNS Healthcare, Atomwise	2017
Bayer	Drug discovery, patient stratification	GNS Healthcare, BenevolentAI	2018
Biogen	Drug discovery, neurodegenerative diseases	IBM Watson, Atomwise	2019

stance, AstraZeneca has collaborated with DeepMind to enhance tissue analysis in oncology, while Novartis leverages Microsoft AI for patient segmentation and trial efficiency. Similarly, Pfizer, Sanofi, and GlaxoSmithKline employ AI platforms such as IBM Watson, Exscientia, and Insilico Medicine to accelerate drug discovery, biomarker development, and clinical trial design. These collaborations reflect AI's expanding role from preclinical modeling to post-marketing applications.

The table has been structured to clearly distinguish AI use cases in discovery (e.g., target identification, virtual screening) versus development (e.g., trial optimization, toxicity prediction), thereby improving reader comprehension and aligning with the pharmaceutical R&D workflow.

3. Bioassay of Drug Candidate

The integration of *in silico*, *in vitro*, and *in vivo* studies is essential for effective and efficient drug discovery. *In silico* studies provide a cost-effective and rapid initial screening of potential drug candidates, which are then rigorously tested through *in vitro* and *in vivo* experiments to ensure their safety and efficacy before proceeding to clinical trials in humans. This multi-stage approach helps streamline the drug discovery process, reducing time and costs while increasing the likelihood of success in developing new treatments.[92]

Recent advances in biomedical engineering and genetic technologies have introduced innovative *in vitro* and *in vivo* techniques that significantly enhance the predictive power and translational relevance of preclinical drug testing.

CRISPR-based assays represent a transformative *in vitro* approach, enabling precise genome editing to model disease-specific mutations and assess gene-drug interactions in human-derived cell lines. These systems would allow researchers to dissect target-specific pathways and identify synthetic lethal interactions, which are particularly valuable in oncology and for rare genetic disorders.[93] CRISPR screening platforms have also been integrated into drug repurposing pipelines, offering scalable tools for high-throughput functional genomics.

In the realm of *in vivo* models, the development of humanized animal models has bridged critical translational gaps by introducing human genes, cells, or tissues into immunodeficient animals. These models are beneficial for studying immunotherapies, infectious diseases, and drug responses related to metabolism.[94] Unlike conventional rodent models, humanized systems enable the evaluation of drug efficacy and toxicity in a context that closely mimics human physiological conditions.

Additionally, organ-on-a-chip technologies, although not strictly *in vitro* or *in vivo*, offer a hybrid system that simulates the dynamic interactions of human tissues and fluids. These microfluidic devices recreate the multicellular architectures and mechanical forces of organs like the lung, liver, and gut, providing valuable insights into drug absorption, distribution, and organ-specific toxicity.[95]

Together, these cutting-edge approaches complement traditional bioassays by enhancing mechanistic understanding, improving predictive accuracy, and supporting the development of safer and more effective drugs.

3. 1. *In vitro* Studies

In vitro studies provide valuable information on the efficacy and safety of drug candidates before *in vivo* animal studies and clinical trials. *In vitro* studies evaluate the effects of potential drug candidates on specific biological targets in an *in vitro* setting. During this phase, cell culture studies are conducted to assess the impact of the candidate drug on cell viability, its apoptotic and necrotic effects, and its genotoxicity as part of toxicity and safety tests to understand the mechanism of action of the drug candidate, its effects on cellular signaling pathways, receptor interactions, and biomolecular processes are examined in detail.[96–99] Pharmacokinetic studies are conducted to investigate how the drug candidate is absorbed, distributed, metabolized, and excreted by the cells.[100] Additionally, pharmacodynamic studies are performed to determine the biological effects and efficacy of the drug on the cells. *In vitro* studies utilizing three-dimensional (3D) cell cultures and organoid models provide more complex and realistic cellular environments, helping to achieve more reliable results.[101,102]

3D cell cultures and organoid systems offer significant advantages over traditional two-dimensional (2D) cultures, as they more accurately mimic the structural and functional complexity of human tissues. They replicate cell–cell and cell–matrix interactions, nutrient and oxygen gradients, and tissue-specific architecture more effectively, enhancing their predictive value for *in vivo* outcomes. However, these models are not without limitations. They can be expensive to establish and maintain, often require specialized scaffolds or materials, and exhibit variability in reproducibility and scalability for high-throughput applications. Furthermore, while *in vitro* systems whether 2D or 3D are invaluable for mechanistic insights, they lack biokinetic context, which may lead to misinterpretation of toxicity or efficacy profiles when extrapolating results to human physiology.[103]

3. 2. *In vivo* Studies

In vivo studies involve testing drug candidates in animal models to evaluate their efficacy, pharmacokinetics, and safety within a living organism.[104] These studies are a critical step to verify the findings from *in vitro* experiments and to evaluate the efficacy and safety of the drug in more complex biological systems.[105] At this stage, ADME studies are conducted to determine the bioavailability and half-life of the drug as part of pharmacokinetic studies. Pharmacodynamic studies are performed to establish dose-response relationships and the degree of efficacy. Acute, subacute, and chronic toxicity tests are conducted as part of toxicity and safety studies. Potential side effects, organ damage, and mortality rates are examined.[106–108] *In vivo* models are crucial for studying the progression of the disease and the effects of the drug on this process. Additionally, they play an important role in observing the response to treatment and in identifying and validating biomarkers to monitor disease progression.[105] Compared to *in vitro* experiments, animal models are more dependable, despite certain limitations such as variations in biokinetics parameters and the inability to extrapolate results to humans.[103] Nonetheless, significant physiological and metabolic differences between animal models and humans can limit the translatability of preclinical findings, necessitating cautious interpretation and validation in human-relevant systems.

4. Discussion

4. 1. What are the Gaps in Drug Development?

The landscape of drug development is characterized by challenges that impede the efficient translation of scientific discoveries into safe and effective therapies. For instance, one of the significant issues in the pharmaceutical industry is the innovation gap, where drug development costs are escalating. In contrast, the number of new drugs approved remains relatively stable.[109] This discrepancy underscores a fundamental challenge in the field, where the increasing financial burden of bringing a new drug to market is not met with a proportional increase in successful outcomes. The high attrition rate in clinical development significantly contributes to the rising drug development costs.[110] This attrition emphasizes the urgent need for more efficient and reliable methods to identify viable drug candidates early in development to alleviate the financial strain on pharmaceutical companies.

The funding landscape is a critical aspect that exacerbates the gaps in drug development. While a significant portion of foundational research for drug discovery receives public funding, there often needs to be more in transitioning these discoveries into viable drug candidates due to funding limitations.[111] This gap between early-stage research and late-stage development highlights the necessity for bridging mechanisms to ensure that promising leads are not abandoned due to financial constraints. Moreover, challenges in developing new drugs are further compounded by the need for more effective therapies despite significant advancements in preclinical research.[112] This gap between preclinical data and clinical success is attributed to suboptimal drug development strategies, particularly in addressing critical genetic alterations in diseases like cancer.

Another crucial gap in drug development lies in pediatric drug therapy, historically lacking a focus on developing medications specifically tailored for children.[113] Pediatric drug development continues to lag behind adult therapeutics due to several scientific, ethical, and regulatory challenges. Children are often excluded from clinical trials, leading to widespread off-label drug use without robust evidence of safety or efficacy in pediatric populations. Ethical concerns such as obtaining informed consent and minimizing risk further complicate trial design. Regulatory agencies have implemented specific frameworks to bridge this gap. In the United States, the Pediatric Research

Equity Act (PREA) mandates pediatric assessments for certain new drugs, and the Best Pharmaceuticals for Children Act (BPCA) provides incentives such as extended market exclusivity for conducting pediatric studies.[114,115] The European Union's Paediatric Regulation (EC No 1901/2006) requires Pediatric Investigation Plans (PIPs) for new medicines. Despite these advances, barriers persist, including limited pediatric patient numbers, age-dependent pharmacokinetics, and formulation challenges. Addressing these obstacles is essential to ensure the development of safe and effective therapeutics for children.

Additionally, gaps in predicting drug metabolism and toxicity—particularly in the liver—pose significant challenges in drug development.[116] The underperformance in this area is largely attributed to limited understanding of the mechanisms driving hepatic injury, highlighting the urgent need for more comprehensive and physiologically relevant approaches to assess drug safety.

Another challenge is that the interval between biomarker discovery and clinical utility hinders drug development progress.[117] While there is a focus on identifying biomarkers for various conditions, there often needs to be more clarity in translating these findings into clinically meaningful applications. This highlights the importance of streamlining the drug approval process and enhancing the translational impact of biomarker research to bridge this gap effectively. Furthermore, the gap in predicting drug-drug interactions (DDIs) poses a substantial complexity in drug development, emphasizing the need for robust predictive models to assess the potential interactions of new drug entities.[118] Improving our ability to predict and manage DDIs is crucial for ensuring the safety and efficacy of drug therapies.

The lack of proactive drug development is evident in infectious diseases, particularly in addressing emerging viral diseases such as COVID-19.[119] The reactive nature of drug development in response to emerging infectious diseases underscores the need for a more proactive approach to shorten the gap between identifying new diseases and developing effective treatments. Additionally, gaps in understanding the ontogeny of drug metabolism and transport present challenges in predicting drug disposition, especially in vulnerable populations like children and the elderly.[120] The reactive nature of drug development in response to emerging infectious diseases underscores the need for a more proactive approach to shorten the gap between identifying new diseases and developing effective treatments. Additionally, gaps in understanding the ontogeny of drug metabolism and transport present challenges in predicting drug disposition, especially in vulnerable populations like children and the elderly.[121] This gap accentuates the importance of addressing fundamental gaps in disease pathophysiology to drive practical drug discovery efforts. Moreover, gaps in drug design and discovery for diseases like the Ebola virus showcase the potential of computational tools in advancing target-based drug design.[122]

In conclusion, the gaps in drug development are multifaceted and span various stages of the drug discovery and development process. They are not challenges that we can afford to ignore. Addressing these gaps requires a concerted and immediate effort from researchers, industry stakeholders, regulatory bodies, and funding agencies. By implementing innovative strategies, leveraging emerging technologies, and enhancing collaboration, we can drive impactful and efficient drug development efforts, underlining the urgency and importance of the issue.

To bridge the innovation gap and overcome funding limitations in drug development, actionable strategies are needed. Public–private partnerships (PPPs) have proven effective. For example, the Innovative Health Initiative (IHI) a €2.4 billion joint undertaking by the European Union and pharmaceutical industry brings together stakeholders from academia, industry, regulators, and patient organizations to accelerate health innovation.[123] In the United States, the Accelerating Medicines Partnership (AMP) supports cross-sector collaboration in fields such as Alzheimer's disease, type 2 diabetes, ALS, and schizophrenia, facilitating the discovery and validation of biomarkers.[124] These partnerships offer standardized frameworks, pooled resources, and data-sharing mechanisms that enhance translational efficiency. Additionally, open-access datasets like AMP-PD democratize research participation and support reproducibility. Regulatory tools such as the FDA's Biomarker Qualification Program (BQP) provide structured processes for developing biomarkers as validated drug development tools.

4. 2. Unlocking the Potential: How AI/ML are Revolutionizing Drug Development

The 20th anniversary of the completion of the draft human genome sequence was observed in 2021, exemplifying a significant milestone that has revolutionized genomics research and generated a substantial amount of genomic data. Genomics research is projected to produce between 2 and 40 exabytes of data in the next decade.[125] With this giant data, AI/ML have emerged as powerful tools in bridging the gaps in genomics by facilitating the integration of complex data sets, enabling more accurate predictions, and enhancing decision-making processes in various fields such as clinical diagnostics, agriculture, oncology, and personalized medicine. The application of AI in genomics has been highlighted in several studies, showcasing its potential to revolutionize the way genetic information is analyzed and utilized.[22,126–128] By leveraging AI technologies, researchers can overcome challenges in understanding genome evolution, function, and disease mechanisms, ultimately leading to groundbreaking discoveries.[129]

In clinical and genomic diagnostics, AI has been instrumental in linking image-derived phenotypes to their genetic origins, offering insights into disease mechanisms and potential treatments.[22] This imaging and genomic data integration can potentially enhance diagnostic accuracy and personalized treatment strategies. Moreover, in the context of precision medicine, AI plays a crucial role in analyzing genomic determinants along with patient symptoms and clinical history to enable personalized diagnosis and prognostication.[130] Moreover, AI applications to medical images, such as MRI classification tasks for neurological and psychiatric diseases[131], have demonstrated the potential of AI-based algorithms in clinical diagnosis with high quality and efficiency. These advancements spotlight the transformative impact of AI/ML in enhancing diagnostic capabilities and treatment outcomes across various medical disciplines. Regarding this, by combining genomic data with AI/ML analyses, researchers can identify novel biomarkers, optimize treatment approaches, and improve patient outcomes.

AI is not just a theoretical concept in oncology, but a practical tool that is already delivering tangible benefits. It simplifies the analysis of imaging-genomics data in diseases like glioblastoma[132], thanks to deep learning algorithms that have made significant strides in image recognition and genome analysis. The integration of molecular and imaging signatures through AI technologies offers practical advantages for early cancer detection, diagnosis, and treatment planning. In the cancer immunity, AI-driven approaches have not only opened up new avenues for comprehensive analyses of tumor immunity using genomics, transcriptomics, proteomics, and cytomics, but also led to the emergence of tumor immunomics as a novel discipline.[133] This is a clear example of how AI is shaping the future of oncology. In addition, the application of AI in bridging the gap between genomes and chromosomes, as demonstrated through single-chromosome sequencing (ChromSeq), has provided valuable insights into genome organization and function.[129,134] By overcoming challenges related to genome and chromosome analysis, researchers can advance our understanding of genetic mechanisms and their implications for various biological processes.

The integration of AI in genomics has extended to fields such as cardiology[135] and kidney cancer[136] management, bringing with it a host of practical benefits. AI technologies, such as machine and deep learning algorithms, can model complex interactions, identify new phenotype clusters, and enhance prognostic capabilities, thereby significantly improving patient care and outcomes. In kidney cancer management, AI can analyze radiographic, histopathologic, and genomic data to tailor personalized treatment strategies.[136]

AI/ML are not just reshaping the landscape of drug development but also effectively addressing critical gaps and challenges, providing a reassuring solution to complex problems. Their impact is particularly evident in drug repurposing, where these technologies enable researchers to systematically identify potential leads, thereby accelerating the drug development process and reducing associated risks through computational means.[137] In this manner, AI/ML have been instrumental in rapidly identifying drugs effective against the coronavirus, bridging the gap between repurposed drugs, laboratory testing, and final authorization.[138] The rapid growth of biomedical data, facilitated by advanced experimental technologies, has made AI/ML indispensable tools for drawing meaningful insights and improving decision-making in drug discovery, particularly in central nervous system diseases.[28] Again, during the COVID-19 pandemic, AI algorithms have played a crucial role in surveillance, diagnosis, drug discovery, and vaccine development, enabling the design of sophisticated drug development pipelines that reduce the time and costs associated with traditional methods.[81] However, it is essential to address biases in ML-based algorithms to ensure their robustness and reproducibility for integration into clinical practice.[139] AI has also been instrumental in developing treatment regimens and prevention strategies and advancing drug and vaccine development for COVID-19 and other infectious diseases.[140] In orthodontics and chronic airway diseases like asthma and chronic obstructive pulmonary disease (COPD), AI/ML have demonstrated effectiveness in mining and integrating large-scale medical data for clinical practice, showcasing their potential in improving patient care and treatment outcomes.[25,141]

The application of AI, particularly deep learning, offers opportunities to discover and develop innovative drugs by analyzing vast datasets and predicting potential drug candidates.[42] Internationally renowned experts have identified key challenges in small-molecule drug discovery using AI and have put forward strategies to address them, emphasizing the groundbreaking potential of AI in this critical area.[142] Importantly, regulatory bodies like the FDA have not only recognized, but also strongly endorsed the importance of AI/ML in medical devices. They have defined ML as a system capable of learning from specific tasks through performance tracking[143], providing a solid framework for the integration of AI in healthcare. This robust endorsement from the FDA has led to an increase in the approval of AI/ML-based medical devices in the USA and Europe. The FDA, for instance, has actively participated in the approval process of over 60 AI-equipped medical devices[144], indicating a growing trend toward incorporating AI technology into the future of medicine.

ML contributes to the automation of various stages in the traditional drug development pipeline. This is evident in studies such as that of Li et al.[145] and Vatansever et al.[28] As for antibiotic discovery, AI has emerged as a powerful ally, accelerating the identification of novel antimicrobial agents, as highlighted in studies like that of Melo et al.[146] By applying AI to computer-aided drug design, we can expedite the discovery of antibiotics and antimicrobial peptides, addressing the global challenge of antibiotic resistance. This is a crucial task that our collective ML research has significantly advanced. By integrating natural language processing (NLP) in AI, we can scan vast amounts of literature to identify potential drug targets. At the same time, AI-driven synthesis robots, a testament to our shared vision, enable the exploration of new reaction spaces to discover novel drug candidates. This automation, a result of our combined expertise, accelerates the drug discovery process and enhances the reproducibility of chemical reactions, leading to the discovery of new compounds with therapeutic potential.

Furthermore, the advancements in AI-driven drug discovery, as discussed in studies like those of Zhavoronkov et al.[87], have not only paved the way for innovative approaches to target identification and generative chemistry but also hold the promise of a brighter future for clinical pharmacology. By leveraging AI/ML trends, researchers can enhance target identification processes, optimize small-molecule drug discovery, and evaluate clinical trial outcomes with greater accuracy and efficiency. These developments can potentially transform the field of clinical pharmacology, offering new avenues for enhancing drug development and therapeutic interventions and instilling a sense of optimism for the future.

Concisely, when harnessed collaboratively, AI/ML can usher in a new era in the pharmaceutical industry. They have the potential to address key gaps in the process, such as expediting drug discovery, optimizing lead compounds, and enhancing clinical outcomes, offering innovative solutions to longstanding challenges. By utilizing these technologies, researchers can significantly improve the efficiency and effectiveness of drug development, ultimately discovering novel treatments for various diseases. However, further research and collaboration, in which each stakeholder plays a crucial role, are imperative to fully realize this potential. As AI continues to evolve, its impact on drug development is poised to revolutionize the field and pave the way for more effective and personalized therapeutic interventions.

4. 3. Overpowering Restraints in AI-Aided Drug Development

The transformative potential of AI in revolutionizing the discovery of new materials is not just tremendous but also holds the promise of developing materials with tailored properties for diverse applications, sparking optimism for the future of pharmaceutical research. However, it's crucial to recognize and address the challenges and limitations to ensure its practical application.[147]

One significant challenge is the necessity for high-quality data, as AI algorithms heavily depend on data for accurate predictions.[148] The interpretability of AI-driven drug discovery processes is another critical limitation, as researchers often need help comprehending how AI algorithms reach conclusions and recommendations.[149] Moreover, the sustainability of resources is a growing concern due to the significant computational resources and data required for AI techniques.[150] Additionally, the current methods and tools may only partially exploit the potential of AI in drug discovery.[151] Overcoming challenges related to data quality, interpretability, resource sustainability, and tool development is not just important, but essential for maximizing the benefits of AI in revolutionizing the drug discovery process. Moreover, one of the other issues is Ethics. Regarding ethical issues in IA regulation, the EU Council recently proclaimed that member states have acknowledged the "Artificial Intelligence Law," which will establish the world's first comprehensive rules for artificial intelligence.[152]

It is crucial to emphasize the importance of addressing challenges in AI-aided drug development. By implementing strategies based on insights from reputable sources, we can overcome these challenges and maximize the benefits of AI in revolutionizing the drug discovery process. The use of specific AI models, such as deep learning and natural language processing, has become crucial for expediting the drug development process and reducing failures.[44] These AI-powered language models have demonstrated potential in assisting drug discovery and development by summarizing advancements and providing computational tools for efficiently identifying new compounds.[78] Additionally, AI/ML, including neural networks and decision trees, have proven to be essential tools for deriving meaningful insights and enhancing decision-making in drug discovery, particularly in diseases such as central nervous system disorders.[28]

Moreover, AI, in collaboration with human expertise, plays a crucial role in facilitating rational drug design, aiding decision-making processes, personalizing therapies, and effectively managing clinical data for future drug development.[76] By incorporating advancements in computer-aided drug design, automated synthetic chemistry, and high-throughput biological screening, initiatives like the NCATS ASPIRE program aim to explore novel chemical spaces more efficiently and cost-effectively. This underscores the importance of human-AI collaboration in maximizing the potential of AI in drug development.[153] Figure 4 summarizes critical applications of AI in both genomics and clinical domains, such as data integration, variant detection, biomarker discovery, and drug repurposing, underscoring its broad utility in precision medicine.

Overall, while AI offers significant potential in drug development, it's important to acknowledge and address potential risks and limitations. These include the need for large, diverse, and high-quality datasets, to avoid **ancestral bias,** which can result in reduced predictive accuracy for underrepresented populations.[154] Another challenge is **model interpretability**: many deep-learning systems remain "black boxes," limiting clinical adoption. For example, recent explainable AI techniques such as *concept-whit-*

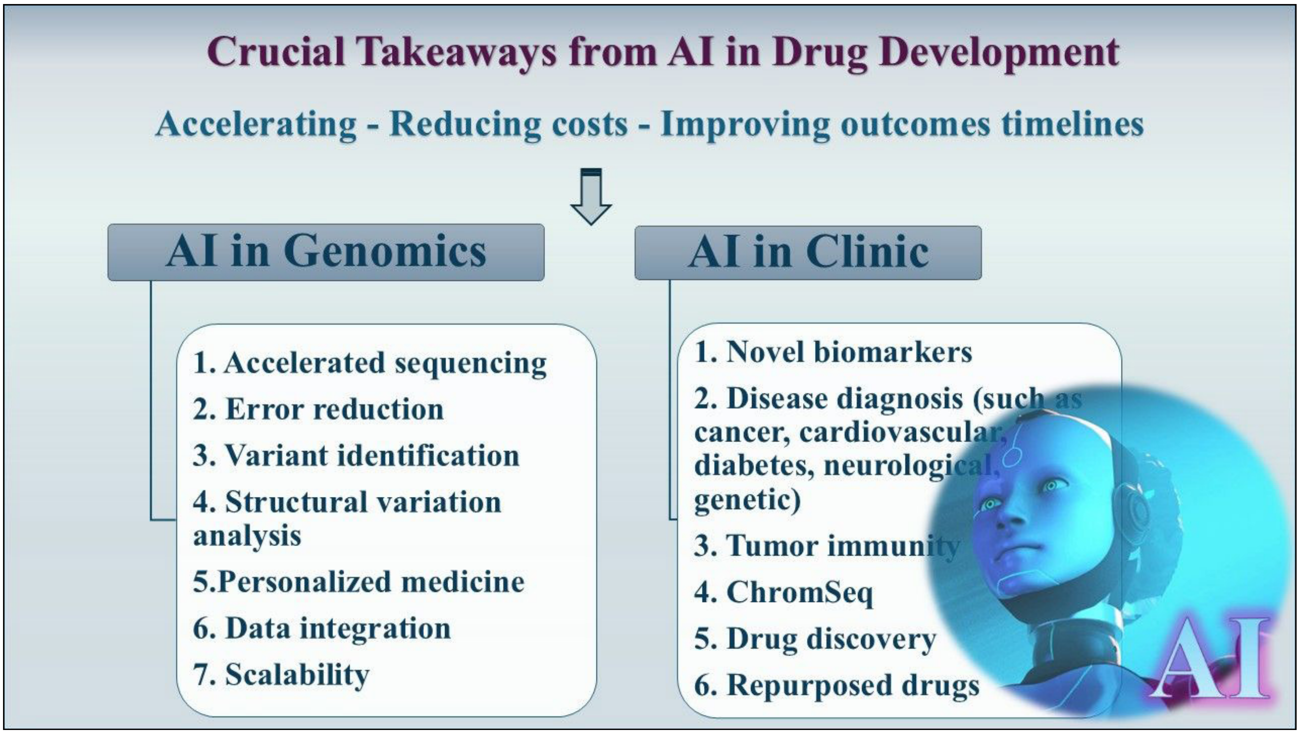

Fig 4. Summary of artificial intelligence applications in drug development, highlighting key contributions in genomics (e.g., data integration, variant analysis) and clinical contexts (e.g., biomarker discovery, disease diagnosis, and drug repurposing).

ening applied in graph neural networks reveal which molecular features drive predictions, thereby enhancing transparency.[155] Additionally, **generalizability between datasets** remains imperfect: models validated on public benchmarks often perform poorly when applied to proprietary or real-world datasets, underscoring the need for rigorous cross-platform validation.[156,157]

By proactively addressing these challenges through explainable frameworks, ancestry-aware model training, and broad validation pharmaceutical researchers can fully leverage AI's promise while maintaining safety, fairness, and confidence in the drug development process.

5. Conclusion

The integration of advanced Technologies particularly AI and ML, computational modeling, and HTS has significantly reshaped the landscape of modern drug development. These tools have demonstrated concrete progress in AI-driven target identification, lead compound optimization, and early-stage ADMET profiling. Together, they contribute to reduced development timelines, improved cost efficiency, and lower failure rates in clinical phases.

Furthermore, emerging *in vitro* 3D models, organoids, and improved *in vivo* models have enhanced translational relevance, thereby bridging the gap between preclinical findings and clinical outcomes. Despite these advancements, challenges remain particularly in areas such as pediatric drug development, biomarker validation, and the development of ethical and regulatory frameworks for the integration of AI.

Future research directions should focus on enhancing the interpretability of AI algorithms, integrating multi-omics datasets for comprehensive decision-making, and developing standardized, reproducible workflows for early-stage evaluation. These efforts will further solidify the role of computational and AI-based systems in delivering safe, effective, and patient-centered therapeutics.

Author's contribution NB, NE, UC, YT: Conceptualization, Formal analysis, Investigation, Methodology, Supervision, Writing - review & editing.

Declarations

Funding

None.

Data availability

No datasets were generated or analyzed during the current study.

Conflict of interest

The authors declare no competing interests.

Ethical approval

Not applicable.

Consent to participate
Not applicable.

Consent to publish
Not applicable.

6. References

1. A. B. Deore, J. R. Dhumane, R. Wagh, R. Sonawane, *Asian J. Pharm. Res. Dev.* **2019**, *7*(6), 62–67. **DOI:**10.22270/ajprd.v7i6.616
2. S. M. Paul, D. S. Mytelka, C. T. Dunwiddie, C. C. Persinger, *Nat. Rev. Drug Discov.* **2010**, *9*(3), 203–214. **DOI:**10.1038/nrd3078
3. W. Fang, S. Wang, X. Gou, *Biophysics Reports*. **2021**, *7*(6), 504–516. **DOI:**10.52601/bpr.2021.210042
4. J. A. DiMasi, H. G. Grabowski, R. W. Hansen, *J. Health Econ.* **2016**, *47*, 20–33. **DOI:**10.1016/j.jhealeco.2016.01.012
5. O. J. Wouters, M. McKee, J. Luyten, *Jama*. **2020**, *323*(9), 844–853. **DOI:**10.1001/jama.2020.1166
6. A. Sertkaya, T. Beleche, A. Jessup, B. D. Sommers, *JAMA Netw. Open.* **2024**, *7*(6), e2415445–e2415445. **DOI:**10.1001/jamanetworkopen.2024.15445
7. G. O. Elhassa, K. O. Alfarouk, *J. Pharmacovigil.* **2015**, *3*(3), 1000e14. **DOI:**10.4172/2329-6887.1000e141
8. C. P. Bourdonnec, P. A. Carrupt, J. M. Scherrmann, S. Martel, *Pharm. Res.* **2013**, *30*(11), 2729–2756. **DOI:**10.1007/s11095-013-1119-z
9. F. Cheng, W. Li, G. Liu, Y. Tang, *Curr. Top. Med. Chem.* **2013**, *13*(11), 1273–1289. **DOI:**10.2174/15680266113139990033
10. J. Dong, N. N. Wang, Z. J. Yao, L. Zhang, Y. Cheng, D. Ouyang, A. P. Lu, D. S. Cao, *J. Cheminform.* **2018**, *10*(1), 29. **DOI:**10.1186/s13321-018-0283-x
11. W. Amelo, E. Makonnen, *Biomed. Research Intl.* **2021**, *1*, 5539544. **DOI:**10.1155/2021/5539544
12. G. Biala, E. Kedzierska, M. Kruk-Slomka, J. Orzelska-Gorka, S. Hmaidan, A. Skrok, J. Kaminski, E. Havrankova, D. Nadaska, I. Malik, *Pharmaceuticals*. **2023**, *16*(9), 1283. **DOI:**10.3390/ph16091283
13. B. Siddalingappa, G. V. Betageri, *Acta Pharm. Sin. B.* **2014**, *4*(1), 3–17. **DOI:**10.1016/j.apsb.2013.12.003
14. J. Chen, Z. Z. Gu, Y. Xu, M. Deng, L. Lai, J. Pei, *Protein Sci.* **2023**, *32*(2), e4555. **DOI:**10.1002/pro.4555
15. Y. Wang, J. Xing, X. Yue, N. Zhou, J. Peng, Z. Xiong, X. Liu, X. Luo, C. Luo, K. Chen, M. Zheng, H. Jiang, *Q. Rev. Biophys.* **2015**. *48*(4), 488–515. **DOI:**10.1017/S0033583515000190
16. S. Alqahtani, *Expert Opin. Drug Metab. Toxicol.* **2017**, *13*(11), 1147–1158. **DOI:**10.1080/17425255.2017.1389897
17. A. E. L. Aissouq, M. Bouachrine, A. Ouammou, F. Khalil, *Turkish J. Chem.* **2022**, *46*(3), 687–703. **DOI:**10.55730/1300-0527.3360
18. T. Banerjee, R. Siebert, *South. Econ. J.* **2017**, *84*(1), 202–228. **DOI:**10.1002/soej.12221
19. D. Delcassian, A. K. Patel, A. B. Cortinas, R. Langer, *J. Drug Target.* **2018**, *27*(3), 229–243. **DOI:**10.1080/1061186X.2018.1438440
20. D. V. Voronin, A. Abalymov, Y. I. Svenskaya, M. V. Lomova, *Int. J. Mol. Sci.* **2021**, *22*(17), 9149. **DOI:**10.3390/ijms22179149
21. J. P Huges, S. Rees, S. B. Kalindjian, K. L. Philpott, *Br. J. Pharmacol.* **2011**, *162*(6), 1239–1249. **DOI:**10.1111/j.1476-5381.2010.01127.x
22. R. Dias, A. Torkamani, *Genome Med.* **2019**, *11*(1), 70. **DOI:**10.1186/s13073-019-0689-8
23. R. Poplin, P. C. Chang, D. Alexander, S. Schwartz, T. Colthurst, A. Ku, D. Newburger, J. Dijamco, N. Nguyen, P. T. Afshar, et al., *Nat. Biotechnol.* **2018**, *36*(10), 983–987. **DOI:**10.1038/nbt.4235
24. J. Jumper, R. Evans, A. Pritzel, T. Green, M. Figurnov, O. Ronneberger, K. Tunyasuvunakool, R. Bates, A. Žídek, A. Potapenko, et al., *Nature.* **2021**, *596*(7873), 583–589. **DOI:**10.1038/s41586-021-03819-2
25. Y. Feng, Y. Wang, C. Zeng, H. Mao, *Int. J. Med. Sci.* **2021**, *18*(13), 2871. **DOI:**10.7150/ijms.58191
26. N. A. Molfino, G. Turcatel, D. Riskin, *Adv. Ther.* **2024**, *41*(2), 534–552. **DOI:**10.1007/s12325-023-02743-3
27. A. Ray, J. Das, S. E. Wenzel, *Cell Reports Med.* **2022**, *3*(12), 100857. **DOI:**10.1016/j.xcrm.2022.100857
28. S. Vatansever, A. Schlessinger, D. Wacker, H. Ü. Kanıskan, J. Jin, M. Zhou, B. Zhang, *Med. Res. Rev.* **2020**, *41*(3), 1427–1473. **DOI:**10.1002/med.21764
29. R. Hamamoto, M. Komatsu, K. Takasawa, K. Asada, S. Kaneko, *Biomolecules*. **2019**, *10*(1), 62. **DOI:**10.3390/biom10010062
30. J. Xu, P. Yang, S. Xue, B. Sharma, M. Sánchez-Martín, F. Wang, K. Beaty, E. Dehan, B. Parikh, *Hum. Genet.* **2019**, *138*(2), 109–124. **DOI:**10.1007/s00439-019-01970-5
31. C. W. L. Ho, K. Caals, *Semin. Nephrol.* **2021**, *41*(3), 282–293. **DOI:**10.1016/j.semnephrol.2021.05.009
32. F. Ugolini, E. Pasqualini, S. Simi, G. Baroni, D. Massi, *Cancers.* **2022**, *14*(15), 3682. **DOI:**10.3390/cancers14153682
33. S. Park, C. Ock, H. Kim, S. Pereira, S. Park, M. Ma, S. Choi, S. Kim, S. Shin, et al., *J. Clin. Oncol.* **2022**, *40*(17), 1916–1928. **DOI:**10.1200/JCO.21.02010
34. Z. Yuan, Y. Li, M. Shi, F. Yang, J. Gao, J. Yao, M. Q. Zhang, *Nat. Commun.* **2022**, *13*(1), 7330. **DOI:**10.1038/s41467-022-34867-5
35. Y. LeCun, Y. Bengio, G. E. Hinton, *Nature*. **2015**, *521*(7553), 436–444. **DOI:**10.1038/nature14539
36. E. R. Parra, A. Francisco-Cruz, I. I. Wistuba, *Cancers.* **2019**, *11*(2), 247. **DOI:**10.3390/cancers11020247
37. D. B. Johnson, J. Bordeaux, J. Kim, C. Vaupel, D. L. Rimm, T. H. Ho, R. W. Joseph, A. Daud, R. M. Conry, et al., *Clin. Cancer Res.* **2018**, *24*(21), 5250–5260. **DOI:**10.1158/1078-0432.CCR-18-0309
38. H. Xu, F. Cong, T. H. Hwang, *Eur. Urol. Focus* **2021**. *7*(4), 706–709. **DOI:**10.1016/j.euf.2021.07.006
39. Y. Gui, X. He, J. Yu, J. Jing, *J. Clin. Med.* **2023**. *12*(4), 1279. **DOI:**10.3390/jcm12041279
40. J. Wu, D. Lin, *Adv. Anat. Pathol.* **2021**, *28*(6), 439–445. **DOI:**10.1097/PAP.0000000000000322

41. G. Wan, Z. Maliga, B. Yan, T. Vallius, Y. Shi, S. Khattab, C. Chang, A. J. Nirmal, K. H. Yu, et al., *Brief. Bioinform.* **2023**, *25*(3), bbae189. **DOI:**10.1101/2023.11.10.566378
42. X. Yang, Y. Wang, R. Byrne, G. Schneider, S. Yang, *Chem. Rev.* **2019**, *119*(18), 10520–10594. **DOI:**10.1021/acs.chemrev.8b00728
43. A. S. Rifaioglu, H. Ataş, M. J. Martin, R. Cetin-Atalay, V. Atalay, T. Doğan, *Brief. Bioinform.* **2018**, *20*(5), 1878–1912. **DOI:**10.1093/bib/bby061
44. S. J. Y. Macalino, V. Gosu, S. Hong, S. Choi, *Arch. Pharm. Res.* **2015**. *38*(9),1686–1701. **DOI:**10.1007/s12272-015-0640-5
45. K. B. Dar, A. H. Bhat, S. Amin, R. Hamid, S. Anees, S. Anjum, B. A. Reshi, M. A. Zargar, A. Masood, S. A. Ganie, *Curr. Top. Med. Chem.* **2019**, *18*(31), 2702–2719. **DOI:**10.2174/1568026619666190119150741
46. L. L. G. Ferreira, R. N. dos Santos, G. Oliva, A. D. Andricopulo, *Molecules* **2015**. *20*(7), 13384–13421. **DOI:**10.3390/molecules200713384
47. M. A. Pak, D. N. Ivankov, *Bioinformatics* **2022**, *38*(18), 4312–4320. **DOI:**10.1093/bioinformatics/btac515
48. C. Yang, E. A. Chen, Y. Zhang, *Molecules* **2022**, *27*(14), 4568. **DOI:**10.3390/molecules27144568
49. F. Stanzione, I. Giangreco, J. C. Cole, *Prog. Med. Chem.* **2021**, *60*, 273–343. **DOI:**10.1016/bs.pmch.2021.01.004
50. I. Hoque, A. Chatterjee, S. Bhattacharya, R. Biswas, *Int. J. Adv. Res. Biol. Sci.* **2017**, *4*(2), 60–71. **DOI:**10.22192/ijarbs.2017.04.02.009
51. J. Vázquez, M. López, E. Gibert, E. Herrero, F. J. Luque, *Molecules*. **2020**, *25*(20), 4723. **DOI:**10.3390/molecules25204723
52. T. Oliveira, M. Silva, E. Maia, A. Silva, A. Taranto, *Drugs Drug Candidates*. **2023**, *2*(2), 311–334. **DOI:**10.3390/ddc2020017
53. D. Vemula, P. Jayasurya, V. Sushmitha, Y. N. Kumar, V. Bhandari, *Eur. J. Pharm. Sci.* **2023**, *181*, 106324. **DOI:**10.1016/j.ejps.2022.106324
54. L. Zhao, H. L. Ciallella, L. M. Aleksunes, H. Zhu, *Drug Discov. Today.* **2020**, *25*(9), 1624–1638. **DOI:**10.1016/j.drudis.2020.07.005
55. E. N. Muratov, J. Bajorath, R. P. Sheridan, I. V. Tetko, D. Filimonov, V. Poroikov, T. I. Oprea, I. I. Baskin, A. Varnek, A. Roitberg, et al., *Chem. Soc. Rev.* **2020**, *49*(11), 3525–3564. **DOI:**10.1039/D0CS00098A
56. N. A. Murugan, G. R. Priya, G. N. Sastry, S. Markidis, *Drug Discov. Today*. **2022**, *27* (7), 1913–1923. **DOI:**10.1016/j.drudis.2022.05.013
57. F. Gentile, J. C. Yaacoub, J. Gleave, M. Fernandez, A. T. Ton, F. Ban, A. Stern, A. Cherkasov, *Nat. Protoc.* **2022**, *17*(3), 672–697. **DOI:**10.1038/s41596-021-00659-2
58. J. M. Stokes, K. Yang, K. Swanson, W. Jin, A. Cubillos-Ruiz, N. M. Donghia, C. R. MacNair, S. French, L. A. Carfrae, Z. Bloom-Ackermann, et al., *Cell.* **2020**, *180*(4), 688–702. **DOI:**10.1016/j.cell.2020.04.001
59. L. L. G. Ferreira, A. D. Andricopulo, *Drug Discov. Today.* **2019**, *24*(5), 1157–1165. **DOI:**10.1016/j.drudis.2019.03.015
60. H. Tian, R. Ketkar, P. Tao, *J. Mol. Model.* **2022**, *28*(12), 408. **DOI:**10.1007/s00894-022-05373-8
61. G. Xiong, Z. Wu, J. Yi, L. Fu, Z. Yang, C. Hsieh, M. Yin, X. Zeng, C. Wu, A. Lu, X. Chen, T. Hou, D. Cao, *Nucleic Acids Res.* **2021**, *49*(W1), W5–W14. **DOI:**10.1093/nar/gkab255
62. S. N. Mali, H. K. Chaudhari, *Open Pharm. Sci. J.* **2018**, *5* (1), 12–23. **DOI:**10.2174/1874844901805010012
63. D. E. Marin, I. Taranu, *Toxins*. **2023**, *15*(7), 421. **DOI:**10.3390/toxins15070421
64. S. Fatima, P. Gupta, S. Sharma, A. Sharma, S. M. Agarwal, *Future Med. Chem.* **2020**, *12*(1), 69–87. **DOI:**10.4155/fmc-2019-0206
65. J. C. Madden, S. Webb, S. J. Enoch, H. E. Colley, C. Murdoch, R. Shipley, P. Sharma, C. Yang, M. T. D. Cronin, *Comput. Toxicol.* **2017**, *3*, 44–57. **DOI:**10.1016/j.comtox.2017.07.001
66. Z. Lin, W. C. Chou, *Toxicol. Sci.* **2022**, *189*(1), 7–19. **DOI:**10.1093/toxsci/kfac075
67. F. Kelleci Çelik, G. Karaduman, *J. Chem. Inf. Model.* **2023**, *63*(15), 4602–4614. **DOI:**10.1021/acs.jcim.3c00687
68. L. Elend, L. Jacobsen, T. Cofala, J. Prellberg, T. Teusch, O. Krämer, I. A. Solov'yov, *Molecules* **2022**, 27(13), 4020. **DOI:**10.3390/molecules27134020
69. Z. J. Baum, X. Yu, P. Y. Ayala, Y. Zhao, S. P. Watkins, Q. Zhou, *J. Chem. Inf. Model.* **2021**, *61*(7), 3197–3212. **DOI:**10.1021/acs.jcim.1c00619
70. D. P. Tran, S. Tada, A. Yumoto, A. Kitao, Y. Ito, T. Uzawa, K. Tsuda, *Sci. Rep.* **2021**, *11*, 10630. **DOI:**10.1038/s41598-021-90245-z
71. K. Terayama, M. Sumita, R. Tamura, K. Tsuda, *Acc. Chem. Res.* **2021**, *54*(6), 1334–1346. **DOI:**10.1021/acs.accounts.0c00713
72. M. Meuwly, *Chem. Rev.* **2021**, *121*(16), 10218–10239. **DOI:**10.1021/acs.chemrev.1c00033
73. J. Zhang, D. Chen, Y. Xia, Y. Huang, X. Lin, X. Han, N. Ni, Z. Wang, F. Yang, L. Yang, Y. Yang, Y. Q. Gao, *J. Chem. Theory Comput.* **2023**, *19*(14), 4338–4350. **DOI:**10.1021/acs.jctc.3c00214
74. J Xu, X. Ye, Z. Lv, Y. H. Chen, X. S. Wang, *Chem. A. Eur. J.* **2024**, *30*(26), e202304279. **DOI:**10.1002/chem.202304279
75. Y. Elbaz, D. Furman, M. C. Toroker, *Adv. Funct. Mater.* **2019**, *30*(18), 1900778. **DOI:**10.1002/adfm.201900778
76. R. Srivastava, *Density Functional Theory-Recent Advances, New Perspectives and Applications*. **2022**, 83–91. **DOI:**10.5772/intechopen.99018
77. C. Selvaraj, I. Chandra, S. K. Singh, *Mol. Divers.* **2021**,*26*(3), 1893–1913. **DOI:**10.1007/s11030-021-10326-z
78. Z. Liu, R. Roberts, X. Chen, R. Huang, W. Tong, *Drug Discov. Today.* **2021**, *26*(11), 2593–2607. **DOI:**10.1016/j.drudis.2021.06.009
79. M. Archer, S. Germain, *Int. J. Digit. Heal.* **2021**, *1*(1), 5. **DOI:**10.29337/ijdh.31
80. M. Y. Shaheen, *SciOpen Prepr.* **2021**, 1–8. **DOI:**10.14293/S2199-1006.1.SOR-.PPVRY8K.v1
81. G. Arora, J. Joshi, R. S. Mandal, N. Shrivastava, R. Virmani, T. Sethi, *Pathogens*. **2021**, *10*(8), 1048. **DOI:**10.3390/pathogens10081048
82. Y. Fu, H. Zhang, E. D. Morris, C. K. Glide-Hurst, S. Pai, A. Traverso, L. Wee, I. Hadzic, P. Lønne, C. Shen, T. Liu, X. Yang, *Plasma Med. Sci.* **2022**, *6*(2), 158–181.

DOI:10.1109/TRPMS.2021.3107454

83. A. Majeed, S. O. Hwang, *Symmetry.***2021,** *14*(1), 16. **DOI:**10.3390/sym14010016
84. J. Jiménez-Luna, F. Grisoni, N. Weskamp, G. Schneider, *Expert Opin. Drug Discov.* **2021**, *16*(9), 949–959. **DOI:**10.1080/17460441.2021.1909567
85. D. J. Griffin, C. W. Coley, S. A. Rank, J. M. Hawkins, K. F. Jensen, *Org. Process Res. Dev*. **2023**, *27*(11), 1868–1879. **DOI:**10.1021/acs.oprd.3c00229
86. A. Sahoo, G. M. Dar, *Appl. Biol. Chem*. J. **2021**, *2*(2), 34–48. **DOI:**10.52679/tabcj.2021.0007
87. A. Zhavoronkov, Q. Vanhaelen, T. I. Oprea, *Clin. Pharmacol. Ther.* **2020**, *107*(4), 780–785. **DOI:**10.1002/cpt.1795
88. Y. Wu, L. Ma, X. Li, J. Yang, X. Rao, Y. Hu, J. Xi, L. Tao, J. Wang, L. Du, et al., *Front. Pharmacol.* **2024**, *15*, 1459954. **DOI:**10.3389/fphar.2024.1459954
89. T. Khinvasara, N. Tzenios, A. Shanker, *J. Complement. Altern. Med. Res.* **2024**, *25*(7), 108–122. **DOI:**10.9734/jocamr/2024/v25i7552
90. G. Schneider, *Nat. Rev. Drug Discov.* **2018**, *17*(2), 97–113. **DOI:**10.1038/nrd.2017.232
91. S. Kant, Deepika, S. Roy, *Discov. Pharm. Sci.* **2025**, *1*(1), 7. **DOI:**10.1007/s44395-025-00007-3
92. O. Pelkonen, M. Turpeinen, H. Raunio, *Clin. Pharmacokinet.* **2011**, *50*(8), 483–491. **DOI:**10.2165/11592400-000000000-00000
93. W. Zhou, H. Han, X. Sun, X. Guo, J. Wen, X. Zhao, *Front. Pharmacol.* **2025**, *16*, 1552741. **DOI:**10.3389/fphar.2025.1552741
94. L. D. Shultz, F. Ishikawa, D. L. Greiner, *Nat. Rev. Immunol.* **2007**, *7*(2), 118–130. **DOI:**10.1038/nri2017
95. S. N. Bhatia, D. E. Ingber, *Nat. Biotechnol.* **2014**, *32*(8), 760–772. **DOI:**10.1038/nbt.2989
96. N. Bilgic, G. G. Duran, *J. Essent. Oil Bear. Plants* **2020**, *23*(6), 1283–1295. **DOI:**10.1080/0972060X.2020.1866681
97. N. Besli, G. Yenmis, M. Tunçdemir, E. Yaprak Sarac, S. Doğan, S. Solakoğlu, G. Kanigur Sultuybek, *Turkish J. Biochem.* **2020**, *45*(3), 295–304. **DOI:**10.1515/tjb-2019-0197
98. H. Ecevit, K. Gunduz, N. Bilgic, M. Izmirli, B. Gogebakan, *Adv. Mod. Oncol. Res.* **2017**, *3*(1), 15. **DOI:**10.18282/amor.v3.i1.170
99. G. Yenmiş, N. Beşli, E. Yaprak Saraç, F. S. Hocaoğlu Emre, K. Şenol, G. Kanıgür, *Turk. J. Med. Sci.* **2021**, *51*(2), 826–834. **DOI:**10.3906/sag-1908-112
100. A. T. Jannuzzi, A. M. Yilmaz Goler, D. Shilkar, S. Mondal, V. N. Basavanakatti, H. Yıldırım, M. Yıldız, H. Çelik Onar, N. Bayrak, V. Jayaprakash, A. F. TuYuN, *Chem. Biol. Drug Des.* **2023**, *102*(5), 1133–1154. **DOI:**10.1111/cbdd.14314
101. S. A. Langhans, *Front. Pharmacol.* **2018**, *9*. **DOI:**10.3389/fphar.2018.00006
102. L. A. Struzyna, M. L. Watt, *Mol. Pharmacol.* **2021**, *99*(4), 256–265. **DOI:**10.1124/molpharm.120.000142
103. S. Saeidnia, A. Manayi, M. Abdollahi, *Pros and Cons. Curr. Drug Discov. Technol.* **2015**, *12*(4), 218–224. **DOI:**10.2174/1570163813666160114093140
104. C. Tang, T. Prueksaritanont, *Pharm. Res.* **2010**, *27*(9), 1772–1787. **DOI:**10.1007/s11095-010-0157-z
105. P. Mukherjee, S. Roy, D. Ghosh, S. K. Nandi, *Lab. Anim. Res.* **2022**, *38*(1), 18. **DOI:**10.1186/s42826-022-00128-1
106. M. Pellegatti, *Expert Opin. Drug Metab. Toxicol.* **2012**, *8*(2), 161–172. **DOI:**10.1517/17425255.2012.652084
107. J. J. Xu, P. V. Henstock, M. C. Dunn, A. R. Smith, J. R. Chabot, D. de Graaf, *Toxicol. Sci.* **2008**, *105*(1), 97–105. **DOI:**10.1093/toxsci/kfn109
108. F. Liu, X. Zhuang, C. Yang, Z. Li, S. Xiong, Z. Zhang, J. Li, C. Lu, Z. Zhang, *Biopharm. Drug Dispos.* **2014**, *35*(5), 296–307. **DOI:**10.1002/bdd.1897
109. P. Bloomingdale, V. A. Nguyen, J. Niu, D. E. Mager, *J. Pharmacokinet. Pharmacodyn.* **2018**, *45*(1), 159–180. **DOI:**10.1007/s10928-017-9567-4
110. B. Fermini, S. T. Coyne, K. P. Coyne, *Slas Discov.* **2018**, *23*(8), 765–776. **DOI:**10.1177/2472555218775028
111. S. T. Cole, *Philos. Trans. R. Soc. B Biol. Sci.* **2014**, *369*(1645), 20130430. **DOI:**10.1098/rstb.2013.0430
112. A. M. Tsimberidou, *Pharmacol.* **2015**, *76*(6), 1113–1132. **DOI:**10.1007/s00280-015-2861-1
113. K. W. Kathy Cheung, B. D. Van Groen, G. J. Burckart, L. Zhang, S. Huang, *J. Clin. Pharmacol.* **2019**, *59*, 56–69. **DOI:**10.1002/jcph.1489
114. M. B. Bernhardt, H. Lindsay, W. Allen-Rhoades, J. H. Foster, *Pediatr. Blood Cancer* **2021**, *68*(3), e28871. **DOI:**10.1002/pbc.28871
115. Pediatric Research Equity Act | PREA | FDA. https://www.fda.gov/drugs/development-resources/pediatric-research-equity-act-prea (accessed 2025-07-21).
116. K. Fraser, D. M. Bruckner, J. S. Dordick, *Chem. Res. Toxicol.* **2018**, *31*(6), 412–430. **DOI:**10.1021/acs.chemrestox.8b00054
117. C. Bime, S. M. Camp, N. G. Casanova, R. C. Oita, J. Ndukum, H. Lynn, J. G. N. Garcia, *Transl. Res.* **2020**, *226*, 105–115. **DOI:**10.1016/j.trsl.2020.06.010
118. M. Shebley, H. J. Einolf, *Clin. Pharmacol. Ther*. **2019**, *105*(6). **DOI:**10.1002/cpt.1394
119. R. M. Meganck, R. S. Baric, *Nat. Med.* **2021**, *27*(3), 401–410. **DOI:**10.1038/s41591-021-01282-0
120. B. D. Van Groen, K. Allegaert, D. Tibboel, *Br. J. Clin. Pharmacol.* **2020**, *88*(10), 4285–4296. **DOI:**10.1111/bcp.14534
121. A. F. Francisco, S. Jayawardhana, F. J. Olmo, M. D. Lewis, S. R. Wilkinson, M. C. Taylor, J. M. Kelly, *Molecules.* **2020**, *25*(12), 2799. **DOI:**10.3390/molecules25122799
122. M. Balmith, M. Faya, S. M. E. Soliman, *Chem. Biol. Drug Des*. **2016**, *89*(3), 297–308. **DOI:**10.1111/cbdd.12870
123. E. Vaudano, *Front. Med.* **2025**, *12*, 1554948. **DOI:**10.3389/fmed.2025.1554948
124. B. Nelson, M. E. Shenton, S. W. Woods, (AMP®SCZ), A. M. P. *Schizophrenia* **2025**, *11*(1), 62. **DOI:**10.1038/s41537-025-00605-1
125. Artificial Intelligence, Machine Learning and Genomics. https://www.genome.gov/about-genomics/educational-resources/fact-sheets/artificial-intelligence-machine-learning-and-genomics, Accesion date: 22.05.2024.
126. K. Asada, S. Kaneko, K. Takasawa, H. Machino, S. Takahashi, N. Shinkai, R. Shimoyama, M. Komatsu, R. Hamamo-

to, *Front. Oncol.* **2021**, *11*, 666937. **DOI:**10.3389/fonc.2021.666937

127. I. Tunali, R. J. Gillies, M. B. Schabath, *Perspect. Med.* **2021**, *11*(8), a039537. **DOI:**10.1101/cshperspect.a039537
128. S. Aneja, E. Chang, A. Omuro, *Curr. Opin. Neurol.* **2019**, *32*(6), 850–856. **DOI:**10.1097/WCO.0000000000000761
129. J. E. Deakin, S. Potter, R. J. O'Neill, A. Ruiz-Herrera, M. de Bello Cioffi, M. D. B. Eldridge; K. Fukui, J. A. Marshall Graves, D. K. Griffin, F. Grützner, et al., *Genes*. **2019**, *10*(8), 627. **DOI:**10.3390/genes10080627
130. K. B. Johnson, W. Wei, D. Weeraratne, M. E. Frisse, K. E. Misulis, K. Rhee, J. Zhao, J. L. Snowdon, *Clin. Transl. Sci.* **2020**, *14*(1), 86–93. **DOI:**10.1111/cts.12884
131. Z. Zhang, G. Li, Y. Xu, X. Tang, *Diagnostics* **2021**, *11*(8), 1402. **DOI:**10.3390/diagnostics11081402
132. D. Liu, J. Chen, X. Hu, K. Yang, Y. Liu, G. Hu, H. Ge, W. Zhang, H. Liu, *Front. Oncol.* **2021**, *11*, 699265. **DOI:**10.3389/fonc.2021.699265
133. Y. Xu, G. H. Su, D. Ma, Y. Xiao, Z. M. Shao, *Signal Transduct. Target. Ther.* **2021**, *6*(1), 312. **DOI:**10.1038/s41392-021-00729-7
134. A. Iannucci, A. Makunin, A. Lisachov, C. Ciofi, R. Stanyon, M. Svartman, V. A. Trifonov, *Genes*. **2021**, *12*(1), 124. **DOI:**10.3390/genes12010124
135. A. Sammani, A. F. Baas, F. W. Asselbergs, A. S. J Riele, *J. Clin. Med.* **2021**, *10*(5), 921. **DOI:**10.3390/jcm10050921
136. M. Lee, S. Wei, J. Anaokar, R. Uzzo, A. Kutikov, *Curr. Opin. Urol.* **2021**, *31*(4), 409–415. **DOI:**10.1097/MOU.0000000000000881
137. Z. Tanoli, M. Vähä-Koskela, T. Aittokallio, *Expert Opin. Drug Discov.* **2021**, *16*(9), 977–989. **DOI:**10.1080/17460441.2021.1883585
138. S. Mohanty, H. A. Rashid, M. Mridul, C. Mohanty, S. Swayamsiddha, *Diabetes Metab. Syndr. Clin. Res. Rev.* **2020**, *14*(5), 1027–1031. **DOI:**10.1016/j.dsx.2020.06.068
139. M. E. Laino, A. Ammirabile, A. Posa, P. Cancian, S. Shalaby, V. Savevski, E. Neri, *Diagnostics.* **2021**, *11*(8), 1317. **DOI:**10.3390/diagnostics11081317
140. M. Senthilraja, *Slas Technol.* **2021**, *26*(2), 123–126. **DOI:**10.1177/2472630320983813
141. Y. M. Bichu, I. Hansa, A. Y. Bichu, P. Premjani, C. Flores-Mir, N. R. Vaid, *Prog. Orthod.* **2021**, *22*(1), 18. **DOI:10.1186/s40510-021-00361-9**
142. P. Schneider, W. P. Walters, A. T. Plowright, N. Sieroka, J. Listgarten, R. A. Goodnow, J. Fisher, J. M. Jansen, J. S. Duca, T. S. Rush, M. Zentgraf, et al., *Nat. Rev. Drug Discov*. **2019**, *19*(5), 353–364. **DOI:**10.1038/s41573-019-0050-3
143. U. J. Muehlematter, P. Daniore, K. N. Vokinger, *Lancet Digit. Health.* **2021**, *3*(3), e195–e203. **DOI:**10.1016/S2589-7500(20)30292-2
144. R. Hamamoto, K. Suvarna, M. Yamada, K. Kobayashi, N. Shinkai, M. Miyake, M. Takahashi, S. Jinnai, R. Shimoyama, et al., *Cancers*. **2020**, *12*(12), 3532. **DOI:**10.3390/cancers12123532
145. C. Li, G. Gandhi, J. M. Lee, W. W. Yeng Yeo, S. B. Choi, *Int. J. Mol. Sci.* **2021**, *22*(16), 8962. **DOI:**10.3390/ijms22168962
146. M. C. R. Melo, J. R. M. Maasch, C. de la Fuente-Núñez, *Commun. Biol.* **2021**, *4*(1), 1050. **DOI:**10.1038/s42003-021-02586-0
147. A. Blanco-Gonzalez, A. Cabezon, A. Seco-Gonzalez, D. Conde-Torres, P. Antelo-Riveiro, A. Pineiro, R. Garcia-Fandino, *Pharmaceuticals* **2023**, *16*(6), 891. **DOI:**10.3390/ph16060891
148. T. T. Van Tran, A. S. Wibowo, H. Tayara, K. T. Chong, *J. Chem. Inf. Model.* **2023**, *63*(9), 2628–2643. **DOI:**10.1021/acs.jcim.3c00200
149. K. K. Kırboğa, S. W. Abbasi, E. U. Küçüksille, *Chem. Biol. Drug Des*. **2023**, 102(1), 217–233. **DOI:**10.1111/cbdd.14262
150. M. Li, J. Zhang, *Chem. Sci*. 2023, *14*(39), 10628–10630. **DOI:**10.1039/D3SC90185H
151. K. Yang, *J. Chem. Inf. Model.* **2024**, *64*(8), 2941–2947. **DOI:**10.1021/acs.jcim.3c01979
152. Artificial Intelligence Act: MEPs Adopt Landmark Law. https://www.europarl.europa.eu/news/en/press-room/20240308IPR19015/artificial-intelligence-act-meps-adopt-landmark-law, Accesion date: 24-05-2024.
153. K. K. Duncan, D. D. Rudnicki, C. P. Austin, D. A. Tagle, *Front. Robot. Ai.* **2020**, *6*, 1–6. **DOI:**10.3389/frobt.2019.00143
154. L. A. Smith, J. A. Cahill, J.-H. Lee, K. Graim, *Nat. Commun.* **2025**, *16*(1), 2144. **DOI:**10.21203/rs.3.rs-3168446/v1
155. M. Proietti, A. Ragno, B. La Rosa, R. Ragno, R. Capobianco, *Mach. Learn.* **2024**, *113*(4), 2013–2044. **DOI:**10.1007/s10994-023-06369-y
156. M. A. Pramudito, Y. N. Fuadah, A. I. Qauli, A. Marcellinus, K. M. Lim, *Sci. Rep.* **2024**, *14*(1), 24045. **DOI:**10.1038/s41598-024-71169-w
157. Q. Ding, R. Yao, Y. Bai, L. Da, Y. Wang, R. Xiang, X. Jiang, F. Zhai, *Drug Des. Devel. Ther.* **2025**, 4501–4516. **DOI:**10.2147/DDDT.S525171

Povzetek

Postopek odkrivanja zdravil tradicionalno dolgotrajen in drag proces, vendar doživlja revolucijo z vključevanjem inovativnih pristopov. V tem članku smo povzeli, kako sodobne tehnike pospešujejo odkrivanje in razvoj zdravil ter hkrati znatno zmanjšujejo stroške. Osredotočamo se na močno sinergijo bioinformatike, umetne inteligence (UI) in visokozmogljivega testiranja (HTS). Bioinformatika pomaga pri identifikaciji in potrjevanju tarč zdravil z analizo obsežnih genomskih in proteomskih podatkovnih zbirk. UI izboljšuje identifikacijo in optimizacijo spojin vodnic s pomočjo napovednega modeliranja in algoritmov strojnega učenja, kar močno skrajša čas, potreben za te faze. HTS omogoča hitro pregledovanje obsežnih knjižnic spojin za odkrivanje potencialnih kandidatov za zdravila. Pristopi, ki temeljijo na UI, kot sta HTS in napovedno modeliranje, izboljšujejo odločanje v zgodnjih fazah, zmanjšujejo poskuse in napake ter prispevajo k stroškovni učinkovitosti skozi celoten proces. Poleg tega napredek v računalniški kemiji in simulacijah molekulske dinamike omogoča globlji vpogled v interakcije med zdravilom in tarčo, kar dodatno pospešuje načrtovanje učinkovitih in selektivnih spojin. Pri odkrivanju zdravil kandidate testirajo v laboratorijskih in živalskih modelih, da se oceni njihova učinkovitost, farmakokinetika in varnost. Z vključevanjem predkliničnih metod se lahko učinkovitost in uspešnost odkrivanja zdravil bistveno izboljšata, kar vodi do učinkovitejših in varnejših zdravil. Ta pregled poudarja pomembno vlogo računalniških tehnologij v sodobnem razvoju zdravil ter raziskuje njihove obetavne implikacije za prihodnje raziskave in klinično uporabo.

Scientific paper

HPLC-DAD Analysis, Antioxidant and Antibacterial Properties of Fruit Extracts from *Pistacia atlantica* Desf.

Younes Douffa[1], Karima Saffidine[1*], Nour Elhouda Belabes[1], Nadjet Azzi[1], Haifaa Laroui[1], Hafsa Silini Cherif[2], Thoraya Guemmaz[1], Fatima Zerargui[1] and Abderahmane Baghiani[1]

[1] *Laboratory of Applied Biochemistry, Faculty of Nature and Life sciences, University Ferhat Abbas Setif1, Setif 19000, Algeria*

[2] *Laboratory of Applied Microbiology, Department of Microbiology, Faculty of Natural and Life, Ferhat Abbas Setif1 University, Setif 19000, Algeria*

* *Corresponding author: E-mail: saffidinekarima@gmail.com*

Received: 05-09-2025

Abstract

Pistacia atlantica is commonly used in traditional medicine to treat various diseases in Algeria. This study was carried out to investigate the antioxidant potential and antibacterial properties of fruit extracts. The results indicated various amounts of polyphenols and flavonoids in different extracts. Quercetin, gallic acid, chlorogenic acid and methyl gallate were the dominant constituents in the ethyl acetate extract (EAE) and crude extract (CrE) quantified by HPLC-DAD. EAE was the most active in scavenging DPPH and hydroxyl ($OH^\cdot$) radicals, hydrogen peroxide (H_2O_2), reducing power and total antioxidant capacity. All extracts have the ability to inhibit lipid peroxidation. A broad spectrum of antibacterial effects (10.66 to 29.33 mm) was obtained. In addition, the time-kill assay and the MBC/MIC ratio indicated that all extracts were bactericidal against most of the test bacteria and their combination with antibiotics showed remarkable synergistic effect. The findings of this study suggest that medicinal plant is a potential source of natural antioxidant and antibacterial compounds, which could be used where these kinds of activities are warranted.

Keywords: *Pistacia atlantica*; HPLC-DAD; Antioxidant; Antibacterial activity.

1. Introduction

Oxidative stress is a common factor in the genesis of several human diseases such as cancer, Alzheimer's, inflammation, arthritis, diabetes, atherosclerosis and Parkinson's disease.[1] This becomes a major area of research, motivating the scientists to look for more therapeutic plants which provide health benefits for human health. In recent decades, there is more interest in natural antioxidants, which mainly have phenolic structure known for their potential to trap frees radicals produced as a result of diverse degradations and disease processes.[2] These phytochemicals have been recognized as safer with fewer side effects than synthetic oxidants, thus reducing the risk of chronic diseases.[3] Furthermore, bacterial infections represent a major public health, that impact millions of individuals every year. Antibiotics are commonly employed to treat microbial infections; however, the high significant genetic variation of harmful pathogens, enable them to acquire resistance to these drugs.[4] This led to a decline in the effectiveness of current antibacterial medications, rendering them less useful or entirely powerless. The increase in multidrug-resistant (MDR) bacteria highlights the necessity of exploring plant-derived products for finding new treatment alternatives and innovative antimicrobial medications. Phenolic compounds are well-known to effectively reduce the damage caused by free radicals and fight off parasites and pathogenic bacteria.[5]

Pistacia atlantica Desf. (Atlas pistachio) commonly known as "Betoum" in Arabic, is one of the plants traditionally used in the treatment of human ailments since ancient times. Atlas pistachio is a tree belonging to the *Anacardiaceae* family, a rare endemic and threatened with extinction species found in the semi-aride, aride and even saharan regions in Algeria.[6] This tree of 3–5 meters produces small unisexual flowers and spherical red drupe fruits with 5 to 6 mm in size. Different parts of this plant (fruits and leaves) are widely used in traditional medicine to treat respiratory and digestive systems, throat infections, heal wounds, heart, kidneys, dyspepsia and peptic ulcer.[7] Scientific research has also revealed many pharmacological activities such as antioxidant, antimicrobial, antihyperglycemic, anti-inflammatory, analgesic, anti-carcinogenic and anti-cholinesterase.[8] Most of these activities are linked to the content of the secondary metabolites of this plant.[9] The main objectives of this study were to estimate the phenolic and flavonoid content, and to evaluate the antioxidant potential as well the antibacterial effect of the hydro-methanolic extract and its fractions from *P. atlantica*.

2. Materials and Methods

2. 1. Plant Material

Fresh fruits of atlas pistachio (*Pistacia atlantica* Desf. 1977) were collected in September 2023, from Tamanrasset situated in the far southern Algerian Sahara. The plant was identified by Professor Chermat Sabah, Department of Pharmacy, Faculty of Medicine, University Setif1Ferhat Abbas, Algeria. The Fruits were cleaned and allowed to dry at room temperature in a shaded area. Then, dry seeds were ground into a powder using electric mill.

2. 2. Extraction Procedure

The hydro-methanolic extract of *P. atlantica* was prepared according to Saffidine *et al.*[10], with slight modification. 500 g of fine powder were macerated with 5000 mL in water-methanol (1: 9) under magnetic agitation for 15 min at 80 °C. The mixture was left to macerate for 7 days. It was then filtered on cotton and filter paper Whatman n° 3. This process was repeated twice again. The filtrates were combined and evaporated at 40 °C in a rotary evaporator under decreased pressure. The residual extract was dried in an oven and stored in refrigerator until use. The percentage yield of this dried crude hydro methanolic extract (CrE) was obtained using the following equation:

$$\text{Yield of extract (\%)} = (w1/w2) \times 100$$

where **w1** is the weight of the extract residue after solvent removal and **w2** is the weight of dried plant powder.

The crude extract (CrE) of *P. atlantica* fruits was fractionated using solvents with increasing polarity, including petroleum ether, ethyl acetate. 25 g of dry extract was suspended in 200 mL of boiling distilled water and let to decant in the refrigerator for 30 min, then filtered through filter paper. First, the aqueous solution was fractionated with petroleum ether to remove lipids, then with ethyl acetate. Three fractions were obtained after this process: petroleum ether (PEE) and ethyl acetate (EAE) and residual aqueous fraction (AqE). These fractions were allowed to dry at 37 °C in an oven after being evaporated at 40 °C under reduce pressure using a rotary evaporator. After that, the dried fractions were stored in a refrigerator until further tests.

2. 3. Determination of Total Phenolic Content (TPC)

P. atlantica extracts were subjected to Folin-Ciocalteu (FC) method to measure the total phenolic content (TPC).[11] This process is based on the reaction of the phenol compounds with the FC reagent (complex of phosphomolybdic and phosphotungstic acids) and the blue color that results is correlated with amount of polyphenols. 200 μL of extracts or Gallic acid as standard (0–200 μg/mL) was mixed with 1 mL of FC reagent (1/10). After 4 min, 800 μL of sodium carbonate (7.5%) was added and the mixture was incubated for 2 hours at room temperature. Then, the absorbance was measured at 765 nm. TPC was expressed in milligrams of Gallic Acid Equivalent per gram of dry extract (mg GAE/g DE).

2. 4. Determination of Total Flavonoid Content (TFC)

Total flavonoid content (TFC) of different extracts was determined using the aluminum chloride ($AlCl_3$) assay.[12] In the presence of aluminum chloride, free hydroxyl groups of flavonoids gave a yellowish complex which is proportional to the quantity of flavonoids presents in the extract. 1 mL of samples or quercetin (0–40 μg/mL) as standard was mixed with 1 mL of $AlCl_3$ solution (2%). The mixture was incubated at room temperature for 10 min and the absorbance was measured at 430 nm. The result was expressed as micrograms of quercetin equivalent per milligrams of dry extract (μg EQ/mg of extract).

2. 5. HPLC-DAD Analysis

Characterization and quantification of phenolic compounds in CrE and EAE extracts of *P. atlantica* was carried out by High performance Liquid Chromatography with Diode Array Detection (HPLC-DAD) method used in this study and was adapted from the protocol established by Gheraibia *et al.* (2020),[13] using an Agilent 1260 series. The separation was carried out using Zorbax Eclipse Plus C8 column (4.6 mm × 250 mm, 5 μm). The mobile phase consisted of solvent A (water) and solvent B (0.05% trifluoroacetic acid in acetonitrile) at a flow rate 0.9 mL/min. The mobile phase was programmed consecutively in a linear gradient as follows: 0 min (82% A); 0–1 min (82% A); 1–11 min (75% A); 11–18 min (60% A); 18–22 min (82% A); 22–24 min (82% A). The multi-wavelength detector was monitored at 280 nm. The injection volume was 5 μL for samples and standards solutions and the column temperature was maintained at 40 °C.

2. 6. Antioxidant Activity

2. 6. 1. DPPH Scavenging Assay

DPPH is a stable free radical commonly used to assess the radical scavenging activity of plant extract due to its high sensitivity. This assay is based on the measurement of the capacity of the extracts to scavenge this free radical. In the presence of antioxidant, the stable radical 2,2-diphenyl-1-picrylhydrazyl (DPPH) losses its characteristic dark purple color and is reduced to yellow diphenylpicril hydrazine. The method consisted in mixing 50 μL of different concentrations of extracts or butyl hydroxytoluene (BHT) as standard with 1250 μl of DPPH solution (0.004% in methanol).[14] After incubation for 30 min in the dark at room temperature, absorbance was measured at 517 nm. The synthetic antioxidant butyl hydroxytoluene (BHT) was used as positive control. Antiradical activity (AR) was calculated using the following equation:

$$AR\ (\%) = [(A_0 - A_1)/A_0] \times 100$$

were $\mathbf{A_0}$ is the absorbance of the solution containing only DPPH radical solution. $\mathbf{A_1}$ is the absorbance of the DPPH solution in the presence of the sample. The IC_{50} value is the concentration of the sample required to scavenge 50% of DPPH free radical.

2. 6. 2. Hydroxyl Radical ($HO^{\bullet}$) Scavenging Assay

This assay was performed based on the method described by Mayouf[15], with few modifications. The reaction mixture consists of 150 μL of extracts or standard (vitamin C) at different concentrations, mixed with 300 μL of a stock solution containing ferric sulfate ($FeSO_4$ 9 mM) and hydrogen peroxide (0.3%). The reaction between $FeSO_4$ and H_2O_2 lead to the generation of hydroxyl radicals according to the Fenton reaction. The mixture was incubated for 15 min at 32 °C. Then 75 μL of salicylic acid (20 mM) was added to the reaction mixture, which was incubated again for 15 min at 32 °C. The absorbance was measured at 562 nm.

2. 6. 3. Hydrogen Peroxide (H_2O_2) Scavenging Assay

The capacity of the extracts to scavenge H_2O_2 is based on the reaction of ferrous ion (Fe^{+2}) with 1,10-phenanthroline, which forms red-orange tri-phenanthroline complex, indicating a potent radical scavenging of H_2O_2 in the media. This assay was performed by mixing 63 μL of ferrous ammonium sulfate (1 mM) with 375 μL of different concentrations of extracts or standard.[16] Then, 16 μL of hydrogen peroxide (5 mM) was added to the mixture and incubated at room temperature in the dark for 5 min. After that, 375 μL of 1,10- phenanthroline (1 mM) was added and incubated again for 10 min. The absorbance of the solution was read at 510 nm. Hydrogen peroxide scavenging activity (HPSA) was calculated according to the following equation:

$$HPSA\ (\%) = (A\ sample/A\ control) \times 100$$

A sample: absorbance of the sample.
A control: absorbance of the control.

2. 6. 4. Reducing Power Assay

This assay is based on the capacity of the extracts to reduce the ferric iron of the ferricyanide complex-Fe^{3+} to ferrous iron-$Fe^{2+}$of blue color. 100 μL of different dilutions of extracts or standard were added to 100 μL phosphate buffer (pH 6.6) and 100 μL potassium ferricyanide (1%). The mixture was incubated at 50 °C for 20 min, followed by addition of 250 μL of trichloroacetic acid TCA (10%) and centrifuged for 10 min at 3000 rpm. Then, 250 μL of the upper layer solution was mixed with 250 μL of distilled water and 500 μL of 0.1% ferric chloride solution ($FeCl_3$). The absorbance was determined at 700 nm against a blank. Ascorbic acid (vitamin C) was used as the standard. The effective concentration (EC_{50}) at which the absorbance reaches 0.5, was used as reducing capacity potential of the extract.[10]

2. 6. 5. Total Antioxidant Capacity (TAC)

Total antioxidant activity of plant extracts was estimated by phosphomolybdenum assay.[17] When antioxidants in the sample reduce the molybdenum complex, a green-colored complex is produced. 100 μL of plant extract or Trolox as standard in different concentrations were added to 1 mL of reagent solution containing 0.6 M sulfuric acid, 28 mM sodium phosphate and 4 mM ammonium molybdate. The mixture was incubated for 90 min at 95 °C. After the solutions had cooled to room temperature, the absorbance was then measured at 695 nm.

2. 6. 6. Lipid Peroxidation Inhibition

The ferric thiocyanate (FTC) method was used to determine the antioxidant property of extracts in lipid like-system.[18] The ferrous iron (Fe^{2+}) is converted to ferric iron (Fe^{3+}) by a hydroperoxides (LOOH) produced when linoleic acid is oxidized. The resultant ions (Fe^{3+}) then combine with thiocyanate to form a red complex that has a maximum absorbance at 500 nm. The emulsion was prepared by mixing 155 μL of linoleic acid and 0.2804 g of Tween 20 in 50 mL of phosphate buffer (0.02 M at pH 7.0). After that, 0.5 mL of extract solution or standard (BHT) was mixed with 2.5 mL of linoleic acid emulsion and incubated for 5 days at 37 °C. A volume (0.1 mL) of the reaction mixture was mixed with 4.7 mL of ethanol (75%) and 0.1 mL of ammonium thiocyanate (30%). Then, 0.1 mL

$FeCl_3$ (0.02 M in 3.5% HCl) was added. The absorbance at 500 nm was measured 3 min later after adding ferrous chloride to the reaction mixture. This procedure was repeated each day. The inhibition of lipid peroxidation was determined for each day using the following formula:

$$\% \text{ inhibition} = (Ac - As / Ac) \times 100$$

where **Ac** is the absorbance of the control reaction and **As** is the absorbance of the sample.

2. 6. 7. Thiobarbituric Acid (TBA) Method

This assay was conducted at the last day of the FTC method to detect the formation of the malondialdehyde (MDA), the final product formed during the oxidation of linoleic acid MDA forms a pink complex with TBA.[19] A volume of 1 mL from the incubated combination of linoleic acid emulsion and extract was added to 2 mL of a 20% solution of trichloroacetic acid (TCA) and 2 mL thiobarbituric acid solution TBA (0.67%). This resulting mixture was subjected to a boiling water bath for 10 min, and once it had cooled down, it was centrifuged at 3000 rpm for 20 min. The supernatant's absorbance was measured at 532 nm.

2. 7. Antibacterial Activity

2. 7. 1. Bacterial Strains

The antibacterial activity was evaluated using referenced strains ATCC (American Type Culture Collection): *Escherichia coli* (ATCC 25922), *Pseudomonas aeruginosa* (ATCC 27853), *Staphylococcus aureus* (ATCC 25923) and clinical strains: *Escherichia coli* 982, *Pseudomonas aeruginosa 982*, *Klebsiella pneumoniae* 982, *Staphylococcus aureus* 995, *Streptococcus pneumonia* 990 acquired from Laboratory of Bacteriology at Setif hospital. Other referenced strains: *Bacillus cereus* (ATCC 10876), *Salmonella typhimurium* (ATCC 13311), *Enterococcus faecalis* (ATCC 49452), *Citrobacter freundii* (ATCC 8090), *Klebsiella pneumoniae* (ATCC 700603), *Listeria monocytogenes* (ATCC 15313) and *Proteus mirabilis* (ATCC 35659) obtained from Laboratory of Natural Substances at the University of Tlemcen, Algeria.

2. 7. 2. Agar Well Diffusion Assay

The antibacterial susceptibility of the tested bacteria to different extracts of *P. atlantica* was evaluated using the agar well diffusion method.[20] Mueller-Hinton agar medium was autoclaved and poured into the Petri dishes. The suspension of each strain from young colonies of 18 to 24 hours was made in nutrient broth and its concentration was adjusted to 0.5 McFarland (10^8 CFU/mL). After that, the inoculums of various bacteria were spread over the surface of Mueller Hinton agar, and four wells of 6 mm in diameter were punched off into the agar medium with sterile cork borer. Three of these wells were filled with 50 μL of extract and the fourth well was poured with 50 μL of sterile distilled water as negative control. The plates were kept for 1 hour at room temperature to allow the diffusion of extracts, and then incubated at 37 °C for 24 h. The results were obtained by measuring the diameter of inhibition zones around the wells. Standard antibiotic discs Cefotaxime (CTX) was used as positive control against *E. coli*, *K. pneumoniae*, *L. monocytogenes*, *C. freundii*. Imipenem (IPM) was used for *B. cereus*, Amoclan (AMC) for *E. faecalis* and *P. mirabilis*. Bactrim (SXT), Oxacillin (OXA), Ceftazidime (CAZ) were tested respectively on *S. typhimurium, S. aureus* and *P. aeruginosa*.

2. 7. 3. Determination of Minimum Inhibitory Concentration (MIC) and Minimum Bactericidal Concentration (MBC).

The minimum inhibitory concentration (MIC) was assessed for plant extracts exhibiting antibacterial activity, by broth microdilution method using 96 wells microplates.[21] A two-fold serial dilution of the extract was prepared in the 10 wells of sterile microplate containing 25 μL Mueller Hinton nutrient broth. The inoculums of the bacterial strains were preparing from fresh cultures of 18 to 24 hours. The turbidity was adjusted to 0.5 McFarland (10^8 CFU/mL) and then these suspensions were diluted (1/10). 5 μL of it were inoculated into all wells except the 11th well which is considered as negative control and the 12th as growth positive control. Subsequently, 70 μL of Mueller Hinton medium was added to 96 wells. The microplates were incubated at 37 °C for 24 hours and MIC was defined as the lowest concentration of the extract displaying no visible growth of the tested microorganism. To determine MBC, 2 μL from each well that did not exhibit any growth was inoculated in parallel streaks of 3 cm on Mueller-Hinton agar plates, and then we incubated at 37 °C for 24 hours. The number of bacterial colonies on the streaks was compared with that on the control plate, which contained the streaks of the diluted inoculums (10^{-1}, 10^{-2}, 10^{-3} and 10^{-4}) of the bacteria. MBC was defined as the lowest concentration of the extract at which the bacterial growth was totally inhibited. The ratio between MBC and MIC was calculated. When this MBC/MIC is less than 4, the extract is considered as bactericidal against the tested strains; while a ratio above 4 means that the extract is bacteriostatic.

2. 7. 4. Time-dependent Antibacterial Activity

The impact of contact time on the antibacterial activity of *P. atlantica* extracts was determined using the spread plate method.[22] The bacterial strain suspensions were prepared from a fresh culture incubated for 18 to 24 hours, with a concentration of 10^6–10^7 CFU/mL. 100 μL of each bacterial suspension were incubated with 10 mL of the extract dissolved in nutrient broth at 200 rpm in a shaker incubator for 2 and 4 hours. After the period incubation, series of 10-fold dilutions were carried out on the combination of the suspension and extract. Then, 100 µL of each dilution was spread onto agar plates, which were incubated for 24 hours at 37 °C. The results were expressed by counting the colonies and comparing them with the control plate to estimate the inhibition activity. The following formula was used to calculate the percentage loss of bacterial viability (LV):

$$LV (\%) = (Nc – Nt) / Nc * 100$$

Nc: the number of colonies in the control plates.
Nt: the number of colonies in the treated plates.

2. 7. 5. Synergistic Antibacterial Assay

To assess the synergistic antibacterial activity, *P. atlantica* extracts were combined with standard antibiotics using disc diffusion method. 20 µL of each extract was dispensed on the antibiotic disk, and then placed on the surface of Mueller-Hinton agar inoculated with the tested bacteria. The plates were incubated at 37 °C for 24 hours and the zones of inhibition produced by the single standard or by the plant extract in combination with standard antibiotics were measured.[21] Synergism is interpreted as when zone of combination > zone of standard antibiotic; if zone of combination = zone of standard antibiotic, it means indifference and if zone of combination < zone of standard antibiotic, it is interpreted as antagonism.

2. 8. Statistical Analysis

All the tests were performed in triplicates. Results are expressed as mean ± standard deviation. Statistical evaluation was conducted with Graph Pad 8. ANOVA one way was employed to establish basic comparison. The differences were statistically considered significant at $P < 0.05$

3. Results and Discussions

3. 1. Yield, Total Phenols and Flavonoids Content of *P. atlantica* Extracts

In the present study, the yield percentage of the different extracts, total phenolic (TPC) and flavonoids (TFC) content are presented in table 1. The result of extraction yield of *P. atlantica* fruits showed that the maximum percent of 67.32 and 22.04% was obtained by aqueous (AqE) and petroleum ether (PEE) extracts, followed by crude (CrE) and ethyl acetate (EAE) extracts.

Table 1. Yield (%), total phenolic and flavonoids content (TPC and TFC) of fruit extracts from *P. atlantica*: crude extract (CrE), petroleum ether (PEE), ethyl acetate (EAE) and aqueous (AqE) fractions. Values are mean ± SD (n = 3). Different superscript letters indicate significant difference within column ($P < 0.05$).

Extract	Yield %	TPC (mg GAE/g)	TFC (µg QE/mg)
CrE	11.58^{c}	145.45±3.49^{b}	35.05±0.04^{b}
PEE	22.04^{b}	45.60±3.404^{c}	11.62±0.59^{d}
EAE	4.08^{d}	266.34±15.50^{a}	62.7±0.42^{a}
AqE	67.3^{2}a	115.64±3.244^{d}	12.77±0.07^{c}

Total phenolic (TPC) and flavonoid (TFC) contents showed significant differences in plant fruit extracts. Thus, the highest amount of TPC and TFC was recorded with EAE (266.34 ± 15.50 mg GAE/g and 62.7 ± 0.42 µg QE/mg), followed by CrE, AqE and PEE.

The differences in the yield of various extracts may be due to the characteristics of the solvent or the nature of phenolic compounds that have being extracted.[23] Moreover, the synthesis of these compounds is influenced by several factors including light, temperature, humidity and nutrient availability.[24] Our results are in agreement with several other studies that demonstrate that *P. atlantica* fruit extracts contain a significant amount of these phenolic compounds.[25,26]

3. 2. HPLC Analysis

The identification and quantification of *P. atlantica* phenolic compounds were performed using HPLC-DAD analysis. The amount and retention time of the identified compounds are presented in table 2 and supplementary information.

15 compounds were identified in each extract with various concentrations. Quercetin (19818.42 µg/g), gallic acid (12871.49 µg/g), chlorogenic acid (3960.28 µg/g) and methyl gallate (3619.76 µg/g) were the dominant constituents in CrE. However, other compounds including rutin, ellagic acid, coumaric acid, syringic acid, coffeic acid and kaempferol were present in moderate concentration, while lowest concentration was showed with vanillin, naringenin, rosmarinic acid, daidzein and ferulic acid. EAE was characterized by high amount of gallic acid (47539.53 µg/g), methyl gallate (31376.82 µg/g), quercetin (28824.60 µg/g) and chlorogenic acid (12184.13 µg/g); followed by ellagic acid, coumaric acid, syringic acid, naringenin, vanillin and daidzein with moderate concentration. Many studies have shown that these phenolic compounds have beneficial effects on human health, owing to their biological activities including antioxidant, anti-inflammatory and antibacterial activities.[27]

Table 2. HPLC analysis of phytoconstituents in crude (CrE) and ethyl acetate (EAE) extracts of *P. atlantica*. **RT**: retention time, **C**: concentration.

Peak	**Compounds**	**CrE**		**E–AE**	
		RT (mn)	**C (µg/g)**	**RT (mn)**	**C (µg/g)**
1	Gallic acid	3.535	12871.49	3.531	47539.53
2	Chlorogenic acid	4.267	3960.28	4.245	12184.13
3	Catechin	–	0.00	–	0.00
4	Methyl gallate	5.386	3619.76	5.382	31376.82
5	Coffeic acid	5.715	314.12	–	0.00
6	Syringic acid	6.151	354.21	6.151	2858.16
7	Rutin	6.841	752.98	–	0.00
8	Ellagic acid	7.194	630.08	7.174	6875.11
9	Coumaric acid	8.314	457.08	8.309	3677.68
10	Vanillin	9.124	163.18	9.083	479.28
11	Ferulic acid	9.440	35.28	9.436	156.42
12	Naringenin	10.122	156.56	10.124	1549.28
13	Rosmarinic acid	10.035	62.71	11.699	80.19
14	Daidzein	15.659	42.51	16.176	225.04
15	Quercetin	17.437	19818.42	17.427	28824.60
16	Cinnamic acid	–	0.00	19.041	6.32
17	Kaempferol	20.307	256.78	20.295	23.83
18	Hesperetin	–	0.00	21.088	58.53

3. 3. Antioxidant Activities

3. 3 .1. DPPH Scavenging Assay

The results of DPPH radial scavenging activity are illustrated in table 3. Among the tested extracts, EAE exhibited the strongest DPPH radical scavenging activity with very low IC_{50} (5.59 ± 0.27 µg/ml) more effective than BHT as standard. CrE and AqE also showed a considerable activity. In contrast, PEE displayed the lowest capacity.

Table 3. Radical scavenging activities of different extracts from *P. atlantica* fruits: crude extract (CrE), petroleum ether (PEE), ethyl acetate (EAE) and aqueous (AqE) fractions; and standards (BHT and Vitamin C). Results were expressed as the mean ± SD (n = 3). ns: no significant difference, ***: P < 0.001, ****: P < 0.0001.

Extracts	**DPPH** IC_{50} **µg/ml**	$OH^{\cdot}$ IC_{50}**mg/ml**	H_2O_2 IC_{50} **µg/ml**
CrE	22.35±0.12^{ns}	0.46 ± 0.02***	158.74±1.92****
PEE	439.04±5.79****	3.91 ± 0.04****	745.7±17.88****
EAE	5.59±0.27***	0.50 ± 0.02****	20.56±5.8^{4n}s
AqE	48.48±1.13****	1.55 ± 0.04****	121.14 ± 6.08****
BHT	20.00± 0.11	–	–
Vitamin C	–	0.29 ± 0.01	36.17±5.49

Our results showed that *P. atlantica* from Algeria is more active in scavenging action than the same plant from different area in the world,[26,28,29] and other species including *P. vera*,[30] *P. lentiscus*,[31] and *P. khinjuk*.[32]

3. 3. 2. Hydroxyl Radical ($HO^{\bullet}$) Scavenging Assay

The Hydroxyl radicals ($OH^{\cdot}$) are formed during the metabolic process in cells, known for their extreme reactivity and capability to interact various biomolecules such as lipids, proteins and DNA, causing harm to the organisms. Hence, human health relies on the removal of these free radicals.[33] According to the table 3, CrE and EAE showed the highest scavenging of hydroxyl radical ($OH^{\cdot}$) with IC_{50} of 0.46 ± 0.02 and 0.50 ± 0.02 mg/mL, respectively. However, AqE and PEE exhibited the lowest activities. These results are in accordance with the findings obtained for the different extract from the leaves of *P. atlantica*,[34] and are more notable than those found in other species such as *P. vera*,[31] and *P. lentiscus*,[32] and *P. khinjuk*.[35]

3. 3. 3. Peroxide (H_2O_2) Scavenging Assay

Hydrogen peroxide itself exhibit a low reactivity, due to its capacity to penetrate cell membrane, it can oxidize various intracellular molecules. Furthermore, its reaction with transition metals like iron produces more reactive species such as hydroxyl radicals.[36] This indicates the importance of removing hydrogen peroxide by the antioxidant defense systems. In hydrogen peroxide scavenging assay, EAE showed a potent scavenging capacity with an IC_{50} = 20.56 ± 5.84 µg/mL, exceeding both the standard and the other extracts (table 3). These results represent the first report on hydrogen peroxide scavenging activity of *P. atlantica* fruits extracts, based on our knowledge. Our findings showed that *P. atlantica* extracts possessed a significant antioxidant potential, which may be explained by the presence of phyto–constituents, especially phenolic acids and flavonoids. These phenolic compounds are well-known for their biological properties,[37,38] acting as radical quenchers by donating a hydrogen atom or through electron transfer.[39]

3. 2. 4. Reducing Power Assay

Reducing power assay results are illustrated in figure 1 and indicted that all the extracts possessed the ability to reduce ferric iron. EAE had the strongest reducing activity (EC_{50} = 7.11 ± 0.10 μg/ml), which was similar to that of the standard vitamin C (5.87 ± 0.06 μg/ml), followed by CrE and AqE. The reducing power of these extracts could be related to the presence of the phenolic compounds which act as electron donor in the reduction process.[40,41]

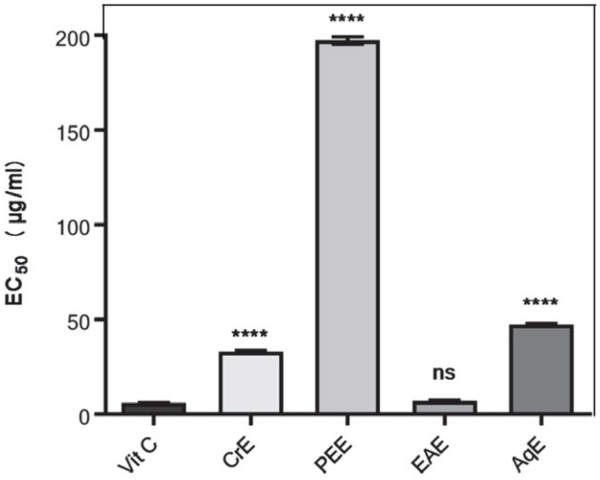

Figure 1. EC_{50} in reducing power of *P. atlantica* extracts: crude extract (CrE), petroleum ether (PEE), ethyl acetate (EAE) and aqueous (AqE) fractions; and the standard (vitamin C). values are expressed as mean ± SD of triplicate. ns: No significant difference, ****: P < 0.0001.

Our results are in agreement with those obtained by Belyagoubi *et al.*[40] and Benmohamed *et al.*[26], but were more effective than those of the study conducted on leaves by Zerkani *et al.*[25]

3. 2. 5. Total Antioxidant Capacity (TAC)

This assay is a quantitative method used to evaluate the sample's ability to reduced phosphate- Mo (VI) to phosphate-Mo (V) through electron or proton donation, during a prolonged incubation at higher temperatures and under acidic conditions.[42,43] According to the results presented in figure 2, EAE showed the strongest antioxidant capacity (EC_{50} = 18.23 ± 0.23 μg/mL) than the other fractions and the standard Trolox. This can be related to the high flavonoids content in this extract. A moderate TAC was exhibited by CrE and AqE.

These results are comparable to that of the study conducted on *P. lentiscus* leaves and seeds.[44] Previous studies have indicated that this plant contain a considerable amount of kaempferol, myricetin, quercetin and its derivatives,[45] which exist in our extracts and these compounds are known for their great capacity as antioxidant.

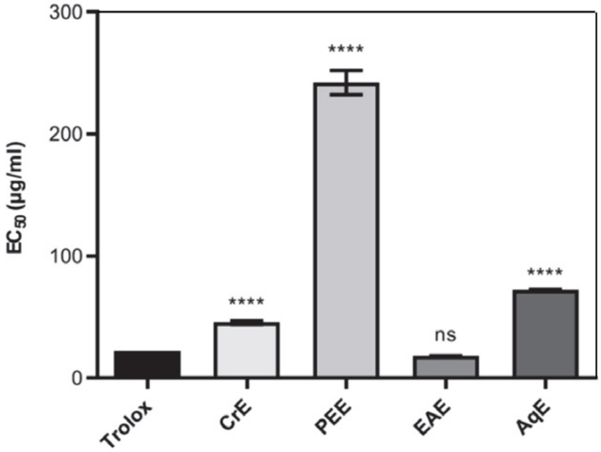

Figure 2. EC_{50} in total antioxidant capacity (TAC) of fruit extracts from *P. atlantica*: crude extract (CrE), petroleum ether (PEE), ethyl acetate extract (EAE) and aqueous (AqE) fractions; and standard (Trolox). Results are mean of 3 replicates values. ns: No significant difference, ****: P < 0.0001.

3. 2. 6. Lipid Peroxidation Inhibition

Lipid peroxidation is a process in which free radicals attack poly-unsaturated lipids in cell membranes, leading to cell damage, which can be inhibited by antioxidants. In this assay, peroxides are formed during the oxidation of linoleic acid and have the ability to oxidize Fe^{2+} to Fe^{3+}. This later forms a red complexe with thiocyanate.[46] The effect of the *P. atlantica* extracts on lipid peroxidation inhibition obtained after five days is represented in figure 3 and showed that EAE and PEE have the highest capacity to inhibit lipid peroxidation with percentage inhibition of 82.86 ± 0.31% and 80.11 ± 2.54%, respectively, and was comparable to that of the standard BHT (81.10 ± 0.68%), followed by CrE (74.83 ± 1.5%).

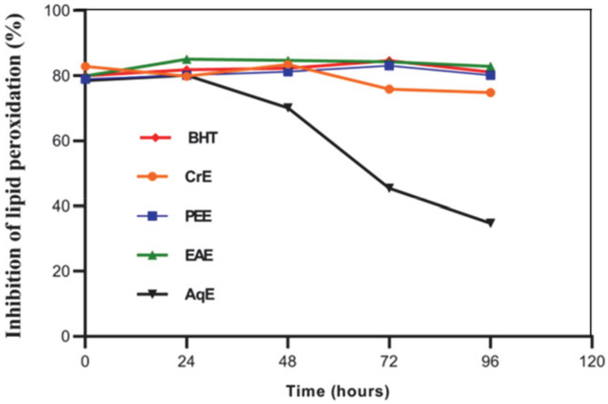

Figure 3. Kinetic of lipid peroxidation inhibition of fruit extracts from *P. atlantica*: crude extract (CrE), petroleum ether (PEE), ethyl acetate extract (EAE) and aqueous (AqE) fractions; and the standard (BHT), at a concentration of 2 mg/mL.

The potent activities of these extracts may be due to the quantity and the quality of extracts compounds, which neutralize free radicals and convert them into more stable form. This stops the radical chain reactions,[47] in case of PEE, its antioxidant capacity may be linked to the presence of lipophilic antioxidants such as fatty acid and terpenoids.[48] These compounds are known for their ability to scavenge free radicals, which can provide protection against lipid peroxidation.[49]

3. 2. 7. Thiobarbituric Acid (TBA) Method

The end product of lipid peroxydation, MDA serves as a biomarker in this experiment and its concentration directly reflects the extent of lipide damage triggered by oxidative stress. The data of this assay are shown in figure 4. EAE was the most effective extract in inhibiting MDA formation (93 ± 1.14%) than BHT (89.37 ± 0.19%), followed by PEE (88.29 ± 0.32%), and CrE (87.59 ± 0.25%).

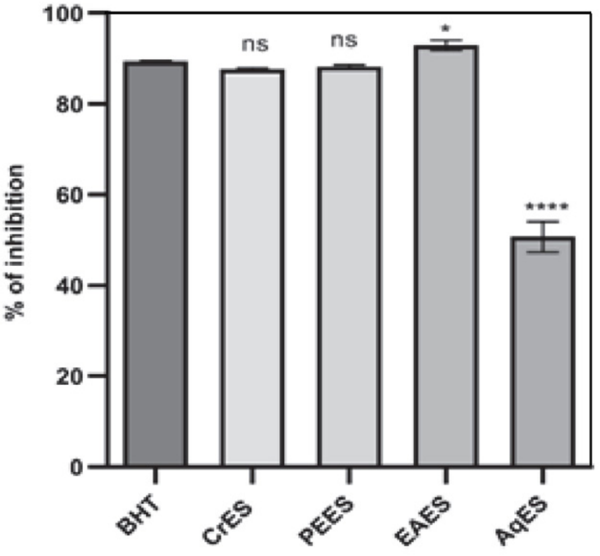

Figure 4. The percent inhibition of MDA formation by *P. atlantica* extracts: crude extract (CrE), petroleum ether (PEE), ethyl acetate extract (EAE) and aqueous (AqE) fractions; the standard (BHT). Values are % means ± SD (n = 3). ns: no significant difference. ****: P < 0.0001.

These obtained activities for *P. atlantica* fruits, were more significant than those reported for leaves extracts of the same plant,[34] and *P. khinjuk* extracts.[35]

3. 3. Antibacterial Activity

3. 3. 1. Well Diffusion Method

The results of the antibacterial activity of *P. atlantica* extracts screened on 15 different bacterial strains using the well diffusion method are indicated in the table 4. All extracts exhibited a broad spectrum of antibacterial activity against both gram-positive and gram-negative pathogenic bacteria with inhibition zones ranging from 10.66 to 29.33 mm. EAE demonstrated the strongest activity against *S. aureus*, *P. aeruginosa* 982, *S. typhimurium*, *S. aureus* 995, *B. cereus*, *E. faecalis*, *C. freundii* and *P. mirabilis*. These antibacterial activities were comparable to that of the standard antibiotics. Moreover, clinical stains: *S. pneumoniae* 990, *K. pneumoniae* 982, and *E. coli* 982 were only sensitive to EAE and their inhibition zones varied from 11 to 14 mm. On the other hand, CrE and PEE showed the highest inhibition zones against *K. pneumoniae* and *S. aureus* 995, respectively; and moderate inhibition zones on *S. aureus*, respectively. However, AqE exhibited the lowest activity.

Our results showed strongest activities against several bacteria species than that of obtained by Benmohamed *et al.*[26], and Benhamou *et al.*[49], and were comparable to those reported for *P. chinensis*,[50] and *P. khinjuk*.[52]

Chemical investigations of various *Pistacia* species have revealed their richness in phenolic compounds,[28,53] which are active against a wide range of microorganisms.[54,55] This may be due to their interaction with bacteria cell membrane[56,57] or the inhibition of enzymes essential for various metabolic processes.[58]

3. 3. 2. Time–dependent Antibacterial Activity

The results of the effect of contact time on the bacterial viability are illustrated by table 5 and showed potent and various antibacterial activities against different bacterial strains. The rates of growth inhibition were expressed in percentage with values ranging from 79.39 to 99.98% and from 22.58 to 100% after the 2 and the 4 hours of incubation period, respectively. Thus, the most active extract was EAE against 11 bacterial strains and the mortality rates varied from 87.41 to 99.86% after 2 hours of contact and remained stable against most of the strains, ranging from 88.48 to 99.98% after 4 hours at a concentration of 10 mg/mL. This extract was bactericidal on almost species.

Significant and similar rates were also recorded for CrE and PEE at a concentration of 20 mg/mL, after 2 and 4 hours of contact time. These extracts were bactericidal against four bacterial strains. Conversely, AqE showed a high mortality rate after 2 hours against *S. typhimurium* and *K. pneumoniae*, which significantly decreased after 4 hours. The strong antibacterial activity of EAE is due to its richness in bioactive compounds such as phenolic acids and flavonoids whose potential antibacterial effect was demonstrated.

3. 3. 4. Determination of Minimum Inhibitory Concentration (MIC) and Minimum Bactericidal Concentration (MBC).

After screening antibacterial activity using the agar-well diffusion assay, the most active extracts were further tested to evaluate their MIC and MBC. As shown in table 6, the MICs varied from 0.02 to 6.25 mg/mL and MBCs ranged from 0.19 to 50 mg/mL. The EAE was the most active with low MIC values on *S. pneumoniae 990*, *B. cereus*,

Table 4. Antibacterial activity of fruit extracts from *P. atlantica*: crude extract (CrE), petroleum ether (PEE), ethyl acetate extract (EAE) and aqueous (AqE) fractions; and the standard antibiotics. The results were expressed as mean ± SD of triplicate determinations.

Bacterial strains	Inhibition zone (mm) CrE	PEE	EAE	AqE	antibiotics
Ec	–	–	12.00 ± 1.00	–	28.00 (CTX)
Pa	–	–	14.00± 1.41	–	11.00 (CAZ)
Sa	16.00 ± 1.00	14.5 ± 0.70	29.33 ± 1.15	–	27.00 (OXA)
Bc	12.66 ± 2.08	17. 5 ± 0.70	18.5 ± 3.53	–	31.50 (IPM)
St	–	–	20.00 ± 2.82	12.33 ± 0.57	25.00 (SXT)
Ef	–	–	17.66 ± 0.57	–	22.50 (AMC)
Cf	–	–	17.66 ± 2.08	–	35.00 (CTX)
Kp	23.00 ± 7.93	22.5 ± 3.35	16.50 ± 2.21	12.33 ± 2.51	22.00 (CTX)
Pm	13.33 ± 1.52	–	17.00 ± 1.00	–	29.00 (AMC)
Ec 982	–	–	11.00 ± 1.41	–	32.00 (CTX)
Pa 982	–	–	21.00 ± 1.00	–	23.00 (CAZ)
Kp 982	–	–	13.50 ± 0.70	–	(CTX)
Sa 995	16.33 ± 1.52	17.16 ± 2.02	19.33 ± 1.15	–	22.00 (OXA)
Sp 990	–	–	14.00 ± 1.41	–	

Ec: *E. coli*, Pa: *P. aeruginosa*, Sa: *S. aureus*, Bc: *B. cereus*, St: *S. typhimurium*, Ef: *E. faecalis*, Cf: *C. freundii*, Kp: *K. pneumoniae*, Pm: *P. mirabilis*, Ec982: *E. coli 982*, Pa *982*: *P. aeruginosa 982*, Kp*982*: *K. pneumoniae 982*, Sa *995*: *S. aureus 995*, Sp*990*: *S. pneumoniae 990.*

Table 5. Loss of bacterial viability (%) with *P. atlantica*: crude extract (CrE), petroleum ether (PEE), ethyl acetate extract (EAE) and aqueous (AqE) fractions, after 2 and 4 hours of incubation.

Bacterial	CrE		PEE		EAE		AqE	
Strains	2 hours	4 hours	2 hours	4 hours	2 hours	4 hours	2 hours	4 hours
Ec	–	–	–	–	93.76±1.25	97.12±0.65	–	–
Sa	99.98±0.08	99.99±0	92.65±0.24	89.82±1.27	99.65±0.04	99.88±0.02	–	–
Bc	–	–	99.88±0.09	99.87±0.03	97.18±0.65	94.69±0.68	–	–
St	–	–	–	–	93.47±1.17	93.65±7.92	89.84±1.06	22.58±0.44
Ef	–	–	–	–	95.02±0.27	94.23±0.50	–	–
Cf	–	–	–	–	99.58±0.04	99.67±0.04	–	–
Kp	99.07±1.29	99.60±0.55	90.77±1.07	95.88±0.24	96.35±1.18	95.31±0.82	79.39±6.46	28.78±3.50
Pm	99.11±0.16	100.00±00	–	–	94.22±0.53	99.35±0.08	–	–
Pa 982	–	–	–	–	95.45±0.26	94.94±0.79	–	–
Kp 982	–	–	–	–	87.41±1.03	88.48±3.45	–	–
Sa 995	99.69±0.41	99.98±0.08	99.84±0.01	99.48±0.04	99.86±0.05	99.98±0.01	–	–
Sp 990	–	–	–	–	95.53±1.15	95.60±1.93	–	–

S. typhimurium, *C. freundii*, and *P. aeruginosa 982*, *E. coli*, *P. aeruginosa*, *S. aureus*, and *S. aureus 995*. Similarly, the CrE displayed a significant MICs for *K. pneumoniae* and *B. cereus*. However, PEE and AqE displayed moderate MIC against the tested bacteria. Our results were better than those reported by Rigane[58], and Hasheminya.[59]

On the other side, the bacteriostatic and bactericidal nature of *P. atlantica* extracts against the selected microorganisms was appreciated through the MBC/MIC ration. As shown in table 5, EAE was bactericidal against 7 strains: *E. coli, S. aureus, B. cereus, P. mirabilis, E. coli 982, K. pneumoniae 982* and *S. aureus 995.* Similarly, the CrE and PEE demonstrated a bactericidal effect against four bacterial strains. However, AqE displayed bactericidal activity only on *K. pneumoniae*.

3. 3. 5. Synergistic Antibacterial Assay

In our study, the plant extracts combined with antibiotic exhibited a significant synergistic ability to inhibit the growth of microorganisms and inhibition zones enhanced between 3 and 13 mm (table 7). EAE showed strong synergistic effect against various bacterial strains, followed by CrE and PEE. However, AqE, has a significant synergistic only on *K. pneumoniae*.

The findings revealed a potent synergy of the plant extracts with standard antibiotics, which could provide new possibilities for treating infectious diseases and reducing the drug resistance.[60] Further studies are needed to explore the molecular basis of the synergistic interaction for developing new natural antibacterial agents.

Table 6. MIC and MBC (mg/mL) of extracts from *P. atlantica*: crude extract (CrE), petroleum ether (PEE), ethyl acetate extract (EAE) and aqueous (AqE) fractions. R = MBC/MIC, bactericidal effect: MBC/MIC ≤ 4, bacteriostatic effect: MBC/MIC > 4.

Bacterial	CrE			PEE			EAE			AqE		
strains	**MIC**	**MBC**	**R**	**MIC**	**MBC**	**R**	**MIC**	**MBC**	**R**	**MIC**	**MBC**	**R**
Ec	–	–	–	–	–	–	0.39	0.39	**1.00**	–	–	–
Pa	–	–	–	–	–	–	0.39	12.50	**32.05**	–	–	–
Sa	1.56	0.78	**0.50**	3.12	3.12	**1.00**	0.39	0.78	**2.00**	–	–	–
Bc	0.19	0.39	**2.00**	1.56	6.25	**4.00**	0.19	0.39	2.00	–	–	–
St	–	–	–	–	–	–	0.19	12.50	**64.10**	6.25	25.00	**4.00**
Ef	–	–	–	–	–	–	3.12	12.50	**4.00**	–	–	–
Cf	–	–	–	–	–	–	0.19	1.56	**8.01**	–	–	–
Kp	0.02	0.19	**0.81**	3.12	0.19	**0.06**	3.12	12.50	**4.00**	1.56	1.56	**1.00**
Pm	6.25	50.00	**8.00**	–	–	–	0.78	1.56	**2.00**	–	–	–
Ec 982	–	–	–	–	–	–	3.12	6.25	**2.00**	–	–	–
Pa 982	–	–	–	–	–	–	0.19	3.12	**16.02**	–	–	–
Kp 982	–	–	–	–	–	–	3.12	6.25	**2.00**	–	–	–
Sa 995	1.56	25.00	**16.02**	1.56	12.5	**8.00**	0.39	0.78	**2.00**	–	–	–
Sp 990	–	–	–	–	–	–	0.04	3.12	**65.10**	–	–	–

Table 7. Antibacterial activity of *P. atlantica* extracts: crude extract (CrE), petroleum ether (PEE), ethyl acetate extract (EAE) and aqueous (AqE) fractions combined with standard antibiotics.

Bacterial	Inhibition zone (mm)				
strains	**CrE+AB**	**PEE+AB**	**EAE+AB**	**AqE+AB**	**AB**
Ec	–	–	31.00 (S)	–	28.00 (CTX)
Pa	–	–	17.00 (S)	–	11.00 (CAZ)
Sa	40.00 (S)	40.00 (S)	39.00 (S)	–	27.00 (OXA)
Bc	43.00 (S)	–	–	–	31.50 (IPM)
St	–	–	25.00 (I)	26.00 (I)	25.00 (SXT)
Ef	–	–	26.00 (S)	–	22.50 (AMC)
Cf	–	–	44.00 (S)	–	35.00 (CTX)
Kp	30.00 (S)	28.00 (S)	25.00 (S)	25.00 (S)	20.00 (CTX)
Lm	–	–	–	–	15.00 (CTX)
Pm	33.00 (S)	–	30.00 (S)	–	27.00 (AMC)
Ec 982	–	–	39.00 (S)	–	32.00 (CTX)
Pa 982	–	–	23.00 (I)	–	23.00 (CAZ)
Sa 995	–	26.00 (S)	–	–	22.00 (OXA)

S: synergy, I: indifference, AB: antibiotic

4. Conclusion

In this study, we evaluated the antioxidant and the antibacterial activities of *P. atlantica* extracts. Our findings indicated that the plant extracts possess strong antioxidant properties against several antioxidant systems and demonstrates potent antibacterial effects. The ethyl acetate extract (EAE) showed a powerful capacity in scavenging radical, reducing power and lipid peroxidation. Furthermore, this extract has an interesting antimicrobial effect against a broad spectrum of bacterial strains. These results describe the biological properties of this plant and provide a scientific foundation for its use in Algerian traditional medicine. Further studies are necessary to study the activities of the characterized phytochemicals by HPLC-DAD, which can be useful for therapeutic applications.

Acknowledgments

This research work was supported by the Algerian ministry of higher education and scientific research (MERS/DGRSDT). We would like to thank Pr. Sabah CHERMAT for the identification of the plant.

5. References

1. A. Muscolo, O. Mariateresa, T. Giulio, R. Mariateresa, *Int. J. Mol. Sci.* **2024**. *25*(6), 3264–3286. **DOI:**10.3390/ijms25063264
2. A. A. Feregrino-Pérez, A. Mercado-Luna, C. A. Murillo-Cárdenas, R. González-Santos, J. L. Chávez-Servín, A. F. Vargas-Madriz, E. Luna-Sánchez, *Agr.* **2024**. *14*(1), 142–155.

DOI:10.3390/agronomy14010142

3. N. Nasim, I. S. Sandeep, S. Mohanty, *The Nucleus.* **2022**. *65*(3), 399–411. **DOI:**10.1007/s13237-022-00405-3
4. G. Mancuso, A. Midiri, E. Gerace, C. Biondo, *Pathogens.* **2021**. *10*(10), 1310–1324. **DOI:**10.3390/pathogens10101310
5. Y. C. Gercek, S. Celik, S. Bayram, *Molecules.* **2021**. *27*(1), 117–130. **DOI:**10.3390/molecules27010117
6. S. Chermat and S. Bounar, *JEAT.* **2020**. *16*(2), 45–50.
7. M. Bozorgi, Z. Memariani, M. Mobli, M. H. Salehi Surmaghi, M. R. Shams-Ardekani, R. Rahimi, *Sci. World J.* **2013**. *2013*(1), 1–33. **DOI:**10.1155/2013/219815
8. C. Bakka, M. Hadjadj, O. Smara, H. Dendougui, S. Mahdjar, *J. Pharm. Sci. Res.* **2019**. *11*(11), 3634–3637.
9. Z. Ben Ahmed, M. Yousfi, J. Viaene, B. Dejaegher, K. Demeyer, Mangelings, D. Vander, Y. Heyden, *Pharm. Biol.* **2017**. *55*(1), 1185–1194. **DOI:**10.1080/13880209.2017.1291690
10. K. Saffidine, F. Zerargui, T. Guemmaz, A. Baghiani, *Trop. J. Nat. Prod. Res.* **2023**. *7*(5), 2996–3001. **DOI:**10.26538/tjnpr/v7i5.23
11. M. Djarmouni, A. Baghiani, M. Adjadj, L. Arrar, *Annu. Res. Rev. Biol.* **2018**. *22*(6), 1–7. **DOI:**10.9734/ARRB/2018/39084
12. M. Adjadj, M. Djarmouni, A. Baghiani, *Asian J. Biotechnol. Bioresour. Technol.* **2018**. *2*(3), 1–9. **DOI:**10.9734/AJB2T/2017/39081
13. S. Gheraibia, N. Belattar, M. A. Abdel-Wahhab, *S. Afr. J. Bot.* **2020.** 131, 222–228. **DOI:**10.1016/j.sajb.2020.02.019
14. T. Guemmaz, L. Arrar, A. Baghiani, *J. Drug Deliv. Ther.* **2020**. *10*(5), 39–44. **DOI:**10.22270/jddt.v10i5.4349
15. N. Mayouf, N. Charef, S. Saoudi, A. Baghiani, S. Khennouf, L. Arrar, *J. ethnopharmacol.* **2019**. *239*, 111914–111923. **DOI:**10.1016/j.jep.2019.111914
16. F. Zerargui, K. Saffidine, T. Guemmaz, H. Laroui, H. Trabsa, A. Baghiani, M. H. A. Zarga, *Trop. J. Pharm. Res.* **2023**. *22*(7), 1417–1425. **DOI:**10.4314/tjpr.v22i7.9
17. A. Deghima, N. Righi, N. Rosales-Conrado, M.E. León-González, E. Gómez-Mejía, Y. Madrid, F. Bedjou, *S. Afr. J. Bot.* **2020**. *132*, 204–214. **DOI:**10.1016/j.jep.2020.113347
18. H. Laroui, T. Guemmaz, F. Zerargui, K. Saffidine, S. Guenifi, L. Arrar, A. Baghiani, *J. Ethnopharmacol.* **2024**. *326*, 117964–117973. **DOI:**10.1016/j.jep.2024.117964
19. A. Bentahar, S. Khennouf, A. Bouaziz, A. Baghiani, S. Dahamna, S. Amira, L. Arrar, *Der Pharma Chemica.* **2016**. *8*(12), 88–99.
20. D. Asmerom, T. H. Kalay, G. G. Tafere, *Int. J. Microbiol.* **2020**. *2020,* 1–6. **DOI:**10.1155/2020/8840857
21. K. Saffidine, F. Zerargui, T. Guemaz, C. Lameche, F. Sahli, A. Baghiani, *TURJAF.* **2023**. *11*(2), 383–389. **DOI:**10.24925/turjaf.v11i2.383-389.5362
22. R. Bouchareb, R. Doufnoune, F. Riahi, H. Cherif-Silini, L. Belbahri, *Mater. Chem.Phys.* **2019**. *243*, 122598–122600. **DOI:**10.1016/j.matchemphys.2019.122598
23. G. Nouioura, M. El Fadili, A. El Barnossi, E. H. Loukili, H. Laaroussi, M. Bouhrim, E. H. Derwich, *Sci. Rep.* **2024**. *14*(1), 8325–8340. **DOI:**10.1038/s41598-024-59087-3
24. P. Pant, S. Pandey, S. Dall'Acqua, *Chem. Biodivers.* **2021.** *18*(11), 2100345–2100359. **DOI:**10.1002/cbdv.202100345
25. H. Zerkani, I. Tagnaout, Z. Khiya, S. Boutahiri, S. Amalich, K. Fadili, T. Zair, *J. Chem.* **2022**. *2022*(1), 7432169–7432172. **DOI:**10.1155/2022/7432169
26. M. Benmohamed, H. Guenane, M. Messaoudi, W. Zahnit, C. Egbuna, M. Sharifi-Rad, M. Yousfi, *Molecules*. **2023**. *28*(1), 349–269. **DOI:**10.3390/molecules28010349
27. S. Sun, Z. Liu, M. Lin, N. Gao, X. Wang, *Front. Nutr.* **2024**. *11*, 1456730–145640. **DOI:**10.3389/fnut.2024.1456730
28. O. Amri, A. Zekhnini, A. Bouhaimi, S. Tahrouch, A. Hatimi, *Pharmacogn. J.* **2018**. *10*(1), 71–76. **DOI:**10.5530/pj.2018.1.14
29. M. Rezaie, R. Farhoosh, M. Iranshahi, A. Sharif, S. Golmohamadzadeh, *Food Chem.* **2015**. *173*, 577–583. **DOI:**10.1016/j.foodchem.2014.10.081
30. 29. H. Dalvand, S.M.M. Hamdi, H. Ahmadvand, *Plant Sci. Today.* **2024**. *11*(1), 513–520. **DOI:**10.14719/pst.2853
30. H. Karageçili, M. A. Yilmaz, S. H. Alwasel, M. Arık, İ. Gülçin, *Rec. Nat. Prod.* **2023**. *17*(5), 918–937. **DOI:**10.25135/rnp.410.2305.2787
31. A. Bouyahya, I. C. C. Assemian, H. Mouzount, I. Bourais, A. Et-Touys, H. Fellah, Y. Bakri, *Ind. Crops Prod.* **2019**. *128*, 62–69. **DOI:**10.1016/j.indcrop.2018.11.001
32. K. Jomova, R. Raptova, S. Y. Alomar, S. H. Alwasel, E. Nepovimova, K. Kuca, M. Valko, *Arch. Toxicol.* **2023**. *97*(10), 2499–2574. **DOI:**10.1007/s00204-023-03562-9
33. A. Peksel, I. N. C. I. Arisan-Atac, R. Yanardag, *J. Food Biochem.* **2010**. *34*(3), 451–476. **DOI:**10.1111/j.1745-4514.2009.00290.x
34. S. Ahmed, S. Saeed-Ul-Hassan, M. Islam, F. Qureshi, I. Waheed, I. Munawar, *Acta Pol. Pharm.* **2017**, *74*(1), 173–178.
35. S. G.Tumilaar, A. Hardianto, H. Dohi, D. Kurnia, D, *J. Chem.* **2024**, *2024*(1), 5594386–5594407. **DOI:**10.1155/2024/5594386
36. J. G. Kim, A. R. Sharma, Y. H. Lee, S. Chatterjee, Y. J. Choi, R. Rajvansh, S.S. Lee, *Aging Dis.* **2024**. *16*(3), 1–24. **DOI:**10.14336/AD.2024.0282
37. T. T. Nhu-Trang, Q. D. Nguyen, N. Cong-Hau, L. T. Anh-Dao, P. Behra, *Molecules.* **2023**. *28*(8), 3470–3487. **DOI:**10.3390/molecules28083470
38. M. Parcheta, R. Świsłocka, S. Orzechowska, M. Akimowicz, R. Choińska, W. Lewandowski, *Materials.* **2021**. *14*(8), 1984–2008. **DOI:**10.3390/ma14081984
39. C. M. C. Andrés, J.M. Pérez de la Lastra, C.A. Juan, F.J. Plou, E. Pérez-Lebeña, *Processes.* **2023**. *11*(9), 2771–2794. **DOI:**10.3390/pr11092771
40. N. Belyagoubi-Benhammou, L. Belyagoubi, F. Atik Bekkara, *J. Med. Plant res.* **2014**. *8*(40), 1198–1207. **DOI:**10.5897/JMPR2014.5554
41. G. Nouioura, M. El Fadili, A. El Barnossi, E. Loukili, H. Laaroussi, M. Bouhrim, J.P. Giesy, M. A. M. Aboul-Soud, Y. A. Al-Sheikh, B. Lyoussi, E. Derwich, *Sci. Rep.* **2024**. *14(1)*, 8325-8344. **DOI:**10.1038/s41598-024-59087-3
42. O. Vergun, O. Bondarchuk, D. Rakhmetov, S. Rakhmetova, O. Shymanska, *Agrobiodivers. Impro. Nutr. Health Life Qual.* **2022**. *6*(2), 180–190. **DOI:**10.15414/ainhlq.2022.0005

43. M. Yemmen, A. Landolsi, J. B. Hamida, F. Mégraud, M. T. Ayadi, *Cell. mol. biol.* **2017**. *63*(9), 87–95. **DOI:**10.14715/cmb/2017.63.9.16
44. N. Belyagoubi-Benhammou, L. Belyagoubi, A. Benmahieddine, D.B. Menni, A. El Zerey-Belaskri, G. Di Marco, S.M. Jafari, *Biocatal. Agric. Biotechnol.* **2024**. *57*(1), 103143. **DOI:**10.1016/j.bcab.2024.103143
45. H. Zaoui, N. Boutaoui, A. Menad, R. Erenler, Z. Lahcene, F. Benayache, S. Ameddah, *Egypt. J. Chem.* **2022**. *65*(12), 695–705. **DOI:**10.21608/ejchem.2022.126336.5600
46. H. Wu, K. H. Bak, G. V. Goran, N. Tatiyaborworntham, *Crit. Rev. Food Sci. Nutr.* **2024**. *64*(15), 4921–4939. **DOI:**10.1080/10408398.2022.2146654
47. B. Šojić, S. Milošević, D. Savanović, Z. Zeković, V. Tomović, B. Pavlić, *Molecules.* **2023**. *28*(5), 2293–2315. **DOI:**10.3390/molecules28052293
48. G. Nouioura, M. El Fadili, N. El Hachlafi, H. A. Abuelizz, A. E. Elidrissi, M. Ferioun, N. Soulo, S. Er-ahmani, B. Lyoussi, E. Derwich, *Heliyon*. **2024**. *10*(8), 29520–29530. **DOI:**10.1016/j.heliyon.2024.e29520
49. N. Benhammou, F. A. Bekkara, T. K. Panovska, *Afr. J. pharm. pharmacol.* **2008**. *2*(2), 022–028.
50. W. Khan, Z. Ullah, D. Shah, M. Ismail, S. Azam, B. M. Khan, J. Khan, *Iheringia, Série Botânica.* **2023**. *78*, 2023022–2023027. **DOI:**10.21826/2446-82312023v78e2023022
51. M. Taran, M. Sharifi, E. Azizi, M. Khanahmadi, *J. Med. Plant.* **2010**. *9*(33), 81–85.
52. F. Khallouki, A. Breuer, E. Merieme, C. M. Ulrich, R. W. Owen, *J. pharma. Biomed. Anal.* **2017**. *134*, 310–318. **DOI:**10.1016/j.jpba.2016.11.023
53. B. Ben Akacha, M. Michalak, I. GeneralićMekinić, M. Kačániová, M. Chaari, F. Brini, A. Ben Hsouna, *Food Sci. Nutr.* **2024**. *12*(1), 574–589. **DOI:**10.1002/fsn3.3780
54. K. Zhao, Y. Jiang, K. Dev, X. He, V. Sharma, X. Pang, *Front. Cell. Infect. Microbiol.* **2024**. *14*, 1481656–1481667. **DOI:**10.3389/fcimb.2024.1481656
55. N. Oulahal and P. Degraeve, *Front. Microbiol.* 2022. *12*, 753518–753549. **DOI:**10.3389/fmicb.2021.753518
56. G. Nouioura, M. El Fadili, H. K. Ghneim, L. Zbadi, S. Maache, O. Zouirech, M. Danouche, M. A. M. Aboul-Soud, J.P. Giesy, B. Lyoussi, E. Derwich, *Arab. J. Chem.* **2024**. *17*, 105726-105742. **DOI:**10.1016/j.arabjc.2024.105726
57. G. Nouioura, M. El Fadili, N. El Hachlafi, S. Maache, I. Mssillou, H. A. Abuelizz, F. Z. Lafdil, S. Er-rahmani, B. lyoussi, E. Derwich, *Front. Chem*. **2024**. *12*, 1369745-1369760. **DOI:**10.3389/fchem.2024.1369745
58. G. Rigane, H. Ghazghazi, C. Aouadhi, R. Ben Salem, Z. Nasr, *Nat. Prod. Res.* **2017.** *31*(6), 696–699. **DOI:**10.1080/14786419.2016.1212035
59. S. M. Hasheminya, J. Dehghannya, *Food Biosci.* **2020.** *34*(1), 100–510. **DOI:**10.1016/j.fbio.2019.100510
60. A. M. Donkor, B. Ahenkorah, A. Yakubu, M. N. Donkor, *Fine Chem. Eng.* **2024.** *5*(1), 73–87. **DOI:**10.37256/fce.5120243648

Povzetek

Pistacia atlantica se v tradicionalni medicini v Alžiriji pogosto uporablja za zdravljenje različnih bolezni. Ta študija je bila izvedena z namenom raziskati antioksidativni potencial in protibakterijske lastnosti izvlečkov plodov. Rezultati so pokazali različne količine polifenolov in flavonoidov v različnih izvlečkih. Kvercetin, galna kislina, klorogenska kislina in metil galat so bile prevladujoče spojine v etil acetatnem izvlečku (EAE) in surovem izvlečku (CrE), določene s HPLC-DAD. EAE je bil najučinkovitejši pri lovljenju DPPH in hidroksilnih (OH•) radikalov, vodikovega peroksida (H_2O_2), pri reducirni moči in skupni antioksidativni kapaciteti. Vsi izvlečki imajo sposobnost zaviranja lipidne peroksidacije. Ugotovljen je bil širok spekter protibakterijskih učinkov (10,66 do 29,33 mm). Poleg tega sta časovno odvisen test ubijanja bakterij in razmerje MBC/MIC pokazala, da so bili vsi izvlečki baktericidni proti večini testiranih bakterij, njihova kombinacija z antibiotiki pa je pokazala izrazit sinergistični učinek. Ugotovitve te študije kažejo, da je zdravilna rastlina potencialen vir naravnih antioksidativnih in protibakterijskih spojin, ki bi jih bilo mogoče uporabiti tam, kjer so tovrstne aktivnosti zaželene.

DOI: 10.17344/acsi.2025.9370 *Acta Chim. Slov.* **2025,** *72,* 613–621

Scientific paper

Fibrous Silica KCC-1 as a Platform for Mn-Based Dual Metal Oxide Adsorbents for CO_2 Capture

Syawal Mohd Yusof,[1,2] Azizul Hakim Lahuri,[1,*] Nurul Asikin Mijan,[2]
Umar Kalmar Nizar,[3] Siti Sarahah Sulhadi,[1] Salma Samidin,[2]
Ainil Hafiza Abdul Aziz[1]

[1] *Department of Science and Technology, Universiti Putra Malaysia Sarawak, Nyabau Road, P.O. Box 396, 97008 Bintulu, Sarawak, Malaysia.*

[2] *Department of Chemical Science, Faculty of Science and Technology, Universiti Kebangsaan Malaysia, 43600, Bangi, Selangor, Malaysia.*

[3] *Chemistry Department, Faculty of Mathematic and Natural Science, Universitas Negeri Padang.*

* *Corresponding author: E-mail: azizulhakim@upm.edu.my*

Received: 06-19-2025

Abstract

The continuous rise in atmospheric CO_2 levels due to industrial emissions and fossil fuel combustion has intensified the need for efficient carbon capture. Solid adsorbents are favoured for their reusability and low energy demand, yet often face limitations in thermal stability and adsorption performance. This study examines the effect of co-loading manganese (Mn) with potassium (K), copper (Cu), and calcium (Ca) on fibrous silica KCC-1 for CO_2 capture over a wide temperature range. KCC-1 was synthesised via a microemulsion method, and metals were introduced using an ultrasonic-surfactant-assisted impregnation technique. Characterisation using XRD, FTIR, BET, FESEM-EDX, and CO_2-TPD confirmed structural integrity, surface functionality, and adsorption behaviour. CaO-MnO@KCC-1 shows the most balanced textural properties and the highest CO_2 uptake due to its strong basicity and varied adsorption site strength. This highlights its potential as a temperature-flexible CO_2 adsorbent.

Keywords: CO_2 capture; Manganese-based catalysts; Fibrous silica KCC-1; Ultrasonic-Surfactant-assisted impregnation; metal dispersion; Basicity and redox properties

1. Introduction

The continuous rise in atmospheric CO_2 concentration due to industrial processes and the burning of fossil fuels has intensified global warming and climate change.[1] CO_2 capture and storage (CCS) technology have therefore become essential for addressing these environmental issues. Solid sorbents have drawn the most attention among the several CCS techniques because of its efficiency, reusability, and potential for large-scale applications.[2–5]

The search for "smart sorbents" that can effectively absorb CO_2 at a variety of temperatures is still an intriguing area of materials science, nevertheless. Despite the progress made in CCS development, challenges remain in designing adsorbents capable of performing efficiently at different operational temperatures. The adsorption performance of a material is primarily influenced by the strength and nature of the interaction between the CO_2 molecules and the active sites on the adsorbent surface, while the desorption profile reflects the thermal stability and binding energy of the adsorbed species. Thus, instead of a single material operating across all temperature regimes, materials tailored with varied binding site strengths are required to target low to high adsorption temperatures. Recent studies have shifted toward developing "smart sorbents" that can respond to temperature variations by adjusting their adsorption behaviour accordingly.

Manganese-based materials are widely recognized for their redox flexibility, thermal stability, and variable surface characteristics, making them excellent candidates for CO_2 capture.[6] The use of manganese oxides introduces moderate basic sites that are favourable for the chemisorption of acidic CO_2 molecules. However, the performance of Mn-based adsorbents alone may be limited by their surface area and pore accessibility. To improve their efficiency, especially under varying thermal conditions, the incorporation of a second metal has been widely explored in the literature.

The combination of manganese with a second metal oxide – such as potassium (K), calcium (Ca), or copper (Cu) – has been investigated to improve CO_2 capture performance. Wang et al.[7] had reported that potassium is well known for enhancing surface basicity, which facilitates CO_2 chemisorption. Study confirmed the calcium can form stable carbonates at elevated temperatures, contributing to long-term CO_2 retention and storage.[8] Meanwhile, copper provides redox-active sites and enhances moderate binding interactions through catalytic surface activation.[9] Bimetallic systems often display improved adsorption profiles, broader active site distributions, and stronger structural stability than their monometallic counterparts.

A new star in adsorbent support of fibrous silica KCC-1, is introduced to provide a playground for highly dispersed of active site and improved gas-solid interactions.[10] Besides, it has large surface area, mesoporous architecture, and distinctive fibrous shape. For example, Nasir et al.[11] investigated the performance of amine-functionalised KCC-1, where TEPA@KCC-1 exhibited a CO_2 adsorption capacity of 4.31 mmol/g under 40 °C and 30 bar of maximum pressure. This study aims to open up new options for creating "temperature-smart" sorbents that can give targeted CO_2 capture performance throughout low, medium, high and extremely high temperature ranges by co-loading manganese onto KCC-1 with K, Cu, or Ca.

An ultrasonic-surfactant-assisted impregnation technique was used to create the adsorbents, which ensured uniform dispersion, preventing from agglomerate and optimal interaction between the metals and the KCC-1 support.[12] In addition to showcasing the exceptional adaptability of Mn-based bimetallic adsorbents, this work offers a guide for customizing materials to satisfy the ever-changing needs of sustainable CCS technology. This work clears the path for creative answers to one of the most important global issues of our day by connecting basic material science with real-world application.

2. Methodology

2. 1. Synthesis of Metals-Mn@KCC-1 Adsorbents

All chemicals used in this study were of analytical grade and applied without further purification. Tetraethyl orthosilicate (TEOS, Merck) was used as the silica precursor for the synthesis of KCC-1. Toluene (R&M Chemicals) served as the oil phase, while 1-butanol (Merck) acted as the co-surfactant. Urea (Merck, Germany) was added to promote hydrolysis and condensation reactions. Cetyltrimethylammonium bromide (CTAB, Sigma-Aldrich) was used as the structure-directing agent during the synthesis of KCC-1 and also in the metal impregnation step. Distilled water was used in all solution preparations.

The fibrous silica KCC-1 support was synthesized using a microemulsion method as reported by Yusof et al.[13] with modifications involving ultrasonic and surfactant-assisted impregnation. In the metal loading step, approximately 1 g of KCC-1 was dispersed in 10 mL of distilled water and sonicated for 10 minutes. Metal precursors manganese(II) nitrate tetrahydrate $Mn(NO_3)_2{\cdot}4H_2O$ (Sigma-Aldrich), potassium nitrate KNO_3 (R&M Chemicals), calcium nitrate tetrahydrate $Ca(NO_3)_2{\cdot}4H_2O$ (Merck), and copper(II) nitrate trihydrate $Cu(NO_3)_2{\cdot}3H_2O$ (Merck) were prepared separately in distilled water in a 1:1 molar ratio (Mn to co-metal) to achieve a 2.5 wt% loading for each metal. CTAB was added to the metal solution at a metal-to-surfactant ratio of 3:10 and sonicated for another 10 minutes.

The metal-containing solution was then mixed with the KCC-1 suspension and further sonicated for 30 minutes to ensure uniform distribution of metals on the support. The resulting mixture was dried on a hotplate at 80 °C until water completely evaporated. The adsorbents were thermally treated (calcined) at 600 °C for 4 hours under nitrogen to remove the residual CTAB surfactant and stabilize the metal oxides, this process is referred to as activation. The final adsorbents were designated as M-MnO@KCC-1, where M refers to K_2O, CaO, or CuO depending on the co-metal used.

2. 2. Characterization

The structural, chemical, morphological, and textural properties of the prepared adsorbents were evaluated using several characterization techniques. X-ray diffraction (XRD) analysis was performed using a Bruker D8 Advance diffractometer with Cu-Kα radiation (λ = 1.5406 Å), operated at 40 kV. The scans were recorded over a 2θ range of 10° to 80° with a step size of 0.02°. Fourier Transform Infrared (FTIR) spectra were obtained using an Agilent Cary 600 in the range of 4000–400 cm^{-1} at a resolution of 4 cm^{-1} with 32 scans per sample. Nitrogen adsorption–desorption isotherms were recorded at 77 K using a Micromeritics Tristar II Plus analyser after degassing the samples at 150 °C for 4 hours under flow of nitrogen gas. The BET method was used to determine surface area, while the Barrett–Joyner–Halenda (BJH) method was applied to derive the pore size distribution from the desorption branch. The surface morphology and elemental distribution were studied using field emission scanning electron microscopy (FESEM) and energy dispersive X-ray spectroscopy (EDX), both conducted on a Zeiss Merlin Compact operated at an accelerating voltage of 5–15 kV.

2. 3. CO_2 Capture Study

The CO_2 capture performance of the adsorbents was evaluated using temperature-programmed desorption of CO_2 (TPD-CO_2). Prior to the desorption step, each sample (approximately 20 mg) was pretreated under a flow of high-purity nitrogen gas (99.999%) at 150 °C for 1 h to remove any physisorbed species. After cooling to 50 °C, the samples were exposed to a continuous flow of 15 % CO_2 balanced with nitrogen at a total flow rate of 15 mL/min for 1 hour to allow adsorption. The adsorption was carried out under saturation mode to ensure complete CO_2 coverage on all available active sites. Following adsorption, the system was purged with nitrogen at the same flow rate for 30 minutes to remove any weakly physisorbed CO_2. The desorption step was then carried out by heating the sample from 50 °C to 900 °C at a rate of 10 °C/min under a nitrogen flow of 15 mL/min. The CO_2 desorption profile was monitored using a thermal conductivity detector (TCD). The desorption patterns obtained were used to analyse the strength and distribution of the CO_2 adsorption sites across the tested temperature range.

3. Result And Discussion

3. 1. Physicochemical Properties of Adsorbents

The structural and composition of Mn co-loaded with potassium (K), calcium (Ca), and copper (Cu) on the fibrous silica KCC-1 support are revealed by the XRD patterns (Figure 1a). All samples exhibit a broad diffraction peak at 15–35°, which is consistent with the amorphous silica structure framework of the KCC-1.[14,15] The typical broad peak associated to the fibrous silica structure's preservation, which is necessary to sustain the large surface area and porosity required for CO_2 capture capacity and the metal dispersion. The absence of noticeable MnO peaks indicates that manganese oxide is well-distributed throughout the KCC-1 surfaces, with particle sizes due to falling below the XRD technique's detection limit.

None of the CaO peaks exist for CaO-MnO@KCC-1 due to the calcium and manganese substrates are widely distributed throughout the KCC-1 surface, making crystallinity invisible to XRD. The CuO-MnO@KCC-1 sample exhibited a peak at 34°, which corresponds to MnO (111) (ICDD 03-065-0638), indicating the existence of crystalline manganese oxide due to increased crystallinity and larger MnO particle domains, which exceed the XRD detection threshold. Strong interactions between copper and the silica framework were also suggested by the identification of a peak at 46° as copper silicate (431) (ICDD 03-032-0346), resulting imbedded of copper mostly on the dendrimer of KCC-1 (outer surface).

Significant peaks in the FTIR spectra of K_2O-MnO@KCC-1, CaO-MnO@KCC-1, and CuO-MnO@KCC-1 validate the chemical and structural properties of the produced materials. The asymmetric stretching and bending vibrations of the Si–O–Si framework are responsible for the strong and broad absorption bands seen in the 800–

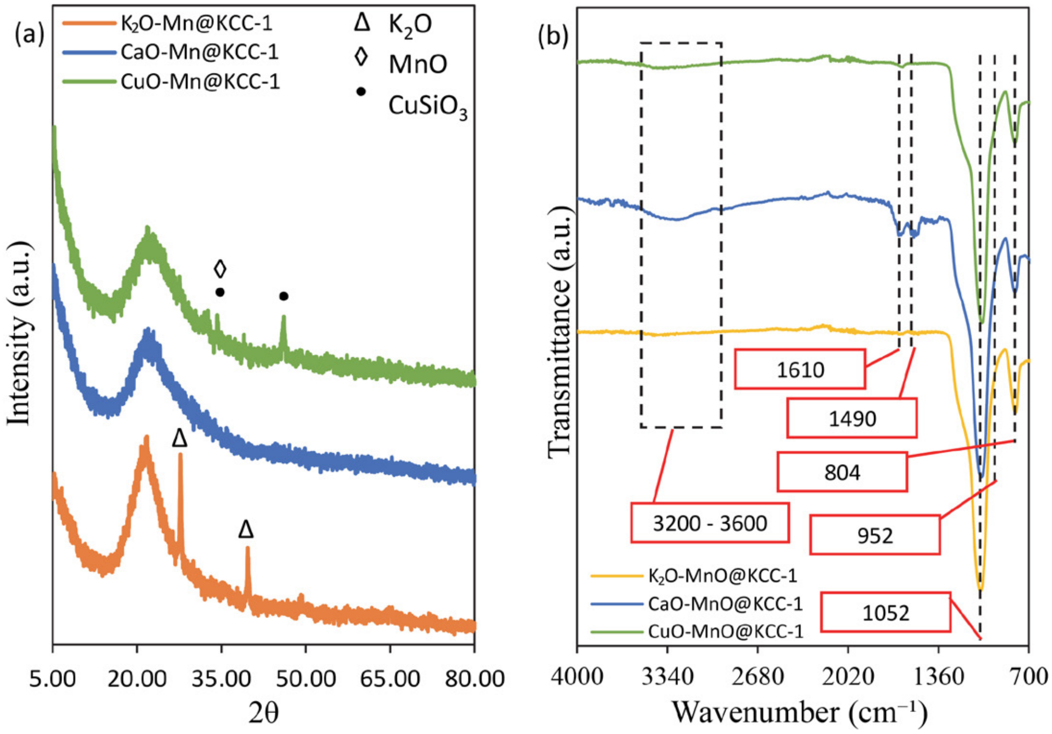

Figure 1: (a) XRD diffractogram and (b) FTIR spectra of the adsorbents.

850 cm^{-1} and 1100–1200 cm^{-1} ranges for all adsorbents.[16,17] These peaks validate the mesoporous properties of the silica structure by showing that it has been preserved inside the KCC-1 framework. All adsorbents exhibit a wide band in the high-frequency range at around 3400 cm^{-1}, which is ascribed to the stretching vibrations of hydroxyl (–OH) groups.[18,19] The presence of surface hydroxyls, which are essential for adsorbent interactions, including the adsorption of molecules like CO_2, is shown by this peak. Due to variations in surface chemistry brought about by the added metals (K, Ca, and Cu), the hydroxyl peak's strength may fluctuate somewhat between the samples due to the hygroscopic of metal particles properties.

The spectra show clear peaks for CaO-MnO@KCC-1 at 1610 cm^{-1} and 1490 cm^{-1}. The peak of H–O–H bending vibration is shown at 1610 cm^{-1} indicates molecularly adsorbed water.[20] This is attributed to the strong basicity of CaO, which readily reacts with atmospheric CO_2. The existence of calcium oxide species is suggested by the peak at 1490 cm^{-1}, which is attributed to CaO.[21] These results are consistent with the XRD data, which demonstrate the well-dispersed nature of calcium species on the KCC-1 framework but do not reveal any identifiable $CaCO_3$ peaks. A carbonate peak also appears for CuO-MnO@KCC-1 at 1610 cm^{-1}, which is consistent with the Cu silicate phases shown by XRD. The presence of carbonate indicates that copper and CO_2 may interact partially, possibly resulting in the formation of weakly bonded carbonates. The idea that copper species are evenly distributed or imbedded in the silica network is supported by the lack of noticeable CuO peaks in XRD. Copper preserves the mesoporous structure of silica while improving redox characteristics that are essential for mild CO_2 adsorption, according to the FTIR data. When compared to XRD, the FTIR results highlight how each metal affects the structural and chemical characteristics of the KCC-1 support. Copper interacts with the silica framework to contribute to mild CO_2 adsorption, but calcium promotes a high basicity with persistent carbonate and oxide forms. The structural and functional changes by the metal impregnation in KCC-1 are better understood according to these combined findings analysis.

The textural properties of the synthesized adsorbents were investigated using nitrogen adsorption–desorption isotherms, pore size distribution (PSD), and BET surface area measurements. All samples exhibit Type IV isotherm with an H1 hysteresis loop, as shown in Figure 2, which is characteristic of mesoporous materials. The presence of this loop indicates capillary condensation in mesopores and confirms that the mesoporous structure of KCC-1 was preserved after metal impregnation. The size of the hysteresis loop varied among the samples, with CuO-MnO@KCC-1 showing a visibly wider loop compared to the other two, indicating a higher pore volume and more developed mesoporous structure as reported before by Maity and Polshettiwar.[22]

Table 1 presents the BET surface area, total pore volume, and average pore size of all samples. The K_2O-MnO@KCC-1 sample provide the lowest surface area (71 m^2/g) and pore volume (0.17 cm^3/g), with an average pore diameter of 9.6 nm. Compared to pristine KCC-1 reported by Hao et al.,[23] which has a BET surface area of approximately 600 m^2/g, a pore volume of 0.91 cm^3/g, and an average pore size of 7.1 nm, this indicates a significant reduction in textural properties, likely due to partial pore blockage by potassium oxide. This is further supported by the broader and less intense PSD peak of K_2O-MnO@KCC-1 in Figure 3, suggesting reduced pore uniformity and lower accessibility, which is consistent with previous findings by Yusof et al.[13]

In contrast, CaO-MnO@KCC-1 exhibited a much higher surface area (296 m^2/g) and pore volume (0.52 cm^3/g), with an average pore diameter of 6.6 nm. The PSD shows a sharper and narrower peak compared to K_2O-MnO@KCC-1, indicating more uniform mesopores. The smaller average pore size observed here is not necessarily stabilizing the structure, but rather reflects the formation of more compact pore networks due to calcium oxide distribution within the KCC-1 matrix. The shift in PSD toward smaller pore diameters suggests a densification of the pore network by CaO incorporation, as reported by Khine et al.[8] without inducing pore collapse.

CuO-MnO@KCC-1 demonstrated the most favourable textural features, with the highest surface area (427 m^2/g), largest pore volume (0.86 cm^3/g), and an average pore size of 7.7 nm. Its isotherm shows a large and well-defined hysteresis loop, wider than those of the other samples, which supports the presence of well-developed mesopores and enhanced gas accessibility. The PSD curve shows moderately uniform pores, suggesting that copper oxide is well integrated and enhances the pore structure without severe blockage. This behaviour is consistent with the formation of copper silicate phases at the dendritic outer layers of KCC-1, as also supported by FESEM and XRD findings. The comparison of PSD peaks clearly shows a shift: Pristine KCC-1: ~7.1 nm,[23] K_2O-MnO@KCC-1:

Table 1: Textural properties of the adsorbents

Samples	BET surface area (m^2/g)	Micropore area (m^2/g)	Total pore volume (cm^3/g)	Average pore size (nm)
K_2O-MnO@KCC-1	71	2.0	0.17	9.6
CaO-MnO@KCC-1	296	5.7	0.52	6.6
CuO-MnO@KCC-1	427	13.2	0.86	7.7

9.6 nm (broader, less defined), CaO-MnO@KCC-1: 6.6 nm (narrow, sharp peak) and CuO-MnO@KCC-1: 7.7 nm (moderately broad). These differences indicate that potassium caused pore expansion but reduced uniformity, calcium led to narrower and denser pore channels, and copper enhanced mesoporosity while maintaining good pore accessibility. Overall, the copper-containing sample exhibits the best balance of surface area, pore volume, and mesostructural quality.

All of the adsorbents' FESEM images (Figure 4) show KCC-1's distinctive fibrous structure, demonstrating that the spherical, dendritic mesoporous silica framework was successfully synthesized.[22] When metal oxides are added, the fibrous and unique morphology further demonstrate

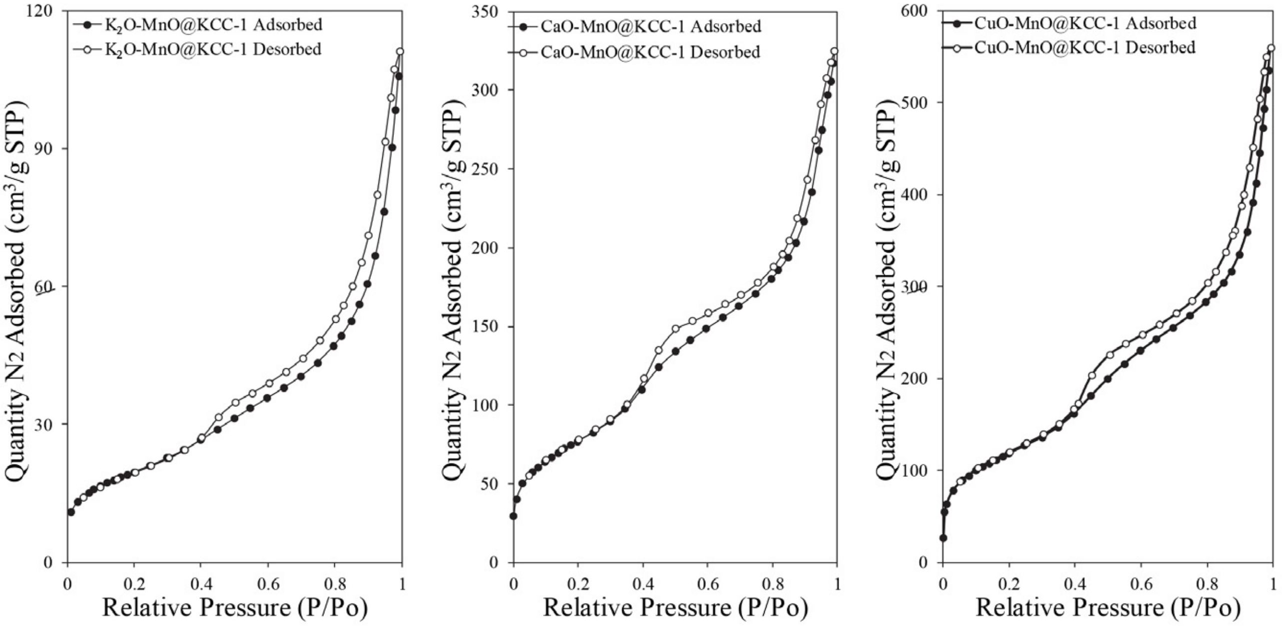

Figure 2: Nitrogen adsorption-desorption isotherm of adsorbents

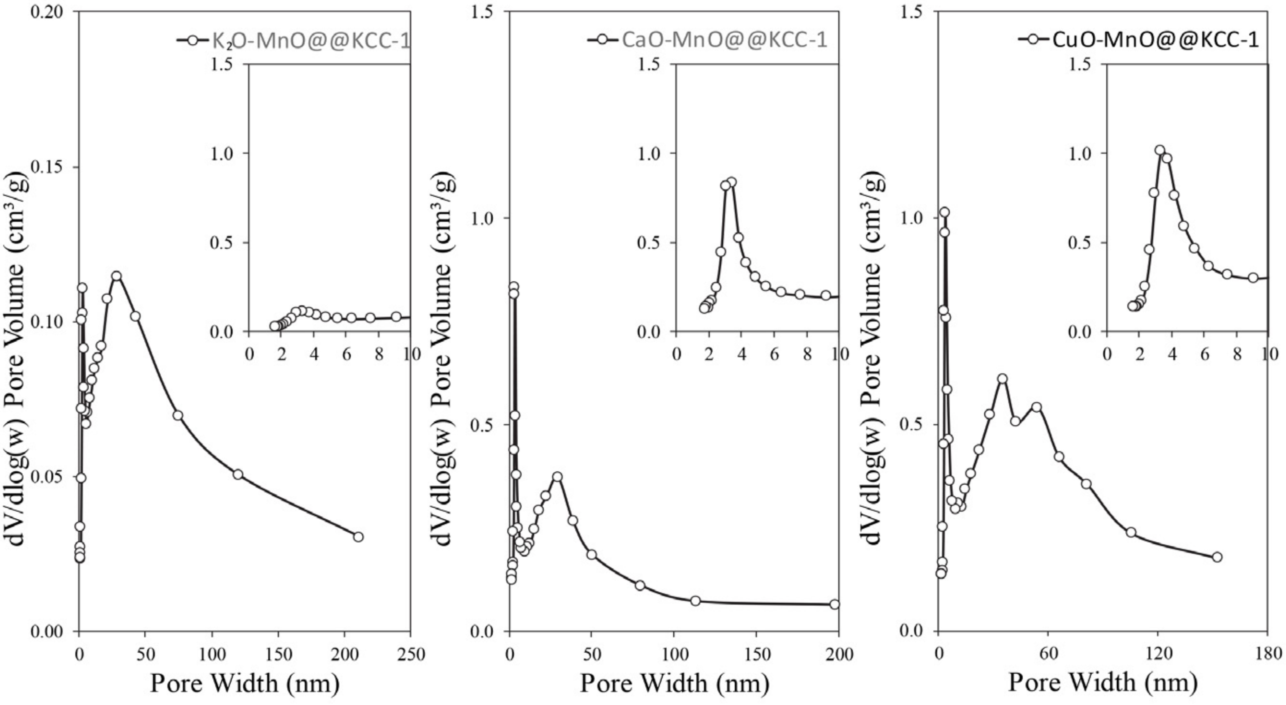

Figure 3: Pore size distribution of adsorbents

the KCC-1 framework's structural stability. However, K_2O-MnO@KCC-1, CaO-MnO@KCC-1, and CuO-MnO@KCC-1 all have somewhat different particle morphologies and surface textures, which offer insight on how metal impregnation affects the adsorbents structure. The FESEM images of K_2O-MnO@KCC-1 reveal that the fibrous network is mostly intact, but the surface seems somewhat rougher than that of pure KCC-1.[24]

Comparing CaO-MnO@KCC-1 to K_2O-MnO@KCC-1, the FESEM pictures reveal more distinct fibrous structure and extremely homogeneous spherical particles. The mesoporous structure's stability and integrity are reflected in this morphology, which is in line with the nitrogen adsorption data's narrow pore size distribution and larger BET surface area. The FTIR spectra ascribed to CaO and $CaCO_3$, indicate that the structural framework is strengthened by calcium incorporation. These results are in line with the XRD data, which show that calcium has a synergistic impact on maintaining the mesoporous architecture by confirming well-dispersed calcium species without noticeable pore collapse. In contrast to CaO-MnO@KCC-1, CuO-MnO@KCC-1 exhibits a somewhat finer surface and well-preserved spherical shape, according to the FESEM images. The large BET surface area and the somewhat uniform pore size distribution, which is centred at 7.73 nm, are consistent with this finding. The presence of carbonate peaks in the FTIR spectrum indicates that there are not many interactions between the silica framework and copper species. The XRD data, which show evenly distributed copper species devoid of notable crystalline CuO peaks, support the FESEM findings that copper impregnation slightly decrease porosity without seriously harming the KCC-1 framework's structural integrity.

Important information on the elemental makeup of the adsorbents K_2O-MnO@KCC-1, CaO-MnO@KCC-1, and CuO-MnO@KCC-1 and their effective integration into the silica framework is provided by the Energy-Dispersive X-ray (EDX) study (Figure 4). The existence of silicon (Si) and oxygen (O), the main constituents of the KCC-1 silica matrix, as well as manganese (Mn) and the corresponding metal modifiers potassium (K), calcium (Ca),

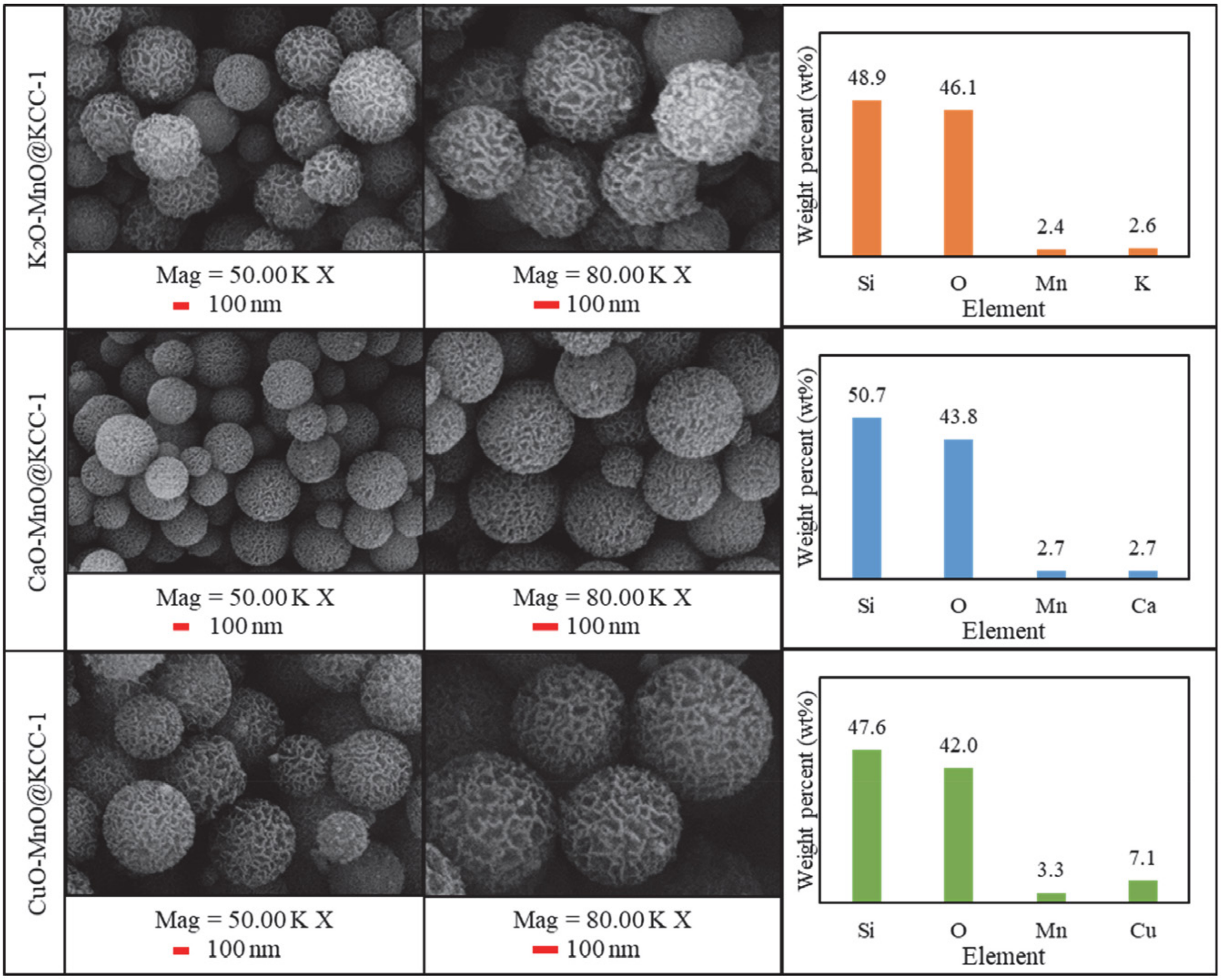

Figure 4: FESEM images and EDX of the adsorbents

and copper (Cu) are confirmed by the EDX spectra of all three materials. In conclusion, the FESEM and EDX study offers an understanding of the structural changes of metal impregnation when combined with XRD, FTIR and N_2 adsorption-desorption data. CaO-MnO@KCC-1 exhibits improved stability and porosity because to calcium stabilizing impact, whereas K_2O-MnO@KCC-1 displays partial structural disruption. Conversely, CuO-MnO@KCC-1 preserves a balance between high porosity and structural integrity, which is a result of copper efficient interaction with the silica framework. These differences demonstrate how important the added metals in modifying the KCC-1-based adsorbents structural and textural characteristics.

3. 2. CO_2 Capture Study

Different CO_2 desorption peaks that correspond to weakly (<250 °C), moderately (251–480 °C), strong (481–700 °C) and very strong (>700 °C) adsorbed CO_2 species are shown in Figure 5 with tabulate in Table 2 (TPD-CO_2 profiles of each adsorbent).[26] The peaks for K_2O-MnO@KCC-1 are mostly weakly bound CO_2 species, suggesting low adsorption energy locations where potassium oxide predominates and the adsorption at 14.74 cm^3/g compared to pristine KCC-1 at 11.65 cm^3/g reported by Yusof et al.[12] Although potassium increases basicity and improves interaction with acidic CO_2 molecules, active sites are less accessible due to partial pore blockage. As a result, especially at higher temperatures, the adsorption capability is increase slightly. Because of potassium prevailing effect, manganese in K_2O-MnO@KCC-1 appears to improve mild CO_2 binding but does not considerably enhance adsorption. On the other hand, very strong, moderate, and weak desorption peaks demonstrate the better adsorption capability of CaO-MnO@KCC-1 at 22.35 cm^3/g. CaO plays a major role in the basicity of the material, which results in strong interactions with CO_2 and the development of carbonates on the surface. The desorption of tightly bonded CO_2 species is shown by the steep peak at higher temperatures, which suggests persistent carbonate production. Manganese function in this system is to balance the adsorption energies by offering sites for moderate CO_2 binding, which enhances the strong basic sites that calcium introduces. Among the three adsorbents, CaO-MnO@KCC-1 is the most effective due to its high affinity and dispersion,[8,25] which further improve the accessibility of active sites.

The TPD-CO_2 profile for CuO-MnO@KCC-1 displays a wider range of desorption peaks, covering weak, moderate, and high binding energies at 19.12 cm^3/g. Manganese promotes CO_2 interaction at higher binding energies, whereas copper's redox characteristics improve moderate CO_2 adsorption through surface activation. The high adsorption peak is less noticeable than in CaO-MnO@KCC-1, however, suggesting that there are fewer stable carbonate-forming sites. Given its high surface area and moderate pore size distribution, which enable quick CO_2 capture and release, it appears that CuO-MnO@KCC-1 depends more on dynamic adsorption-desorption processes than on strong chemical binding.[27] When comparing the adsorbents, manganese presence in all systems is crucial for improving moderate adsorption sites and bridging the gap between the co-loaded metals capacities. Manganese partially mitigates the poor adsorption of potassium in K_2O-MnO@KCC-1, whereas it enhances the strong binding of calcium in CaO-MnO@KCC-1, resulting in a wider variety of adsorption sites. For CuO-MnO@KCC-1, manganese strengthens the material ability to bind CO_2 moderately and ensures stable performance across varying conditions. To sum up, the TPD-CO_2 data demonstrate how manganese and the co-loaded metals interact to influence adsorption efficiency. Copper encourages moderate adsorption, calcium strengthens strong carbonate production, while potassium favours weak binding. All the adsorbents demonstrate a beneficial synergistic interaction with manganese, contributing to a balanced distribution of CO_2 adsorption sites across weak, moderate, and strong binding regions. As illustrated in Figure 5, CaO-MnO@KCC-1 exhibits the most comprehensive and intense desorption profile, indicating a high density of active basic sites. Its significant CO_2 uptake over a broad temperature range confirms its superior adsorption performance. This can be attributed to the presence of strong basicity, thermally stable carbonate formation, and a well-preserved mesoporous structure, making CaO-MnO@KCC-1 the most promising candidate for efficient CO_2 capture under varying operational conditions.

4. Conclusion

In order to improving their CO_2 adsorption capabilities, manganese was co-loaded onto dendritic fibre silica

Table 2: CO_2 Adsorption capacity of the adsorbents

Samples	**CO_2 adsorption capacity (cm^3/g)**				
	Weak (<250 °C)	**Medium (251–480 °C)**	**Strong (481–700 °C)**	**Very Strong (>700 °C)**	**Total**
K_2O-MnO@KCC-1	3.38	9.89	–	1.48	14.74
CaO-MnO@KCC-1	6.13	7.46	–	8.72	22.35
CuO-MnO@KCC-1	3.23	8.91	–	6.98	19.12

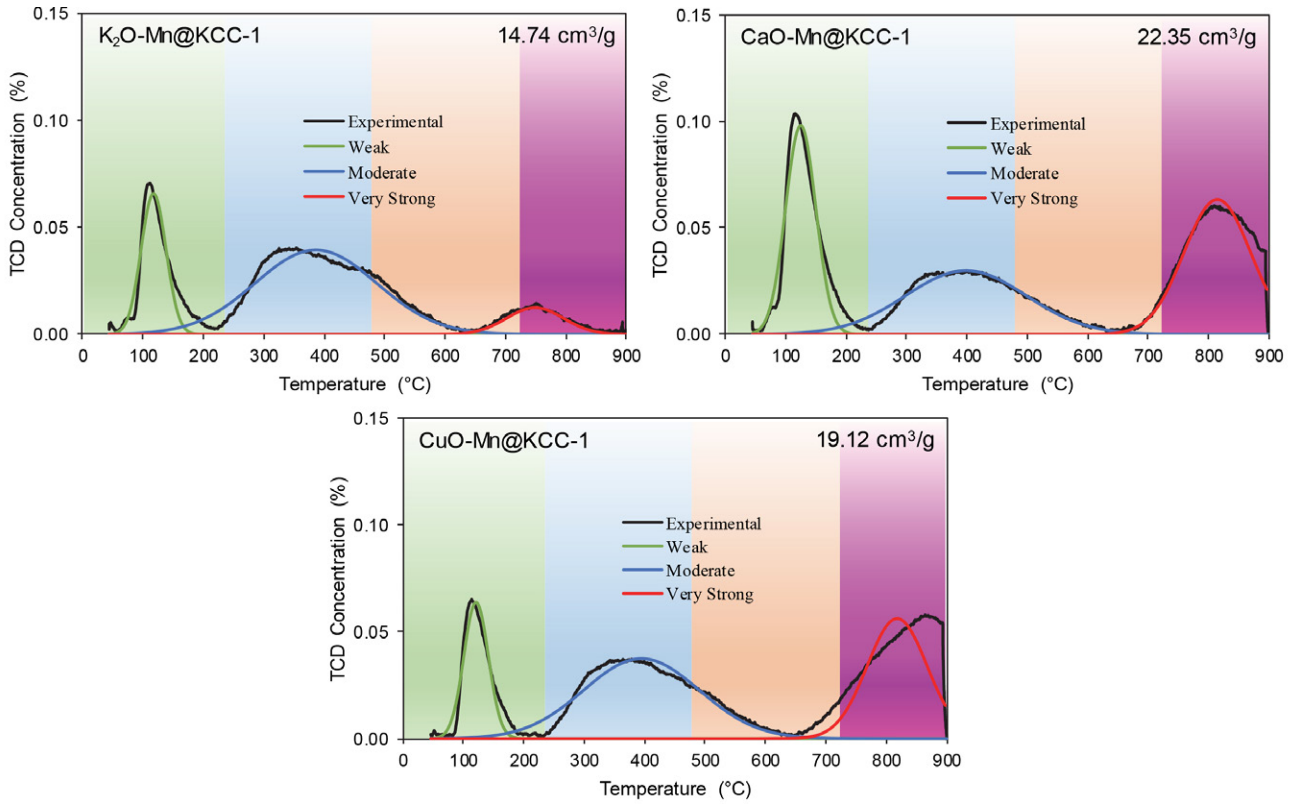

Figure 5: TPD-CO_2 profile of the adsorbents.

KCC-1 together with potassium, calcium, and copper. The characterization results demonstrated that metals were successfully incorporated into the KCC-1 framework, with distinct effects of each metal on the chemical, structural, and textural characteristics. According to TPD-CO_2 analysis, K_2O-MnO@KCC-1 mainly prefers weakly bound CO_2 species, CaO-MnO@KCC-1 has a higher adsorption capacity because of its strong basicity and stable carbonate formation, and CuO-MnO@KCC-1 has redox characteristics allow it to efficiently balance moderate and strong adsorption sites. The results illustrate how manganese plays a crucial role in enhancing each metals adsorption behaviour. CaO-MnO@KCC-1 was found to be the most efficient adsorbent, indicating its potential for tailored CO_2 capture throughout a range of temperatures.

AKNOWLEDGEMENT

The authors would like to acknowledge the funding support provided by Universiti Putra Malaysia under grant number 9795800 and the authors also express their gratitude to OCIM Sdn. Bhd. for supporting this research through grant number 6300940 awarded to Universiti Putra Malaysia.

Author contributions

S.M.Y. and A.H.L. designed and performed the experiments. S.M.Y., S.S.S., S.S., and A.H.A.Z. performed the studies and data analysis. A.H.L, N.A.M. and U.K.N. supervised the research. All authors contributed to the writing and editing of the manuscript.

Conflicts of interest

The authors declare no conflicts of interest.

5. References

1. S. A. Rawool, Y. Kar, V. Polshettiwar, *Mater. Adv.* **2022**, *3*, 8449–8459. **DOI:**10.1039/D2MA00809B
2. Y. Guo, L. Luo, Y. Zheng, T. Zhu, *ACS Omega* **2020**, *5*, 9641–9648. **DOI:**10.1021/acsomega.9b03374
3. M. Younas, M. Sohail, L. L. Kong, M. J. K. Bashir, S. Sethupathi, *Int. J. Environ. Sci. Technol.* **2016**, *13*, 1839–1860. **DOI:**10.1007/s13762-016-1008-1
4. S. Y. Lee, S. J. Park, *J. Ind. Eng. Chem.* **2015**, *23*, 1–11. **DOI:**10.1016/j.jiec.2014.09.001
5. N. Mittal, A. Samanta, P. Sarkar, R. Gupta, *Energy Sci. Eng.* **2015**, *3*, 207–220. **DOI:**10.1002/ese3.64
6. V. Mahdavi, M. Mardani, *Mater. Chem. Phys.* **2015**, *155*, 136–146. **DOI:**10.1016/j.matchemphys.2015.02.011
7. S. Wang, J. Zhan, K. Chen, A. Ali, L. Zeng, H. Zhao, W. Hu, L. Zhu, X. Xu, *ACS Sustain. Chem. Eng.* **2020**, *8*, 8214–8222. **DOI:**10.1021/acssuschemeng.0c01151
8. E. E. Khine, D. Koncz-Horvath, F. Kristaly, T. Ferenczi, G. Karacs, P. Baumli, G. Kaptay, *J. Nano. Res.* **2022**, *24*, 139. **DOI:**10.1007/s11051-022-05518-z

9. B. Boukoussa, A. Hakiki, N. Bouazizi, A. P. Beltrao-Nunes, F. Launay, A. Pailleret, F. Pillier, A. Bengueddach, R. Hamacha, A. Azzouz, *J. Mol. Struct.* **2019**, *1191*, 175–182. **DOI:**10.1016/j.molstruc.2019.04.035
10. K. Palanichamy, S. Umasankar, S. Ganesh, N. Sasirekha, *Int. J. Hydrogen Energy* **2023**, *48*, 11727–11745. **DOI:**10.1016/j.ijhydene.2022.12.076
11. M. S. R. M. Nasir, M. P. Khairunnisa, N. W. C. Jusoh, A. A. Jalil, *IOP Conf. Ser. Earth Envi. Sci.* **2020**, *476*, 1, 12084. **DOI:**10.1088/1755-1315/476/1/012084
12. H. Hamrayev, S. Korpayev, K. Shameli, *J. Res. Nanosci. Nanotechnol.* **2024**, *12*, 1–24. **DOI:**10.37934/jrnn.12.1.124
13. S. M. Yusof, R. Othaman, H. D. Setiabudi, L. P. Teh, *J. Solid State Chem.* **2021**, *294*. **DOI:**10.1016/j.jssc.2020.121845
14. S. N. Bukhari, C. C. Chong, H. D. Setiabudi, Y. W. Cheng, L. P. Teh, A. A. Jalil, *Chem. Eng. Sci.* **2021**, *229*, 116141. **DOI:**10.1016/j.ces.2020.116141
15. M. S. R. M. Nasir, M. P. Khairunnisa, N. W. C. Jusoh, A. A. Jalil, *IOP Conf. Ser. Mater. Sci. Eng.* **2020**, *808*, 012031. **DOI:**10.1088/1757-899X/808/1/012031
16. M. Safar, B. J. Lin, W. H. Chen, D. Langauer, J. S. Chang, H. Raclavska, A. Pétrissans, P. Rousset, M. Pétrissans, *Appl. Energy* **2019**, *235*, 346–355. **DOI:**10.1016/j.apenergy.2018.10.065
17. Q. Li, H. Zhang, F. Peng, C. Wang, H. Li, L. Xiong, H. Guo, X. Chen, *Energ. Fuel.* **2020**, *4*, 2097–2106. **DOI:**10.1021/acs.energyfuels.9b03997
18. M. Pishnamazi, H. Hafizi, M. Pishnamazi, A. Marjani, S. Shirazian, G. M. Walker, *Sci. Rep.* **2021**, *11*, 535. **DOI:**10.1038/s41598-020-79983-8
19. X. Yan, X. Hu, S. Komarneni, *RSC Adv.* **2014,** *4*, 57501–57504. **DOI:**10.1039/C4RA09626F
20. F. Zarei, A. Marjani, A. Hassani Joshaghani, *J. Environ. Chem. Eng.* **2019**, *7*. **DOI:**10.1016/j.jece.2019.103309
21. C. Diningsih, L. Rohmawati, *Indonesian Phys. Rev.* **2022**, *5*, 208–215. **DOI:**10.29303/ipr.v5i3.174
22. W. Guan, F. Ji, Y. Cheng, Z. Fang, D. Fang, P. Yan, Q. Chen, *J. Nanomater.* **2013**, *2013*, 542109. **DOI:**10.1155/2013/542109
23. A. Maity, V. Polshettiwar, *Chem. Sus. Chem.* **2017**, *10*, 3866–3913. **DOI:**10.1002/cssc.201701076
24. P. Hao, B. Peng, B.Q. Shan, T.Q. Yang, K. Zhang, *Nanoscale Adv.* **2020**, *2*, 1792–1810. **DOI:**10.1039/D0NA00219D
25. A. Maity, A. Das, D. Sen, S. Mazumder, V. Polshettiwar, *Langmuir* **2017**, *33*, 13774–13782. **DOI:**10.1021/acs.langmuir.7b02996
26. A. H. Lahuri, M. A. Yarmo, T. S. Marliza, M. N. Abu Tahari, W. Z. Samad, N. Dzakaria, M. R. Yusop, *Mater. Sci. Forum.* **2017**, pp. 479–484. **DOI:**10.4028/www.scientific.net/MSF.888.479
27. W. N. R.W. Isahak, Z. A. C. Ramli, M. W. Ismail, K. Ismail, R. M. Yusop, M. W. M. Hisham, M. A. Yarmo, *J. CO_2 Util.* **2013**, *2*, 8–15. **DOI:**10.1016/j.jcou.2013.06.002

Povzetek

> Nenehno naraščanje ravni CO_2 v ozračju zaradi industrijskih emisij in izgorevanja fosilnih goriv je povečalo potrebo po učinkovitem zajemanju ogljika. Trdni adsorbenti so priljubljeni zaradi možnosti večkratne uporabe in nizke porabe energije, vendar pogosto naletijo na omejitve v toplotni stabilnosti in adsorpcijski zmogljivosti. Ta študija preučuje učinek sočasnega nalaganja mangana (Mn) s kalijem (K), bakrom (Cu) in kalcijem (Ca) na vlaknasto siliko KCC-1 za zajemanje CO_2 v širokem temperaturnem območju. KCC-1 je bil sintetiziran z metodo mikroemulzije, kovine pa so bile dodane z ultrazvočno impregnacijo s pomočjo površinsko aktivnih snovi. Karakterizacija z uporabo XRD, FTIR, BET, FESEM-EDX in CO_2-TPD je potrdila strukturno celovitost, funkcionalnost površine in adsorpcijsko obnašanje. CaO-MnO@KCC-1 kaže najbolj uravnotežene teksturne lastnosti in najvišjo absorpcijo CO_2 zaradi svoje močne bazičnosti in raznolike moči adsorpcijskih mest. To poudarja njegov potencial kot temperaturno prilagodljiv adsorbent CO_2.

DRUŠTVENE VESTI IN DRUGE AKTIVNOSTI
SOCIETY NEWS, ANNOUNCEMENTS, ACTIVITIES

Vsebina

Contents

Društvene vesti in druge aktivnosti

KOLEDAR VAŽNEJŠIH ZNANSTVENIH SREČANJ S PODROČJA KEMIJE IN KEMIJSKE TEHNOLOGIJE

SCIENTIFIC MEETINGS – CHEMISTRY AND CHEMICAL ENGINEERING

2025

September 2025

25–27 29TH INTERNATIONAL SYMPOSIUM ON SEPARATION SCIENCES (ISSS2025BELGRADE)
Belgrade, Serbia
Information: https://isss2025belgrade.rs/

29–1 GDCh SCIENCE FORUM CHEMISTRY 2025 (SFC 2025)
Karlsruhe, Germany
Information: https://www.gdch.science/

30 5th VIRTUAL CHEMBIOTALKS
Online
Information: https://www.universiteitleiden.nl/en/science/led3/chembiotalks

October 2025

1 UNESCO/IUPAC POSTGRADUATE COURSE IN POLYMER SCIENCE
Prague, Czech Republic
Information: https://www.imc.cas.cz/events/unescoiupac/current-course

6–10 INTERNATIONAL CHEMICAL BIOLOGY SOCIETY/EUROPEAN CHEMICAL BIOLOGY SYMPOSIUM JOINT MEETING (ICBS/ECBS JOINT MEETING)
Paris, France
Information: https://www.eu-openscreen.eu/newsroom/ecbs.html

10–11 10TH SYMPOSIUM OF CHEMISTRY STUDENTS (SiSK)
Zagreb, Croatia
Information: https://sisk.hkd.hr/

18–19 16TH STUDENS' CONGRESS OF SOCIETY OF CHEMISIST AND TECHNOLOGIST OF MACEDONIA
Skopje, Republic of N. Macedonia
Information: https://congress.sctm.mk/event/5/

November 2025

1–6 45TH INTERNATIONAL SYMPOSIUM ON HALOGENATED PERSISTENT ORGANIC POLLUTANTS (POPs)- (Dioxin 2025)
Antalya, Türkiye
Information: https://www.dioxin2025.org/

23–25 25TH EUROPEAN MEETING ON ENVIRONMENTAL CHEMISTRY (EMEC 25)
Chania, Crete
Information: https://www.emec25.tuc.gr/en/home

December 2025

1	ORGANIC CHEMISTRY POSTER SYMPOSIUM 2025 London, United Kingdom
Information:	https://www.rsc.org/events/detail/81676/organic-chemistry-poster-symposium-2025
10–11	WORKSHOP ON Lc-Ms Method Validation and Performance Rome, Italy
Information:	https://www.spettrometriadimassa.org/conference-2025-Methods_Validation_2025
11–12	ReSource 2025: INTERNATIONAL CONFERENCE ON BIOWASTE TRANSFORMATION TO ENERGY & CHEMICALS La Rochelle, France
Information:	https://www.resource-conference.com/

Acta Chimica Slovenica

Author Guidelines

Submissions

Submission to ACSi is made with the implicit understanding that neither the manuscript nor the essence of its content has been published in whole or in part and that it is not being considered for publication elsewhere. All the listed authors should have agreed on the content and the corresponding (submitting) author is responsible for having ensured that this agreement has been reached. The acceptance of an article is based entirely on its scientific merit, as judged by peer review. There are no page charges for publishing articles in ACSi. The authors are asked to read the Author Guidelines carefully to gain an overview and assess if their manuscript is suitable for ACSi.

Additional information

- Citing spectral and analytical data
- Depositing X-ray data

Submission material

Typical submission consists of:

- full manuscript (PDF file, with title, authors, abstract, keywords, figures and tables embedded, and references)
- supplementary files
  - ***Full manuscript*** (original Word file)
  - ***Statement of novelty*** (Word file)
  - ***List of suggested reviewers*** (Word file)
  - ***ZIP file containing graphics*** (figures, illustrations, images, photographs)
  - ***Graphical abstract*** (single graphics file)
  - ***Proposed cover picture*** (optional, single graphics file)
  - ***Appendices*** (optional, Word files, graphics files)

Incomplete or not properly prepared submissions will be rejected.

Submission process

Before submission, authors should go through the checklist at the bottom of the page and prepare for submission.

Submission process consists of 5 steps.

Step 1: Starting the submission

- Choose one of the journal sections.
- Confirm all the requirements of the ***checklist.***
- Additional plain text comments for the editor can be provided in the relevant text field.

Step 2: Upload submission

- Upload full manuscript in the form of a Word file (with title, authors, abstract, keywords, figures and tables embedded, and references).

Step 3: Enter metadata

- First name, last name, contact email and affiliation for all authors, in relevant order, must be provided. Corresponding author has to be selected. Full postal address and phone number of the corresponding author has to be provided.
- ***Title and abstract*** must be provided in plain text.
- Keywords must be provided (max. 6, separated by semicolons).
- Data about contributors and supporting agencies may be entered.
- ***References*** in plain text must be provided in the relevant text filed.

Step 4: Upload supplementary files

- Original Word file (original of the PDF uploaded in the step 2)
- ***List of suggested reviewers*** with at least five reviewers with two recent references from the field of submitted manuscript must be uploaded as a Word file. At the same time, authors should declare (i) that they have no conflict of interest with suggested reviewers and (ii) that suggested reviewers are experts in the field of the submitted manuscript.
- All ***graphics*** have to be uploaded in a single ZIP file. Graphics should be named Figure 1.jpg, Figure 2.eps, etc.
- ***Graphical abstract image*** must be uploaded separately
- ***Proposed cover picture*** (optional) should be uploaded separately.
- Any additional ***appendices*** (optional) to the paper may be uploaded. Appendices may be published as a supplementary material to the paper, if accepted.
- For each uploaded file the author is asked for additional metadata which may be provided. Depending of the type of the file please provide the relevant title (Statement of novelty, List of suggested reviewers, Figures, Graphical abstract, Proposed cover picture, Appendix).

Step 5: Confirmation

- Final confirmation is required.

Article Types

Feature Articles are contributions that are written on Editor's invitation. They should be clear and concise summaries of the author's most recent work written with the broad scope of ACSi in mind. They are intended to be general overviews of the authors' subfield of research but should be written in a way that engages and informs scientists in other areas. They should contain the following (see also general guidelines for article structure below): (1) an introduction that acquaints readers with the authors' research field and outlines the important questions for which answers are being sought; (2) interesting, novel, and recent contributions of the author(s) to the field; and (3) a summary that presents possible future directions. Manuscripts should normally not exceed 40 pages of one column format (font size 12, 33 lines per page). Generally, experts who have made an important contribution to a specific field in recent years will be invited by the Editor to contribute a **Feature Article**. Individuals may, however, send a proposal (of no more than one page) for a **Feature Article** to the Editor-in-Chief for consideration.

Scientific articles should report significant and innovative achievements in chemistry and related sciences and should exhibit a high level of originality. They should have the following structure:

1. Title (max. 150 characters),
2. Authors and affiliations,
3. Abstract (max. 1000 characters),
4. Keywords (max. 6),
5. Introduction,
6. Experimental,
7. Results and Discussion,
8. Conclusions,
9. Acknowledgements,
10. References.

The sections should be arranged in the sequence generally accepted for publications in the respective fields and should be successively numbered.

Short communications generally follow the same order of sections as Scientific articles, but should be short (max. 2500 words) and report a significant aspect of research work meriting separate publication. Editors may decide that a Scientific paper is categorized as a Short Communication if its length is short.

Technical articles report applications of an already described innovation. Typically, technical articles are not based on new experiments.

Preparation of Submissions

Text of the submitted articles must be prepared with Microsoft Word. Normal style set to single column, 1.5 line spacing, and 12 pt Times New Roman font is recommended. Line numbering (continuous, for the whole document) must be enabled to simplify the reviewing process. For any other format, please consult the editor. Articles should be written in English. Correct spelling and grammar are the sole responsibility of the author(s). Papers should be written in a concise and succinct manner. The authors shall respect the ISO 80000 standard [1], and IUPAC Green Book [2] rules on the names and symbols of quantities and units. The Système International d'Unités (SI) must be used for all dimensional quantities.

Graphics (figures, graphs, illustrations, digital images, photographs) should be inserted in the text where appropriate. The captions should be self-explanatory. Lettering should be readable (suggested 8 point Arial font) with equal size in all figures. Use common programs such as MS Excel or similar to prepare figures (graphs) and ChemDraw to prepare structures in their final size. Width of graphs in the manuscript should be 8 cm. Only in special cases (in case of numerous data, visibility issues) graphs can be 17 cm wide. All graphs in the manuscript should be inserted in relevant places and **aligned left**. The same graphs should be provided separately as images of appropriate resolution (see below) and submitted together in a ZIP file (Graphics ZIP). Please do not submit figures as a Word file. In **graphs**, only the graph area determined by both axes should be in the frame, while a frame around the whole graph should be omitted. The graph area should be white. The legend should be inside the graph area. The style of all graphs should be the same. **Figures and illustrations** should be of sufficient quality for the printed version, i.e. 300 dpi minimum. **Digital images and photographs** should be of high quality (minimum 250 dpi resolution). On submission, figures should be of good enough resolution to be assessed by the referees, ideally as JPEGs. High-resolution figures (in JPEG, TIFF, or EPS format) might be required if the paper is accepted for publication.

Tables should be prepared in the Word file of the paper as usual Word tables. The captions should appear above the table and should be self-explanatory.

References should be numbered and ordered sequentially as they appear in the text, likewise methods, tables, figure captions. When cited in the text, reference numbers should be superscripted, following punctuation marks. It is the sole responsibility of authors to cite articles that have been submitted to a journal or were in print at the time of submission to ACSi. Formatting of references to published work should follow the journal style; please also consult a recent issue:

1. J. W. Smith, A. G. White, *Acta Chim. Slov.* **2008**, *55*, 1055–1059.
2. M. F. Kemmere, T. F. Keurentjes, in: S. P. Nunes, K. V. Peinemann (Ed.): Membrane Technology in the Chemical Industry, Wiley-VCH, Weinheim, Germany, **2008**, pp. 229–255.
3. J. Levec, Arrangement and process for oxidizing an aqueous medium, US Patent Number 5,928,521, date of patent July 27, **1999**.
4. L. A. Bursill, J. M. Thomas, in: R. Sersale, C. Collela, R. Aiello (Eds.), Recent Progress Report and Discussions: 5th International Zeolite Conference, Naples, Italy, 1980, Gianini, Naples, **1981**, pp. 25–30.
5. J. Szegezdi, F. Csizmadia, Prediction of dissociation constant using microconstants, http://www. chemaxon.com/conf/Prediction_of_dissociation _constant_using_microco nstants.pdf, (assessed: March 31, 2008)

Titles of journals should be abbreviated according to Chemical Abstracts Service Source Index (CASSI).

Special Notes

- Complete characterization, **including crystal structure**, should be given when the synthesis of new compounds in crystal form is reported.
- Numerical **data should be reported with the number of significant digits corresponding to the magnitude** of experimental uncertainty.
- **The SI system of units and IUPAC recommendations** for nomenclature, symbols and abbreviations should be followed closely. Additionally, the authors should follow the general guidelines when citing spectral and analytical data, and depositing crystallographic data.
- **Characters** should be correctly represented throughout the manuscript: for example, 1 (one) and l (ell), 0 (zero) and O (oh), x (ex), D7 (times sign), B0 (degree sign). Use Symbol font for all Greek letters and mathematical symbols.
- The rules and recommendations of the **IUBMB** and the **International Union of Pure and Applied Chemistry (IUPAC)** should be used for abbreviation of chemical names, nomenclature of chemical compounds, enzyme nomenclature, isotopic compounds, optically active isomers, and spectroscopic data.
- **A conflict of interest** occurs when an individual (author, reviewer, editor) or its organization is in-

volved in multiple interests, one of which could possibly corrupt the motivation for an act in the other. Financial relationships are the most easily identifiable conflicts of interest, while conflicts can occur also as personal relationships, academic competition, etc. **The Editors** will make effort to ensure that conflicts of interest will not compromise the evaluation process; potential editors and reviewers will be asked to exempt themselves from review process when such conflict of interest exists. When the manuscript is submitted for publication, **the authors** are expected to disclose any relationships that might pose potential conflict of interest with respect to results reported in that manuscript. In the Acknowledgement section the source of funding support should be mentioned. The statement of disclosure must be provided as Comments to Editor during the submission process.

- **Published statement of Informed Consent.** Research described in papers submitted to ACSi must adhere to the principles of the Declaration of Helsinki (***http://www.wma.net/e/policy/b3.htm***). These studies must be approved by an appropriate institutional review board or committee, and informed consent must be obtained from subjects. The Methods section of the paper must include: 1) a statement of protocol approval from an institutional review board or committee and 2), a statement that informed consent was obtained from the human subjects or their representatives.
- **Published Statement of Human and Animal Rights.**When reporting experiments on human subjects, authors should indicate whether the procedures followed were in accordance with the ethical standards of the responsible committee on human experimentation (institutional and national) and with the Helsinki Declaration of 1975, as revised in 2008. If doubt exists whether the research was conducted in accordance with the Helsinki Declaration, the authors must explain the rationale for their approach and demonstrate that the institutional review body explicitly approved the doubtful aspects of the study. When reporting experiments on animals, authors should indicate whether the institutional and national guide for the care and use of laboratory animals was followed.
- To avoid conflict of interest between authors and referees we expect that not more than one referee is from the same country as the corresponding author(s), however, not from the same institution.
- Contributions authored by **Slovenian scientists** are evaluated by non-Slovenian referees.
- Papers describing **microwave-assisted reactions** performed in domestic microwave ovens are not considered for publication in *Acta Chimica Slovenica.*
- *Manuscripts that are **not prepared and submitted** in accord with the instructions for authors are not considered for publication.*

Appendices

Authors are encouraged to make use of supporting information for publication, which is supplementary material (appendices) that is submitted at the same time as the manuscript. It is made available on the Journal's web site and is linked to the article in the Journal's Web edition. The use of supporting information is particularly appropriate for presenting additional graphs, spectra, tables and discussion and is more likely to be of interest to specialists than to general readers. When preparing supporting information, authors should keep in mind that the supporting information files will not be edited by the editorial staff. In addition, the files should be not too large (upper limit 10 MB) and should be provided in common widely known file formats to be accessible to readers without difficulty. All files of supplementary materials are loaded separately during the submission process as supplementary files.

Proposed Cover Picture and Graphical Abstract Image

Graphical content: an ideally full-colour illustration of resolution 300 dpi from the manuscript must be proposed with the submission. Graphical abstract pictures are printed in size 6.5 x 4 cm (hence minimal resolution of 770 x 470 pixels). Cover picture is printed in size 11 x 9.5 cm (hence minimal resolution of 1300 x 1130 pixels)

Authors are encouraged to submit illustrations as candidates for the journal Cover Picture*. The illustration must be related to the subject matter of the paper. Usually both proposed cover picture and graphical abstract are the same, but authors may provide different pictures as well.

* The authors will be asked to contribute to the costs of the cover picture production.

Statement of novelty

Statement of novelty is provided in a Word file and submitted as a supplementary file in step 4 of submission process. Authors should in no more than 100 words emphasize the scientific novelty of the presented research. Do not repeat for this purpose the content of your abstract.

List of suggested reviewers

List of suggested reviewers is a Word file submitted as a supplementary file in step 4 of submission process. Authors should propose the names, full affiliation (department, institution, city and country) and e-mail addresses of five potential referees. Field of expertise and at least two references relevant to the scientific field of the submitted manuscript must be provided for each of the suggested reviewers. The referees should be knowledgeable about the subject but have no close connection with any of the authors. In addition, referees should be from institutions other than (and countries other than) those of any of the authors. Authors declare no conflict of interest with suggested reviewers. Authors declare that suggested reviewers are experts in the field of submitted manuscript.

How to Submit

Users registered in the role of author can start submission by choosing USER HOME link on the top of the page, then choosing the role of the Author and follow the relevant link for starting the submission process.

Prior to submission we strongly recommend that you familiarize yourself with the ACSi style by browsing the journal, particularly if you have not submitted to the ACSi before or recently.

Preprints Policy

Acta Chimica Slovenica allows also a submission of manuscripts which have already been made available as a preprint prior to submission to the journal. Authors are encouraged to update any pre-publication versions with a link to the final published article. It is advised that authors don't assign copyright during the preprint process, instead authors should retain copyright on their work when posting to a preprint server. If a DOI is assigned to a preprint, *Acta Chimica Slovenica* will assign a new DOI to the accepted article.

Correspondence

All correspondence with the ACSi editor regarding the paper goes through this web site and emails. Emails are sent and recorded in the web site database. In the correspondence with the editorial office please provide ID number of your manuscript. All emails you receive from the system contain relevant links. **Please do not answer the emails directly but use the embedded links in the emails for carrying out relevant actions.** Alternatively, you can carry out all the actions and correspondence through the online system by logging in and selecting relevant options.

Proofs

Proofs will be dispatched via e-mail and corrections should be returned to the editor by e-mail as quickly as possible, normally within 48 hours of receipt. Typing errors should be corrected; other changes of contents will be treated as new submissions.

Submission Preparation Checklist

As part of the submission process, authors are required to check off their submission's compliance with all of the following items, and submissions may be returned to authors that do not adhere to these guidelines.

1. The submission has not been previously published, nor is it under consideration for publication in any other journal (or an explanation has been provided in Comments to the Editor).
2. All the listed authors have agreed on the content and the corresponding (submitting) author is responsible for having ensured that this agreement has been reached.
3. The submission files are in the correct format: manuscript is created in MS Word but will be **submitted in PDF** (for reviewers) as well as in original MS Word format (as a supplementary file for technical editing); diagrams and graphs are created in Excel and saved in one of the file formats: TIFF, EPS or JPG; illustrations are also saved in one of these formats. The preferred position of graphic files in a document is to embed them close to the place where they are mentioned in the text (See ***Author guidelines*** for details).
4. The manuscript has been examined for spelling and grammar (spell checked).
5. The ***title*** (maximum 150 characters) briefly explains the contents of the manuscript.
6. Full names (first and last) of all authors together with the affiliation address are provided. Name of author(s) denoted as the corresponding author(s), together with their e-mail address, full postal address and telephone/fax numbers are given. Provision of an ORCID ID is optional but highly encouraged.
7. The ***abstract*** states the objective and conclusions of the research concisely in no more than 150 words.
8. Keywords (minimum three, maximum six) are provided.
9. ***Statement of novelty*** (maximum 100 words) clearly explaining new findings reported in the manuscript should be prepared as a separate Word file.
10. The text adheres to the stylistic and bibliographic requirements outlined in the ***Author guidelines***.
11. Text in normal style is set to single column, 1.5 line spacing, and 12 pt. Times New Roman font is recommended. All tables, figures and illustrations have appropriate captions and are placed within the text at the appropriate points.
12. Mathematical and chemical equations are provided in separate lines and numbered (Arabic numbers) consecutively in parenthesis at the end of the line. All equation numbers are (if necessary) appropriately included in the text. Corresponding numbers are checked.
13. Tables, Figures, illustrations, are prepared in correct format and resolution (see ***Author guidelines***).
14. The lettering used in the figures and graphs do not vary greatly in size. The recommended lettering size is 8 point Arial.
15. Separate files for each figure and illustration are prepared. The names (numbers) of the separate files are the same as they appear in the text. All the figure files are packed for uploading in a single ZIP file.
16. Authors have read ***special notes*** and have accordingly prepared their manuscript (if necessary).
17. References in the text and in the References are correctly cited. (see ***Author guidelines***). All references mentioned in the Reference list are cited in the text, and vice versa.
18. Permission has been obtained for use of copyrighted material from other sources (including the Web).
19. The names, full affiliation (department, institution, city and country), e-mail addresses and references of five potential referees from institutions other than (and countries other than) those of any of the authors are prepared in the word file. At least two relevant references (important recent papers with high impact factor, head positions of departments, labs, research groups, etc.) for each suggested reviewer must be provided. Authors declare no conflict of interest with suggested reviewers. Authors declare that suggested reviewers are experts in the field of submitted manuscript.
20. Full-colour illustration or graph from the manuscript is proposed for graphical abstract.
21. ***Appendices*** (if appropriate) as supplementary material are prepared and will be submitted at the same time as the manuscript.

Privacy Statement

The names and email addresses entered in this journal site will be used exclusively for the stated purposes of this journal and will not be made available for any other purpose or to any other party.

ISSN: 1580-3155

Koristni naslovi

Slovensko kemijsko društvo
www.chem-soc.si
e-mail: chem.soc@ki.si

Wessex Institute of Technology
www.wessex.ac.uk

SETAC
www.setac.org

European Water Association
http://www.ewa-online.eu/

European Science Foundation
www.esf.org

European Federation of Chemical Engineering
https://efce.info/

International Union of Pure and Applied Chemistry
https://iupac.org/

Novice europske zveze kemijskih društev EuChemS najdete na:

Brussels News Updates
http://www.euchems.eu/newsletters/

www.nalgesin.si

Hitro opravi z bolečino.

Učinkuje v 15 minutah.(1)

Nalgesin S vsebuje natrijev naproksenat.

Ali ste vedeli, da deluje do **12 ur**?

1. Sevelius H et al. Bioavailability of Naproxen Sodium and Its Relationship to Clinical Analgesic Effects. Br J Clin Pharmacol 1980; 10: 259–63.

KRKA

Pred uporabo natančno preberite navodilo!
O tveganju in neželenih učinkih se posvetujte z zdravnikom ali s farmacevtom.

ActaChimicaSlovenica
ActaChimicaSlovenica

This review highlights the convergence of artificial intelligence, molecular modeling, and bioinformatics in modern drug discovery. By integrating advances in clinical data and structural biology, it provides a comprehensive perspective on innovative therapeutic strategies for the future. See page 581.

Year 2025, Vol. 72, No. 3